Chapter 7: Image Processing and Analysis Methods

Sergio Bernardes
Center for Geospatial Research, Department of Geography, University of Georgia, Athens, GA, USA

Marguerite Madden
Center for Geospatial Research, Department of Geography, University of Georgia, Athens, GA, USA

Contributing Authors:
Ike Astuti
Center for Geospatial Research, Department of Geography, University of Georgia, Athens, GA, USA

Emilio Chuvieco
Environmental Remote Sensing Research Group, Department of Geology, Geography and Environment. Universidad de Alcalá, Spain

David Cotten
Center for Geospatial Research, Department of Geography, University of Georgia, Athens, GA, USA

Philip E. Dennison
Department of Geography, University of Utah, Salt Lake City, UT, USA

Iryna Dronova
Department of Landscape Architecture and Environmental Planning, College of Environmental Design, University of California Berkeley, Berkeley, CA, USA

Ioannis Gitas
Laboratory of Forest Management and Remote Sensing, School of Forestry and Natural Environment, Aristotle University of Thessaloniki, Greece

Peng Gong
Center for Earth System Science, Tsinghua University, Beijing, China

Belen Franch-Gras
University of Maryland, Department of Geographical Sciences, College Park, MD, USA
NASA Goddard Space Flight Center, Greenbelt, MD, USA

Matt Hancher
Google, Mountain View, CA, USA

Akira Hirano
Japan International Research Center for Agricultural Sciences, Tsukuba, Ibaraki, Japan

Allison Howard
Department of Psychology, University of Georgia, Athens, GA, USA
Department of Biology, University of Maryland, College Park, MD, USA

Xuefei Hu
Department of Environmental Health, Rollins School of Public Health, Emory University, Atlanta, GA, USA

Alfredo Huete
University of Technology, Sydney, Sydney, Australia

Thomas Jordan
Center for Geospatial Research, Department of Geography, University of Georgia, Athens, GA, USA

Chris Justice
Department of Geographical Sciences, University of Maryland, College Park, MD, USA

Rick L. Lawrence
Spatial Sciences Center, Montana State University, Bozeman, MT, USA

Linlin Lu
Institute of Remote Sensing and Digital Earth, Chinese Academy of Sciences, Beijing, China

Deepak R. Mishra
Center for Geospatial Research, Department of Geography, University of Georgia, Athens, GA, USA

Sachidananda Mishra
Dow Agrosciences LLC, Indianapolis, IN, USA

Tomoaki Miura
Department of Natural Resources and Environmental Management, University of Hawaii at Manoa, Honolulu, HI, USA

Giorgos Mountrakis
Department of Environmental Resources Engineering, State University of New York College of Environmental Science and Forestry, Syracuse, NY, USA

Mahesh Pal
Department of Civil Engineering, National Institute of Technology, Kurukshetra, Haryana, India

Caren Remillard
Center for Geospatial Research, Department of Geography, University of Georgia, Athens, GA, USA

Dar A. Roberts
Department of Geography, University of California, Santa Barbara, CA, USA

Jean-Claude Roger
Department of Geographical Sciences, University of Maryland, College Park, MD, USA
NASA Goddard Space Flight Center, Greenbelt, MD, USA

Kunwar K. Singh
Center for Geospatial Analytics, North Carolina State University, Raleigh, NC, USA
Department of Forestry & Environmental Resources, North Carolina State University, Raleigh, NC, USA

Ben Somers
Division of Forest, Nature and Landscape, Katholieke Universiteit Leuven, Leuven, Belgium

Dimitris Stavrakoudis
Laboratory of Forest Management and Remote Sensing, School of Forestry and Natural Environment, Aristotle University of Thessaloniki, Greece

Wanxiao Sun
Grand Valley State University, Allendale, MI, USA

Guoqing Sun
Department of Geographical Sciences, University of Maryland, College Park, MD, USA
NASA Goddard Space Flight Center, Biospheric Sciences Lab, Greenbelt, MD, USA

David Thau
Google, Mountain View, CA, USA

Laurent Tits
Flemish Institute for Technological Research (VITO), Remote Sensing Unit, Mol, Belgium

E. Lynn Usery
U.S. Geological Survey, Rolla, MO, USA

Eric Vermote
NASA Goddard Space Flight Center, Greenbelt, MD, USA

Cuizhen Wang
Department of Geography, University of South Carolina, Columbia, SC, USA

Mingshu Wang
Center for Geospatial Research, Department of Geography, University of Georgia, Athens, GA, USA

Qihao Weng
Center for Urban and Environmental Change, Department of Earth and Environmental Systems, Indiana State University, Terre Haute, IN, USA

Wenjing Xu
Center for Geospatial Research, Department of Geography, University of Georgia, Athens, GA, USA

Tian Yao
Universities Space Research Association, Goddard Earth Sciences and Technology Center, NASA Goddard Space Flight Center, Biospheric Sciences Lab, Greenbelt, MD, USA

Hiroki Yoshioka
Aichi Prefectural University, Nagakute, Japan

Lei Zhang
Center for Urban and Environmental Change, Department of Earth and Environmental Systems, Indiana State University, Terre Haute, IN, USA
The State Key Laboratory of Information Engineering in Surveying, Mapping and Remote Sensing, Wuhan University, Wuhan, China

Qingyuan Zhang
Universities Space Research Association, Goddard Earth Sciences and Technology Center, NASA Goddard Space Flight Center, Biospheric Sciences Lab, Greenbelt, MD, USA

Zhi Zhang
School of Public Administration, China University of Geosciences, Wuhan, China

1 INTRODUCTION

Recent developments for acquiring and distributing remotely-sensed data have greatly increased data availability to the user community. The past two decades have witnessed an explosion in data acquisition by a variety of ground, airborne and orbital sensors. The popularization of Unmanned Aerial Systems (UAS) and the development of reduced cost orbital platforms should guarantee that even higher data volumes will be available to future analysts. The past decades also saw the opening of image data archives (e.g., Landsat, CBERS, Sentinel), making access to a rich database of moderate resolution satellite images a reality across the globe. This increased volume and variety of remotely-sensed data increases the demand for methods and procedures for data handling and information extraction. This chapter, *Image Processing and Analysis Methods*, describes recent efforts to expand the analyst's data processing toolset and includes the theory and strategies used in manipulating remotely-sensed data by digital systems. The text focuses on presenting algorithms and techniques for image processing and analysis and emphasizes recent developments not covered by previous editions of the ASPRS Manual of Remote Sensing. Although the main topics covered by the chapter involve the direct processing of images, the text also covers concepts involved in processing remote sensing data that may not have been collected or stored as images, such as spectral curves

acquired by spectroradiometers. Several sections of this chapter match this description, including Spectral Vegetation Indices and Spectral Mixture Analysis. Image processing includes not only the analysis of images, but also the necessary steps involved in preparing images for analysis, such as geometric correction, atmospheric correction and several techniques associated with image enhancement. Spectral indices resulting from the combination of multiple spectral bands are presented, with emphasis on the description of vegetated targets. A detailed treatment is given to the mixture problem resulting from the contribution of multiple materials within the instantaneous field of view (IFOV) of a given sensor. Because multiple applications can benefit from the increased explanation power provided by a large number of spectral bands, hyperspectral data processing is also presented and discussed. Further, the chapter addresses the benefits and challenges involved in combining datasets acquired by different systems (Data Fusion). Image classification addresses multiple strategies involved in assigning classes to images (e.g., Support Vector Machine, and Decision Trees); and includes advances in Object-Based Image Analysis (OBIA), particularly those related to image segmentation in preparation for classification. Given the increasing length of remotely-sensed data time series, particular attention is given to preparing sequences of images and data, including multiple techniques for smoothing, spike removal and the retrieval of metrics associated with temporal variations of targets. The chapter also brings multiple examples of use of products derived from processing remotely-sensed data as input to a variety of workflows, including modeling and analysis efforts. Finally, very current topics involving recent advances in image acquisition and availability, are presented for generating 3D surfaces from multiple images using Structure from Motion (SfM); processing of very large datasets (Big Data); and processing of images in the cloud are presented.

2 GEOMETRIC CORRECTION

2.1 *Introduction*

Remotely-acquired images and data are ubiquitous and traditional aerial- and satellite-based images are now only a part of the data being collected and made available to the public. With expanding use of sensor technology and innovative platforms such as small satellites, unmanned aerial systems, and stationary sensor fields, many new image and data forms are available. Uses of these remotely-sensed data in combination with other data sources, particularly geospatial data in geographic information systems (GIS), require geometric correction to ground coordinate systems. The traditional approach to geometric correction comes from photogrammetry and early satellite image correction systems. These methods of geometric correction include physical and mathematical models. Ground control points (GCPs) are essential to these mathematical models and may also be used with physical models. These basic models are described below and are well documented in current remote sensing textbooks and college courses.

Many factors can affect the characteristics and geometric quality of remotely-acquired data, ultimately defining the ability to identify targets correctly and to measure their physical, chemical or biological properties accurately. Physical models attempt to describe mathematically all the various types of distortion resulting from the platform, sensor, and Earth systems during the data collection process. These distortions include the position, velocity, and orientation of the platform; view angles, IFOV, and panoramic effects of

the sensor; the ellipsoid and relief representations of the Earth; and the cartographic projection (Toutin, 2004).

2.2 *Sources of Geometric Distortion*

Sources of geometric distortion in images can be categorized into observer and observed components (Toutin, 2004). Observer component parts of the image generation system include the platform and sensor. Geometric distortion also results from observed components which include the atmosphere and Earth system, and the cartographic projection (Toutin, 2004). A detailed presentation of different types of distortion is presented in Bernstein (1983).

2.2.1 *Platform*

The platform from which sensor data are acquired contributes to geometric distortion because of departures from the nominal altitude. The orbital period, eccentricity, and the actual inclination of the platform with respect to the Earth's surface also contribute distortion to orientation and shapes in the acquired image data. In addition, velocity variations change line-spacing or create line gaps and overlaps in images.

2.2.2 *Sensor*

Distortions specific to the sensor are a function of sensor characteristics and design, including frame, mode of acquisition (whiskbroom, push broom), and viewing geometry (nadir, fore, aft, and across-track views). The effects of viewing geometry can be particularly relevant in some active systems, such as radar, LiDAR, and sonar. Uncertainty in the calibration of focal length and the IFOV for visual and infrared sensors, and timing for synthetic aperture radar (SAR) are sources of geometric distortion. The attitude of the sensor, including roll, pitch, and yaw; the scan skew for scanning sensors; and the velocity of the platform relative to the area of the Earth being sensed introduce distortion in the final images.

2.2.3 *Earth System*

The Earth system causes distortion in image geometry because of rotation, curvature, and terrain relief. Rotation causes displacements between image lines that are latitude-dependent. Curvature causes variation in pixel spacing and relief creates parallax in the scanner direction (Toutin, 2004).

2.2.4 *Cartographic Projection*

Map projection distortions are approximated to a reference ellipsoid of the geoid and the projection of the reference ellipsoid on a tangent plane. These distortions are well understood and covered amply in the literature (Usery *et al*., 2009). The nature of the "correction" depends upon the ultimate use of the data. For area measurements, one should use an equal area projection, and for shape measurements one should use a projection that preserves the angular relationships of the scene.

2.3 *Correction Models*

2.3.1 *Physical Models*

Many methods exist for correcting distortions and these are often characterized as physical and/or general models (Toutin, 2004; Dave *et al.*, 2015). A physical model can describe all distortions mathematically. These include: the platform's position, velocity, or orientation; the sensor's view angles, IFOV, panoramic effects; the Earth's ellipsoid and relief; and the cartographic projection. Such a model needs both-orbit and sensor information, as well as a small number of GCP's to compute and refine the parameters of the mathematical model.

2.3.2 *General Models*

General models for geometric correction have a long history and were developed with the original Landsat images by the National Aeronautics and Space Administration (NASA) and others (Bernstein, 1983). These models represent a generalized form of the collinearity equations between object space coordinates, *X*,*Y*,*Z* and image space coordinates *x*,*y* as in Equation 7-1.

$$\begin{cases} x - x_0 = -f \frac{m_{00}(X-X_c)+m_{10}(Y-Y_c)+m_{20}(Z-Z_c)}{m_{02}(X-X_c)+m_{12}(Y-Y_c)+m_{22}(Z-Z_c)} \\ y - y_0 = -f \frac{m_{01}(X-X_c)+m_{11}(Y-Y_c)+m_{21}(Z-Z_c)}{m_{02}(X-X_c)+m_{12}(Y-Y_c)+m_{22}(Z-Z_c)} \end{cases} \quad (7\text{-}1)$$

where: X_C, Y_C, Z_C are the spatial coordinates of the perspective center of the sensor at the instant the image was taken; f is the focal length, x_0, y_0 represent the image coordinates of the principal point; and m_{ij} are the elements of an orientation matrix which is determined entirely by three rotation angles (ν, f, k).

The standard model uses two and three dimensional polynomials and is a standard process taught in remote sensing curricula, as shown in Equations 7-2 and 7-3.

$$P_{2d}(X,Y) = \sum_{i=0}^{m} \sum_{j=0}^{n} a_{ij} X^i Y^j \quad (7\text{-}2)$$

$$P_{3d}(X,Y,Z) = \sum_{i=0}^{m} \sum_{j=0}^{n} \sum_{k=0}^{p} a_{ijk} X^i Y^j Z^k \quad (7\text{-}3)$$

In the last 15 years or so, the form of polynomials has shifted to the rational function model (Yang, 1997; Dowman and Dolloff, 2000; Di *et al.*, 2003). The rational functional model uses ratios of polynomials as shown in Equation 7-4 and 7-5 (after Yang, 1997).

$$x_f = \frac{F_1(X_m,Y_m,Z_m)}{F_2(X_m,Y_m,Z_m)} \quad (7\text{-}4)$$

$$y_f = \frac{F_3(X_m,Y_m,Z_m)}{F_4(X_m,Y_m,Z_m)} \quad (7\text{-}5)$$

where: F_i is a polynomial with the following form:

$$F(X,Y,Z) = \sum_{i=0}^{N} \sum_{j=0}^{i} \sum_{k=0}^{j} c_n \times X^{i-j} \times Y^{j-k} \times Z^k \quad (7\text{-}6)$$

where: N is the polynomial order, c_n are coefficients, and the subscript n is determined by:

$n = \frac{i\times(i+1)\times(i+2)}{6} + \frac{j\times(j+1)}{2} + k$. The total number of coefficients for each polynomial is:

$\frac{(N+1)\times(N+2)\times(N+3)}{6}$. For example, when N = 3, Equation 7-6 becomes a 3rd order three-dimensional polynomial with 20 coefficients (Equation 7-7), which is the most common form used by software vendors.

$$F(X,Y,Z) = c_0 + c_1X + c_2Y + c_3Z + c_4X^2 + c_5XY + c_6XZ + c_7Y^2 + c_8YZ + c_9Z^2 + c_{10}X^3 + c_{11}X^2Y + c_{12}X^2Z + c_{13}XY^2 + c_{14}XYZ + c_{15}XZ^2 + c_{16}Y^3 + c_{17}Y^2Z + c_{18}YZ^2 + c_{19}Z^3 \quad (7\text{-}7)$$

The first order rational functions above become the formulation of the direct linear transformation (DLT). The collinearity equations are similar and translatable directly to rational functions if the sensor has a single perspective center, the interior orientation is linear, and the object space is the same as the map coordinate system (Yang, 2000).

Replacement sensor model (Dowman and Dollof, 2000) is a generic term for methods using ratios of polynomial functions that provide a transformation from object space to image space by fitting to a regular spatial grid. There are four approaches to developing this replacement sensor model: polynomials and rational functions as discussed above, grid interpolation methods, and an extended version of the Universal Sensor Model (USM) abstract specification (OGC, 1999). The Rational Functional Model (RFM) is considered to be a generic sensor model (Hu *et al.*, 2004) and, compared to polynomial models, it is more generic and technically applicable to all types of sensors including frame, pushbroom, whiskbroom, and SAR (Tao *et al.*, 2000; Hu and Tao, 2002). Tao and Hu (2001) address the theoretical properties and practical aspects of the RFM and derive both the direct and iterative least squares solutions under terrain independent and terrain dependent scenarios.

2.4 *Application to Data Types for Geometric Corrections*

The RFM has been applied to many different sensors beginning with Space Imaging Inc.'s adoption of the RFM as an alternative sensor model for image exploitation. Tao and Hu (2001); Palsule *et al.* (2004); Singh *et al.* (2008); and Yilmaz *et al.* (2004) applied the RFM successfully to model Cartosat-1 data. Maglione *et al.* (2014) successfully applied RFM to WorldView-2 data in a project to extract coastlines.

2.5 *Conclusions and Outlook*

Geometric corrections of remotely-sensed images are readily available in products from providers, either as corrected images, physical model parameters for the spacecraft and sensor, or as coefficients of rational functions for the simulated model. Users have the alternative to perform geometric correction if needed, and the methods are well documented and available in commercial and open source software. Educational materials on geometric correction for remotely-sensed images are available from universities and other educational institutions on the World Wide Web.

3 TOP OF THE ATMOSPHERE CORRECTION OVER LAND SURFACES

3.1 *Theoretical Background, History and Recent Advances*

Atmospheric effects have a non-negligible impact on Earth observations acquired by polar-orbiting or geosynchronous satellites. Those systems, designed initially to produce "pictures" in the visible solar spectrum of the earth and clouds, have evolved into complex sensing systems capable of acquiring quantitative measurements of the radiation field at several wavelengths, directions, and polarizations, which are the input data for sophisticated inversion algorithms for retrieval of land, ocean and atmosphere physical properties. Specifically, over land and ocean, the process that decouples the signal coming from the surface, and from the atmosphere above it, to obtain "surface reflectance" is called "atmospheric correction" or "atmospheric compensation" to allude to the fact that the process is not perfect.

The difficulty is achieving a high level of accuracy in deriving the surface reflectance, or the reflectance "value as measured by an ideal sensor held at the same view geometry and located just above the Earth's surface assuming an absence of atmosphere". It is impossible to validate reflectance without any assumption/calculation, except on the surface of the moon for example, which has limited value as far as Earth monitoring is concerned. Another problem in the validation is scale. Remotely-sensed observations averaged over several *decameters* or *kilometers* are compared typically to ground-based decimeter radius observations acquired by handheld validation instruments. Even though some sensing systems nowadays have high spatial resolution (≥ one *meter*), the signal measured over the "validation" target is also coming from the surrounding areas up to a fairly large distance at short wavelengths (i.e., the so-called adjacency effect), making it necessary to rely on a model and iterative processes to come to closure on validation.

Atmospheric correction over land, even if imperfect, is needed as input for higher-level surface geophysical parameters, including Vegetation Indices (VIs), Bidirectional Reflectance Distribution Function (BRDF)/Albedo, Leaf Area Index (LAI)/Fraction of Photosynthetically Active Radiation (FPAR), Burned Areas, Land Cover, Thermal Anomalies, and Snow Cover. It is also necessary to use the surface reflectance product in multitemporal or multispectral (MS) image-based applications aimed at detecting and monitoring changes on Earth's surface (e.g., anthropogenic impacts, red-green-blue images).

Rather than discuss all approaches extensively for atmospheric correction in various domains, it is perhaps better to focus on the physically-based approach adapted to continuous near global application instead of episodic local studies. Thus, we present the theoretical basis for modeling the atmospheric effect in the solar spectrum based largely on the Second Simulation of a Satellite Signal in the Solar Spectrum Vector (6SV) code formalism (see Vermote *et al*., 1997), and used practically in solving the problem of large data volume inversion. In the following, we discuss briefly the performances of several radiative transfer codes available to the public, along with their merits and limitations. We then focus on the main challenge of atmospheric correction in the solar Spectrum; namely, the aerosol effect. We present several near-operational approaches for aerosol inversion and discuss their strengths and weaknesses. The next part will be devoted to a detailed error analysis and performance evaluation using the Moderate Resolution Imaging Spectroradiometer (MODIS) surface reflectance product as an example. Finally, we conclude with recommendations for improving land surface reflectance and its validation.

3.2 *Theoretical Basis*

3.2.1 *Simplified Formalism*

The atmospheric "perturbation" of a directional surface reflectance signal depends on the type and characteristics of atmospheric particles interacting with incident solar radiation. Different gas molecules scatter radiation according to Rayleigh's law (i.e., molecular scattering) and absorb it within specific spectral bands whose bandwidths vary among gas species and depend on the vertical atmospheric pressure and temperature profiles. Aerosols are particles with sizes ranging from ~$10^{-3}\mu m$ to ~$20\mu m$ that scatter and absorb radiation in accordance with the Mie and Geometric Optics theories.

In the idealized case of a Lambertian Surface[1] and within narrow spectral bands outside of the main absorption features of water vapor, the top-of-atmosphere (TOA) reflectance can be simulated as Equation 7-8:

$$\rho_{TOA}(\theta_s,\theta_v,\varphi,P,\overbrace{\tau_A,\omega_0,P_A}^{Aer},U_{H_2O},U_{O_3}) = Tg_{OG}(m,P)Tg_{O_3}(m,U_{O_3})\left[\begin{matrix}\rho_{atm}(\theta_s,\theta_v,\varphi,P,Aer,U_{H_2O}) + \\ Tr_{atm}(\theta_s,\theta_v,P,Aer)\frac{\rho_s}{1-S_{atm}(P,Aer)\rho_s}Tg_{H_2O}(m,U_{H_2O})\end{matrix}\right] \quad (7\text{-}8)$$

where: ρ_{TOA} is the reflectance at the TOA; ρ_{atm} is the atmosphere intrinsic reflectance, Tr_{atm} is the total atmosphere transmission (downward and upward); S_{atm} is the atmosphere spherical albedo; and, ρ_s is the surface reflectance to be retrieved by the atmospheric correction procedure;

The geometrical conditions are described by the solar zenith angle θ_s, the view zenith angle θ_v, and the relative azimuth ϕ (or the difference between the solar and view azimuth angles);

P is the pressure that influences the number of molecules and the concentration of absorbing gases in the atmosphere, Tg designates the gaseous transmission by water vapor (Tg_{H_2O}), ozone (Tg_{O_3}), or other gases (Tg_{OG}), U_{H_2O} is the integrated water vapor content, U_{O_3} is the integrated ozone content, and m is the so-called "air-mass" computed as $1/cos(\theta_s)+1/cos(\theta_v)$;

τ_A, ω_0, and P_A describe the aerosol properties and are spectrally dependent: τ_A is the aerosol optical thickness, ω_0 is the aerosol single scattering albedo, and P_A is the aerosol phase function.

The effect of water vapor on intrinsic atmosphere reflectance can be approximated as:

$$\rho_{atm}(\theta_s,\theta_v,\phi,P,Aer,U_{H_2O}) = \rho_R(\theta_s,\theta_v,\phi,P) + \left(\rho_{R+Aer}(\theta_s,\theta_v,\phi,P,Aer) - \rho_R(\theta_s,\theta_v,\phi,P)\right)Tg_{H_2O}(m,\frac{U_{H_2O}}{2}) \quad (7\text{-}9)$$

where: ρ_R represents the reflectance of the atmosphere due to molecular scattering (Rayleigh) and ρ_{R+Aer} represents the reflectance of the mixture of molecules and aerosol particles. Accounting correctly for the mixing and the so-called coupling effect (Deschamps *et al.*, 1983) is important for achieving a high accuracy of atmospheric effect modeling. This approximation conserves the correct computation of the coupling

[1] Accounting for surface BRDF is necessary in a rigorous approach for modeling the so-called surface BRDF-Atmosphere coupling (see Vermote *et al*., 1997), however it represents a second order effect and is expected to introduce only a consistent bias and not to influence an inter-annual variability analysis (see Franch *et al*., 2013).

and assumes that water vapor is mixed with aerosol particles and that molecular scattering is not affected by water vapor absorption.

3.2.2 *Radiative Transfer and Practical Implementation*

In addition to the geometrical conditions, several key parameters are required to perform the forward modeling of the problem (computation of the different terms that describe the atmosphere of Equations 7-8 and 7-9): the aerosol characteristics (optical thickness, size distribution, refractive indices, and vertical distribution[2]), the atmospheric pressure, the ozone amount, and the column integrated water vapor.

Forward modeling is done using the 6SV Radiative Transfer Model (RTM) code. 6SV is an advanced RTM designed to simulate reflection of solar radiation by a coupled atmosphere-surface system, including polarization effects. This code was developed on the basis of its scalar predecessor, 6S, which was the underpinning of the MODIS atmospheric correction algorithm (Vermote *et al.*, 1997). 6SV provides a variety of options to simulate an aerosol atmosphere including a special option to incorporate Aerosol Robotic Network (AERONET) measurements. Ground surface modeling includes simulations of homogeneous and in-homogeneous surfaces with, or without, a directional effect. The code operates on the basis of the Successive Order of Scattering (SOS) method, and accounts for polarization of radiation in the atmosphere by calculating the Q and U components of the Stokes Vector (Lenoble *et al*., 2007). 6SV has been validated extensively since its release by comparison with other commonly used radiative transfer (RT) codes and valuable benchmarks such as Monte Carlo simulations and Coulson's tabulated values (Coulson *et al*., 1960). The code's overall theoretical accuracy is within 1%, which conforms to the standard RT code accuracy requirement (Muldashev *et al*., 1999). The complete validation effort is summarized in two manuscripts (Kotchenova *et al*., 2006; Kotchenova and Vermote, 2007) that are available on the official 6SV Web site (*http://6s.ltdri.org/*).

The 6SV validation effort also demonstrates the importance of using vector code for atmospheric correction. In the majority of modeled cases, ignoring the effects of polarization leads to a large relative error of up to 7.2% for a mixed molecular-aerosol atmosphere in simulated TOA reflectances.

The 6SV is used to build look-up tables for each spectral band where the TOA signals are computed for a reduced set of geometrical conditions: solar zenith from 0.0 to 80.0 degrees by steps of 5 degrees, view zenith from 0.0 to 75.0 degrees by steps of 2.0 degrees, relative azimuth from 0.0 to 180.0 by variables depending on solar and view angle to maintain a maximum difference in scattering angle between two successive geometry of 2.0 degrees.

For each geometric situationy, the signal is computed at 20 discrete values of Aerosol Optical Thickness (AOT) at 550*nm* (from 0. to 5.0), seven levels of atmospheric pressure, and four basic aerosol types.

The gaseous absorptions (Tg_{H_2O}, Tg_{O_3} and Tg_{OG}) are computed separately (see Equations 7-8, 7-9) using a semi-empirical method that depends on air-mass and absorber amounts.

[2] The size distribution is usually assumed (even in AERONET retrieval (Dubovik *et al*., 2000)), although it could have an impact on the accuracy of the forward modeling in specific instances (Dechamps *et al.*, 1983).

3.3 *Aerosol Inversion*

3.3.1 *Method*

In practice, several sources of ancillary data could be used for most atmospheric parameters (e.g., ozone, water vapor, atmospheric pressure) but the most problematical parameter to obtain is the aerosol that needs to be obtained at a suitable temporal (e.g., near-coincident in time) and spatial resolution (on the order of 1*km* or better, if possible) with a reasonable accuracy. Fundamentally, aerosols are concentrated in the lower layers of the atmosphere and their average lifetime is a few days. This is the reason for their high spatial and temporal variability. The most important aerosol characteristic is the optical depth that drives several terms of Equation 7-8 directly, and needs to be estimated from the data themselves. Early efforts, tried to detect dark targets in the image automatically, where the surface reflectance could be approximated to be negligible (e.g., the Case-I ocean color algorithm for atmospheric correction in the near-infrared (NIR) and at longer wavelengths) and the signal observed is the atmospheric intrinsic reflectance, ρ_{atm}, from which the optical depth can be inverted. One problem over land is the difficulty in finding such dark targets reliably. One solution is to use the shorter blue wavelength where most surfaces are dark (e.g., 412*nm*) as is done in the Deep Blue algorithm (Hsu *et al*., 2006), in which case one still must estimate the surface reflectance at 412*nm* and possibly account for directional effects. This usually results from a database derived from carefully selected data (i.e., composite).

Some other methods used on instruments capable of acquiring directional observations, such as the Multi-angle Imaging SpectroRadiometer (MISR) (Diner *et al*., 1998), use the hypothesis that the directional effect from the surface is the same at two different wavelengths (e.g., red and NIR), thereby reducing the number of unknowns in the problem and allowing for inversion of some key aerosol properties (Aerosol Optical Depth (AOD), size range, single scattering albedo.) The performances of the aerosol inversion from MISR have been evaluated extensively over land surfaces (Kahn *et al*., 2010). Roughly, between 50% (dust and hybrid case) and 75% (biomass burning, continental and urban) of the AOD retrievals at 550*nm* are within the 0.05 or 20% x AOD error bars.

The MODIS aerosol group developed the MOD04 algorithm that uses spectral correlation between Shortwave Infrared (SWIR) (2.1μm) and Visible (0.47μm and 0.67μm), once again to reduce the number of unknowns and derive AOD and Angstrom Exponent[3]. Levy *et al*. (2010) provides a very detailed assessment of the performance of the so-called MODIS dark-target aerosol algorithm, overall the 77% of the AOD retrieval is within expected error bars, ± (0.05+0.15 AOD); although one limitation of this algorithm is that over-bright targets such as a desert site (e.g., one of the AERONET locations called Solar Village), the AOD is not retrieved, given the relatively simple form of the basic spectral relation used in the retrieval.

An alternative approach has been under development and validation in the past few years that aims at making the relationship used in the MOD04 retrieval less generic and more variable, both spatially and temporally. Basically, it uses a time series of data instead of a single observation to infer a better estimate of the ratio between SWIR and Visible bands. Some preliminary evaluation of this approach over seven AERONET sites (Lyapustin *et al.*, 2011) shows that Multi-Angle Implementation of Atmospheric

[3] The performance of Angstrom Exponet retrievals over land are marginal and will be removed from future versions of the algorithm (Levy *et al*., 2010).

Correction (MAIAC) and MOD04 have similar accuracy over dark and vegetated surfaces, and that MAIAC generally improves accuracy over brighter surfaces and provides aerosol retrievals over the Solar Village AERONET site (bright desert).

The flexibility of MAIAC has been combined with the simplicity of MOD04, and the availability of MISR retrievals over a variety of surfaces from 2000-2010, to design the MOD09 Collection-6 aerosol retrieval portion of the algorithm (i.e., atmospheric correction over land surfaces). See Vermote and Kotchenova (2008) for the Collection-5 algorithm.

The Collection-5 algorithm uses the red band (670*nm*) and four bands in the blue and SWIR (412*nm*, 443*nm*, 470*nm*, 490*nm* and 2130*nm*) to derive both the AOT and the most suitable aerosol model (chosen from four candidate models) by minimizing the "model residual" computed as:

$$Model\ residual = \frac{\sum_{i=1}^{4}\left(\rho_i^s - r_{i,red}\rho_{red}^s\right)^2}{4} \quad (7\text{-}10)$$

where: ρ^s_{red} is the surface reflectance retrieved at 670*nm* by using the optical thickness derived from 470*nm*, assuming a constant ratio, 0.5, between ρ^s_{red} and ρ^s_{470nm}, and $r_{i,red}$ are empirical spectral coefficient (ratios) between the 412*nm*, 443*nm*, 490*nm*, 2130*nm* bands and the 670*nm* band.

In the Collection-5 algorithm, the ratio between 670*nm* and the other bands are fixed and correspond to values typically observed over vegetation (i.e., 0.4 at 412*nm*, 0.45 at 443*nm*, 0.5 at 470*nm*, 0.54 at 490*nm* and 2.0 at 2130*nm*).

In the Collection-6 algorithm the ratio values are location and time dependent. The time dependence is achieved by allowing the ratios to vary linearly with the Normalized Difference Water Index (NDWI) such as:

$$r = r_{cte} + r_{slope}\, NDWI \quad (7\text{-}11)$$

where: $NDWI = \frac{(\rho_{870nm} - 0.5\rho_{2130nm})}{(\rho_{870nm} + 0.5\rho_{2130nm})}$ (7-12)

The time and location dependence are established by correcting the MODIS Terra TOA data from the Climate Modeling Grid product (i.e., 0.05 degree latitude, longitude resolution) using the available MISR data on a daily basis for 2000 to 2010. An example of the spatial variation of the ratio at 470*nm* is shown in Figure 7-1. Over vegetated areas other than dense forest, the ratio is around 0.5 (i.e., yellow and orange on the color scale), which was the value assumed in Collection-5 over dense forest. In Brazil, central Africa, South East Asia, and Canada, the ratio is higher ~0.8 (i.e., red to dark red); but, since the reflectance is smaller at 670*nm*, the resulting "error" on the aerosol optical depth is not large compared to other sources of error (e.g., aerosol absorption, size distribution etc.). Over arid surfaces like the Sahara, Middle East, Central Australia, and South Africa, the ratio is slightly lower ~0.4-0.3 (i.e., green and blue on the color scale); but, having an accurate ratio over those bright surfaces is particularly important as a small error in the ratio translates to a bigger error on the assumed surface reflectance; and subsequently, on the AOT.

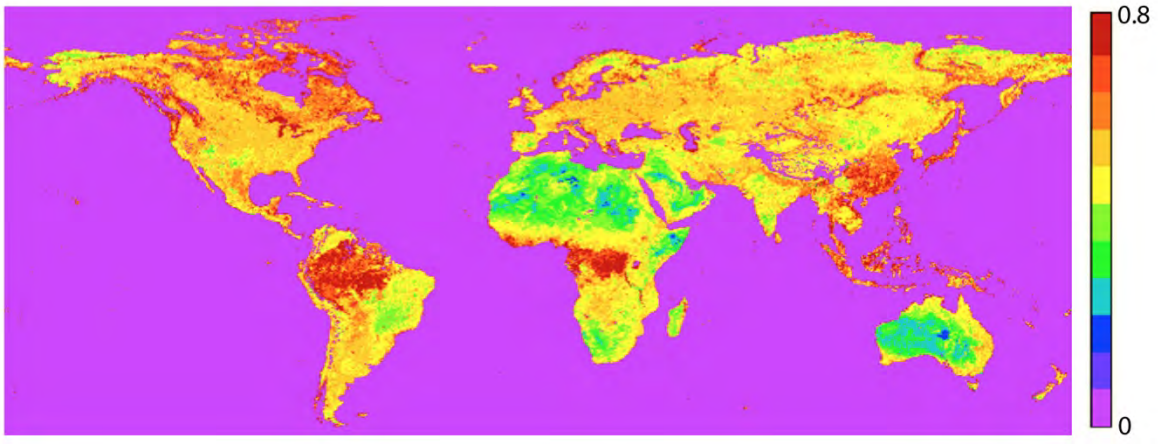

Figure 7-1. Map of the ratio between MODIS Terra band 3 (470*nm*) and band 1 (670*nm*). This is the average ratio observed over a period of 10 years using coincident MODIS/MISR observations and the optical thickness from MISR to perform atmospheric correction.

3.3.2 *Aerosol Optical Depth Validation*

Evaluation of the MODIS Collection-6 aerosol over land was performed over the same sites used by Lyapustin *et al*. (2011). A collection of "dark" and "bright" sites tested the limit of the inversion. Validation was conducted for both Aqua and Terra from 2000 to 2014. The analysis was performed by averaging the aerosol retrievals over a subset of 11×11 pixels centered on the AERONET instrument location. Cloud, snow and water were excluded in the averaging, but no other filtering was done (i.e., MOD04 and MAIAC exclude some of the highest or lowest AOT retrieval before averaging). The results are presented in Figure 7-2 for the East Coast sites (i.e., Goddard Space Flight Center (GSFC), Stennis, Walker Branch and Wallops Island); Figure 7-3 for the West Coast sites (i.e., UCLA and Fresno); and Figure 7-4 for the Solar Village site (i.e., a bright desert site in Saudi Arabia). The results are highly similar both in slope and correlation to those presented in (Lyapustin *et al.*, 2011), and even show better correlation (0.88 versus 0.66) and lower intercept (0.04 versus 0.13) for the Solar Village site that is particularly challenging in terms of aerosol retrieval. It should be noted that MOD04 and MOD09 Collection-5 do not retrieve aerosols over Solar Village. MOD09 Collection-6 shows good performance in aerosol retrieval on a site by site basis based on the correlation observed, although there is a systematic bias in the slope of the relationship over the Lyapustin *et al.* (2011) analysis. This systematic bias could be due to an inadequate choice of the aerosol model used in the inversion that is currently limited to four basic types based on (Dubovik *et al.*, 2002): (1) Urban clean (based on the GSFC site); (2) Urban polluted (based on the Mexico City site); (3) Smoke low absorption (based on Amazonian and Bolivian sites); and, (4) Smoke high absorption (based on the Mongu site in Southern Africa). The results are presented in the next section. To some extent, surface reflectance validations indicate that the bias in optical thickness is partially compensated in the atmospheric correction process, where the same model is used for the inversion and the correction.

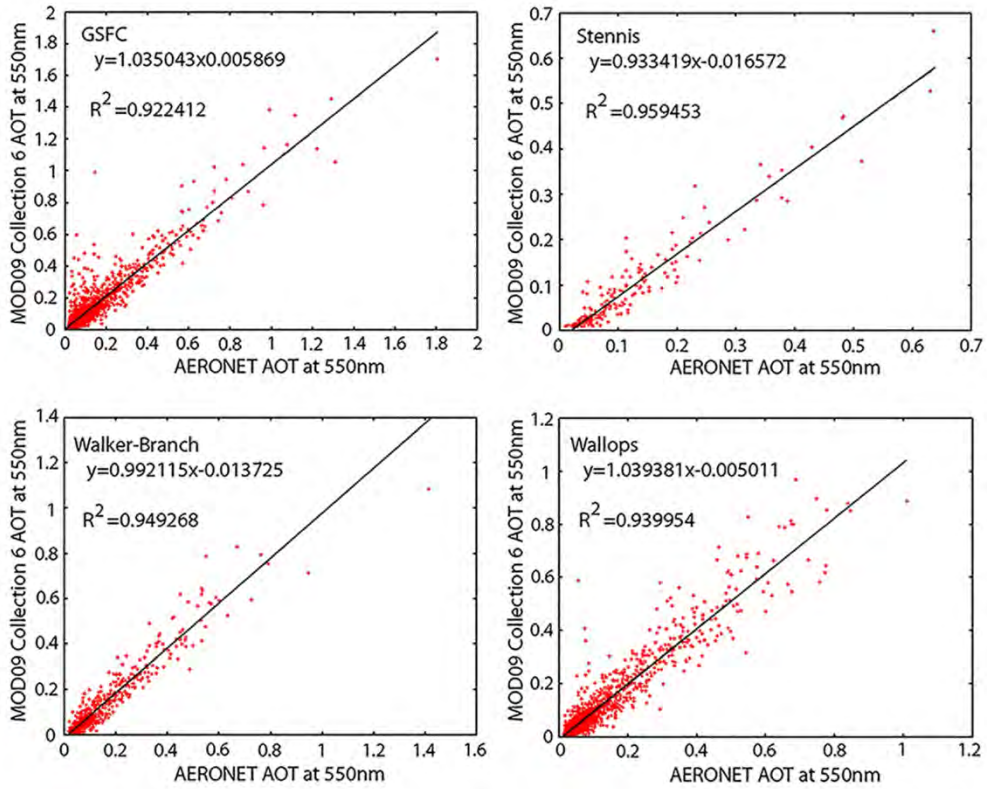

Figure 7-2. Scatterplot of the MOD09 AOT at 550*nm* versus the AERONET measured AOT at 550*nm* for East Coast sites: GSFC (top left), Stennis (top right), Walker Branch (bottom left) and Wallops (bottom right).

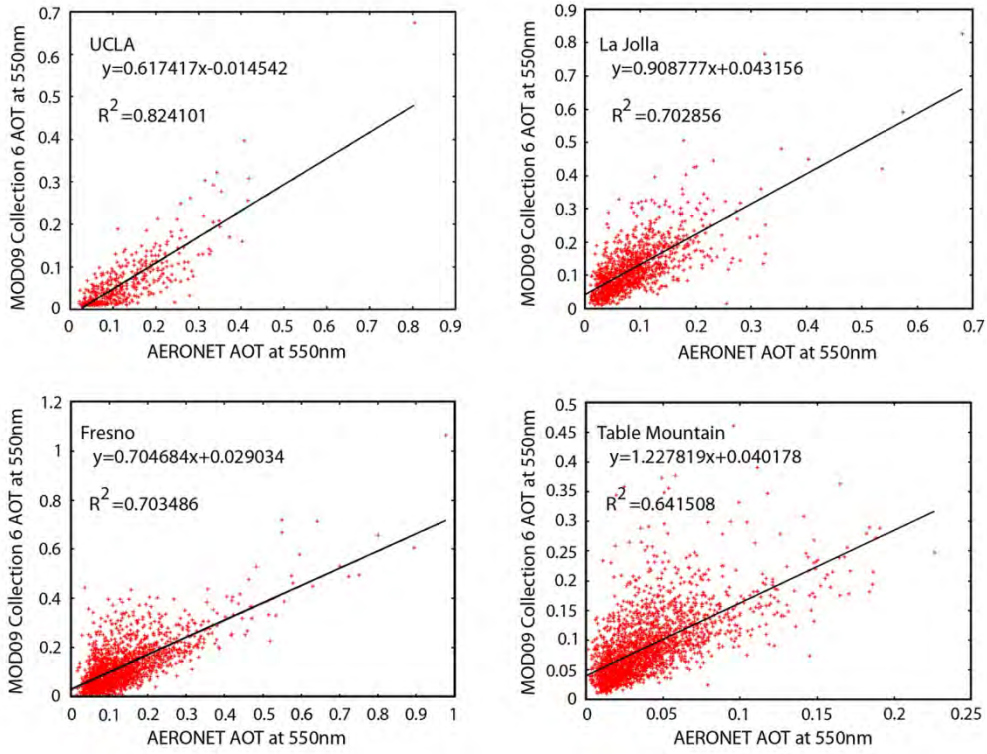

Figure 7-3. Scatterplot of the MOD09 AOT at 550*nm* versus the AERONET measured AOT at 550*nm* for the West Coast sites: UCLA (top left); La Jolla (top right); Fresno (bottom left); and Table Mountain (bottom right).

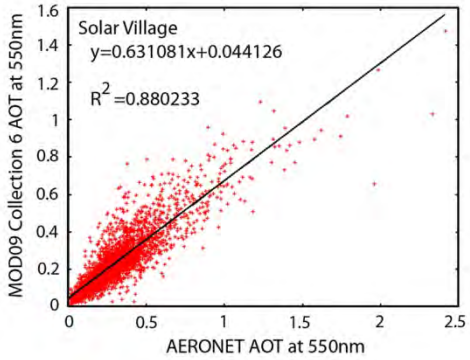

Figure 7-4. Scatterplot of the MOD09 AOT at 550*nm* versus the AERONET measured AOT at 550*nm* for a very bright site in Saudi Arabia (Solar Village).

3.4 *Surface Reflectance Validation*

The direct validation of land surface reflectance is problematical since there are no systematic measurements of the spatial and spectral resolutions that would permit validation of aerosol optical thickness using AERONET. Like many others, an indirect approach using the AERONET data associated with an accurate radiative transfer code is applied to provide a validation proxy. This indirect approach is described in detail in Vermote and Kotchenova (2008) for analyzing the Collection-5 MOD09 product. It relies on a reference dataset created by 6SV using AERONET measurements as input to determine the accuracy, precision, and uncertainty (APU) of the surface reflectance product. The APU were originally defined by the National Polar-Orbiting Operational Environmental Satellite System (NPOESS) project to evaluate a variety of Earth Data Records (EDR) and are computed as follows in Equations 7-13, 7-14, and 7-15:

$$A = \frac{\sum_{i=1}^{N}\left(\mu_i^e - \mu_i^t\right)}{N} \tag{7-13}$$

$$P^2 = \frac{\sum_{i=1}^{N}\left(\mu_i^e - \mu_i^t - A\right)^2}{N-1} \tag{7-14}$$

$$U^2 = \frac{\sum_{i=1}^{N}\left(\mu_i^e - \mu_i^t\right)^2}{N} \tag{7-15}$$

where: in this case, μ^e is the operational surface reflectance of the sensor considered and $\mu^t$is the surface reflectance 'truth'.

Table 7-1 and Figures 7-5, 7-6 and 7-7 present the APU for the MODIS Collection-6 shorter central wavelength bands usable over land: band 4 (550*nm*) and band 1 (645*nm*). The blue bands are excluded from this analysis because they are used in the aerosol inversion, and therefore are meaningless after correction (Vermote and Kotchenova, 2008). The APUs for these bands are almost always within, or better than, specification (magenta line), even for the West Coast and Solar Village sites that had a systematic bias in the AOT retrieval, and that a compensation effect is occurring.

Table 7-1. Performance of MODIS APU Band 4 Surface Reflectances.

Site	Number of Points	Average Truth	Accuracy	Precision	Uncertainty
GSFC	67365	0.07159	-0.00084	0.00417	0.00436
Stennis	7163	0.04853	0.00196	0.00262	0.00331
Walker Branch	15605	0.05723	0.00085	0.00324	0.00350
Wallops	16961	0.06381	-0.00024	0.00336	0.00338
UCLA	8457	0.06844	0.00229	0.00352	0.00464
La Jolla	9766	0.09018	-0.00371	0.00350	0.00529
Fresno	29914	0.10513	-0.00250	0.00482	0.00553
Table Mountain	72679	0.08338	-0.00352	0.00321	0.00478
Solar Village	125952	0.25639	-0.00580	0.00590	0.00860

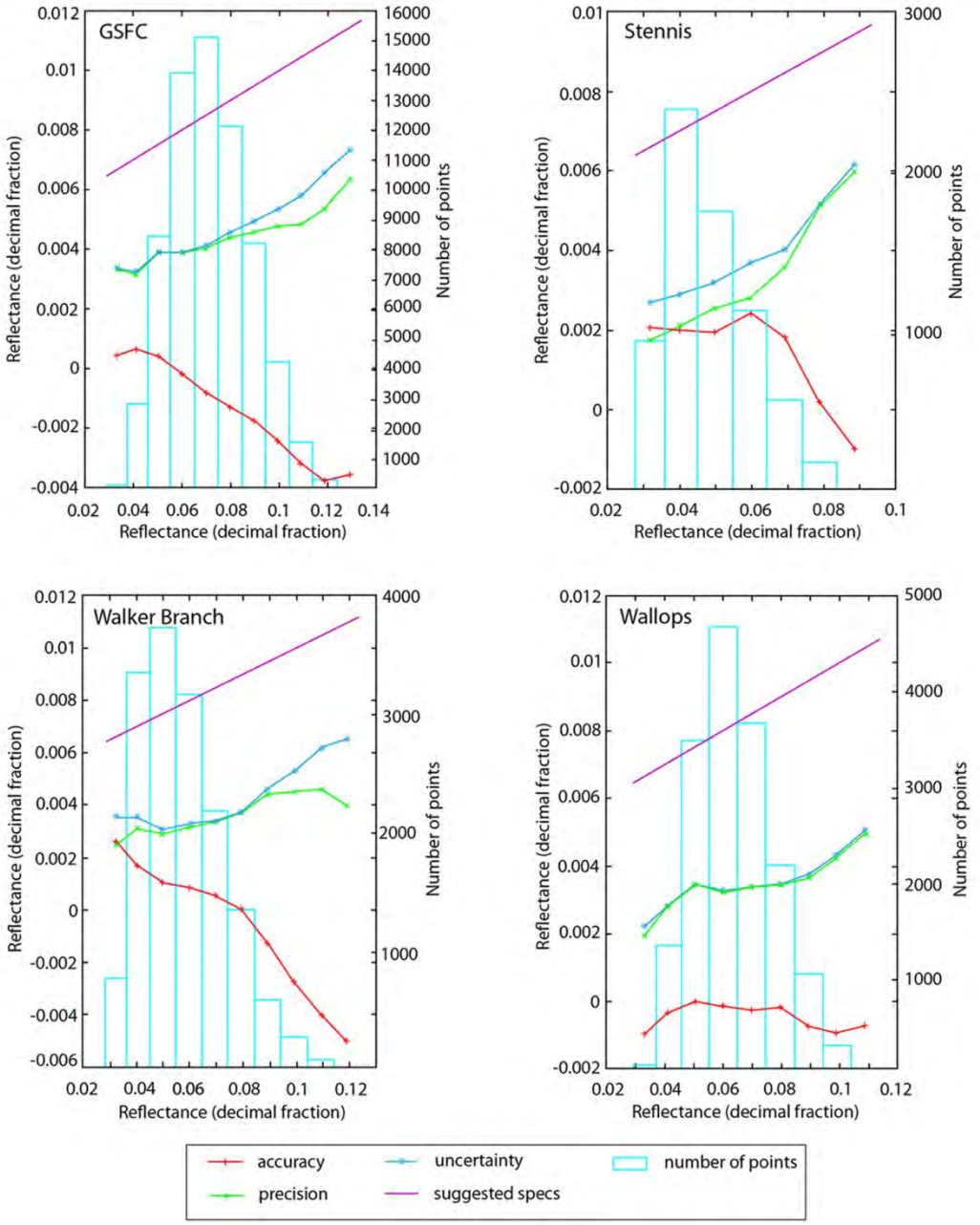

Figure 7-5. APU of the reflectance product for MODIS Terra green band over the East Coast sites: GSFC (top left), Stennis Space Center (top right), Walker Branch (bottom left) and Wallops (bottom right).

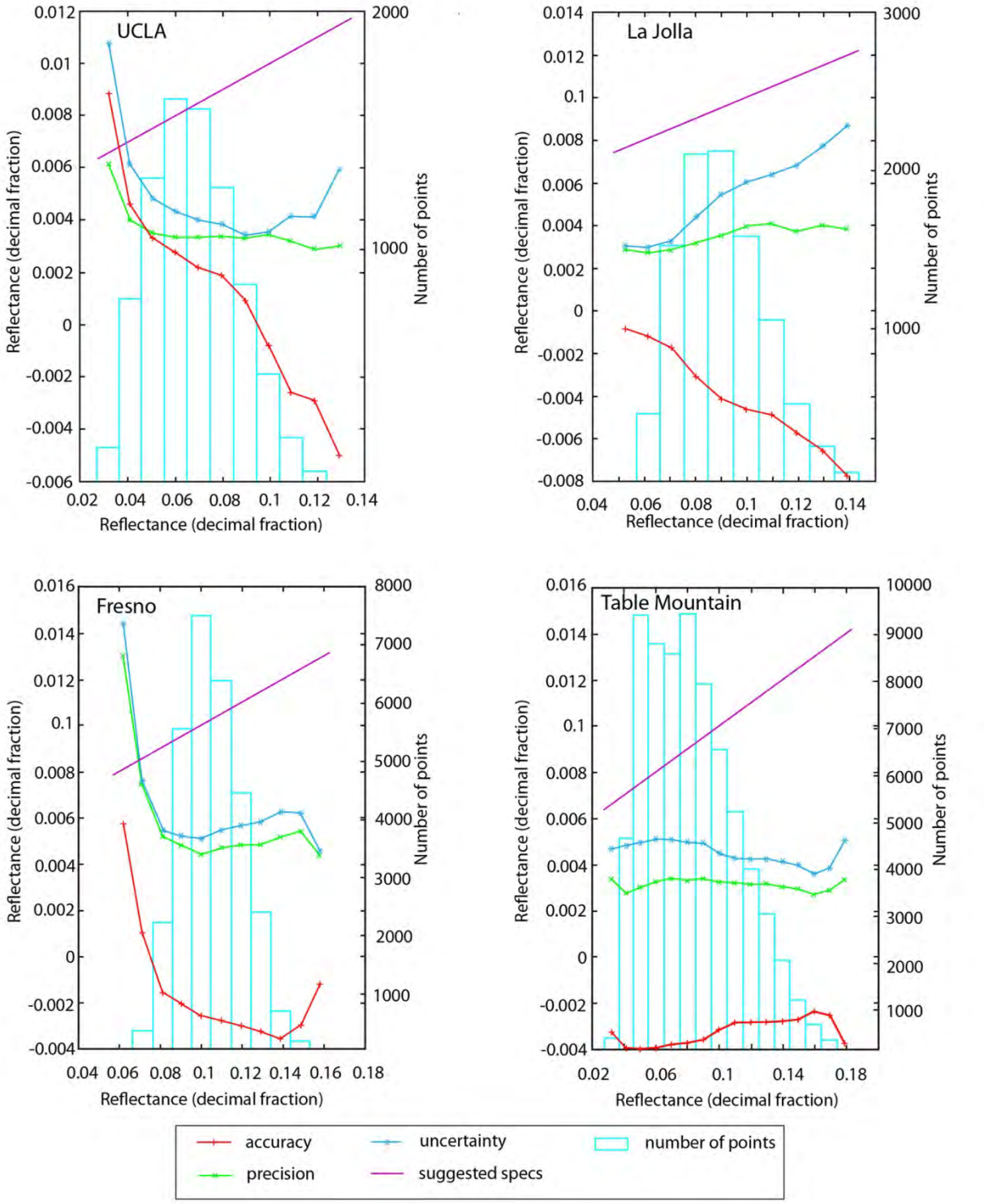

Figure 7-6. APU of the reflectance product for MODIS Terra green band over the West Coast sites: UCLA (top left), La Jolla (top right), and Fresno (bottom left) and Table Mountain (bottom right).

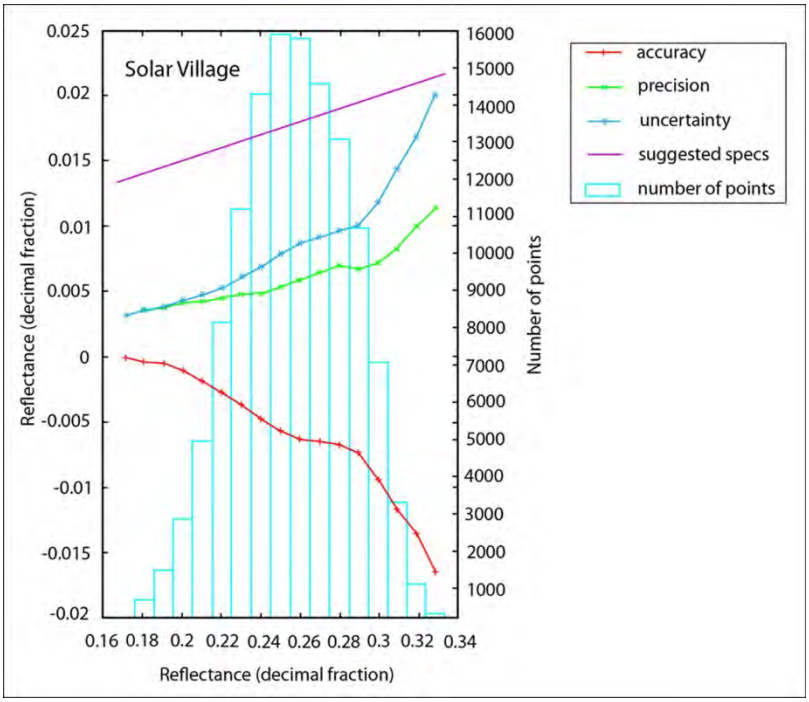

Figure 7-7. APU of the reflectance product for MODIS Terra (green band) for the Solar Village site.

3.5 *Conclusion*

Progress in atmospheric correction over land during the past 20 years has been impressive. Critical to those improvements was launching high quality instruments designed for land observations in the Earth Observing System (EOS) era, among them MODIS and MISR. Equally critical was the availability of systematic, accurate and detailed measurements of aerosols from the AERONET global network, which were developed during the period. Direct validation of surface reflectance is limited by the availability of systematic spectral surface reflectance measurements at the proper spatial scale. The application of the above method currently underway for the Landsat class of sensor of 30*m* or better spatial resolution is a first step toward direct validation, provided that the current surface radiation measurement networks are upgraded with spectral measurements. In the meantime, the "indirect" approach that uses AERONET measurements is a valid alternative for providing a robust statistical assessment of surface reflectance products. However, a detailed protocol for using AERONET needs to be specified to ensure consistency between the surface reflectance products from different approaches and instruments.

4 MULTI-DOMAIN ANALYSIS AND IMAGE TRANSFORMS

4.1 *Fractals*

Fractal-based texture analysis is a relatively novel class of spatial technique that has generated considerable interest in the remote sensing community in the past three decades (Pentland, 1984; De Cola, 1989; Lam, 1990; De Jong and Burrough, 1995; Myint, 2003; Sun, 2006; Sun *et al.*, 2006; Ju and Lam, 2009; Liu *et al*., 2012; Silvetti and Delrieux, 2013; Riccio and Ruello, 2015; Xie *et al*., 2015; Feng *et al.*, 2017).

Fractal techniques are well suited to the analysis of textural features in remotely sensed images, as the environmental features captured in the image are often complex and fragmented (Burrough, 1981; Lorimer *et al*., 1994). A remotely sensed image can be viewed as a hilly terrain surface whose "elevation" is proportional to the image grey level value. Technically, an image can be interpreted as a 3D space where the *x, y* coordinates represent 2D position on the image plane and the *z* coordinate represents the grey level values or digital numbers (DN).

This Section focuses on the state-of-the-art of fractal analysis techniques in remote sensing. First, three key concepts of fractals are introduced, i.e., fractals, fractal dimension, and self-similarity. The section then presents and describes seven commonly used methods for estimating the fractal dimension of remotely sensed imagery. Fractal applications in remote sensing are subsequently presented. Results from empirical studies applying fractal techniques are compared. Directions for future research are also discussed. The section is concluded with a brief discussion of the limitations of the fractal approach.

4.1.1 *Fractals, the Fractal Dimension, and Self-Similarity*

Fractal geometry was introduced and popularized by Mandelbrot (1977, 1982) to model complex natural phenomena as well as other complex objects that classical Euclidean geometry fails to analyze. In Euclidean geometry, dimensions are integers or whole numbers, (e.g., 1 for lines, 2 for areas, and 3 for volumes). These are called topographic dimensions. Topographic dimensions remain constant no matter how irregular a line or an area may be.

In fractal geometry, on the other hand, dimension is treated as a continuum and is called fractal dimension. The fractal dimension, denoted as *D*, is a central construct of fractal geometry. The *D* value can be a non-integer and can be used as an indicator of the complexity of curves and surfaces. For example, a curve's fractal dimension can take on any non-integer value between 1 and 2, depending on the degree of irregularity of its form. The more contorted a line is, the higher its dimension. Similarly, a surface's fractal dimension may be a non-integer value between 2 and 3.

According to Mandelbrot (1977) the term *fractal* comes from the Latin adjective *fractus*, which is also the root for fraction and fragment and means "irregular or fragmented." Formally, a fractal is defined as a set for which the Hausdorff-Besicovitch (or fractal) dimension strictly exceeds the topological dimension (Mandelbrot, 1977). It is called the fractal dimension because it is a fractional (or non-integer) number.

A fundamental characteristic of fractal objects is that their measured metric properties, such as length or area, are a function of the scale of measurement. A classic example to illustrate this property is the "length" of a coastline (Richardson, 1961; Mandelbrot, 1967). When measured at a given spatial scale δ, the total length of a crooked coastline $L(\delta)$ is estimated as a set of N straight-line segments of length δ. Because small details of the coastline (e.g., peninsulas) not recognized at lower spatial resolutions become apparent at higher spatial resolutions, the measured length $L(\delta)$ increases as the scale of measurement δ increases. Mandelbrot (1967, 1977) generalized and expanded on Richardson's (1961) empirical findings and showed that the relationship between length and measuring scale can be described by the power law:

$$L(\delta) = K\delta^{(1-D)} \tag{7-16}$$

where: the exponent D is called the fractal dimension, and K is a constant.

The idea of using *D* to describe irregular shapes is a powerful one, because it captures what is lost in classical geometric representation of form. Figure 7-8 displays three fractal surfaces and their corresponding images representing *D* = 2.1, 2.5, and 2.9. The fractal surfaces are generated using the shear displacement method (Saupe, 1988). A higher fractal dimension value means a more spatially complex surface.

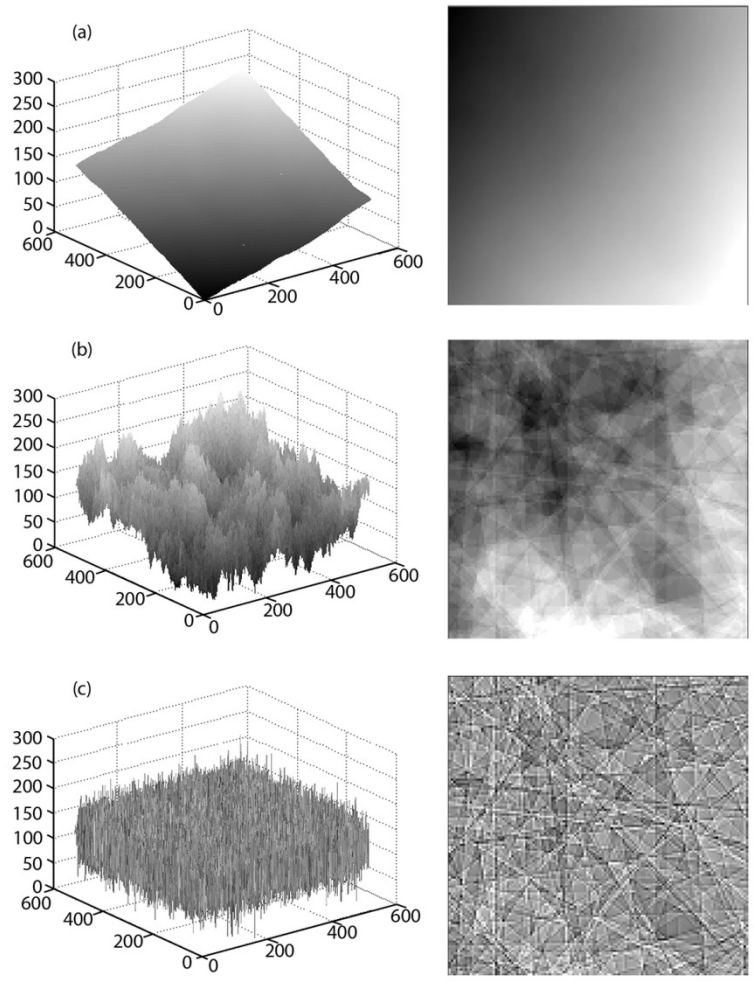

Figure 7-8. Three fractal surfaces and their corresponding images, representing *D* = 2.1 (a), 2.5 (b), and 2.9 (c), generated using the shear displacement method.

Self-similarity is another key concept of fractals. Self-similarity is defined as a property where a subset, when magnified to the size of whole, is indistinguishable from the whole (Mandelbrot, 1977; Voss 1988). The property of self-similarity implies that the form of an object is invariant with respect to scale. In other words, a strictly self-similar object can be thought of as being constructed of an infinite number of copies of itself.

In the geosciences, the property of self-similarity may be better termed scale-independence (Clarke, 1986). The forms of natural phenomena are often erratic as "chance" or random factors often play an important role in their generating processes (Mandelbrot, 1977). As such, unlike mathematical fractals, natural objects generally do not display exact self-similarity. Instead, they may exhibit a certain degree of statistical

self-similarity over a limited range of scales. Statistical self-similarity refers to scale-related repetitions of overall complexity, but not of the exact pattern (Voss, 1988).

Self-similar objects are isotropic (i.e., rotation invariant) upon scaling. If rescaling of an object is anisotropic, then the object is said to be self-affine. Formally, with self-affine fractals the variation in one direction scales differently than the variation in another direction (Mandelbrot, 1985).

Remotely sensing images are not only spectrally and spatially complex, but they often exhibit certain similarities at different spatial scales (Lam and De Cola, 1993a). How to extract the complex and erratic textures in the image and use spatial information to improve image understanding and classification has been a major research issue in remote sensing for decades (Haralick *et al*., 1973; Gong and Howarth, 1990; Gong *et al*., 1992; Tso and Mather, 2009). In this context, fractal geometry is especially appealing because it offers important tools for charactering complex objects and land surface patterns in remotely sensed imagery.

4.1.2 *Methods to Compute Fractal Dimension*

The fractal dimension *D* of strictly self-similar objects can be derived mathematically and is given by (Mandelbrot, 1977):

$$D = \frac{\log(N)}{\log(1/r)} \tag{7-17}$$

where: *N* represents an object of *N* parts scaled down by a ratio of *r*. The *D* derived from Equation 7-17 is called the shape's similarity dimension (Mandelbrot, 1977). Figure 7-9 illustrates the relationship between the number of parts or steps (*N*) and the similarity ration (*1/r*). The *D* value of a curve, such as a coastline, is estimated by measuring the length of the curve using various step sizes.

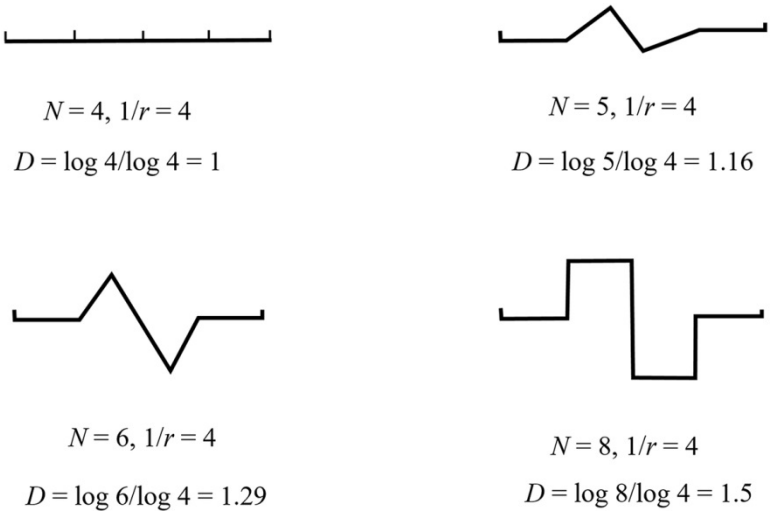

Figure 7-9. Relationships between fractal dimension (*D*), number of steps (*N*), and similarity ratio (1/*r*) (after Lam, 1990).

For non-mathematical objects, however, the fractal dimension cannot be derived analytically. Instead, it must be empirically estimated. A variety of methods have been proposed to compute the fractal (*monofractal*) dimension of natural objects. Sun *et al.* (2006) provide a review of six commonly used methods for estimating the *D* of surface features, such as topographic surfaces and image intensity surfaces. These

methods use some version of the statistical relationship between the measured quantities of an object and step sizes to derive the estimates of *D*. The "quantity" of an object is expressed in terms of, for example, length, area, or number of boxes (cells) needed to cover the object. "Step size" refers to the scale or resolution of measuring units used. The procedure common to most of the methods discussed in this section consists of three steps:

- First, measure the quantities of the object under consideration using various step sizes.
- Second, plot log (measured quantities) versus log (step sizes) and fit a least squares regression line through the data points. The log-log plot is often referred to as the Richardson plot.
- Third, use the slope of the regression line to derive the *D* of the object.

4.1.2.1 The Triangular Prism Method

The triangular prism method was developed by Clarke (1986) primarily to calculate the *D* of topographic surfaces, but it has been applied extensively to remotely sensed images. The method makes use of a raster representation of the elevations of the Earth's surface such as in a digital elevation model (DEM). Based on this data structure, the method takes elevation values or the equivalent of DN values in an image at the corners of squares (i.e., analysis windows), interpolates a center value, divides the square into four triangles, and then computes the top surface areas of the prisms which result from raising the triangles to their given elevations. By repeating this calculation for geometrically increasing square sizes (δ), the relationship between the total upper surface area of the prisms (i.e., the sum of areas *A*, *B*, *C*, and *D* in Figure 7-10) and the spacing of the squares (i.e., step size δ) can be established, and used to estimate *D* (Table 7-2). The only input parameter required in this method is the number of step sizes.

Several modifications have been proposed. Clarke's original algorithm used step size squared (δ^2) in the regression. Lam *et al.* (2002) have shown that step size (δ) instead of step size squared should be used to derive the correct *D*. Sun (2006) has proposed three implementations of the triangular prism method. Sun's methods differ from Clarke's method in the choice of alternative pixels other than corner pixels of the square and the use of actual DN of the central pixel. Sun (2006) shows that the modified triangular prism methods perform better than Clarke's (1986) original method when applied to images with complex textures. Ju and Lam (2009) introduced a new algorithm of the triangular prism method for extending its applications within a local window, called the divisor-step method. It is a sampling strategy and is used to improve the window coverage.

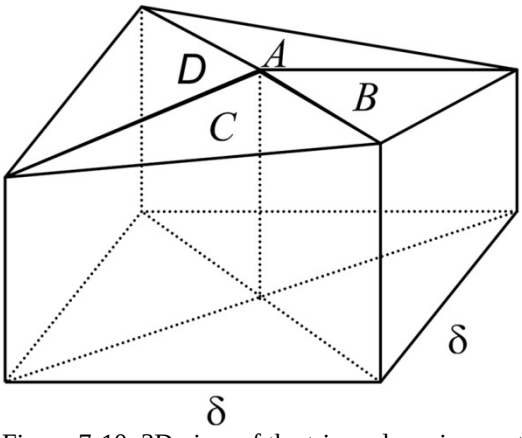

Figure 7-10. 3D view of the triangular prism method (after Clarke, 1986).

Table 7-2. Methods for Computing the Fractal Dimension (D) of Surface Features[a].

Method	Relation used	Basic formula	Estimate of D
Triangular prism	Total area of the tops of prisms vs. side length of analysis windows	$A(\delta) \propto \delta^{2-D}$ $A(\delta)$ = area δ = side length of analysis windows	Plot log $A(\delta)$ versus log (δ), slope is $(2 - D)$ $D = 2 -$ slope
Differential box counting	Number of boxes needed to cover an image vs. box size	$N \propto (1/r)^{-D}$ N = number of boxes $r = s/M$ s = side length of boxes M = side length of the image	Plot log N versus log $(1/r)$, Slope is $-D$ $D =$ -slope
Isarithm	Length of contour line vs. step size	$L(\delta) \propto \delta^{1-Dcontour}$ $L(\delta)$ = length of contour line (i.e., number of boundary cells) δ = step size	For each contour line, plot log $L(\delta)$ versus log (δ), slope is $(1 - D_{contour})$ D = average of all $D_{contour} + 1$
Variogram	Mean squared elevation (or DN) difference vs. distance	$E[(Z_p - Z_q)^2] \propto (d_{pq})^{2H}$ Z_p, Z_q = elevations or DNs at points p and q d_{pq} = distance between p and q	Plot log $E[(Z_p - Z_q)^2]$ versus log (d_{pq}) slope is $2H$ $D = 3 - H = 3 -$ slope/2
Robust fractal estimator	Length of profile vs. step size	$L(\delta) \propto \delta^{1-Dprofile}$ $L(\delta)$ = length of profile δ = step size	For each cell, take the average of $D_{profile}$ in both EW and NS directions D obtained by combining fractal dimensions of each cell using a weighted average and adding 1
Hurst coefficient	Greatest difference in brightness within a neighborhood vs. distance	$E[(BV_b - BV_d)] \propto (d_{pc})^H$ BV_b, BV_d = DNs of brightest and darkest pixels b and d d_{pc} = distance between pixel p and the center c of the neighborhood	Plot log $E[(BV_b - BV_d)]$ versus log (d_{pc}) Slope is H $D = 3 - H$
Power spectrum	Fourier power spectral density vs. the frequency	$P(f) \propto f^{-(5 - 2Dprofile)}$ $P(f)$ = the power f = the frequency	Plot log $P(f)$ versus log (f), slope is $-(5 - 2D_{profile})$ $D = D_{profile} + 1$

[a] $D_{contour}$ = fractal dimension of a contour line; $D_{profile}$ = fractal dimension of a profile. For references see section 4.1.2.

4.1.2.2 The Differential Box-Counting Method

The differential box-counting (DBC) method was proposed by Sarkar and Chaudhuri (1992) to compute the D of digital images. This method can be thought of as a variant of the well-known box-counting approach (Goodchild, 1980; Voss, 1988). In the DBC, N in Equation (7-17) is counted in the following manner. If an image of size $M \times M$ pixels is scaled down to a size $s \times s$, where $M/2 \geq s > 1$ and s is an integer, then we have a ratio of $r = s/M$. Consider the image as a 3D space with (x, y) denoting the image plane and (z) denoting the grey level. The (x, y) space is partitioned into grids of size $s \times s$. On each grid there is a column of boxes of size $s \times s \times s'$. If G denotes the grey level range of the image (e.g., 256), s' is calculated by $[G/s'] = [M/s]$. This ensures that the grey level range G is also scaled down by a ratio of r. Let the minimum and maximum grey level of the image in $(i,j)^{th}$ grid fall in box number z_{min} and z_{max}, respectively.

Then $n\ (i,j) = z_{max} - z_{min} + 1$ is the contribution of N in $(i, j)^{th}$ grid. Taking contributions from all grids, we have:

$$N = \sum_{i,j} n(i,j) \tag{7-18}$$

For different values of r, that is, different values of s or step sizes, the quantity of N is counted. D is then computed from the least-squares linear fit of log (N) versus log ($1/r$) (Table 7-2). In a sense, the DBC method makes a digital approximation of thickness of the blanket that covers the image intensity surface at a particular resolution.

4.1.2.3 The Isarithm Method

The isarithm method (Shelberg *et al*., 1983) is based on the premise that the complexity of isarithm or contour lines may be used to approximate the complexity of a surface. It is based on the widely accepted walking-divider method for calculating the fractal dimension of line features (Klinkenberg, 1992). The method starts with a matrix of *z*-elevations (i.e., DN values), an isarithm interval is selected and isarithm lines are constructed on the surface. For each isarithm line, its lengths are calculated in terms of the number of boundary cells over a number of step sizes, log (number of boundary cells) is regressed against log (step size), and the slope of the regression line is used to derive the D of the isarithm line. This process is repeated for every isarithm line. The surface's D is obtained by averaging the D values of all the isarithm lines that have $R^2 \geq 0.9$ and adding one (1) (Table 7-2). Three input parameters must be specified by the user: 1) the number of step sizes; 2) the isarithm interval; and 3) the direction in which the computation is implemented (row, column, or both).

4.1.2.4 The Variogram Method

In this method, the mean of the squared elevation (or DN) difference (i.e., variance) is calculated for different distances, and D is estimated from the slope (b) of the regression between the logarithms of variance and distance (see Figure 7-11) so that $D=3 - b/2$ (Mark and Aronson, 1984; see also Table 7-2). Variations of the variogram method exist. Roy *et al*. (1987), for example, calculated D using four different implementations of the variogram method. The variogram method is based on the assumption that the surface being analyzed is a fractional Brownian surface. However, studies have shown that natural phenomena are not truly fractal (Mark and Aronson, 1984; Roy *et al*. 1987). Another issue that requires attention in variogram analysis is the sampling strategy used to determine the point pairs (Klinkenberg, 1994; Roy *et al*. 1987). The method is computationally intensive.

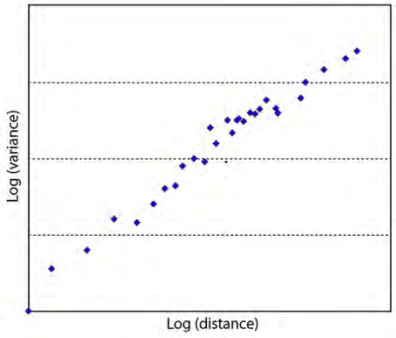

Figure 7-11. The log (variance) versus log (distance) plot used in the variogram method.

4.1.2.5 The Robust Fractal Estimator

The robust fractal estimator was proposed by Clarke and Schweizer (1991) in an attempt to provide stability in the computation of *D*. Using the walking-divider method, the robust fractal estimator computes for each cell the *D* of each profile in both the east-west and north-south directions and places the average of the two in a new array. The *D* of the entire surface is obtained by combining the *D* values of each cell using a weighted average and adding one (1). Clarke and Schweizer (1991) noted that the method is primarily designed to calculate *D* for natural surfaces using data from United States Geological Survey (USGS) DEMs, but it should work equally well on any gridded surface data.

4.1.2.6 The Hurst Coefficient

A particularly efficient method for computing the fractal dimension of surfaces (e.g., elevation images) is the Hurst coefficient, or rescaled range analysis (Hurst *et al*., 1965; Feder, 1988; Russ, 1990). Hurst coefficient computation technique has been used for various segmentation applications. Originally applied to time-series data, the Hurst coefficient was expanded by Russ (1990) to estimate fractal dimensions of two-dimensional images.

Russ (1990) described how two-dimensional circular filters were used for computing the Hurst coefficient. The algorithm examines the pixels in the neighborhood (window) around each pixel location in the original image, with a radius (distance) typically from 5 to 10 pixels. For each window, the distance of each pixel from the center of the window is calculated and is put in distance classes. The number of pixels at each distance within the window is also counted. The brightest and darkest pixel values in each of the distance classes are found, and their differences are used to construct a Hurst plot. Performing a least-squares fit for the log (brightness difference) versus log (distance) relationship, determines a slope of the regression line. The slope is the Hurst coefficient. It is directly related to fractal dimension *D: D* = 3 – *H* (Russ, 1993).

An enhanced method to estimate the Hurst coefficient in surfaces was proposed by Silvetti and Delrieux (2013), where a quadratic self-correlation coefficient is evaluated. In this method, the determination of brightness variation takes into account all pairs of pixels in each distance class within the window, not just those involving the central pixel. Silvetti and Delrieux (2013) introduced a method, called the normalized integral fit, an alternative to the least squares fit. This method is used to overcome the inherent instabilities that the least squares fit might introduce (Russ, 1993, 2017). The normalized integral fit performs a weighted average of localized brightness variation exerting more influence at smaller distances.

4.1.2.7 The Fourier Power Spectrum Method

Another technique for computing the *D* of surface features is the use of Fourier analysis. The Fourier method uses the power spectrum derived from the surface (Pentland, 1984; Burrough, 1981). It can be shown that the Fourier power spectrum, *P(f)*, of a fractional Brownian function (*f*) is proportional to $f^{(-2h-1)}$, where $h=2 - D_{profile}$ (Pentland, 1984). The fractal dimension of the profile ($D_{profile}$) is obtained from the slope of the regression line of the log-log plot of *P(f)* versus *f*. The *D* of the surface is computed as $D=D_{profile} + 1$ (Table 7-2). Detailed descriptions of the steps required to perform a spectral analysis for fractal applications can be found in Peitgen and Saupe (1988) and Turcotte (1992). Spectral methods should

only be applied to self-affine curves (i.e., profiles) since they will always return a $D=1$ for self-similar curves (Peitgen and Saupe, 1988).

4.1.3 *Applications of Fractal Techniques to Remote Sensing Image Analysis*

A main application of fractal techniques to remotely sensed imagery is to measure the roughness or texture complexity of land surface features. This section focuses on the use of computed *D* in four major application areas: 1) to characterize the overall spatial complexity of an image, 2) to supply image classification with textual information, 3) to describe the geometric complexity of the shape of feature classes in a classified image, and 4) to examine the scaling behavior of environmental phenomena.

4.1.3.1 Using *D* to Characterize the Overall Spatial Complexity of Remotely Sensed Imagery

The use of *D* to characterize the overall textural complexity of remotely sensed imagery is perhaps the most obvious utility of fractal models in image analysis (Lam, 1990; Qiu *et al.*, 1999; Read and Lam, 2002). Only a single *D* is computed for the entire image. Such a global *D* can be calculated for remotely sensed data of different land cover types, sensor, and bands. This type of application is attractive because global *D* values can be computed without the need to first classify the image.

Lam (1990), for example, used the isarithm method to measure the spatial complexity of three Landsat Thematic Mapper (TM) images representing three different land cover types in coastal Louisiana. Results showed that the estimated *D* values of three TM surfaces were generally higher than those of most real-world terrain surfaces. Among the three land cover types, the highest *D* occurred in an urban area, followed by a complex coastal area, and a rural area. The work also compared the *D* values of the three land cover types across seven spectral bands and found that the *D* values of the same land cover type turn out to be quite different in different bands. The urban landscape has its highest *D* values occurring in bands 2 and 3, whereas the coastal and rural areas both exhibit high *D* values in band 1.

In an analysis of two Airborne Visible/Infrared Imaging Spectrometer (AVIRIS) images of the Los Angeles area, Qiu *et al.* (1999) found that the computed *D* values for urban landscapes were higher than those for rural landscapes. The authors confirmed Lam's (1990) finding that the estimated *D* values of the same land cover type varied significantly across bands. The work by Qiu *et al*. (1999) shows that textures of land cover types may be better characterized by certain band(s) than by others. As such, identifying the bands in which the contrast in computed *D* between different land cover types is most distinct may be a necessary step when working with MS images.

A global *D* has been considered useful when incorporated into image metadata, or when employed as a tool for data mining and change detection (Jaggi *et al*., 1993; Lam *et al*., 2002). In addition, *D* can be used as an initial screening tool for examining information contained within different spectral bands. Variations in *D* values across bands may be used as a guide for identifying noisy bands or for selecting bands for image classification (Lam, 1990; Qiu *et al*., 1999).

4.1.3.2 Use of *D* as a Texture Measure to Segment and Classify Images

Several investigations have applied fractal techniques to describe image textures and segment various types of images (Pentland, 1984; Keller *et al*., 1989; De Jong and Burrough, 1995; Myint, 2003; Zhou and Lam, 2005; Sun *et al*., 2005; Sun, 2006; Ju and Lam, 2009; Silvetti and Delrieux, 2013). These works

consider that local variations in computed *D* can be used as texture measures and that different land cover types may have characteristic textures or roughness that could be described by different *D* values. Ideally, if there were a one-to-one relation between the texture of a land cover type and a unique *D* value, then the *D* could be viewed as the "fractal signature" of that land cover type and used to exact it from the image. Pentland (1984) considered the image intensity surface as a fractal Brownian function (fBf) and estimated *D* from Fourier power spectrum of fBf. The work successfully segmented several types of images using computed *D* values.

De Jong and Burrough (1995) proposed a so-called "local *D* algorithm," a method that can be thought of as a local implementation of the triangular prism concept (Clarke, 1986). In the "local *D* algorithm," a kernel (window) of 9 by 9 pixels is moved over the image and, at each position of the kernel, a *D* is computed within the kernel, resulting in a new image file containing the estimated local *D* values. This new layer of *D* values was then used as texture measures in the classification procedure. The "local *D* algorithm" was applied to the classification of six Mediterranean vegetation types in two remotely sensed images. The results seem somewhat mixed. While the "local *D* algorithm" appeared effective in separating five of the six land cover types in a Landsat TM image, the method could not sharply distinguish between any of the six land cover types in an airborne Geophysical Environmental Research Imaging Spectrometer (GERIS) image. This result was explained by the poor quality of the GERIS image and authors concluded that, although local *D* values for TM imagery seemed to reflect different land cover types, *D* values by themselves were insufficient for the classification of TM images.

In a study comparing the discriminatory power of several texture analysis methods, Myint (2003) found that the computed *D* values for the same image vary with the computational method and spectral band used. The work concluded that fractal-based textual discrimination methods are applicable, but these methods alone may be ineffective in identifying different land cover types in remotely sensed images.

Ju and Lam (2009) compared the accuracy and robustness of three sampling methods. In that study, a set of small simulated surfaces with 16 sizes ranging from 9 x 9 to 69 x 69 pixels were generated. These window sizes were selected because this series cover most windows used in the previous image classification or segmentation research related to local fractal measurements (De Jong and Burrough, 1995; Emerson *et al*., 2005; Myint and Lam, 2005). For each window size, 50 surfaces were generated for each of the five theoretical fractal dimensions (i.e., 2.1, 2.3, 2.5, 2.7, and 2.9). The divisor-step algorithm (Ju and Lam, 2009) was tested using 4,000 simulated surfaces and an IKONOS subset, and is found to be more robust and accurate than the geometric-step and arithmetic-step sampling algorithms (Quattrochi *et al*., 1997; Lam *et al*., 1998; Emerson *et al*., 2005).

Silvetti and Delrieux (2013) reported that the quadratic self-correlation coefficient gives more precise local fractal estimations than the Hurst coefficient (linear self-correlation method), but at the expense of a higher computation cost. They compared four methods, that is, quadratic self-correlation with least squares fit, quadratic self-correlation with normalized integral fit, linear self-correlation, and divisor step, in term of precision, accuracy, and invariance properties both with synthetic and real remote sensing images using different window sizes (e.g., 3, 5, 7, 9, and 11). The work demonstrated how the normalized integral fit and least squares fit make quadratic self-correlation a robust tool which allows for both precise and accurate local fractal estimations.

4.1.3.3 Fractal Characterization of Classified Image Features

Fractal analysis can be of descriptive value when investigating the spatial complexity of classified image features. Lovejoy (1982), for example, analyzed the perimeter - area relationship of rain and cloud areas identified from satellite and radar images. Results showed that the degree of contortion of the perimeter of cloud regions could be described by D=1.35 over a range of cloud sizes.

De Cola (1989) used the perimeter-area relationship to describe the shape of regions of eight land cover classes extracted from a Landsat TM image of north-west Vermont. The work associated land cover types with D values (e.g., forests had high D and large regions, while agriculture activities had large regions with D inversely related to the intensity of cultivation, and urban land use yielded small regions with relatively high D). Fractal descriptions of those land cover types were then used as input to GIS. Results demonstrated how the analysis of individual land cover regions can be used to investigate the location and description of individual regions and to check the reliability of classification.

Finally, fractal description of classified image features can provide useful descriptive statistics for characterizing the aggregate feature classes. In this context, knowledge about the characteristic D values of different feature classes may be valuable in understanding the processes that generate the phenomena under consideration (Lovejoy, 1982).

4.1.3.4 Scaling Characteristics of Remotely Sensed Images

Fractal models have been used to study the scaling behavior of geographic features and the knowledge generated by this type of research may be valuable for determining the optimum resolution of pixels used in remote sensing (Goodchild, 1980; Lovejoy, 1982; Mark and Aronson, 1984; Goodchild and Mark, 1987; Emerson *et al*., 1999; Lam *et al*., 2002; Sun and Southworth, 2013; Feng *et al.*, 2017).

Emerson *et al*. (1999) examined the effect of changing pixel size on the computed D values of Normalized Difference Vegetation Index (NDVI) images of two study areas. In the example of Huntsville Alabama, it was found that the estimated D values of NDVI images of agriculture, forest, and urban areas responded differently to aggregation. The image of the agriculture area grew more complex as the pixel size was increased from 10m to 80m, while the D value of forested area grew slightly smoother and the complexity of urban area remained approximately the same. The analysis of the image data of the East Humboldt Range in Nevada showed a more complex relation between pixel size and D, and this relation changes between seasons.

Feng *et al.* (2017) proposed to use spatial resolution as the modified scale parameter to calculate the fractal dimension D. The work analyzed the relationship among fractal dimension, spatial resolution, and the size of geo-object in remotely sensed imagery. Results showed that it is possible to choose feature scales to best characterize the specific objects or phenomena under consideration. The analysis indicates that feature scales are related to the actual sizes of the geo-object. With high spatial resolution image data, such as QuickBird, the optimal observation scale is no longer equivalent to the actual size of the geo-object. On the contrary, the actual size of the geo-object may be a multiple of the optimal observation scale (i.e., spatial resolution or pixel size). These results suggest that the modified fractal methods appear effective in capturing the pixel-based scale effect existing in remotely sensed data.

4.1.4 *Discussion*

4.1.4.1 Performance of Various Computational Methods

The utility of *D* as a texture measure depends to a large extent on the reliability of computational methods. Seven computational methods have been introduced and most of them have their theoretical and/or practical limitations. Generally, the triangular prism method is the most accurate for images having higher spatial complexity and is less computationally intensive than other methods, such as the variogram or Fourier power spectrum methods (Clarke, 1986; Lam *et al*., 2002; Ju and Lam, 2009). Sarkar and Chaudhuri (1992) have shown that the DBC method is both accurate and computationally efficient. Despite this, the method has not been widely applied to remote sensing problems (Tso and Mather, 2009). Shelberg *et al.* (1983) pointed out that the isarithm method can be used to estimate the *D* for non-self-similar surfaces and it is one of the most often used methods in the field (Lam, 1990; Lam and De Cola, 1993b, Qiu *et al.*, 1999, Emerson *et al.*, 1999, Lam *et al.*, 2002).

Klinkenberg and Goodchild (1992) found that the variogram method produced consistent estimates of *D* when applied to topographic data. Clarke and Schweizer (1991), on the other hand, reported that for the same dataset, the variogram method yielded consistently higher *D* values than those obtained from the triangular prism method and the robust fractal estimator. Lam *et al.* (2002) suggested that the variogram method was a comparatively poor estimator for all the simulated surfaces in their study. Clarke and Schweizer (1991) reported that the robust fractal estimator consistently yielded a lower *D* value than those obtained from the triangular prism and variogram methods. Further, several investigations have pointed out that the power spectrum method involves sophisticated data preprocessing and is computationally complex (Fox and Hayes, 1985; Clarke, 1986).

4.1.4.2 Factors Influencing Computed *D* Values

Remotely sensed images with different textural characteristics are expected to have different *D* values. However, differences in image texture are not the only factor influencing the computed *D* values. Many studies have reported that different fractal computational methods often yield significantly different *D* values for the same feature and/or same dataset (Roy *et al.*, 1987; Lam, 1990; Clarke and Schweizer, 1991; Klinkenberg and Goodchild, 1992; De Jong and Burrough, 1995; Lam *et al*., 2002; Myint, 2003; Sun *et al.*, 2006).

Several factors may be responsible for the differences in estimated *D* using different methods (Klinkenberg, 1994). First, fractal methods are not all measuring the same fractal quantity. For example, the isarithm method measures the length of isarithm lines, while the triangular prism methods measure the area of triangles, and the DBC method the number of boxes. Second, fractal methods may be inappropriately applied. For example, the robust fractal estimator can only be applied to self-affine data (Clarke and Schweizer, 1991). Violation of this requirement could lead to erroneous results.

Third, the choice of input parameter values may also affect the resulting *D* values. This means that the selection of the smallest and largest step sizes and the interval spacing is critical as these parameters may affect the slope of the regression line and hence the computed *D*. However, there are no established guidelines for choosing the beginning or ending step size. Shelberg *et al.* (1982) proposed to use one-half of the average distance between every pair of adjacent points as the smallest step size. In practice, the smallest

step size is often chosen to be close to the limiting resolution of the datasets used (Clarke and Schweizer, 1991). Several investigations have suggested using a reduced largest step size. It is widely accepted that for statistical reasons, step size should increase as a power of two (i.e., geometric step).

The divisor-step algorithm proposed by Ju and Lam (2009) utilizes the entire window fully and computes the number of steps according to the window size (*W* is an odd number). The step size should be a divisor of (*W*-1). Using a set of divisor steps of (*W*-1) will guarantee 100% coverage of the entire window at all steps. For example, in an 11 x 11 window, there are four steps and step sizes are 1, 2, 5, and 10.

It should be noted that local *D* values provide meaningful results only for image portions larger than the smallest step size used. In other words, texture variations at scales smaller than the smallest step size will be overlooked in fractal analysis. This is often referred to as the blurring effect. How to choose an "appropriate" window size and how to deal with the boundary effect, as well as the blurring effect, are two important issues that deserve attention in computing local *D* values.

4.1.4.3 Are Remotely Sensed Images Fractal?

The self-similarity property underlying the fractal model predicts that for truly fractal surfaces, the computed *D* should be constant at all scales, at all locations, and in all directions. Numerous studies have shown that the estimated *D* values of most natural phenomena are unstable with respect to scale, location, and/or orientation (Mark and Aronson, 1984; Roy *et al*., 1987; Klinkenberg and Goodchild, 1992; Burrough, 1993). The consensus is that, as far as natural phenomena are concerned, self-similarity is exhibited only in a statistical sense and such statistical self-similarity, when present, is exhibited only in limited regions and over limited ranges of scale (Goodchild and Mark, 1987; Milne, 1991).

Are remotely sensed images fractal? Most research published to date has suggested that real remotely sensed images are not true fractals and that the estimated *D* is stable only over limited ranges of scale. A number of studies have found that the estimated *D* of real remotely sensed images vary with the resolution of the image used and the region and direction in which *D* was computed (Lam, 1990; De Jong and Burrough, 1995; Emerson *et al*., 1999; Lam *et al*., 2002; Sun *et al*., 2006). De Jong and Burrough (1995) suggested that most remotely sensed images are not strictly self-similar; instead, they may be at most only statistically self-similar over a limited range of pixel sizes. The observation that most remotely sensed images may not be even statistically self-similar brings up an important issue, that is, does it make sense to use *D* to describe image textures? Some researchers argued that lack of self-similarity is not a limitation to the fractal technique, and it could be simply seen as a method for extracting information from the Richardson plot (Orford and Whalley, 1983; Kennedy and Lin, 1986; Normant and Tricot, 1993). There is still considerable uncertainty regarding to what extent remotely sensed images are statistically self-similar. More research is clearly needed in this area.

De Jong and Burrough's (1995) demonstrated how to locally compute the *D* of real remotely sensed images. Few studies have attempted to systematically calculate local *D* values and use such information to classify real images. How to develop efficient algorithms to compute local *D* values from real images and use local *D* values as information to improve image classification is an area that holds great potential for future research.

4.1.5 *Conclusions*

Fractal geometry provides a useful tool for charactering textural features in remotely sensed images because most of what we measure in remote sensing – boundaries of land covers, patched of landscapes, rivers and water bodies, tree crowns, etc. – is discontinuous, complex, and fragmented. Fractal techniques have been applied to measure the "roughness" or geometric complexity of land surface features in unclassified and classified images. Quantitative information about local variations in estimated *D* values has been used as a texture measure to segment and classify remotely sensed images. Fractal techniques have also been used to investigate the scaling behavior of environmental phenomena and the results from this stream of research may prove valuable for choosing "optimal" resolutions for the study of environmental phenomena at different scales in remote sensing and GIS.

Despite the potential utility of fractal techniques, several methodological and practical measurement issues have been encountered. For example, the computed *D* is supposed to capture the differences in the characteristic of image textures. However, a host of factors other than image texture, such as the computational method used, the choice of input parameter values, input images, and so forth, may all have an effect on the computed *D*. Research has shown that significant variations in computed *D* can be introduced by computational methods. Therefore, the choice of method is an important issue.

A major drawback in fractal techniques is that they can be applied only to single bands. It appears desirable to develop what may be called "multivariate fractal methods". Such multivariate fractal methods should enable the analysis of all bands together and would represent a tremendous improvement to the existing methods. Existing fractal techniques rest mostly on the assumption that image textures can be described by a single (i.e., monofractal) dimension. Evidence suggests that the structures underlying most natural phenomena are most likely multifractals. Further research is needed to determine whether multifractal models could do a better job in characterizing image textures.

While fractal dimension appears able to capture certain aspects (i.e., geometric complexity of the shape) of the surface properties of remotely sensed images, use of *D* alone cannot sufficiently describe image textures and achieve satisfactory classification results. Other factors such as the size and distribution of a textural feature and its spatial relations to other features may also play an important part in differentiating one type of texture from another. It appears that the utility of *D* may be explored to a fuller extent when it is used in conjunction with other texture measures and perhaps spectral classification approaches as well.

4.2 *Domain Transforms and Analyses Using Fourier and Wavelets*

4.2.1 *Introduction*

Remotely-sensed data can be processed and analyzed considering multiple data representation domains (e.g., spatial, temporal, frequency). Analyses in the spatial domain are widely used in remote sensing and image processing and have traditionally employed multiple forms of convolution and digital filtering to enhance or reduce feature contrast, to delineate boundaries and to manipulate signals with low or high spatial variability, among multiple other applications. Some of these approaches have been successfully applied in analyses involving the temporal domain (e.g., smoothing of time series of satellite images for spike removal).

An alternative way of representing and characterizing datasets in remote sensing draws from signal processing and the analysis of harmonic series, and uses amplitude oscillations, including their frequencies, to represent the variability of targets or phenomena over space and time. These analyses consider that data acquired by remote sensors can be described and represented by variations in DNs or brightness values, such as high or low frequency of change (i.e., oscillations) and sudden changes in values (i.e., transients). In two-dimensional analyses, for instance, smooth regions in images indicate reduced variation in brightness, while boundaries or sharp transitions represent abrupt changes.

The ability to explain the spatiotemporal variability in signal oscillations and shap changes in brightness using the frequency domain is a powerful tool in image processing and two related analytical approaches (e.g., Fourier and Wavelets) have found multiple applications in remote sensing. Section 3.2 addresses the frequency domain in data analysis and introduces those two approaches. Examples of applications are presented and include noise removal, image fusion, data compression and time series analysis.

4.2.2 *Fourier*

Fourier transforms and analyses, including the linear decomposition of spatial or time signal into sine and cosine components, have found multiple applications in a variety of fields, including remote sensing. The analysis is based on the ability to explain spatiotemporal variability of data series by using infinity bound sinusoids at different frequencies and phases and the transformation of signals (e.g., images or other remotely-sensed data) from the spatial or time domain into the frequency domain. This section presents an overview of techniques involved in Fourier analysis. For a more mathematical and in-depth review on the topic the reader is directed to a variety of texts exploring Fourier and Fourier Transforms, including Brigham (1988) and Bloomfield (2000).

Among other applications, Fourier-based transformations of remotely-sensed images from spatial to frequency domains have been used for noise removal, image matching and registration, and in support of pattern/feature recognition (e.g., Chen *et al.*, 1994; Fattahi *et al.*, 2009; Zacharov and Toutin, 2012; Varghese *et al.*, 2016). Using the frequency domain, specific frequencies in the original data can be identified and individually analyzed and processed (e.g., frequencies characteristic of noise can be removed). An inverse transformation can then be used to convert the frequency domain image back to the spatial domain. Figure 7-12 exemplifies this workflow and shows the results of multi-step image processing involving: 1) a forward Fast Fourier Transform (FFT) to transform an image to the frequency domain; 2) the computation of a power spectrum to identify a threshold to filter out noise; 3) the application of a Hanning mask to the FFT image; and 4) the use of an inverse FFT to transform the image back to the spatial domain. Processing involved adding noise to the original image (Figures 7-12a and 7-12b). A shifted FFT is presented in Figure 7-12c. Figure 7-12d shows reduced noise following filtering using a Hanning filter and the transformation of results back to spatial domain. Figure 7-12e to 7-12j illustrate the use of Fourier analysis to reduce regular noise added to Figure 7-12e. Figure 7-12f shows the shifted FFT transform for the original image. Figures 7-12g and 7-12h show the representation of horizontal lines in the spatial and frequency domains. Figure 7-12i has the frequency of horizontal lines identified and masked out. Figure 7-12j shows results from the transformation of the frequency domain image back to the spatial domain.

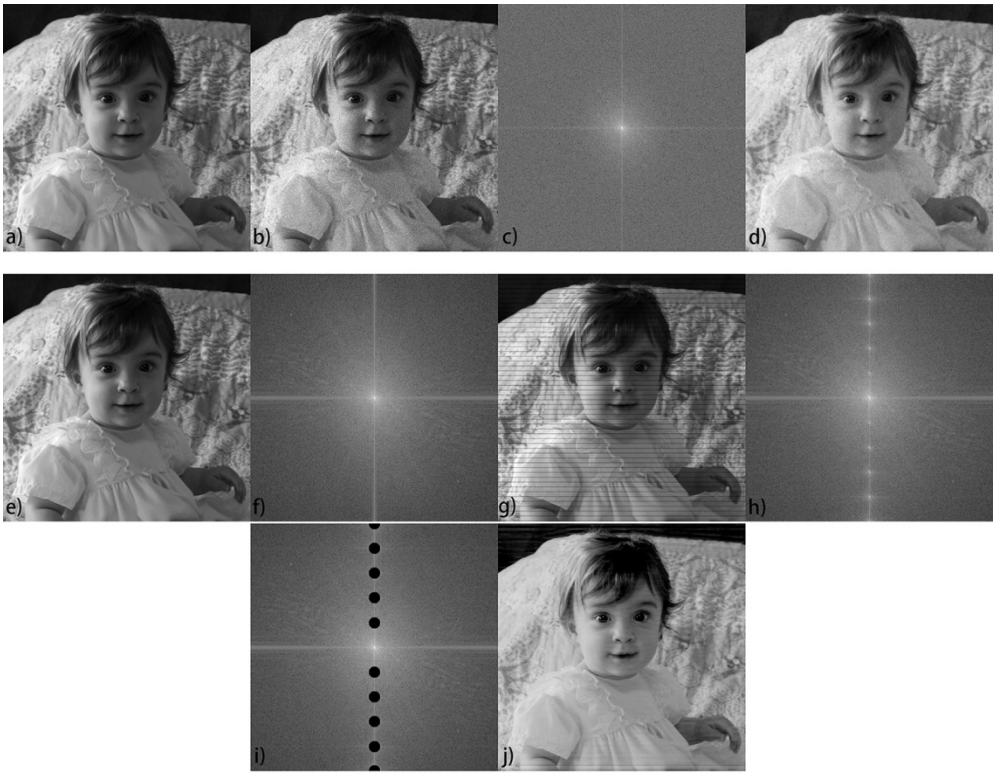

Figure 7-12(a-j). Noise removal using forward FFT image filtering and inverse FFT (see text for description of images).

Figure 7-13(a,b,c) illustrates a one-dimensional analysis and decomposition of a time series of sinusoid signals into two frequencies of different amplitudes. Figure 7-13a shows the combined signal, which is analogous to a temporal cross-section of digital values for a given single pixel and multiple dates showing two seasonality patterns. The components of the time signal are decomposed into individual frequencies (Figure 7-13b). Figure 7-13c shows the results of an FFT analysis of the signal and resulting plot indicating frequencies (50 *Hz* and 200 *Hz*) and amplitudes (1 and 1.5) for the data.

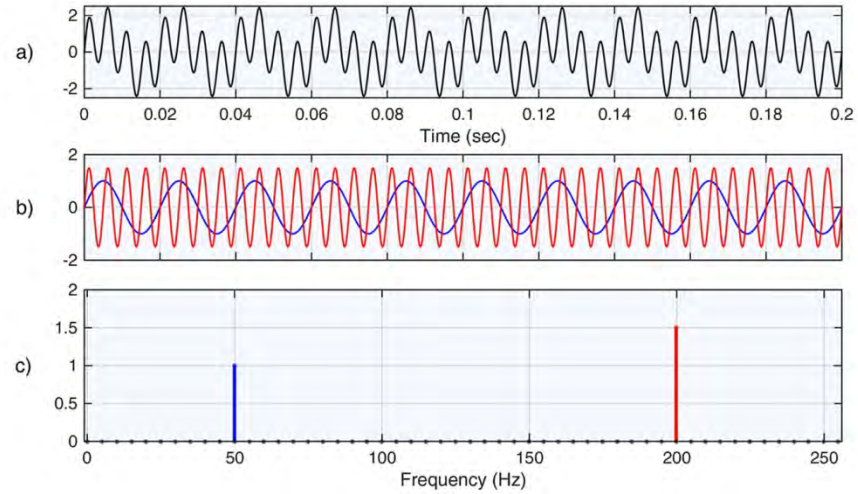

Figure 7-13 a, b, c. One-dimensional representation of time signal decomposition by sinusoids: (a) original time series; (b) decomposition of time series into two frequencies; and (c) representation of the original time series (time domain data) in the frequency domain indicating frequencies and amplitudes of the original data.

Harmonic analysis of time series through the decomposition of the time signal has been used to investigate spatio-temporal variations in seasonalities and plant phenology using a variety of remotely sensed data and over large spatial domains (e.g., Jakubauskas *et al.*, 2001; Wagenseil and Samimi, 2006; White *et al.*, 2009). For instance, White *et al.* (2009) used a 1982-2006 time series of NDVI data derived from Advanced Very High Recolution Radiometer (AVHRR) and multiple approaches, including the Harmonic Analyses of NDVI Time-Series – Fast Fourier Transform (HANTS-FFT), to derive spring phenology in North America. The work fitted multiple frequencies to the NDVI time series and coefficients from the FFT were then used to generate a daily NDVI series and to derive a start of the season metric. The approach can be extended to the decomposition of time series into sets of images of amplitude and phase and the identification of periodic components from the vegetation signal to identify specific phenological patterns and to map vegetation-soil-climate complexes (Azzali and Menenti, 2000). Other applications of Fourier in time series analysis include time series reconstruction by denoising and gap filling (e.g., Roerink *et al.*, 2000; Zhou *et al.*, 2016).

Limitations to the use of the frequency domain by Fourier analysis include the loss of localization associated with the technique. Fourier transforms present limitations also when regions of steep variability (i.e., abrupt changes in space or time) need to be characterized. In its original form, sum of sine and cosines that extend to infinity reduce the efficiency of representing abrupt changes in signals or images. Variations of the Fourier transform, including the Short-Time Fourier Transform (STFT) address some of these limitations. Some of these solutions, however, provide localization in space or time, at the cost of reducing the frequency resolution. The next section introduces an alternative approach to frequency domain characterization based on wavelets.

4.2.3 *Wavelets*

Wavelets bring advantages over the use of sines-cosines by Fourier analysis, as wavelets are defined by finite intervals or duration and have spatial or frequency localization. Spatio-frequency localization including temporal localization when processing time series, is critical in determining abrupt changes in the data series over the dimension of analysis and is key for the characterization of sharp changes in data values and edge detection. Wavelet analysis can be based on one or more "mother wavelets", which represent oscillations starting at zero amplitude, reaching a maximum/minimum and then reaching zero amplitude again. A variety of wavelet configurations has been proposed to address data variability (Figure 7-14). The approach provides flexibility to define functions represented by infinite series of wavelets and/or different mother wavelets.

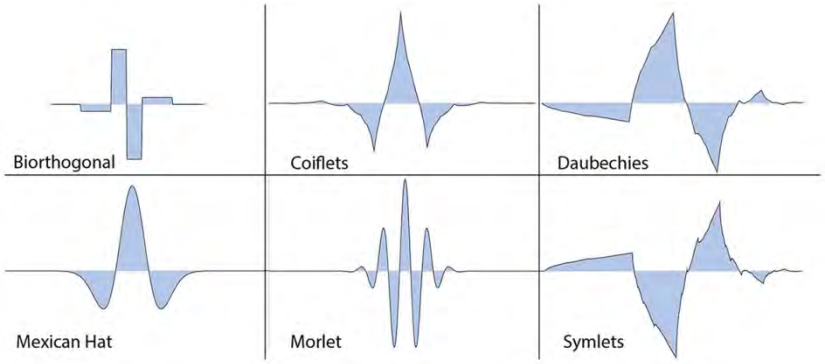

Figure 7-14. Examples of wavelet configurations proposed to address data variability.

Wavelet transforms use versions of wavelets that are scaled in space or time, by shrinking or stretching mother wavelets. By stretching a wavelet (i.e., increasing scale), the frequency of the wavelet is reduced. Conversely, increased frequency and transients or abrupt changes in space or time can be represented by compressed (i.e., reduced scale) versions of the wavelet. In addition to scaling, shifting of the scaled wavelet over the extent of the domain is used to capture and represent the variability presented by the remotely-sensed signal. Figure 7-15 illustrates the use of scaling and shifting a Morlet wavelet (i.e., blue lines) in the one-dimensional space by using a temporal profile of a single MODIS NDVI pixel (i.e., red line). Readers interested in a more complete description of wavelets are invited to visit Mallat (2009).

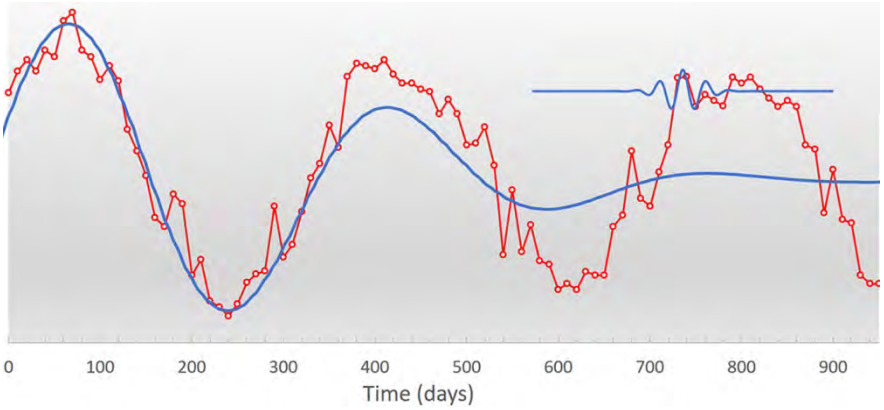

Figure 7-15. Wavelet analysis using scale and shifting of a mother wavelet (Morlet) over a temporal profile of MODIS NDVI.

Wavelets have found multiple applications in image processing and remote sensing, including image compression (Dragotti *et al.*, 2000; Karami *et al.*, 2012); dimensionality reduction (Bruce *et al.*, 2002; Kaewpijit *et al.*, 2003); image fusion (Ranchin, *et al.*, 2003; Amolins *et al.*, 2007); crop phenology detection (Sakamoto *et al.*, 2005; White *et al.*, 2005); feature and change detection (Niedermeier *et al.*, 2000; Bovolo and Bruzzone, 2005); and retrieval of biophysical variables (Blackburn and Ferwerda, 2008; Cheng *et al.*, 2014); among many others. Widely used methods include a variety of wavelet transforms (e.g., Discrete Wavelet Transform (DWT); Continuous Wavelet Transform (CWT), Stationary Wavelet Transform – (SWT)) with specific implementations/behaviors when performing wavelet scaling and shifting. Figures 7-16 to 7-19 provide examples of image processing using wavelets, including wavelet decomposition, noise removal, image fusion and image compression. Figure 7-17 shows the use of SWT for noise removal considering a one-dimensional time series (7-17a to 7-17c) and a 2D image (7-17d and 7-17e).

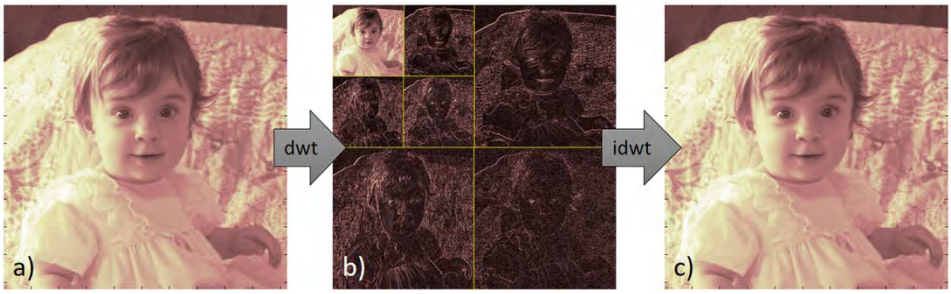

Figure 7-16. Wavelet decomposition for 2D image (a) original image, (b) image decomposition using DWT; (c) synthesized image resulting from (IDWT.)

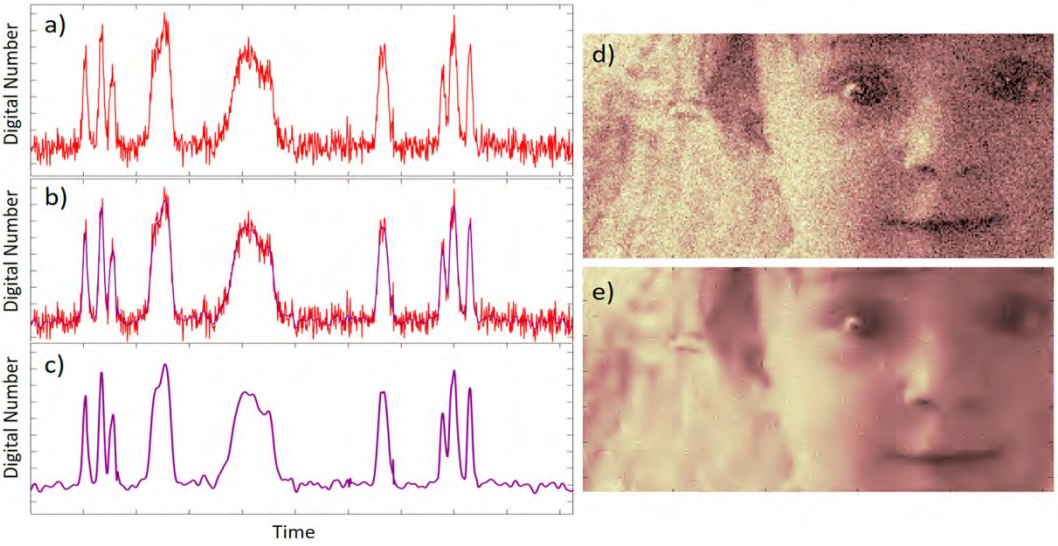

Figure 7-17. Noise removal using SWT: (a) one-dimensional time series with noise; (b) time series after noise removal overlaid to time series with noise; (c) time series after noise removal; (d) image with noise; (e) image after noise removal.

Image fusion capabilities of wavelets is demonstrated by Figure 7-18. The fusion technique involves the DWT of images to be fused and the decomposition of the original images. Fusion methods include the fusion of decompositions, followed by IDWT.

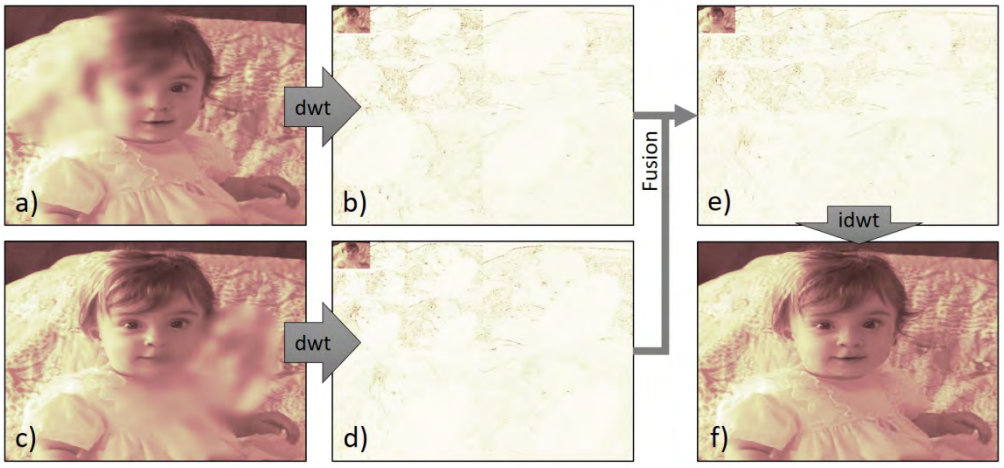

Figure 7-18. Use of wavelets for image fusion and detail enhancement: (a) image with reduced detail in region 1; (b) decomposition of image "a" using a DWT; (c) image with reduced detail in region 2; (d) decomposition of image "c" using a DWT; (e) fusion of decompositions; (f) fused image using an IDWT.

Wavelets have shown remarkable ability to compress images and have been widely used for image compression and storage. The JPEG 2000 compression standard and its lossless compression results from the incorporation of wavelet transform (Christopoulos *et al.*, 2000). Figure 7-19 shows the use of wavelets for image compression by wavelet-based image decomposition.

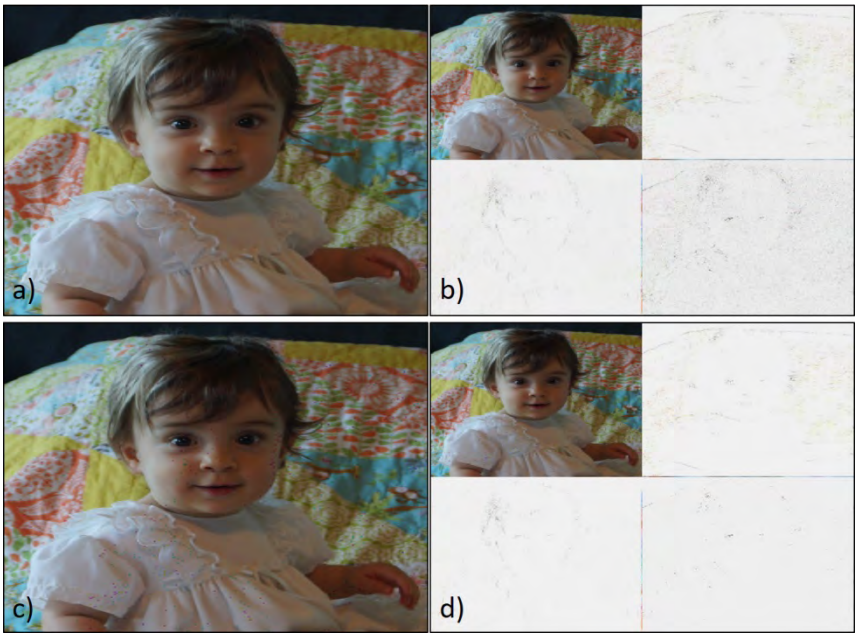

Figure 7-19. Image compression using wavelet-based image decomposition: (a) original image; (b) wavelet decomposition of original image; (c) compressed image (76.33% compression); (d) wavelet decomposition of compressed image.

5 SPECTRAL VEGETATION INDICES

5.1 *Introduction*

Vegetation indices (VIs) are spectral measures of the green foliage status of a canopy, commonly referred to as '*greenness*'. They are highly robust and transparent satellite measurements computed seamlessly across all pixels in time and space, irrespective of land cover, sun-view geometry, and soil background. They are computed easily from measurements made with spectroradiometers and spectral cameras handheld or mounted on towers, unmanned aerial vehicles (UAV), and aircraft; and thus, are amenable to cross-sensor comparisons and validation with satellite sensors. As a result, they are among the most widely used satellite products that provide key measurements of vegetation productivity and phenology for biogeochemical modeling and biodiversity studies. They have become indispensable tools across an array of climatological, ecological, hydrological, and agricultural resource management, and public health applications. Following a comprehensive review of Huete *et al.* (2014), this Section presents the current status and recent developments in satellite VIs with a focus on operational satellite VI products. The section concludes with a discussion on future research needs for the development of robust satellite VI products.

5.2 *Description of Vegetation Indices*

The theoretical basis for VIs can be understood by comparing leaf spectral reflectance to those of a soil and senesced plant (Figure 7-20). The reflected energy from a green leaf is very low in the visible spectrum due to high absorption of visible light, referred to as *photosynthetically active radiation* (PAR), by leaf pigments. In the NIR, nearly all of the radiation is scattered (i.e., reflected and transmitted) in a manner dependent on leaf type, morphology and cellular structure. Maximum contrast will occur in healthy, structurally-developed leaves, and minimal contrast will occur in stressed, diseased, and senesced leaves. VIs are spectral transformations of two or more bands that quantify the contrast between the red and NIR reflectances, sensitive measures of variations in leaf physiological status (e.g., leaf age, morphology and pigment content), foliage amount and structure (e.g., vegetation fraction, leaf angles, and leaf area), and area-averaged canopy photosynthetic capacity.

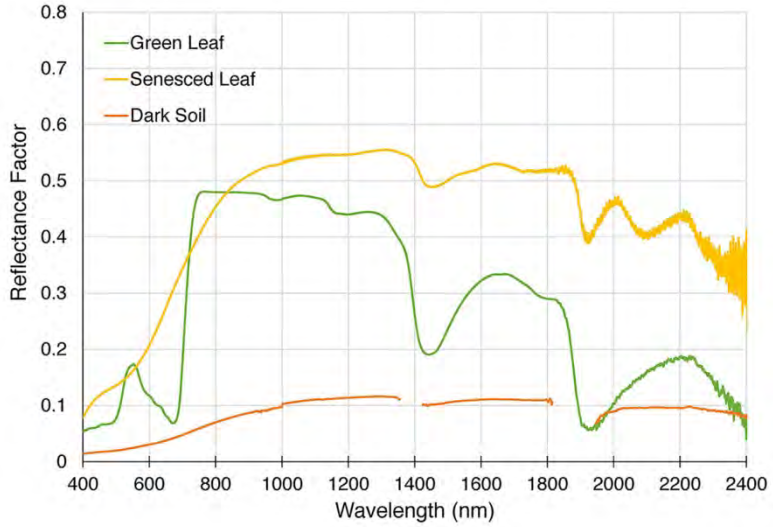

Figure 7-20. Spectral reflectance of green leaf, senesced leaf, and dark soil. Courtesy, Alfredo Huete.

5.2.1 *Index Formulations*

A variety of ways in which two or more spectral bands may be combined to quantify the red-NIR contrast have been introduced, resulting in a multitude of VI formulas that vary from two-band ratios, normalized differences, linear spectral band combinations, angle based VIs, and optimized band combinations. The NDVI in Equation (7-19) is the most commonly used VI in remote sensing (Tucker, 1979):

$$NDVI = (SR - 1)/(SR + 1) = (\rho_{NIR} - \rho_{red})/(\rho_{NIR} + \rho_{red}) \quad (7\text{-}19)$$

where: ρ_{red} = red reflectance; ρ_{NIR} = NIR reflectance; and SR = simple ratio. This normalized version of the simple ratio of NIR to red reflectances (Rouse *et al.*, 1973) constrains values between −1 and +1.

Linear band combination indices (LCI), such as the Tasseled Cap greenness index (Kauth and Thomas, 1976) and spectral mixture analysis (SMA) have been applied to Landsat imagery and MODIS imagery (Justice *et al.*, 1998; Crist and Cicone, 1984; Lobser and Cohen, 2007), as shown in Equations 7-20 and 7-21. These indices have the added advantage of generating multiple measures of components within a pixel, including vegetation, soil, shade, and other scene elements (Souza *et al.*, 2003):

$$\text{LCI} = a \cdot \rho_{\text{NIR}} + b \cdot \rho_{\text{red}} + \sum_{i=0}^{n-2} c_i \cdot \rho_i \quad (7\text{-}20)$$

where: ρ = reflectance; *a*, *b*, and *c* = weights of each band to the VI; and *n* = number of bands.

Optimized indices employ simplified radiative transfer theory of soil-vegetation interactions (e.g., Huete, 1988; Gobron *et al*., 2000). The soil-adjusted vegetation index (SAVI) is an optimized combination of red and NIR bands designed to extract canopy greenness independent of the underlying canopy background (soil, water, and litter) brightness variations.

$$\text{SAVI} = (1 + L) \cdot (\rho_{\text{NIR}} - \rho_{\text{red}}) / (\rho_{\text{NIR}} + \rho_{\text{red}} + L) \quad (7\text{-}21)$$

where: *L* = canopy background adjustment factor.

The structure of the SAVI equation encompasses a large proportion of existing VIs, including the NDVI and linear combination indices through the '*L*' term, which is based on Beer's law. When *L* = 0, the SAVI becomes the NDVI, Equation (7-19) and when *L* is very large (i.e., *L* > 10 to infinity), the SAVI becomes the LCI, Equation (7-20).

5.2.2 *Vegetation Index and Vegetation Biophysical Isolines*

Having VIs fixed to be constant, VI models such as Equations (7-19) to (7-21) can be seen as relationships between the red and NIR reflectances. The relationship formed from a set of reflectance spectra, or the line of a constant VI value, is the vegetation "index isoline." The index isolines define the manner in which VIs quantify the subpixel amount of vegetation present in a pixel and, thus, depict key theoretical differences among VIs (Price, 1992). The paragraphs below describe relationships between different VIs illustrated in Figure 7-21.

In Figure 7-21, the isolines of three different VIs (i.e., NDVI, SAVI, and perpendicular vegetation index (PVI)) are compared in the NIR-red reflectance space. Diverging out from the origin are the NDVI isolines which are characterized with steeper slopes for higher NDVI values but zero-intercepts for the entire NDVI dynamic range. The PVI, representing LCIs, forms parallel index isolines with a constant slope, but increasing NIR intercepts with increasing index values. The SAVI isolines are similar to the NDVI isolines, but different from them in that the origin of the SAVI isolines is shifted away from that of the NIR-red reflectance space. Therefore, both the slope and intercept of the SAVI isoline increase with increasing index values.

Plotted also in Figure 7-21 are "actual" red and NIR reflectances of a cotton canopy over different soil backgrounds measured at various growth stages over a growing season. Red and NIR reflectances of bare soil form a "soil line" above the 1:1 line, representing the boundary condition of "zero" vegetation (Richardson and Wiegand, 1977). Each set of reflectance spectra, or a set of red-NIR reflectance pairs, measured at a certain growth stage, i.e., constant biophysical conditions (e.g., any fixed LAI, and structural arrangement) but varying soil background reflectances, also forms a line with a specific slope and intercept to the biophysical condition (Figure 7-21). This line of constant vegetation is referred to as the vegetation "biophysical isoline" (Huete 1988; Baret and Guyot, 1991; Verstraete and Pinty 1996; Yoshioka *et al*., 2000a). The biophysical isoline can be considered as the optical representation of vegetation biophysical conditions and therefore are subject to change with leaf physiological status and sun-target-view geometric conditions even for the same LAI and structural arrangement.

Comparing the VI isolines with the vegetation biophysical isolines provides a means of improving or designing optimal VIs and, thus, the development of optimized VIs has been influenced to some extent by the shape of the biophysical isolines (Huete, 1988; Verstraete and Pinty, 1996; Yoshioka *et al.*, 2000b). The SAVI, one of optimized VIs, was derived by shifting origin of the index isolines with the *L* adjustment factor, which best aligned its index isolines with the observed biophysical isolines (Huete, 1988).

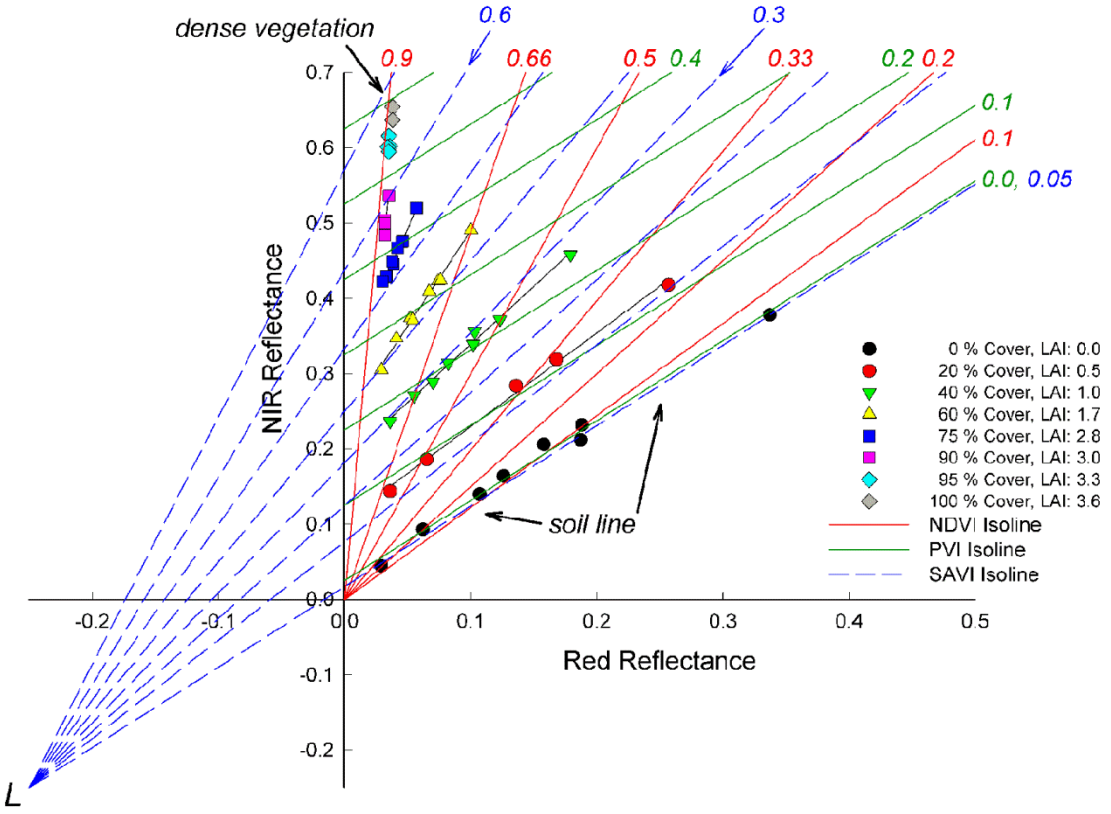

Figure 7-21. Vegetation index isolines for NDVI, SAVI, and PVI in NIR-red crossplot. The isolines are superimposed on the triangular cloud of actual crop (cotton) canopy spectral measurements over a growing season. Adapted from Huete *et al*. (2014).

5.2.3 *Hyperspectral Indices*

A large number of hyperspectral indices have been formulated and proposed, utilizing narrow spectral bands to capture fine resolution biochemical spectral variability associated with species, leaf age, and plant stress variations (Carter and Knapp, 2001). These indices offer higher sensitivity in the retrieval of foliage biochemical properties than broadband VIs and quantify canopy absorption processes associated with pigments, water, and ligno-cellulose compounds from litter and woody material (Ustin *et al*., 2004). The photochemical reflectance index (PRI), Equation (7-22) uses two narrow bands and provides a scaled light-use efficiency (LUE) measure (Gamon *et al*., 1992; Middleton *et al*., 2011):

$$\mathrm{PRI} = (\rho_{531nm} - \rho_{570\mathrm{nm}})/(\rho_{531nm} + \rho_{570nm}) \qquad (7\text{-}22)$$

Spectral variations at 531*nm* are associated closely with the dissipation of excess light energy by xanthophyll pigments to protect the photosynthetic leaf apparatus (Ripullone *et al*., 2011). Other examples of hyperspectral indices include the modified chlorophyll absorption ratio index (MCARI) and transformed

chlorophyll absorption ratio index (TCARI) (Haboudane *et al*., 2004; Tan *et al.*, 2013). Various studies also applied and compared the normalized difference of every pair of bands in a hyperspectral dataset to assess their optimum relationships and correlations with biophysical parameters of interest (e.g., Thenkabail *et al.*, 2013). Launches of new hyperspectral missions such as the Hyperspectral Infrared Imager (HyspIRI) and Hyperspectral Imager Suite (HISUI) should provide opportunities for scaling and extending leaf physiologic processes and phenology from species to ecosystem scales, as well as from ecosystem to regional and global scales, through data fusions with coarse resolution satellite VIs.

5.2.4 *Operational Indices*

Current operational satellite VI products include the NDVI and the enhanced vegetation index (EVI). The EVI is an optimized combination of red, NIR, and blue bands, designed to extract canopy greenness, independent of the underlying canopy background brightness and atmospheric aerosol variations, with extended sensitivity into higher biomass regions (Huete *et al*., 2002) Equation (7-23). The index gains its heritage from the SAVI and the atmospherically-resistant VI (Kaufman and Tanré, 1992):

$$\mathrm{EVI} = 2.5 \cdot (\rho_{\mathrm{NIR}} - \rho_{\mathrm{red}}) / (\rho_{\mathrm{NIR}} + C_1 \cdot \rho_{\mathrm{red}} - C_1 \cdot \rho_{\mathrm{blue}} + L) \quad (7\text{-}23)$$

where: ρ_{blue} = blue reflectance; L = canopy background adjustment factor; and C_1 and C_2 = aerosol resistance weights. The EVI coefficients of L = 1; C_1 = 6 and C_2 = 7.5 were adopted for Landsat Enhanced Thematic Mapper Plus (ETM+) and MODIS spectral bands (Huete *et al*., 2002). The EVI can be computed from many sensors that have a blue band, including SPOT-VEGETATION (Xiao *et al.*, 2003) and Advanced Earth Observing Satellite-II (ADEOS-II) Global Imager (GLI) (Yamamoto *et al.*, 2005).

A two-band enhanced vegetation index (EVI2), which is functionally equivalent to the EVI, was developed for use in sensors without a blue band by Jiang *et al*. (2008), Equation (7-24):

$$\mathrm{EVI2} = 2.5 \cdot (\rho_{\mathrm{NIR}} - \rho_{\mathrm{red}}) / (\rho_{\mathrm{NIR}} + C_1 \cdot \rho_{\mathrm{red}} + L) \quad (7\text{-}24)$$

where: L = 1 and C_1 = 2.4 are the EVI2 coefficients derived for Terra and Aqua MODIS. The EVI2 has been found useful even for those sensors equipped with a blue band (e.g., Pfeifer *et al.*, 2012; Morton *et al.*, 2014). The consistency of EVI values across different sensors may be more problematic than that of the NDVI due to variable and more difficult atmospheric correction schemes of the blue reflectance (Fensholt *et al.*, 2006a).

Although many VIs are well correlated with one another and some (e.g., NDVI and simple ratio vegetation index (SR)) are functionally equivalent, there are important differences in the way VIs depict vegetation foliage as described in Section 5.2.2; and, thus, the use of multiple VIs offers a more complete characterization of canopy properties (Huete *et al.*, 2014). The EVI, SAVI, PVI, and Tasseled Cap greenness are more sensitive spectrally to the NIR and contain information from multiple canopy leaf layers, whereas the NDVI is most sensitive to the canopy-absorbing red band and senses primarily the uppermost leaf layers. This spectral sensitivity difference, for example, allows the first set of indices to have extended sensitivity over high LAI/biomass areas where the NDVI saturates (Fensholt *et al*., 2004; Huete *et al*., 2006). The NDVI and ratio-based VIs, on the other hand, have the advantage of minimizing noise and influences attributed to variations in irradiance and topography.

5.3 *Developing Satellite Vegetation Index Products*

A sequence of data processing steps is generally applied to derive satellite VI products of high quality, i.e. cloud-free, atmosphere-corrected, and globally consistent VI values. First, satellite-measured radiances are normalized by exoatmospheric solar irradiances to TOA reflectances that are then corrected to varying degrees for atmospheric effects such as molecular scattering and absorption influences, stratospheric aerosols, or all of atmospheric constituents including tropospheric aerosols, to better approximate field- and tower-based VI measurements. Finally, the retrieved indices are composited temporally and spatially to produce globally consistent VI values. In this final step, cloud masks are often utilized to remove pixels contaminated with cloud, cloud shadow, and/or heavy aerosol artifacts.

One key process in generating high quality satellite VI products is temporal compositing. In this process, sequential input reflectance images over a set time interval (e.g., 7-day, 10-day, or 16-days) are composited into a single image consisting of least cloud- and atmosphere-contaminated, near-nadir viewing pixel observations.

5.3.1 *Maximum Value Compositing and Constraint View Angle Maximum Value Compositing*

Standard compositing methods used in coarse resolution satellite data are based on the maximum value composite (MVC) concept developed for AVHRR NDVI time series data by Holben (1986). In the MVC method, the highest NDVI value over a compositing period is selected to represent the greenness status of a given pixel for that period. In the early AVHRR era, the highest NDVI was presumed to occur on days with the least cloud and atmospheric contamination, and for the smallest atmospheric optical depth (i.e., the closest-to-nadir viewing geometry). The compositing method was applied to data that were not corrected for atmospheric or sun-target-sensor geometry effects. For vegetated surfaces, the atmosphere increases red reflectance and decreases NIR reflectance, resulting in a negative bias in the NDVI (e.g., Vermote and Kotchenova, 2008). The Global Inventory Modeling and Mapping Studies (GIMMS) AVHRR NDVI3g time series data have been temporally composited with the MVC method (Table 7-3).

The MVC approach has become less useful as advancements in operational atmospheric correction have evolved. The sun-target-sensor geometry effect, described by the bidirectional reflectance distribution function, becomes more prominently revealed in the atmospherically-corrected data. The sun-target-sensor geometry alters the effective proportion of sunlit and shaded vegetation viewed by a sensor and illuminated by the sun, which can alter the spectral contrast drastically between red and NIR reflectances, resulting in angular biases in VIs (Cihlar *et al*., 1997; Schaaf *et al*., 2002). In general, the NDVI decreases in backscattering direction because of high red reflectances relative to NIR, whereas the NDVI increases in forescattering direction as red reflectances are reduced more strongly due to shadowing relative to the scattered NIR (Fensholt *et al*., 2006b). The EVI varies in an opposite manner, having a positive bias in the sunlit, backscattering direction due to the stronger NIR signal (Sims *et al*., 2011). For the atmospherically-corrected data, the MVC method has been shown to confuse high NDVI values associated with lower residual cloud/atmosphere contamination with those caused by off-nadir viewing (Cihlar *et al.*, 1994; van Leeuwen *et al.*, 1999). In the atmospherically-corrected data, overcorrection of atmosphere may also result in high NDVI values due to a negative bias in red reflectances, further complicating the effectiveness of the MVC approach.

The MODIS VI algorithm has adopted a constraint view angle MVC (CVA-MVC) approach (Huete *et al.*, 2011). This method improves upon the MVC approach by attempting to restrict pixel selections to within ±30° view zenith angles by choosing the closest-to-nadir view pixel from 2 or 3 highest NDVI values in the compositing period (i.e., minimized for BRDF influences). In the MODIS VI algorithm, per-pixel quality assessment (QA) information is also used to filter out problematic and noisy pixels potentially contaminated by residual clouds, cloud shadow, and/or high aerosol loadings, and/or due to large viewing geometries before the CV-MVC application. Chuvieco *et al.* (2005) found that the MODIS VI compositing procedure provided close to nadir observation angles and good spatial coherency, while the traditional MVC method provided poor results for mapping burned area over the Iberian Peninsula. This CV-MVC procedure was also used in generating AVHRR NDVI and EVI2 global temporally-composited datasets (Table 7-3) (Didan *et al.*, 2015).

Table 7-3. Comparison of AVHRR Global Vegetation Index Time Series Datasets.

	GIMMS 3g (Pinzon and Tucker, 2014)	LTDR V4 (*http://ltdr.nascom.nasa.gov*)	VIP (Didan *et al.*, 2015)
Index	NDVI	NDVI	NDVI, EVI2
Grid resolution	0.08°	0.05°	0.05°
Temporal resolution	15-day	Daily	Daily, 7-day, 15-day, monthly
Temporal coverage	1981-2013	1981-present	1981-1999
Source data	AVHRR GAC	AVHRR GAC	LTDR V4 AVHRR
Source coverage	07/1981-02/1985 NOAA-7 03/1985-10/1988 NOAA-9 11/1988-08/1994 NOAA-11 09/1994-01/1995 NOAA-9 01/1995-10/2000 NOAA-14 11/2000-12/2003 NOAA-16 01/2004-12/2008 NOAA-17 01/2009-12/2011 NOAA-18 01/2012-12/2013 NOAA-19	06/1981-02/1985 NOAA-7 01/1985-11/1988 NOAA-9 11/1988-09/1994 NOAA-11 01/1995-12/1999 NOAA-14 11/2000-12/2005 NOAA-16 07/2005-12/2009 NOAA-18 05/2009-present NOAA-19	06/1981-12/1999 LTDR V4
Radiometric calibration	Ocean and cloud vicarious calibration (Vermote and Kaufman, 1995), and desert calibration (Los, 1993) for NOAA-7 to 14; desert vicarious calibration (Cao *et al.*, 2008; Wu *et al.*, 2010) for NOAA-16 to 19	Ocean and cloud vicarious calibration (Vermote and Kaufman, 1995)	Adopted from LTDR V4
Orbit drift correction	Empirical mode decomposition (Pinzon *et al.*, 2005) for NOAA-7 to 14	BRDF-based normalization to nadir view and 45° sun zenith angle (Vermote *et al.*, 2009)	Adopted from LTDR V4
Atmospheric correction	Corrected for El Chichon and Mt. Pinatubo stratospheric aerosol effects (Vermote *et al.*, 1997)	Corrected for molecular and aerosol effects	Adopted from LTDR V4
Temporal compositing	Maximum NDVI (Holben, 1986)	N/A	Constraint view-angle maximum NDVI (van Leeuwen *et al.*, 1999)
Inter-sensor calibration	Inter-calibrated across platforms using Bayesian Methods with SeaWiFS	None	Cross-calibrated to MODIS using per-pixel simple linear regression

5.3.2 *BRDF-based Compositing*

BRDF models may be employed to further reduce angular variations in VI products. This has been accomplished in the MODIS Nadir BRDF-Adjusted Reflectance (NBAR) product. NBAR reflectances are adjusted to nadir through BRDF model inversions applied to seven or more good quality, cloud-free observations within a composite cycle (Schaaf *et al.*, 2002). The MODIS NBAR reflectances are adjusted for local solar noon angle, whereas the MODIS VI product is produced at local solar zenith angle (as they represent actual observations). Therefore, these datasets contain seasonal sun angle variations, which however do not present a problem in inter-annual time series data and trend analyses, given there is no sensor calibration or orbital drift (Wang *et al.*, 2012). AVHRR Land Long-term Data Record (LTDR) reflectance and NDVI datasets are standardized for a nadir viewing and constant solar zenith angle geometry using MODIS BRDF kernels (Table 7-3).

In contrast to other BRDF products, the MAIAC is based on a radiative transfer model that does not make a Lambertian assumption in correcting for atmosphere (Lyapustin *et al*., 2012). The MAIAC compositing approach is based on a cloud screening and atmospheric correction algorithm that takes advantage of an adaptive time series analysis with processing of groups of pixels, to derive atmospheric aerosol concentration and surface reflectance. It was first derived for Amazon forests and then extended to the African tropics and has been a key product in resolving debates and controversies on dry-season and drought satellite greening studies in Amazonian rainforests (Morton *et al*., 2014; Saleska *et al*., 2016). Whereas Morton *et al*. (2014) reported no seasonality in Amazon forests, evidence from MAIAC-based studies (Guan *et al*., 2015) and *in situ* and tower flux studies, show tropical forest 'greening' during higher sunlight and annual dry seasons, suggesting they are limited more by light than water. In summary, satellite products may use models to correct artifacts (e.g., MAIAC and NBAR) or compositing algorithms designed to minimize such artifacts (e.g., standard MODIS VIs). Any of these data products, however, will typically output either climatological values or lower quality pixels when there is an absence of better-quality pixels, and for this reason, it is important to employ QA filtering of such products.

5.4 *Vegetation Index Continuity Among Sensor Systems*

There is a need for accurate, long term satellite measurements to assess climate change impacts on ecosystems. VI datasets from a number of Earth observing satellites can fill this need as they can be used to generate seamless, continuous long-term data records for climate change studies. The Visible Infrared Imaging Radiometer Suite (VIIRS) sensor series on the Joint Polar Satellite System (JPSS) program will continue the VI data streams initiated with National Oceanic and Atmospheric Administration (NOAA) AVHRR and NASA Earth Observing System MODIS (Cao *et al.*, 2014). Both NDVI and EVI have been selected as geophysical products for the JPSS program (Vargas *et al.*, 2013). It is of great importance to investigate multi-sensor VI continuity/compatibility (e.g., among AVHRR, MODIS, and VIIRS) and to develop a mechanistic understanding of VI continuity across disparate sensor systems.

Numerous investigations have evaluated NDVI continuity and consistency empirically across multiple AVHRR sensors (e.g., Los, 1993; Roderick *et al*., 1996). Many of these investigations have focused on ensuring consistent calibration over time and across sensors (Vermote and Kaufman, 1995; see also Table 7-3) as AVHRR sensors were not equipped with on-board calibration devices and as orbital drift created

trends in NDVI time series through the BRDF effects with gradually increasing solar zenith angles. A strong emphasis has been placed on calibration for the current and newer sensors (Slater *et al.*, 2001).

With the launch of a new generation of satellite sensors, including AVHRR/3, MODIS, and Landsat-7 ETM+ in the late 1990s, attempts to reconcile multi-sensor VI data for sensor characteristics and algorithm differences evolved (Teillet *et al*., 1997). Many studies developed empirical inter-sensor spectral calibration equations using: (1) quadratic regression for the NDVI (Trishchenko *et al.*, 2002; Miura *et al.*, 2006; Trishchenko, 2009; Gonsamo and Chen, 2013); (2) simple linear regression for the NDVI (Steven *et al.*, 2003); and (3) for the EVI and EVI2 (Kim *et al.*, 2010) across a large number of sensors, including MODIS, VEGETATION, AVHRR, Sea-viewing Wide Field-of-view Sensor (SeaWiFS), Landsat ETM+, and VIIRS. Several studies employed weighted averaging of two or more narrow spectral bands to derive a broadband-based AVHRR-equivalent NDVI from MODIS (Gitelson and Kaufman, 1998; Gao, 2000) and Medium Resolution Imaging Spectrometer (MERIS) (Gunther and Maier, 2007). Using SeaWiFS NDVI data as a bridge, Pinzon and Tucker (2014) applied Bayesian methods to cross-calibrate AVHRR/2-NDVI and AVHRR/3-NDVI. Yet another approach was proposed by Yoshioka *et al*. (2012), which used vegetation biophysical isolines to inter-calibrate two-band indices spectrally, including NDVI, SAVI, and EVI2, across sensors. Obata *et al*. (2013 and 2016) extended this isoline-based translation approach to the EVI and derived a MODIS-compatible EVI from VIIRS spectral bands. This bottom-to-top theoretical approach provided a better mechanistic understanding and predictive modeling of cross-sensor relationships for the NDVI, EVI, and input reflectances. It is noted, however, that all these methods have been designed to compensate for spectral bandpass differences across sensors.

Consideration of additional factors is required to derive long term VI records from disparate sensor systems. They include spatial resolution differences and platform orbital differences that result in view and sun angle differences, and algorithmic differences associated inherently with sensor characteristics (e.g., van Leeuwen *et al.*, 2006; Swinnen and Veroustraete, 2008; Miura *et al.*, 2013). The historical AVHRR record will continue to serve as a critical dataset for climate science and establishing the continuity or compatibility with the AVHRR record remains a challenge. It may also be beneficial to extend backwardly the EVI2 and other 2-band VIs to the historical AVHRR record to complement the NDVI (Marshall *et al.*, 2016). Overall, more rigorous examinations of inter-sensor VI continuity and compatibility are desired and will be critical in support of climate science and ecosystem sustainability studies.

5.5 *Validation of Satellite Vegetation Index Products*

Validation is an essential part of satellite VI product development to evaluate their quality, and spatial and temporal consistency, and to provide accuracy and reliability information for research and applications. Earlier validation efforts involved finer resolution airborne and satellite imagery, field radiometer measurements, biophysical field sampling, and automated ground observation networks (Privette *et al*., 2000), all having an objective to validate VIs through independent radiometric and biophysical measurements. Accuracy and precision values for the MODIS VIs are generally within 0.02 to 0.05 VI values (MODIS Land Team, 2015).

In context of the Committee on Earth Observation Satellites (CEOS) Land Product Validation (LPV) subgroup, validation of a satellite product is achieved progressively from Stage 1 to Stage 3 by expanding

the areal coverage and time period from which product quality and accuracy are assessed (URL: http://lpvs.gsfc.nasa.gov). This is necessary and logical as the quality of satellite VI retrievals vary in space and time because of geographic and seasonal variations in cloud cover, quality of atmospheric correction, and sensor performance (Miura *et al.*, 2000; Wolfe *et al.*, 2002; Samanta *et al.*, 2010). Recently, the CEOS LPV subgroup has developed an additional stage, Validation Stage 4, and proposed a framework for achieving its implementation. This framework consists of a citable protocol, fiducial reference data, and automated subsetting, recommending the adoption of more systematic, automated validation exercises than previous protocols (e.g., Fernandes *et al*., 2014). Below are methods and approaches that have been used to validate MODIS VIs and VIIRS VIs with a brief discussion on infrastructures that can be utilized for Stage 4 validation of satellite VI products.

5.5.1 *Reflectance-based Vegetation Index Validation*

Independent, top-of-canopy (TOC) and nadir reflectance measurements are means to validate satellite VI products (Huete *et al.*, 2002; Fensholt *et al.*, 2006a). VIs are readily computed from TOC reflectances measured with ground-based spectroradiometers, tower-mounted sensors, and airborne instruments. Calibrated and traceable "transfer radiometers" mounted on light aircraft or UAVs can be flown at altitudes of 10*m* to 300*m* above ground level (AGL) to acquire TOC reflectances with nadir looks at prescribed sun angles for independent characterization of VIs (Huete *et al*., 1999). This extends locally-constrained, sub-canopy scale field radiometric measurements to kilometer length scales, suitable for validating coarse resolution VI products. This approach is primarily to validate satellite reflectances and provide uncertainties in atmosphere correction which may be translated to accuracies and uncertainties in the satellite VI measures (Vermote and Kotchenova, 2008). Such nadir, TOC reflectance values can also aid in characterizing the uncertainties in a satellite VI compositing scheme by assessing the extent to which the compositing algorithm is able to retrieve close-to-nadir VI values.

5.5.2 *Ground Observation Networks*

In situ observation networks have evolved into highly calibrated and traceable sensor systems that offer great potential for providing temporally-continuous, higher quality (e.g., finer spatial and temporal resolution) measurements than the satellite. These networks complement field and airborne validation data acquired as spatial snapshots in time that can enhance quality, reduce uncertainty, and permit cross-sensor continuity assessments of satellite VIs. They include the AERONET (Holben *et al*., 2001), Baseline Surface Radiation Network (BSRN)/Surface Ratiatin Budget (SURFRADS) (Augustine and Dutton, 2013), PhenoCam (Richardson *et al.*, 2009), and global tower flux network FLUXNET (Running *et al.*, 1999).

5.5.2.1 AERONET

The AERONET Surface Reflectance Validation Network (ASRVN) collects operational satellite data at over 100 AERONET sites and retrieves surface reflectances from these satellite data with a rigorous atmospheric correction algorithm and *in situ* AERONET atmospheric measurements (Wang *et al*., 2009). Computed VIs from ASRVN surface reflectance data can be compared against their equivalent satellite products (Huete *et al.*, 2014). Compared to ground-based, aircraft, and finer resolution satellite measurements, this approach has the advantage of identical spectral, spatial, and observation geometry sampling with the

satellite measurement. The sun photometer-based atmosphere correction is applicable to relatively large areas around an AERONET site for more rigorous spatial analysis. It is also applicable to off-nadir viewing conditions that allow realistic assessments of accuracies and uncertainties in VIs due to variability in atmosphere and over a range of sensor observation viewing angles. Recently, Shabanov *et al.* (2015) evaluated the performance of VIIRS TOC NDVI and EVI using their respective counterparts produced with *in situ* AERONET atmospheric measurements as a reference.

5.5.2.2 Surface Radiation Networks

Many towers are now instrumented with sensors measuring PAR and shortwave solar radiation fluxes at high temporal frequencies. A broadband version of the NDVI and EVI2 can be derived from these radiation measurements (Huemmrich *et al.*, 1999; Rocha and Shaver, 2009), which are useful to monitor and quantify vegetation seasonal changes and land cover dynamics, and thus suitable for validation of the satellite counterparts. Wilson and Meyers (2007) demonstrated how well these tower-derived NDVI time series data could trace MODIS NDVI across numerous tower sites as independent verifications of NDVI data over smaller, but homogeneous footprint areas. Wang, Q. *et al*. (2004) found the tower-based broadband NDVI to be a good index to describe physiological activity of a pine forest during certain periods, providing a means for obtaining other physiological parameters that are required by ecosystem models.

5.5.2.3 Global Tower Flux Network

FLUXNET coordinates observations from micro-meteorological tower sites, and their regional and global analysis (Running *et al*., 1999). The tower sites use eddy covariance methods for continuous measurements of carbon dioxide, water vapor, and energy exchanges between terrestrial ecosystems and the atmosphere. This provides potential opportunities to evaluate satellite VI measures of vegetation growth, phenology, and seasonal dynamics. Strong, multiple-biome satellite EVI relationships with tower gross primary production (GPP) measurements have been reported for MODIS and the SPOT VEGETATION satellite data across AmeriFlux tower sites and tropical forests in the Amazon and Southeast Asia (Xiao *et al*., 2004 and 2005; Rahman *et al*., 2005; Sims *et al*., 2006; Huete *et al*., 2008). High resolution tower GPP time series measurements have been used as a means to validate the temporal trajectory of reconstructed daily EVI2 from LTDR AVHRR data (Zhang, 2015).

5.5.3 *Biophysical Validation*

Field-based vegetation biophysical sampling may be useful for validating and assessing VI performance in space and time. Numerous studies examined relationships between VIs and vegetation biophysical properties using field experimental and radiative transfer model simulated data (e.g., Asrar *et al.*, 1984; Gao *et al.*, 2000; Fensholt *et al.*, 2004; Gitelson *et al.*, 2014). A good correspondence between VIs and field biophysical measurements reported in these and other studies provides confidence in using VIs as surrogates for biophysical variables that are otherwise difficult to sample in the field.

Although results from these studies have contributed to biophysical validation of VIs across numerous environments, most VI-biophysical relationships derived from empirical field measurements are at local scales, which therefore have limited spatial extension to other areas or different spatial scales. Another dilemma in using LAI and FPAR to validate VIs is that these biophysical parameters do not distinguish

among quality of greenness (chlorophyll levels) nor phenological age of the leaf (i.e., young, developing, mature); total FAPAR and LAI encompass a variety of leaves of different levels of maturity of varying levels of greenness and photosynthetic efficiency. Yet, another complication in the biophysical validation of VIs is a lack of consensus on what VIs explicitly measure about a canopy and how to interpret a VI value. The large number of co-varying canopy properties makes it difficult to quantify explicitly one variable from the others, and hence to retrieve specific biophysical details from the integrative VI 'greenness' signal (Huete *et al.*, 2014).

5.6 *Recent Findings and Development*

5.6.1 *Phenology Studies*

VI time series data derived from moderate resolution sensors, including MODIS, AVHRR, and VEGETATION, are now widely used to characterize seasonal dynamics of vegetation and their inter-annual variability with quantifiable metrics, such as the onset date of greening, peak greenness date, and growing season length, at regional to global scales (Zhang *et al.*, 2006; Reed *et al.*, 2009). Phenology is the study of recurring biological events (van Vliet *et al.*, 2002) and is an important integrative science for quantifying vegetation responses and feedbacks to climate change (Penuelas *et al*., 2009).

Zhang X. *et al.* (2014) extracted the two phenological metrics of the onset date of greening and the growing season length from AVHRR and MODIS EVI2 time series data and analyzed the metrics for interannual variability and trends for a period of 1982 to 2010 across the entire globe. They report that the trends of vegetation phenology were substantially variable across the globe during the last three decades. Their trend analysis was conducted conservatively by separating the two periods of 1982–1999 and 2000–2010 because of different qualities and some inconsistencies observed between AVHRR LTDR (see Table 7-3) and MODIS data.

Recently, Melaas *et al.* (2013) presented a method for characterizing both long-term average and interannual dynamics of the phenology of temperate deciduous broadleaf forests using multi-decadal Landsat EVI time series data. Spring and autumn phenological transition dates extracted from Landsat EVI data agreed closely with *in situ* phenology measurements at these forest sites. Their results indicate the potential utility of high-resolution satellite VIs not only for landscape-scale phenology studies, but also for bridging *in situ* phenological measurements to those extracted from coarse resolution sensors such as MODIS, AVHRR, and VIIRS.

5.6.2 *Ecosystem Resilience*

Satellite data can reveal useful information on vegetation dynamics and provide opportunities to measure ecosystem changes and responses to climate variability. The AVHRR-NDVI data record is widely used to assess vegetation resilience, land degradation, and drought responses to climate variability. For example, Brandt *et al*. (2015) reported a greening trend in the Sahel region of Africa based on trend analysis of long time series rainfall and AVHRR-NDVI data (1987–2013). They showed a 36% increased greening response, due to increasing tree cover, driven by a 40% increase in rainfall over this period.

Some studies normalize the vegetation response by the magnitude of changes to the climate signal, as in the approach used by Ponce-Campos *et al*. (2013), who applied rain use efficiency (RUE) and water use efficiency (WUE) measures to assess vegetation responses and resilience during the early 21st Century extreme hydroclimatic events. Comparisons of vegetation resilience across different parts of the world are difficult to assess without accounting for variations in magnitude of climatic disturbances. RUE enables cross-biome comparisons and establishes a hypothetical threshold beyond which ecological transitions or ecosystem collapse may occur.

DeKeersmaecker *et al*. (2015) used the GIMMS3g AVHRR-NDVI to assess and quantify vegetation sensitivity and resilience of global biomes while simultaneously taking climate variability into account. Seddon *et al*. (2016) formulated the Vegetation Sensitivity Index (VSI) using monthly MODIS EVI-greenness responses to variability in water availability, cloudiness and air temperature. The VSI quantifies patterns and drivers of ecological sensitivity by identifying ecologically sensitive areas that exhibit either amplified or slowed responses to climate variability in comparison to other regions, and includes a 'weighting' for the various climate factors that contribute to ecological change.

5.6.3 *Solar-induced Fluorescence*

Spectral VIs convolve leaf chlorophyll content, leaf demography and ontogeny, biomass, and canopy structure, to provide aggregate measures of their variations at moderate, weekly to monthly, time scales. Complementing VI measurements, space-based estimates of Sun-Induced chlorophyll Fluorescence (SIF) have recently become available. SIF is an electromagnetic signal emitted in the 650-850*nm* spectral window as a by-product of photosynthesis, representing a more direct measure of photosynthesis (Meroni *et al*., 2009).

In contrast to spectral VIs and other satellite vegetation products such as LAI and fAPAR, chlorophyll fluorescence provides estimates of actual photosynthetic rates, and has been shown to be highly correlated with GPP estimates (Guanter *et al*., 2012). SIF is more dynamic than greenness, and will respond much more quickly to environmental stress, through both change in stress-induced LUE and canopy light absorption (Porcar-Castell *et al*., 2014). It is thus seen as one way to increase the effective temporal remote sensing of vegetation photosynthesis, essentially to near real-time with promising potential capabilities to improve carbon cycle models and provide more accurate projections of ecosystem productivity and climate impacts on production.

The first global maps of SIF were derived using data from the Greenhouse Gases Observing Satellite (GOSAT) (Guanter *et al*., 2012), and more recently, a global SIF data set with better spatial and temporal sampling than that from GOSAT was produced using spectra from the Global Ozone Monitoring Experiment-2 (GOME-2) instrument onboard the Meteorological Operational (MetOp-A) platform (Joiner *et al*., 2013). Several future missions are also being prepared, including the European Fluorescence Explorer (FLEX) satellite mission (Meroni *et al*., 2009) and the Sentinel-5 Precursor Tropospheric Monitoring Instrument (TROPOMI) satellite mission (Veefkind *et al*., 2012).

5.7 *Future Directions and Challenges*

New challenges and demands for robust remote sensing tools address up-coming ecological challenges. More accurate and longer term VI data records will be needed for climate and ecosystem sustainability studies, requiring multi-sensor data fusions and continuity/compatibility analyses. Despite the success of VIs, there are increasing demands to better define what VI values represent and measure in characterizing a canopy. Future advancements in hyperspectral and solar-induced fluorescence offer much potential in advancing remote sensing based landscape monitoring and applications. VIs will continue to be used widely and may become the preferred products for monitoring Earth's changing ecosystems. This is due primarily to their consistency, robustness, and overall transparency. Thus, VIs are an important first step in looking at the state of an environment, and from which higher level products and/or *in situ* datasets can be involved to assess important mechanisms responsible for VI signal variance.

6 SPECTRAL MIXTURE ANALYSIS

6.1 *Introduction*

Early in the history of MS remote sensing, it was recognized that the relatively coarse spatial resolution of spaceborne sensors would result in multiple materials being present in any given ground instantaneous field of view (GIFOV) of a sensor; thus creating a "mixed pixel". The potential of "unmixing" coarse spatial resolution MS data was first proposed by Horowitz *et al.* (1971), prior to the launch of the Landsat systems. SMA is one of several terms used to describe the process by which a spectrum produced by light reflecting from multiple materials within an IFOV is unmixed using "pure" spectra, called endmembers, to generate estimates of fractional abundance for each material. Alternative terms include "mixture decomposition" (Hall *et al.*, 1995), "spectral unmixing" (Keshava and Mustard, 2002) and "mixture modeling" (Ichoku and Karnieli, 1996) to name a few. In this review, we use the term SMA.

One of the earliest applications of SMA was in planetary geology. Singer and McCord (1979) used a two-component mixture to better understand the impact of aeolian dust on Martian spectra. This work was followed subsequently by laboratory-based studies of synthetic mixtures using lunar samples collected during the Apollo Missions (Johnson *et al.*, 1985), and synthetic mixtures of alluvial fan materials of varying composition and particle size (Shipman and Adams, 1987) and analysis of imagery collected by the Viking Lander (Adams *et al.*, 1986), in which the impact of changing illumination was modeled by including a shade component. The first refereed publication focused on terrestrial vegetation was published by Smith *et al*. (1990), who applied SMA to Landsat TM data acquired over Owens Valley, California to estimate shrub cover. Other early adoptions included Shimabukuro and Smith (1991), who proposed using constrained least squares regression for fraction estimation and related changes in shade fraction to Eucalyptus stand ages. Gillespie (1992) further proposed a thermal unmixing approach by introducing the concept of virtual cold; and Quarmby *et al*. (1992), who applied a mixing model to estimate crop area fraction in AVHRR data.

From these early beginnings, SMA has become a mainstream analysis tool applied routinely to broadband MS and hyperspectral data. Using Google Scholar and primarily targeting refereed sources, the

authors identified over 330 highly ranked manuscripts focused on SMA or one of its variants (Figure 7-22). As can be observed, research focused on SMA has increased steadily from early applications in 1990, peaking at 24 papers between 2005 and 2006, with a steady stream of papers published each year since 2006. It should be noted that more recent publications are underestimated because poorly cited or uncited papers will be ranked low in a search. The important contribution of these studies has been recognized by a large number of citations, totaling close to 40,000 according to Google Scholar™ and over 20,000 in the Web of Science in September, 2015. It should also be noted that many papers use SMA products, but do not include any indication of mixture analysis in the title, key word or abstract and thus go unrecognized by this type of analysis.

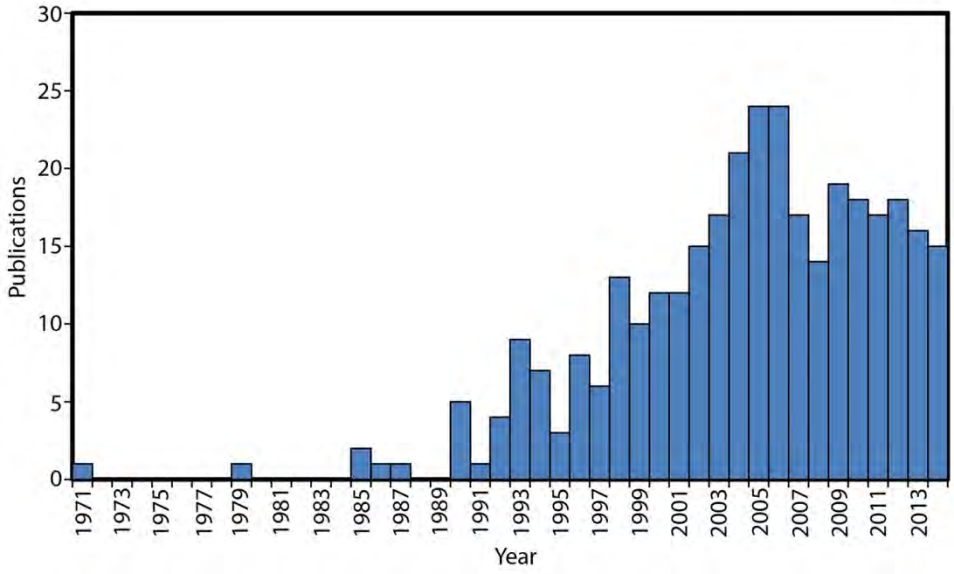

Figure 7-22. The number of SMA publications from 1971 to 2014.

SMA has broadened considerably from its early origins in planetary geology. Ecological applications have become prominent, focusing on issues as diverse as estimating forest structure (e.g., Hall *et al.*, 1995; Lu *et al.*, 2004; Roberts *et al.*, 2004; Sonnentag *et al.*, 2007), mapping tropical deforestation (e.g., Shimabukuro *et al.*, 1994; Roberts *et al.*, 2002; Souza *et al.*, 2013), selective logging and forest degradation (e.g., Asner *et al.*, 2004; Souza *et al.*, 2005), pasture degradation (e.g., Numata *et al.*, 2007; Davidson *et al.*, 2008), fire severity and post-fire recovery (e.g., Riano *et al.*, 2002; Quintano *et al.*, 2006; Veraverbeke and Hook, 2013), sub-pixel tree-fall gaps (e.g., Negrón-Juárez *et al.*, 2011), plant species (e.g., Dennison and Roberts, 2003a,b; Plourde *et al.*, 2007; Youngentob *et al.*, 2011; Somers and Asner, 2013, 2014). Urban remote sensing has also been a strong focus area, with a primary interest in estimating impervious surface fraction and vegetation cover (e.g., Small, 2001; Phinn *et al.*, 2002; Wu and Murray, 2003; Powell *et al.*, 2007; Weng and Lu, 2008; Roberts *et al.*, 2012). Precision agriculture and crop mapping have also been a common application, including: (a) crop area mapping (e.g., Quarmby *et al.*, 1992; Lobell and Asner, 2004; Ozdogan, 2010); (b) estimates of crop production (e.g., Somers *et al.*, 2009a/b; Tits *et al.*, 2012) and (c) mapping plant pathogens and diseases (e.g., Fitzgerald *et al.*, 2004; Coops *et al.*, 2006). Other applications include snow-grain size/snow-covered area mapping (e.g., Painter *et al.*, 1998; 2003), fire temperature and area estimation (e.g., Dennison *et al.*, 2006; Eckmann *et al.*, 2008; Matheson and Dennison, 2012), sediment

estimation in water (e.g., Mertes *et al.*, 1993; Warrick *et al.*, 2004), estimates of kelp biomass (e.g., Cavanaugh *et al.*, 2011) and extensive use in biological microscopy (e.g., Zimmerman *et al.*, 2003). Methodological developments have always been, and remain to be a major focus in SMA, with over 100 papers published since 1990 incorporating some methodological elements that include innovations in fraction inversion (e.g., Shimabukuro and Smith, 1991; Heinz and Chang, 2001; Nascimento and Dias, 2005), endmember extraction (e.g., Winter, 1999; Xiong *et al.*, 2011; Roth *et al.*, 2012), or the strategic use of spatial information (e.g., Martin and Plaza, 2011; Zare *et al.*, 2013; Deng and Wu, 2013); temporal information (e.g., Dennison and Roberts, 2003b; Ozdogan, 2010; Somers and Asner, 2013) or spectral subsets (e.g., Asner and Lobell, 2000; Somers *et al.*, 2009b; 2010a).

This section has provided a brief introduction to SMA. The concept of linear and non-linear mixtures and important concepts such as endmembers, fraction constraints, and endmember variability have been introduced. We have provided graphical examples of the unmixing process and an example of simple and multiple endmember SMA applied to AVIRIS data used to map vegetation and impervious surface cover. We conclude with a discussion of current research needs and future directions. Several excellent reviews exist and the reader is encouraged to read early reviews on SMA by Adams *et al.* (1993), Ichoku and Karnelli (1996), Keshava and Mustard (2002), Adams and Gillespie (2006) and reviews focused specifically on hyperspectral SMA (e.g., Bioucas-Dias *et al.*, 2012) and endmember variability (e.g., Somers *et al.*, 2011; Zare and Ho, 2014). At least one journal special issue is devoted entirely to SMA (e.g., Plaza *et al.*, 2011).

6.2 *The Mixing Problem*

A spectral mixture occurs whenever the reflectance, reflected radiance, or emitted radiance within the IFOV of an instrument originates from two or more spectrally distinct materials. In the case where photons only interact significantly with one material along their path between the source, surface and sensor, the mixture is often called a “checkerboard mix”, in which the measured spectrum is the sum of the spectra of each component within the (FOV), weighted by the areal fraction of each material in the FOV (Figure 7-23).

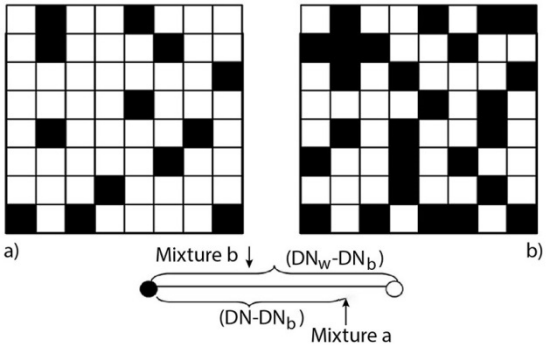

Figure 7-23. Black and white image of a checker-board: a) represents a checkerboard consisting of a majority of white squares while b) has many more black squares. Aggregated into a single pixel, the spectrum on the left would have higher reflectance because of the larger proportion of white pixels. A graphical representation of a two component, single band mixture is shown below the images. DN is “digital number” but could be reflectance or radiance as well. Subscripts refer to white (w) or black (b).

A defining property of the "checkerboard" mixing case is that, provided the pure spectrum of each component is properly identified and noise is minimal, the areal abundance retrieved using SMA and the actual fractional cover will be the same. This is called a linear spectral mixture and is based on the assumption that no photon interaction occurs between materials in the FOV. In the example shown above, with only two components, the fraction of the white endmember can be calculated as the brightness difference between the mixture and the dark component, divided by the brightness difference between the bright and dark endmember (f_w = (DN-DN$_b$)/(DN$_w$-DN$_b$). Gramm-Schmidt Orthogonalization operates on a principle similar to this example, but in *n*-dimensional space.

In cases where photons interact with more than one material between the source, surface and sensor, it is called an intimate mixture, and the mixing process is considered to be non-linear. Intimate mixtures were first described in detail by Nash and Conel (1974), in which two to three component mixtures of powdered plagioclase, pyroxene and ilmenite were created in the laboratory. Whereas mineral mixtures between the transparent minerals plagioclase and pyroxene produced spectra that were intermediate in proportion to the amount of each mineral in the mixture, mineral mixtures involving the opaque mineral ilmenite produced surface darkening far in excess of the percentage of ilmenite in the mixture. In other words, fractions determined by a linear model with ilmenite did not match mineral abundance (Figure 7-24).

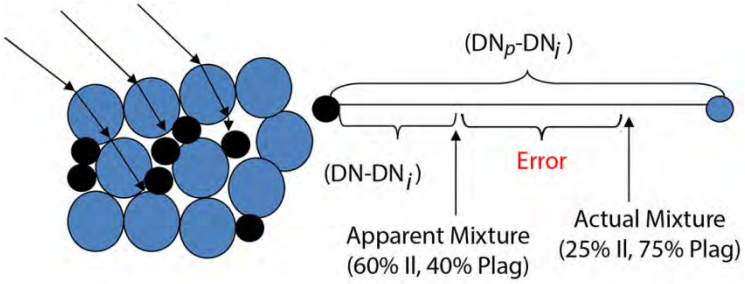

Figure 7-24. Illustration of a 75%/25% plagioclase/ilmenite mixture. In this two-component mixture, the fraction of plagioclase is calculated as f_p = (DN-DN$_i$)/(DN$_p$-DN$_i$). Spectrally a 75/25% mixture of plagioclase and ilmenite grains looks like a 40/60% mixture. Numbers extracted from Conel and Nash (1974).

Intimate (non-linear) mixtures occur whenever photons encounter more than one component along their path. In theory, non-linear mixtures should dominate all mixtures, but provided multiple scattering is minimal, non-linear mixtures can often be neglected. Examples where this is not the case include intimate mineral mixtures (Nash and Conel, 1974; Shipman and Adams, 1987), sediments in water (Mertes *et al.*, 1993), highly absorbing particulates in snow, or transparent vegetation over a bright substrate (Huete, 1987; Roberts, 1991; Somers *et al.*, 2009a). For other applications, the simplest case assuming linear mixing is the dominant model.

6.3 *Linear Unmixing*

6.3.1 *Simple Mixing Models*

In simple mixing models, photon interactions between materials are neglected and linear mixing between a constant set of spectra is used to model every pixel in an image. In this case, a measured spectrum is

modeled as the sum of two or more pure spectra, called endmembers, each weighted by the spectral fraction of the material within the IFOV, Equation (7-25).

$$M_\lambda = \sum_{z=1}^{n} EM_{\lambda z} \cdot f_z + \varepsilon_\lambda \quad (7\text{-}25)$$

where: a mixed spectrum, M, is modeled as the sum of n endmembers, EM_z, each weighted by fraction f_z. Whatever spectral information cannot be accounted for by the model is contained in a spectral residual, ε_λ. The spectral residual can also be considered a measure of model fit and is often summarized as the Root Mean Square Error (RMSE) (Equation 7-26):

$$RMSE = \sqrt{\sum_{i}^{m} \varepsilon_\lambda^2 /(m-1)} \quad (7\text{-}26)$$

where: m equals the number of bands used in the model. Mixing solutions are often constrained, forcing fractions to sum to one (e.g., Adams *et al.*, 1993; Settle and Drake, 1993), or to sum to one with all fractions being positive (e.g., Shimabukuro and Smith, 1991; Heinz and Chang, 2001). Theoretically, the number of endmembers that can be included in a spectral mixture is equal to one more than the number of bands, although the actual number of endmembers that can be included is often significantly fewer because of spectral degeneracy (i.e., collinearity) between endmember combinations (Sabol *et al.*, 1992; Van Der Meer and de Jong, 2000; Chen X. *et al.*, 2011). More typically 3 to 4 endmembers are included in a model (Roberts *et al.*, 1993).

6.3.2 *Endmembers*

An important notion is the concept of an endmember and many techniques have been developed specifically to define endmembers for SMA. Endmembers can be derived from many sources including imagery (i.e., image endmembers; e.g., Dennison and Roberts, 2003a), laboratory measurements (e.g., Smith *et al.*, 1990), field spectra (e.g., Roberts *et al.*, 2004), radiative transfer (e.g., Painter *et al.*, 1998; Dennison *et al.*, 2006; Sonnentag *et al.*, 2007; Tits *et al.*, 2012) or as virtual endmembers that enclose the potential mixing space (e.g., Gillespie, 1992; Tompkins *et al.*, 1997). While reference endmembers (i.e., spectra of known materials measured in the laboratory or the field) are desirable, it is often impractical to use them because of a lack of adequate spectral libraries that capture large numbers of materials as well as the spectral variation within specific material types. In addition, reference endmembers may not match those in the image due to differences in sensors, atmospheric effects and illumination conditions (e.g., Tompkins *et al.*, 1997). Examples of studies that have used reference endmembers to unmix broad-band and hyperspectral images include Smith *et al.* (1990), Roberts *et al.* (1993; 1997b; 2002; 2004), and Negrón-Juárez *et al.* (2011).

A more common practice is to use image endmembers, spectra selected from the image that are assumed to consist of a single cover class. Candidate image endmembers can be identified using semi-automated approaches, such as the Pixel Purity Index (PPI) (Boardman *et al.*, 1995), fully automated approaches such as N-FINDR (Winter, 1999), Vertex Component Analysis (VCA) (Nascimento and Dias, 2005), and Piecewise Endmember Detection (PCE: Zare and Gader, 2010) or fully automated approaches with spatial constraints (e.g., Deng and Wu, 2013; Zare *et al.*, 2013). For example, Souza *et al.* (2013), used PPI to identify

a set of candidate endmembers from Landsat TM data, and then used them to generate models of green vegetation (GV), non-photosynthetic vegetation (NPV), soil, shade and cloud fraction to map deforestation and forest degradation across the Amazon Basin over a ten year period (Souza *et al.*, 2013).

The concept of image and reference endmembers is illustrated in Figure 7-25. This figure shows a high spatial resolution synthetic image consisting of a mixed pixel of tree, shadows and soil (Figure 7-25a). This image was generated with a physically-based ray-tracer (PBRT) (Pharr and Humphreys, 2004), using a virtual citrus orchard which was calibrated using field spectral measurements (Stuckens *et al.*, 2009). The resulting spectrum of the mixed pixel is shown in Figure 7-25b and image endmembers of tree canopy and soil extracted from the image are shown in Figure 7-25c. In two-dimensional array space, the Soil, Tree and Shade endmembers define a triangle, with all possible mixing combinations contained within the triangle (Figure 7-25d). Image endmembers define the vertices of the triangle representing the extremes present within the scene. Reference endmembers plot outside of the triangle defined by the image endmembers, since they are more pure representatives then the image endmembers (Figure 7-25d). In this example, the image endmember for tree includes some shadows and minor gaps and is thus a mixed pixel. The image endmember for soil is nearly identical to a reference endmember.

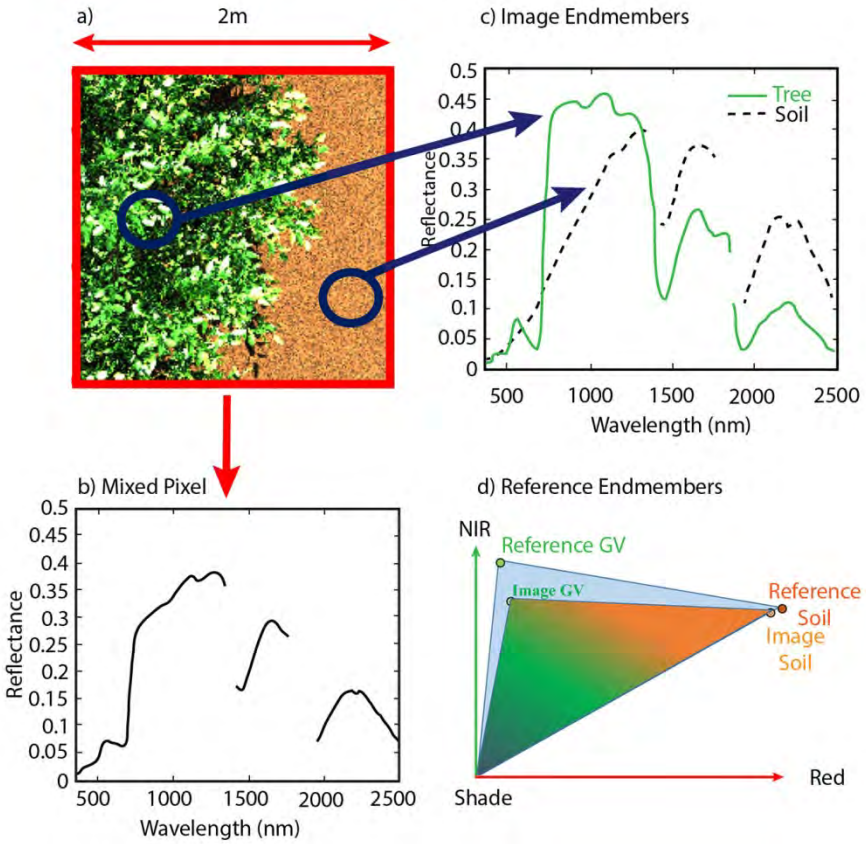

Figure 7-25. A mixed pixel consisting of three endmembers: Tree, Soil and Shade. A fine spatial resolution image is shown in (a). The resulting "mixed pixel", calculated as the average of all spectra within the field of view is shown in (b). Frame (c) shows image endmembers identified as extremes of the mixing triangle (d) for Green Vegetation and Soil. Reference endmembers (d) lie outside of the triangle defined by image endmembers, representing more pure components.

In a naturally vegetated system, common endmembers include GV (also called photosynthetic vegetation), NPV (e.g., Roberts *et al.*, 1993), soil or some other substrate and shade. For reflectance data, the shade endmember is often modeled as spectrally flat (i.e., photometric shade), although some models include a variable shade (i.e., vegetation shade: e.g., Roberts *et al.*, 1993; Fitzgerald *et al.*, 2005), while others do not include shade (e.g., Okin, 2007; Tits *et al.*, 2012). For radiance data, the shade endmember can include an atmospheric scattering component (e.g., Dennison *et al.*, 2006). Thus, a typical forested ecosystem may be modeled as a mixture of GV, exposed branches (NPV), architecturally dependent shadows (i.e., shade) and potential exposed soil. In an urban environment a common endmember would be impervious surface; ash or char would be important endmembers in a fire scar; snow or ice spectra would be important in frozen terrain; and lakes and rivers may require water spectra with sediments. Essentially, the endmembers used in a mixing model depend on the scene content and objectives of the research. They are also scale dependent. For example, a sun lit crown may be an appropriate endmember at a forest scale, but a sun lit branch or leaf may be more appropriate at sub-canopy scales.

6.3.3 *Abundance Estimation and Limitations*

Numerous approaches have been proposed to solve for fractions given a population of endmembers. Examples include constrained and weighted least squares (Shimabukuro and Smith, 1991), Gramm-Schmidt orthogonalization (e.g., Adams *et al.*, 1993), singular value decomposition (Boardman, 1989), and fully-constrained least squares (Heinz and Chang, 2001) with its variants (e.g., Wang L. *et al.*, 2013).

The unmixing process can be illustrated graphically considering cases of two endmember unmixing with no shade (Figure 7-26a), two endmember mixing with shade (Figure 7-26b), three endmember mixing with a third band (Figure 7-26c) and four endmember mixing showing a mixing volume (Figure 7-26d). In Gramm-Schmidt orthogonalization, fractions are always calculated as the projection of a mixed pixel onto mixing lines, planes or volumes defined by the endmembers. Figure 7-26a shows the case of a two-endmember mixture of soil and tree with no shade included in the model. Here the soil fraction is calculated as the distance between the tree endmember and the projection of the mixture on the line, divided by the spectral distance between the soil and tree endmembers (Figure 7-26a). Comparison to the checkerboard mixed case (Figure 7-23) shows that the form is identical except with a two-band system and two endmembers, the departure off the mixing line provides a measure of error (RMSE). When a third endmember (shade) is added, the three endmembers form a mixing triangle (Figure 7-26b). Given two bands and three endmembers, all combinations fall within a plane and there is thus no longer a measure of error. In this case, fractions are calculated as the projected distance between the mixture and the mixing line between two of the endmembers. For example, tree fraction is calculated as the distance between the mixture and the soil-shade mixing line, divided by the spectral distance between the tree endmember and this line. In the two-endmember case that involves a bright endmember and shade, the bright endmember fraction is simply the projected distance along the shade-endmember mixing line.

Adding a third wavelength with three endmembers generates a mixing plane (Figure 7-26c). In this case, the mixture is projected on to the plane and fractions are calculated as shown in Figure 7-26b. However, with three bands and three endmembers, we also have a measure of fit error, calculated as the distance between the mixed spectrum and the mixing plane (Figure 7-26c). Wavelength specific differences between

the measurement and model are the residuals. Adding a fourth endmember, defines a mixing volume (Figure 7-26d). With four endmembers and three bands, all combinations are possible and there is no RMSE. Fractions are calculated as the projected distance between the mixed pixel and a mixing plane defined by the other endmembers. Thus, the tree fraction is calculated as the distance between the mixed pixel and the mixing plane defined by Shade, NPV and Soil, divided by the distance between the tree endmember and this same plane. With four or more bands, four or fewer endmembers can be included in the model while retaining a fit error. With imaging spectrometers, there is the potential for an immense number of endmembers but, due to spectral degeneracy the number of endmembers is typically far fewer than the number of bands.

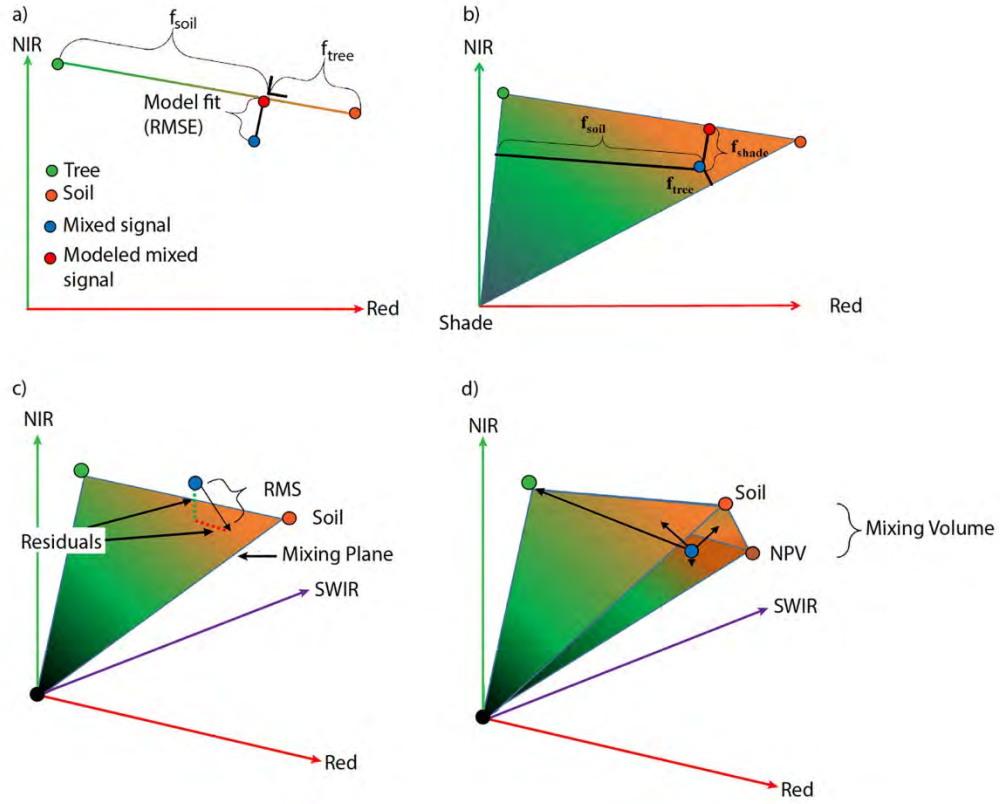

Figure 7-26. Examples of two-, three-, and four-endmember cases. Figure 7-26a shows a mixing model between tree and soil with no shade included. In 7-26b, tree and soil endmembers are the same, but a shade endmember has been added to accommodate the spectral misfit resulting in no measure of error. In 7-26c a third (SWIR) wavelength defines a mixing plane and RMSE again expresses the error between the model and measurement. Figure 7-26d shows a mixing volume consisting of four endmembers (GV, NPV, Soil and Shade). In this example, given four endmembers and three wavelengths, RMSE will be zero.

A significant limitation for all simple mixing models is the fundamental assumption that a single set of endmembers can be used to unmix an entire scene. The general assumption with a simple mixing model is that: (a) all pixels can be represented by the same set of endmembers; (b) all endmembers are equally separable and; (c) spectral variation within an endmember category is negligible. More often, the number of endmembers required to unmix a pixel varies within an image. For example, a well irrigated lawn may be modeled adequately with a two-endmember mixture consisting of GV and shade, whereas natural shrublands may require GV, Soil, NPV and Shade. In the simple case, a four endmember model applied to a pixel

that only has two materials present may generate erroneous fractions for materials that were *absent*, while a two endmember model applied to the more complex shrubland will generate error for materials that were *present*, but not included in the model. Spectral contrast is also an important concept. Materials that have high spectral contrast (e.g., GV and Soil) will be readily separable with low error, but materials that have low contrast (e.g., NPV and Soil) may be difficult to include in the same model without generating error (Roberts *et al.*, 1993; Okin *et al.*, 2001; Asner and Heidbrecht, 2002). The importance of spectral contrast is illustrated in Figure 7-27. In this example, four endmembers (i.e., GV, NPV, Soil and Shade) and three wavelengths are shown. The endmembers define a mixing volume. High spectral contrast between GV, Soil and Shade results in physically reasonable fraction estimates. Low spectral contrast between NPV and Soil is manifested as a mixing volume that only shows minor departures from a mixing plane. Even minor variation that causes mixed spectra to plot outside of the mixing volume will result in large super positive (>100%) or negative fractions.

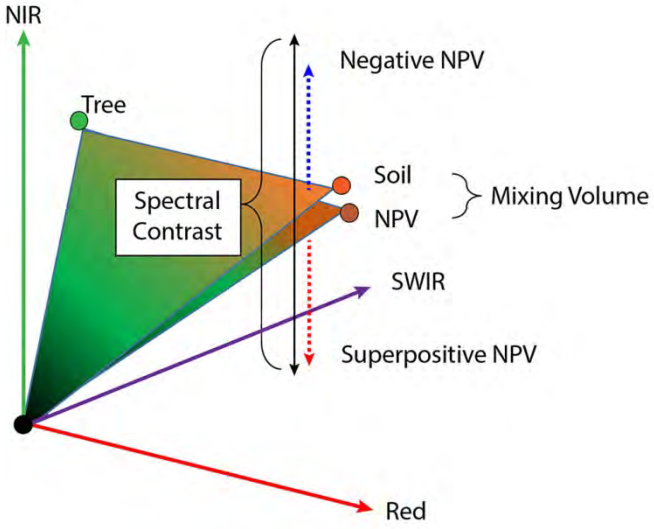

Figure 7-27. Spectral contrast can be defined as the spectral difference between one material and another within a range of wavelengths. Tree, Soil and Shade spectra have unique spectra at many wavelengths and thus have a high spectral contrast, are easily discriminated, and can be unmixed at high accuracy. Soils and NPV spectra can be very similar except in the SWIR, where moderately strong ligno-cellulose bands in NPV distinguish them (Roberts *et al.*, 1993). This low contrast translates to a relatively "thin" mixing volume, generating superpositive (>100%) or negative fractions when a mixture lies only slightly outside of the mixing volume defined by the endmembers.

Natural spectral variation within the same endmember (i.e., endmember variability) is also a source of error. Spectral differences between the endmember and the actual materials in the modeled image will result in fraction error and/or increased RMSE. For example, a broadleaf deciduous plant endmember used to unmix a conifer spectrum will generate errors in fractions as well as model fit. Techniques have been developed to minimize some of these errors. For example, Somers *et al.* (2009b) proposed a means to suppress the impact of endmember variability by selecting portions of the spectrum that are the least variable within a class. Alternatively, spectral contrast between endmember classes can be accentuated, as in van der Meer and de Jong (2000). Non-linear mixing models, such as Artificial Neural Networks (ANN) can accommodate variability within an endmember class as well (Carpenter *et al.*, 1999). The issue of endmember variability is discussed in more detail in Section 6.3.5.

6.3.4 *Example Simple Mixing Model*

To illustrate some of the potential and weaknesses of the simple mixing model, an example is shown of a mixed natural and anthropogenic scene imaged by AVIRIS (Figure 7-28). This data set was acquired on July 19, 2011 to evaluate the relationship between plant species, fractional cover, and land surface temperature (Roberts *et al.*, 2015); and, to map GV, NPV (i.e., litter, stems and bark), soil, rock, roof and paved surfaces in the urbanized zones (Roberts *et al.*, 2016).

In this example, image endmembers were extracted from reference polygons defining the major biotic and abiotic components within the scene (Figure 7-28d). Iterative Endmember Selection (IES) was used to identify a subset of 90 spectra that produced accurate fractions for all of the major components (Roth *et al.*, 2012) (see Section 6.3.5). From that set, one GV, one Soil, and one NPV endmember was selected as the single spectrum for each class that modeled the most area within the natural portions of the scene. A commercial roof spectrum is included to show how some impervious surfaces are spectrally distinct from soils. Lowest spectral contrast is apparent between the Soil and NPV spectra.

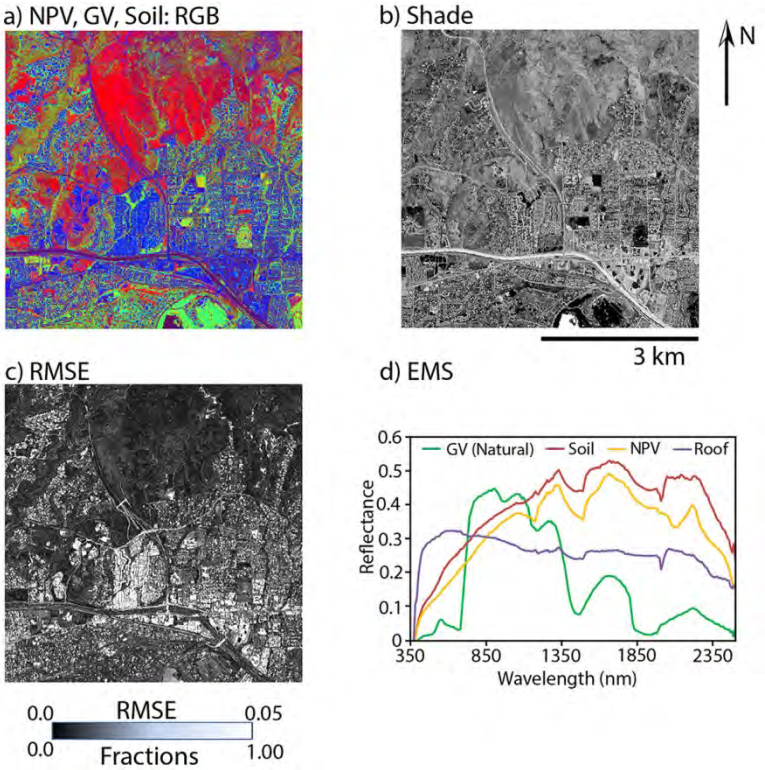

Figure 7-28. (a) Fraction image showing NPV, GV and Soil displayed as RGB. A shade fraction image is shown in (b) and RMSE is shown in (c). These images were generated using a four-endmember model of NPV, GV, Soil and Shade using the spectra shown in (d).

Figure 7-28 shows an example from a subset of AVIRIS imagery in the interface between natural vegetation to the north and urban surfaces to the south. In this example, NPV has high fractions along the northern half of the scene, mapping large areas of senesced grasslands shown in magenta (Figure 7-28a). GV is most abundant along riparian corridors in the north, with the highest GV fractions found in the southern portion of the scene for irrigated grasses and parks. Soil fraction is highest in urbanized areas to the south, where impervious surfaces are erroneously mapped as soils because they are most similar spectrally to soils.

Shade fractions are highest over water in the far south and over dark surfaces such as asphalt roads (Figure 7-28b). High shade fractions are also evident on northeast facing slopes and in the more forested portions of the scene. RMSE errors are low in most of the natural vegetation, but are very high in the urbanized areas, where the Soil endmember fits impervious surface spectra poorly, resulting in high RMSE.

6.3.5 *Multiple Endmember Models*

Limitations of simple mixing models were first recognized by Sabol *et al.* (1992). In that seminal study, the authors evaluated the impact of sensor noise, the number of wavelengths and the number of endmembers on the accuracy of SMA. They showed that fraction errors increased with an increase in sensor noise; were highest for materials with low spectral contrast (i.e., Soil and NPV); were minimized when the correct number of endmembers was used in the model; and were lower for hyperspectral data compared to broad band data. To illustrate endmember variability, we show spectra of two of seven endmember classes present in the AVIRIS scene shown in Figure 7-28. Here, we selected 25 GV spectra from nine vegetation classes and 33 roof spectra from eight roof classes. Spectral variability is present within a single species (e.g., the curve for avocado trees shown in magenta color in 7-29a) or commercial roof types (commercial roofs shown in turquoise in 7-29b), and also occurs within broader classes of materials (e.g., willow vs. oak or commercial vs. red-tile roof). All of this variability must be taken into account when applying SMA to a scene, yet a single pixel still typically requires only three to four endmembers to account for the mixture with low error.

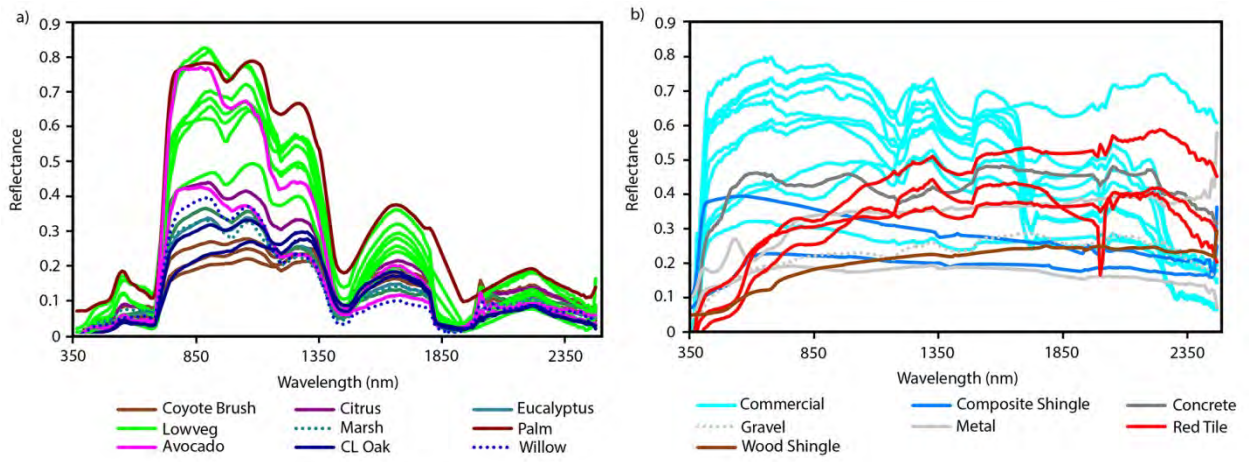

Figure 7-29. Examples of nine GV spectra (a) and seven commercial roof spectra (b) extracted from 2011 AVIRIS data are used as endmembers.

Numerous solutions have been proposed to address the impact of "endmember variability" within an endmember class; and/or, the requirement that the number and identity of endmembers required to unmix a pixel varies from one pixel to the next (Somers *et al.*, 2011). Among the first were Roberts *et al.* (1998), who proposed Multiple-Endmember Spectral Mixture Analysis (MESMA). Using MESMA, the number and types of endmembers are varied on a per-pixel basis. Candidate models are selected from a pre-defined spectral library, with viable models constrained such that they meet a fraction requirement (typically set at physically reasonable fractions, accommodating some noise) and meet a fit constraint, typically set by a maximum RMSE. Given multiple candidates for each pixel, MESMA selects the model that provides the

lowest RMSE (Painter *et al.*, 1998). In the two-endmember case involving shade and a bright endmember, MESMA has been used as a classifier based on the type of endmember selected for that pixel (Dennison and Roberts, 2003a). Since the introduction of MESMA, spectral variation within an endmember population has become recognized widely as a challenge for SMA (Somers *et al.*, 2011).

A similar approach to MESMA, in which the numbers of endmembers are fixed, but are allowed to vary per pixel, was proposed by Maselli (1998). Rogge *et al.* (2006) proposed iterative spectral unmixing, in which a fixed set of endmembers is used, but the number of endmembers is allowed to vary on a per pixel basis. Bateson *et al.* (2000) proposed the concept of endmember bundles, where multiple representatives of each endmember class are included in a spectral library. Using the endmember bundle concept, Asner and Heidbrecht (2002) developed Automatic Montecarlo Unmixing (AutoMCU), by which candidate spectra for each endmember class are drawn randomly from a population and used to generate statistical estimates of fractional cover and an error measure (i.e., standard deviation of the fractions). AutoMCU has the advantage that it is completely automated, provided a representative spectral library for a region has been developed. As examples, AutoMCU has been used to estimate changes in fractional cover associated with selective logging (Asner *et al.*, 2004), arid land degradation (Asner and Heidebrecht, 2003; 2005) and pasture degradation (Davidson *et al.*, 2008).

Iterative unmixing procedures can become unwieldy if the number of potential endmembers in each class becomes large. Results can also become difficult to interpret. As a solution, several pre-processing steps have been suggested for iteratively unmixing methods described above to ensure that an optimal spectral library is used as input. Roberts *et al.* (1997a) proposed an additional component to MESMA, in which a candidate spectral library developed for MESMA is subset to identify the endmember sets that provide the best separation between endmembers with the fewest number of endmembers used to unmix the image. Several approaches have been proposed to improve endmember separability while lowering the number of endmembers in a spectral library. Among these are: (a) Count-based endmember selection (COB) (Roberts *et al.*, 2003); (b) Endmember Average RMSE (EAR) (Dennison and Roberts, 2003a); (c) Mean Average Spectral Angle (MASA) (Dennison *et al.*, 2004); and most recently (d) IES (Schaaf *et al.*, 2011; Roth *et al.*, 2012). COB selects the subset of endmembers that models the largest number of spectra within its class. EAR operates within each class to select endmembers that model their class with the lowest average RMSE. MASA operates similar to EAR but uses the mean spectral angle as the fit metric.

COB, EAR and MASA do not account for potential confusion between endmember classes, since each metric is based solely on performance within the same class. IES is an automated approach that selects endmembers that best model their own class while minimizing confusion with other classes as measured by the kappa coefficient (Congalton, 1991). For each iteration in IES, the endmember that best improves kappa is added to the library. To avoid issues associated with sub-optimal initial selections, IES tests all previous endmembers selected by removing them from the library and evaluating whether endmember removal increases kappa. IES continues to add and subtract endmembers until kappa stabilizes (Schaaf *et al.*, 2011; Roth *et al.*, 2012). Another approach to optimizing endmember library definition and size was suggested by Iordache *et al.* (2014a) in their Hyperspectral Unmixing via Multiple Signal Classification and Collaborative Sparse Regression (MUSIC-CSR) algorithm. Based on the goodness of fit between the image

to be unmixed and the reference endmember library, signatures that do not contribute to explaining the variability in the image are discarded from the library.

Numerous studies have used MESMA with endmember selection to:

- Map plant species (Dennison and Roberts, 2003a; Li *et al.*, 2005; Rosso *et al.*, 2005; Youngentob *et al.*, 2011; Roth *et al.*, 2012; Roberts *et al.*, 2015);
- Monitor crop vitality (Iordache *et al.*, 2014b);
- Map vegetation and impervious fractions in urban areas (Powell *et al.*, 2007; Franke *et al.*, 2009; Roberts *et al.*, 2012; Demarchi *et al.*, 2012);
- Map arid landforms (Ballantine *et al.*, 2005); and,
- Map semi-arid vegetation cover (Okin *et al.*, 2001; Thorp *et al.*, 2013).

Non-biotic studies include retrieving snow covered area and grain size (Painter *et al.*, 1998; 2003), fire temperature and area (Dennison *et al.*, 2006; Eckmann *et al.*, 2008), river sediment concentrations (Kilham and Roberts, 2011), fire severity (Quintano *et al.*, 2013), surface expression of coal mines (Fernandez-Manso *et al.*, 2012) and mapping lunar materials (Li and Mustard, 2003). Recently, Somers *et al.* (2012), Deng and Wu (2013) and Zare *et al.* (2013) extended the MESMA concept to the spatial domain, proposing automated approaches for identifying endmember subsets that allow the types of endmembers to vary within a region of a scene while automatically extracting the optimal subset from within that region.

Another option for accounting endmember variability is to suppress their impacts through strategic band selection. Asner and Lobell (2000) proposed autoSWIR, in which spectra are normalized to a SWIR-2 band that maximizes separability between soil, NPV and GV in the SWIR while minimizing the effect of variable brightness and multiple-scattering. Use of the 2078*nm* band, followed by Monte-Carlo Unmixing generated stable, accurate fractions of NPV, soil, and GV at the Jornada Long-Term Ecological Site (LTER) site in New Mexico. Somers *et al.* (2010a) proposed Stable Zone Unmixing (SZU), in which a subset of bands is selected that minimizes spectral variation within a class, while optimizing spectral separability between classes. Somers *et al.* (2010a) applied this concept to a set of scenarios generated from *in situ* measured hyperspectral data. The scenarios covered both urban and natural environments under differing conditions. Furthermore, refinements included development of Uncorrelated Stable Zone Unmixing (USZU), in which band subsets were reduced further to remove highly correlated bands that provided little improvement in separation (Somers and Asner, 2013) and weighted SMA (wSMA), in which spectral bands less sensitive to endmember variability are given a higher weight in SMA (Somers *et al.*, 2009b). SZU has been applied to imaging spectrometry to improve map accuracy of vegetation impacted by marine oil spills (Peterson *et al.*, 2015). USZU has been applied to time series data to improve separation between native and invasive tree species in Hawaii (Somers and Asner, 2013; 2014), while wSMA has been applied to hyperspectral data to improve canopy fraction estimates in an orange grove (Somers *et al.*, 2009b), and to monitor defoliation in mixed-aged Eucalyptus plantations using Landsat and Hyperion data (Somers *et al.*, 2010b).

6.3.6 *Example of Multiple-Endmember Spectral Mixture Analysis*

To illustrate the potential of MESMA, an example is included using MESMA to unmix the same AVIRIS scene used in Section 6.3.4. However, in this analysis endmember variability is accommodated and the numbers of endmembers are allowed to vary on a per-pixel basis. Endmembers were selected initially using

IES, generating a library of 563 endmembers. This library was further reduced by removing endmembers that performed well in the library, but not on the image (e.g., Powell *et al.*, 2007; Roberts *et al.*, 2012). This reduced library, consisting of 376 spectra, became the library used to classify urban images into 23 classes based on the endmember that best fit a mixture between a bright endmember and shade (Figure 7-30d). Classification is a different process than sub-pixel mapping. For example, a mixed class such as an orchard may be a viable class on a map, but may actually consist of a mixture between two other endmember classes, e.g., Soil and GV. To unmix a scene into fractions of pure endmember classes, all mixed-class spectra should be removed. Removing mixed spectra further reduced the library to 258 endmembers. However, this still represents an unwieldy number of combinations and also includes considerable spectral degeneracy – spectra that are distinct in two endmember models, but not distinct when included in a three or four endmember model. A procedure was developed to reduce spectral degeneracy, resulting in a final model consisting of 90 spectra. For a more detailed description of this process see Roberts *et al.* (2016). This final library included 25 GV spectra, 7 NPV, 3 Rocks, 7 Soils, 15 paved spectra and 33 roof spectra. Both natural and anthropogenic materials are incorporated into the model, and several surfaces that could not be modeled separately using SMA (i.e., rocks, paved, roof) are now modeled.

Comparison of Figures 7-28 and 7-30 illustrates important differences between simple SMA and MESMA. In the first frame, the NPV-GV-Soil model from MESMA is similar for NPV, although there tends to be more pure pixels (i.e., pixels mapped as NPV and shade). Endmember variability in NPV tends to be modeled as a sub-pixel fraction of soil or a minor amount of GV. The GV fraction image shows high GV in the same places, but overall the GV fraction appears higher in MESMA. This is because endmember variability manifests itself as brightness differences within GV, and differences in NIR-to-red contrast within a plant spectrum or between species, is modeled as modest fractions of soil, NPV or shade; or possibly negative soil or NPV fractions. The most obvious differences are found in urban areas, which are modeled as Soil in simple SMA, but modeled as Roof or Paved Ground in MESMA (Figure 7-30b). The Rock-Paved ground-Roof model (Figure 7-28b) distinguishes clearly between impervious and non-impervious surfaces and also distinguishes clearly between paved impervious (green) and roof materials (blue). However, confusion between rock fractions and paved ground are evident in some areas. Overall, the RMSE is considerably lower in the MESMA model (Figure 7-30c compared to Figure 7-28c) with much lower RMSE in urbanized areas and only minor decreases in RMSE in natural areas; notably senesced grasslands which were modeled as NPV and shade in the MESMA model.

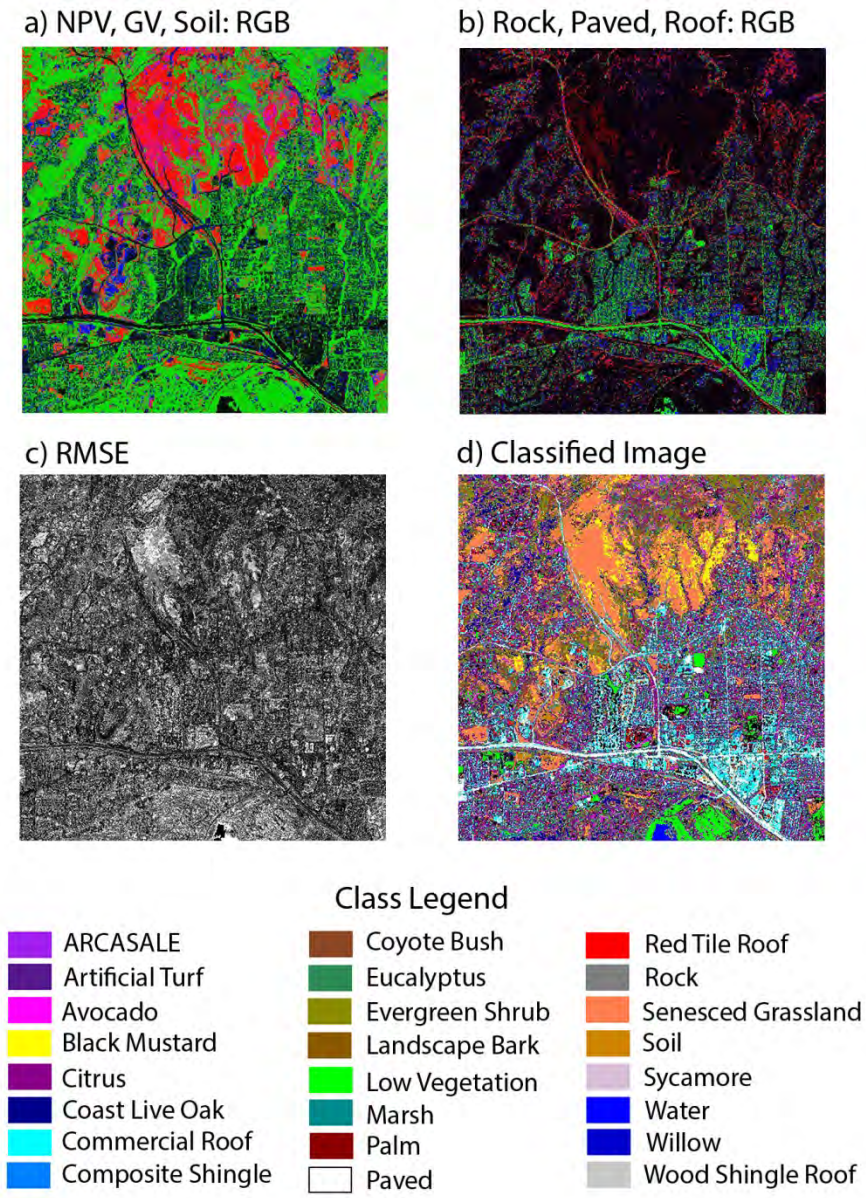

Figure 7-30. Mixing models generated using MESMA and a 90 endmember spectral library. (a) an NPV-GV-Soil mixing model displayed as RGB; (b) a Rock-Paved-Roof model; and (c) an RMSE image. It is also possible to use a two-endmember model to classify an image based on the endmember that is selected. This is illustrated in (d), generated from a 376 endmember spectral library that included spectrally degenerate materials within a class (e.g., two GV spectra from different species that are similar spectrally) as well as mixed pixels representing a class (e.g., avocado orchards containing mixture of canopy and soil). All fractions were shade normalized.

To illustrate further the advantages of MESMA over the simple mixing model, Figure 7-31 compares fractions from the mixing models to fractions derived from validation polygons used by Roberts *et al.* (2012) and Roberts *et al.* (2016). Fractions were validated for simple SMA using a five endmember model (NPV, GV, SOIL, ROOF, PAVED GROUND), and (IMPERVIOUS) using endmembers shown in Figure 7-28d, and the 90 endmember model shown in Figure 7-30.

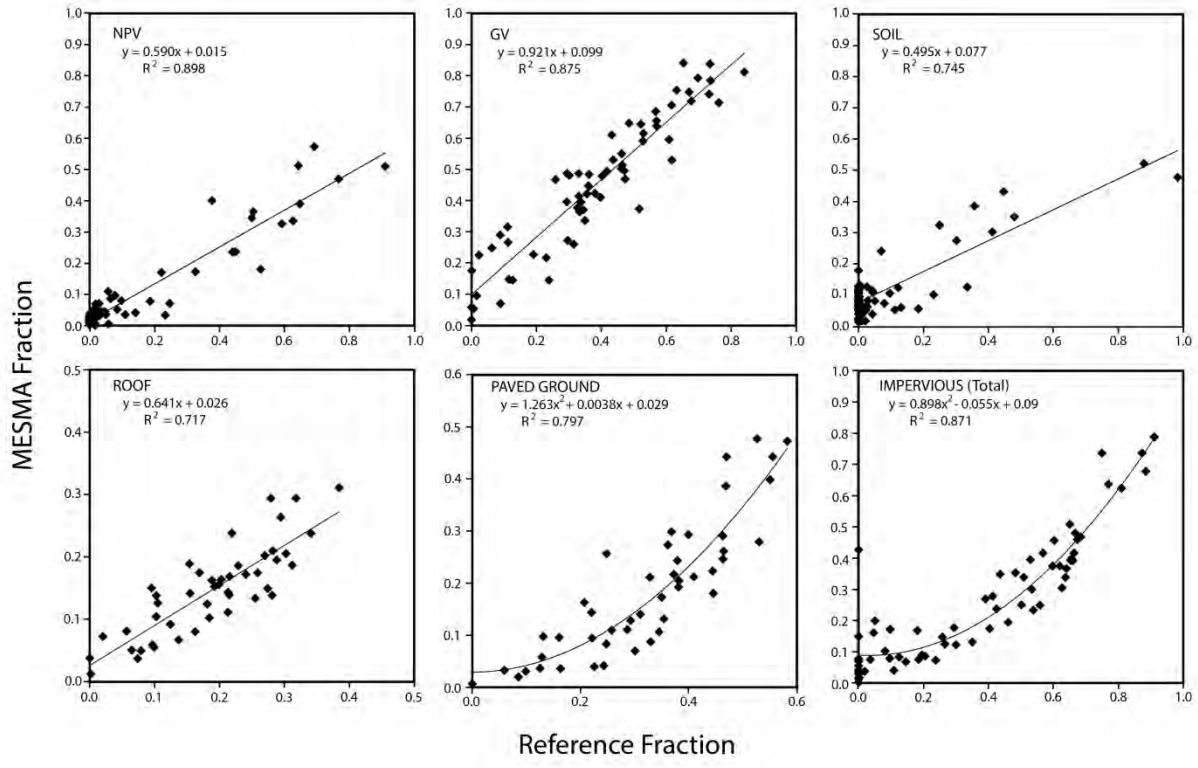

Figure 7-31. Fraction validation for NPV, GV, SOIL, ROOF, PAVED GROUND and IMPERVIOUS (Roof+Road). Reference fractions are shown on the x-axis; MESMA fractions are on the y-axis.

MESMA fractions are highly correlated linearly to NPV, GV, Soil and Roof fractions, with r^2 values ranging from a high of nearly 0.9 for NPV to a low of 0.745 for Soil (Figure 7-31). Paved ground, and the sum of Paved Ground and Roof is also highly correlated, but the relationship is non-linear, demonstrating that MESMA underestimates the paved ground fraction except when the Paved Ground category is high. With the exception of the GV fraction, it should be noted that MESMA underestimates fractional cover for most surfaces, likely because it is failing to identify every material within a mixed pixel (Slope < 1.0).

Simple SMA produces lower accuracies than MESMA for all materials except GV. This high accuracy is a product of the high spectral contrast of GV relative to the other materials in the scene. NPV fractions are also highly correlated and, in fact, show a near 1:1 relationship between the reference fractions and the model, even though the scatter is significantly higher (Figure 7-32). This suggests that MESMA is most likely adding endmembers erroneously to spectra that were better modeled as either pure NPV or a mixture of NPV with minor amounts of exposed soil. Impervious fractions show a remarkably similar pattern between the models, but the Soil fraction has much lower accuracy. Simple SMA cannot accommodate soil, NPV and Impervious without generating significant fraction errors.

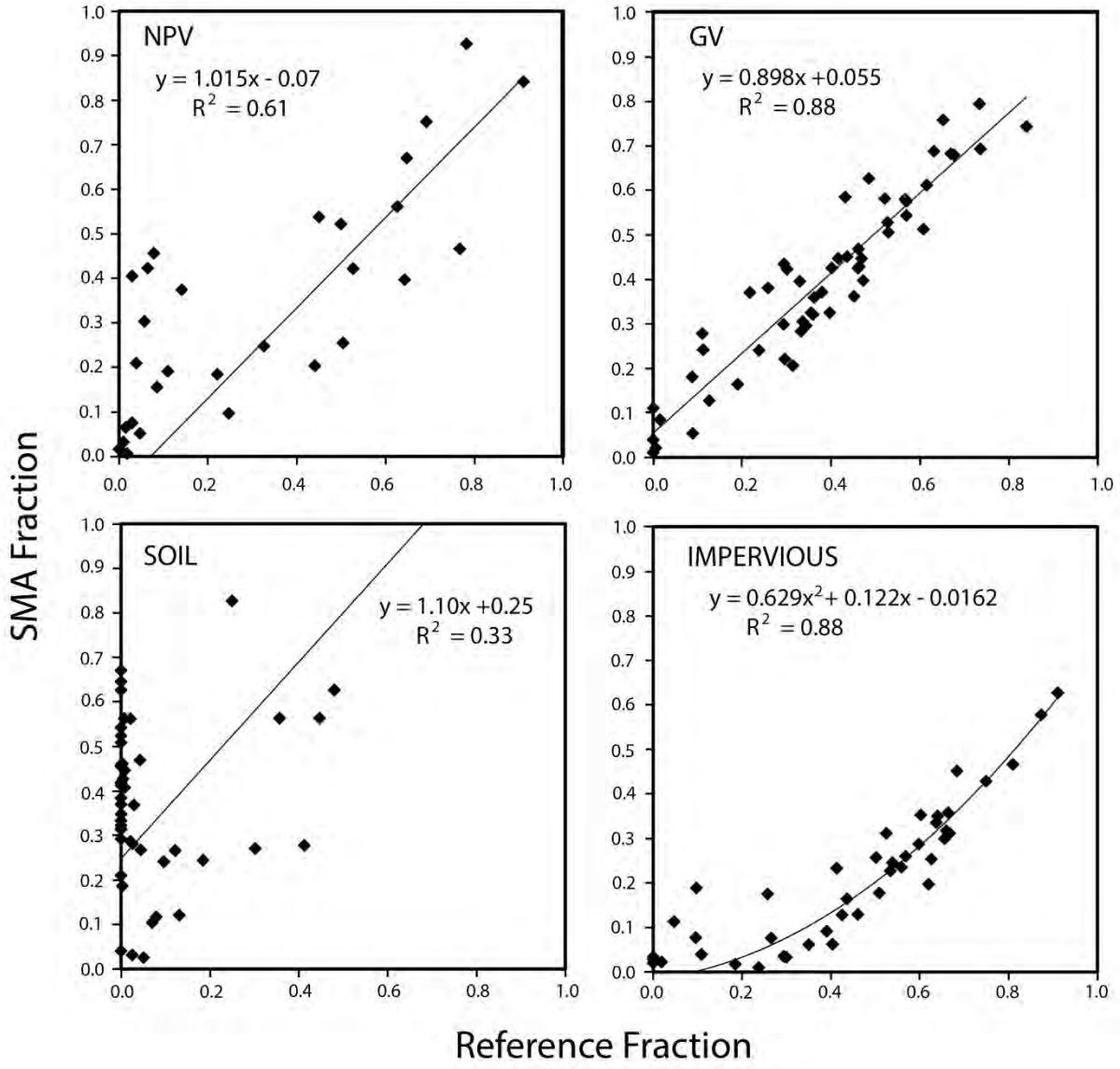

Figure 7-32. Fraction validation for NPV (litter, bark and stems), GV (green leaves), Soil and Impervious (Roof). Reference fractions are shown on the x-axis, SMA fractions on the y-axis.

6.4 *Non-linear Unmixing*

Non-linear mixing results when photons interact with more than one material along the path from source target to sensor, as described in Section 6.2. One early solution to the problem with mineral mixtures was proposed by Shipman and Adams (1987), who transformed mineral spectra to single scattering albedo, effectively linearizing the problem. Similarly, Mertes *et al.* (1993) linearized the mixing problem by developing a look up table between estimated sediment fraction and actual sediment fractions in water/ sediment mixtures. Sediment concentrations are non-linearly related to water reflectance because increased scattering with elevated sediment concentrations increases water absorption along the path, resulting in a progressively smaller increase in reflectance for each equal increase in sediment concentrations. By constructing a

look up table between sediment fraction, retrieved using SMA, and actual concentrations, the authors could estimate sediment concentrations accurately.

Non-linear mixing has the potential of impacting SMA significantly with vegetation-soil mixtures because leaves transmit and scatter NIR radiation (Roberts, 1991; Huete, 1987). As an illustration of how much scattering occurs, an image of a highly transparent maple leaf placed in front of a white and black background is shown (Figure 7-33). Reflectance transects of red, green and NIR show that leaf reflectance is enhanced by almost a factor of two in the NIR compared to the same leaf placed over a black background. A prominent NIR halo surrounds the leaf with NIR reflectance increasing and exceeding 100% at the unshaded edge of paper adjacent to the leaf. Over the black background, and at red wavelengths where leaves are highly absorbing, leaf reflectance does not change and no halo is present.

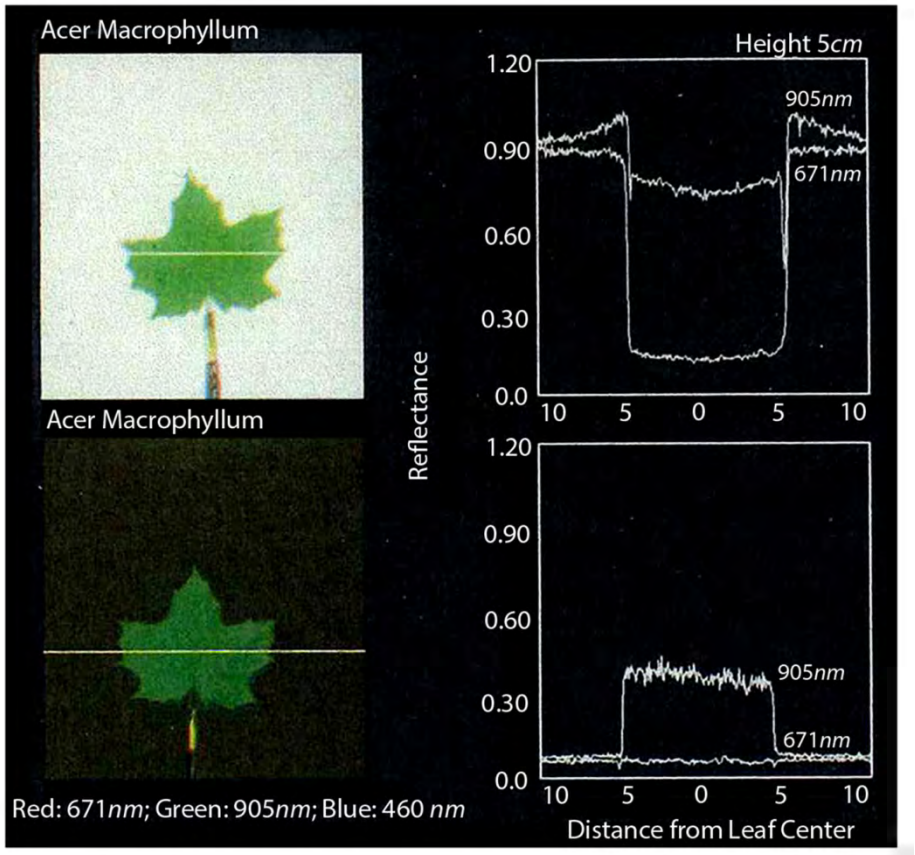

Figure 7-33. Digital photograph of the same maple leaf positioned over a white (top) and black background. Colors displaced are Red (671*nm*), NIR (905*nm*) and Blue (460*nm*) as RGB. From Roberts (1991).

Importantly, the effect of multiple NIR scattering on endmembers can be modeled. Roberts *et al.* (1990) developed a simple photon scattering model that allowed up to eight multiple scattering events between a simulated scene made up of horizontal leaves of varying dimensions placed at varying heights above a surface. Comparison between modeled, and measured simulated leaves (Roberts, 1991) demonstrated excellent correspondence, suggesting that the model was capable of simulating the interaction between two scattering surfaces well (Figure 7-34).

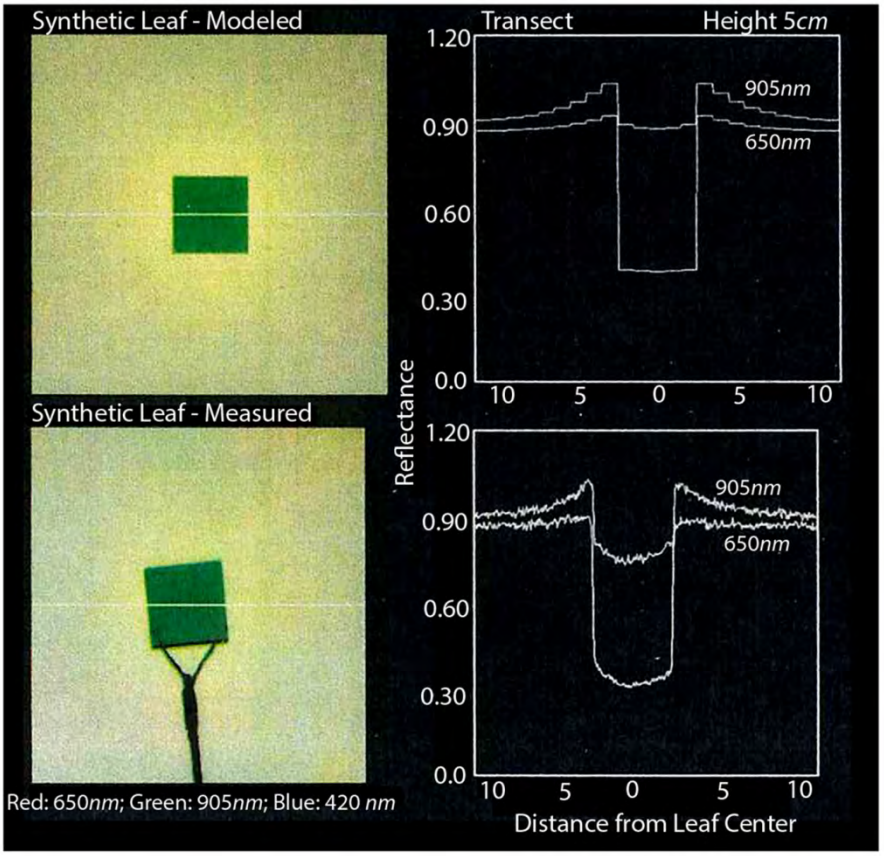

Figure 7-34. Computer simulation of a synthetic leaf placed over a white background (top), compared to a measured image using a digital camera. Simulations were run using the same reflectance and transmittance properties for the synthetic leaf and same height above the white background. Elevated reflectance is observed in the NIR along the margins of the synthetic leaf and on the adjacent white background. The minimum pixel size of computer simulations was one centimeter.

A computer model offers the opportunity to evaluate how multiple scattering impacts endmembers and spectral mixture models. Roberts (1991) evaluated how the spectra of a substrate and overlying leaf changed as a function of substrate reflectance and percent cover (Figure 7-35) Considering three cases of sparse (1%), intermediate (25%) and dense cover (>70%), one can observe significant changes in the NIR reflectance of the substrate and simulated leaf endmember. At 1% cover, leaf reflectance is influenced strongly by adjacent and shaded substrate, resulting in a minor increase in red, but significant increase in NIR reflectance. At the same time, the impact of leaf on adjacent substrate is minimal because cover is low. At intermediate cover, leaf NIR reflectance begins to drop as more substrate is shaded, while NIR reflectance of the substrate increases as more photons scatter between leaves and substrate. At dense cover, leaf NIR reflectance is still 20% higher than it would be over a black, non-scattering background, but substrate reflectance is now highly elevated and, in fact, has taken on some of the spectral properties of a leaf.

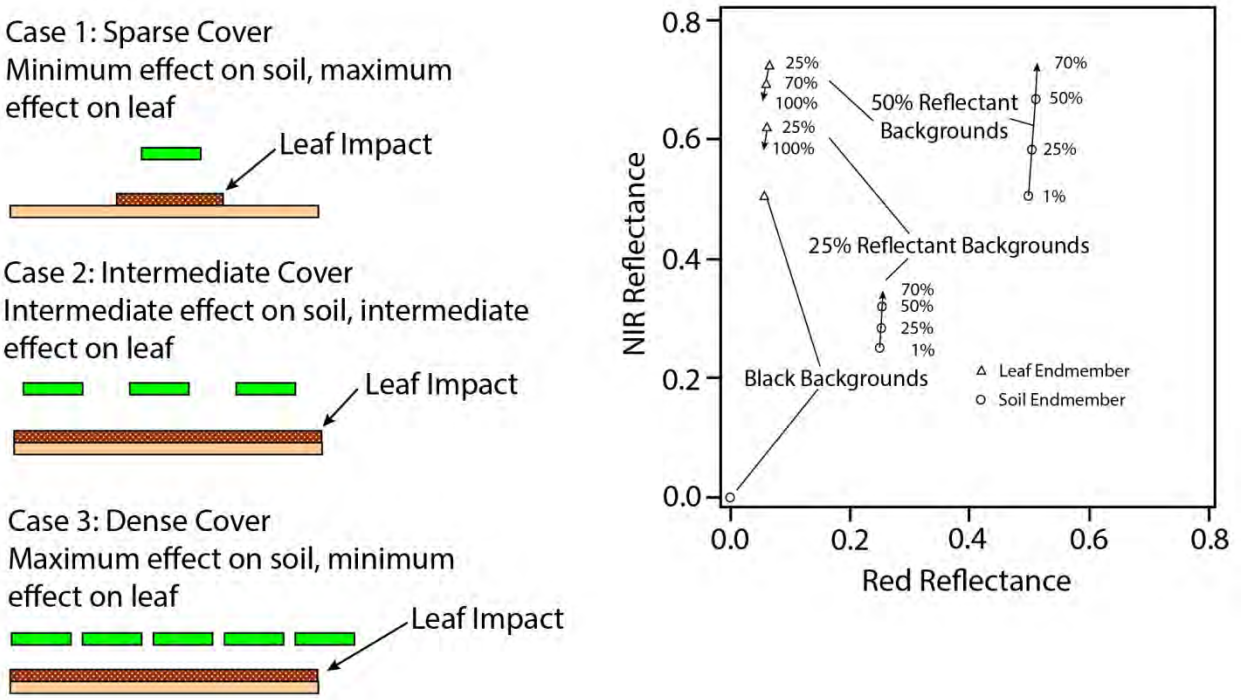

Figure 7-35. Computer simulation of how leaf and substrate reflectance change as a function of fractional cover and substrate reflectance. Three cases are illustrated graphically on the left, the case of sparse cover (Case 1), intermediate cover (Case 2) and dense cover (Case 3). A scatter plot showing changes in NIR and red reflectance is shown on the right. Courtesy, D.A. Roberts.

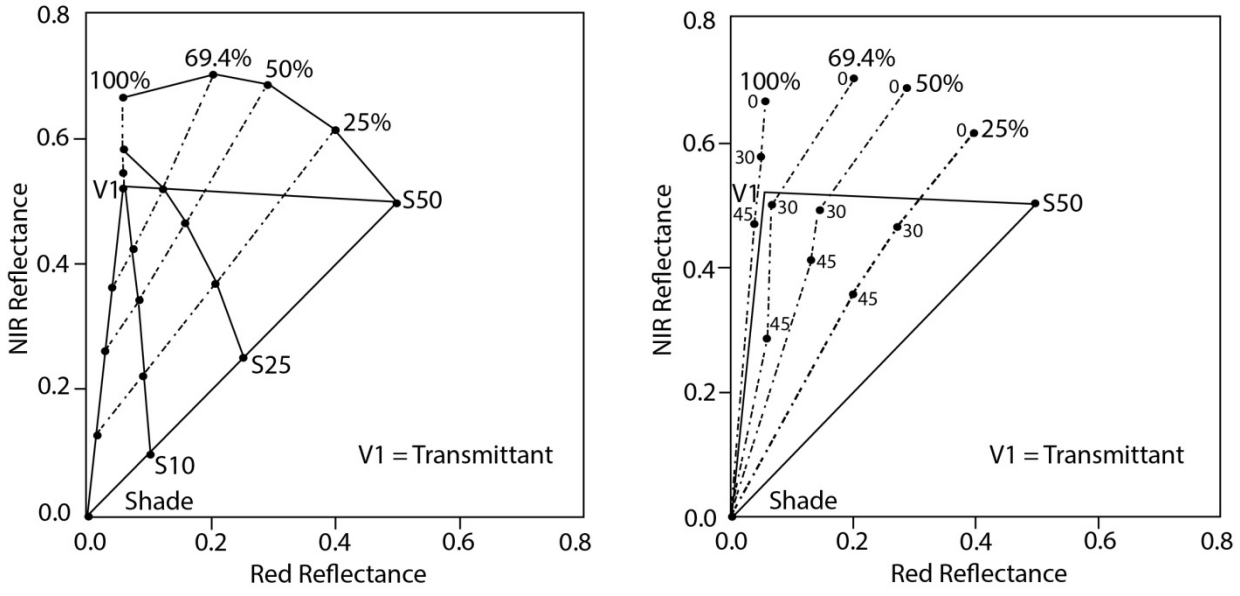

Figure 7-36. NIR to red scatterplot showing how mixing lines of equal cover change as a function of substrate reflectance (left) and zenith angle (right). At nadir illumination, leaf reflectance is over 20% higher than it would be in a non-transmittant leaf. The mixing line between 100% substrate (S50) and 100% leaf is curved and lines of equal fractional are subparallel to the substrate-shade mixing line. As solar zenith increases, and shade increases, mixing lines of equal cover bend towards 0% red, because leaves are nearly opaque in the red, but scatter NIR light.

Computer simulations make it possible to observe how the relationship between NIR and red reflectance changes as a function of fractional cover, substrate reflectance and solar zenith (Figure 7-36). The strictly linear mixing case with no scattering is illustrated by a mixing triangle between leaf (V1), substrate (S50) and shade (0% reflectance). In the presence of transparent leaves and NIR scattering, mixing lines between pure substrate and pure leaf (GV) are curved and lines of equal GV cover are subparallel to the substrate-shade mixing line (Figure 7-36, left). By varying solar zenith but fixing substrate reflectance at 50%, lines of equal fractional cover bend towards 0% red reflectance. This is because shadows cast by leaves include NIR transmitted/scattered photons, but few red photons due to chlorophyll absorption. We find it notable that computer simulations in Figure 7-36, are similar to measured relationships observed by Huete *et al.* (1985), when varying canopy fractional cover and substrate reflectance. Using a radiosity-based radiative transfer model, Borel and Gerstl (1994) demonstrated similar, significant impacts of multiple NIR scattering on canopy and substrate reflectance. They also evaluated non-vegetated, rough surfaces, demonstrating that non-linear mixing is significant for all scattering surfaces, not just leaf-substrate mixtures.

When linear SMA with non-scattering endmembers is used to unmix images where NIR-scattering is occurring, the linear model overestimates the GV fraction, underestimates shade but determines the soil fraction correctly (Figure 7-37). This is because the scattered radiation has the spectral signature of a plant and thus adjacent, unshaded substrate is modeled as having some plant cover, and plant-shade substrate is modeled as a mixture of vegetation and shade. While this suggests that substrate fraction is correctly modeled, this only holds true as long as shade is included in the model. If, however, the shade fraction is not included, or the shade fraction is normalized out (i.e., all non-shade fractions divided by the sum of all fractions absent shade), this model suggests that GV will be overestimated, and substrate fraction underestimated. The magnitude of error will depend upon leaf/canopy transmittance (i.e., greater opacity equals decreased non-linearity) and the brightness of adjacent substrates (i.e., darker substrates will reduce scattering).

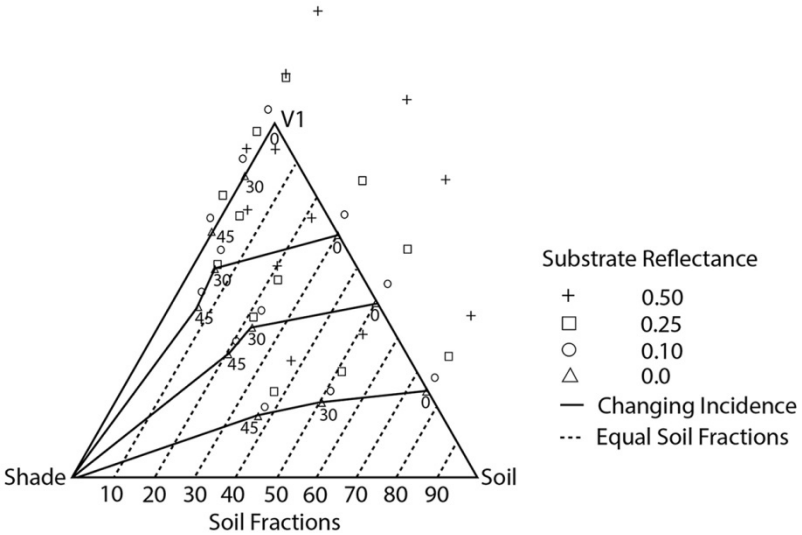

Figure 7-37. Ternary diagram showing fraction estimates from a linear mixing model applied to simulated mixtures of GV, substrate and shade allowing for multiple scattering. Mixing lines are parallel to the lines of equal soil fraction, but exceed 100% for GV (V1). GV is overestimated in all cases, and shade is underestimated.

Since all surfaces scatter radiation to some extent, non-linear mixing is present in all cases where two spectrally contrasting materials are present in the same pixel. Various approaches have been proposed to minimize the impact of non-linear mixing on estimated fractions. Fundamentally, non-linear mixing can be viewed as a scale-dependent process. Thus, a mineral mixture between a highly absorbing and non-absorbing mineral will form a non-linear mixture, yet two soils placed adjacent to each other on a flat surface will form a linear mixture. Non-linearity can also be accounted for by incorporating multiple scattering into endmembers. Thus, for example, a single leaf may represent an inappropriate GV endmember, but a branch or canopy spectrum, which includes NIR scattering, may represent a better candidate. However, because the canopy spectrum influences adjacent substrates and may be influenced by adjacent substrates, this does not fully remove the effect of non-linearity (Somers *et al.*, 2009a).

Roberts *et al.* (1993) proposed using "vegetation shade" combined with leaf stacks as a way of reducing the impact of non-linearity. However, because vegetation shade itself will vary (Fitzgerald *et al.*, 2005) this may not be a viable solution. Ray and Murray (1996) proposed a non-linear mixing model in which the interactive terms are included in the model as the multiplicative product between pure endmember spectra. Thus a mixing model would include pure GV, pure soil and GV-soil spectrum to model interaction between them. Chen and Vierling (2006) also observed significant non-linear effects when comparing spectra measured from a balloon system, to modeled spectra based on field spectra and estimated surface fractions. Similar to Ray and Murray (1996) they proposed a non-linear model that included interactive terms. Somers *et al.* (2009a), when comparing actual surface fractions to linear models of surface fractions in an orange orchard, found similar significant non-linear effects. They also proposed a non-linear model that included interactive terms, but partitioned the error, artificial fraction of the interactive term, back into the original cover estimates with the partitions varying depending upon the cover of the main components. Finally, there are numerous situations where non-linear mixing is minimized. For example, mixing models that only use non-scattering wavelengths (visible, SWIR) tend to be more linear (Asner and Lobell, 2000; Chen and Vierling, 2006). Alternatively, surfaces such as snow-covered terrain mixed with conifer forest also represent a more linear case. Conifers tend to be less transparent than broadleaf deciduous trees (Roberts *et al.*, 2004) while snow reflectance decreases significantly as wavelength increases in the NIR, also reducing multiple scattering opportunities.

Heylen *et al.* (2014) provided a review of non-linear mixing. However, considerable research is still needed to address the potential significance of non-linear mixing. In-depth analysis of nonlinear mixing in vegetated areas is currently hampered by a critical lack of well-validated datasets. It can also be difficult to separate the impact of endmember variability from the impact of non-linear mixing. A full quantitative and qualitative assessment of nonlinear mixing effects in vegetated areas would provide crucial inputs for calibrating and developing nonlinear mixture models, better modeling the actual mixing process. To this end, datasets consisting of mixtures of tree, soil, weeds and shade have been designed and made freely available (Tits *et al.*, 2014). With the exact cover fractions (CFs) as well as the exact spectral signature for each component known for each pixel and for each component, the datasets enable an objective evaluation of different nonlinear mixing models, as exemplified in Dobigeon *et al.* (2014) for a range of bilinear mixing models. However, these remain simulated datasets, and the design of a real hyperspectral benchmark dataset

remains crucial in the design and the operational implementation of high-performance nonlinear mixing models.

6.5 *Conclusions*

SMA is a powerful technique that has been applied widely to broad band and hyperspectral data to solve problems. Since its first introduction in 1971, it has evolved considerably and remains an area of very active research and development. A critical element of SMA is endmember selection and the quality of endmembers relates to the validity of the retrieved fractions. Another critical element is the problem of addressing endmember variability in which one spectrum is not representative of the diversity of spectra within one class. For example, it is neither reasonable, nor desirable, to attempt to define a single vegetation spectrum that can unmix every possible type of vegetation on Earth through all seasons and years. Approaches have been developed to suppress the impact of endmember variability, while alternate approaches embrace that diversity to improve material discrimination.

Currently, there are several areas where SMA could be improved. First, there is a general absence of high-quality validation data sets. Given the immense diversity of techniques developed to extract endmembers and retrieve CFs, it is critical that the community gain a better understanding of the advantages and disadvantages of each approach. The absence of key test data sets with sufficient validation has made this challenging. It also should be noted that there is likely no single-best solution to each problem. An optimal approach for one research application may not be optimal for another. Thus, the solution for improved tropical tree species mapping may not be the same as one for mapping impervious surface cover, fire temperatures, water depth, or mineral abundance. Linear mixture models have proven to be very effective tools to address numerous environmental situations. However, further research is needed to improve insight into nonlinear mixing behavior in real life scenes.

7 HYPERSPECTRAL IMAGE DATA PROCESSING

7.1 *Introduction*

Hyperspectral remote sensing, also commonly referred to as imaging spectrometry, is a mode of spectral data acquisition at a very narrow spectral bandwidth (i.e., fine spectral resolution) with up to a couple hundred contiguous spectral bands. Hyperspectral data collection aims to capture a subtle spectral pattern, often, spectral reflectance pattern or signature, of the target features, and to use that rich spectral information to identify target materials to diagnose the condition of the target; or, more simply, to classify the image data.

Early in the 1980s, the value of hyperspectral remote sensing and its use was exploited actively by the geological community and after almost four decades of research efforts involving a wide spectrum of disciplines, the range of hyperspectral applications is widening. Through laboratory measurements, geologists are aware that common minerals exhibit unique spectral reflectance signatures, or spectra, particularly in terms of absorptions in the SWIR wavelength region. The MS images observed by early Landsat satellites, although their spectral resolving power with broad, MS bands were somewhat limited, suggested: (1) the

possibility of determining the mineralogy of the substrate over an extensive area; and, (2) developing crude maps of mineral distribution on the Earth's surface. The big impact of this approach and its future direction at that time was well documented in Goetz *et al.* (1985). In those early days, vegetation cover was often considered to be noise. Unlike minerals, vegetation composed of essentially the same kind of cells generally exhibited similar spectral signatures. However, through subsequent in-depth investigations, hyperspectral data started offering great promise in providing both biophysical and biochemical properties of vegetation. A comprehensive summary of such applications can be found in Thenkabail *et al.* (2012).

7.2 *Advantages and Challenges*

Increased numbers of spectral bands and more detailed spectral signatures support increased accuracy in identifying materials. Since hyperspectral remote sensing collects an entire spectrum for every pixel, it is able to capture much more detail on every pixel than commonly used MS remote sensing. In addition, since hyperspectral data contain a substantial amount of information about atmospheric characteristics at the time of image acquisition, the image data themselves can be used with atmospheric models to compute quantities such as the total atmospheric column water vapor content (Gao and Goetz, 1990).

Increased dimensionality poses a challenge for data transfer and processing; handling of hyperspectral data is expensive computationally in nature. However, this challenge is now being slowly overcome thanks largely to advances in computing.

What's more of a pressing challenge is that spectral signatures being recorded by a hyperspectral sensor on an aircraft or on a satellite platform contain noise. Remotely-sensed spectra are distorted by the atmosphere. This calls for atmospheric corrections that remove atmospheric effects (e.g., attenuation) from the spectral signals being recorded. However, atmospheric correction algorithms may not be reliable enough to enable "matching" remotely-sensed and terrestrial spectra.

In many applications, most pixels contain a mixture of materials. A pixel might be 30*m* by 30*m* or so depending on the hyperspectral sensor; the chance of that pixel containing one material is usually very small. So, work is needed to "unmix" spectra into their constituent materials. Doing so either requires a spectral library or to pre-identify pure spectra for basic components of a scene (i.e., "endmember"). The spectral library consists of spectra of pure materials and often involves using spectroradiometers in the field or in the laboratory. In most cases, identifying endmembers still requires some kind of manual identification. See section 6 of this chapter for a detailed description of the techniques involved in SMA.

7.3 *Hyperspectral Sensors*

Many operational hyperspectral sensors are available today, with the majority of them being airborne. However, multiple spaceborne hyperspectral sensors are now being proposed that should be operational in the near future. A brief discussion of those operational and planned hyperspectral sensors is presented below.

7.3.1 *Commonly Used Hyperspectral Sensors*

Jensen and Yang (2009) provided a comparative description of some commonly used hyperspectral sensors in the 3rd edition of the *Manual of Remote Sensing* (Table 7-4). The list is still relevant because no spaceborne hyperspectral sensors with high spatial resolution have become operational since the time of its publication. Detail of these hyperspectral remote sensing systems can be found in Jensen and Yang (2009).

Table 7-4. Some Widely Used Hyperspectral Remote Sensing Systems (After Jensen and Yang, 2009).

Hyperspectral Sensor	Spectral Resolution (*nm*)	Spectral Interval (*nm*)	Number of Bands	Swath Width*	Quantization (bits)	Platform
AVIRIS	400-2500	10	224	667	12	Airborne
HyMap	450-2500	10-20	100-200	512	12-16	Airborne
SEPS-H	430-1050	Variable	76	512	16	Airborne
	1500-1800		32			
	2000-2500		32			
	8000-12500		12			
AISA+	430-970	Programmable	244	512	12	Airborne
CASI	400-1000	Programmable	288	550	14	Airborne
	380-1050			1500		
HYDICE	400-2500	7.6-16	210	208	12	Airborne
Hyperion	400-2500	10	220	7.5*km* at nadir	12	Spaceborne
MODIS	405-14385	Variable	36	10*km* at nadir	12	Spaceborne

*Pixels for airborne; *km* for spaceborne

Of these existing hyperspectral remote sensing systems, the AVIRIS and Hyperion are particularly unique. The AVIRIS system, developed by NASA's Jet Propulsion Laboratory (JPL) has been collecting hyperspectral images for scientific research and applications since 1987. Extensive research was conducted and hundreds of publications using the AVIRIS data worldwide representing a variety of application fields are available from the AVIRIS workshop (*http://aviris.jpl.nasa.gov/*). Hyperion, NASA's first spaceborne hyperspectral sensor, collected the first science-grade high spatial resolution hyperspectral images from space. The knowledge gained from Hyperion is relevant to future spaceborne hyperspectral remote sensing programs (Table 7-5).

7.3.2 *Proposed Spaceborne Hyperspectral Sensors*

Table 7-5 provides description of three future spaceborne hyperspectral sensors soon to be placed in orbit.

Table 7-5. Description of HyspIRI, HISUI, and EnMAP: Three Spaceborne Hyperspectral Remote Sensing Systems.

Hyperspectral Sensor	Spectral Resolution (*nm*)	Spectral Interval (*nm*)	Number of Bands	Swath Width (*km*)	Spatial Resolution (*m*)	Revisit Cycle (days)
HyspIRI-VSWIR	380-2510	10	210	153	60	19
HISUI-Hyperspectral Imager	400-970 970-2500	10 12.5	185	30	30	60
EnMAP-Hyperspectral Imager	420-1000 900-2450	6.5 10	244	30	30	27

7.3.2.1 Hyperspectral Infrared Imager

Hyperspectral Infrared Imager (HyspIRI) is a NASA global mission focused on unique and urgent Earth science and applications objectives being addressed by continuous spectral measurements in the visible to short-wave infrared (VSWIR) portion of the spectrum, and measurements from eight discrete MS bands in the thermal infrared wavelength region (*http://hyspiri.jpl.nasa.gov/*). The VSWIR hyperspectral sensor will cover the range 380–2510*nm* in 10*nm* contiguous bands. The instrument has a swath of 153*km* with a spatial resolution of 60*m* at nadir. The dedicated HyspIRI satellite will be in a low Earth orbit at an altitude of 626*km*, and will have a revisit cycle of 19 days. Launch is expected to occur after 2022.

7.3.2.2 Hyperspectral Imager Suite

Hyperspectral Imager Suite (HISUI) consists of both a hyperspectral and a MS imager being developed by the Japanese Ministry of Economy, Trade, and Industry (METI). HISUI will be one of the mission instruments of the Japanese Aerospace Exploration Agency (JAXA) Advanced Land Observing Satellite 3 (ALOS-3), scheduled for launch in 2019. The swath of the Hyperspectral Imager will be 30*km* at a spatial resolution of 30*m*; however, the sensor will be equipped with a cross-track pointing mechanism which tilts the Hyperspectral Imager ±3 degrees. The sensor consists of a reflective telescope and two spectrometers that cover the Visible-Near Infrared (VNIR) wavelength region with 10*nm* spectral intervals, and the SWIR wavelength region with 12.5*nm* spectral intervals. With these two spectrometers, Hyperspectral Imager will provide physical properties of the surface materials with 185 bands (Tachikawa *et al*., 2012).

7.3.2.3 Environmental Mapping and Analysis Program

The Environmental Mapping and Analysis Program (EnMAP) is a German hyperspectral satellite mission that aims to monitor and characterize Earth's environment on a global scale (*http://www.enmap.org*). The satellite system is being developed entirely in Germany under the guidance of the Space Administration Division of the German Aerospace Center (DLR); the German Research Center for Geosciences (GFZ) is taking the scientific leadership. Two hyperspectral sensors will record reflected energy from the Earth at wavelengths between 420*nm* and 2450*nm* with 244 contiguous spectral bands. The swath of EnMAP hyperspectral sensors will be 30*km* at a spatial resolution of 30*m*. The satellite is scheduled for launch in 2018. Further detail of this mission is documented in Kaufmann *et al*. (2012).

7.4 *Hyperspectral Data Processing*

7.4.1 *Pre-processing*

For hyperspectral data to be useful for extracting information of the target features on the ground, the raw hyperspectral at-sensor radiance needs to be converted to apparent surface reflectance and ultimately to surface reflectance. This requires both radiometric calibration and geometric correction. These procedures are similar to those involving conventional MS data. However, they are particularly important when manipulating hyperspectral data because these procedures allow the remotely-sensed spectra to be compared quantitatively with *in situ* spectra collected on the ground, for instance using a handheld spectroradiometer, or with laboratory-derived spectra (Jensen, 2005).

7.4.2 *Radiometric Calibration*

There are different approaches for radiometric calibration of hyperspectral data depending on the availability of *in situ* spectral measurements. When *in situ* spectral measurements are available, the digital numbers in the image can be converted directly to reflectance using the empirical line correction method (Kruse *et al.*, 1990). This requires concurrent *in situ* spectral measurements at two or more targets within the image. When *in situ* spectral measurements are not available, the DNs need to be converted to "at-sensor" radiance and transformed to radiance or reflectance at the Earth's surface. Doing so requires sensor calibration, flight information, and information about site-specific atmospheric conditions at the time of image acquisition. Since direct measurements of atmospheric properties are rarely available, radiative transfer atmospheric correction models are commonly used to estimate surface reflectance. Some examples of such models include the Moderate Resolution Atmospheric Transmission (MODTRAN) radiative transfer code (Berk *et al*., 1987), Atmospheric/Topographic CORrection (ATCOR®) that uses look-up tables calculated with MODTRAN code (Richter and Schläpfer 2014a, 2014b), and Fast line-of-sight Atmospheric Analysis of Spectral Hypercubes (FLAASH®) (Perkins e*t al*., 2012) which is available in the ENVI® software. When neither *in situ* spectral measurements nor atmospheric data needed for radiative transfer atmospheric correction models are available, radiometric normalization techniques can be adopted; but they are usually not preferred.

7.4.3 *Geometric Correction*

The procedures for geometrically correcting hyperspectral data to a known datum and map projection are essentially the same as for conventional MS data. Full description of these procedures is not repeated here. However, it is important to note that since most operational hyperspectral data are currently obtained on aircraft, correction is required to account for motion and altitude of the aircraft. In such cases, on-board global positioning systems (GPS) and Inertial Navigation System (INS) technology are often used. In addition, geometric correction of hyperspectral data usually takes longer compared to that of MS data because there are simply more bands to process.

7.5 *Thematic Information Extraction*

Extracting thematic information accurately and efficiently is an important issue in hyperspectral remote sensing. Although standard image processing and analytical techniques developed for conventional multispectral data apply to virtually all hyperspectral data, a wide array of techniques and methods has been developed for hyperspectral image processing and analysis to take advantage of the full spectral information present in hyperspectral data. A comprehensive overview of such image processing techniques can be found in Jensen (2005); some of more advanced techniques such as the ANN and Support Vector Machines (SVM) particularly in the context of vegetation studies are presented in Thenkabail (2012). These image processing techniques have been implemented in many general purpose image processing software packages such as ENVI®, ERDAS IMAGINE®, and IDRISI®. Some of these techniques and procedures used for information extraction are presented below.

7.5.1 *Dimensionality Reduction*

The number of spectral bands in a remote sensing system is referred to as its data dimensionality. Hyperspectral data with many hundreds of bands have high spectral dimensionality and often contain noise and spectral redundancy. The most commonly used technique to reduce spectral redundancy of conventional MS data is Principal Component Analysis (PCA). Unfortunately, PCA alone is often not sufficient for reducing the high dimensionality of hyperspectral data. A useful algorithm developed specifically for this purpose is the Minimum Noise Fraction (MNF) transformation which uses two cascaded principal component analyses (Chen *et al.*, 2003a). MNF determines the inherent dimensionality of hyperspectral image data, and collapses the useful information into a much smaller set of MNF images to reduce the computational requirements for subsequent processing (Boardman and Kruse, 1994).

7.5.2 *Spectral Mapping and Matching Approaches*

A group of algorithms was developed to compare hyperspectral data to known reference spectra and to assign each pixel in an image to one particular class. This group includes binary encoding (Mazer *et al*., 1988), Spectral Angle Mapper (SAM) (Kruse *et al*., 1993), and Spectral Feature Fitting (SFF) (Clark *et al*., 1990). Another group of algorithms involving sub-pixel classification is used to determine the proportional abundances of target materials, or endmembers, in each pixel of an image. SMA of hyperspectral data includes linear spectral unmixing (Adams *et al*., 1995), and matched filtering (Harsanyi and Chang, 1994).

7.5.3 *Spectral Indices Approach*

Like traditional indices developed for use with conventional MS data, spectral indices can also be used with hyperspectral data. For example, NDVI can be calculated by using narrow-spectral band in the red and NIR regions of the spectrum. Many other narrow-band indices have been suggested, such as the PRI (Gamon *et al.*, 1992) and the Transformed Chlorophyll Absorption in Reflectance Index/Optimized Soil-Adjusted Vegetation Index (TCARI/OSAVI) (Haboudane *et al.*, 2002).

7.5.4 *Derivative Spectroscopy Approach*

Derivative spectroscopy uses changes in spectral reflectance or radiance with respect to wavelength (a measure of rate-of-change or slope) to sharpen spectral features, emphasize desired information, or eliminate less useful information (Jensen, 2005). The technique can be used to compare spectral curves mathematically from hyperspectral data to spectral curves generated in a laboratory, in the field, or from other hyperspectral data. Some examples of derivative techniques applied to hyperspectral data include Demetriades-Shah *et al*. (1990), Tsai and Philpot (1998) and Adams *et al.* (1999).

7.6 *Conclusion*

After almost four decades of extensive research and instrument development, hyperspectral remote sensing is approaching its promise. Until now, hyperspectral sensors have been flown primarily in aircraft for experimental and commercial purposes. However, more spaceborne hyperspectral sensors are now close to being operational, which should improve both their spatial and temporal coverages. Various image

processing techniques developed and matured specifically through the use of high-quality airborne hyperspectral data are expected to make newly available data even more useful.

8 IMAGE DATA FUSION

8.1 *Introduction*

Remote sensing data fusion is a technique commonly used for integrating information acquired with different spatial and spectral resolutions from sensors mounted on satellites, aircraft, and ground platforms. It aims to produce a dataset that contains more detailed information than each of the sources taken individually (Zhang, 2010). The term *data fusion* is often synonymous with merging, combination, synergy, and integration in the literature. In the remote sensing community, the following definition has been adopted: "Data fusion is a formal framework in which are expressed means and tools for the alliance of data originating from different sources. The process aims to obtain information of greater quality, where the exact definition of 'greater quality' will depend upon the application" (Wald, 1999).

Due to a lack of available datasets, analysis of remotely-sensed data has been performed until recently, using a single satellite image. The emerging suite of products currently available provides exceptionally good coverage in space, time, and the electromagnetic spectrum. These wide-ranging sets of data allow analyses of time series created by combining different sensor types and scales, thus providing better integration with ancillary data and models. Data fusion combining data from several sources is becoming increasingly important and necessary in many remote sensing applications (Solberg, 2006).

8.2 *Background*

Within the realm of optical remote sensing, some satellite sensors provide the spectral bands needed to distinguish features spectrally but not spatially, while other satellite sensors provide the spatial resolution for distinguishing features spatially but not spectrally (Wang, Z. *et al.*, 2005). However, many remote sensing applications can benefit by combining data from multiple sensors to attain more comprehensive information.

The most common applications of data fusion are to sharpen images, improve geometric accuracy, provide stereo-photogrammetry, enhance features not visible in a single data set, improve classification (as in the case study provided in this section), detect changes over time, and fill gaps caused by missing or defective data (Pohl and van Genderen, 1998).

Fusing panchromatic (PAN) (i.e., high spatial but low spectral resolution) to MS (i.e., low spatial but high spectral resolution) is commonly called pan-sharpening. These types of images have reverse characteristics because of the physics behind how photons are acquired to produce imagery. Since MS sensors typically have narrower bandwidths (i.e., are sensitive to fewer wavelengths), they receive less energy and therefore require more time to produce the same intensity response as PAN images. This intensity response also allows for a smaller pixel size to be used in the PAN sensors, thus producing higher spatial resolution images.

Many studies require both high spatial and high spectral resolutions, yet combining two different sets of imagery can be difficult. Even if images from different sensors are registered geometrically and acquired at nearly the same time and perspective, the physics behind data collection of the different spectral bands must be taken into account (Thomas *et al.*, 2008). Figure 7-38 shows the spectral response for different wavelengths using different sensors on the QuickBird satellite. These responses are similar for sensors on other spacecraft but the exact function describing their sensitivity to different wavelengths will differ (i.e., full width at half maximum (FWHM), bandwidth, and center wavelength).

Object occultation is common when combining sensors with different spectral bands. Certain features may be obvious in one image but could be completely absent in another image using a different sensor. These effects can be observed directly in Figure 7-38 because an object reflecting solar energy at ~715*nm* will be missing from the red and NIR bands, and will only be visible in the PAN image. Another side effect is contrast inversion. This occurs when one sensor records a decrease in reflectivity while another sensor detects an increase over the same range (Thomas *et al.*, 2008). Using Figure 7-38, the PAN sensor will record a weaker signal for an object reflecting at 500*nm* compared to an object reflecting at 600*nm*, while the opposite is true for the Blue sensor.

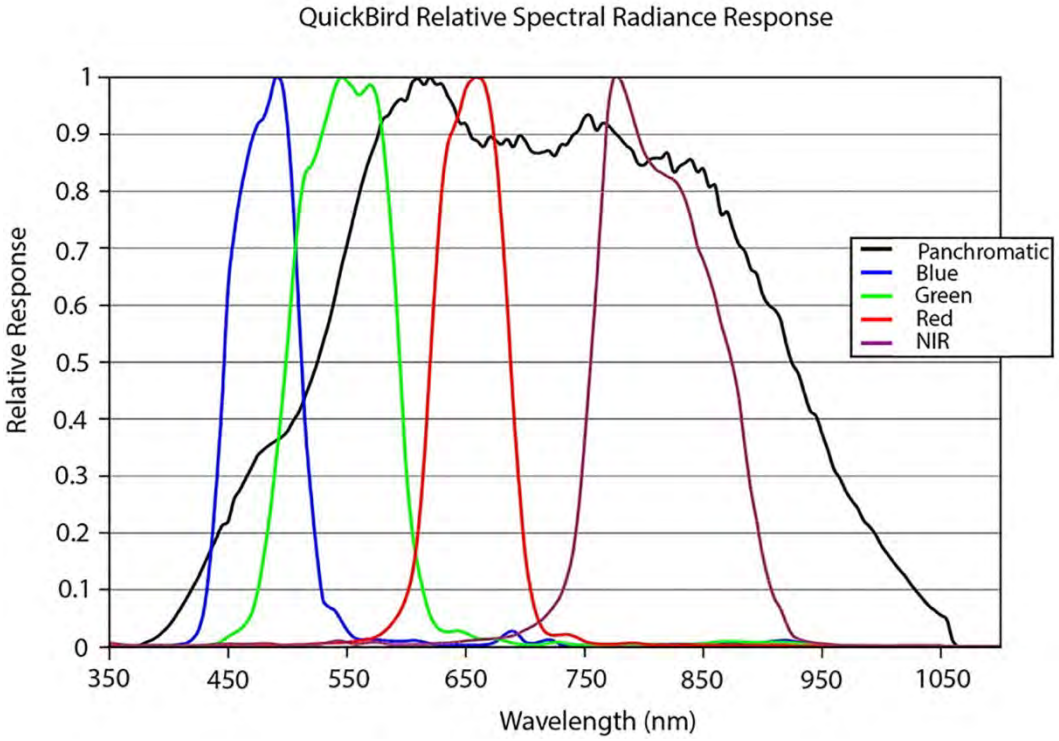

Figure 7-38. Quickbird spectral response curve (Image Credit: Digital Globe).

8.3 *Methods*

To best determine what datasets should be fused and what types of approaches should be implemented, users need to answer the following questions: (1) what questions can be answered by the data?; (2) what available data sets are most applicable to these needs?; (3) what techniques and data combinations might

provide the most effective answers?; and (4) how do the data need to be preprocessed before they can be fused? (Pohl and van Genderen, 1998).

Merging multi-source data can create a more consistent interpretation of the scene compared to an interpretation based on data from a single sensor. Research on data fusion has a long history in remote sensing because fusion products are the basis for many applications. However, integrating remotely-sensed data, especially multi-source data, remains challenging due to various requirements for accurate data co-registration, the complexity of the landscape, and the temporal and spectral variations within the input data set (Zhang, 2010).

When integrating data from different sensors, it is critical that they be co-registered (i.e., transformed into one coordinate system). If the data are georeferenced, the co-registration process involves simply resampling the images to a common map projection. In many cases however, an image matching step is necessary to obtain sub-pixel accuracy in matching. A full image registration process is composed of four steps: feature extraction, feature matching, transformation selection, and image resampling. The image registration process detailed above is a prerequisite for data fusion.

In general, remote sensing fusion techniques can be classified into three different levels: the pixel/data level, the feature level, and the decision level (Pohl and van Genderen, 1998). Pixel level fusion is the combination of raw data from multiple sources into single resolution data. This fusion technique generally falls into two categories: image differencing and image ratioing (Li and Yeh, 1998). Pixel-based fusion consists of merging information from different images on a pixel-by-pixel basis to improve the performance of image processing tasks such as segmentation. Data fusion occurs at the lowest processing level since the data being merged are actual physical parameters, rather than resulting from analysis of the original data set. Advantages of pixel level fusion include its simplicity (i.e., no special classifier software needed), correlation between sources, and use for change detection. These offer the greatest flexibility of use whereas feature-level and decision-level based fusion methods are usually related to specific application examples.

Feature-level fusion extracts various features from different data sources and then combines features into one or more feature maps that may be used instead of the original data for further processing. The methods applied to extract features usually depend on the characteristics of the individual source data, and processing workflows may include multiple methods, if the datasets used are heterogeneous. Typically, such fusion requires a precise (i.e., pixel-level) registration of the available images. Therefore, the feature maps obtained are used as input to pre-processing algorithms for image segmentation or change detection (Zhang, 2010). Like pixel-level fusion, advantages of feature-level fusion include its simplicity (i.e., no special classifier software needed) and its suitability for change detection. However, its sensor-specific features give it an advantage over pixel-based fusion.

The purpose of the feature extraction step is to extract regions, edges, and contours that can be used to represent tie-points in a set of images to be matched. This is a critical step, as the registration accuracy can be no better than the accuracy achieved for the tie points (Solberg, 2006).

The approaches to feature extraction are known as area-based methods, feature-based methods, and hybrid approaches. Area-based methods are best suited for images from the same or highly similar sensors because the grey levels of the images are used directly for matching, often by statistical comparison of pixel values in small windows. Feature-based methods are usually application dependent since the features to be

use as tie points need to be tailored to the application. Hybrid approaches use both area-based and feature-based techniques by combining both a correlation-based matching with an edge-based approach, and they are useful for matching data from heterogeneous sensors (Solberg, 2006).

Decision-level fusion combines the results from multiple algorithms to yield a final fused decision. When the results from different algorithms are expressed as confidences rather than decisions, it is called *soft fusion*; otherwise, it is called *hard fusion*. Methods of decision fusion include voting methods, statistical methods, and fuzzy logic. These three levels do not encompass all possible fusion methods, since input and output of data fusion may be different at different levels of processing. In practical operations, the applied fusion procedure is often a combination of the three levels. Advantages of decision-level fusion include its usefulness for data with different probability densities and modeling abilities. However, unlike pixel-level and feature-level fusion, decision-level fusion often requires special software (Solberg, 2006).

In summary, pixel-based fusion consists of merging information from different images on a pixel-by-pixel basis to improve the performance of image processing tasks such as segmentation. Feature-based fusion consists of merging features extracted from different signals or images. In feature-level fusion, features are extracted from multiple sensor observations, then combined into a concatenated feature vector and classified using a standard classifier. Symbol-level or decision-level fusion consists of merging information at a higher level of abstraction. Based on the data from each single sensor, a preliminary classification is performed. Fusion then consists of combining the outputs from the preliminary classifications (Solberg, 2006).

8.4 *Details on Pixel Level Fusion Techniques*

Wang, Z. *et al.* (2005), and references within, describe the different specific pixel-based methods used in image fusion. Intensity Hue Saturation (IHS) and the Brovey Transform (BT) are common fusion procedures that use three image bands for processing. IHS relies on the color properties (i.e., intensity, hue, saturation) of the bands being used, typically red, green, blue (RGB), while BT normalizes the three bands in question before they are multiplied with the PAN image. This method transforms the luminance information from the MS image into a high-resolution PAN image while retaining the corresponding spectral features of each pixel.

High Pass Filtering (HPF) preserves the spatial information of high-resolution data by transforming them into the frequency domain and filtering the result using a high-pass filter. This information is obtained by putting data through a boxcar, which involves averaging each pixel with its neighboring pixels. The size of the boxcar will determine what types of features are removed: a large boxcar will affect large features while a small boxcar will affect small features. A high-pass filter removes regions smaller than the boxcar in the PAN image (Aiazzi *et al.*, 2002). By combining these filtered high-resolution PAN data with the low-resolution MS imagery a high resolution MS image is produced.

In comparison to the methods above, PCA can be used for data fusion and can incorporate any number of bands. PCA computes principal components by transforming the original correlated dataset into a smaller set of uncorrelated variables (i.e., principal components) while still representing most of the information from the original dataset (Ricotta *et al.*, 1999). Each principal component is a linear combination of the original variables. The set of principal components is ordered by the amount of variance explained in the

original data set. The first component contains the maximum proportion of variance and low components are often discarded because the principal component image contains information that is common to all the bands. The first principal component from the low-resolution MS imagery is then replaced by the high-resolution PAN data creating a high-resolution MS image (Wang, Z. *et al.*, 2005).

PCA has the advantage of identifying patterns in the data, and the transform does not lead to information loss. However, this method is implementation-dependent and results may vary depending on the software used. The time between image acquisitions may also affect the results of PCA-based image fusion. Even if specific features exist in each scene to be fused and these features remain unchanged, if other features experience a change, those pixels may affect the overall output (Gupta *et al*., 2013).

A common use of data fusion is to combine transformation methods. One such technique, ARSIS, developed by Ranchin *et al.* (2003), has been used to map urban areas, air quality, and agriculture. The method uses a multiscale model (MSM) to generate an approximation image and detail image from the higher spatial resolution image, where the detail image contains features close to the original image resolution. This produces a map of spatial variabilities that can be inverted and applied to the low-resolution image. The model for both image sets is performed for several iterations, to produce the most informative model. The output from the MSM can be input into an Inter-Band Structure Model (IBSM) that relates the spatial features to spectral features.

8.5 *Case Study for Data Fusion of Optical Images*

Here, an example of data fusion is presented using OBIA to fuse high spatial resolution (e.g., WorldView-2 imagery) with eight 2*m* MS bands and one 0.5*m* PAN band) and hyperspectral (e.g., 242-band Hyperion image with 30*m* resolution) satellite data for geological strata classification. The study uses fusion methods to combine the advantages of both datasets effectively to accurately classify geological strata.

The study area covers 2.73*km* in the western Tarim basin, located on the southern flank of the Wulagen syncline in Wuqia, Xinjiang, western China (Figure 7-39). It is bounded by upper left longitude 39°9'12" and latitude 74°57′32", lower right longitude 39°38′5" and latitude 74°58′28". At an elevation of approximately 2,400*m* above sea level, the study area lies to the west of the Wulagen lead-zinc (Pb-Zn) deposit, which is a sandstone-hosted unit with a prospective Pb-Zn reserve greater than 10 Megatons of Pb-Zn at 3.62% concentration. The area represents a typical sedimentary landscape.

A standard level 2A WorldView-2 image acquired on 21 August 2011 was used. It includes one PAN layer, eight MS, layers and calibration metadata that were used for radiometric correction. The PAN image has the spectral range from 450*nm* to 800*nm*, with 0.5*m* spatial resolution. The MS image with 2*m* spatial resolution is composed of eight bands: Coastal blue (400-450*nm*), Blue (450-510*nm*), Green (510-580*nm*), Yellow (585-625*nm*), Red (630-690*nm*), Red edge (705-745*nm*), NIR1 (760-895*nm*), and NIR2 (860-1040*nm*). Geo-rectification was already applied to this product and no further normalization was necessary for topographic relief.

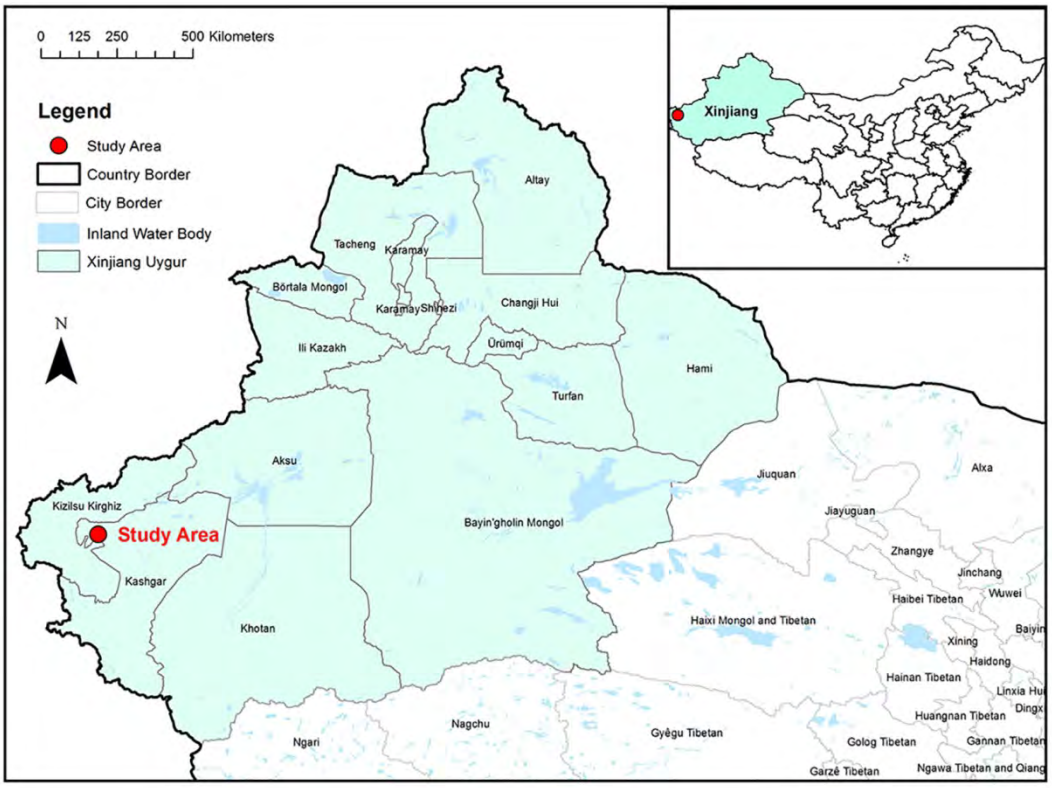

Figure 7-39. Study area as a subset area of Xinjiang.

The Hyperion image was acquired on 29 September 2003 and was downloaded from the USGS archives. Hyperion is an along-track sensor mounted on the EO-1 spacecraft collecting optical data in 242 bands ranging from VNIR to SWIR, with each band having a spectral resolution ~10*nm* and spatial resolution of 30*m*. Because vegetation coverage is sparse in the study area, and almost free of human activity, the stratigraphy was considered to be spatially stable between September 2003, acquisition date of the Hyperion image and August 2011, the acquisition date of the WorldView-2 image.

8.5.1 *Methods*

Object-Based Image Analysis (OBIA) is characterized by the ability to use multi-source data as input. Usually, images with relatively high spatial resolution are used as initial inputs in the OBIA workflow, in conjunction with data sources such as DEMs, LiDAR, and others. To examine whether the additional spectral information could improve the accuracy for image analysis, OBIA used the original high-resolution data (i.e., WorldView-2) alone to compare with the method that relies on the synergy of WorldView-2 and Hyperion data. Figure 7-40 shows the data processing protocol involved in the proposed OBIA method for this study. Data preprocessing and accuracy assessment for the two methods were carried out using ENVI (i.e., v. 5.0, Harris Geospatial Solutions) image processing software, whereas the OBIA section was conducted by Trimble's eCognition Developer 8.0 software, formerly known as Definiens.

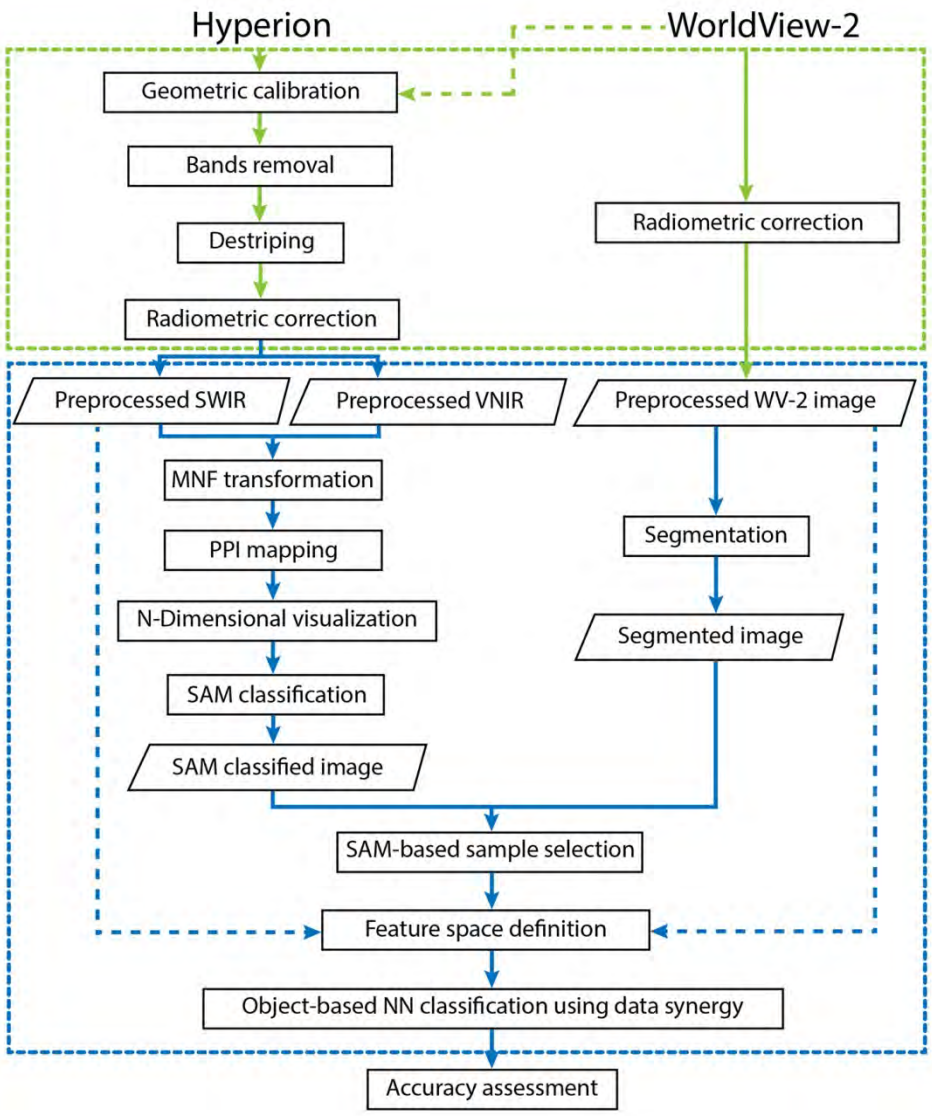

Figure 7-40. Workflow of data fusion based on the integration of Hyperion and WorldView-2 images. WV-2=WorldView-2; PPI=Pixel Purity Index; SAM=Spectral Angle Mapper.

8.5.2 *Preprocessing*

For the WorldView-2 image, preprocessing focused mainly on radiometric correction, calibration and atmospheric correction. Raw DNs were converted to radiance by applying the ENVI WorldView Calibration utility. The FLAASH® atmospheric correction module was used to correct for atmospheric effects and to derive surface reflectance, thus providing comparable spectral values for fusion with Hyperion data.

Hyperion image preprocessing consisted of four steps. Initially, the image was geometrically registered to align with the WorldView-2 scene with total RMSE = 0.46, the pixel size of Hyperion. Next, non-calibrated bands 1-7, 58-76, and 225-242 were removed, since only 50 of 70 VNIR bands and 148 of 172 SWIR bands of Hyperion were calibrated. The remaining 198 bands had a spectrum range from 426*nm* to 2395*nm* (Beck, 2003). Additional bands, 120-132; 165-182; 185-187 and 221-224 were removed because of their sensitivity to water absorption and susceptibility to atmospheric scattering. Bands 77 and 78 were also

removed due to their low signal to noise value (Petropoulos *et al.*, 2012). This resulted in 50 VNIR bands and 108 SWIR bands that were processed separately because of their differing structure (Datt *et al.*, 2003) and for OBIA application purposes, as explained later in Sections 8.5.3 and 8.5.4. Following destriping to account for differences in gain and offset of different detectors of the Hyperion sensor, radiometric corrections were performed on the images. Similar to the radiometric correction conducted on WorldView-2, the DNs were first converted to "at-sensor" radiance and then to surface reflectance using FLAASH®.

8.5.3 *Spectral Angle Mapper Classification of Hyperion Data*

Spectral Angle Mapper (SAM) was first applied to Hyperion data to generate an initial classified image, which was used as a reference for further sample selection in OBIA (Kruse, 2003). MNF of all 158 bands was carried out, followed by general mapping using PPI. Then, spectral endmembers were selected in n-dimensional space (Boardman, 1993) and later identified by a geology expert. The final preprocessing goal was to obtain the SAM results, which were optimized with input from the geology expert and combined with the segmented image to guide sample selection in the classification step.

8.5.4 *Segmentation of WorldView-2*

OBIA consists of two sequential parts: segment generation and segment labeling. Image segmentation splits an image into separate and homogeneous objects; namely, segments and classification techniques were used to label the objects with specific class attributes. The classes in this area have inherent intraclass spectral variability that is captured in high-resolution imagery as texture features. OBIA deals with such images by classifying them into homogeneous objects, which in this example represent patches of specific stratum values with differing spectral and textural signatures.

Eight bands of WorldView-2 MS were used during segmentation. Though the software allows users to assign different weights ranging from 0 to 1 for each band, 1 was assigned to all bands to include the full spectral information in the segmentation process. In eCognition, images can be segmented considering three parameters: shape, compactness and scale.

Shape and compactness can be assigned values between 0 and 1 to control the homogeneity of objects. While the shape parameter adjusts weights put on spectral homogeneity and shape, the compactness factor balances compactness and smoothness when determining the object shape (Platt and Rapoza, 2008). For sedimentary strata, shape is less significant for object identification than spectral homogeneity. Thus, 0.1 was assigned to the shape parameter to focus on spectral information and assigned 0.5 to compactness. This resulted in smoothness being assigned automatically as 0.5.

Scale is the most important parameter in image segmentation as it determines homogeneity tolerance for the segments (Platt and Rapoza, 2008; Thomas *et al.*, 2003). The value assigned to the scale parameter depends greatly on the user's requirement of object size based on their specific study goals. The higher the scale value, the larger is the size of the output object. Several experiments were run with several scale parameters and visual assessments in order to identify the optimal scale that allowed the algorithm to distinguish objects on the ground. Scales from 100 to 500 with intervals of 50 were tested with the value of 250 giving the best results. As verified by visual inspection, values greater than 250 generated segments that consisted of more than one stratum and values smaller than 250 tended to generate considerable noise.

These variations cause ambiguities resulting in over-segmentation or under-segmentation of the image, respectively.

8.5.5 *Classification of the Segmented Image*

The standard Nearest Neighbor (NN) classifier (Definiens, 2009) was applied to assign stratigraphic class values to segmented objects. This classifier is preferred when only a few features are used but results in objects not being well separated. Specifically, the procedure included sample selection, feature space definition, classification, output review and optimization. Data synergy was realized through the first two steps.

First, a set of output segments was selected as training samples representing different classes, similar to pixel-based supervised classification. The labels derived from the previously obtained SAM result were used as references. This action falls into the category of soft decision-level data synergy according to Zhang (2010). Segments can be considered as sample regions only when a cover class from SAM covers over 90% of the area contained in these segments. This procedure was named "SAM-based sample selection". The details of this process are illustrated in Figure 7-41. For an object eligible to be a sample, object-based segmentation decides the spatial region of this sample and SAM decides its class attributes. By combining the results from SAM and segmentation, ambiguity in sample selection can be minimized.

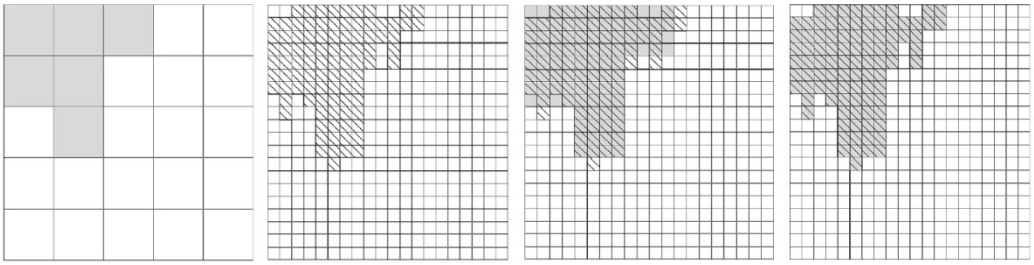

(a) Result of SAM. Grey area was classified as Class X.

(b) Result of segmentation. Shadowed area was segmented as a heterogeneous region.

(c) Combined the two results.

(d) When the 90% rule is met, it is eligible to be a sample. Assign class label "X" to this region.

Figure 7-41. SAM-based sample selection.

Once the samples have been selected, a feature space must be defined. The standard NN approach in eCognition allows the feature space to be constructed using original, composite, transformed, or customized bands. Though the WorldView-2 image has relatively abundant spectral information (i.e., 8 bands) compared with QuickBird and IKONOS (i.e., 4 bands), the relative absence of spectral information in SWIR still produces uncertainty in classification.

The SWIR spectral range covers spectral features of hydroxyl-bearing minerals, sulfates, and carbonates common to many geologic units (Kruse, *et al*., 2003). Therefore, the SWIR bands in Hyperion were introduced to provide additional spectral information for feature space definition. MNF was used to reduce the data dimensionality of the remaining 108 SWIR bands and added the resulting 20 MNF bands to the analysis (Green *et al.*, 1988). Thus, 29 bands were considered in the feature space construction (i.e., 8 MS bands, 1 PAN band and 20 SWIR MNF bands). The best combination of spectral and spatial features was calculated and optimized by feature space optimization tools in the software to determine the most effective parameters

describing each class. Sixty-eight features were considered initially as potential sources for feature space construction (Table 7-6). Of these, five features were selected for the final classification (Table 7-7).

Segments generated by the previous step were also classified using only the nine WorldView-2 bands (i.e., no Hyperion SWIR bands). This single-data classification was used as a standard procedure to which results of OBIA with data synergy were compared. For the standard procedure, WorldView-2 only. five features (Table 7-7) were used to classify the segments that were selected from the 26 attributes (Table 7-6).

Table 7-6. Object-Based Features Considered.

Abbreviation of Feature	Name of Feature	Description
Mean	Mean Value of Band	Average reflection value of each segment in a selected Band
StanDev	Standard Deviation	Reflective standard deviation for each segment in a selected Band
GLCM	Grey Level Co-occurrence Matrix Value*	Calculated for each segment from the values in PAN band, measurement for texture
IHS	IHS Transformation Components**	IHS transformation using a false color composite comprising band 4-3-2 of MS

* Including homogeneity, contrast, dissimilarity, entropy, standard deviation, and correlation.
** Including intensity, hue, and saturation.

Table 7-7. Features Selected by the Feature Space Optimization Tool for Classification in the Two Procedures.

OBIA with only WorldView-2	OBIA with Data Fusion
Mean MS band 5	Mean MS band 6
Mean MS band 6	Mean SWIR MNF band 11
Stadv MS band 5	Mean SWIR MNF band 17
IHS hue	Stadv SWIR MNF band 18
GLCM contrast PAN	IHS hue

8.5.6 *Results*

In the study area, clastic sedimentary formations are dominant. It may be possible to detect stratigraphic differences visually, but boundaries between classes are difficult to delineate (Figure 7-42a). Visually, the two classification results (Figures 7-42b and 7-42c) show that stratigraphic classes replicated the sedimentary structure of the rocks and the boundaries could be identified easily because data fusion maintained the fine pixel size found in WorldView-2.

When OBIA was run on WorldView-2 alone, rocks from one stratigraphic unit were sometimes classified into two or more classes (Figure 7-42b). For example, some segments of C1 in the upper part of the image were classified incorrectly due to spectral variations (i.e., brighter and darker) caused by shadows. For these shadowed areas, VNIR reflectance variations among bands were reduced compared with non-shadowed area. Hence, areas with and without shadow effects can be misclassified easily as two classes when only looking at MS bands, which are fewer in number and have wider bandwidths. On the other hand, results produced by OBIA with data fusion took advantage of the spectral response in a wider band range, from VNIR to SWIR, to record spectral features of this class, thus minimizing spectral ambiguities with other classes.

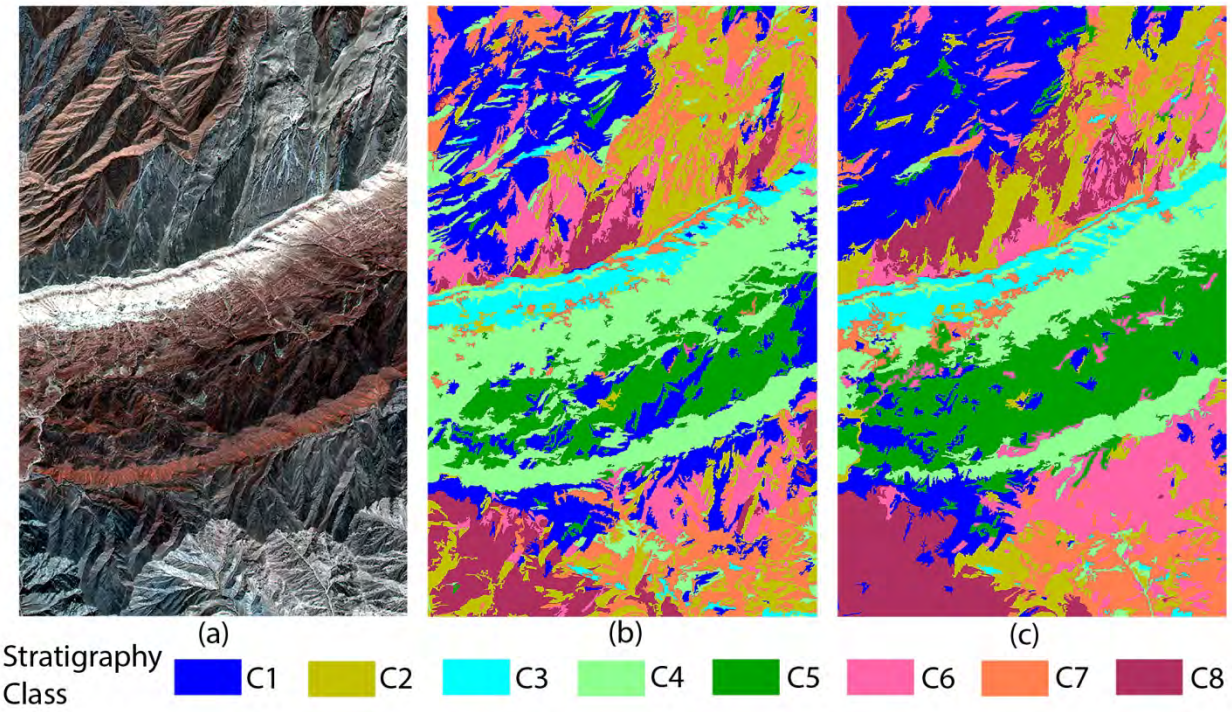

Figure 7-42. (a) Original bands of WorldView-2 (composited bands 4-3-2; (b) classified image using OBIA with WorldView-2 only; and (c) classified image using OBIA with data fusion of WorldView-2 and Hyperion data.

This improvement is attributed to additional spectral information from data synergy that can be further explained by comparing the spectral plots of the two classes (i.e., C1 and C3). As shown in Figure 7-43, the shapes of VNIR band plots for C1 and C3 (i.e., spectral information contained in WorldView-2) were similar. In terms of the range of values, the non-shadowed part of C1 was closer to C3 than the shadowed part of C1. This is one source of ambiguity causing misclassification between C1 and C3 when looking only at information derived from the WorldView-2 MS image. If SWIR spectra from Hyperion are added, (a) and (b) have similar shapes but are distinctly different from (c). Using the higher resolution data reduced the ambiguity between the two classes efficiently, balancing the within-patch spectral variation, in this case data range differences due to shadows.

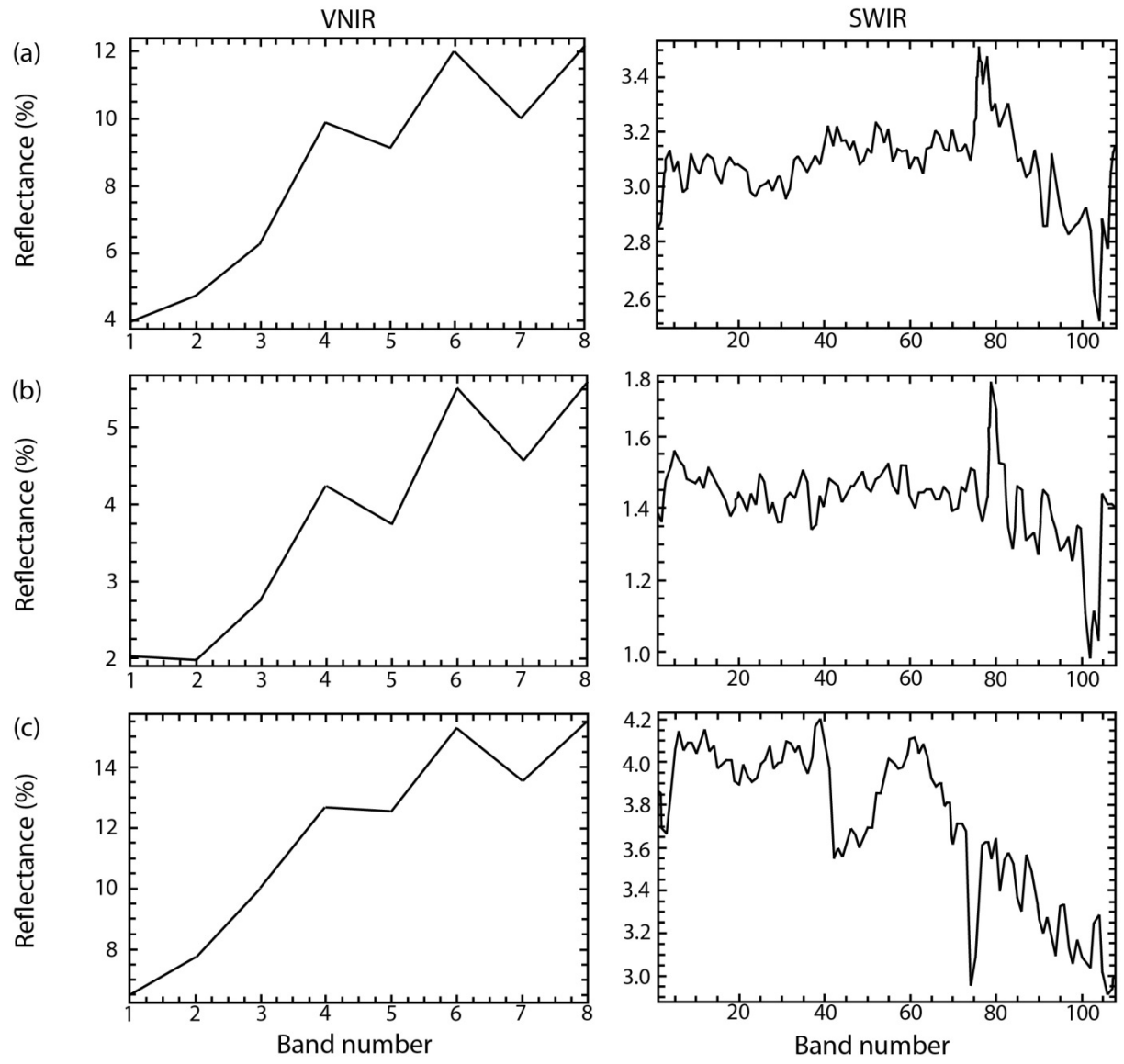

Figure 7-43. Spectral plot of (a) the non-shadowed part of C1; (b) the shadowed part of C1; and (c) C3.

A comparison between the accuracy of results from the error matrices further demonstrates that OBIA with data fusion generally performs better in class identification. OBIA with data fusion had an overall accuracy of 86.3%, which increased the classification accuracy by 11.3% when compared to the method using only WorldView-2 having 75% overall accuracy. Kappa coefficient increased from 0.7120 to 0.8434.

C1 and C2 were unchanged in the two matrices, but the other classes showed improvement. For OBIA without data synergy, C2, C4 and C7 had relatively low user's accuracy. This was due mainly to their spectral overlap with other classes. For example, C2 is mixed spectrally with C6 and C7 in VNIR bands. Therefore, 19 test pixels of C6 and 21 test pixels of C7 were classified mistakenly as C2. However, an increase in their user's accuracy shows that their over-representation had been effectively reduced by the OBIA with data synergy. C3 had relatively high accuracy in both the methods (i.e., 96.3% and 88.9% of user's accuracy, 100% and 92.3% of producer's accuracy in the two methods respectively). This is because

it is especially high reflectance makes it distinguishable from surrounding classes. This feature was further emphasized when additional spectral information from Hyperion was taken into consideration and its producer's accuracy reached 100% in the new method.

Table 7-8a shows the error matrix for the OBIA classification using WorldView-2 data only. Table 7-8b shows the error matrix for the OBIA classification with data synergy.

Table 7-8a. Error Matrix for the OBIA Classification with WorldView-2 Only.

	C1	C2	C3	C4	C5	C6	C7	C8	User's Accuracy (%)
C1	75	0	0	0	6	5	2	0	85.23
C2	1	64	2	0	0	19	11	4	63.37
C3	6	0	48	0	0	0	0	0	88.89
C4	12	2	2	50	4	0	6	0	65.79
C5	2	0	0	3	46	0	0	0	90.20
C6	0	2	0	2	0	24	0	6	70.59
C7	4	12	0	1	1	7	36	1	58.06
C8	0	3	0	0	0	4	0	47	87.04
Producer's Accuracy (%)	75	77.11	92.31	89.29	80.7	40.68	65.45	81.3	

Overall accuracy=75.00%
Kappa Coefficient=0.7120

Table 7-8b. Error Matrix for the OBIA Classification with Data Synergy.

	C1	C2	C3	C4	C5	C6	C7	C8	User's Accuracy (%)
C1	75	0	0	0	0	1	0	2	93.75
C2	2	64	0	0	2	0	4	0	91.43
C3	0	0	52	0	0	0	2	0	96.30
C4	0	0	0	50	0	0	2	0	96.15
C5	5	0	0	3	54	0	0	0	87.10
C6	17	1	0	0	1	53	2	0	72.62
C7	1	6	0	3	0	5	45	0	75.00
C8	0	12	0	0	0	0	0	56	82.35

Overall accuracy=86.35%
Kappa Coefficient=0.8434

8.5.7 *Discussion and Conclusions*

High-resolution imagery improved access to spatial details for mapping dramatically. Integrating spectral information from additional data sources, for example Hyperion hyperspectral imagery, has shown to be an effective form of image analysis. For remote sensing of geological strata, spectral and textural information in images is determined by component and granularity of sediments. Therefore, the synergy of WorldView-2 and Hyperion was able to contribute to classification accuracy. In contrast to traditional pixel-based image analysis, OBIA allows objects on the ground to be distinguished as meaningful pixel-grouped segments rather than a set of separate pixels. OBIA in eCognition offers a semi-automated way to analyze targets based on image segmentation, allowing users to integrate information from several data sets at the feature-level or decision-level. Results from such analyses can be inserted directly into a GIS system.

It should be noted that human intervention is still necessary when using OBIA. For example, the selection of optimal segmentation parameters depends on the heterogeneity of the features over the study area, and those parameters should be defined on a case-by-case basis. Furthermore, the study area for this research represents a natural landscape almost devoid of human disturbance and therefore gradual spectral transitions between geological features are intact. Conversely, an anthropogenic landscape may have many artificial elements with spectrally abrupt transitions such as impervious surfaces and agricultural fields. As a result, the internal heterogeneity for each class is likely to vary and the viability of the proposed method would need to be assessed. Hence, it would be beneficial to extend this study to include areas with differing landscape characteristics. Also, the time gap between the two images used in this study cannot be ignored. Classification is expected to be improved by using data collected at the same time.

Auxiliary spectral bands cannot always guarantee effectiveness for every stratigraphic class. More robust data fusion relies on a comprehensive understanding of spectral features from each of the target classes. For example, C5 and C8 showed some decrease in user's accuracy with the new method. A careful examination of the error matrix revealed that there was confusion among C1, C4 and C5. These classes are similar in reflectance considering the bands used (both VNIR with lower spectral resolution and SWIR with higher spectral resolution). The additional spectral information in SWIR failed to make the classes more distinguishable from each other. One possibility is their spectral features, which could be detected more easily using VNIR bands with higher spectral resolution. For class C8, the classification overlap with C2 increased to a certain extent after introducing the SWIR bands, but its confusion with C6 has been eliminated. It shows that the efficiency of data synergy is on a class-by-class basis. If the spectral characteristics of two classes are similar in the additional bands, the introduction of these bands will create obstacles to accurate classification rather than facilitate it. On the other hand, using bands that show distinctive spectral features of the two classes due to data synergy, as described in Figure 7-41, increases class separability.

The proposed method employed a single set of parameters for segmentation. However, considering the range of sizes of objects on the ground and varied information that may be available at different scales, a single parameter set may not always be optimal to identify all the objects on an image (Kim *et al.*, 2009; Laliberte and Rango, 2009). A multi-scale OBIA, where different parameters can be set for different cover classes, may yield better results.

Generally, the classification of most of the classes in this study took advantage of the spectral response of the SWIR band in Hyperion. These were not included in the analysis when only using WorldView-2 imagery. The results demonstrated the potential to apply OBIA for remote sensing of geology. With data synergy, spectral advantages from Hyperion and spatial advantages from WorldView-2 are combined, improving the stratigraphic classification accuracy. Effective data synergy can be achieved by selecting auxiliary data based on specific spectral reflectance features of target objects. Further studies based on this method will focus on using multi-scale OBIA for different landscape areas such as mountains, urban landscapes, forests, agricultural areas, among others.

9 IMAGE CLASSIFICATION

9.1 *Introduction*

Data classification and interpretation are major tasks in remote sensing and encompass multi-step workflows, which typically include:

- prediction and identification of thematic classes (i.e., categorical data);
- identification and preparation of input variables (i.e., predictors) to be used during the classification or interpretation process;
- selection of classification method and use of classifier for class identification and labelling of thematic units; and,
- assessment and evaluation of the classification results.

All steps involved in the classification and interpretation of remotely-sensed data are critical to the final quality of results and analysts greatly benefit from understanding classification algorithms for proper classification method selection (e.g., pixel based vs. region based; supervised vs. unsupervised); use and result evaluation. Below, are summaries of some image classification approaches often used in remote sensing, including: SVM; decision tree classifier (DTC); fuzzy clustering; SAM, and OBIA.

9.2 *Support Vector Machines*

Since their introduction in the 1970s (Vapnik, 1979), SVMs have become a popular choice for image classification tasks. One major appeal of SVMs is their ability to generalize from a small training data set; it has been shown that SVMs can produce results with higher classification accuracy than other commonly used methods (Mantero *et al.*, 2005). SVMs are a supervised classification technique as labeled samples are essential. They fall under the non-parametric category as they do not make (or require) an underlying assumption on the data distribution. During the training phase, an SVM uses key training points to identify hyperplanes that separate classes in the classification feature space (Zhu and Blumberg, 2002). The operation is iterative, which is time-consuming, however faster than other popular machine learning methods, such as back propagation neural networks. In Figure 7-44, adapted from Burges, 1998, an example is shown of a SVM training for a two-class problem. The algorithm will select the key training points, called support vectors, to formulate the optimal hyperplane for separation of classes by maximizing the margin width.

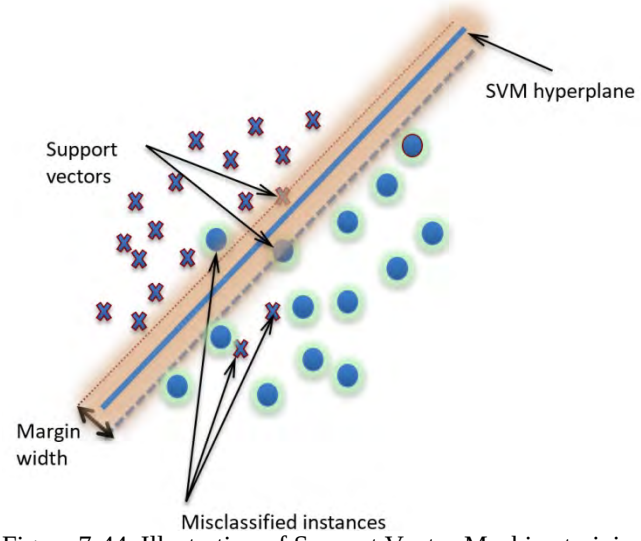

Figure 7-44. Illustration of Support Vector Machine training.

Because in their original form SVMs separate the feature space using hyperplanes, in essence linear functions, sometimes they fail to capture complex class distributions. To overcome this limitation, several kernel-based transformations have been introduced, that allow transformation to a different non-linear space where hyperplanes could potentially separate classes. Further discussion on SVM kernels is available (Scholkopf and Smola, 2001). In addition, originally SVMs were developed for two-class problems, in essense binary classifications. While for remote sensing classification SVMs could be applied by grouping all but one class and then attempt to separate that group from that class (i.e., one-against-all method) other methods have been proposed to handle multi-class separation more effectively (Knerr *et al.*, 1990).

A wide range of applications of SVM has been reported in the literature and Mountrakis *et al.* (2011) provide a recent review on the use of SVM in remote sensing. Typical tasks employing the technique involve the classification of MS and hyperspectral data in high and medium spatial resolutions (<40m pixel size). Uses include mapping and biophysical parameter estimation, for example chlorophyll concentration (Kwiatkowska and Fargion, 2003; Bazi and Melgani, 2007; Sun *et al.*, 2009). Several works dealing with urban mapping have benefited from using SVM. For example, Watanachaturaporn *et al.*, (2008) identified that SVMs outperformed other classifiers in an urban classification task. SVMs also are commonly used in crop mapping. For instance, Camps-Valls *et al.* (2004) found that in a crop classification task using hyperspectral imagery SVMs outperformed typical neural networks. The authors reported that SVMs were not as affected by reduced training sample size. A method comparison involving general land cover classification showed that SVMs and neural networks outperformed the maximum likelihood method, while the SVMs were much faster to train (Dixon and Candade, 2008). SVMs also have been applied to other classification tasks, including the reconstruction of cloud-contaminated multMSispectral images (Melgani, 2006).

SVMs also have inherent limitations. The most notable one is the kernel transformation, which requires extensive testing. Furthermore, in the effort to increase separability of classes, the resulting dimensionality increase may lead to unexpected results, especially when the dimensionality is already high (e.g., hyperspectral images). Another methodological concern relates to how SVMs handle noisy data. Because SVMs

by design look for support vectors to establish the separation hyperplanes, they are more susceptible to noise, a typical occurrence in remotely sensed data.

As mentioned, there are numerous studies comparing the algorithmic performance of SVM with other popular classification methods. In this regard, Khatami *et al.* (2016) aimed to establish general guidelines for researchers and practitioners while using SVM and performed a meta-analysis looking back 15 years of published works. The study aggregated comparative investigations from the five most popular remote sensing journals and findings suggest that SVMs tend to outperform slightly neural networks and decision trees, while offering considerable gains when compared with simpler algorithms such as the maximum likelihood.

To conclude, SVMs have found fruitful ground in remote sensing applications. Numerous efforts have been pursued to address algorithmic limitations and implement SVMs in a wide range of remote sensing tasks. If trends from other domains are an indication for high volume remote sensing tasks, SVMs may be sidelined by deep learners in the near future. However, for localized studies with limited reference datasets, SVMs should be given serious consideration.

9.3 *Decision Tree Classifier*

9.3.1 *Introduction*

Parametric statistical procedures, such as the maximum likelihood classifier, are based on the assumption that the data follow some pre-defined model, such as a Gaussian normal distribution. Other statistical procedures each have explicit or implied assumptions as to the structure of the data. The performance of any statistical classification will depend on how well the data match the assumptions underlying the statistical method. It is unlikely that any remote sensing-based dataset will precisely follow the assumptions of any classifier, but the complex structure of these data can be particularly problematic for parametric methods that have particularly strict distributional assumptions. The maximum likelihood classifier is a single-stage classifier, because an observation is given the label of one of a predetermined number of classes in a single step. This approach to classification has two significant drawbacks (Swain and Hauska 1977):

- Only one of the possible combinations of features (i.e., spectral bands and ancillary data) is used in the classification.
- Each sample is tested against all classes.

An inherent weakness of the maximum likelihood procedure is that the subset of features used in classification is not necessarily the optimal choice for all classes. Usually, a set of features is selected either simply by what features are available or, if feature selection does take place, by the criterion of maximum average interclass separability (i.e., in a multi-class multi-feature classification the set of features with largest pair-wise separability is used). The problem of using only one feature subset as the basis of a classification is particularly severe in cases where the dataset has a large number of classes. In principle, one could combine the features that are useful in discriminating between all possible combinations of pairs of classes and use the combination of these features in a single stage classifier; however, a feature that is valuable for distinguishing certain classes might increase confusion between other classes.

As progress in new sensor technology for Earth observation remote sensing continues, increasingly high spectral resolution multi/hyper-spectral imaging sensors are being developed. These sensors provide more detailed and complex data with increased dimensionality. As the number of spectral features, number of training samples, and classification accuracy are interrelated in a complex fashion, one may need to know how many features should be used to maximise the overall classification accuracy. Where training sample size is limited and the dimensionality of the feature space is high, then the estimate of first and second-order statistics (e.g., as required by maximum likelihood classifier) cannot accurately summarise all information that is contained in the data and results are thus less reliable.

For such problems, it would be preferable to have a classification system that could decompose the classification problem into several stages leading to a simplified decision-making process by taking decisions at successive stages. The technique of decomposing the classification problem into several stages is termed multistage classification. It has several attractive features, the most important of which, perhaps, is interpretability, because the model structure can be transparent to the analyst. In many instances, taking such partial decisions is conceptually simpler, as each decision involves only using information relevant to the current stage, which has led to the increased popularity of multistage decision making for remote sensing classifications.

9.3.2 *Decision Tree Classifiers*

Several multistage classification techniques, based on the way they are constructed, have been proposed in literature. Decision tree classifiers, which sequentially reject classes along a path to a finally accepted class label, are an effective implementation of a multistage classifier and became increasingly popular due to their conceptual simplicity and computational efficiency in remote sensing. A DTC has a simple form, which can be compactly stored and classifies test data efficiently. A DTC also carries out automatic feature selection and complexity reduction. The tree structure provides easily understandable and interpretable information regarding the generalisation ability of the data.

The significant advantages of DTCs are their non-parametric nature (Quinlan, 1993), simplicity, flexibility, and computational efficiency (Safavian and Landgrebe, 1991; Hansen *et al.*, 1996; Friedl and Brodley, 1997; Pal and Mather, 2003), which makes them an effective tool for remote sensing classifications (Hansen *et al.*, 1996). Decision tree classifiers are found in the remote sensing and statistical literature under various names (e.g., decision trees, classification tree analysis (CTA), classification and regression trees (CART), or binary recursive partitioning).

Two approaches are generally used to design a DTC (Swain and Hauska, 1977). Both approaches are similar in principle, but differ significantly in the way the tree is developed.

- Heuristic search method
- Manual design method

Construction of a classification tree using the heuristic approach is a supervised classification approach; thus, it is initiated using a training data set consisting of feature vectors and their corresponding class labels. The decision tree is then constructed by recursively partitioning the training data set into purer, more homogenous, subsets on the basis of a set of tests applied to one or more attribute (feature) values at each branch or node in the tree. This procedure involves three steps: splitting nodes, determining which nodes

are terminal nodes, and assigning class label to terminal nodes. The assignment of class labels to terminal nodes is straightforward: labels are assigned based on a majority vote or a weighted vote when it is assumed that certain classes are more likely than others. This enables associated probabilities to be applied to the resulting classes at each terminal node.

A tree constructed this way is composed of a root node, containing all the data, a set of internal nodes (i.e., splits), and a set of terminal nodes (i.e., leaves). Each node in a decision tree has only one parent node and two or more descendent nodes (see Figure 7-45). A data set is classified by moving down the tree and sequentially subdividing it according to the decision framework defined by the tree until a terminal node is reached.

In comparison to heuristic methods, manual methods use statistics such as the mean vector and covariance matrix calculated for all classes using single feature. A graph called coincident spectral plot is then plotted for each feature using the mean and variances of all the classes. This method is not suitable for the data using two or more features together, which is generally the case with remote sensing classifications.

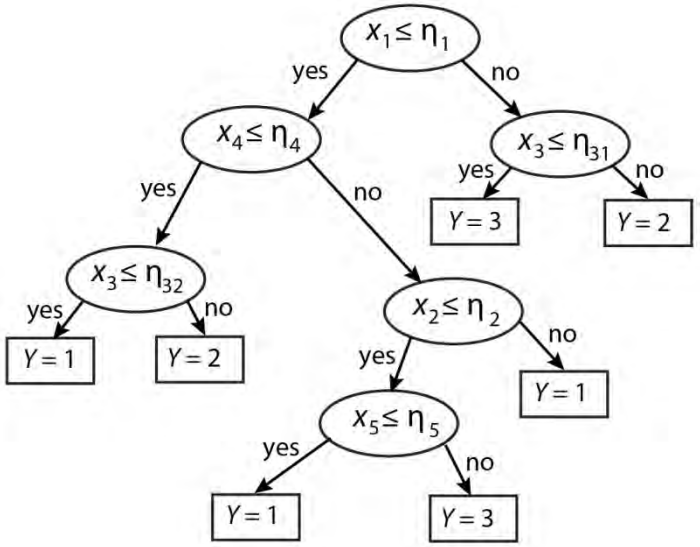

Figure 7-45. A classification tree for a five-dimensional feature space and three classes. The x_i are the feature values, the η_i are the thresholds, and Y is the class label.

9.3.3 *Decision Tree Design Approaches*

Numerous tree construction approaches have been developed in the last forty or so years, but most of the research in DTC design has concentrated in the area of finding splitting rules, which finally gives the idea of the termination rules. Being the most important element of a DTC, several algorithms are proposed to split the training data at each internal node of a decision tree into regions that contain data from just one class. These algorithms either minimize the impurity of the training data or maximize the goodness of split. The main approaches to design a decision tree are:

- Top-down approach
- Bottom-up approach
- Hybrid approach

Top down approach of designing a DTC is the most commonly used for remote sensing classification and consists of the following three tasks:

- Selection of a node splitting rule,
- Decision as to which nodes are terminal,
- Assignment of each terminal node to a class label.

The class assignment problem is the easiest in above-mentioned design tasks. Terminal nodes that have the highest probabilities by using a basic plurality rule are assigned to the classes. The basic idea in choosing any splitting criterion at an internal node is to make the data in the descendent nodes purer.

The approach adopted by the top-down method of designing a decision tree is to choose the attribute that best divides the training data into classes and then partition the data based on the value of selected attribute. This process is applied recursively to each partitioned subset, with the procedure terminating when all data in the current subset have the same class or, in some implementations, a minimum number of observations is reached. The result is represented as a tree in which each node specifies an attribute and each branch emanating from a node specifies a possible value of that attribute.

Thus, the main task of this process is to select the attribute (i.e., feature) to be used as criterion, because at each node in the development of a decision tree there will be a set of observations and a number of attributes to classify them. One cannot select an individual attribute without first determining the "quality" of all of the attributes and seeing how well each one separates the data into various classes. The quality of an attribute should reflect the useful information provided by that attribute. There are two major approaches to estimate the quality of an attribute.

In the first approach, the quality of an attribute may be estimated by ignoring the other attributes, therefore assuming independence of attributes. In the second approach, the quality of an attribute may be estimated in the context of other attributes. The first approach is also called the myopic approach (Kononenko and Hong, 1997), which has the advantage of computational speed. The latter approach is computationally more demanding but has the potential to discover higher-order dependencies among the attributes.

9.3.3.1 Attribute Selection Measures

Many approaches are proposed for selection of attributes (i.e., features) used in the design of DTC (Breiman *et al.*, 1984, Mingers, 1989a; Quinlan, 1993; Murthy *et al.*, 1994; Kononenko and Hong, 1997). Some approaches measure the “goodness of split” (Breiman *et al.*, 1984), while other approaches try to minimize the impurity of the training data.

The quality of an attribute in classification is defined in term of the purity of classes of training data, and most approaches assign a quality measure directly to the attribute. A set of observations is pure if all the observations belong to the same class, whereas the set is maximally impure if the proportion of observations in all classes is uniform. The impurity function measures the impurity of a set of observations and achieves the minimum for a pure set, and maximum for a maximally impure set. Impurity functions are mainly used in selecting the best attribute to further split the current node. The most frequently-used impurity measures in decision tree induction are:

- Information Gain and Information Gain Ratio criterion (Quinlan, 1993)

- Gini Index (Breiman *et al.*, 1984)
- Twoing rule (Breiman *et al.*, 1984)
- Chi-square statistics (Mingers, 1989a)
- Entropy (Apte and Weiss, 1997)

(1) Information Gain and Information Gain Ratio Criterion

Quinlan (1993) proposed the use of the information gain and information gain ratio, based on a classic formula from information theory that measures the theoretical information content of a code as $-\sum p_i \log(p_i)$ where p_i is the probability of the i^{th} message and the term $-\sum p_i \log(p_i)$ is a measure of homogeneity of a node and also referred as Entropy (Apte and Weiss, 1997). The value of this measure depends on the likelihood of the various possible messages. If they are all equally likely (i.e., the p_i are equal), there is the greatest amount of uncertainty and the information gained will be greatest. The less equal the probabilities, the less information would be gained. The value of the function also depends on the number of possible messages (Quinlan, 1993).

For a given training set *T*, selecting one case at random and saying that it belongs to some class C_i, has the following probability of being correct:

$$f((C_i, T)/|T|) \tag{7-27}$$

where: $f(C_i, T)$ stands for the number of cases in *T* that belongs to class C_i and $|T|$ denotes the number of cases in *T*. The information gained by splitting T using a test Z that can partition T into k outcomes can be measured by the quantity:

$$\text{gain}\ (Z) = \text{info}(T) - \text{info}_z(T) \tag{7-28}$$

This criterion is called the gain criterion (Quinlan, 1993). The gain criterion, select a test to maximise the information gain. This is also known as the "mutual information between the test *Z* and the class" (Quinlan, 1993).

The drawback of the gain criterion is that it has a strong bias towards the tests with many outcomes. The bias inherent in the gain criterion can be rectified by normalization in which the apparent gain with many outcomes is adjusted. If the information content of a message pertaining to a case that indicates not the class to which the case belongs but the outcome of the test then, by analogy with the definition of info (*T*) (Quinlan, 1993), the information generated by dividing *Z* into n subsets is given by:

$$Split\ info\ (Z) = -\sum_{j=1}^{k} \frac{|T_j|}{|T|} \times log_2\left(\frac{|T_j|}{|T|}\right). \tag{7-29}$$

This gives an idea of the potential information generated by dividing *Z* into *k* subsets, whereas the gain measures the information useful for classification that arises from the same division. Then, the ratio gain ratio (*Z*) = gain (*Z*)/split info (*Z*) provides the proportion of information generated by a split that is useful for classification and used in C4.5, an extensively used decision tree software for remote sensing classifications. These criteria recursively split the *T* so as to maximize the gain ratio at each node of the tree. This procedure continues until each terminal node contains only observations from a single class, or further splitting yields no increase in information.

(2) The Gini Index

The Gini index is widely used in decision tree software and used in remote sensing studies. Breiman *et al.* (1984) proposed this attribute selection measure called the Gini index of diversity. The Gini function measures the impurity of an attribute with respect to the classes. The general Gini function for a given training set *T* can be defined by:

$$\sum\sum_{j\neq i}(f\ (C_i,T)/|T|)\left(f\left(C_j,T\right)/|T|\right) \quad (7\text{-}30)$$

The Gini index is simple and can be computed quickly. This index uses the rule that assigns an object selected at random from the node to the class *i* with probability f (C_i, *T*)/ |*T*|, instead of using the plurality rule to classify objects in a node.

(3) The Twoing Rule

The twoing rule has been less commonly used in remote sensing studies, and at least one study found it to be inferior for that purpose than the Gini index (Zambon *et al.*, 2006). It separates the classes into two super-classes, $C_1 = \{j_1, \ldots \ldots, j_n\}$, and $C_2 = C - C_1$ (Breiman *et al.*, 1984). For a given split of a node, the decrease in impurity that results from this split of the node can be computed as:

$$(|T_L|/|T|) * (|T_R|/|T|) * (\sum_i |L_i/|T_L| - R_i/|T_R||)^2 \quad (7\text{-}31)$$

where: $|T_L|$ and $|T_R|$ are the number of examples on the left and right of a split at the node and L_i and R_i are the number of examples in class *i* on the left and right side of the split. This decrease in impurity is known as the twoing value. The twoing value is actually a goodness of fit measure rather than an impurity measure.

(4) The Chi-square Contingency Table Statistic

This method of attribute selection is based on traditional statistics for measuring the association between two variables in a contingency table (Mingers, 1989a). This approach works by comparing the observed frequencies with the frequencies that one would expect if there were no association between the attributes. The resulting statistic is distributed approximately as chi-square, with larger values indicating greater association. The basic equation for this function is

$$\chi^2 = \sum\sum \frac{\left(x_{ij}-E_{ij}\right)^2}{E_{ij}} \quad (7\text{-}32)$$

where: $E_{ij} = X_i X_j / N$, i.e., the expected value for each cell in the contingency table. A study by Pal and Mather (2003) used MS data to examine the performance of four attribute selection measures in terms of classification accuracy. They used a univariate DTC with error-based pruning. A total of 2700 data for training and 2037 for testing were used. Figure 7-46 provide a plot of classification accuracy achieved by different attribute selection algorithms and confirms the findings of Breiman *et al*. (1984) and Mingers (1989a) that classification accuracy is not much affected by the choice of attribute selection measure, whereas another study by Zambon *et al*. (2006) compared four attribute splitting rules (i.e., gini, entropy, class probability, and twoing) across diverse remote sensing-based datasets (e.g., multispectral moderate and high-spatial resolution and hyperspectral) and found differences up to 6% overall accuracy, especially with hyperspectral data.

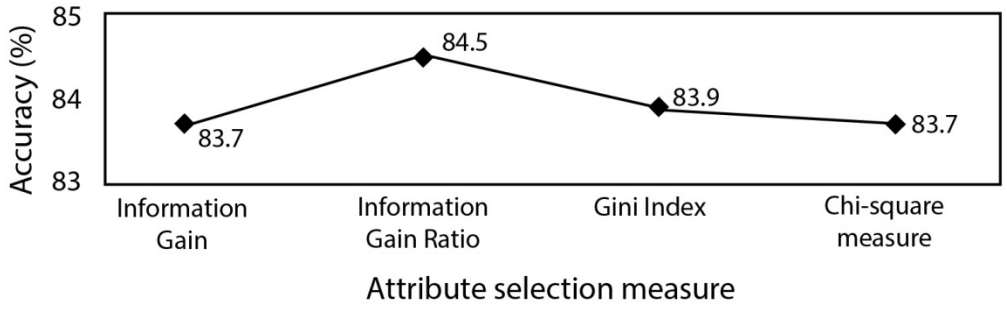

Figure 7-46. Variation in classification accuracy with different attribute selection measure.

The final stage in top-down DTC design is the determination of when splitting should be stopped. Initial approaches to selecting terminal nodes were of the form where a threshold $\beta > 0$ is set, and node t is declared as a terminal node if $\max_{S \in T} \Delta i(S(t), t) < \beta$. Where $\Delta i\,(S, t)$ is decrease in impurity because of the split S at every internal node t (Breiman *et al.*, 1984). The problem with this rule is that partitioning might be halted too soon at some nodes and too late at some others. Breiman *et al.* (1984) suggested that the stopping rule has a greater impact on the performance of DTC than the splitting rules and suggested that, instead of using a stopping rule, one should continue splitting until all the terminal nodes are pure, or nearly pure, thus generating a large tree. This large tree is then selectively pruned, producing a decreasing sequence of sub-trees. Finally, select the subtree that has the lowest estimated misclassification rate. This general approach has become the commonly used method.

The bottom-up approach of creating a decision tree uses a distance measure, such as the Mahalanobis distance (Landeweered *et al.*, 1983), to construct a binary tree using training dataset. The pairwise distances between *a priori* defined classes are computed, and the two classes with the smallest distance are merged to form a new group in each step. The mean vector and covariance matrix for each group are computed from training data in that group, and the process is repeated until a single group is left at the root. The hybrid methods of designing a DTC use both the bottom-up and top-down approaches sequentially and have been found to have several advantages over both top-down and bottom-up approaches (Kim and Landgrebe, 1991). They are found to converge to classes of informational value, because the cluster initialization provides early guidance in this direction, while the straightforward top-down approach does not guarantee such convergence. The hybrid approach can also use overlapping classes, which is not possible with bottom-up approach. Another approach called as growing-pruning method (Gelfand *et al.*, 1991) of constructing a DTC was proposed so as to deal with the problem of limited data sets. This approach works by dividing the whole dataset into two subsets of nearly equal size. A tree is grown using the first data subset until pure terminal nodes are reached. A pruned sub-tree is then selected by minimizing an estimate of the error rate based on the second data subset over all pruned sub-trees. This procedure is then iterated, using the second data subset to grow a tree starting from the terminal nodes of the previously selected pruned sub-tree and continued until the sequence of selected pruned sub-trees converges.

9.3.4 *Classification Algorithms Based on Data Splitting Method*

Decision tree classification algorithms can also be divided based on the criteria of using a uniform or a heterogeneous set of algorithms to split the data at internal nodes. Traditional approaches of designing a

decision tree are based on homogenous classification models for which a single algorithm is used to estimate each split. Generally speaking, there are two types of decision trees based on homogenous hypothesis space: univariate decision trees (i.e., by far the most commonly used in remote sensing studies) and multivariate decision trees.

A hybrid hypothesis space combines different homogenous hypothesis spaces to construct a decision tree. The learning algorithms used to estimate a hybrid tree allow different splitting methods to be applied within different subtrees of the larger decision tree (Friedl and Brodley, 1997).

9.3.4.1 Univariate Decision Trees

A univariate decision tree is a type of decision tree in which the decision boundaries at each node of the tree are defined by a single feature of the input data (Swain and Hauska, 1977). The data at each internal node of a univariate decision tree are split into two or more subsets on the basis of a test on a single feature (i.e., attribute) of the input data, and each test is required to have a discrete and finite number of outcomes. Thus, a univariate decision tree classification proceeds by recursively partitioning the input data until a terminal node is reached, and the class label associated with the node is then assigned to the observation. The specific values of the decision boundaries in a univariate decision tree are estimated empirically from the training data. In the case of continuous data, a boolean test of the form $X_i > b$ is estimated at each internal node of a decision tree from the training data, where X_i is a feature in the data space and b is a threshold in the observed range of X_i. The value of b can be estimated by using some objective measure that maximises dissimilarity or minimises similarity of the descendent nodes.

9.3.4.2 Multivariate Decision Trees

In case a class structure depends on combination of features, performance of a univariate decision tree will decline (Breiman *et al.*, 1984; Utgoff and Brodley, 1990; Brodley and Utgoff, 1992). In problems where a linear structure is suspected, the set of allowable splits is extended to include linear combinations of features in the input data. Multivariate decision trees are similar to univariate decision trees except that the splitting test at each node is based on more than one feature of the input data. In one approach, set of linear discriminant functions is estimated at each interior node of a multivariate decision tree, and the coefficients for the linear discriminant function at each interior node are estimated from the training data. The test at each node has the form:

$$\sum_i a_i X_i \leq c \tag{7-33}$$

where X_i represent the features in the data space, a is the vector of coefficients of the linear discriminant functions, and c is a threshold value. An alternative approach is the logistic model trees, where the split at each node is determined by a logistic regression model (Landwehr *et al.*, 2005). Multivariate decision trees are often found to be more compact and can also be more accurate (Brodley and Utgoff, 1992; Lawrence and Moran, 2015). The higher complexity of multivariate decision tree algorithms introduces a number of factors that affect their performance. First, different algorithms can be used to split the data at internal nodes, whereas each method can perform differently depending on the data and classification problem. Second, as the split at each internal node of a multivariate decision tree is based on one or more features,

so different feature selection algorithms can be used to perform feature selection at each internal node within a multivariate decision tree.

9.3.4.3 Hybrid Decision Tree Classifier

A hybrid decision tree is a decision tree in which different classification algorithms may be used in different subtrees of a larger tree. The implementation of hybrid decision tree based classification approach is based on the fact that different algorithms exhibit selective superiority during classification (Friedl and Brodley, 1997) and the optimal classification algorithm depends on the data set to be classified. If different classification algorithms are allowed within the framework of a single hybrid tree, the data set can be partitioned in a fashion such that the different classifiers can be applied to different subsets of the data.

9.3.5 *Prunning Decision Trees*

Decision tree classifiers divide the training data into subsets, until each subset contains data belonging to a single class. This procedure of data division usually results in a very large and complex tree. As training samples might not be perfectly representative of the population from which they are sampled, fitting a decision tree until all terminal nodes contain data for a single class potentially overfits any noise in the training data. This can lead to poor performance by the classifier on data not used to create the model. Alternatively, even if overfitting does not take place, the creation of a large, complex tree might result in a non-parsimonious model, where a large portion of the tree adds very little, if any, explanatory value. These problems of overfitting and lack of parsimony can be reduced by pruning the original tree, which will lead improved performance by the classifier (Pal and Mather, 2003).

A decision tree is not usually simplified by deleting the whole tree in favor of a terminal node. Instead, parts of the tree that do not contribute to classification accuracy on unseen cases are removed, thus producing a less complex and more comprehensible tree. Two different approaches are used to produce a simplified decision tree (Breiman *et al.*, 1984):

- To remove retrospectively some part of the tree structure built by recursive partitioning
- By deciding not to divide a set of training data any further

First approach of simplifying the decision tree involves allowing the tree to grow to its full depth, when all leaves contain data for a single class. This is often modified to allow some heterogeneity, by limiting the number of observations at terminal nodes to a small number, but certainly more than one. This fully-grown tree is then pruned. This method requires more computation in building parts of the tree that are subsequently discarded, but this cost is offset by the benefits due to more thorough exploration of possible partitions. Pruning a decision tree will result in terminal nodes that do not necessarily contain training data from a single class, leading to higher misclassification error of training data. Instead of a class associated with a terminal node, there will be a class distribution specifying, for each class, the probability that training data at the terminal node belongs to that class.

The second approach is generally called stopping or pre-pruning with the advantage of not wasting time in assembling a tree structure that is not used in the final simplified classifier. In-spite of its simplicity, major problem with this approach is to specify a correct stopping rule (Breiman *et al.*, 1984). If the threshold value used to stop the growth of tree is too high it can terminate division before the benefits of subsequent

splits become evident, while too low a value results in little simplification of the tree. The example below shows a decision tree generated by using a univariate decision tree (see, Figure 7-47) using a two-class dataset before and after pruning.

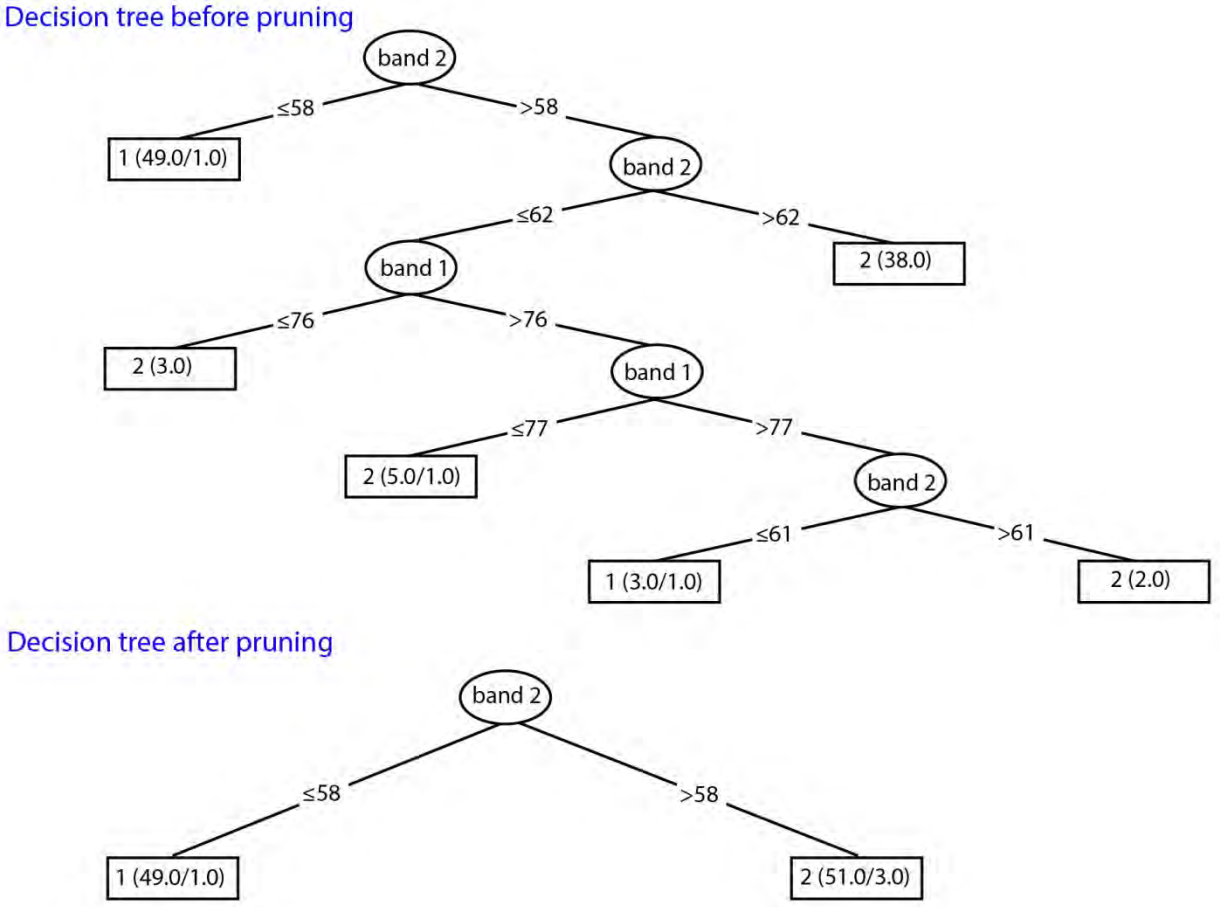

Figure 7-47. Example of decision tree generated by using a univariate decision tree (C4.5) including a two-class dataset before and after pruning.

Decision trees are usually simplified by removing one or more subtrees and replacing them with leaves. The process of pruning can be started from the bottom of the tree by examining each subtree. This procedure is called the bottom-up approach. Alternatively, in the top-down approach, the process starts from the root and moves towards the leaves of the tree by examining the branches. The tree is pruned if replacement of a subtree with a terminal node would lead to a lower predicted error rate. The error rate for whole tree decreases as the error rate of any of its subtrees is reduced, and this process will lead to a tree whose predicted error rate is minimal with respect to the allowable form of pruning. As mentioned earlier, pruning always increases error on training data, so it is necessary to have a suitable technique for predicting error rates.

Two families of techniques to predict error rates of a pruned tree are available. In the first family, the error rate of the tree and its subtrees is predicted by using a new data set that is separate from the training data. Since these cases were not examined at the time the tree was constructed, the estimate obtained from them can be independent, depending on how they were collected relative to the training data. This approach works well if sufficient data are available. The second approach uses training data itself to predict these

error rates and pruning the tree, generally through a cross validation approach. The important techniques for pruning the decision tree are as follows:

- Cost-complexity pruning (Breiman *et al.*, 1984)
- Reduced-error pruning (Quinlan, 1987)
- Pessimistic pruning (Quinlan, 1993)
- Error based pruning: (Quinlan, 1993)
- Critical value pruning (Mingers, 1989b)

9.3.5.1 Cost-complexity Pruning

In cost-complexity pruning (CCP), the predicted error rate of a tree is modelled as the weighted sum of its complexity and error on training data, with the separate data set being used primarily to determine an appropriate weighting. This technique is a two-stage process in which first stage involves in creating a sequence of sub-trees from original decision tree generated by using training data set. Each sub-tree is obtained by replacing one or more sub-trees of previous sub-tree with leaves until the final tree is just a terminal node.

In the second stage of this process, the best tree from the sequence of sub-trees with respect to the predictive accuracy criterion is selected. Two different methods can be used to estimate the true error rate of each tree in the family. The first method is based on cross-validation, whereas the other method uses an independent pruning data set. In case the test set containing N' cases are used for classification with each sub-tree and E' be the minimum number of errors observed with any sub-tree, with the standard error of E' being given by:

$$Se(E') = \sqrt{E' \times (N' - E')/N'} \tag{7-34}$$

The smallest sub-tree whose number of errors on test dataset does not exceed $E' + Se(E')$ is selected as final tree.

9.3.5.2 Reduced-error Pruning

This method uses a separate test dataset to assess the error rates of the tree and its components. In this method, the original tree classifies all the test data. The changes in misclassification over the test data that would occur if a sub-tree is replaced by the best possible terminal node are examined. If the new tree would give an equal or smaller number of errors, and if sub-tree contains no subsequent sub-tree with the same property, then the sub-tree is replaced by the terminal node. The process continues until no further replacements would increase the number of errors over the test set.

Similar to the CCP, this method generates a sequence of trees. The final tree is the most accurate and smallest sub-tree of the original tree with respect to the test data set. This method of pruning the decision tree would be quite effective when training and test data are abundant but can lead to poorer-performing trees when data are scarce.

9.3.5.3 Pessimistic Pruning

This approach of pruning the decision tree increases the estimated error rates of subtrees to reflect the size and composition of the training subsets and replaces every subtree whose predicted error rate is not

significantly lower than that of a terminal node (Quinlan, 1987). It aims to avoid the necessity of a separate test data set or cross validation as required by reduced error pruning and cost complexity pruning. A continuity correction for the binomial distribution is used to obtain a more realistic estimate of the misclassification rate than using error ratio determined by training dataset.

The continuity correction obtained this way can still produce an optimistic error rate on training dataset. To avoid this problem, Quinlan (1993) suggested pruning the subtree unless its corrected number of misclassifications is lower than that for the node by at least by one standard error of reference tree. As this algorithm evaluates each node starting at the root of the tree (i.e., top-down approach), it does not need to consider nodes that are in subtrees that have already been pruned.

9.3.5.4 Error-based Pruning

This is an improved pessimistic pruning method and based on a far more pessimistic estimate of the expected error rate and implemented in the C4.5 and C5.0 algorithms (Quinlan, 1993). Unlike the pessimistic pruning method, this method visits the nodes of the full-grown tree according to a bottom-up, post-order traversal strategy instead of a top-down strategy.

9.3.5.5 Critical Value Pruning

This method relies on estimating the importance of a node from classifications done at the tree creation stage. In creating the original tree, a goodness of split measure determines the attribute at a node. The value of the measure reflects how well the chosen attribute splits the data between the classes at the node. The pruning method specifies a critical value and prunes those nodes that do not reach the critical value, unless a node further along the branch does reach that value. The larger the critical value selected, the greater the degree of pruning and the smaller the resulting tree. In practice, a series of pruned trees is generated using increasing critical values (Mingers, 1989b). A single tree can be chosen in the same way as for cost-complexity pruning. The particular critical value used depends on the measure used in creating the tree. A study by Pal and Mather (2003) suggests that the choice of suitable pruning method is an important factor in the design of a DTC (Figure 7-48). They compared C4.5 decision tree with a maximum likelihood classifier in terms of classification accuracy and suggested that C4.5 classifier produces a higher level of classification accuracy than maximum likelihood classifier. Figure 7-49 provides classified images of the study area obtained by using a C4.5 decision tree and maximum likelihood classifiers.

Another approach for pruning DTC considers a stopping criterion while tree is being grown. In spite of its simplicity, major problem with this approach is to specify a correct stopping rule (Breiman *et al.*, 1984). If the threshold value used to stop the growth of tree is too high, it can terminate division before the benefits of subsequent splits become evident, while too low a value results in little simplification of the tree.

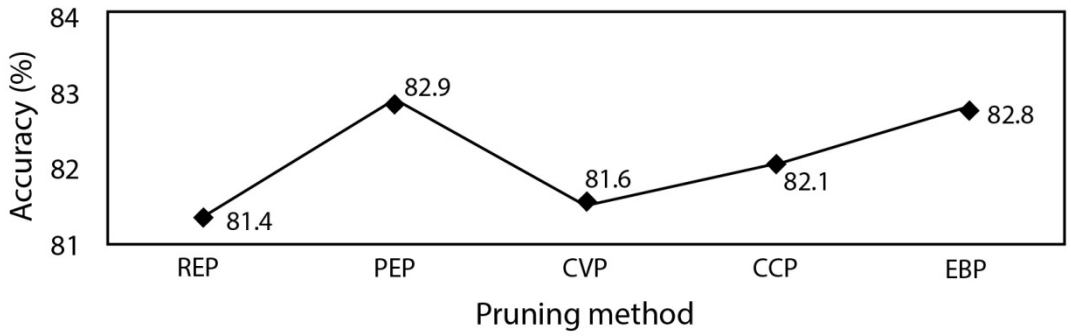

Figure 7-48. Variation of classification accuracy with the choice of pruning method.

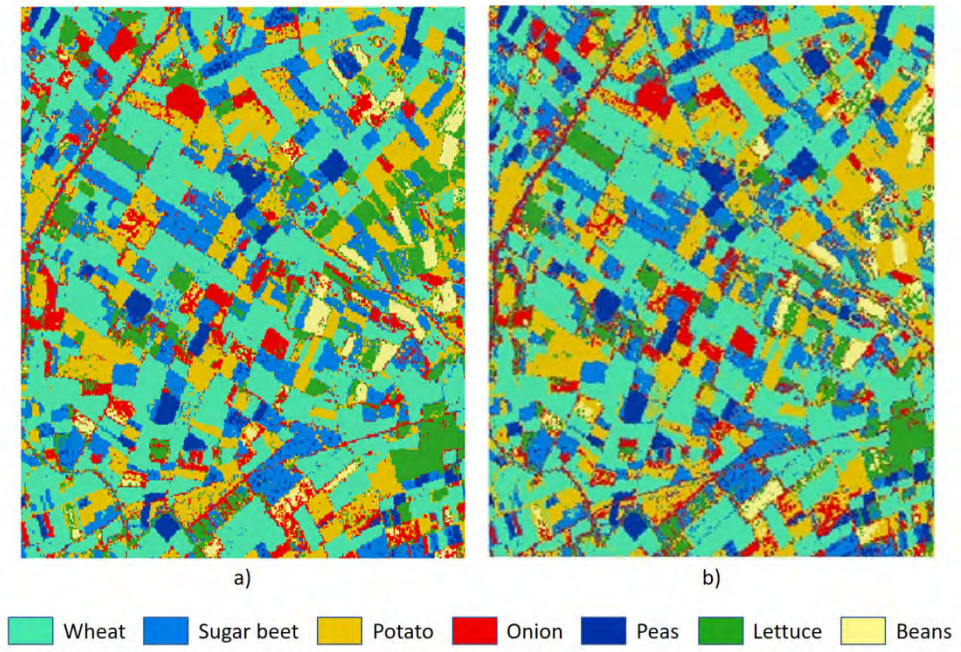

Figure 7-49. Classified image of the study area using (a) C4.5 decision tree classifier and (b) maximum likelihood classifier.

9.3.6 *Problems Using Decision Tree Classifiers*

Decision tree classifiers are an effective and general machine learning tool and have been used intensively in the field of remote sensing image classification. Like other classifiers based on different assumptions, these classifiers inevitably have some limitations that can have an impact on their performance. The factors affecting the DTCs can be summarized as:

- Type of classifier, whether it is univariate or multivariate.
- Attribute selection measure used in designing a classifier.
- Pruning methods used to prune the tree.
- Number of training observations required for the optimum classification results.
- Balance of training observations among classes.
- The level of errors in the training data.

Few studies report the effects of these factors on land cover classification accuracy. Friedl and Brodley (1997) studied the behavior of different DTCs, such as univariate, multivariate, and hybrid classifiers, for land cover classification. They found that hybrid decision classifiers outperform other types of decision trees. Pal and Mather (2003) suggest that it is the pruning method that affects the classification accuracy more than attribute selection methods. On the other hand, Zambon *et al.* (2006) found that attribute selection methods could have significant effects on final accuracies, and Lawrence and Moran (2015) found that logistic model trees performed statistically significantly better than univariate trees across 30 remote sensing-based datasets.

Both inaccuracies and outliers in the training data can adversely affect decision trees, because such data can potentially account for a large portion of the variability in the data (Friedman, 2001). Decision tree algorithms can, therefore, concentrate on correctly classifying this erroneous or extreme data to the detriment of correctly classifying other data. This type of data is typical in remote sensing training data where, for example, a training polygon for rangeland containing 50 pixels might be expected to have several pixels with a predominance of bare ground. Finally, the presence of an unbalanced data set with some classes more heavily represented than others can affect the performance of decision trees, because the sparsely represented classes do not account for substantial variance and can therefore fail to be separated from other classes. Lawrence and Moran (2015) found that decision trees were particularly poor at classifying rare classes when compared to several other classifiers using 30 remote sensing-based datasets.

9.3.7 *Decision-tree-based Ensemble Classifiers*

Several methods, including boosting and bagging, have recently been developed to address the shortcomings of classification tree algorithms (Bauer and Kohavi, 1999; Friedl *et al.*, 1999; DeFries and Chan, 2000; Pal, 2007). These methods, sometimes called voting or ensemble methods, operate by generating multiple trees and classifying observations based on a plurality vote of the multiple trees (Opitz and Maclin, 1999). The primary difference among these methods is how the multiple trees are developed. Two major types of methods have been developed, those that develop new classification trees based on the results of previous classification trees (i.e., boosting methods) and those that rely on subsets of the training data to develop new classification trees (i.e., bagging methods) (Bauer and Kohavi, 1999). Many variants of these basic methods exist (Opitz and Maclin, 1999).

Boosting methods have generally produced the greatest increases in accuracy, although under certain circumstances lower accuracies can result (Bauer and Kohavi, 1999; Opitz and Maclin, 1999). Boosting methods begin by producing a standard classification tree (Freund and Schapire, 1996; Freund *et al.*, 1999). Training data are then assigned weights in such a way to give more weight to incorrectly classified data given greater weight. The process is repeated for a specified number of iterations, and the set of resulting classification trees vote on the correct classification. Boosting has been shown to improve classification tree performance in many cases, while performing at least as well as classification tree algorithms in most remaining cases (e.g., Freund and Schapire, 1996; Freund *et al.*, 1999; Opitz and Maclin, 1999). One boosting program, C5.0, has found wide use in remote sensing, both for GAP analysis and the U.S. National Land Cover Database. Boosting does not, however, assist with inaccurate training data, outliers, or unbalanced data sets. ‘‘Outliers,’’ training data that are incorrectly labeled or that are especially hard to

distinguish from other classes, for example, can have an adverse effect on boosting, because the algorithm will place emphasis on these observations, since they will be the worst classified and given the greatest weight in the boosted classification trees (Bauer and Kohavi, 1999; Freund and Schapire, 1996; Freund *et al.*, 1999; Opitz and Maclin, 1999).

Bagging methods are bootstrapping approaches where multiple classification trees are developed by repeatedly selecting random subsets of the original training data (Breiman, 1996). A user-specified number of iterations is performed and, as in boosting, observations are classified based on the most common prediction from among the multiple classification trees. In a comparison of traditional classification trees, bagging, and boosting, bagging consistently produced higher classification accuracies than single classification trees, but was often less accurate than boosting (Opitz andMaclin, 1999).

RandomForest is a bagging operation, where multiple classification trees are developed, each one based on a random subset of the training data observations (Breiman, 2001; Pal, 2005; Lawrence *et al.*, 2006). In addition to this normal bagging function, in RandomForest, each classification tree split is based on a random subset of the input variables, in our case spectral information. The multiple classification trees then vote on the correct classification. RandomForest has been used successfully in numerous studies (Pal, 2005; Lawrence *et al.*, 2006). RandomForest has several advantages over other tree-based approaches (Breiman, 2001; Liaw and Wiener, 2002). Pruning of trees is not necessary and the approach is robust to overfitting, a problem that plagues classification trees. It is easier to use than many other ensemble classification methods, with the only parameters to be set being the number of trees grown and the number of variables used at each tree split; however, it has been shown to be not very sensitive to the setting of either of these parameters. It also is claimed that RandomForest can provide a reliable estimate of error using the data that is randomly withheld from each iteration of tree development (i.e., the ‘‘out-of-bag’’ portion), making it unnecessary to have an independent accuracy assessment data set (Breiman, 2001).

Stochastic gradient boosting (SGB) is a hybrid of the boosting and bagging approaches (Friedman, 2001, 2002; Lawrence *et al.*, 2004; Baker *et al.*, 2006). First, instead of using the entire data set to perform the boosting, a random sample of the data is selected at each step of the boosting process. Second, boosting is based on a steepest gradient algorithm, with the gradient defined by deviance (i.e., twice the binomial negative log-likelihood) as a surrogate for misclassification rates. Finally, instead of developing full classification trees at each stage of the boosting procedure, relatively small trees are developed, with 6 terminal nodes being a common size. Each tree developed during the process, often 100–200 trees, is summed, and each observation is classified according to the most common classification among the trees. The combined effect of these differences from other boosting methods reduces SGBs sensitivity to inaccurate training data, outliers, and unbalanced data sets. SGB has been shown in most cases to produce substantially higher accuracies with independent data (i.e., data that were not used to develop the trees) than either CTA or other boosting methods. For instance, in a comparison between single, univariate decision trees and SGB for mapping wetland and riparian area with Landsat imagery, SGB was able to better detect the wetland and riparian areas, achieving 86% overall accuracy compared to 73% for the simple decision tree (Baker *et al.*, 2006). Finally, SGB also is highly resistant to overfitting.

In a comparison of univariate, single decision trees to random forests and C5.0 across 30 datasets, random forests and C5.0 consistently and significantly outperformed the single decision trees (Lawrence and

Moran, 2015). Random forests slightly outperformed C5.0, although the difference was statistically significant. More recent reported results across 45 remote sensing datasets, with comparisons among 14 classification algorithms, also support higher accuracies from these ensemble methods (Lawrence, 2017).

9.4 *Fuzzy Clustering*

9.4.1 *Introduction*

Satellite acquired imagery has been used for land use and land cover classification and estimation of fractional cover, including vegetation fraction and impervious surface fraction. Numerous techniques have been developed for extracting fractional images. Among those techniques, linear spectral mixture analysis (LSMA) is the algorithm which has been widely applied; recently with a fair amount of success (Lee and Lathrop, 2005; Lu and Weng, 2004, 2006; Wu, 2004; Wu and Murray, 2003). Although LSMA has been used widely, it contains fundamental limitations (Foody *et al.*, 1997). LSMA is based on an assumption that mixtures of reflectance of land cover features are linear. However, when scattered photons interact with multiple components, the mixture becomes non-linear (Gilabert *et al.*, 2000; Roberts *et al.*, 1993), such as multiple scattering by overstory, understory vegetation and soil. In many cases, the nonlinearity of mixture is significant and cannot be neglected (Ray and Murray, 1996; Roberts *et al.*, 1993), and LSMA is sensitive to non-linear interactions (Linderman *et al.*, 2004). As a result, to apply LSMA, non-linear mixtures have to be ignored or assumed to be insignificant (Gilabert *et al.*, 2000; Roberts *et al.*, 1993). The second drawback of LSMA is related to endmember selections. The number of endmembers is determined by the dimensionality of the images and correlations between bands (Small, 2001). The limited number of endmembers reduces the capability of un-mixing due to the image spectra being under-sampled (Small, 2001). Endmember selection is a challenge also because of within-class spectral variability (Foody *et al.*, 1997). Each land cover class could be located in different places within the feature space (Atkinson and Tatnall, 1997), which could make the selected endmembers to not represent the spectra of each land cover class thoroughly.

To tackle these issues, non-linear un-mixing techniques need to be developed. Fuzzy classification may be used as a non-linear un-mixing technique, which has been widely applied in previous research, including: (1) land use/land cover classifications (Fisher and Pathirana, 1990; Foody, 1996, 1998; Foody and Cox, 1994; Lee and Lathrop, 2002; Mohan *et al.*, 2000; Tang *et al.*, 2007; Zhang and Foody, 1998, 2001); (2) Vegetation classification (Filippi and Jensen, 2006; Tapia *et al.*, 2005; Townsend, 2000); (3) Change analysis (Okeke and Karnieli, 2006a,b); (4) Flooded area mapping (Amici *et al.*, 2004); (5) Cloud cover classification (Ghosh *et al.*, 2006); and (6) Geology (Ranjbar and Honarmand, 2004). As an un-mixing technique, fuzzy classification has no assumption about the nature of the mixing, considering linear mixing as a special case of the non-linear mixing. Therefore, it might be hypothesized that fuzzy classification can achieve better estimation of fractional images than LSMA.

9.4.2 *Fuzzy Classification*

Fuzzy sets are classes without sharp boundaries and the transition from non-membership to membership is gradual. A fuzzy set is measured by a fuzzy membership grade (possibilities) which ranges from 0.0 to

1.0, indicating from a 0% membership to 100% membership. Fuzzy sets can provide better representation for geographical information. Both information classes and spectral classes can be represented as fuzzy sets. Spectral space can be divided into fuzzy sets without sharp boundaries, which can be mathematically expressed in Equation 7-35 as:

$$\begin{aligned} &\forall x \in X \\ &0 \le f_{F_i}(x) \le 1 \\ &\sum_{x \in X} f_{F_i}(x) > 0 \\ &\sum_{i=1}^{m} f_{F_i}(x) = 1 \end{aligned} \tag{7-35}$$

where: F_1, $F_2 \ldots F_m$ represent the spectral classes, X is the whole pixels, m is the number of the classes, x is the pixel measurement vector, and f_{F_i} is the membership function of the fuzzy set F_i ($1 \le i \le m$) (Wang, 1990).

To calculate the fuzzy representation for each spectral class, the probability measures of fuzzy events was applied. The mathematical expression can be defined in Equation 7-36 as:

$$p(A) = \int_{\Omega} f_A(x) dP \tag{7-36}$$

where: f_A is the membership function of the spectral class A ($0 \le f_A(x) \le 1$), Ω is the spectral space, and $p(A)$ is the probability measure of the spectral class A (Wang, 1990).

Then, fuzzy signatures can be extracted from original images using a chosen algorithm (Wang, 1990). Fuzzy mean and fuzzy covariance can be calculated for each information class to yield fuzzy signatures. The mathematical expression of fuzzy mean is defined in Equation 7-37 as:

$$\mu_c^* = \frac{\sum_{i=1}^{n} f_c(x_i) x_i}{\sum_{i=1}^{n} f_c(x_i)} \tag{7-37}$$

where: n is the total number of training pixel measurement vectors, x_i is a training pixel measurement vector ($1 \le i \le n$), and f_c is the membership function of class c.

The mathematical expression of fuzzy covariance is defined in Equation 7-38 as:

$$\sum_c^* = \frac{\sum_{i=1}^{n} f_c(x_i)(x_i - \mu_c^*)(x_i - \mu_c^*)}{\sum_{i=1}^{n} f_c(x_i)} \tag{7-38}$$

where: μ_c^* is the fuzzy mean, n is the total number of training pixel measurement vectors, x_i is a training pixel measurement vector ($1 \le i \le n$), and f_c is the membership function of class c.

The membership function for class c can be expressed in Equations 7-39 and 7-40 as:

$$f_c(x) = \frac{p_c^*(x)}{\sum_{i=1}^{m} p_i^*(x)} \tag{7-39}$$

$$p_i^*(x) = \frac{1}{(2\pi)^{N/2}\left|\sum_i^*\right|^{1/2}} . \exp\left[-\frac{1}{2}\left(x-\mu_i^*\right)^T \sum_i^{*-1}\left(x-\mu_i^*\right)\right] \tag{7-40}$$

where: N is the dimension of the pixel vectors, and m is the number of the classes ($1 \le i \le m$).

Fuzzy signatures can then be inputted into a fuzzy classifier to calculate the fuzzy membership of each information class for each pixel. The membership value is determined by the standardized Euclidean distance of each pixel to the mean spectra of a signature on each band using a sigmoidal membership function. Although there are many types of membership functions, such as sigmoidal, J-shaped, and linear, the sigmoidal membership-function is the most commonly used in fuzzy set theory. The sigmoidal membership function is calculated in Equations 7-41 through 7-44 as:

$$\mu = \cos^2 \alpha \tag{7-41}$$

where: μ is the sigmoidal membership function, in the case of a monotonically decreasing function:

$$\alpha = (x\text{-point } c)/(\text{point } d\text{-point } c)*pi/2 \tag{7-42}$$

when: $x < \text{point } c,\ \mu = 1$;

where: in the case of a monotonically increasing function:

$$\alpha = (x\text{-point } a)/(\text{point } b\text{-point } a)*pi/2 \tag{7-43}$$

when: $x >$ *point b*, $\mu = 1$. (Points *a*, *b*, *c*, and *d* refer to the control points)

The fuzzy classifier provides fuzzy set membership images corresponding to each class as well as an image of classification uncertainty. Classification uncertainty indicates the degree to which no class clearly stands out above others in the assessment of fuzzy set membership of a pixel. It is calculated in Equation 7-44 as:

$$\textit{Classification Uncertainty} = 1 - \frac{\max - \frac{sum}{n}}{1 - \frac{1}{n}} \tag{7-44}$$

where: max is the maximum set membership value for the pixel; *sum* is the sum of the fuzzy set membership value for the pixel; and *n* is the number of classes (i.e., signatures) (Eastman, 2006).

In the study conducted by Hu and Weng (2011), the fuzzy classification was conducted to extract impervious surfaces. Training data were manually selected from the original imagery. Training in the fuzzy classifier was similar to training site selection in traditional supervised classification. The difference was that the training site needed to be homogeneous for conventional supervised classification, which was not required for the fuzzy classifier. For each image, thirty training samples for each land cover class, including

high albedo, low albedo, soil, and vegetation, were manually selected on the original imagery. Each sample had different size and contained a set of training pixels, ≥ than 30 pixels. Four fuzzy membership images plus one classification uncertainty image were yielded. Four fuzzy membership images included a high albedo image, a low albedo image, a vegetation image, and a soil image. An impervious surface fraction image was then generated by adding two fuzzy membership images (i.e., high albedo and low albedo). Spectrally confused materials (e.g., water, shade, and dry soils) were removed to improve the quality of the impervious surface map using the method proposed by Wu and Murray (2003). Figure 7-50 illustrates the fuzzy membership images.

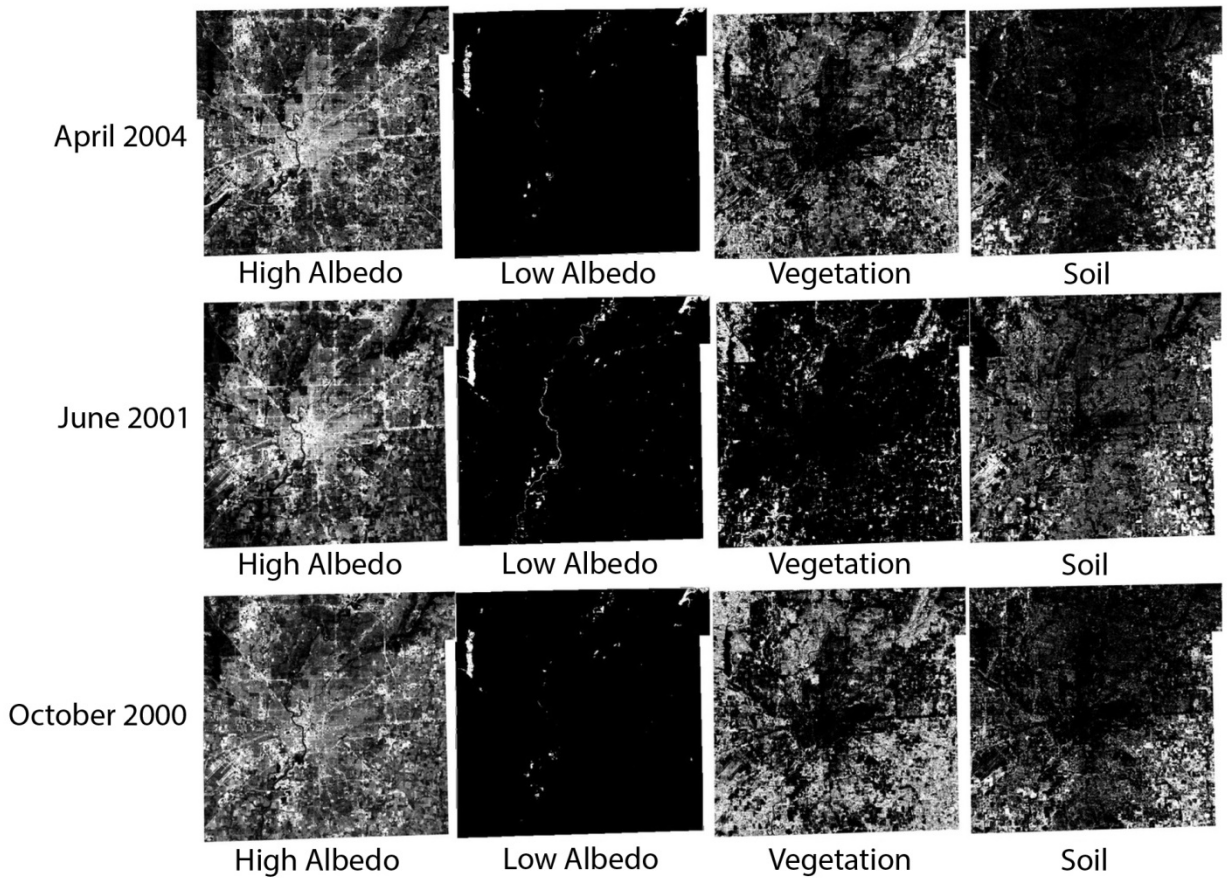

Figure 7-50. Fuzzy membership images of Indianapolis derived from ASTER images (Hu and Weng, 2011). The pixel value indicates the fuzzy membership of a class within that pixel.

Although the fuzzy classification can yield better results of impervious surface estimation than LSMA, the quality of fuzzy signatures relies heavily on identifying the fuzzy membership grade for all classes in each training site. Some important parameters need to be appropriately defined, such as z-score, which may impact significantly the accuracy of the final results. The fuzzy set membership was determined by the distance of a pixel to the signature means, and the z-score value was the distance where the fuzzy set membership value became zero. The fuzzy set membership at the signature means is one. If the distance increased, the fuzzy set membership would decrease until it became zero, where the *z*-score distance was reached. The *z*-score value was determined by the quality of the signature and the width of each class. If the signature was pure and the class width small, a small *z*-score should be selected; otherwise, a large *z*-

score would be necessary. Compared to the fuzzy classifier, LSMA is a simpler model which is both time and computation efficient. Therefore, LSMA has recently become widely accepted as a sub-pixel classifier.

9.4.2.1 Kernel Fuzzy C-means Clustering

Using time series satellite imagery for land cover classification and change detection has attracted increased attention in recent years (Zhu and Woodcock, 2014). The temporal domain of satellite imagery has showed its advantages in resolving spectral confusion between classes with similar spectral characteristics (Schneider, 2012; Bhandari *et al*., 2012). Landsat time series data have been applied successfully to map dynamics of urban areas due to their long record of continuous measurement at effective spatial resolution and temporal frequency (Gao *et al.*, 2012; Sexton *et al.*, 2013; Li *et al*., 2015; Zhang and Weng, 2016a). However, these methods focused on spectral differences or temporal consistency after classification. Little attention was paid to temporal data mining methods to differentiate urban areas from other land cover using dense time series of Landsat images.

Time series clustering can be effective in time series data mining (Liao, 2005; Fu, 2011). Kernel fuzzy C-means (KFCM), proposed by Zhang and Chen (2003), has shown potential to provide a more robust signal-to-noise ratio and less sensitivity to cluster shapes in comparison to other clustering algorithms (Du *et al*., 2005). Given time series data $X = \{x_1, x_2, \cdots, x_n\}$, $x_k \in R^d$ $(k = 1,2, \cdots, n)$, d was temporal dimension, n was the number of samples, KFCM partitions X into c fuzzy subsets by minimizing the following objective function shown in Equation 7-45.

$$J_m(U,V) = 2\sum_{i=1}^{c}\sum_{k=1}^{n} u_{ik}^m(1 - K(x_k, v_i)) \quad (7\text{-}45)$$

where: c is the number of clusters; v_i was i^{th} cluster centroid; u_{ik} is the membership of x_k in class i, and $\sum_i u_{ik} = 1$; $m \in [1, +\infty]$ is the weighting exponent determining the fuzziness of the clusters. $K(x_k, v_i)$ is the kernel function, aiming to map x_k from the input space X to a new space with higher dimensions. In this study, radial basis function (RBF) kernel was adopted as shown by Equation 7-46.

$$K(x_k, v_i) = exp(-\|x_k - v_i\|^2/\sigma^2) \quad (7\text{-}46)$$

where: the parameter σ was computed by:

$$\sigma = \frac{1}{c}\left(\sqrt{\frac{\sum_{i=1}^{n}\|x_i - m\|^2}{n}}\right). \quad (7\text{-}47)$$

To search for new clusters, the objective function was minimized:

$$Min\, J_m(U,V) = 2\sum_{i=1}^{c}\sum_{k=1}^{n} u_{ik}^m\big(1 - K(x_k, v_i)\big) \quad (7\text{-}48)$$

$$s.t. \quad \sum_{i=1}^{c} u_{ik} = 1, k = 1,2, \cdots, n \quad (7\text{-}49)$$

Lagrange function converted the constrained objective as an unconstrained optimization model. By optimizing the objective function, the membership u_{ik} and centroid v_i could be updated (Equations 7-50 and 7-51):

$$u_{ik} = \frac{\left(\frac{1}{\left(1-K(x_k,v_i)\right)}\right)^{\frac{1}{m-1}}}{\sum_{j=1}^{c}\left(\frac{1}{\left(1-K(x_k,v_i)\right)}\right)^{\frac{1}{m-1}}} \quad (7\text{-}50)$$

$$v_i = \frac{\sum_{k=1}^{n} u_{ik}^{m} K(x_k,v_i) x_k}{\sum_{k=1}^{n} u_{ik}^{m} K(x_k,v_i)} \quad (7\text{-}51)$$

Labeled time series samples were derived from stable time series, and remaining time series were considered as unlabeled samples. Given a time series, X, consisting of X_l and X_u, X_l included labeled samples, and X_u included unlabeled samples.

The whole process of semi-supervised KFCM algorithm was shown as: (1) Initialized the values of σ and u_{ik} using X_l and X_u. For X_l, the value of component u_{ik} was set to 1 if the data x_k were labeled with class i, and 0 otherwise. For X_u, positive random values within [0,1] were set to unlabeled data. The initial set of centroid v_i was calculated using Equation 7-52 as:

$$v_i^0 = \frac{\sum_{k=1}^{n'}\left(u_{ik}^{l}\right)^{m} x_k^l}{\sum_{k=1}^{n\wedge\prime}\left(u_{ik}^{l}\right)^{m}} \quad (7\text{-}52)$$

where: n' was the number of labeled data, and (2) Updated the membership u_{ik} in X_u and centroid v_i until the objective function was minimized.

Finally, inconsistent labeled pixels were mapped comparing the LST L and BCI B clustering results. For those pixels, if the maximum membership $max(u_{ik})^L$ of the pixel k in L was higher than $max(u_{ik})^B$ in B, the pixel was labeled as the class with $max(u_{ik})^L$ in L, and *vice versa*. However, if the values were equal, the pixel was labeled as the class with $max(u_{ik})^L$.

The study conducted by Zhang and Weng (2016b), aimed at extracting urban areas using a semi-supervised fuzzy time series clustering method through Biophysical Composition Index (BCI) (Deng and Wu, 2012) and Land Surface Temperature (LST) time series and applied the method to the Pearl River Delta, China, from 1990 to 2014. BCI and LST time series images were derived because of their strong correlation with urban areas (Zhang and Weng, 2016a). BCI aimed to identify different urban biophysical compositions, which has been demonstrated to be effective in identifying the characteristics of impervious surfaces and vegetation and in distinguishing bare soil from impervious surfaces (Deng and Wu, 2012). LST, as a significant parameter in urban environmental analysis, tended to be correlated positively with urban expansion (Weng and Lu, 2008; Yuan and Bauer, 2007). Figure 7-51 shows derived urban areas using time series fuzzy clustering.

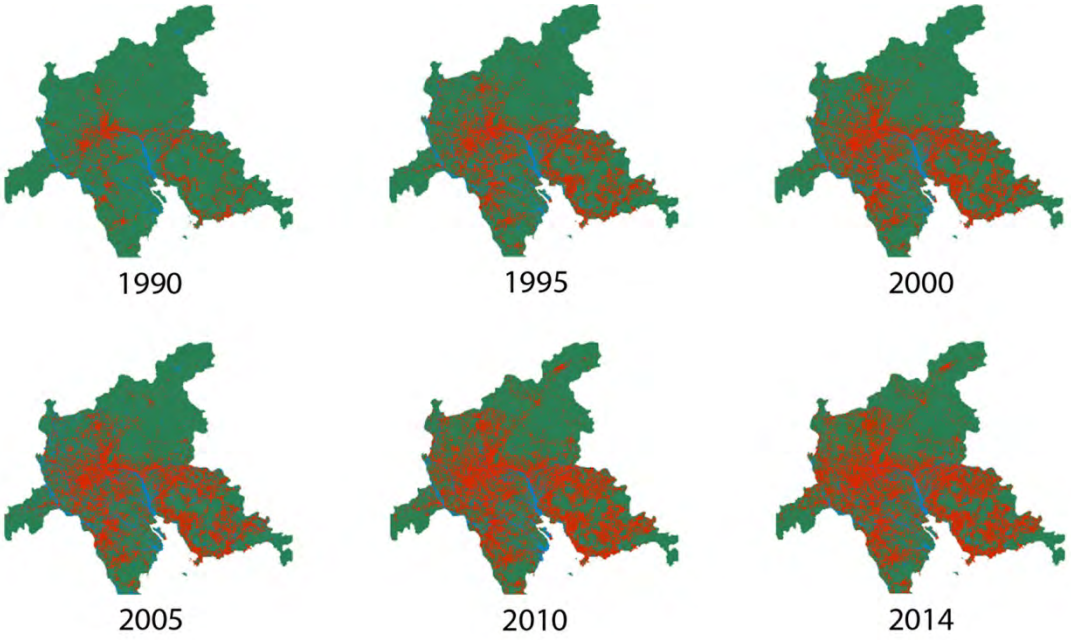

Figure 7-51. Annual urban areas from 1990 to 2014 in Pearl River Delta (modified after Zhang and Weng, 2016b). The red color represented urban area, the blue color showed water bodies, and the green color showed non-urban area.

The annual clustering yielded accuracies from 78.23% to 91.32%, which showed the effectiveness of the time series clustering method. However, the clustering accuracy varied yearly and fewer number of satellite images in a year could obscure the information of land cover changes and reduce the separability of temporal features of urban areas from non-urban areas. Especially, the trend of vegetation phenology was weakened. Furthermore, time series clustering suggested the value of imagery with cloud contamination or Scan Line Corrector (SLC)-off data in identifying urban areas. Although cloud contamination and SLC-off data caused significant noise and resulted in incomplete time series, the method of gap filling and smoothing (Zhang and Weng, 2016a) was helpful to solve the problem of missing data through enhancing temporal resolution of the time series.

9.5 *Spectral Angle Mapper Classifier*

Spectral Angle Mapper (SAM) is one of several supervised classifiers developed specifically for comparing hyperspectral images and reference spectra (Kruse *et al*., 1993). SAM takes an atmospherically-corrected *n*-band pixel from hyperspectral data and compares the pixel to reference spectra in the same *n*-dimensions. This technique treats an observed reflectance spectrum as a vector in a multidimensional space, where the number of dimensions equals the number of spectral bands. In other words, each pixel in an *n*-band hyperspectral image can be considered as an *n*-dimensional vector.

Each vector defines a set of angles with coordinates representing the band, which can be used to compare two spectra, such as a pixel-derived spectrum to a reference spectrum in a spectral library, or to an "endmember" (i.e., purest spectrum pre-identified in the image). When conducting comparisons, multidimensional vectors are defined for each spectrum and the angle between the two vectors is calculated. The SAM classifier considers the angular distance between pixels as a measure of distance (van der Meer, 2006).

If this angle is smaller than a given tolerance level, the spectra are considered to match. On this particular point, SAM classifier is similar to the NN classifier commonly used with conventional multispectral data. For example, Figure 7-52 shows the simplified two-band representation of a test pixel spectrum (derived from an unknown pixel in the image) and two reference spectra (derived from a laboratory measurement or from an endmember). When two dimensions are considered, the angle $\alpha 2$ is smaller than $\alpha 1$, which indicates the test pixel is likely to match the reference spectrum $r2$. However, adding a third dimension to this picture reveals the angle $\alpha 1$ is actually smaller than $\alpha 2$. Consequently, the test pixel spectrum is considered to match the reference spectrum $r1$. The increased number of bands of hyperspectral data can make angular distance comparisons process intensive. In addition, the dimensionality of the space in which the vectors are located becomes too large for human visualization.

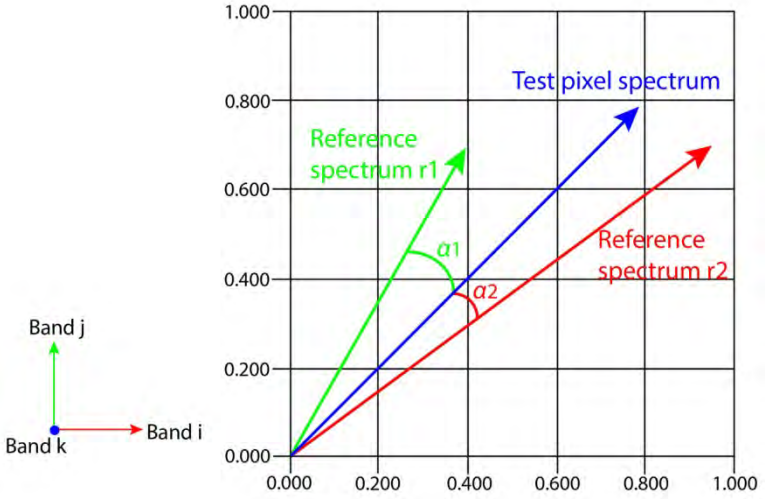

Figure 7-52. The logic of SAM classification (adapted from Kruse *et al.*, 1993).

The advantage of SAM is that it is relatively insensitive to the magnitude of the pixel vectors since only the angular distances between vectors are used in establishing class membership. If the overall illumination increases or decreases due to the presence of a mix of sunlight and shadows or topographic shading, the length of the vector can increase or decrease; but its angular orientation will remain constant. This is shown schematically in Figure 7-53 (Lillesand *et al.*, 2015) where a two-band "spectrum" for a particular material will lie somewhere along a line passing through the origin of a two-dimensional space. Under low illumination conditions, the length of the vector will be short, and the point will be located closer to the origin of the multidimensional space (i.e., point *A* in Figure 7-53). When illumination increases, the length of the vector will increase, and the point will move farther from the origin (e.g., point *B*), but the angle stays the same.

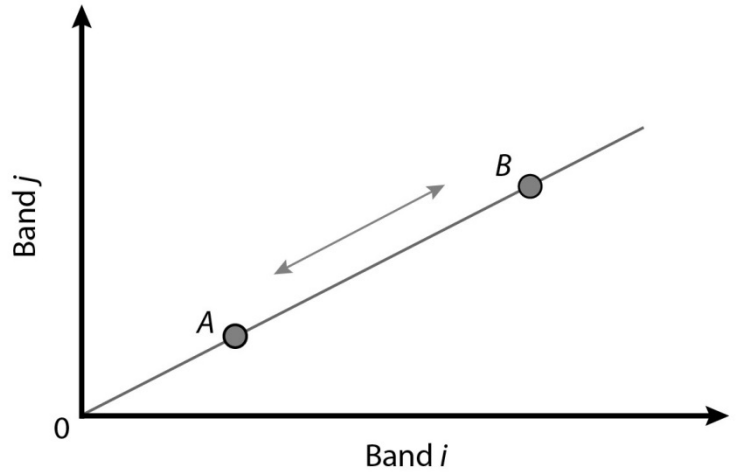

Figure 7-53. For a particular material, the vector corresponding to its spectrum will lie along a line passing through the origin, with the magnitude of the vector being smaller (*A*) or larger (*B*) under lower or higher illumination, respectively (adapted from Lillesand *et al.,* 2015).

9.6 *Object-Based Image Analysis and Feature Extraction*

9.6.1 *Introduction*

Extracting landscape information from remote sensing data has been greatly facilitated by advances in Object-Bbased Image Analysis (OBIA), which treats landscapes as mosaics of meaningful semantic objects composed of image pixels. Within the OBIA workflow, objects are first generated from the input data using *image segmentation* techniques, followed by *object classification* based on their spectral, textural, geometrical, and/or contextual (i.e., describing spatial relationships with other scene elements) characteristics. Image objects, or segments, represent groups of pixels that share some degree of similarity in digital values and maintain geometric and geographic relationships to their corresponding ground elements of the real-world landscape.

By utilizing a larger pool of information at the object unit level than at pixels or grid cells, the OBIA framework allows extracting landscape features that are ecologically and semantically closer to research targets determined by human cognition (Blaschke and Strobl, 2001; Benz *et al.*, 2004; Blaschke *et al.*, 2008 and 2014; Holt *et al.*, 2009; Lang *et al.*, 2009; Blaschke, 2010). Smoothing of the local spatial variation in pixel values of image objects may improve spectral contrast among classes or entities of interest and alleviate the infamous problem of "salt-and-pepper" speckle resulting from classifications of high-resolution pixels exhibiting spectral variation inside semantically defined objects (Blaschke, 2010; Dronova *et al.*, 2012). Finally, OBIA framework also allows to account for the hierarchical organization of landscape entities, patches and cover types and to perform analyses at different spatial scales of these nested layers.

In recent decades, OBIA use has spanned across a broad array of landscape studies, including analyses of surface composition and change in urban as well as "wildland" terrestrial, wetland and aquatic ecosystems and wildlife studies (Blaschke, 2010; Dronova *et al.*, 2015; Witharana and Lynch, 2016; Huang *et al.*, 2017) and in the fields historically less focused on remote sensing, such as public health (Holt *et al.*, 2009; Kelly *et al.*, 2011). These applications have been further stimulated by advances in very high-resolution

imaging and UASs (Laliberte *et al*., 2011; Mafanya *et al*., 2017). A critical determinant of OBIA success in these diverse efforts is delineation of objects via image segmentation, the primary focus of this section.

9.6.2 *Image Segmentation as a Critical Step in Object-Based Image Analysis Workflow*

Image segmentation is the process by which individual pixels are grouped into image objects (i.e., segments) intended to represent ground features, landscape zones or other spatial units relevant to research objectives. Various segmentation techniques have long been used in computer vision (CV) studies and eventually adopted in environmental remote sensing (Benz *et al.*, 2004; Blaschke and Strobl, 2001; Clinton *et al.*, 2010). Early segmentation techniques focused primarily on color and texture as the basis for delineating groups of pixels as segments (Dubuisson-Jolly and Gupta, 2000; Hofmann *et al.*, 1998). Present-day applications increasingly aim to accommodate complex multi-scale structure and hierarchical organization of landscapes where not only color, but also shape and contextual relationships among ground elements determine object relevance to semantic targets (Baatz and Schäpe, 2000; Benz *et al.*, 2004).

The primary goal of segmentation is often to recover relevant landscape entities at a given spatial resolution, such as buildings, trees and road elements recognizable from aerial or high-resolution satellite images in urban landscapes. However, in areas with complex cover type composition and variable geometry of patches it may be challenging to identify representative objects for different landscape categories, and segmentation is used to generate "primitive" objects, or smaller sub-elements of patches. These primitives help to reduce local noise and provide mapping units for subsequent classification. Spectral, geometric and contextual properties of delineated target objects or primitives strongly depend on the choice of segmentation approach and parameters as discussed in Section 9.6.3.

Importantly, the criteria for segmentation "success" and "relevance" of features highly vary among studies. Hence, the definition of the "best" or "most appropriate" segmentation depends on how well the relevant real-world boundaries are recovered and how object units ultimately affect the outcome of classifications (Figure 7-54). Even in studies using smaller primitive objects, size and spatial layout affect the contrast between landscape cover types and hence the outcomes of classifications using objects as mapping units (Wang L. *et al.*, 2004). For instance, in several analyses of heterogeneous mixed-cover landscapes, object-based classification accuracy tended to initially increase with greater object size relative to pixel-based outcomes, but eventually reaching a peak and starting to decline due to inclusion of multiple classes and higher chance of spectral confusion among larger more heterogeneous objects (Dronova *et al.*, 2012; Kim *et al.*, 2011). Similarly, object-level modeling of ecosystem parameters, such as biomass and LAI of vegetation, may be sensitive to the size and intrinsic heterogeneity of object units (Addink *et al.*, 2007), highlighting the importance of segmentation in representing landscape composition for a given research question.

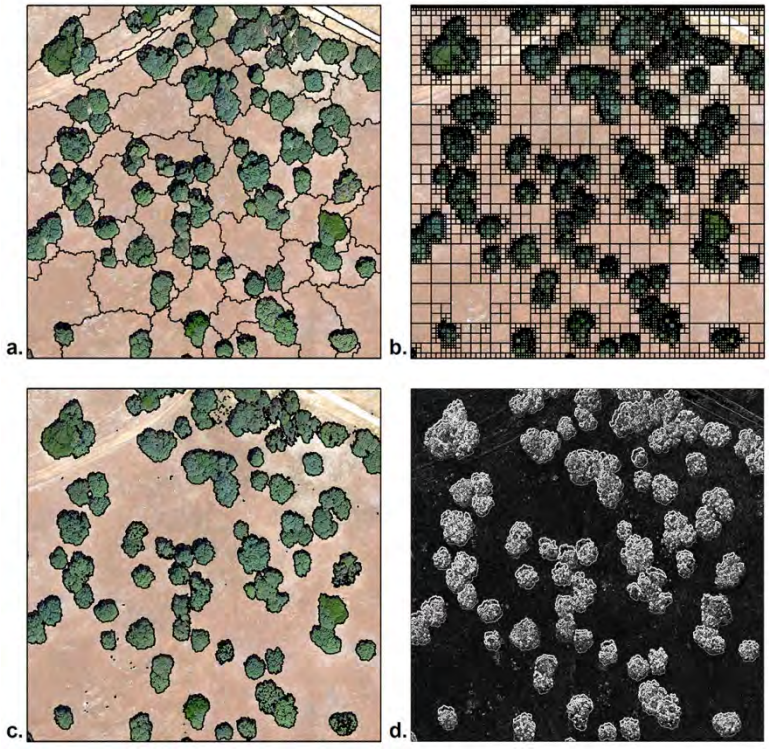

Figure 7-54. Application of different segmentation approaches to delineate oak trees from an aerial image with 0.15 *m* pixel resolution: (a) multi-resolution segmentation with scale 120, shape 0.3 and compactness 0.5; (b) quadtree based segmentation with scale 130; (c) contrast split segmentation using red image band and minimum bright area of 0.5; and (d) Sobel edge detecting filter applied to the NIR band.

9.6.3 *Image Segmentation Methods*

9.6.3.1 The Objectives of Image Segmentation

Specific objectives of image segmentation vary among studies and present an important consideration for choosing an appropriate segmentation method. Very often the goal is to delineate known ground landscape elements as semantic objects in the image, provided that the input spatial resolution is sufficient to differentiate the targets from their surroundings. In this case, the user needs to consider which characteristics make the target class unique when compared to the rest of the landscape, and choose a segmentation technique where these characteristics can be adjusted easily. In contrast, when the objective is to map patches of different landscape cover types with variable spectral and geometric attributes, image segmentation is more used typically to delineate primitives of cover classes in a way that would maximize their difference in relation to the rest of the landscape and thus provide meaningful units for subsequent classification. These uses of segmentation tend to emphasize spectral and textural properties, while the complex geometry of landscape entities is recovered later following the classification of primitive objects. Primitives also provide a powerful way to smooth local noise, which may be especially notorious with high-resolution data. This benefit was noted by a broad array of studies using optical aerial and satellite images at various spatial resolutions and radar data that may exhibit substantial speckle even at relatively large pixel sizes.

Segmentation may also be applied as an intermediate step within more elaborate sequences of OBIA procedures. For example, it may be used to delineate broad landscape zones prior to delineation of class-

specific patches within those, or to split a large heterogeneous feature into smaller units to refine class boundaries. In such applications, relatively simpler and computationally less demanding techniques are used that aggregate pixels into simple blocky units to be modified later; or that rely on predetermined spectral thresholds as a basis to create object zones.

Finally, some applications require image regions to conform to pre-existing spatial units such as administrative boundaries, topography and soil types. Such units are often not visible to remote sensors and thus may be difficult to discern based on their spectral, textural or geometrical properties alone. In these cases, external spatial datasets can be incorporated directly into segmentation workflow to enforce the boundaries into the layouts of generated objects.

9.6.3.2 Input Information Required by Segmentation

The outcomes of most segmentation methods are dictated by digital values of image pixels, their local variation, and other geographic attributes of individual locations. The most common types of input information used by segmentation algorithms to generate objects include:

- Values of individual image pixels (e.g., spectral values, or color) or raster grid cells (e.g., elevation), sometimes from multiple sources such as optical images and LiDAR datasets;
- Patterns of local variation in pixel values (e.g., image texture);
- Criteria defining relative importance of shape versus spectral properties (e.g., color);
- Any existing relevant boundaries of landscape features derived externally in raster or vector form (e.g., geographic vector datasets, administrative units, previous classification results, etc.).

It is important to note that the segmentation procedures do not split pixels. Image pixels remain the minimum mapping units of the original data used as input for segmentation, and object boundaries resulting from the latter still follow the "blocky" pixel outline. Some of the software packages, such as eCognition, allow exporting segmentation results with smoothed object boundaries. Although such smoothing reduces the blocky appearance of object units, it does not automatically ensure accurate reproduction of the real-world boundary within the pixel. For these reasons, it may be more challenging to recover "true" positions of landscape boundaries with coarser-resolution input imagery, and the primary utility of segmentation with such data lies in capturing the majority of relevant spatial unit extents by image objects.

9.6.3.3 Common Segmentation Methods

This section reviews several segmentation techniques commonly used in environmental applications of remote sensing data at different landscape scales. With the exception of cases when objects have to be derived from pre-existing datasets, information contained in pixel values and their local patterns provide the primary basis for delineating object units. Common segmentation methods fall into two broad groups: "global" approaches focusing on pixel value similarities in the image data space, rather than spatial domain, and "locally operating" methods focusing on spatial relationships among pixels within local neighborhoods, or image regions. By their nature, global algorithms emphasize the spectral proximity of pixel values and thus tend to perform not so well with high-resolution data, where high variation of pixel colors may exist within semantically "whole" features. In contrast, methods focusing on local neighborhoods operate on small regions which may encompass spectrally contrasting, but spatially neighboring, pixels, and thus are especially useful for detailed high-resolution input data.

(1) Global Methods

(a) Thresholding Approaches

Thresholding methods allocate pixels into image objects based on pre-specified ranges of values to which these pixels belong. The cut-off thresholds may be provided by the user (e.g., based on the prior knowledge or arbitrary threshold choices), or determined using automated histogram-slicing methods such as the Otsu algorithm (Otsu, 1979), histogram shape-based methods, entropy-based techniques and others. For example, in eCognition software two algorithms (multi-threshold segmentation and contrast split segmentation) generate objects by "slicing" the image based on cutoff values specified for a designated image band. The multi-threshold algorithm requires one or more threshold values provided in advance, while the contrast split method evaluates the scene automatically based on user-specified pixel attributes (e.g., spectral band), search data range and step, contrast mode, constraints on minimum object size, and minimum proportions of study area below and above the cutoff threshold.

The main advantage of thresholding methods lies in the relative simplicity of their implementation, particularly if the input characteristics exhibits natural zonation due to topography (van Den Eeckhaut *et al*., 2012), or have a multi-modal distribution with clear transition points between modal zones. Figure 7-54c illustrates the application of eCognition's contrast split segmentation to delineate green oak trees in a landscape where they contrast with the matrix of dry senescent grasses. However, these techniques may be less successful when optimal threshold values vary spatially; or when the feature of interest has a unimodal distribution with no clear transition points. Another shortcoming is the over-splitting of heterogeneous semantic entities, such as detection of small gaps with contrasting color in some of the tree crowns in Figure 7-54c.

(b) Clustering

Unsupervised clustering methods, such as K-Means algorithm or ISODATA, can also be used to delineate objects as groupings of pixels based on their proximity in the data space formed by image spectral bands or other pixel attributes. Automated clustering methods typically compare the spectral value of each pixel with a specified number of cluster centers and modify cluster means iteratively so that each cluster has the majority of its closest pixels in the "optimal" solution. The advantage of clustering algorithms lies in their relative ease of implementation, which does not require specialized OBIA software. The important shortcoming, however, lies in the "global" nature of approaches focusing on regions in the data space rather than landscape's spatial domain, and thus, the inability to account for spatial context of pixels. The latter issue becomes an especially serious constraint with high-resolution input imagery where clusters formed by spectral similarity may not account for pixel value dispersion among the objects and may lead to over-splitting of target units.

(2) Methods Based on Local Metrics

(a) Edge-based Methods

Edge-based segmentation methods delineate objects by detecting meaningful boundaries within local neighborhoods that contain spectrally contrasting pixels. Various techniques exist such as Sobel filtering and contour generation, that are relatively easy to apply using moving window operations on raster data and converting the outputs to vector format. However, due to several important limitations, edge-based methods in environmental remote sensing have been much less common compared to region-based approaches.

The primary shortcoming of edge-based filtering is sensitivity to local noise, leading to undesirable over-splitting of the objects. These techniques perform especially poorly on textured objects with intrinsic patterns of contrasting color values; this problem is illustrated in Figure 7-54d where tree crowns have multiple edges detected by Sobel filter due to sharp local differences between sunlit and shadowed foliage. Fuzzy edges of landscape entities, common in transitional landscapes, mixed-cover areas, also represent a challenge leading to multiple proximal edges close to each other. Finally, as with any filtering techniques, the thickness and orientation of detected edges may be sensitive to local neighborhood or moving window specifications.

(b) Simple Top-down (Split) and Botton-up (Merge) Region Methods

Local region-based segmentation methods are based on the iterative algorithms which test similarity of image pixels or already delineated regions against other pixels or regions. Such algorithms can operate in a *bottom-up* direction, starting with a set of "seed" pixels and growing objects from those, or in a *top-down* direction, starting with the entire extent and splitting it into regions. Hybrid region-based approaches combine top-down and bottom-up principles and optimize object delineation through a series of "split-and-merge" iterations.

An example of a top-down splitting algorithm is the quadtree based segmentation in eCognition software that creates different-sized square objects by splitting pixels into a 'quad tree' using a specified parameter of scale that constrains intrinsic heterogeneity of segments (Figure 7-54b). Larger, spectrally homogeneous portions of the landscape are represented by squares of larger area, while locally heterogeneous locations, such as patch edges, become small squares.

A number of bottom-up algorithms also exist, with one common family being watershed segmentations operating in analogy with topographically complex terrain where accumulation of water starts from the points of minimal elevation. Region growing begins from the local minima in pixel values in a manner of "flooding the basins", until basins attributed to different starting locations are "filled". The "watershed lines" formed by the boundaries between adjacent regions become object outlines. Another popular region-growing method is multi-scale, or multi-resolution segmentation discussed in the next section.

(c) Multi-resolution Segmentation

Multi-resolution segmentation is a special case of a bottom-up region-merging approach where pixels are grouped into objects based on a number of input properties (Table 7-9) with the aim to recover some degree of variation in shape and size of real-world landscape elements (Figure 7-54a). The outcomes of multi-resolution segmentation are especially sensitive to the parameters of *scale*, controlling maximum allowed heterogeneity of objects and hence their size, *shape*, which denotes relative importance of geometric

shape and compactness criteria versus spectral information, and *compactness*, which specifies the degree of deviation from a very compact shape with low perimeter-to-area ratio, such as circle or square. Characteristics of the input images, such as sensitivity to spectral differences among classes or entities of interest, are also important, and their relative contributions may be further regulated by selecting different weights for relevant bands. For instance, studies focusing on the contrast between water and land may choose to weight near- and shortwave-infrared bands, if available, higher due to low water reflectance in these spectral regions, leading to smoother appearance and darker color of water bodies.

Table 7-9. Parameters and Inputs Affecting Multi-resolution Segmentation Results in eCognition.

Parameter	Description	Potential Effect on Segmentation Results
Scale	A metric of maximum allowed within-object spectral heterogeneity	Larger scale value allows for more heterogeneous and hence larger-sized objects in the output
Shape	Weight coefficient denoting relative importance of geometric properties versus color	Higher value reduces the relative impact of spectral (color) on the output, allowing for higher spectral variations inside objects but smoother boundaries and lower variation in shape
Compactness	Weight coefficient for the criterion denoting object deviation from a compact shape (circle or square)	Higher compactness values lead to more compact objects with lower perimeter-to-area ratio and may be especially useful for delineating blocky or round-shaped features such as trees
Input image bands and their weights	Choice of band weight coefficient for available input image layers	Specific effects vary depending on the sensitivity of available image bands to contrasts among target entities or their classes
Use of thematic information	Decision to include any ancillary ("thematic") geospatial layers to inform object generation by multi-resolution segmentation	Vector thematic boundaries may be enforced on the boundaries of resulting objects, while raster thematic layers such as classification maps provide additional criteria for homogeneity of image regions

The multi-resolution segmentation approach has been extremely popular in a wide variety of OBIA applications, in both human-dominated and wild landscapes. One of its most common uses involves constructing "primitive" objects corresponding to smaller-sized surface patches or patch components that are subsequently classified as different cover types and may be combined into larger patches in this process (Addink *et al.*, 2007; Clinton *et al.*, 2010; Kim *et al.*, 2011). Because multiple multi-resolution segmentation parameters may lead to a large number of possible segmentation results, it may be difficult to choose the "optimal" outcome from these options. Furthermore, specific parameter combinations may produce objects matching only particular classes of landscape elements (Clinton *et al.*, 2010; Holt *et al.*, 2009; Moffett and Gorelick, 2013). For example, in Figure 7-55a the choice of relatively large-scale value together with high compactness and moderate shape weights highlights building roofs and backyard lawns as individual objects, yet fails to accurately reproduce the trees. In contrast, higher weights for shape and compactness with relatively lower scale value in Figure 7-55b allow capturing trucks in the parking lot and a number of trees and tree shadow objects while over-splitting streets, buildings and open areas. Finally, low settings for shape and

compactness together with a high scale value in Figure 7-55c lead to successive reproduction of linear street features, yet also an excessive generalization of fine-scale urban elements.

Examples shown in Figures 7-54a and 7-55 illustrate the challenge of selecting an optimal set of multi-resolution segmentation parameters to accommodate *all* entities or classes of interest, which applies to many segmentation methods. However, these decisions may be to some extent facilitated by several guiding principles and semi-automated selection approaches discussed in section 9.6.4 below.

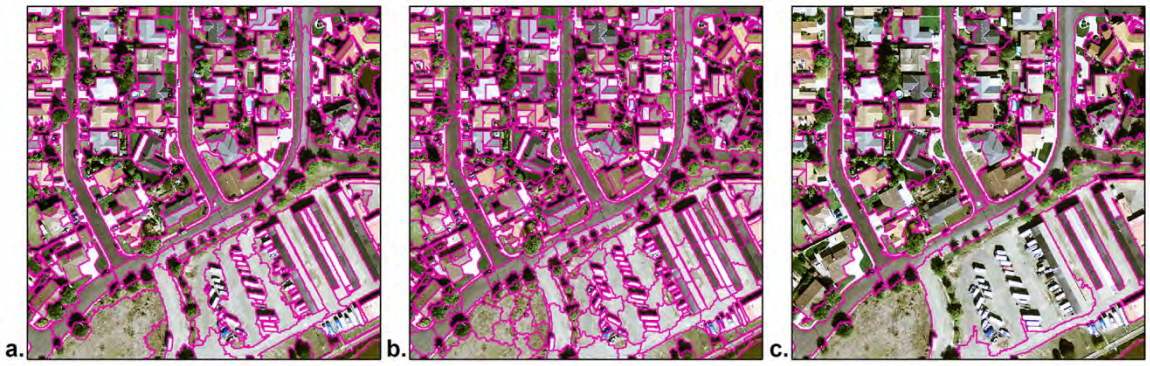

Figure 7-55. Multi-resolution segmentation results for different parameter combinations applied to a 30*m* resolution aerial photo of an urban area: (a) scale 130, shape 0.3, compactness 0.7; (b) scale 60, shape 0.5, compactness 0.9; and (c) scale 400, shape 0.1, compactness 0.1.

9.6.4 *Choosing an Optimal Segmentation Method*

9.6.4.1 Major Considerations in Selecting a Segmentation Approach

A major task within the segmentation process is selecting the appropriate method, its parameters and input data to maximize the chance of achieving research objectives. The first critical determinant of the outcome concerns the *spatial resolution of the input data* and *its potential to represent target landscape elements*. Overly coarse resolution is likely to absorb the boundaries among semantically relevant ground features, up to the point of making segmentation meaningless (Figure 7-56b). At the same time, overly high resolution is likely to accentuate within-object dispersion of spectral values due to variation in color, shadowing, illumination and presence of irrelevant elements of the ground or canopy surface. The latter issue is of lower concern with OBIA because some of the local noise may be smoothed by objects; nevertheless, it may affect the choice of the segmentation method.

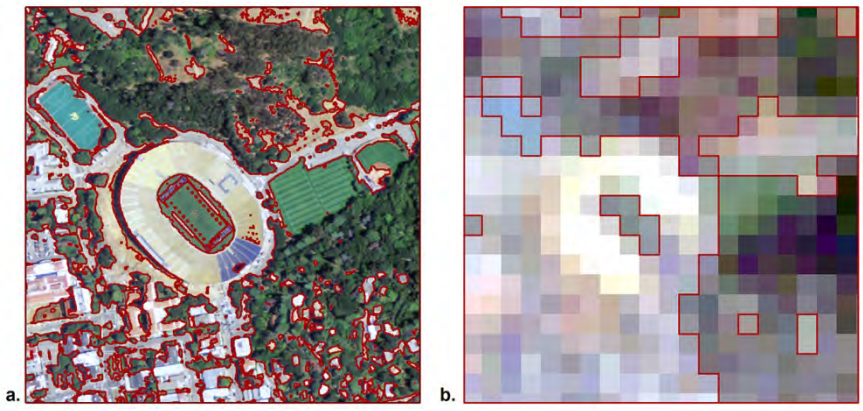

Figure 7-56. The effects of spatial resolution on thresholding-based segmentation applied to delineate green vegetation for the same area within two remote sensing images acquired in June 2009: (a) the National Agricultural Imagery Program aerial photo at 1*m* resolution, and (b) Landsat-5 TM scene at 30*m* resolution.

The choice of segmentation technique and its parameterization also depends on *whether this step aims to recover whole landscape features versus primitive objects.* In general, landscape features with little dispersion in their characteristic attributes, such as trees in Figure 7-54 may be easier to reproduce with a single segmentation run than entities whose properties vary substantially, such as urban elements in Figures 7-55 and 7-56a. In contrast, primitive object delineation may allow for higher flexibility in parameter choice because entities of interest such as cover type patches are recovered later at the step of classification. However, success and accuracy of the latter ultimately depends on how well primitives of one class can be separated from those of others, which may call for some pre-testing of parameters using unsupervised approaches.

Relative importance of geometry versus color is another key determinant of segmentation. Detecting target entities that exhibit geometric typologies, such as rectangular buildings and round trees, but that show high inter-class variation in color are likely to benefit from weighting shape and geometry higher than spectral information. In contrast, delineation of entities with variable shape but pronounced spectral contrasts, such as different vegetation and surface types in mixed-cover natural landscapes, should weight spectral properties higher. For instance, water bodies may be present in the landscape as narrow, linear water courses and channels as well as more compact, round ponds and lakes. In these cases different criteria may be applicable to different typologies of the same class; or perhaps primitive objects should be considered that can be classified later based on spectral and textural properties of water. It is also advisable to weight color higher when segmentation's objective is to generate homogeneous small primitives whose shapes are less relevant than spectral contrasts among target cover classes.

Finally, it is important to consider whether target objects are likely to be spectrally homogeneous or exhibit intrinsic variation that should be preserved within the object boundaries. For instance, uneven illumination may cause a variable degree of shadowing on tree crowns or building roofs (see Figures 7-54 and 7-55). In such cases, segmentation parameters controlling size and heterogeneity may need to be adjusted to allow for larger, less homogeneous segments. However, caution is needed since allowing for greater size may eventually increase the risk of merging portions of multiple classes within the same object. In contrast, more spectrally uniform targets may call for homogeneous and relatively small object primitives to facilitate between-class contrasts while still accounting for local color variation.

9.6.5 *Approaches for Ranking and Comparing Segmentation Outputs*

(a) Unsupervised Methods for Segmentation Comparison

In complex landscapes where ground features may be less recognizable to the human eye, it is often more challenging to choose and parameterize an appropriate segmentation method, and decisions are still frequently based on trial-and-error (Dronova, 2015). These tasks can be facilitated by unsupervised methods to evaluate segmentation results, which have a long history of use in image processing and CV studies (Clinton *et al.*, 2010; Holt *et al.*, 2009; Levine and Nazif, 1985). These strategies tend to focus primarily on spectral and textural outcomes of segmentation, such as homogeneity within objects or classes, and

compare these among different object layouts to determine which parameter sets provide the closest match to desired representation of the actual landscape.

Recently, some of the unsupervised comparison methods have been adapted for the popular Multiresolution Segmentation (MRS) approach in eCognition. For instance, the Estimation of Scale Parameter (ESP) tool (Dragut *et al.*, 2010, 2011, 2014) uses a metric of local variance (LV) and its rate of change across different segmentation scales to evaluate scales where substantial changes in LV may indicate capture of a set of meaningful objects. The latest version of this method (Dragut *et al.*, 2014) incorporates multiple image bands simultaneously. Another example is the Plateau Objective Function (Martha *et al.*, 2011), which uses spatial auto-correlation and within-object variance to optimize segmentation properties, also for the multi-resolution segmentation algorithm.

An important advantage of such methods is recognizing the multi-scale nature of landscape structure where more than one set of segmentation parameters may be needed to identify features of interest. The current limitation of these methods, however, is in the chief focus on segmentation scale and the fact that methods lack automated capacity to test for multiple parameters simultaneously. In addition to scale, parameters such as shape, compactness or weights of the input bands can provide significant contributions to analyses. In complex landscapes with variable patch sizes, these techniques may be further limited by the absence of "characteristic" scales and hence smooth, continuous change in LV metric.

(b) Supervised Approaches to Evaluate the Match with Reference Objects

When segmentation is aimed at delineating recognizable ground entities, identification of the most suitable segmentation result may benefit from the *supervised* approaches that link computer-produced result with human-determined targets. Such approaches, sometimes referred to as empirical discrepancy methods (Holt *et al.*, 2009), focus on the geometric match between known objects and segmentation results, with the primary criteria centered on the degree of spatial overlap and/or positional difference between reference and mapped object units (Clinton *et al.*, 2010; Holt *et al.*, 2009; Moeller *et al.*, 2007; Radoux and Defourny, 2007). For instance, to assess the degree of aerial overlap between image segments and reference objects x_i from a set X, the following metric can be computed as Equation 7-53 (after Holt *et al.*, 2009):

$$Total\ area\ matched = \sum_{i=1}^{m} \frac{\sum_{j=1}^{n} area(y_j)}{area(x_i)}, y_j \in Y_i^* , \quad (7\text{-}53)$$

where: Y_i^* is the subset of all the delineated segments y_i that intersect a given reference object x_i so that at least one of their centroids is inside the other object, or their mutual aerial overlap exceeds 50% of x_i, or y_i (after Clinton *et al.* (2010)).

A common strategy to evaluate segmentation's capacity to recover semantic target objects focuses on the balance between *oversegmentation*, or excessive splitting of the target units, and *undersegmentation*, or insufficient recovery of the object boundaries as shown in Equations 7-54, 7-55 and 7-56:

$$Undersegmentation_{i,j} = 1 - \frac{area(x_i \cap y_j)}{area(x_i)}, y_j \in Y_i^* , \quad (7\text{-}54)$$

and

$$Oversegmentation_{i,j} = 1 - \frac{area(x_i \cap y_j)}{area(y_j)}, y_j \in Y_i^* . \quad (7\text{-}55)$$

Over- and under-segmentation metrics can be further combined into a metric of "closeness", essentially representing their RMSE (Clinton *et al.*, 2010; Levine and Nazif, 1985):

$$Closeness_{ij} = \sqrt{\frac{Oversegmentation_{ij}^2 + Undersegmentation_{ij}^2}{2}}. \quad (7\text{-}56)$$

An important caveat with supervised approaches to segmentation optimization is that different human perceptions or research objectives may identify "objects" differently (Clinton *et al.*, 2010; Holt *et al.*, 2009; Moffett and Gorelick, 2013). Although objective ranking methods using over- and under-segmentation criteria may facilitate decisions, in some cases landscape composition may be so versatile that different sets of segmentation parameters become suitable for delineating different types of objects (Figure 7-55). If a particular object class is of special interest, then segmentation parameter selection should be prioritized based on the properties of that class. However, if multiple landscape classes with different characteristic objects are important, then solutions may require multi-step OBIA procedures. Strategies may include, for instance, alternating segmentation procedures with temporary or partial classifications of the landscape, using hierarchical approaches that involve splitting larger regions, merging primitive objects, or both, or alternating different segmentation techniques as discussed in the next section.

9.6.5.2 Combining Multiple Segmentation Methods to Achieve the Objectives

Applications of most common segmentation methods rely on the assumption that some characteristic scales or parameter combinations are especially well suited for representing landscape entities of interest. This assumption may not be well satisfied when properties of target entities exhibit high variability, and even multi-resolution segmentation may fail to recover a full range of object sizes and shapes in a single run, even after a careful parameter selection. This challenge may be addressed by sequential application of different segmentation algorithms to facilitate detection of the target units when individual methods fail to recover them in a single run.

A particularly successful strategy has been to combine with a top-down splitting or thresholding approach, which allows one to subdivide the study area into broad regions as landscape strata, or to correct already delineated object boundaries by splitting mixed objects (Delaplace *et al.*, 2010; Dezso *et al.*, 2012; Platt and Rapoza, 2008; van Den Eeckhaut *et al.*, 2012). This approach may be especially beneficial when thresholding or splitting uses a complementary layer of information, such as land surface elevation or LiDAR-based digital surface model to create initial regions, followed by a region-based segmentation utilizing spectral data from the image (O'Neil-Dunne *et al.*, 2013; Van Den Eeckhaut *et al.*, 2012). The disadvantage of adding multiple segmentation operations to OBIA workflow is, however, in the need for additional trial-and-error parameterization for each method, and increased complexity of the analysis procedure.

9.6.5.3 Assessing Segmentation Accuracy

The issue of accuracy with respect to delineated object boundaries is related closely to the problem of choosing the optimal segmentation parameters. Overall, the assessment of accuracy in OBIA is less common for segmentation outputs than for classification results, and is needed primarily when the objective is to delineate whole objects or ground entities. Accuracy may then be quantified as the match between image

segments and reference objects using over- and under-segmentation criteria and "closeness" metrics described, or the approaches accounting for positional accuracies and variable distributions of object sizes (Radoux *et al.*, 2011; Radoux and Defourny, 2007). Because reference objects are often derived from field tracing of landscape patches or digitized from images, maps and other data sources, some degree of mismatch with image objects mapped from pixel units is expected, even in highly satisfactory segmentation outcomes (Holt *et al.*, 2009; Radoux and Defourny, 2007; Yu *et al.*, 2006).

Note that the correspondence between segmentation results and real-world entities may be more difficult to validate in landscapes with less certain, more variable-shaped features and fuzzy boundaries even if high-resolution imagery or ground-traced boundaries are available for such verification (Moffett and Gorelick, 2013; Yu *et al.*, 2006). Furthermore, segmentation in such areas is often used to produce primitive objects that are rarely validated (Dronova, 2015). Of higher interest becomes the ability of primitives to represent spectral contrasts among classes, which can be verified by comparing spectral distances among object class samples at different segmentation scales, such as Jeffrey-Matusita or Bhattacharya distances between class sample means (Wang, L., *et al.*, 2004). Following the classification of primitive objects, accuracy is assessed typically as a thematic match between mapped and "actual" classes for a given spatial reference unit using contingency matrices and fuzzy methods (Congalton and Green, 2009); or, as a spatial match between the boundaries of mapped class patches and known reference units (Radoux *et al.*, 2011; Radoux and Bogaert, 2014). The choices of image classification algorithm and sampling strategy to determine testing objects become critical determinants of the outcome in addition to segmentation approach and input data properties (Dronova *et al.*, 2012; Radoux and Bogaert, 2014; Wang, L. *et al.*, 2004).

9.6.6 *Object-Based Image Analysis and Image Segmentation Software*

Applying image segmentation for landscape feature extraction has been facilitated greatly by the growing capacity and accessibility of OBIA software platforms. Among commercial packages, a popular choice over the last nearly two decades has been the eCognition Developer suite by Trimble Inc. (formerly, Definiens Inc.). These packages offer a user-friendly interface with the ability to develop custom sequences of procedures (or "rule sets") for segmentation, classification, and other types of feature extraction; and, to perform analyses at multiple, hierarchically linked, spatial levels. A number of segmentation methods are available in this package, from a simple "chessboard" algorithm breaking the image into uniform square blocks of specified size, to more complex iterative methods such as multi-resolution segmentation as described in section 9.6.3.3(2)(C).

Examples of other commercial software include ENVI (Zoom) feature extraction module for ENVI (Harris Geospatial Solutions), the IMAGINE Objective add-on for ERDAS® Imagine (Hexagon Geospatial Inc.), BIS Cloud (formerly BerkeleyImgSeg) and new Segmentation and Classification toolset in ArcGIS 10.3 (Esri, Inc.). Open-source OBIA packages have also been developed, such as Monteverdi and Monteverdi2 by Orfeo Toolbox; SPRING by the National Institute for Space Research of Brazil (INPE); and InterImage by the Computer Vision Laboratory of the Department of Electrical Engineering at Catholic University of Rio de Janeiro, Brazil. It is important to note that not every segmentation method requires a pre-designed software package. Simpler methods that derive objects based on thresholds in the data, or clustering algorithms, may be generated by applying these algorithms to images in non-OBIA remote

sensing or GIS software, and converting raster outputs to vector datasets. Even more complex types of segmentation requiring iterative splitting and merging of local regions (Section 9.6.3.3(2)) may be coded using Python language or data processing platforms such as R or Matlab (Mathworks, Inc.), though advanced programming skills may be required.

9.6.7 *Summary*

Image segmentation is a critical part of the OBIA workflow that establishes the connection between human perception of landscape structure and information content of the digital remote sensing data. Navigating among various segmentation techniques for a given objective requires careful consideration of tradeoffs that affect spectral, geometric and contextual properties of resulting objects; and hence, their match with the target entities of interest and utility for subsequent analysis steps. Particularly important criteria include emphasizing spectral versus geometric properties of target features, preserving intrinsic heterogeneity versus maximizing spectral contrasts with other features, and the decision on delineating whole entities of interest versus their primitive elements that could be classified later to recover entire features.

Among diverse segmentation approaches, global methods, such as thresholding and clustering, partition the landscape based on the proximity of pixels in the spectral domain determined by the values of input data. In contrast, locally operating methods, such as region-based and edge-based techniques focus on pixel values and spatial patterning within narrower neighborhoods and allow spatial adjacency to be incorporated in object generation. For a given image, the choice of a "suitable" segmentation method and parameter set is dictated by the properties of target features and by constraints resulting from spatial resolution and spectral content of the input data. Various supervised and unsupervised metrics may be used to compare and rank segmentation outcomes based on their match with target entities, the degree of over- and under-splitting, or changes in local variation and spatial autocorrelation of the input pixel values. Some of these metrics may be used also for assessing segmentation accuracy.

Finally, in developing a successful segmentation strategy, it is important to consider using segmentation results in succeeding steps of the analysis. Regardless of whether segmentation aims to recover whole landscape entities or "temporary" primitive objects, the outcomes will affect strongly the subsequent object-based classification or spatial modeling at object unit level. Hence it is important to coordinate the desired segmentation outcomes, such as the degree of the initial match with semantic features, with the broader research goals and the capacity of resulting spectral, textural, geometrical, and contextual attributes to represent the role of the extracted features in the fabric of landscape structure and underlying processes.

10 CHANGE DETECTION AND TIME SERIES ANALYSIS

10.1 *Relevance of the Temporal Dimension in Remote Sensing Data Analysis*

Earth is a very dynamic planet. Both biophysical and human-induced processes imply continuous changes (Lippitt *et al*., 2015). Atmospheric gases and aerosols are constantly moving from one region to another by global or local winds and are influenced by solar radiation, evapotranspiration, biomass burning,

industrial or agricultural activities. Oceans change rapidly too, as ocean currents transfer heat, sediments, and organic compounds to neighboring and distant places. Land seems to be more stable, but still shows remarkable dynamism in some areas, particularly where intense human activities are intermixing with natural areas: agricultural and urban frontiers, mining operations, or other large infrastructures. Conservation areas are particularly sensitive to temporal changes (Willis, 2015).

Better science requires a better understanding of the extent and impact of all those environmental changes that interact to create complex effects. Agricultural expansion frequently implies deforestation that affects carbon sinks from forested areas. In addition, agricultural expansion is associated commonly with forest burning, which in turn implies aerosols and gas emissions (e.g., CO_2, CH_4, NOx) that affect atmospheric processes.

Monitoring change is a real challenge because some of the relevant transformations are dynamic and/or affect large territories. Observations based on fixed ground sensors cover the temporal variation very well, but they are frequently incapable of capturing spatial variations of those processes. Weather data and hydrological networks are typically very sparse, especially in developing countries. Therefore, representation of the spatial complexity of processes relies on interpolating methods that are frequently not very reliable (Bolstad, 2008).

Remotely-acquired observations and data are a very good alternative for obtaining a two-dimensional view of trends, as they make it possible to acquire spatially comprehensive data from the surface at different spatial and temporal resolutions. In fact, monitoring dynamic processes is one of the most important contributions of satellite observation behind environmental studies (Chuvieco, 2016). Since sensors are mounted in satellites with recurrent orbits, the acquired data are collected at repetitive intervals, at the same altitude, from the same sensor, from the same spectral bands, and frequently at the same local hour, to facilitate change detection. Manned missions of the Space Shuttle and the International Space Station do not offer systematic observation, but their photographs can be used for visual-qualitative comparisons. Airborne sensors do not provide systematic observations either; but, they can be used to detect changes between fixed dates, and they are of particular interest in analyzing long-term changes (Song *et al*., 2015).

The actual observation frequency of satellite remote sensing systems depends mainly on satellite orbital characteristics and sensor field-of-view, being more frequent for images acquired from higher satellites with wider FOV sensors. Geostationary satellites, located at orbital heights of 36,000*km* observe a wider area, actually the full Earth disk, while low-altitude satellites require more orbits to cover the whole planet. Sensors with wide FOV, such as MODIS, VIIRS, MERIS or AVHRR acquire daily images, even if they are orbiting at similar heights as Landsat-TM/OLI or SPOT-HRV/HRG, which require 2-3 weeks to observe the same area.

In practical terms, the nominal temporal resolution of a sensor is not the same as the actual observation cycle for several reasons. First, cloud-cover reduces the number of useful observations using optical sensors. Second, not all sensors have systematic acquisitions. Some sensors collect data continuously, but others are activated when passing over areas of interest, either to save energy or to execute data downloads. Commonly, coarse spatial resolution sensors provide much higher temporal resolution (e.g., hours to a few days) than the fine-spatial resolution sensors (e.g., several days or weeks). To alleviate their low temporal orbital observation, most high-spatial resolution sensors include pointing capabilities, being able to observe

areas of interest off-nadir of the orbital path. Finally, even though all sensors include some on-board storage capacity, they rely on networks of ground receiving antennas. Depending on the density of the receiving network, some areas may not have a good historical record. This is the case of Landsat-TM/ETM data acquired over Africa and Asia. Lack of local acquisition is also behind the limited data stored in historical archives of the HRPT-AVHRR sensors, at least until 1992 when global storage was established. Today, these images are valuable for analyzing long-term land cover changes at a degraded resolution (0.05°) in the case of the LTDR database: *http://ltdr.nascom.nasa.gov/cgi-bin/ltdr/ltdrPage.cgi*.

During the first years of Earth observation, spatial resolution was the most appreciated, but nowadays temporal resolution is also considered critical for monitoring natural events, particularly when updated monitoring is decisive. For example, observing hurricanes with very fine spatial resolution imagery every week would be virtually worthless. Since clouds are very dynamic, monitoring them requires very high observation frequency even at the cost of losing spatial detail. The same applies to other natural hazards like fire, floods, and icebergs.

Two dimensions of temporal change can be analyzed from Earth observation images: seasonal trends and stable transformations (Chuvieco, 2016). In the first case, the main interest is detecting stable transformations of ground cover, caused either by short-duration catastrophic events such as floods, earthquakes, volcanic eruptions, hurricanes, and fire; or by slow-duration phenomena such as urban sprawl, crop change, and desertification, among other phenomena. Typically, images acquired in two reference periods, such as before and after a sudden or devastating event or events separated by a fixed time span, are compared visually, or digitally (Luneta and Elvidge, 1998; Sader and Winne, 1992; Smits and Annoni, 2000).

The second temporal case aims to detect phenological changes in land cover throughout the year. For example, cultivated land will show a soil reflectance if it has been planted recently, but will appear as GV when the crop is in full development and virtually hides the soil. A few weeks later the field may show a senescent vegetation signal, and later a mixture of soil and straw. The interpreter interested in seasonal changes tries to follow the vegetation dynamics in different periods (Willis, 2015), which is very useful to better discriminate associations or even species. Many authors have used images from different times of the year in their classification process (Latifovic *et al*., 2004; Lo *et al*., 1986). A seasonal separability analysis helps identify which season is more appropriate to discriminate particular land covers (Schriever and Congalton, 1995). Analysis of seasonal changes in long-term time series (e.g., 20-30 years) helps to identify trends caused by global warming or local climate changes (Alcaraz-Segura *et al*., 2010), as well as the impact of major disturbances such as fire, wind storms, and drought (Chuvieco *et al.*, 2016; Fraser *et al.*, 2003). This approach is described further in Section 10-4.

The historical coverage of Landsat sensors, along with their evolving spatial and spectral resolutions have proven to be ideal for monitoring significant land surface transformations worldwide. Two initiatives are remarkable: the United Nations Environmental Program's (UNEP's) *Atlas of Our Changing Environment*, which provides selected examples of land cover changes in different domains and continents (*http://na.unep.net/atlas/*), and Google's *Earth Engine*, which compiles the entire Landsat archive from 1984-2012 for the land surface, with interactive capacity to observe changes for the 28-year period (*https://earthengine.google.org/*). Similar to the UNEP initiative is the newly-released image portal from NASA named *World of Change* with selected examples of changes based on several satellite missions:

http://earthobservatory.nasa.gov/Features/WorldOfChange/. Figure 7-57 is an example of temporal change in the surface area of the Aral Sea over a 15 year span.

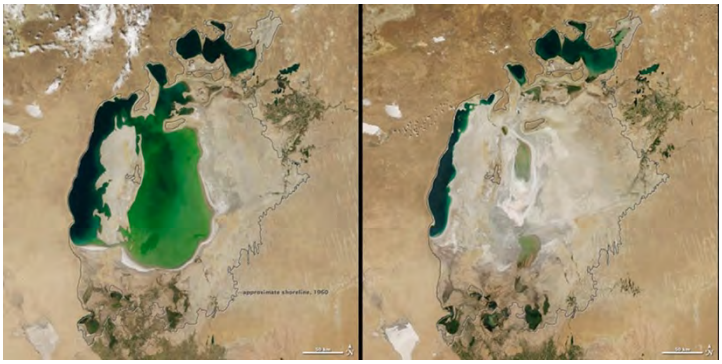

Figure 7-57. Multi-temporal variation of the Aral Sea (Kazakhstan) between 2000 and 2015 (Source *https://earthobservatory.nasa.gov/WorldOfChange/AralSea.)*

The growing capacity of computer processing systems makes it possible to process the historical Landsat archive to retrieve changes even at global scale. This is the case of the forest change detection map based on Landsat composites from 2000 and 2012 (Hansen *et al.*, 2013). Similar efforts are being developed for crop and burned area monitoring based on new Landsat-8 sensors and the recently launched Sentinel-2 Multispectral Imager (Roy *et al.*, 2014).

10.2 *Factors Affecting the Retrieval of Change in Remotely-Sensed Images*

To retrieve change detection from satellite remote sensing images, one should keep in mind that ground cover changes are not the only factor of radiometric change when comparing multitemporal images. Other variables affect the radiance detected by the sensor, potentially mixing actual and apparent changes, which is the main challenge for time-sensitive analyses. Apparent changes are those associated with perturbance factors, geometric or radiometric, which should be removed before actual temporal change extraction is made.

The most obvious perturbance factor between two images acquired at different times in the same area is precise co-registration. If the two images do not overlap precisely, any comparisons will be misleading: one might identify as *change* what it is, in fact, *displacement*. Another important source of temporal differences relates to atmospheric influences. It is well-known that atmospheric conditions affect both incoming and outgoing radiance, either by absorption or scattering that impact sensor-detected radiance even when land cover is stable. More relevant is the effect of non-lambertian behavior that most land covers present. This implies that the same cover may have different reflectances depending on the illumination and observation angles. For this reason, to retrieve consistent temporal series, it is important to perform BRDF corrections (Schaaf *et al.*, 2002), particularly in wide field-of-view sensors.

In summary, radiometric and geometric corrections are particularly critical for temporal analysis, as otherwise apparent changes will be confused with real ones. Interpreters need to be sure that the same variable and the same area are being compared for all images involved in the temporal analysis, or else the

comparison will be meaningless. The following subsections review methodological options to carry out these corrections.

10.2.1 *Multitemporal Matching*

Multitemporal comparisons require that input images be co-registered precisely to ensure that the exact area is being compared. Misregistration effects can be quite serious for the case of heterogeneous landscapes with great spatial variability, such as in urban areas (Gordon, 1980), and especially with high-spatial resolution sensors (Roy, 2000). Even in the case of coarse-resolution sensor imagery, it has been shown that up to 50% of the change observed between two images can be due to displacements when the mean registration residual among images exceeds one pixel (Townshend *et al.*, 1992). The same study estimates that geometric accuracies better than 0.2 pixels are required to keep comparison errors below10% (Townshend *et al.*, 1992).

Geometric matching for multitemporal images relies commonly on automatic techniques that are able to find common points between any image and a reference image. Since the area is the same for all the temporal series, only those areas affected by clouds or cover changes will differ, but most of the image area will have the same features. Several algorithms have been proposed to perform this automatic searching (Eugenio and Marqués, 2003; Gao *et al*., 2009). Once the matching points are found, a statistical algorithm can be computed to obtain the corrected images, in a way very similar to that commonly performed for single images.

10.2.2 *Radiometric Calibration*

Once the images are properly overlapped, multitemporal comparisons require radiometric correction, which implies that all input bands of the different dates are measured in the same physical units. This correction implies three phases: calibration, atmospheric correction and topographic correction.

Calibration implies converting raw Digital Levels (DLs) to radiance values. They require accessing sensor calibration coefficients by Equation 7-57.

$$L_k = b_k DL_{,k} + g_k \tag{7-57}$$

where: L_k is the spectral radiance of band k (in $Wm^{-2}sr^{-1}\mu m^{-1}$), DL_k is the raw digital level of the same band, and b_k and g_k are the bias and gain coefficients of the same band k. These coefficients are provided by the sensor manufacturer and usually are included in the image header file.

When using a long time series of sensor data such as those from NOAA-AVHRR or Landsat TM/ETM+, calibration coefficients may change throughout the sensor life. In some cases, even the spectral characteristics of a sensor may be modified throughout its life time (e.g., the AVHRR sensor configuration was altered from the NOAA-14 to the NOAA-15 satellites). Therefore, correction algorithms need to be adapted to the different spectral bands (Khlopenkov and Trishchenko, 2007; Trishchenko *et al.*, 2002). For the Landsat historical archive, calibration values provided by Chander *et al.* (2009) are commonly used, and they are routinely included in the header file.

Radiance to top of the atmosphere (*ToA*) reflectance (ρ) conversion is performed using Equation 7-58.

$$\rho_{ToA} = \frac{\pi \cdot L_k \cdot d^2}{E_{0,k} \cos\theta_s} \tag{7-58}$$

where: d is the Earth-Sun distance in astronomical units, L_k is the spectral radiance of band k; $E_{0,k}$ is *ToA* solar irradiance in the same band (see parameters in Chander *et al.*, 2009 for Landsat sensors), and θ_s, and the solar zenith angle extracted from the day, time and latitude of image acquisition.

For the thermal bands, *ToA* temperature (T_{ToA}) is computed in Equation 7-59 as:

$$T_{ToA} = \frac{K2}{ln(\frac{K1}{L_k}+1)} \tag{7-59}$$

where: $K1$ and $K2$ are calibration constants, varying with each sensor.

10.2.3 *Atmospheric Correction*

As mentioned previously, atmospheric perturbations in the detected signal may be relevant for monitoring change processes, and therefore a multitemporal comparison requires first removing the absorption and scattering effects. There is a wide variety of algorithms to carry out atmospheric corrections for both optical and thermal data (see, Section 3 for a detailed discussion on this topic). For solar bands, the general formula is:

$$\rho_k = \frac{d^2\,\pi(L_k - L_{a,k})/\tau_{k,0}}{E_{0,k}\cos\theta_i \tau_{k,i} + E_{d,k}} \tag{7-60}$$

where: $L_{a,k}$. accounts for atmospheric scattering, $\tau_{k,i}$, and $\tau_{k,0}$ are incoming and outgoing atmospheric transmissivity and $E_{d,k}$ is diffuse irradiance.

Atmosphere correction is a quite complex process requiring information on atmospheric properties at the time of image acquisition. This information is usually not available so corrections are based on estimates. The most common methods are data extracted from simultaneous measurements of external sensors (King *et al.*, 1999), on radiative transfer models (Ju *et al*., 2012; Kotchenova *et al.*, 2008) and on estimates based on image properties.

The latter are the more operative, particularly in the thermal infrared where the two bands commonly available in the thermal spectral region make it possible to estimate atmospheric absorption reliably (Li *et al.*, 2013b). For optical bands, methods based on image characteristics assume that atmospheric scattering can be estimated from spectral radiance of dark objects (Chavez, 1988; Chavez, 1996). This method assumes that any image has some areas with high-absorption materials, where the reflectance should be close to zero (e.g., water, shadows). Therefore, the minimum DL of each band is used to estimate L_a. This method assumes that atmospheric scattering is constant throughout the image, since it is computed from a single value. Some authors have proposed establishing a network of dark surfaces distributed in the image, which might be used to account for the spatial variation of the atmospheric optical depth (Ouaidrari and Vermote, 1999). In addition to this problem, this simple method does not take into account the additive effects of diffuse irradiance.

10.2.4 *Topographic Correction*

Once the atmospheric effects are removed, another relevant issue for multitemporal comparison is the impact of terrain shadows, which affect data products differently, depending on the day and hour of image acquisition. Winter images will present longer shadows, and therefore reflectance of off-solar slopes will present lower reflectances than for summer images.

Topographic shadow removal is performed in two steps as shown in Figure 7-58 (Chuvieco, 2016). The first one involves modelling the position of shadows at the time of satellite acquisition. It simply implies to "illuminate" a DEM with the same angles as the Sun (i. e., zenith and azimuth) when the image was acquired. The output of this analysis is the cosine of the illumination angle for each pixel (γ_i). The DEM should have a similar, or better, spatial resolution as the image to be corrected.

From the "shade" image, removal of shadows in the image may be accomplished using different models (Hantson and Chuvieco, 2011). The simplest ones assume a Lambertian behavior of the target surface (Teillet *et al.*, 1982) given in Equation 7-61:

$$\rho_{h,i} = \rho_i \left(\frac{\cos\theta_i}{\cos\gamma_i}\right) \quad (7\text{-}61)$$

where: $\rho_{h,i}$ is the reflectance of pixel i in horizontal terrain, ρ_i the reflectance on a slope (corresponding to the image before correction), θ_i the solar zenith angle of the scene, and γ_i the illumination angle. When assuming a non-lambertian surface, the correction model becomes more complex, as we need to estimate the roughness of each observed cover in the different bands. An intermediate complex model was proposed by Teillet (1982) using a semi-empirical approach given in Equation 7-62.

$$\rho_{h,i} = \rho_i \left(\frac{\cos\theta_i + c_k}{\cos\gamma_i + c_k}\right) \quad (7\text{-}62)$$

where: c_k is a constant computed from the regression of the reflectance image and the illumination image. Several variations of this model have been proposed with good results for multitemporal analysis (Hantson and Chuvieco, 2011).

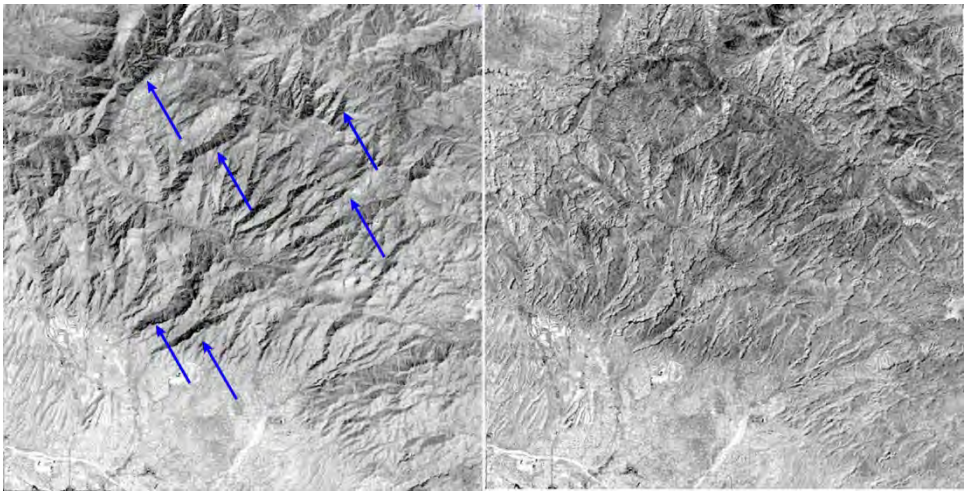

Figure 7-58. Impact of topographical correction over a Landsat-TM image of the Tucson area. Arrows indicate the strongest shadow effects (after Chuvieco, 2016).

10.2.5 *BRDF Correction*

The final relevant factor to be corrected in multi-temporal image comparisons relates to the impacts of having images acquired from different observation geometries. This is very common in wide FOV sensors, which are precisely those with higher temporal resolution. The effect is caused by the non-lambertian behavior of most land covers that causes a relevant change in reflectance as the same cover is observed/illuminated from different angles.

To address these corrections one should consider the BRDF of each observed surface. The goal is to standardize all observations to the same geometry, so the temporal series becomes more consistent. The directional effects of reflected radiance for any given combination of viewing and solar illumination angles are expressed in Equation 7-63 (Sandmeier and Itten, 1999) as:

$$f(\theta_i, \phi_i; \theta_r, \phi_r, \lambda) = \frac{dL(\theta_r, \phi_r, \lambda)}{dE(\theta_i, \phi_i, \lambda)} \quad (7\text{-}63)$$

where: dL is the reflected radiance at a given view zenith (θ_r) and azimuth angle (ϕ_r), and dE is the incident irradiance at a specified solar zenith (θ_i) and azimuth (ϕ_i) direction.

BRDF corrections have been proposed for the most common wide field-of-view sensors, such as AVHRR (Shepherd and Dymond, 2000) and MODIS data, which offers a standard BRDF-corrected reflectance product (termed MOD43: Román *et al.*, 2009; Schaaf *et al.*, 2002).

10.3 *Change Detection Techniques*[4]

Change detection techniques have been used widely with remotely-sensed images, since they are applicable to a broad range of disciplines (Mouat *et al.*, 1993). They aim to identify what features were modified between two or more dates. In this section we will cover those changes that are related to more stable modifications of the ground cover, versus the seasonal or phenological changes that will be covered by the following one. Examples of stable changes are those related to urbanization processes, agricultural expansion, dessication of wetlands, impacts of volcanic eruptions and earthquakes. Phenological changes are those that occur during the yearly cycle, either in crops or natural vegetation.

Most alterations detected by remotely-sensed data are associated with spectral changes (e.g., reflectance, temperature, etc.), but changes in spatial features can also be observed. This is the case of modifications of agricultural landscapes, either by increasing size or modifying shapes of crop plots. These changes can be approached by using texture measurements, as well as segmentation and object-oriented classification techniques (Bontemps *et al.*, 2008; Bruzzone and Fernández-Prieto, 2000; Hazel, 2001). See Section 9.6 for a description of OBIA and segmentation.

10.3.1 *Multitemporal Color Composites*

This technique uses the same basis as a standard color composite, but it combines different dates of the same band instead of using different bands of the same date. When mixing three dates in RGB composition, those areas with similar values in all dates would display in gray levels, while areas affected by change would display in shades of color. This technique has been used successfully in several change detection

[4] This section is adapted from the Change Detection Techniques chapter of Chuvieco, E., 2016. *Fundamentals of Satellite Remote Sensing: An Environmental Approach*, CRC Press, Boca Raton (FL).

studies (Martin, 1989; Sader and Winne, 1992). Figure 7-59 shows an example of these color compositions using NDVI images computed from Landsat TM scenes acquired in 1990 and 2010 over the Acre state of Brazil. Grey tones correspond to stable areas, while those pixels that reduced their DLs from the first to the second date (i.e., lower NDVI should be associated to deforestation) are displayed in red, and those with increased DLs in cyan (green+blue: reforestation).

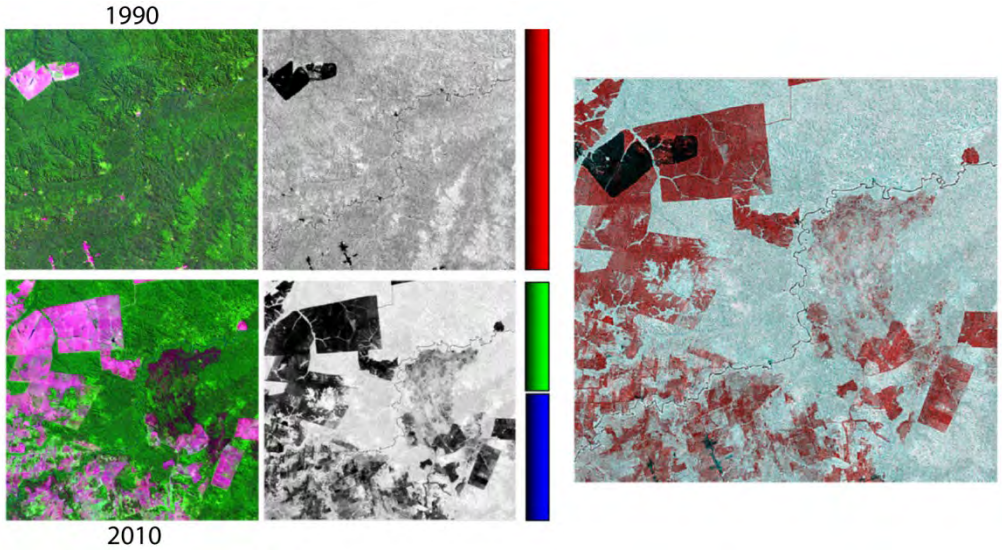

Figure 7-59. Multi-temporal color composite of NDVI values (after Chuvieco, 2016).

10.3.2 *Image Differencing and Ratios*

In many cases color composite images provide a very clear distinction of changes, but those changes need to be identified visually afterwards. When trying to extract them digitally, other techniques need to be applied. A simple one is image differencing as given in Equation 7-64:

$$DL_c = DL_{t2} - DL_{t1} \tag{7-64}$$

where: DL_{t2} and DL_{t1} are the values of the second and first date being compared, respectively. DL can be either reflectance or temperature (Pilon *et al.*, 1988) or any kind of spectral indices (Coppin and Bauer, 1994; Martín and Chuvieco, 1995). Negative values will categorize areas with decreasing values, and positive values regions will categorize areas with increasing values.

Temporal differencing reflects absolute changes between two dates, but this absolute value may not reflect the significance of the observed increases or decreases properly. For instance, a decrease of 0.1 in NDVI may be very critical when the original value is 0.2 or almost irrelevant when the original value is 0.7. To obviate this, an alternative to the temporal difference is the use of ratios, either absolute or normalized ones, as defined in Equations 7-65 and 7-66:

$$DL_c = (DL_{t2}/DL_{t1}) \tag{7-65}$$

$$DL_{i,j,c} = (DL_{t2} - DL_{t1})/(DL_{t2} + DL_{t1}) \tag{7-66}$$

with parameters defined as in Equation 7-64. Multitemporal ratios have been used in agricultural inventories (Lo, *et al.*, 1986), deforestation studies (Singh, 1986), and to detect areas affected by forest fires (Kasischke *et al.*, 1993).

It should be noted that these ratios are asymmetrical, which means that the result is dependent on what date is in the numerator. An increase of twice the DL from 50 to 100 would give a value of 2 or of 0.5 depending on whether the numerator is the first or the second date. In summary, the ratio is a nonlinear transformation of the temporal relationships. To solve this problem, some authors recommend applying a logarithmic conversion of the result (Eastman *et al.*, 1994).

10.3.3 *Principal Components*

Principal Component Analysis (PCA) is used generally to summarize a wide set of variables by preserving the common information found in the input variables. However, when using PCA in change detection, the input variables are a mixture of bands acquired on different dates. The main components are precisely those that refer to invariant information (i.e., features that do not change), while secondary components show the transformations (i.e., "dynamic" components). Therefore, in this case, the most interesting components are not necessarily the main ones, but sometimes those with less variance, particularly if the area has not been affected by major changes (Fung and LeDrew, 1988; Ingebritsen and Lyon, 1985).

The PCA transformation of the twelve bands of the Brazil multitemporal images have been computed bands 1 to 7 of 1990 and 2010, excluding the thermal band. The resulting eigenvectors (see, Table 7-10) show the treeless area, with strong and negative contrast between the NIR and other bands in the 2010 image. The second component shows vegetation changes between the two images, although the spectral contrast is not very clear, with negative values for the Blue-Red-SWIR bands and positive in the NIR in the most recent image and contrary in the oldest one. It shows higher values for areas that have changed from soil to vegetation. The third component also corresponds to changes, but in this case mainly those related to vegetation lost, while the forth implies moderate reforestation.

Table 7-10. Eigenvectors of the Multi-Temporal Analysis of the Acre Image (Brazil).

	2010						1990					
	B1	B2	B3	B4	B5	B7	B1	B2	B3	B4	B5	B7
PCA1	0.168	0.136	0.266	-0.029	0.841	0.408	0.023	0.016	0.024	0.018	0.074	0.032
PCA2	-0.020	-0.004	-0.040	0.367	-0.025	-0.086	0.138	0.126	0.178	0.355	0.758	0.298
PCA3	-0.003	-0.043	0.031	-0.887	-0.109	0.068	0.103	0.079	0.130	-0.092	0.348	0.174
PCA4	0.028	0.040	0.020	0.230	0.003	-0.047	0.060	0.020	0.090	-0.924	0.215	0.171

10.3.4 *Regression Analysis*

In context of change detection, linear regression is used to compare the values of the second date with those estimated from the first date, assuming that no change has occurred. The regression is built from DL values or stable pixels between the two dates. Once the regression model has been fitted, the DLs of the second date may be estimated from those of the first date using Equation 7-67.

$$\widehat{DL}_{t2} = a + b * DL_{t1} \tag{7-67}$$

The residuals of the regression model can be used as a change detection index:

$$DL_c = \widehat{DL}_{t2} - DL_{t2} \tag{7-68}$$

As they will show either higher or lower values than those expected if the area had been stable.

10.3.5 *Change Vector Analysis*

Change Vector Analysis (CVA) tries to identify the magnitude and the direction of change by using a bivariate space of transitions between the two dates. The vector that links the location of pixels in that bivariate and multitemporal space will contain information about the intensity and orientation of change. The angle of the change vector indicates the meaning of the change, while the magnitude of the vector indicates the importance of that particular change.

The components of CVA can be computed from simple geometric rules. The intensity, *I*, of the change vector will be obtained by Equation 7-69 while the direction will be defined by the angle (α) in Equation 7-70.

$$I_{i,j,c} = \sqrt{(DL_{i,t1} - DL_{i,t2})^2 + (DL_{j,t1} - DL_{j,t2})^2} \quad (7\text{-}69)$$

$$\alpha = arctan(\frac{DL_{j,t1} - DL_{j,t2}}{DL_{i,t1} - DL_{i,t2}}). \quad (7\text{-}70)$$

for the spectral band *i, j* between the two periods of interest (t_1 and t_2).

CVA has been used widely (Chen, J., *et al.*, 2003; Friedl *et al.*, 2002). Figure 7-60 shows an example of this analysis from the Brazil multitemporal TM pairs. The direction of change shows lower angles for those areas affected by deforestation processes, particularly those where soils were dominating, the burned area did not show such a clear trend. The image for intensity of change shows higher values for areas converted from forest to crops, pasture or bare soil, while lower intensity of change values are shown for the burned area. Areas remaining as forested and plots deforested before the first image also show low intensity values.

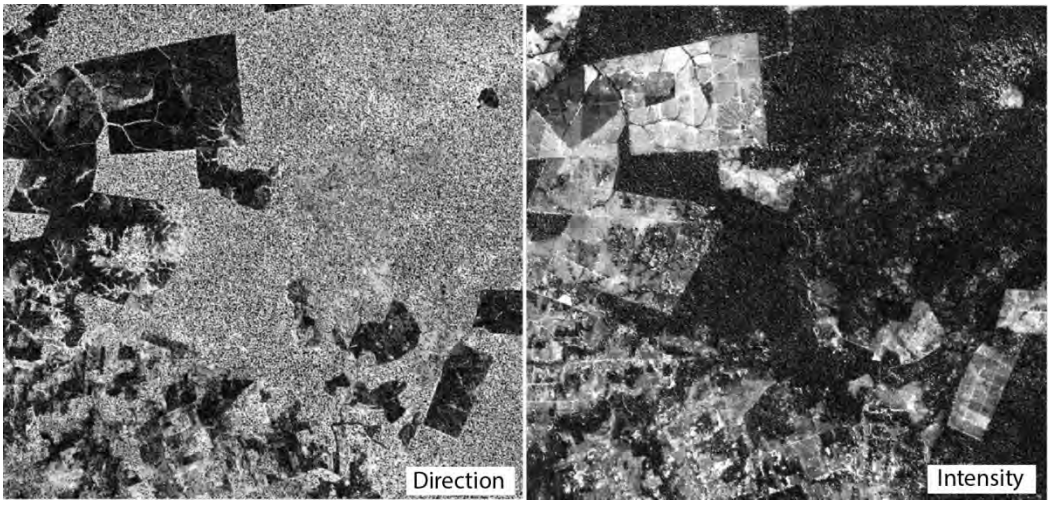

Figure 7-60. Direction and intensity of the change vectors in the Brazil Acre study site.

10.3.6 *Defining Change Thresholds*

All methods so far reviewed produce continuous images of change. In other words, the output images show a continuous scale of change, from low to high digital level values. However, interpreters often seek to generate a categorized image that distinguishes changed from stable areas. It is therefore necessary to

segment the change images generated by the aforementioned techniques to create significant groups of change.

Thresholds are commonly stablished using the mean and the standard deviation, but there is no objective way to select the most suitable multiple values of standard deviation to fix those thresholds. Some authors recommend changing them gradually and assessing the impact on the resulting change image (Fung and LeDrew, 1988; Fung, 1992). Other authors suggest using the sensor signal-to-noise ratio (Smits and Annoni, 2000). Some recommend extracting the thresholds from spatial differences of the potential change pixel and the neighbor characteristics. The spatial context is commonly estimated from a moving window of different size, which serves to account for the background trend. When a pixel has a strong contrast with the surrounding areas, it is labeled as potential change. This spatial context has been used extensively for cloud detection (Saunders and Kriebel, 1988) and for mapping burned areas (Chuvieco *et al.*, 2008, Fernández *et al.*, 1997).

10.3.7 *Multitemporal Analysis of Classified Images*

Identifying changes can also be handled using classification techniques. In this case, it is not required to define a change threshold, since classification already implies transformation of the continuous scale of DLs into a nominal scale of cover classes. Therefore, change analysis can be based on analyzing transitions between categories in two or more dates.

The first approach to using classification techniques for change detection analysis is based on classifying two or more dates simultaneously. Using either supervised or unsupervised methods, the interpreter needs to identify both the significant stable covers and the relevant cover changes. Therefore, the resulting classification includes stable and dynamic covers. Stable urban or transition from rural to urban or from rainfed to irrigated agriculture are good examples of such categories.

Another approach to multitemporal change detection analysis is to classify two dates of the same area and then compare those classifications to detect which areas maintain or have changed their cover. For doing so, the same categories should be used in both dates. Transition or stable pixels can be obtained by cross-tabulation analysis, in which pixels from one date are compared with the other one and all crossings are computed (Table 7-11). Stable pixels (those with the same category on both dates) will be located in the diagonal of this table, while the dynamic pixels will occupy the other cells. The analysis of this matrix provides critical information on the transitions between the two dates. When comparing just the total areas covered by certain categories in the two dates, the net difference provides a first insight into the evolution of that cover (increase or decrease), but the multitemporal table facilitates determination of the categories to which, or from which, these transitions have occurred. Actually, the total difference in area covered does not reveal the full set of transitions, since in the same area, gains and losses of the same category occur and they may be cancelled by considering only the totals (Pontius *et al.*, 2004).

Table 7-11. Cross-Tabulation of the Brazil Images.

		2010				
		Forest	Crops	Water	Burned	Total
1990	Forest	346888	192349	1745	51048	592030
	Crops	794	16233	47	260	17334
	Water	371	66	477	44	958
	Total	348053	208648	2269	51352	610322

The multitemporal table also provides an excellent framework for computing change metrics. For instance, the Kappa index or other agreement metrics facilitate a quantitative evaluation of temporal stability between two dates. Transitions of each category may be accounted for by computing initial and final areas covered by that category. For instance, in Table 7-11, the transitions of the sample area between 1990 and 2010 account for 40% of the total area, from which the vast majority was changed from forest to crops (i.e., net loss 41%). Thirty-two percent of original forested area is now crops, while 8.6% is burned. The crop area of 1990 has been mostly maintained (i.e., 93% remained as crops) with a very low percentage changing to forested area (i.e., 4.5%). Total crop area in 2010 was mainly forested in 1990 (i.e., 92%).

A final remark on change detection concerns to the complexity of displaying changes in dynamic maps clearly. Even with a small number of input categories (e.g., say, 8 per date) the number of potential transitions (i.e., 64) exceeds the number of readable classes in a map. Even though some of those transitions will not exist, since some changes are very unlikely or impossible, the cartographic representation of changes is always a challenge (Figure 7-61). An alternative to representing changes would be to show them in a series of maps, one for each category on the first date, and each showing the output category in the second date. When the number of cross-categories is large, it may be preferable to create a series of maps (e.g., one for each input category, showing the transitions between the two dates). For instance, for the Brazil case study, three transitional maps may be created, one for each category of the first date (e.g., forest, crops, and water), showing in thematic colors the final cover at the second date. With this representation, a clearer view of the relevance of stable and transition covers is perceived.

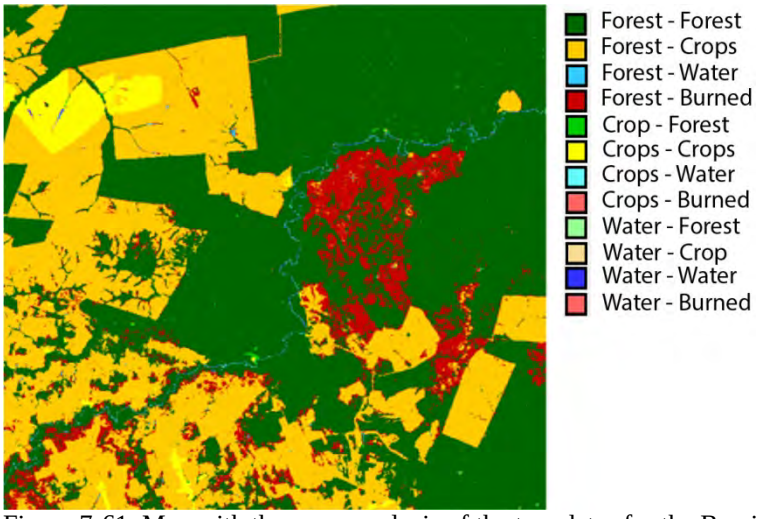

Figure 7-61. Map with the cross-analysis of the two dates for the Brazil site.

10.3.8 *Validation of Change Detection Studies*

The validation of multitemporal analysis is especially challenging as it complicates the comparison of reference and classified data with an additional time dimension. This implies errors associated with proper overlapping between the two images, as well as the difficulty of gathering reference information for historical periods. Summarizing these aspects, one can name the main differences in verification applied to change detection studies:

- Increase in the number of categories in the error matrix. The potential number of categories ("stable," "from," and "to") for two dates is the square of the number of categories in one date. All these classes must be considered during error evaluation, and at the end the confusion matrix will have n^4 cells; n being the starting number of classes for one date (Table 7-12).
- More complexity in the sampling scheme due to the great increase in number of categories to be verified. Since some of the potential changes will be uncommon or impossible (e.g., two urban areas to water bodies), one must increase considerably the sample size to verify these intersections. In these cases, stratified sampling or one based on auxiliary information can be a better alternative (Biging *et al.*, 1998).
- Difficulty in obtaining the reference information for past dates. In most cases, one will not have detailed information of terrestrial covers for distant past dates, which complicates the assessment of the oldest image. Aerial photography or cartographic documents of similar dates can solve this problem, although they may not always be reliable.

When one attempts to verify change detection, the confusion matrix traditionally used in validation studies gets notably complicated. To illustrate this process, consider a simple example of validation: a change detection product, taken from Biging *et al.*, 1998. Consider also that there are three classes for two different dates. This would imply nine possible categories of change. To verify these transitions, one needs a confusion matrix of 81 cells (i.e., the 9 true by the 9 estimated changes), which includes both the permanent classes, those with the same category between dates, as well as the dynamic classes. All these potential transitions/permanencies require verification. Therefore, the confusion matrix will include the tabulation of pixels that the map of changes presents as "from class X to class Y," while in reality, they may be that or some other kind of transition. As in the case of simple confusion matrices, the diagonal will include the true detections of change, those sampled pixels that were detected correctly as stable or as affected by a real change, and outside the diagonal the incorrect changes will be present.

By being more specific, one can better explain the structure of a confusion matrix using the notation described by Biging *et al.* (1998) in Table 7-12. The cells annotated with 1 are estimated stable areas that really are constant, while the cells with 2 are classified accurately as changed. The addition of 1 and 2 indicates the global accuracy of the change detection performed by the interpreter. The rest are errors due to several possibilities: 3 indicates stable areas classified incorrectly to other stable categories; 4 indicates changes when the cells maintained their category (i.e., commission errors, identified as a change for something that did not); 5 marks real changes that were not detected as such (i.e., omission errors); and 6 denotes identified changes inaccurately (detected changes, but assigned to another class, i.e., omission or commission errors, depending on the class considered).

Table 7-12. Confusion Matrix for Change Detection Analysis.

		Reference								
		Stable			Change					
		A	B	C	A	A	B	B	C	C
		A	B	C	B	C	A	C	A	B
Classification	AA	1	3	3	5	5	5	5	5	5
Stable	BB	3	1	3	5	5	5	5	5	5
	CC	3	3	1	5	5	5	5	5	5
	AB	4	4	4	2	6	6	6	6	6

	AC	4	4	4	6	2	6	6	6	6
	BA	4	4	4	6	6	2	6	6	6
Change	BC	4	4	4	6	6	6	2	6	6
	CA	4	4	4	6	6	6	6	2	6
	CB	4	4	4	6	6	6	6	6	2

A,B,C are different thematic categories. See text above Table 7-12 for explanation. Adapted from Congalton and Green (2009) and Biging *et al.* (1998).

10.4 *Time Series Analysis: Recent Advances in Software, Sensors and Data Availability*

Remote sensing time series analysis offers a powerful tool for revealing land surface dynamics, analyzing their magnitude, and estimating their impact on the environment within a defined monitoring time span (Lasaponara and Lanorte, 2012). Obviously, such an analysis requires appropriate spatio-temporal datasets as well as the necessary tools for mining the underlying information. Perhaps most importantly, a clear focus on which variables can, and should be, monitored continuously through remote sensing instruments is of most importance. This section provides an overview of recent advances in time series analysis, on the basis of these three axes: processing software, new types of sensors and data, and essential climate variables (ECVs). Although not the only useful application of remote sensing-based time series analysis, the mitigation of climate change constitutes the main driver for establishing most recent initiatives on persistent and systematic Earth observation data collection.

10.4.1 *Time Series Analysis Software*

The ever-increasing availability of freely-distributed time series of remotely-sensed data offers new possibilities for monitoring and analyzing land surface dynamics. However, the analysis and interpretation of such data is a challenging task, with many processing issues remaining open (Ma *et al.*, 2015). Remote sensing time series are actually 4D signals defined on a spatiotemporal domain, with each image comprising a number of spectral bands. As the spatial resolution of satellite sensors decreases continuously, the volume of data increases substantially, necessitating development of new tools for handling spatiotemporal "big data" efficiently.

Over the last few years, a number of software tools have been developed for analyzing remote sensing time series. Most of them attack the problem of the high volume of information through dimensionality reduction techniques. For example, deriving VIs results in a compression of the spectral dimension, whereas multitemporal composition or image differences reduce the temporal dimension. Moreover, open-source, or otherwise freely-distributed solutions, have increased considerably in the past few years, broadening their utilization by a much wider audience.

Software for Processing and Interpreting Remote Sensing Image Time Series (SPIRITS) is a free software environment for analyzing satellite-derived image time series (*http://spirits.jrc.ec.europa.eu*). SPIRITS was developed by VITO for the Monitoring Agricultural ResourceS (MARS) team of the Joint Research Center (JRC) (Eerens *et al.*, 2014). It provides a simple graphical user interface (GUI) for easing the analysis (see, Figure 7-62) and was originally developed as a toolbox for crop monitoring. As such, it can perform specialized operations such as crop production anomalies and yield assessments. Nevertheless, it has evolved into an independent tool for processing and analyzing time series raster data. To this end, it provides a range of useful processes for general time series analysis, such as smoothing procedures to

remove noise, similarity analysis to identify the most similar year, and databases with regional statistics, among others.

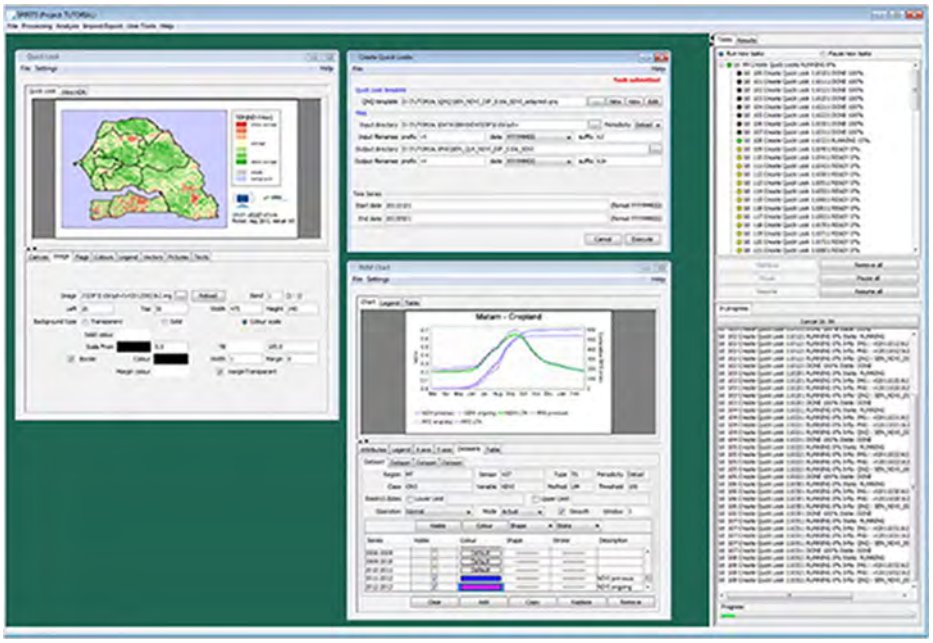

Figure 7-62. The SPIRITS graphical user interface (from Eerens *et al*., 2014).

TIMESAT (Jönsson and Eklundh, 2002, 2004) is a software package distributed freely for analyzing time series satellite sensor data (http://web.nateko.lu.se/timesat/timesat.asp). Since the temporal domain holds important information about short- and long-term vegetation changes, it targets primarily the seasonality of satellite time series data and their relationship to dynamic properties of vegetation, such as phenology and temporal development. TIMESAT consists of a set of MATLAB® and Fortran routines, bundled within a graphical interface written in MATLAB® (Jönsson and Eklundh, 2015). Precompiled binary versions of the program are also provided. Its output consists of seasonality parameters (Figure 7-63), as well as fitted function files containing smooth renditions of the original data. TIMESAT has been used in a number of applications, such as multi-year rice crop phenology monitoring (Boschetti *et al.*, 2009), tracking seasonal changes in coniferous forests (Jönsson *et al.*, 2010), examining spatiotemporal patterns of growing seasons in Ireland (O'Connor *et al.*, 2012), and mapping freshwater phytoplankton phenology (Palmer *et al.*, 2015), among others. Although it has been originally intended for handling noisy time series of AVHRR/NDVI, it has evolved to handle different types of remotely-sensed time series, such as MODIS (Boschetti *et al.*, 2009), MERIS (Palmer *et al.*, 2015), and HJ-1 A/B data (Pan *et al.*, 2015).

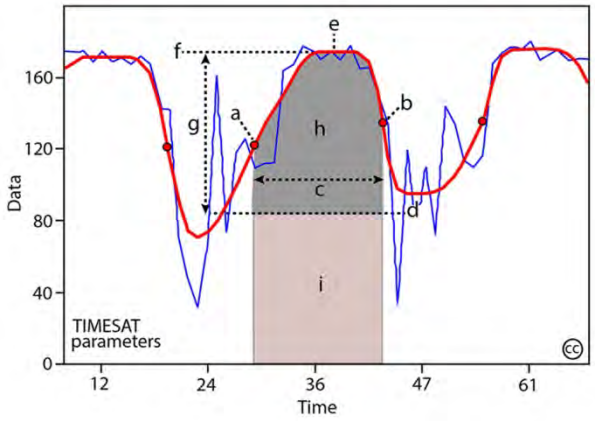

Figure 7-63. Some of the seasonality parameters generated in TIMESAT: (a) beginning of season, (b) end of season, (c) length of season, (d) base value, (e) time of middle of season, (f) maximum value, (g) amplitude, (h) small integrated value, (h+i) large integrated value (source: *http://web.nateko.lu.se/timesat/timesat.asp*).

Advanced remote sensing time series analysis is also possible using the R language (*https://www.r-project.org*). "R" is a programming language and environment for statistical computing and graphics. Its functionality has been augmented substantially over the years, by means of dedicated extensions (called packages) that target specific applications. Because of its ease of use and the simple syntax its language offers, it has been used increasingly for remote sensing data analysis. Several packages exist specifically for remote sensing time series analysis. The Breaks For Additive Season and Trend (BFAST) package (http://bfast.r-forge.r-project.org), for example, provides generic functionality for continuous change monitoring, trend analysis, and near-real time disturbance detection of any kind of disturbance or change process (Verbesselt *et al.*, 2010, 2012). BFAST estimates the time and number of abrupt changes iteratively within time series, and characterizes change by its magnitude and direction. It also offers generic change detection functions for time series segmentation and near-real time monitoring for any kind of time series like for example rainfall, temperature, or dendrochronology series. The closely related bfastSpatial package (http://github.com/dutri001/bfastSpatial) automates the application of many preprocessing steps required for the employing the trend analysis. The TimeSyncR package (*https://github.com/johanez/multifuse*) is based loosely on the TimeSync method of Cohen *et al.* (2010) and provides a tool to aid visualizing and interpreting Landsat time series data for calibrating and validating change detection methods. The MODIS package (*http://modis.r-forge.r-project.org*) consists of a set of functions for downloading, mosaicking, resampling, reprojecting, analyzing, and visualizing MODIS data, with special attention given to spatio-temporal filtering, change detection and phenological metric extraction. Finally, the recent MulTiFuse package (*https://github.com/jreiche/bayts*) provides functions for fusing optical and SAR time series (Reiche *et al.*, 2015). Application of the aforementioned tools is not supported by some dedicated GUIs, but rather requires knowledge of the R programming language and environment. Nevertheless, R offers sophisticated tools for visualizing any type of data, together with many other statistical analysis processes.

The Landsat-based Detection of Trends in Disturbance and Recovery (LandTrendr), for example, comprises a set of preprocessing and analysis algorithms written in the Interactive Data Language (IDL) programming language (*http://landtrendr.forestry.oregonstate.edu*), specifically targeted to capturing trends in Landsat-derived time series (Kennedy *et al.*, 2010). The LandTrendr algorithm tracks land cover changes

across years, whereas intra-year variability is considered noise. Each pixel's temporal trajectory is constructed considering only the best values for each year, after removing clouds, shadows, and data gaps. The core step is applying a temporal segmentation process, whereby the overall change trends are identified after simplifying the time series to remove noise and spikes. Therefore, significant changes can be identified on a yearly basis and are subsequently visualized through change maps. Because of the yearly temporal resolution of LandTrendr's approach, it has been used mainly for (1) analyzing forest biomass dynamics (Powell *et al.*, 2013; Pflugmacher *et al.*, 2014); (2) to distinguish between different forest disturbances (Senf *et al*., 2015); and (3) to identify spatiotemporal changes in fish species populations (Kennedy *et al*., 2015).

All the aforementioned software packages are either open-source or otherwise distributed freely for scientific purposes. Nevertheless, many commercial packages have also started incorporating some functionality for analyzing time series data. One notable example is the TerrSet geospatial software system (*https://clarklabs.org/terrset*), which incorporates the former IDRISI image analysis software and augmented it with enhanced trend analysis and change modeling functionalities. Specifically, it includes a module for general Earth trend modeling applications, providing advanced time series preprocessing and de-noising algorithms, tools for examining the relationship between time series and trends in seasonality, as well as methodologies for analyzing patterns of variability across temporal scales. Moreover, the Land Change Modeler (LCM) module allows analyzing land cover changes, empirically model relationships to explanatory variables, and simulating future land change scenarios, thus supporting the design of policies for climate change mitigation.

10.4.2 *New Sensors, More Data, New Perspectives*

Over the past 40 years, a large number of satellite sensors have been monitoring Earth and its changing patterns. The lessons learned are being used to further develop the efficiency, relevancy, and timeliness of new Earth-observing missions. Emphasis is being given to global time series collection of consistent measurements. For example, the various satellite missions of the Sentinel program have been designed to have a short revisit time; whereas the Sentinel-2 sensor includes specific aerosol content bands to ease atmospheric correction. The latter is important not only for obtaining consistent measurements along different time points, but also for accurately calculating many useful biophysical parameters that are based on ground reflectance measurements. The rapid deterioration of our planet's climate and global initiatives established in response, detailed in the next subsection, have also pushed development of new Earth-observing missions designed to collect measurements on multiple variables for land, sea, and atmosphere. Moreover, the technological advent of remote sensors facilitates monitoring physical properties that conventional optical sensors were not designed to quantify. As such, a diverse range of new application-based on remotely-sensed data, and time series data in particular, have emerged.

Synthetic aperture radar (SAR) sensors are active systems that transmit beams of radiation in the microwave region of the electromagnetic spectrum. They are not affected by light or heat conditions, can penetrate clouds, and their signals can be used to infer ground elevation. Although SAR time series have shorter history than those collected by other optical systems, relatively adequate records exist. For example, ERS-

1 and -2 have collected SAR time series since the early 1990s, retired in 2012, whereas new satellite missions such as Sentinel-1, are already operational.

A prominent application of SAR time series data relates to altimetry, which can be used to infer ground deformation through interferometry (InSAR) (Iglesias *et al.*, 2015). Specific applications range from landslide deformation mapping (Motagh *et al.*, 2013; Shi *et al.*, 2015) and estimation of its velocity (Figure 7-64) (Lauknes *et al.*, 2010) to assessment of structural damage (Arangio *et al.*, 2014; Tofani *et al.*, 2014) and land subsidence in residential areas (Cascini *et al.*, 2013; Chen *et al.*, 2013, 2015; Kim *et al.*, 2015b) and monitoring volcanic activity (Parks *et al.*, 2012; Meyer *et al.*, 2015). SAR signals are also sensitive to water content. For example, smooth water surfaces generally appear as dark areas in SAR images. This property has been exploited to observe seasonal changes in water surface areas (Heine *et al.*, 2014), analyzing flood events (Khan *et al.*, 2014; Shang *et al.*, 2014), and simulating coastal inundation through tidal models (Medeiros *et al.*, 2013). SAR time series data have been employed for monitoring ice-shelf decomposition (Kim *et al.*, 2015a), identifying changes in ice cover thickness of Arctic shallow lakes (Surdu *et al.*, 2014), discriminating types of sea ice (Ressel *et al.*, 2015), and estimating water equivalent dry snow (Leinss *et al.*, 2015).

The ability of SAR signals to penetrate clouds makes them useful also for land change monitoring. Data gaps because of cloud cover are a significant problem in landcover change mapping through optical sensors, especially in tropical regions. Usually this is achieved by fusing the data provided by optical and SAR time series (Lehmann *et al.*, 2015; Reiche *et al.*, 2015), although approaches that employ SAR imagery exclusively also exist (Shiraishi *et al.*, 2014; Betbeder *et al.*, 2015; Dong *et al.*, 2015). Other reported applications of SAR time series data include soil moisture determination (Panciera *et al.*, 2014), LAI retrieval (Beriaux *et al.*, 2013), and estimation of crop phenology parameters (De Bernardis *et al.*, 2015).

LiDAR is active sensor technology that uses light in the form of a pulsed laser to measure ranges (variable distances) to point returns from objects at the surface. Its application the last few years has increased substantially, because of the increasing availability of LiDAR data obtained by airborne sensors. Space Lidar technology is still in its infancy, with the only system being NASA's experimental Ice, Cloud and land Elevation Satellilte (ICESat) Mission, which operated from 2003 to 2009. The primary objectives of ICESat were to measure ice sheet mass balance, cloud and aerosol heights, surface topography and vegetation characteristics. Although the Mission's operational period was short, a number of satellite Lidar time series scientific studies have been conducted, focused mainly on monitoring changes of Earth's permanent ice sheets (Herzfeld and Wallin, 2014; Herzfeld *et al.*, 2014; Wang *et al.*, 2014). Nevertheless, other interesting uses have also been reported, such as analyzing lake water balance changes (Zhang, G., *et al.*, 2013) and estimating forest canopy height (Duncanson *et al.*, 2010, Li *et al.*, 2011). Following the Mission's success, the ICESat-2 follow-up Mission is under development and slated for launch in 2017, with the additional envisaged objective to generate an estimate of global vegetation biomass.

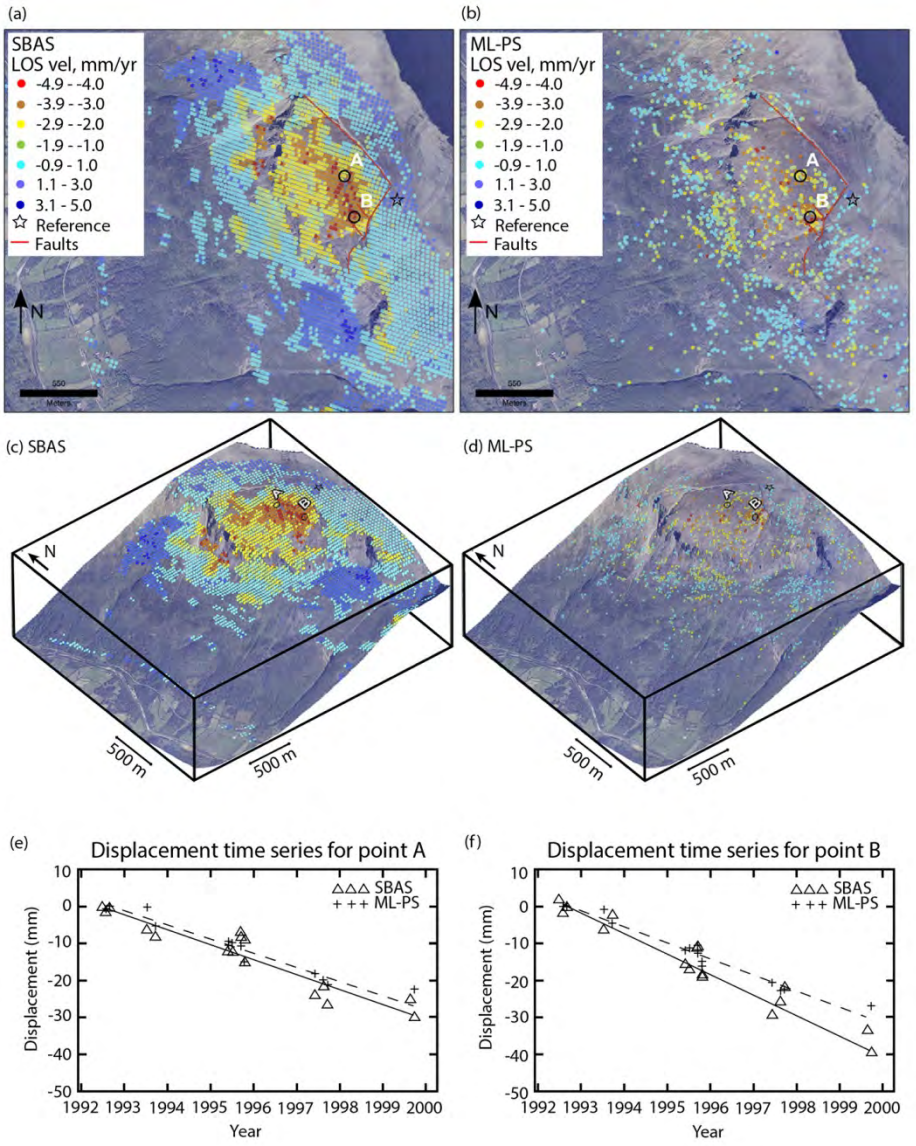

Figure 7-64. Landslide velocity estimation using time series of ESR-1 and ESR-2 SAR data from 1992 through 1999. The SAR sensor is only sensitive to displacement changes with a component in the radar line-of-sight (LOS) direction, whereas two alternative approaches for estimating the average yearly displacement are compared, namely: (a) the Small BAseline Subset (SBAS) algorithm; (b) the Maximum Likelihood Persistent Scatterer (ML-PS); (c-d) the same results in a three dimensional perspective view using a DEM. Yearly displacement of two points, marked as A and B relatively, to the reference star is shown in (e) and (f), respectively, where the solid lines represent the linear model fitted to SBAS, and the dashed lines the one fitted to ML-PS. Generally, SBAS has the advantage of having regional-scale coverage, whereas ML-PS can be used for detailed or complementary studies (source: Lauknes *et al*., 2010).

The wealth of historical records of remote sensing observations available today facilitates time series studies on a global level. A prominent example was the Global Irrigated Area Map (GIAM) project (Thenkabail *et al.*, 2009), whose objective was to identify and map irrigated areas on a global scale. Although the project was conducted at the end of the previous millennium, it serves even today as an example of the potentials offered by remote sensing time series data. GIAM combined the information provided by multiple datasets, many of which were obtained through time series observations. The information was

compiled into a single multi-source and multi-temporal data cube (Figure 7-65) and was subsequently analyzed through advanced pattern recognition algorithms on the spatiotemporal domain.

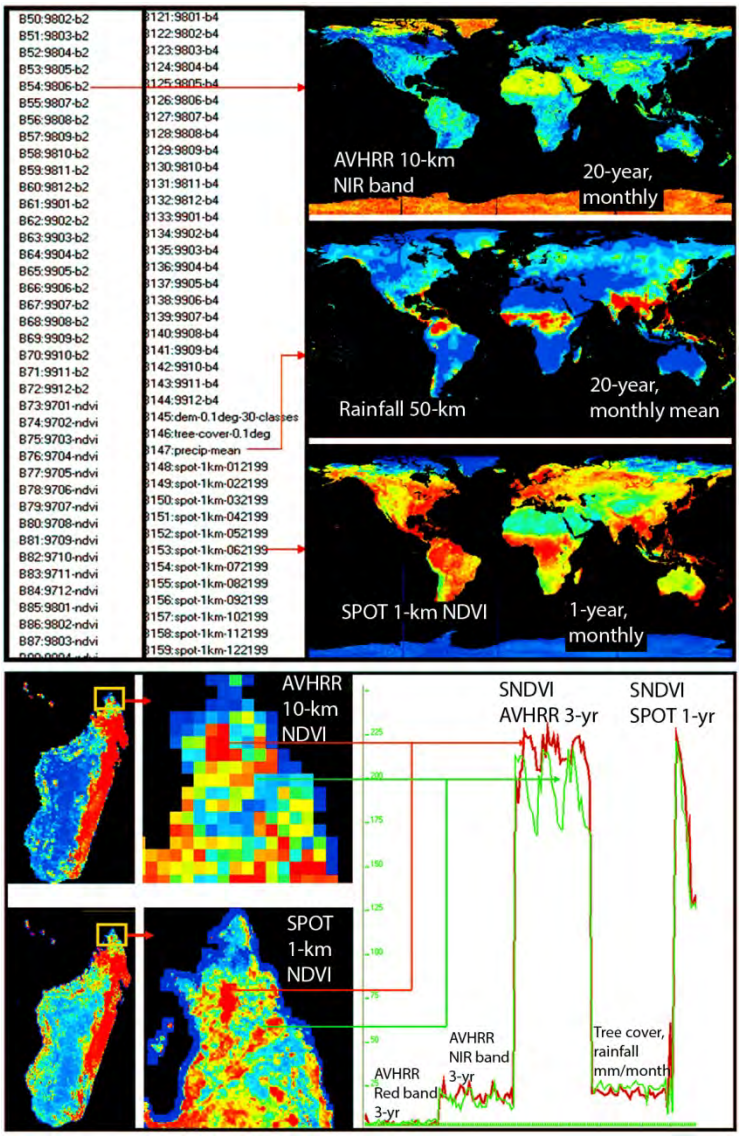

Figure 7-65. Global mega-file data cube comprising 159 data layers, consisting of time series from various sources and providing characteristics from all data layers at any single point (adapted from Thenkabail *et al.*, 2009).

10.4.3 *Remote Sensing as a Source of Data forMeasuring Essential Climate Variables*

The face of Earth is constantly changing at measurable rates, the consequences of which are not fully understood and are still contentious politically, economically, and scientifically. Forest ecosystems are diminishing at an alarming speed, urban and agricultural areas are expanding into surrounding natural spaces, and sea level rise appears to be changing coastal ecosystems. Nowadays, there is a broad consensus that Earth's climates are changing, some at alarming rates, and that there is an urgent need to reduce further degradation and to mitigate negative impacts as much as possible. A number of global initiatives have been established for this purpose, such as the United Nations Framework Convention on Climate Change

(UNFCCC), the Intergovernmental Panel on Climate Change (IPCC), the World Climate Programme (WCP), and the UNEP, along with many other national and transnational initiatives.

To fully identify the trends of climate change, understand its impacts, and design efficient policies for their mitigation, constant monitoring of our planet is essential. In 1992 the Global Climate Observing System (GCOS) was established as an international, interagency, interdisciplinary framework for ensuring that the observations and information needed to address climate-related issues are obtained and made available to all potential users (Houghton *et al.*, 2012). GCOS is a long-term, user-driven operational system capable of providing the comprehensive observations required for monitoring the climate system, for detecting and attributing climate change, for assessing the impacts of climate variability and change, and for supporting research to improve understanding, modeling, and prediction of the climate system. In aggregate, as a system of climate-relevant observing systems, it constitutes the climate observing component of the Global Earth Observation System of Systems (GEOSS).

To provide guidance for collecting climate-related Earth-observing data, GCOS has developed the concept of essential climate variables (ECVs), which have been adopted broadly in science and policy circles and is updated frequently (GCOS, 2010). An ECV is a physical, chemical, or biological variable or a group of linked variables that contribute immensely to characterizing Earth's climate (Bojinski *et al.*, 2014). A variable is identified as an ECV if it fulfils three criteria: (a) it is critical for characterizing the climate system and its changes (relevance); (b) observation is technically feasible through proven scientific methods (feasibility); and (c) generating and archiving data on the variable is affordable (cost-effectiveness). GCOS currently identifies 50 ECVs (GCOS, 2010) that are required for supporting the work of the UNFCCC and the IPCC (Table 7-13).

Table 7-13. The Essential Climate Variables as Currently Identified by GCOS (2010).

Domain	Essential Climate Variables	
Atmospheric	Surface:	Air temperature, Wind speed and direction, Water vapor, Pressure, Precipitation, Surface radiation budget
	Upper-air:	Temperature, Wind speed and direction, Water vapor, Cloud properties, Earth radiation budget (including solar irradiance)
	Composition:	Carbon dioxide, Methane, and other long-lived greenhouse gases, Ozone and Aerosol supported by their precursors (in particular nitrogen dioxide, sulphur dioxide, formaldehyde, and carbon monoxide)
Oceanic	Surface:	Sea-surface temperature, Sea-surface salinity, Sea level, Sea state, Sea ice, Surface current, Ocean color, Carbon dioxide partial pressure, Ocean acidity, Phytoplankton
	Sub-surface:	Temperature, Salinity, Current, Nutrients, Carbon dioxide partial pressure, Ocean acidity, Oxygen, Tracers
Terrestrial		River discharge, Water use, Groundwater, Lakes, Snow cover, Glaciers and Ice caps, Ice sheets, Permafrost, Albedo, Land cover: including vegetation type, fraction of absorbed photosynthetically active radiation (FAPAR), LAI, Above-ground biomass, Soil carbon, Fire Disturbances and Soil moisture

In response to the GCOS ECV specifications, the European Space Agency (ESA) has launched the Climate Change Initiative (CCI) to provide satellite-based climate data records (CDRs) that meet the challenging requirements of the climate community (Hollmann *et al.*, 2013). The aim of the initiative is to realize

the full potential of the long-term Earth observation archives that both ESA and third parties have established that includes data acquisition, calibration, algorithm development, validation, maintenance, and provision of the data to the climate research community. For the current program, 13 of the 50 ECVs have been selected:

- Atmosphere: ozone, clouds, aerosols, and greenhouse gases (GHGs);
- Ocean: sea level, sea surface temperature (SST), ocean color, and sea ice; and
- Terrestrial: land cover, fire disturbance, soil moisture, glaciers and ice caps, and ice sheets.

ESA CCI aims to provide as complete, and as consistent, a time series of multi-sensor global satellite data products as possible for climate research and modeling. For this purpose, the data from a number of globally available satellite instruments are being employed (Figure 7-66), with the length of the record varying between ECVs. For each variable, the best available technique for producing the record is selected, whereas new algorithms are also developed by the respective teams (Merchant *et al.*, 2015). Ultimately, a prototype product is created that will be verified, validated, and assessed openly for its utility to climate science by independent teams.

	SST	Sea level	Ocean colour	Sea-ice	Clouds	GHG	Aerosol	Ozone	Fire	Land cover	Glaciers	Soil moisture	Ice sheets
AATSR/ATSR-2/ATSR-1	●				●		●		●				
MERIS			●		●		●		●	●			
SPOT VGT									●	●	●		
Landsat TM/ETM+											●		●
SAR (ENVISAT/ERS/ALOS/TSX/PALSAR)										●			●
SEVIRI	●												
MODIS			●		●								
Sciamachy						●	●	●					
GOSAT						●							
GOME-1/2							●	●					
AVHRRs	●				●		●						
GOMOS							●	●					
IASI						●							
AIRS						●							
AMSU						●							
ACE						●		●					
SeaWIFS			●										
MIPAS						●		●					
OMI							●	●					
Radar Altimeters (TOPEX-POSEIDON)		●											
Radar Altimeters (JASON-1/2)		●											
Radar Altimeters (ENVISAT, ERS)		●		●							●		●
Scatterometers												●	
SMMR				●								●	
TMI	●											●	
SMOS												●	
AMSR-E	●			●								●	
WINDSAT												●	
SSM/I & SSMIS				●								●	
PARASOL							●						
ASTER											●		●
ICESAT											●		
OSIRIS								●					
SMR								●					
POLDER							●						

Figure 7-66. Satellite sensors contributing to ECV monitoring in the framework of the ESA CCI program (source: Hollmann *et al.*, 2013).

CCI will provide a wealth of consistent, validated, and timely data for a number of climate-related studies. A number of new algorithms for developing more accurate products has been proposed for land cover mapping (Radoux *et al.*, 2014), clouds (Karlsson and Johansson, 2014), seal level rise (Ablain *et al.*, 2015), glacial areas, elevation changes and velocity (Paul *et al.*, 2015), and ozone (Coldewey-Egbers *et al.*, 2015). Moreover, systematic validation of well-established techniques has also begun (Dils *et al.*, 2014, Dorigo *et al.*, 2015, Kern *et al.*, 2015, Padilla *et al.*, 2015). All products created within the CCI framework are available at no cost for download, through a single point of access (*ftp://anon-ftp.ceda.ac.uk/neodc/esacci*) for key data products; whereas, the full suite of products is accessed via the dedicated site for each ECV.

An equivalent CDR program has also been established in the United States of America (USA) carried out by the NOAA (Drobot *et al.,* 2004). Currently, various ECV related time series datasets are assimilated and validated, including aerosol optical thickness, cloud properties, surface radiation budget, ozone, precipitation solar irradiance, sea ice concentration, SST, LAI, FAPAR, and snow cover extent, in the northern hemisphere. Moreover, the list of products is updated continuously, exploiting incoming data from new scheduled missions. All generated data and products are becoming available as soon as they are generated and at no cost through NOAA's dedicated file transfer protocol (FTP) server (*ftp://data.ncdc.noaa.gov/cdr*). Finally, the European Organization for the Exploitation of Meteorological Satellites (EUMETSAT) is also supporting the GCOS implementation plan, collecting and processing a number of ECVs, related mostly to meteorological observations (Schulz *et al.,* 2009).

Remote sensing time series analysis is a broad field with many practical applications. Nevertheless, monitoring ECVs for designing climate change adaptation policies constitutes the main driver for most of the more recent and future satellite missions, even if this objective has been considered complementory with other factors. For example, well before the launch of the first Sentinel-1 satellite, the potentials offered by the whole Sentinel program in terms of monitoring ECVs was assessed and a recommendation was made to prioritize future missions and derived products based on the Malenovský principles (Malenovský *et al.,* 2012). Designing and implementing the Indian Earth Observation System was also influenced strongly by the need for consistent collection of ECV time series (Navalgund and Singh, 2011). ESA's Earth Explorer Missions within the Living Planet Programme aim to monitor specific ECVs that were difficult to observe with previous conventional sensors (e.g., biomass, chlorophyll fluorescence, and greenhouse gases with high spatial resolution).

All the climate change-related initiatives undertaken over the past three decades have resulted in compiling long time series of consistent measurements that enable assessment of climate change trends, as well as the derivation of relatively safe projections of their possible future trends. The activities of GCOS and the Group on Earth Observations (GEO) have facilitated freely available remote sensing time series of climate change data. The various CDR programs are starting to provide consistent and validated time series of various biophysical parameters over a statistically adequate time span. As a consequence, the works based on remote sensing time series data have multiplied over the last few years, especially after 2009. A number of scientific works analyze LAI and FAPAR variables (Camacho *et al.,* 2013; D'Odorico *et al.,* 2014; Verger *et al.,* 2015), because of their importance in carbon stock and ecosystem models and the availability of long time series from sensors such as MODIS, SPOT VEGETATION, and MERIS, among others. Nevertheless, diverse time series applications are also emerging, based on land cover mapping (Blanco *et al.,* 2013), forest fire variability analysis (Vasconcelos *et al.,* 2013), measuring glacial retreat velocities (Dehecq *et al.,* 2015), and determining surface water temperature (Riffler *et al.,* 2015).

10.5 *Image Enhancement for Time-series Analysis and Analysis Methods*

10.5.1 *Introduction*

Image enhancement refers to improving image interpretability and perception of information for specific applications (Maini and Aggarwal, 2010). Various techniques have been developed for image enhancement

in the spatial domain, including the widely used local contrast enhancement techniques through two-dimensional convolution of pixels in a moving window (e.g., *Low Pass*, *High Pass* and various statistical filters) (Pratt, 2014). Image enhancement is also performed by adjusting global contrast using image histograms (e.g., *Min-Max Stretch, Standard Deviation Stretch, Gaussian Stretch* and *Histogram Match)* (Jensen, 2015). In the spatial frequency domain, image enhancement may involve computing a Fourier transform of the image (e.g., FFT and Inverse Fast Fourier Transform (IFFT)), applying the transform, and producing the enhanced image (Russ, 2011). These spatial enhancement methods were documented and described in previous editions of the *Manual of Remote Sensing*.

Here, we introduce the recent development of time-series image enhancement in the temporal domain. Since the 1980s, global observations at *km* scales have been available from satellite systems such as the NOAA's AVHRR, Terra/Aqua MODIS, and SPOT VEGETATION (VGT). Frequent acquisitions of satellite imagery reveal land surface phenology (de Beurs and Henebry, 2004) and its inter-annual responses to climate dynamics (Myneni *et al*., 1997). Satellite-derived NDVI time series have been used commonly for land cover delineation (Wang *et al.*, 2011; 2015) and for analyses of land cover trends under various anthropogenic (e.g., land-use change) and natural (e.g., short-term weather dynamics and long-term climate change) impacts (Elmore *et al*., 2003; White *et al*., 2002). However, raw NDVI trajectories are influenced highly by cloud, atmospheric conditions and systematic noise during image acquisition. Time-series enhancement aims to suppress these kinds of data noise to reconstruct high-quality data sets for improved time-series analysis.

10.5.2 *Time-series Noise Reduction*

Vegetated land surfaces possess inherent growth cycles that can be described by time-series image data. Cloud contamination results in abnormal spikes along those time series, and even on cloud-free days, spectral indices such as NDVI vary with aerosol concentration, BRDF effects from Sun-Earth-sensor geometry, and land surface disturbances. A number of threshold-based noise reduction algorithms have been developed to better approximate vegetation growth cycles.

10.5.2.1 Maximum Value Composite

Early approaches to reducing temporal noise in daily remotely-sensed data include the MVC technique (Holben, 1986), which retains the highest NDVI value in a compositing period by assuming that all contamination (e.g., clouds) results in decreased NDVI. A single value is used to represent the composite period, and therefore, the temporal resolution of the output is reduced. Common examples of MVC composites are: (1) the 8*km*, 10-day Pathfinder AVHRR Land (PAL) datasets, available since the 1980s; (2) the 1*km*, 10-day VGT S10 products available since 1998; and (3) MODIS products at various temporal intervals (8-day, 16-day, and monthly) at spatial resolutions (250*m*, 500*m* and 1,000*m*), available since 2000. In wet growing seasons, however, cloud spikes in these products often remain when clouds cover the whole composite period (Wang *et al*., 2011).

10.5.2.2 Best Index Slope Extraction

As an alternative to MVC, Viovy *et al*. (1992) proposed a threshold-based Best Index Slope Extraction (BISE) approach to suppress noise without reducing temporal resolution. In this approach, a threshold for

acceptable NDVI increase (e.g., 20%) is used to define the upper envelope in a pre-determined scanning time period. High-frequency noise (i.e., sudden increases and decreases of NDVI) do not satisfy the threshold and are eliminated. In spite of its better retention of seasonal variation than MVC, the selection of scanning periods for BISE is subjective, as it depends on the experience of the analyst and varies with land surface dynamics. Like all threshold-based methods, the BISE approach may result in erroneous interpretation, such as shifted start and end of seasons when extracting phenologic descriptors (Jönsson and Eklundh, 2002).

10.5.3 *Time-series Smoothing*

Vegetated land surfaces possess complex growth cycles that vary with biome, climate and human activities. As a result, different smoothing techniques may be needed to extract their phenology behaviors optimally (Zhang *et al*., 2003). The 250*m*, 16-day MODIS NDVI (MOD13Q1) product in 2012-2014 demonstrates some common approaches of time-series smoothing. Three year NDVI time series data for three vegetated areas were representing areas in the North China Plain include: (a) deciduous forest; (b) winter wheat single cropping; and (c) winter wheat-corn double cropping. Their raw NDVI time series and smoothed curves are shown in Figure 7-67. The TIMESAT software was used to extract these curves (Jönsson and Eklundh, 2004).

Forest lands (Figure 7-67a) present single annual cycles from spring to late fall. Winter wheat in the North China Plain is planted in October and harvested the following June (Lu *et al*., 2014). After planting, two growth peaks are apparent: one in winter with a smaller NDVI peak and another in spring with the primary NDVI peak (Figure 7-67b). The North China Plain is dominated by double cropping, (i.e., winter wheat, followed by corn, sometimes cotton). Figure 7-67c reveals two primary peaks (i.e., two growth cycles) within a one-year period – winter wheat in spring and corn in fall. A secondary growth peak of wheat in winter is also apparent. In original NDVI curves, cloud or snow spikes (e.g., the one in early 2014) are observable. Actually, in Figure 7-67c, the secondary growth peak of wheat in winter 2012 is lost due to a spike in this period. The sharp local variation and jagged trajectories of original NDVI values indicate the need for time-series smoothing. A variety of methods have been employed to smooth time series of spectral indices, including those based on local polynomial fitting and the use of logistic and asymmetric Gaussian functions, as presented below.

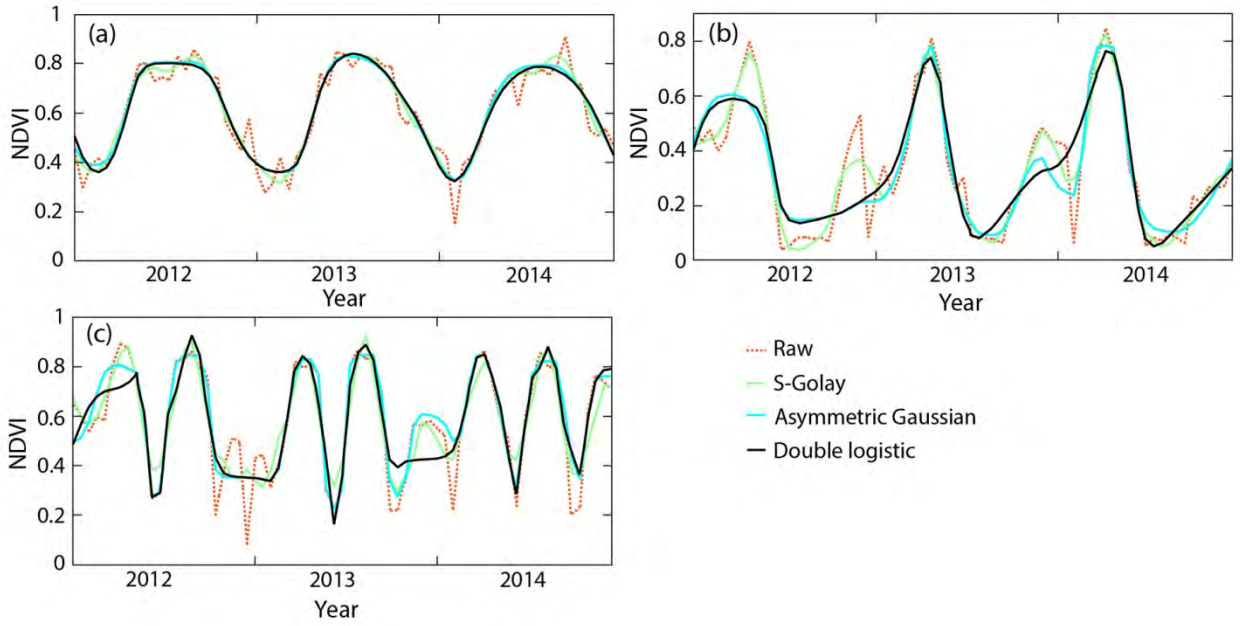

Figure 7-67. NDVI time series from MOD13Q1 for the North China Plain: (a) deciduous forest; (b) winter wheat single cropping and (c) winter wheat-corn double cropping.

10.5.3.1 Local Polynomial Fitting

The most commonly adopted polynomial fitting is the Savitzky-Golay filter (Savitzky and Golay, 1964). Basically, it is a weighted least-square moving average defined by a 2nd-order polynomial regression. Given a filter window $2n+1$, the smoothed NDVI, $NDVI^s(t)$, at a temporal position, t, can be calculated by Equation 7-71 as:

$$NDVI^s(t) = \sum_{j=-n}^{n} w_j \, NDVI'_{j+t} \quad (7\text{-}71)$$

where: $w_j = 1/(2n+1)$ is the weight of the moving average at point j in the window, with $j \epsilon (-n, n)$. $NDVI'$ is the fitted NDVI with a quadratic polynomial function using all $2n+1$ points in the window. At a temporal position, t, the regressed NDVI in a period of $2n+1$ is given by Equation 7-72 as:

$$NDVI'_j = c_0 + c_1 t_j + c_2 t_j^2 \quad (7\text{-}72)$$

where: c_0, c_1, and c_2 are the fitting parameters to be solved in the function.

The Savitzky-Golay filter, referred to as the S-Golay filter in Figure 7-67, provides a simple yet useful smoothing process to reduce cloud contamination in NDVI time series. As shown in the Figure, the S-Golay smoothed curves reduce local variations effectively, especially spikes, in the raw NDVI curves, although the trajectories are still jagged. Among all filters displayed in the Figure, the Savitzky-Golay smoother remains maximally the secondary winter growth of wheat.

Recent studies modified this filter for improved noise reduction. Chen *et al*. (2004) proposed an iterative Savitzky-Golay filter by fitting the upper envelope of NDVI to account for negatively biased noise. Swets *et al*. (1999) incorporated a weighted least squares linear regression, while Bradley *et al*. (2007) weights NDVI values asymmetrically above and below the baseline with an exponential weighting function to better extract the local maxima of NDVI. Jin and Xu (2013) combined several statistical filters into a Running Median-Maximum-Endpoint-Hanning (RMMEH) smoother to reconstruct optimally the MODIS NDVI

time series. These noise-reduction processes often serve as the first step of time-series cleaning before curve fitting (Bradley *et al*., 2007; Wang *et al*., 2011).

10.5.3.2 Logistic Function

Zhang *et al*. (2003) developed a piecewise logistic model to fit the MODIS NDVI time-series curves for extracting phenological metrics. Basically, a complete growth cycle is divided into a series of pieces of temporal changes (e.g., growth or senescence). Defining the curvature as the derivatives of NDVI along the time series, each piece is determined by the transition dates calculated as the minimal or maximal rate of curvature change (i.e., the 2nd derivative of NDVI). For each piece, the NDVI time series is simulated in Equation 7-73 as:

$$NDVI^s(t) = \frac{NDVI_{max}}{1+e^{a+b\times t}} + NDVI_{base} \quad (7\text{-}73)$$

where: $NDVI_{max}$ is the maximal variation of this piece and $NDVI_{base}$ is it's base level, with peak NDVI = $NDVI_{max}$ + $NDVI_{base}$. The simulation of this piece is determined by the exponential function e^{a+bt} with a and b as the fitting parameters.

The piecewise logistic model needs *a priori* knowledge about the numbers of pieces in a growth cycle. Simplifying land surfaces to a single-season growth cycle containing two pieces (i.e., growth and senescence), Beck *et al*. (2006) modified the model to a double logistic function in Equation 7-74 as:

$$NDVI^s(t) = NDVI_{max}\left(\frac{1}{1+e^{-b_1\times(t-a_1)}} + \frac{1}{1+e^{b_2\times(t-a_2)}}\right) + NDVI_{base} \quad (7\text{-}74)$$

where: the terms b_1 and b_2 represent the slopes in the two functions, while a_1 and a_2 are the two inflection points of each slope.

The double logistic filter performs well for forests with single growth cycles (Figure 7-67a). It removes local variations and maintains the smooth trajectories maximally along the time series. For non-ideal growth curves, however, its performance becomes less optimal. As shown in Figures 7-67b and 7-67c, while maintaining the primary growth peaks for winter wheat and corn, the secondary peak of wheat in winter is lost in the double logistic smoothing.

10.5.3.3 Asymmetric Gaussian Function

Asymmetric function fitting methods are more flexible when applied to land surfaces with irregular growth cycles, for example cool-season grasses with a prolonged duration in the USA Great Plains (Wang C. *et al*., 2013). To account for the asymmetric curvatures between growth and senescence, the growth cycle is split into two Gaussian functions (Jönsson and Eklundh, 2004) in Equation 7-75:

$$NDVI^s(t) = \begin{cases} c_1 + c_2 e^{-\left(\frac{t-a_1}{a_2}\right)^{a_3}} & if\ t > a_1 \\ c_1 + c_2 e^{-\left(\frac{a_1-t}{a_4}\right)^{a_5}} & if\ t < a_1 \end{cases} \quad (7\text{-}75)$$

where: two Gaussian functions are split at temporal position a_1: growth in the left ($t < a_1$) and senescence in the right ($t > a_1$). The terms a_2 and a_4 control the slope, a_3 and a_5 are the kurtosis (i.e., flatness) of each function, while c_1 and c_2 determine the base level and the amplitude of the NDVI trajectories.

An interesting modification of the asymmetric Gaussian method is the Double Gaussian model that is suitable in double-season agricultural lands, such as the winter wheat-corn double cropping that is dominant in the North China Plain. In this case, the annual NDVI curve is represented by a combination of two Gaussian functions (Lu *et al*., 2014) in Equation 7-76.

$$NDVI^s(t) = c_1 e^{-\left(\frac{t-a_1}{a_2}\right)^{a_3}} + c_2 e^{-\left(\frac{t-a_4}{a_5}\right)^{a_6}} \quad (7\text{-}76)$$

where: a_1, a_2…, a_6 are the fitting parameters. Different from the asymmetric Gaussian function above, c_1 and c_2 are added to represent the amplitudes of the two Gaussian functions, respectively.

The need for solving multiple parameters to simulate a complete cycle increases the computational complexity of the Gaussian filters. Similar to the double logistic filter, the asymmetric Gaussian filter performs well for land surfaces with simple growth cycles such as forest (Figure 7-67a). In Figure 7-67b and 7-67a, it picks up the secondary growth cycle of wheat in winter 2013, but not the one in winter 2012. These observations agree with Wang *et al*. (2011) that these filters are often ill-suited for land surfaces with complex growth cycles, and fail in areas without strong seasonality. Also, the asymmetric Gaussian filter shifts the temporal position of the peak NDVI slightly, resulting in lower peak values than the double logistic filter, which may become problematic in extracting phenological metrics such as SOS.

10.5.3.4 Fourier Series Function

Fourier fitting methods perform harmonic analysis of satellite time series (Sellers *et al*., 1994; Cihlar, 1996; Roerink *et al*., 2000). In these approaches, a time series is split into a series of symmetric sinusoidal functions. For example, a second-order Fourier series requires five parameters to describe the seasonality of NDVI trajectories (Beck *et al*., 2006) as shown in Equation 7-77:

$$NDVI^s(t) = \sum_{j=0}^{2}(a_j\, cos(j \times \phi_t) + b_j\, sin(j \times \phi_t)) \quad (7\text{-}77)$$

where: $\varphi = 2\pi(t-1)/n$, with n representing the total number of points in the time series. The terms a_0, a_1, a_2, b_1, b_2 are the fitting parameters in a 2nd-order simulation.

Harmonic decomposition of NDVI time series has been applied to identify annual crops relying on their symmetric and inter-annually consistent development cycles (Jakubauskas *et al*., 2002). Most land cover classes, however, do not possess ideally symmetric curves due to dynamic weather conditions and human disturbances. Therefore, Fourier analysis is less applicable to global land surface analyses.

10.5.3.5 Conclusions

High-quality satellite time series are crucial to regional and global vegetation monitoring as well as for environmental change and sustainability research (Bradley *et al*., 2007; Turner *et al*., 2007). Time series enhancement suppresses spectral noise and fits image trajectories optimally into theoretical model functions. Smoothed time series improve our assessment of land surface phenology as well as long-term trends of terrestrial lands under the accelerated pressure of climate change and human disturbances. However, it should be noted that different smoothing approaches may be applied depending on the growth cycles of land surfaces. Filters tend to work well in forested lands that present simple, single growth cycles. The double logistic filter fails to detect any of the secondary growth cycle of wheat in the winter season, while the asymmetric Gaussian filter performs better to depict this cycle when the land is not affected by snow or

cloud spikes. On the other hand, the double logistic filter seemed to better represent the peak NDVI values and temporal positions than the asymmetric Gaussian filter. In short, caution is needed in selecting the optimal smoothing approaches in time series analysis. Multiple techniques have been proposed to analyze time series of remotely-sensed data following image enhancement and time series reconstruction. Details regarding one of these techniques, the Empirical Mode Decomposition (EMD) method, are presented below.

10.6 *Further Methods in Time Series Analysis*

10.6.1 *Empirical Mode Decomposition in Remotely Sensed Image Processing*

The Hilbert-Huang Transform (HHT) was proposed by Huang *et al.* (1998) as a frequency-based method for nonlinear and nonstationary time-series analysis. HHT consists of two parts: EMD and Hilbert Spectral Analysis. The techniques have been applied extensively in Earth science research (Huang and Wu, 2008). Still, the remote sensing community has seen an increase in adopting and customizing EMD for signal/image processing. Given its popularity in the past two decades, this text summarizes the status of EMD applications in remote sensing.

EMD assumes that at any given time, the input dataset may have many coexisting simple oscillatory modes of significantly different frequencies, one superimposed on the other. With an *a posteriori* defined basis derived from the input data, EMD self-adaptively decomposes the dataset into a finite number of components, also known as Intrinsic Mode Function (IMF). Each IMF satisfies the following conditions: (1) in the whole data set, the number of extrema and the number of zero crossings must either be equal to, or differ at most, by one; and (2) at any data point, the mean value of the envelope defined using the local maxima and the envelope defined using the local minima is zero. IMF is generated through a process called sifting. A brief description of the sifting process is shown below; a complete description of the EMD algorithm can be found in (Huang *et al.,* 1998; Huang and Wu, 2008). Given a data set $X(t)$:

Step 1: Initialize: $r_0 = X(t)$, $I = 1$.

Step 2: Set $h_{j-1} = r_{i-1}$, $j=1$. Obtain all local maxima and minima of r_{i-1} and create the upper envelope $u_{\max}$ and lower envelope $u_{\min}$ of h_{j-1}.

Step 3: Define: $mn = (u_{\max} + u_{\min})/2$; then $h_j = h_{j-1} - mn$.

Step 4: Check the properties of h_j. If h_j is not an IMF, set $j=j+1$ and repeat *Step 2* and *Step 3*.

Step 5: Calculate the residual $r_i = r_{i-1} - \text{IMF}i$, $i=i+1$. Repeat the sifting process (from *Step 2* to *Step 4*) to obtain the remaining IMFs. This loop (from *Step 2* to *Step 4*) will not stop until the residual is below a predetermined level, or the residual has a monotonic trend. After EMD, the data set $X(t)$ can be re constructed as:

$$X(t) = \sum_{i=1}^{m} \text{IMF}i + r_m. \qquad (7\text{-}78)$$

An example of the EMD process is illustrated in Figure 7-68, in which the input dataset is decomposed into eight IMFs with a residual term. From IMF 1 to IMF 8, the frequency of each IMF decreases.

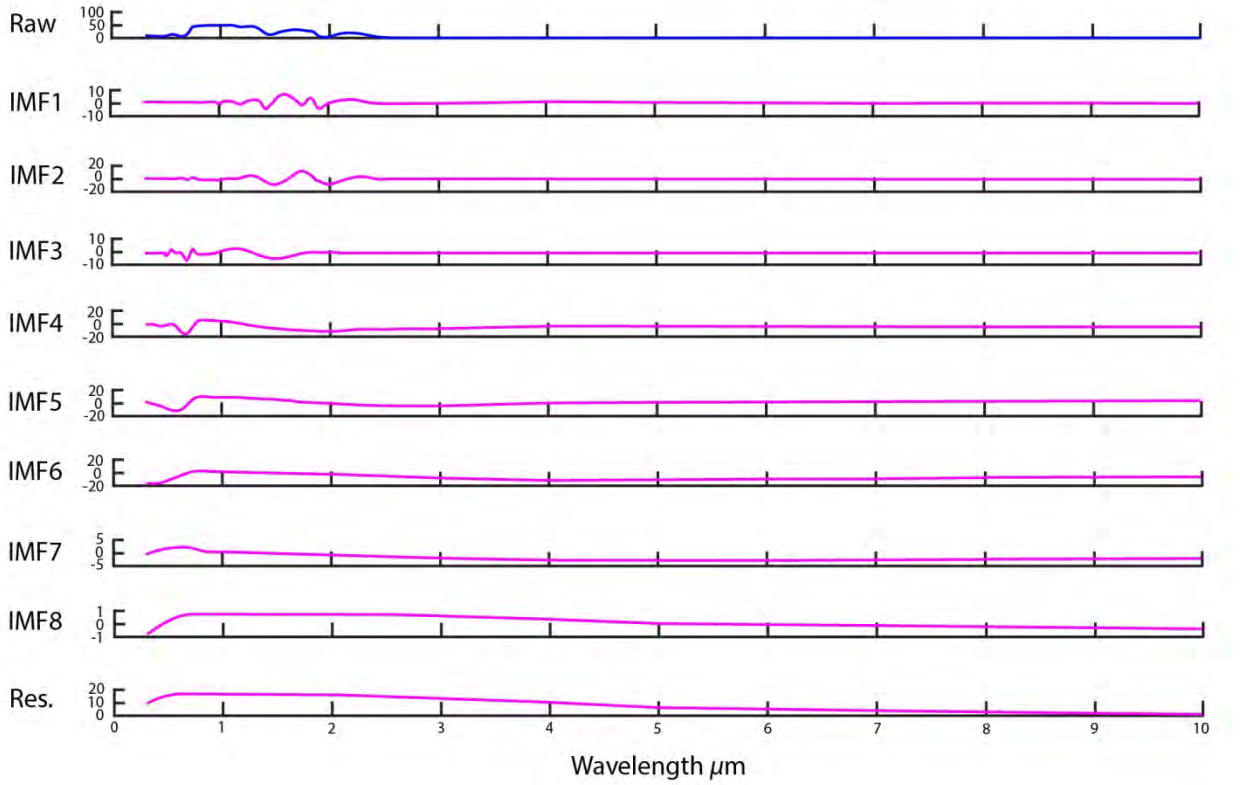

Figure 7-68. Illustration of EMD. Raw refers to the input dataset; Res. Refers to the residual.

Since the development of HHT and the above-mentioned original EMD process, advances have been made in both theory and application. In particular, two important developments benefited remote sensing studies directly: (1) Ensemble EMD (EEMD), a noise-assisted data analysis method; and (2) Two-dimensional Empirical Mode Decomposition (2DEMD) for image analysis.

Although EMD is a simple and efficient self-adaptive method to analyze both non-stationary and nonlinear datasets, one drawback of EMD is the mode mixing, which is defined as a single IMF either consisting of signals of widely disparate scales, or as a signal of similar scale residing in different IMFs (Huang and Wu, 2008). As a solution, Wu and Huang (2009) proposed the EEMD method, which contains the following steps in addition to the original EMD workflow described above:

Step 1: Add a white noise signal to the target dataset.

Step 2: Decompose the data containing added white noise into IMFs.

Step 3: Repeat *Step 1* and *Step 2* with different white noise series each time.

Step 4: Calculate the ensemble means of corresponding IMFs as the final result.

In EEMD, the input dataset can be conceptualized as the summation of the true signal and noise. An assumption in EEMD is that although the input dataset may be acquired with different levels of noise, the ensemble mean value is close to the true signal. Therefore, adding white noise may facilitate extracting the true signal from the input dataset. The magnitude of added white noise can be controlled by Equation 7-79.

$$\varepsilon_n = \frac{\varepsilon}{\sqrt{N}} \tag{7-79}$$

where: N is the number of ensemble members; ε is the amplitude of the added noise; ε_n is the final standard deviation of error, defined as the difference between the input signal and the corresponding IMFs.

Compared to the original EMD, EEMD is a time-consuming algorithm. Implementation of parallel processing with a Graphics Processing Unit (GPU) has been used to increase the processing speed of EEMD (Ren *et al.*, 2014).

Both EMD and EEMD were developed originally for one-dimensional data analysis. To apply this method to two-dimensional data, a row-column EMD is proposed based on one-dimensional EMD (Chen *et al.*, 2008), where EMD is performed on both rows and columns. However, one drawback of this row-column EMD is a striping effect (Teo and Lau, 2012). Recently, several versions of 2DEMD were proposed. Each version contains a fitting surface generated by different algorithms because there is not a universal way to determine the fitting surface to the identified maxima and minima. For example, Sinclair and Pegram (2005) applied a multiquadrics approach, while Demir and Erturk (2010) used a spline method. Moreover, Damerval *et al.* (2005) incorporated Delaunay triangulation and piecewise cubic polynomial interpretation to get the fitting surface; while Xu *et al.* (2006) provided an additional approach by using a mesh fitting method based on finite elements. However, all these two-dimensional approaches are expensive computationally. To improve computational efficiency, a pyramid-based 2DEMD was proposed to extract the IMF from the reduced layer (Teo and Lau, 2012).

10.6.1.1 Applications of Empirical Mode Decomposition in Image Processing

In remote sensing, HHT is generally used for time-series analysis. EMD, a critical part of HHT, was proposed originally as a frequency-based method for nonlinear and nonstationary time-series analysis. Perhaps the most profound application of EMD is to correct the orbit drift of AVHRR (Tucker *et al.*, 2005), where EMD is applied to minimize effects of orbital drift by removing common trends between time series of solar zenith angle and NDVI. Importantly, the GIMMS algorithm uses EMD to separate the surface NDVI reflectance from signal interference (Guay *et al.*, 2014; Tian *et al.*, 2015).

Table 7-14 compares three frequency-based image analysis methods: Fourier Transform, Wavelet Transform, and HHT. Given the characteristics of HHT, there is an increasing trend to use EMD as a complement or replacement for Fourier and Wavelet transforms in remote sensed image processing. In particular, the technique can be used for noise reduction, feature extraction and image fusion. The following sections will introduce EMD applications in time-series and image processing.

Table 7-14. Comparison of Fourier, Wavelet, and HHT Analysis (adopted from Huang and Wu, 2008).

	Fourier Transform	Wavelet Transform	HHT
Basis	*a priori*	*a priori*	*a posteriori* adaptive
Frequency	convolution over global domain, uncertainty	convolution over global domain, uncertainty	differentiation over local domain, certainty
Presentation	energy in frequency	energy in time-frequency space	energy in time-frequency space
Nonlinearity	no	yes	yes
Nonstationarity	no	yes	yes
Feature extraction	no	discrete (no) continuous (yes)	yes
Theoretical base	complete mathematical theory	complete mathematical theory	empirical

EMD and EEMD are effective and efficient tools to reduce noise (usually from high-frequency IMFs), analyze seasonality at varied temporal granularities (usually from low-frequency IMFs) and extract trend (usually from the residual of the input dataset) from time-series. EMD is one of the nine major methods to create and fit NDVI time-series (Kandasamy and Fernandes, 2015). For instance, Chen, C.F. *et al.* (2011) used EMD to smooth MODIS NDVI time-series; Son *et al.* (2013) applied EMD to smooth time series of MODIS spectral indices, including EVI, land surface water index (LSWI), normalized difference built-up index (NDBI), and the difference in the values of EVI and LSWI. Moreover, Hawinkel *et al.* (2015) applied EEMD to detect the time scales and timing of episodes of inter-annual variations of NDVI time-series; Rios *et al.* (2015) used EMD to decompose time series into stochastic and deterministic components, allowing for insights into vegetation dynamics.

With the deluge of big data and *Internet of Things*, more time-series of remotely-sensed and user-generated geospatial data will be available to the remote sensing community. Existing studies have focused on applying EMD or EEMD to investigate vegetation dynamics and most studies used NDVI data. There is, however, huge potential in the application of these algorithms to other data or products for noise reduction and temporal feature extraction.

Similar to time-series smoothing, EMD and EEMD have been applied widely to reduce noise associated with different remote sensing products. For example, Han *et al.* (2002) employed EMD to reduce speckle in SAR images; Demir and Erturk (2010) utilized EMD to reduce noise in hyperspectral imagery and Song *et al.* (2014) applied the technique to filter InSAR data. Given their capability for noise reduction, EMD and EEMD have been used also to enhance hyperspectral image classification results (Ren *et al.,* 2014).

Another main application of EMD involves image fusion. It is reported that EMD-based image fusion methods often perform better than traditional image fusion approaches. Teo and Lau (2012) applied pyramid-based 2DEMD to fuse high-frequency IMF of PAN images with low-frequency IMFs and residuals from MS images, showing that the proposed method out-performs row-column EMD, PCA and Wavelet Transform in terms of RMSE, correlation coefficient, and entropy. Similarly, Dong *et al.* (2014) found that when measured by RMSE, correlation coefficient and spectral information, fusion results from 2DEMD are better than those using wavelet, though both methods are successful in keeping spectral information while enhancing details. Some empirical studies incorporate both EMD and Wavelet Transform, such as in Chen *et al.* (2010), where Atrous Wavelet Transform was used to extract details from SAR imagery. The authors then employed a generalized IHS transform framework in which EMD was used for the fusion of low-resolution MS images and SAR imagery.

11 IMAGE ANALYSIS AND MODELING

This section contains multiple examples of remotely-sensed data as input to a variety of data processing workflows, including modeling and product generation. Examples include the use of remotely-acquired data to: (a) develop algorithms to investigate chlorophyll$_a$ concentration in coastal waters; (b) monitor forest fire; (c) characterize habitats and model species distribution; and (d) support the application of radiative transfer theory involving the use of PAR by vegetation.

11.1 *Coastal Water Algorithms (Chlorophyll$_a$)*

11.1.1 *Introduction*

Coastal environments represent a complex ecosystem where terrestrial outputs meet with the marine environment and interaction among biotic and abiotic habitants occurs, making it one of the most productive ecosystems in the world (Harvey *et al.,* 2015). Coastal ecosystems perform various ecological and economical services including biological, physical, and chemical modifications of the water column, sediment, and submerged and emergent vegetation, food provision, water supply, tourism and recreation, and transportation, among others (Mishra, 2014). However, due to their proximity to terrestrial environments, coastal ecosystems are prone to many anthropogenic disturbances (Mouw *et al.,* 2015). Nutrient over-enrichment through sediment deposition is a widespread threat to coastal water systems because these threats can trigger various harmful effects that hinder the services provided by the water body (Mélin and Vantrepotte, 2015). Timely monitoring of water in estuarine and coastal environments is necessary to sustain ecological functions and overall ecosystem health. Manual water quality sampling and monitoring is challenging because not only does it fail to provide an insight into the spatio-temporal dynamics but also because it is time consuming, labor intensive, and therefore expensive. To obviate these issues with point sampling, researchers and water quality managers have been using remotely-acquired data as an efficient means to monitor water quality parameters such as Chlorophyll$_a$, (Chl$_a$), total suspended solids (TSS), organic sediments, inorganic sediments, and colored-dissolved organic matter (CDOM). These parameters can be accurate proxies for the overall quality and productivity of water systems and are often referred to as optically active constituents (OACs).

Chl$_a$ is often used as a proxy for phytoplankton biomass, which is an indicator of water quality, trophic status, and productivity of aquatic environments. It is also one of the most frequently monitored water quality parameters using remote sensing techniques. Development of remote sensing based methods and algorithms to quantify Chl$_a$ dates back to the 1970s. Despite this long developmental effort, remote estimation of Chl$_a$ still remains a challenge because of factors such as the optical complexity of water, interference of bottom reflectance in shallow water systems, errors associated with atmospheric correction over nearshore shallow waters, and eutrophic coastal waters. In addition to these factors, high uncertainty in Chl$_a$ estimation algorithms over such waters is still observed due to other issues such as difficulties of parameterization, spectral slope derivation, and limited satellite band choices (Mishra and Mishra, 2012; Harvey *et al.,* 2015).

From a remote sensing perspective, reflectance from coastal waters can be complex in their spectral shape due to the presence of several OACs such as Chl$_a$, CDOM, and sediments from riverine inputs (Attila *et al.,* 2013). The following section presents a brief description on various Chl$_a$ algorithms that have been developed and applied to coastal waters with a focus on estuaries, lakes, gulfs and bays. Examples are provided from a wide array of publications from early 1980s to 2010s in these water ecosystems. Current challenges associated with Chl$_a$ algorithm development and future recommendations are also presented briefly.

11.1.2 *Technical Fundamentals*

Remote sensing instruments measure electromagnetic radiation reflected or emitted by the Earth's surface. In ocean color remote sensing, water-leaving radiance (L_w) and remote sensing reflectance (R_{rs}) are derived from the TOA radiance (L_t) measurements using an appropriate atmospheric correction scheme. Remote sensing based OACs estimation procedures often rely on the relationship between L_w and water quality parameters (Kirk, 1996). Despite the absence of well-defined terms and explicit agreements, all remote sensing based Chl$_a$ algorithms can be classified into two broad categories: (1) empirical algorithms, and (2) semi/quasi analytical algorithms. A list of representative empirical and semi/quasi analytical Chl$_a$ algorithms is presented in Table 7-15.

Table 7-15. List of Representative Empirical and Semi-Quasi Analytical Chl$_a$ Algorithms.

Study Region	Model Type	Reference
Empirical Algorithms		
Asian Inland Waters	Empirical, hybrid	Matsushita *et al*., 2015
Northern Gulf Coast, Chesapeake Bay, USA	Empirical, NDCI	Mishra and Mishra, 2012
Chesapeake Bay, USA	Empirical	Tzortziou *et al*., 2007
Global Ocean	Empirical, OC4	O'Reilly *et al*., 2000
Global Ocean	Empirical, OC3	O'Reilly *et al*., 1998
Global Ocean	Empirical	Dierssen, 2010
Global Ocean	Empirical, FLH	Letelier and Abbott, 1996
Semi-quasi Analytical Algorithms		
Azov Sea	Semi-analytical	Moses *et al*., 2012
Reservoirs of the Dnieper River, Azov Sea	Semi-analytical	Moses *et al*., 2009
The IJssel Lagoon, The Netherlands	Semi-analytical	Gons *et al*., 2002
Global Ocean	Semi-analytical	Maritorena *et al*., 2002
Global Ocean	Quasi-analytical	Lee Z. *et al*., 2002
The IJssel Lagoon, The Netherlands, Scheldt Esturary, Belgium, and Lake Tai, China	Semi-analytical	Gons, 1999

11.1.2.1 Empirical Chlorophyll$_a$ Algorithms

Apparent Optical Properties (AOPs) such as L_w and R_{rs} measured over a water column is a function of absorption and scattering of incident light by OACs present in the water column. Therefore, information about OACs can be obtained from AOPs. Empirical Chl$_a$ algorithms, often in the form of linear regression, multiple-linear regression, and non-linear regression, are employed to model the statistical relationship between Chl$_a$ and AOPs, and indices representing reflectance band ratios or band differences (O'Reilly *et al.*, 1998; Tzortziou *et al.*, 2007; Moses *et al.*, 2009; Mishra and Mishra, 2012; Tebbs *et al.*, 2013).

11.1.2.2 Semi-quasi Analytical Chl$_a$ Algorithms

Semi-quasi analytical algorithms are based on radiative transfer equation (Gordon *et al.*, 1988) and link inherent optical properties (IOPs) with AOPs in water bodies (Gons, 1999; Gons *et al.*, 2002; Lee and Lathrop, 2002; Maritorena *et al.*, 2002; Dall'Olmo and Gittelson, 2005). Semi-analytical models employ physical understanding of light propagation and attenuation in the water column to estimate OACs such as Chl$_a$. The simplified relationship that is commonly used as the basis of semi-quasi analytical algorithm is given in Equation 7-80.

$$R_{rs}(\lambda) \approx f(\lambda)\frac{b_b(\lambda)}{a(\lambda)+b_b(\lambda)} \quad (7\text{-}80)$$

where: $f(\lambda)$ (rs^{-1}) is a coefficient accounting for the air-water interface effect, the angular variation of $R_{rs}(\lambda)$ and the effect of multiple scattering; $a(\lambda)$ and $b_b(\lambda)$ are absorption and backscattering coefficients with units of m^{-1}; $a(\lambda)$ and $b_b(\lambda)$ are expressed as the sum of all contributing OACs and often written as:

$$a(\lambda) = a_w(\lambda) + a_{ph}(\lambda) + a_{dg}(\lambda) \quad (7\text{-}81a)$$

$$b_b(\lambda) = b_{bw}(\lambda) + b_{bp}(\lambda) \quad (7\text{-}81b)$$

where: a_w, a_{ph}, and a_{dg} are absorption coefficients of water, phytoplankton, and colored detrital matter; and b_{bw}, and b_{bp} are backscattering coefficients of water and particulate matter in the water column. Semi-quasi-analytical approach utilizes radiative transfer principles to retrieve absorption coefficients of individual components from R_{rs} measurements through inversion modeling and further uses specific-absorption coefficient of Chl_a to estimate Chl_a concentration from Chl_a absorption (Zheng *et al.,* 2014).

11.1.3 *Applications, Potentials and Limitations*

11.1.3.1 Empirical Chlorophyll$_a$ Algorithms

Early assessment of chlorophyll concentration in coastal waters involved qualitative studies relating spatial distribution of Chl_a and radiometric parameters derived from Coastal Zone Color Scanner (CZCS) in Gulf Guinea and Gulf of Lions, Mediterranean Sea (Viollier *et al.,* 1978; Caraux and Austin, 1983) and empirical studies relating Chl_a concentration with airborne spectral reflectance in Georgian Bay (Miller *et al.,* 1977). These early studies showed the potential of remote sensing to assess Chl_a dynamics in surface waters. Although qualitative assessment is relatively easy to perform, it required experience and background knowledge of the analyst and often subjected to personal bias.

In open ocean waters, IOPs are influenced primarily by phytoplankton biomass and water molecules. As all other OACs co-vary with phytoplankton biomass, Chl_a concentration can be derived empirically from $R_{rs}(\lambda)$ with reasonable accuracy. Regressions ranging from linear to quadratic models have been proposed by researchers in a wide range of areas. NASA's SeaWiFS models designed initially for global oceans come in different variants ranging from ocean color-1 (OC-1) linear models to OC-4 cubic polynomial models (O'Reilly *et al.,* 1998), making use of SeaWiFS bands at 412*nm*, 443*nm*, 490*nm*, 510*nm*, and 555*nm*. Studies applying these models report differing results. For example, a study in Alaskan waters compared these global models tested in coastal waters, and they reported that OC-2 performed OC-4. This could be due to the fact that the OC-4 training dataset contain very little data from Polar Regions with high productivity ($Chl_a > 8 mgm^{-3}$) (Montes-Hugo *et al.,* 2005). A study in the Bay of Bengal, India showed that OC-4 overestimated Chl_a values when chl-*a* concentration was greater than $2 mgm^{-3}$ and OC-5 appeared to be the most suitable algorithm for both coastal and open ocean waters (Tilstone *et al.,* 2011). It should be noted that all these algorithms use R_{rs} blue-green band ratio as the predictor which primarily represent a change in the total absorption coefficient in the blue spectral region (Lee *et al.,* 2010). In coastal waters, where colored detrital matter concentration vary independently, a change in $a(\lambda)$ due to $a_{dg}(\lambda)$ could be translated as a change in Chl_a concentration. This is the primary source of poor performance of blue-green OC algorithms in coastal waters. It also appears that empirical models lose their accuracy when there is a change in the

IOPs in the study region. To avoid this issue, global models may need to be regionally parameterized for better accuracy.

Further advancement in Chl_a modeling was triggered by the development of satellite technology and field instruments. More options on operational sensors with improved spectral, spatial, radiometric, and temporal attributes supported the development of remote sensing-based Chl_a monitoring. The launch of MODIS with relatively higher spectral resolution became more suitable for resolving optical complexities. MODIS band configuration was exploited to derive fluorescence line height (FLH) using normalized radiance measured at MODIS bands 13 (665.1*nm*), 14 (676.7*nm*), and 15 (746.3*nm*) (Letelier and Abbott, 1996; Gons *et al.*, 2008). One of these wavelengths is closer to the chlorophyll fluorescence maximum (~ 683*nm*), while the rest were used for backscattering correction, shaping a baseline below the fluorescence peak. Figure 7-69 shows a FLH product computed from MODIS TOA radiance data over Vancouver Island area. High FLH values indicate high surface Chl_a concentration in the study area (Gower and Borstad, 2004). The advantage is that FLH is less sensitive to interference caused by the presence of other absorbing substances in surface waters, and it does not saturate at high chlorophyll concentrations unlike other algorithms relying on 443*nm* (Letelier and Abbott, 1996). However, prediction accuracy of MODIS FLH in an oligotrophic bay (i.e., Chl_a range 0.37 – 0.75mgm^{-3}, r = 0.89) could not be repeated with MERIS FLH-based Chl_a algorithm in Green Bay waters with a range of Chl_a 11-131mgm^{-3} (Gons *et al.*, 2008). MERIS FLH algorithm with 665*nm* and 708*nm* as baseline has been criticized for lower accuracy in coastal waters with more than 4mgm^{-3} Chl_a (Gilerson *et al*., 2007, 2008). However, Gower and King (2007) have demonstrated use of MERIS FLH with two NIR bands in waters with Chl_a up to 20mgm^{-3} with reasonable accuracy (Figure 7-70). Gilerson *et al*. (2007, 2008) reported that MODIS FLH performs well only for waters with Chl_a less than 4mgm^{-3} since particulate backscattering in turbid waters contaminates the MODIS FLH signal.

In productive waters, MERIS FLH could underestimate Chl_a values due to the shift of Chl_a fluorescence peak. For higher Chl_a waters, the fluorescence peak shifts to longer wavelengths (i.e., up to 710*nm*). Because of the "red shift", FLH derived with the three-band baseline method may be underestimated for highly productive waters (Hu *et al.*, 2005). Another limitation associated with the FLH algorithm is the need for precise band placement, and difficulties interpreting FLH data (Harding, Jr., *et al*., 1994).

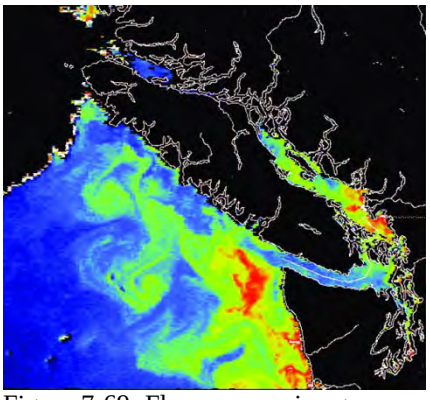

Figure 7-69. Fluorescence image computed from MODIS TOA radiance data acquired on 22 September 2000 over Vancouver Island. Warmer tones represent high fluorescence levels. Land and cloud pixels are masked. From Gower and Borstad (2004).

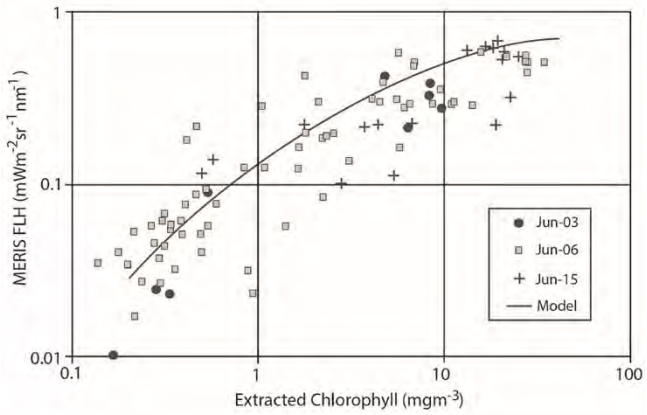

Figure 7-70. Empirical relationship between the MERIS FLH product and surface Chl$_a$ concentration from the Canadian west coast. From Gower and King (2007).

Another study investigated Chl$_a$ sensitivity using AVIRIS hyperspectral data and bio-optical model in coastal waters in the Netherlands (Hoogenboom *et al.,* 1998). A ratio of one of the AVIRIS bands around 713*nm* to the band at 677*nm* was found to be most sensitive to change in Chl$_a$. Simulation results showed that AVIRIS can estimate Chl$_a$ with an accuracy of 20% for relatively low Chl$_a$ values (<10mgm^{-3}) and ~12% for Chl$_a$ values more than 30mgm^{-3}.

Several indices using green-red-NIR spectral regions have been proposed by researchers to model Chl$_a$ in optically complex coastal waters. The Red Green Chl$_a$ Index (RGCI) was developed for MODIS and SeaWiFS with the ratio $R_{rs}(667)/R_{rs}(547)$ and $R_{rs}(670)/R_{rs}(555)$, respectively. The best equation to estimate Chl$_a$ concentration was formulated as Equation 7-82.

$$Chl_a = 0.86 * e^{5.1*RGCI} \quad (7\text{-}82)$$

Validation of the linear regression model showed reasonable accuracy in Tampa Bay, Fld., USA for Chl$_a$ ranging between 1.0 and 30.0mgm^{-3}. Authors documented that modeling uncertainty from RGCI was lower than the traditional blue-green band ratio algorithms.

Dall'Olmo and Gitelson (2005) developed a three-band Chl$_a$ estimation model using red and NIR bands. The three-band model architecture is shown in Equation 7-83.

$$\text{Chl}_a \propto [R_{rs}^{-1}(665) - R_{rs}^{-1}(708)] \times R_{rs}(753) \quad (7\text{-}83)$$

The three band algorithm was based on several assumptions including, (1) the absorption by suspended solids and CDOM beyond 700*nm* is approximately equal to that at 665-675*nm* and the difference between them is very small and can be neglected; (2) the total Chl$_a$, CDOM, and TSS absorption beyond 730*nm* is nearly zero; and (3) the backscattering coefficient of Chl$_a$ is spectrally invariant. The algorithm was successful for predicting Chl$_a$ in turbid productive water bodies with a wide range of optical complexity. Moses *et al.*(2009) further validated the three band algorithm using MERIS data from the Azov Sea and documented that it was able to retrieve Chl$_a$ concentration with a RMSE of 5.02mgm^{-3}, for a Chl$_a$ range: 18.37-47.86mgm^{-3}. In the same study, Moses *et al.* (2009) also presented a simplified two-band model using red and NIR bands to quantify Chl$_a$ in turbid productive waters. To match the band configuration of MERIS sensor, the conceptual model was designed as Equation 7-84.

$$\text{Chl}_a \propto R_{rs}^{-1}(665) \times R_{rs}(708) \quad (7\text{-}84)$$

They applied the two-band algorithm to MERIS images over Azov Sea in Russia and reported the high accuracy potential of the model to estimate Chl_a in turbid productive waters. Similarly, Tzortziou *et al.* (2007) collected an extensive bio-optical dataset to examine the relationship between IOPs and AOPs in the mid-Chesapeake Bay, USA. They observed a fairly strong relationship (R^2=0.54) between R_{rs} ratio at 677*nm* and 554*nm*, $R_{rs}(677)/R_{rs}(554)$, and Chl_a concentration in the bay compared to blue-green spectral band ratios.

Similarly, Mishra and Mishra (2012) proposed a Normalized Difference Chlorophyll Index (NDCI) to quantify Chl_a concentration in optically complex coastal waters. The basis for the index was to take advantage of the 708*nm* reflectance peak and 665*nm* absorption peaks to maximize Chl_a sensitivity. NDCI followed the basic structure of the most widely used VI, NDVI to retain the benefits of a normalized band difference index and formulated below as Equation 7-85.

$$NDCI = \frac{R_{rs}(708)-R_{rs}(665)}{R_{rs}(708)+R_{rs}(665)} \quad (7\text{-}85)$$

NDCI was calibrated and validated using an extensive simulated dataset as well as field and MERIS satellite data from northern Gulf of Mexico coastal waters and Chesapeake Bay. NDCI based quadratic polynomial model (i.e., Equation 7-86) was successful in quantifying Chl_a with 12% overall bias (Figure 7-71). Mishra and Mishra (2012) also warned that erroneous atmospheric correction of MERIS data could impact the model performance adversely by predicting extreme Chl_a values.

$$Chl_a\ (mgm^{-3}) = 13.55 + 87.99 * NDCI + 212.6 * NDCI^2 \quad (7\text{-}86)$$

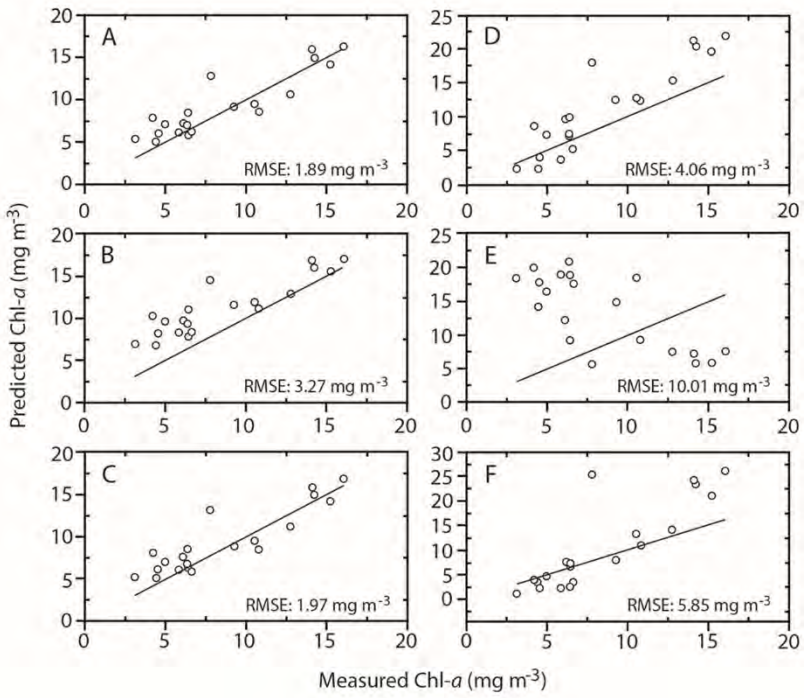

Figure 7-71. Validation of NDCI chlorophyll algorithm performance and its comparison with other algorithm considered in that research; (A) NDCI, (B) Moses *et al.* (2009), (C) Dall'Olmo and Gitelson (2005), (D) Gons *et al.* (2008), (E) Tzortziou *et al.* (2007), and (F) MERIS case 2 Chl_a product (Algal-2). Straight lines on the plots are the 1-to-1 lines. From: Mishra and Mishra (2012).

Gons *et al.* (2008) used a nested band ratio approach to quantify surface Chl_a concentration in Keweenaw Bay. The band ratio model (i.e., Equation 7-87) produced an R^2 of 0.81 with standard error of 0.049 mgm^{-3}. The algorithm, Morel's modified blue-green algorithm, was tested for a composite of samples from three different sites with Chl_a concentration varying from 0.37 to 131mgm^{-3}.

$$Chl_a = 7.45\left[\frac{R_w(510)}{R_w(443)/R_w(560)}\right]0.6 \quad (7\text{-}87)$$

In another study, a multiple linear regression model was developed using Landsat TM bands 2 and 3 ratio. The model was able to explain 72-76% of Chl_a variation in estuarine waters in Australia (Lavery *et al.*, 1993). Similarly, a log-based empirical model was applied to quantify variation of Chl_a in Chesapeake Bay in Equation 7-88 (Harding, Jr., *et al.*, 1994).

$$log_{10}Chl_a = a + b\left(-log_{10}\frac{R_{490}^2}{R_{460}*R_{520}}\right), \quad (7\text{-}88)$$

where: R_n is radiance measured at (n) *nm*.

Another group of empirical algorithms have also been proposed to quantify Chl_a in natural waters which are purely statistical in nature. These algorithms employ machine learning principles including ANN, support vector machine, random forest, and other similar methods to model Chl_a. These models are completely data-driven and are often hard to interpret due to lack of physical principles. One major advantage of machine learning approaches is that, unlike traditional regression approach, it can model non-linear trends in the data. For example, ANN approach has been exemplified in many waters with varying chl-$_a$ range such as in Delaware Bay using Landsat TM images (Keiner and Yan, 1998) and in Rias Baixas, Spain using MERIS data (González Vilas *et al.*, 2011). Results showed that the ANN algorithm was better than the MERIS case II regional processor (C2R) routine. Similar performance was obtained when the algorithm was tested for the same study area but in different condition (i.e., upwelling) (Spyrakos *et al.*, 2011). However, ANN method is also considered as site specific, which is hardly transferable to other geographic areas.

11.1.3.2 Semi-quasi Analytical Algorithms

As discussed earlier, semi-quasi analytical algorithms are used to invert Equations 7-80 and 7-81a, b to estimate IOPs from R_{rs} data. There have been three primary types of approaches reported for analytical inversion of R_{rs} data including: (1) bottom-up; (2) top-down; and (3) inversion using the red-NIR band ratio. Examples of algorithms falling into the category of bottom-up approaches are the linear matrix inversion (Wang, P. *et al.*, 2005) and spectral optimization algorithm (Maritorena *et al.*, 2002). Bottom-up approach requires the algorithm to use bio-optical models for each component during the inversion and retrieves the bulk and individual components simultaneously.

On the other hand, algorithms in top-down approach such as Lee, Z., *et al.* (2002)s Quasi-Analytical Algorithm (QAA) does not require bio-optical models or spectral shapes for individual components during inversion. Rather, QAA independently retrieves bulk absorption at first and further decomposes to retrieve individual absorption components (Craig *et al.*, 2006). As the first step, QAA converts $R_{rs}(\lambda)$ to sub-surface remote sensing reflectance, $r_{rs}(\lambda)$ and retrieves absorption coefficient $a(\lambda)$ empirically from $r_{rs}(\lambda)$ at a reference wavelength (λ_0), where $a(\lambda_0)$ is dominated by $a_w(\lambda_0)$. It further estimates particulate backscattering coefficient at the same wavelength $b_{bp}(\lambda_0)$ by using bio-optical relations derived from radiative transfer

equations. Then, it estimates $b_{bp}(\lambda)$ using a wavelength dependent hyperbolic function and eventually retrieves $a(\lambda)$ spectrum analytically from measured $R_{rs}(\lambda)$. $a(\lambda)$ is further decomposed into phytoplankton absorption coefficient $a_{ph}(\lambda)$ and absorption coefficient of colored detrital matter $a_{dg}(\lambda)$. Finally, Chl$_a$ concentration is retrieved by dividing $a_{ph}(\lambda)$ by the specific absorption coefficient of chlorophyll, $a^*_{chl}(\lambda)$. Earlier versions of QAA were primarily designed for open ocean waters. However, researchers have demonstrated the application of QAA to coastal waters by moving the reference wavelength to longer wavelengths such as 640*nm*, 710*nm* based on the level of productivity and turbidity (Lee, Z. *et al.*, 2002; Le *et al.*, 2009; Mishra *et al.*, 2013).

One example of third semi-analytical algorithm approach which can be applied to optically complex coastal waters is a three-band algorithm proposed by Gitelson *et al.* (2008). A three-band model designed for MERIS sensor in the following form (Equation 7-89):

$$Chl_a = (23.09 \pm 0.98) + (117.42 \pm 2.49) * [\, R_{rs}^{-1}(660 - 670) - R_{rs}^{-1}(700 - 730)] * R_{rs}(740 - 760) \quad (7\text{-}89)$$

and, a two band-model for MODIS sensor, form shown in Equation 7-90.

$$Chl_a = -(16.2 \pm 1.8) + (136.3 \pm 3.2) * [R_{rs}^{-1}(662 - 672) * R_{rs}(743 - 753)] \quad (7\text{-}90)$$

The models were calibrated and validated for lakes and reservoirs in Eastern Nebraska with a wide range of Chl$_a$ concentration (1.2 - 236mgm^{-3}).

In another study, Simis *et al.* (2005) proposed a semi-analytical algorithm to retrieve Chl$_a$ concentration in optically complex waters of Lake Loosdrecht and Lake Ijsselmeer in The Netherlands. The Chl$_a$ absorption equation was formulated as Equation 7-91.

$$a_{chl}(665) = (\{[R(709)/R(665)] * [a_w(709) + b_b]\} - b_b - a_w(665)) * \gamma^{-1} \quad (7\text{-}91)$$

where: R is subsurface irradiance reflectance at wavelength λ and depth 0; a_w and b_b are water absorption coefficient and back-scattering coefficients respectively; and γ is the correction factor that links retrieved absorption versus measured absorption by pigments at a particular wavelength. Once $a_{chl}(665)$ is estimated, *Chl-$_a$* concentration can be obtained by using the Equation 7-92.

$$Chl_a\ (mg\ m^{-3}) = \frac{a_{chl}(665)}{a^*_{chl}(665)} \quad (7\text{-}92)$$

where: $a^*_{chl}(665)$ is the *Chl$_a$* specific absorption coefficient at 665*nm*.

11.1.4 *Conclusion*

There exists a suite of empirical and semi-analytical algorithms to quantify Chl$_a$ in coastal waters (Table 7-15). Since the beginning of satellite remote sensing era, the ocean color community has put its effort to model Chl*a* concentration in open ocean waters. Traditionally, blue-green band ratio algorithms have been successfully used to model Chl$_a$ in the open ocean where IOPs are dominated by phytoplankton pigments and water. However, these algorithms tend to perform poorly in optically complex coastal, estuarine, and inland waters where terrestrial colored dissolved organic matter and detrital matter often strongly influence the AOPs in the blue spectral region. To overcome this issue, researchers have used red-NIR band ratios to retrieve Chl$_a$ in coastal and inland waters. Although, red-NIR band ratios are not completely immune to the presence of other OACs, relative interference of CDOM and detrital matter is much lower than blue-green

or green-red band ratios. For eutrophic waters with Chl_a concentration greater than $10 mg\ m^{-3}$ red-NIR band ratios are preferred for Chl_a retrieval as the relative contribution of colored detrital matter is often very small or negligible (Gons *et al.,* 2002; Gitelson *et al.,* 2007; Moses *et al.,* 2009; Mishra and Mishra, 2012).

In addition to empirical algorithms, MERIS and MODIS FLH have great potential for retrieving Chl_a in optically complex waters. It has been reported that suitable band configuration of MERIS provides a better FLH product than MODIS (Gower and Borstad, 2004). However, the main disadvantage of FLH is the requirement of specific spectral bands to estimate FLH. Due to lack of specific band configuration, FLH algorithm cannot be applied to many past and current sensors such as CZCS, SeaWiFS, and VIIRS.

Semi-quasi analytical algorithms have somewhat addressed the limitation of empirical algorithms by providing better retrievals of IOPs and Chl_a concentration in optically complex coastal waters. The major disadvantage of semi-quasi analytical algorithms is its sensitivity to the errors in atmospheric correction to obtain water leaving reflectance data. A bad atmospheric correction can produce erroneous IOPs eventually affecting the retrieval accuracy of Chl_a. Similarly, these algorithms are also highly sensitive to Chl-*a* specific absorption coefficient values, which is used to retrieve the concentration of Chl_a. Another challenge associated with semi-quasi analytical algorithms is the requirement of a robust bio-optical dataset including *in situ* IOPs, AOPs, pigment measurements and pigment-specific absorption coefficients for model calibration and validation (CAL/VAL). Collection of these bio-optical dataset is not only expensive but also time consuming. Therefore, regional parameterization of these algorithms is often a challenging task. Moreover, IOPs are constantly changing in coastal and global ocean (Dierssen, 2010). To address the continuous change in water optical properties, semi-quasi analytical algorithms may require constant CAL/VAL efforts for keeping them as accurate and reliable as possible.

11.2 *Forest Fire Modeling*

Forest fires affect ecosystem processes and functions at broad scales: driving succession; maintaining biodiversity; and regulating biogeochemical cycles (Cochrane, 2003; Herawati *et al.,* 2015). In recent years, changes in climatic and anthropogenic processes have altered the driving forces that govern wildfires in natural systems. For example, while temperature increases are expected to cause frequent fires of different magnitude and at broader scales (Balch, 2014; Gauthier *et al.,* 2015), intensive human activities lead to an increased number of fires. The complexities of these dynamic systems complicate wildfire management and, therefore, entail modeling with data that address critical aspects of forest fire dynamics.

Successful wildfire management requires landscape-scale information on: (1) fire regime - the temporal change in fire frequency, severity, extent, seasonality, and successive effects within an ecosystem; (2) fuel load - accumulation and distribution of fuels in both vertical and horizontal space; and (3) landscape characteristics such as moisture content, forest types, and topography. Fire regimes influence the abundance and distribution of fuel, thus affecting fire behavior over time (Rollins *et al.,* 2004). Complexity of fuel types and their high spatiotemporal variability poses a challenge to mapping but recent advancements in sensors and improved algorithms show promise for achieving high accuracy in information for successful fire management. Therefore, in-depth analysis of fire regimes can inform strategies that reduce fuel load, and improve fire resilience.

Several methods are in use currently to estimate fire regime, fuel load and landscape characteristics using optical remote sensing, ground surveys and statistical modeling (Keane *et al.*, 2001). However, none of them are comprehensive enough to address all these methods at broad scales. For example, maps of fuels and fire regimes based on gradient modeling can provide variables that determine fire regimes at broad scales. However, due to data sparsity, this approach requires integrating extensive field databases, multiple sources of fire history information, optical remote sensing data, and biophysical modeling to map fuels and fire regimes (Keane *et al.*, 2001; Rollins *et al.*, 2004). To fill these gaps, a growing number of studies have used remote sensing methods to model forest fires incontext of both the vertical and horizontal distribution of species along environmental gradients.

Remote sensing provides a cost-effective broad scale alternative to extensive field data collection for forest fire modeling (Table 7-16). There is a wide range of sensors and algorithms for deriving information about fire regimes and forest fuel distribution. The sensors available for these analyses provide a means for comprehensive coverage. For example, optical satellite sensors can be used to characterize vegetation types and their horizontal distribution. LiDAR measures the three-dimensional arrangement of forest stands and, therefore, is suitable for the accurate and precise estimates of forest structure and composition that is crucial for assessing forest fuels.

Table 7-16. Available Forest Fire Applications to Model Fire Behavior, Effects, and Regimes that Use Survey and Satellite Products.

Forest fire modeling	Applications	Characteristics	Geospatial database
Fire behavior	Behave plus	Models fire behavior, fire effects, and fire environment	LANDFIRE
	FlamMap	Fire behavior and growth across the landscape	
	FARSITE	Wildfire growth and behavior	
Fire effects	FFE-FVS	Forest growth model	Field surveyed tree parameters
	FIRE SEVerity Mapping Tools	Evaluate fire severity maps	Uses satellite image products
	First order fire Effects Model	Predicts tree mortality, fuel consumption, smoke production	Input values are derived from fuel models based on forest cover types
	FuelCalc	Measures crown fuels	Ground, surface, and canopy fuel Characteristics
Monitoring	FFI: Ecological Monitoring	Collection, storage and analysis of ecological information	Field survey data
	FIREMON: Fire Effects Monitoring and Inventory System	Links data with satellite imagery, and maps the sampled data across the landscape *via* image processing	Uses satellite imagery

Information source: *www.firelab.org*

11.2.1 *Optical Remote Sensing*

Optical remote sensing has been used widely for assessing the effect of fire on vegetation. Products derived from optical sensors assist in evaluating plant response to fire severity and exposure. Accuracy of

these analyses depends on a sensor's spatial, spectral, and radiometric characteristics (Arroyo *et al.*, 2008). Medium to low resolution MS data (e.g., Landsat and SPOT) are used to classify forest into vegetation categories, and then fuel characteristics are assigned to each category. Spectral indices are used widely to predict fire severity, exposure and geographic extent using ground reference data to relate spectral properties to forest fire (Epting *et al.*, 2005). While these data are useful for delineating fire severity, exposure, and extent at broad scales, accuracies for mapping fuel types are uncertain. Alternatively, very high-resolution data such as from QuickBird and IKONOS have provided forest characteristics and fuel types at submeter resolutions (Mitri and Gitas, 2008). Hyperspectral data are useful for discriminating spectral and spatial attributes of fire-related vegetation (Veraverbeke *et al.*, 2014). However, due to spectral similarity and mixing problems, these data often have limited success in estimating fuel types and loads with high accuracy (Jin and Chen, 2012). For example, mapping fuel based on forest types such as deciduous and evergreen is easy, but it is difficult to map fuel types based on two different maple species. Moreover, optical sensors are unable to provide vegetation height, which is a critical variable for classifying fuel types.

11.2.2 *LiDAR Remote Sensing*

LiDAR remote sensing has been applied successfully to forest fire studies. Compared to optical sensors, LiDAR sensors can capture three-dimensional forest structure, making them a key data source for forest fire modeling (Andersen *et al.*, 2005). LiDAR facilitates accurate representation of forest structure from stands to individual trees, and provides landscape characteristics such as elevation, slope, aspect, and other important properties of the canopy and surface.

11.2.2.1 Applications of LiDAR in Forest Fire Modeling

As LiDAR data are becoming more cost effective, forest managers are approving data applications to forest fire modeling. The accurate height-above-ground and topography information make LiDAR data highly effective compared to other remote sensing data. For example, due to their capacity to record accurate elevation information below vegetation cover, the last returns of LiDAR data provide a potential for creating high-resolution DEMs. DEM parameters such as slope, elevation, aspect and solar radiation index are used in fire management decision support systems (Morsdorf *et al.*, 2004). These inputs are essential to successful fire behavior prediction models such as fire area simulator (FARSITE) and fire behavior prediction and fuel modeling system (BEHAVE) (Burns, 2012). DEM and digital surface models (DSM) are used together to estimate canopy heights for assessing fuel metrics over large areas (Andersen *et al.*, 2005; Morsdorf *et al.*, 2004). LiDAR has been used to generate fuel metrics such as canopy fuel weight, canopy bulk density (CBD), canopy base height (CBH), and canopy height. Estimated fuel output can also be used directly for an accurate prediction of fire spread and intensity. Due to the similarity between LiDAR and field measured canopy height, LiDAR height measurements are suitable for estimating biomass and offer an alternate to field surveys. Thus, accurate height-above-ground and topography information not only make LiDAR data suitable for mapping fuel and topographic features of targeted forest landscapes, but also for integrating LiDAR data directly to available forest fire behavior models.

11.2.3 *Estimating Forest Canopy Fuel*

Fuel assessments based on ground surveys have been questionable due to their inability to capture spatial heterogeneity of fuels at stand and landscape levels. Skowronski *et al.* (2007) used first-return LiDAR measurements to quantify forest structure and fuels. In another study, height-above-ground data were used to estimate forest fuel parameters, including CBD and CBH (Agca *et al.,* 2011). Andersen *et al.* (2005) used LiDAR-based fuel prediction models to develop canopy fuel maps for Pacific Northwest forests, and recommend using LiDAR for accurate measurement of forest structure over extensive areas. Combining LiDAR with optical sensors is also profitable. For example, Haala *et al.* (2004) combined a terrestrial scanner and a panoramic camera accurately for recognizing tree species. LiDAR returns stratified into height intervals along with spectral information can provide accurate fuel type maps. Gajardo *et al.* (2014) findings suggest that LiDAR and optical data together map fuel properties more accurately due to the synergy of the structural and spectral information than using any of these sensors alone.

11.2.4 *Fire Severity Assessment*

The complexity of forest landscapes, including extreme changes in slope, inaccessibility of area, vegetation heterogeneity, and high biodiversity makes mapping fire severity across a landscape a challenging task, in particular, using traditional field methods. Spectral remote sensing can detect changes resulting from fire easily due to the reduction in chlorophyll. Reduced chlorophyll causes an increase in the visible and a decrease in the NIR region of the electromagnetic (EM) spectrum (Escuin *et al.,* 2008). However, it is difficult to categorize remnant fuel loads from spectral remote sensing. Montealegre *et al.* (2014) have suggested that *canopy relief ratio* and *percentage of all return from LiDAR data* are significant variables for creating a fire severity map. LiDAR-based studies are often done at the pre-fire stage and/or during the fire to characterize fuels for fire management. Gajardo *et al.* (2014) suggested that multi-temporal LiDAR data also have high potential at the post-fire stage to estimate burn severity and vegetation regeneration.

11.2.5 *Large Area Forest Fire Modeling*

Forest managers use wildfire behavior models to inform strategies that mitigate the possibility of large area forest fire such as forest thinning and prescribed fires. Modeling requires spatial data that represent forest landscape, structure, and composition accurately, such as elevation, slope, aspect, canopy height, canopy cover, crown base height, crown bulk density, and forest fuel types. Jakubowski *et al.* (2013) found that these parameters can be predicted accurately using LiDAR with MS images, but noticed that specific fuels were difficult to identify in dense forest stands. Large area fire modeling has been performed using geoscience laser altimeter system (GLAS) data. Peterson *et al.* (2013) used vegetation structure and fuel layers from GLAS and the Landscape Fire and Resource Planning Tools (LANDFIRE) layers to model fire behavior. Their study suggests that including GLAS data enabled better landscape-level characterization of vegetation structure for a better forest fire modeling.

11.2.6 *Commonly Used LiDAR Metrics*

11.2.6.1 Canopy Base Height

Scott and Reinhardt (2001) define CBH as the lowest height above the ground at which there is sufficient canopy fuel to propagate fire vertically through the canopy. There are several ways to estimate CBH at plot level; namely, Lorey's mean, the arithmetic mean, and percentiles. Maguya *et al.* (2015) used a moving voxel method to estimate the height of the gaps below tree crowns for modeling CBH. This approach accommodates variations in LiDAR data that occur due to seasonality (e.g., leaf-on and leaf-off) and tree species. Often, the presence of dense shrubs in forests leads to underestimation of CBH. To account for this, an improved classification of the point cloud can distinguish between over- and understory vegetation. Ladder fuels are difficult to quantify. Kramer *et al.* (2014) suggest LiDAR as a way forward to better characterize ladder fuels.

11.2.6.2 Canopy Bulk Density

CBD is the density of available canopy fuel in a stand. This metric can be estimated using LiDAR, field measurements from the foliage biomass, and crown volume. Several studies have used LiDAR to estimate CBD at both the plot and landscape levels. CBD is used as an input to decision support systems such as FARSITE (Erdody and Moskal, 2010). This is also used in the First Order Fire Effects Model (FOFEM) to determine the proportion of the crown that might be consumed in a wildfire (Erdody and Moskal, 2010; Molina *et al.*, 2014). These metrics form the basis of fuel maps.

11.2.6.3 Canopy Cover Fraction

Canopy cover is expressed as a percentage of total ground area. It is a relative amount of ground area covered by the vertical projection of tree crown perimeters, and the metric is related inversely to the laser pulse penetration rate into the canopy. Thus, canopy cover can be computed as the proportion of the canopy returns over all the LiDAR returns. LiDAR provides highly accurate canopy cover compared to field-based estimates.

11.2.7 *Recent Developments in Forest Fire Modeling*

Two trends in forest fire modeling have emerged. The first trend combines structural and spectral data to address the needs for wildfire growth and behavior modeling. For example, FORSITE, which is a fire simulation model, requires information on topography and fuels along with weather and wind data. The combined use of these data in fire modeling programs improves the quality and accuracy of their prediction. The second trend involves integrating LiDAR data into the LANDFIRE program for mapping vegetation and fuel. These are used to model fire behavior at large scales. Peterson, B., *et al.* (2015) developed a tool called *Creating Hybrid Structure from LANDFIRE/LIDAR Combinations* that allows one to develop a set of vegetation structure and fuel parameters from LiDAR data and integrating them into existing LANDFIRE data sets. Increasing availability of large area lidar data sets will help fill gaps of otherwise sparse LiDAR data in LANDFIRE or other similar programs.

11.3 *Species Distribution Modeling and Remote Sensing*

11.3.1 *Introduction to Species Distribution Modeling*

Many mathematical modeling tools have been developed to link species observation records with environmental variables for characterizing natural distributions of organisms across landscapes based on areas of similar environmental composition. The resulting distribution models are known commonly as species distribution models, ecological niche models, environmental niche models, bioclimatic envelope models, and predictive habitat distribution models (aka, species distribution models (SDM)). These models vary in their utility based on the quality and type of data used as input, the degree to which the species is at equilibrium in its environment, and the temporal and spatial extent of the input data and the resulting model (i.e., the need for extrapolation) (Elith and Leathwick, 2009).

SDMs are commonly used to describe aspects of species ecology, revealing for example, species' land use patterns, habitat and micro-habitat preferences, community- and population-level interactions, or patterns of allopatry for further investigation (Carpenter *et al.*, 1993; Peterson, 2006; Raxworthy *et al.*, 2007). These models are also applied increasingly to predictive questions such as the prediction of species' historical ranges based on paleoclimate layers (e.g., Richards *et al.*, 2007), species' predicted responses to future climate scenarios (e.g., Beaumont and Hughes, 2002; Hilbert, 2004; Thuiller, 2004), extrapolation of observed records to distributions of broader or different geographic extents (e.g., Anderson *et al.*, 2002), and the predicted future extent of invasive species (Peterson *et al.*, 2003; Ficetola *et al.*, 2007; Mainali *et al.*, 2015). These predictive models are often applied to conservation problems and used to support decision making regarding endangered species, critical habitats, biological invasions, and more (Guisan *et al.*, 2013). Serious challenges arise in predictive modeling of species distribution due to issues regarding the selection and availability of appropriate environmental predictor variables, the identification of an appropriate spatial extent for modelling, and problems with identifying distributions for non-equilibrium species (e.g., invasive species) (Mainali *et al.*, 2015). These challenges may be moderated by including dominant species/environment patterns while excluding hyper-local species/environment interactions (Mainali *et al.*, 2015).

Two broad categories of SDM techniques emerge based on the types of species occurrence data or response variables they require: presence/absence records or presence-only data (Hernandez *et al.*, 2006). While presence-absence records provide a more complete picture regarding the species' use of space and habitats, these data are typically more difficult to obtain and the vast repository of museum and historical records are largely presence-only data. Repositories of presence-only data represent a wealth of information that statisticians and ecologists have worked to develop tools to analyze (Elith *et al.*, 2009; Phillips *et al.*, 2009). Kumar and Stohlgren (2013) give a detailed description of the algorithms used and the data required by the various SDM tools described in Table 7-17.

Table 7-17. Commonly Used Models for Predicting Species Distributions (from Morain, *et al.*, 2013).

Model	Advantages*	Disadvantages
Maxent (Phillips *et al.*, 2006)	P; Nl; Np; NS-C; RIV; E; U	Pseudo-absence or background data
GARP (Stockwell and Nobel 1992; Stockwell and Peters 1999)	P; Nl; Np; NS-C; U; NE	Pseudo-absence or background data; no RIV
Classification and Regression Tree (CART) (Breiman *et al.*,	Np; Nl; P/A; E; RIV	Absence data needed

1984)		
Random Forest (Breiman, 2001)	Np; Nl; P/A; RIV	Absence data needed
Boosted Regression Tree (Friedman, 2001; De'ath, 2007)	Np; Nl; P/A; RIV	Absence needed, limited spatial data; need more statistical details
Logistic Regression (McCullagh and Nedler, 1989)	P/A	Absence data needed; sensitive to multi-collinearity
BIOCLIM (Busby, 1991)	P; simple	Needs absence data; less accurate than other niche models
DOMAIN (Carpenter *et al*., 1993)	P; simple	Needs absence data; less accurate than other niche models
Mahalanobis distance (Farber and Kadmon, 2003)	P; Nl	No absence data
Environmental niche factor analyses or ENFA (Hirzel *et al*., 2002)	P	No absence data
Artificial Neural Network (ANN) (Pearson *et al*., 2002)	P/A	Absence data needed
(Jarnecivh *et al*., 2009)	P or A only can be run	All environmental factors are weighted equally

* Codes: P = species presence; P/A = Presence/Absence; Np = Nonparametric; Nl = Non-linear; NS-C = not sensitive to multi-collinearity; RIV = relative importance of variables; CRV = continuous response variables; E = Efficiency; W = widely used.

11.3.2 *Remote Sensing and Species Distribution Models*

Characterizing species' distributions over geographic space requires quantifying topographic and biophysical features of the landscape that are gradational and continuous in nature. To link landscape and species patterns effectively, the quantification of landscape features or predictor variables must occur at spatial and temporal resolutions compatible with the modeled species' ecology, behavior, and the density of observation records used for modeling (Elith and Leathwick, 2009). Advancements in the field of remote sensing have generated a broader range of remotely-sensed predictor variables at increasingly higher spatial and temporal resolutions, and have subsequently improved species distribution model predictions (He *et al.*, 2015). Remotely-sensed products can be used to clip the modeled geographic extent to only pixels deemed suitable for a species' distribution. The inclusion of remotely-sensed predictor variables representative of biophysical characteristics (e.g., chlorophyll content, leaf area indices, soil moisture estimates) can further enhance descriptions and predictions of species distributions (Zimmermann *et al.*, 2007; He *et al.*, 2015). Continued development of high spatial, temporal, and spectral resolution sensors (e.g., WorldView-2, IKONOS, radar, LiDAR, CubeSat programs) and increased accessibility of UAVs also enhance studies of this type (e.g., Hodgson *et al.*, 2013). In selecting remotely-sensed predictor variables for modeling, it is important to consider the impacts these choices may have on model outcomes; as Bradley *et al.* (2012) point out, use of remotely-sensed predictor variables may inadvertently bias one's model toward actual species presence rather than habitat suitability for a species of interest. This is particularly relevant in the case of modeling plant distributions, where using VI or land cover classification data as predictor variables may bias distribution models toward the species' presently used habitat (Bradley *et al.*, 2012).

In addition to providing data on predictor variables, remote sensing technology has the potential to transform the development of SDMs through the derivation of response variables or species occurrence data (He *et al.*, 2015). Remotely-sensed occurrence data have been implemented for detecting and estimating populations of both plant (e.g., Wilfong *et al.*, 2009; Tuanmu *et al.*, 2010) and animal (e.g., Fretwell *et al.*, 2014) species. Detection of plant presence is facilitated by unique phenological properties or plant chemistry, and

detection of animal presence is facilitated by large body size or topographic footprint (e.g., coral reef structure, large woody nesting sites) and unobstructed aerial observations (He *et al.*, 2015).

11.3.3 *Summary*

Species distribution modeling is based on a broad range of statistical tools and techniques, and the value of model output depends on the suitability of modeling choices relative to the species, environment, and data in question. SDMs have a wide range of applications, from the descriptive study of species ecology and interactions to the application of model results to impending conservation issues. These modeling efforts and their associated applications can be enhanced by including remotely-sensed data as both predictor and response variables. Increasing accessibility of remotely-sensed, high resolution data that represent biophysical parameters and species occurrence has, and will continue, to transform species distribution modeling for greater and more accurate applications to questions of species ecology.

11.4 *Vegetation Radiative Transfer Theory and Modeling with PROSAIL2*

Acronyms/Abbreviations: community land model (CLM); carbon dioxide, (CO_2);) photosynthesis, (PSN); photosynthetically active radiation, (PAR); absorbed PAR, (APAR); fraction of PAR absorbed by a whole canopy, $fAPAR_{canopy}$, also referred to as FPAR; fraction of PAR absorbed by all the leaves of a canopy, $fAPAR_{foliage}$; fraction of PAR absorbed by chlorophyll throughout a canopy, $fAPAR_{chl}$; fraction of PAR absorbed by non-chlorophyll components of all the leaves of a canopy, $fAPAR_{non\text{-}chl}$; leaf area index, LAI; gross ecosystem production (GEP); gross primary production, (GPP); net primary production, (NPP); light use efficiency, (LUE); Moderate Resolution Imaging Spectrometer, MODIS; bi-directional distribution function, (BRDF); radiative transfer model, (RTM).

11.4.1 *Fractions of Light Absorption by Chlorophyll, Foliage and Canopy*

A vegetation canopy is partitioned into foliage and non-foliage (hereafter referred to as stem) components, and the foliage is further partitioned into chlorophyll, non-photosynthetic pigments (hereafter referred to as brown pigment**)** and dry matter. Therefore, one can calculate the fraction of PAR absorbed by these components and LAI as: $fAPAR_{canopy}$ (Goward and Huemmrich, 1992), $fAPAR_{foliage}$, $fAPAR_{chl}$, $fAPAR_{non\text{-}chl}$ and LAI_{chl} (Zhang, Q., *et al.*, 2005; 2006; 2009; 2012; 2013; 2014; Zhang; Q., Cheng, Y.B, 2015) with the following Equations (7-93 through 7-96):

$$fAPAR_{canopy} = fAPAR_{foliage} + fAPAR_{stem} \quad (7\text{-}93)$$

$$fAPAR_{foliage} = fAPAR_{chl} + fAPAR_{non-chl} \quad (7\text{-}94)$$

$$fAPAR_{non-chl} = fAPAR_{dry\ matter} + fAPAR_{brown\ pigment} \quad (7\text{-}95)$$

$$LAI_{chl} = LAI \times \frac{fAPAR_{chl}}{fAPAR_{foliage}} \quad (7\text{-}96)$$

where: $fAPAR_{canopy}$, $fAPAR_{foliage}$, $fAPAR_{stem}$, $fAPAR_{chl}$, $fAPAR_{non\text{-}chl}$, $fAPAR_{dry\_matter}$, and $fAPAR_{brown\_pigment}$ are fractions of absorbed PAR by canopy, foliage, stem, chlorophyll in foliage, non-chlorophyll components in foliage, dry matter in foliage, and brown pigment in foliage, respectively.

11.4.1.1 The MODIS $fAPAR_{chl}/LAI_{chl}$ Algorithm Description and Proof-of-Concept Studies

SAIL2, a canopy-level RTM, is coupled with a leaf-level RTM (PROSPECT) in this algorithm (hereafter called PROSAIL2). SAIL2 is a modified version of the SAIL model (Andrieu *et al.*, 1997; Badhwar *et al.*, 1985; Braswell *et al.*, 1996; Goel and Deering, 1985; Goel and Thompson, 1984; Jacquemoud *et al.*, 2000; Major *et al.*, 1992). The algorithm uses an improved version of the PROSPECT model, which includes other pigments except photosynthetic pigments (i.e., lumped together as "brown pigment") and has five leaf-level variables: a leaf internal structure variable (N); leaf total chlorophyll content (C_{ab}); leaf dry matter content (C_m); leaf water thickness (C_w) and leaf brown pigment (C_{brown}) (Baret and Fourty, 1997; Demarez *et al.*, 1999; Di Bella *et al.*, 2004; Hosgood *et al.*, 1995; Jacquemoud and Baret, 1990; Newnham and Burt, 2001; Verhoef and Bach, 2003). The PROSAIL2 model has three groups of parameters: (1) observation viewing geometry variables; (2) an atmospheric condition (i.e., visibility) variable; and (3) biophysical and biochemical variables (Table 7-18). The fourteen biophysical and biochemical variables are plant area index (PAI), stem fraction (SFRAC), cover fraction (CF), stem inclination angle (STINC), stem BRDF effect variable (STHOT), leaf inclination angle (LFINC), leaf BRDF effect variable, five leaf variables that simulate leaf optical properties (N, C_{ab}, C_m, C_w, C_{brown}), one soil/litter variable that simulates soil/litter optical properties ($SOIL_A$), and one variable that simulates stem optical properties ($STEM_A$). MODIS observations are used here to describe parameter retrievals with PROSAIL2. For the MODIS observations, all seven land spectral bands designed for studies of vegetation and the land surface are utilized to invert the PROSAIL2 model: blue (459-479*nm*), green (545-565*nm*), red (620-670*nm*), near infrared (NIR_1: 841-875*nm*; NIR_2: 1230-1250*nm*), and the shortwave infrared ($SWIR_1$: 1628-1652*nm*, $SWIR_2$: 2105-2155*nm*). For atmospherically corrected MODIS data, the atmospheric visibility variable was set to be large and constant throughout this algorithm. Solutions for $fAPAR_{canopy}$, $fAPAR_{foliage}$, $fAPAR_{chl}$, $fAPAR_{non\text{-}chl}$ and LAI_{chl} are derived using the PROSAIL2 model and Equations 7-93 to 7-96.

Table 7-18. List of Variables in the PROSAIL2 Model and Their Search Ranges.

	Variable	Description	Unit
Biophysical /biochemical variables	PAI	Plant area index, i.e., leaf + stem area index	m^2/m^2
	SFRAC	Stem fraction	
	CF	Cover fraction: area of land covered by vegetation/total area of land	
	C_{ab}	Leaf chlorophyll a + b content	$\mu g/cm^2$
	N	Leaf structure variable: measure of the internal structure of the leaf	
	C_w	Leaf equivalent water thickness	*cm*
	C_m	Leaf dry matter content	g/cm^2
	C_{brown}	Leaf brown pigment content	g/cm^2
	LFINC	Mean leaf inclination angle	degree
	STINC	Mean stem inclination angle	degree
	LFHOT	Leaf BRDF variable: length of leaf/height of vegetation	*m*/*m*
	STHOT	Stem BRDF variable: length of stem/height of vegetation	*m*/*m*
	$STEM_A$	Stem reflectance variable range (for a fitted function)	
	$SOIL_A$	Soil reflectance variable range (for a fitted function)	
Atmospheric condition variable	VIS	Diffuse/direct variable: scope of atmospheric clarity	*km*

Each MODIS reflectance observation [ρ_{obs}] for the seven land bands (red, NIR_1, blue, green, NIR_2, $SWIR_1$ and $SWIR_2$), and associated view zenith angle [θ_v, in degrees], relative view azimuth angle [ϕ, in

degrees], and solar zenith angle [θ_s, in degrees] contains some noise, although small differences in angles may be ignored. Each reflectance observation can be treated as a sample of Equation 7-97.

$$\rho \sim \{\rho_{obs}(\lambda, \theta_v(1+3\mathrm{N}(0,1)), \theta_s(1+3\mathrm{N}(0,1)), \phi(1+3\mathrm{N}(0,1)))\} \cdot (1+0.05\mathrm{N}(0,1)) \quad (7\text{-}97)$$

where: N(0,1) is the normal distribution with a mean of zero and SD = 1. Processing can use as many samples from the distribution from Equation 7-97, as needed.

Inversion of RTMs requires careful choices of optimization procedures and multiple approaches have been employed for model inversion. In this example, the PROSAIL2 model was inverted using the Metropolis algorithm (Metropolis *et al.* 1953; Hurtt and Armstrong 1996; Braswell *et al.* 2005), a type of Markov Chain Monte Carlo (MCMC) estimation procedure. This method estimates posterior probability distributions of the variables and thus can provide estimates of uncertainty (e.g., such as standard deviations and confidence intervals) of individual variables, by inspecting the retrieved distributions. At each step out of a predetermined number of iterations, the algorithm uses the current variable estimate to generate a new "proposal" estimate randomly in variable space. This new variable estimate will be the input for a new model run. Model-retrieved and observed reflectance values are used to calculate the likelihood of an error probability model. The Metropolis algorithm then accepts the new variable estimate with a certain probability. The resulting Markov Chain of accepted variable values converges to the posterior distribution of the variables conditional on the observations after a transient "burn-in" period. MCMC theory assures that such a sampling scheme provides Markov chains, whose values represent draws from the posterior distributions. In the following formalism, Pr(·) denotes probability in a general sense, or more specifically, the value of a probability density function; Pr(v) denotes the prior distribution assumed for the set of variables; Pr(v_{new}|data); and, Pr(v_{old}|*data*) refers to the conditional probabilities of "new" and "old" variable estimates (i.e., variable points) given the known "data".

According to Bayes' theorem,

$$\Pr(\mathrm{v} \mid data) \propto \Pr(\mathrm{v}) \Pr(data \mid \mathrm{v}) \quad (7\text{-}98)$$

$$\text{Let } L(\mathrm{v}) = \Pr(data \mid \mathrm{v}) \quad (7\text{-}99)$$

$$\Pr(\mathrm{v} \mid data) \propto \Pr(\mathrm{v}) L(\mathrm{v}) \quad (7\text{-}100)$$

where: $L(\cdot)$ is the likelihood function. In this example, it is assumed a set of independent uniform prior distributions for the variables. Let $X_i = [x_{i1}, \cdots, x_{ip}]$ (p=7, the 7 MODIS bands), i is the subscript of data point, subscripts 1, …, p mean spectral bands, and x is reflectance.

This algorithm assumes that the observed spectral values X_i differ from the model predicted values $U_i = [u_{i1}, \cdots, u_{ip}]$ according to a mean zero p-variate Gaussian error model that results in the likelihood function.

$$L = \prod_{i=1}^{n} \frac{1}{\left(\sqrt{2\pi}\right)^p \left|\Sigma\right|^{1/2}} e^{-(X_i - U_i)' \Sigma^{-1} (X_i - U_i)/2} \quad (7\text{-}101)$$

where: n is the number of data points sampled according to Equation 7-100 and Σ is the variance-covariance matrix of X. Σ is estimated by the usual sample variances and covariances in each step of the algorithm:

$$\Sigma_e = \left(s_{ij}\right)_{p\times p}$$
$$s_{ij} = \frac{1}{n}\sum_{k=1}^{n}(x_{ki} - u_{ki})(x_{kj} - u_{kj}) \quad .i, j = 1, \ldots, p \tag{7-102}$$

The natural logarithm of the likelihood, the "log-likelihood" (*log(L)*, is used in the algorithm during its operation (e.g., Bishop, 1995).

The algorithm defines the probability of accepting the new point as following:

$$\Pr_{accept} = \min\left(1, \frac{\Pr(v_{new} \mid data)}{\Pr(v_{old} \mid data)}\right), \tag{7-103}$$

If the algorithm accepts the new point, it will become the "old" point in the next iteration; otherwise, the old point will still be the "old" point in the next iteration.

To accelerate the speed of convergence of the Metropolis algorithm, the adaptive algorithm used in other studies (e.g., Hurtt and Armstrong 1996; Braswell *et al.* 2005) can be modified as follows:

In each iteration, one variable is selected to change as:

$$v_{new,s} = v_{old,s} + r \times (v_{\max,s} - v_{\min,s}) \tag{7-104}$$

where: *s*=1, … , 14, is the number of variables in PROSAIL-2 that are allowed to search for solutions, *r* is randomly selected at each step between $\pm 0.5 \cdot T_s$, $v_{\max,s}, v_{\min,s}$ are the maximum and minimum values allowed for the search, and T_s is the adaptive length parameter. If $v_{new,s}$ is accepted, then T_s is increased by a factor of 1.006569. If it is rejected, then T_s is decreased by a factor of 0.99. By changing *the adaptive length parameters* in this way, the T_s (*s*=1, … , 14) of all variables are adjusted until varying any given variable leads to acceptance of about 23% to 44% of the time, which is considered an ideal acceptance rate for the Metropolis algorithm (Gelman *et al.*, 2000).

From the posterior distribution above, solutions can be obtained for $fAPAR_{canopy}$, $fAPAR_{foliage}$, $fAPAR_{chl}$, $fAPAR_{non\text{-}chl}$ and LAI_{chl} according to the PROSAIL2 model and Equations 7-93 to 7-96, which would be derived posterior distribution.

11.4.1.2 Examples with 500*m* MODIS Images

For this example, the $fAPAR_{chl}/LAI_{chl}$ algorithm was applied to nine 500*m* Terra/MODIS images (i.e., the 8-day composite reflectance product) that covered the Harvard Forest site in 2008. Selected days of year were 105, 149, 185, 233, 241, 265, 289, 297 and 305. $fAPAR_{chl}$ was mapped for the area as 500*m* (9×9) pixel blocks where the central pixel covered a flux tower. Figure 7-72 exhibits seasonal and spatial (9×9) dynamics of $fAPAR_{chl}$. The evergreen forest pixels had greater $fAPAR_{chl}$ values than deciduous forest pixels on day of year (DOY) 105. All pixels had their greatest $fAPAR_{chl}$ values in mid-summer on DOY 185. Deciduous forests had a different $fAPAR_{chl}$ pattern from evergreen forests during the senescence period.

Validation of the $fAPAR_{chl}$ product has used MODIS images obtained over a five-year period to analyze the seasonal and inter-annual variability of $fAPAR_{chl}$ and LUE for the Southern Old Aspen flux tower site located in Canada. Using the additional information provided by flux tower-based measurements of gross ecosystem production (GEP) and incident PAR, 90-minute averages for absorbed photosynthetically active

radiation (APAR) and LUE (slope of GEP: APAR) have been determined for both the physiologically active foliage and for the entire canopy (Equations 7-105 and 7-106).

$$(LUE_{chl} = \frac{GEP}{PAR \times fAPAR_{chl}}) \quad (7\text{-}105)$$

$$(LUE_{canopy} = \frac{GEP}{PAR \times fAPAR_{canopy}}) \quad (7\text{-}106)$$

The flux tower measurements of *GEP* were strongly related to the MODIS-derived estimates of $APAR_{chl}$ (r^2 = 0.78) but only weakly related to $APAR_{canopy}$ (r^2 = 0.33). Gross LUE between 2001 and 2005 for LUE_{chl} was 0.0241 µmol C µmol^{-1} Photosynthetic Photon Flux Density (PPFD) whereas LUE_{canopy} was 36% lower. The five-year time series of LUE_{chl} corresponded well with both the seasonal phase and amplitude of LUE from the tower measurements but this was not the case for LUE_{canopy} (Figure 7-73). It is interesting to note that both LUE_{chl} and LUE_{tower} are greater than the maximum *LUE* used by the MOD17 GPP product for this biome type. LUE_{chl} derived from MODIS observations could provide a more physiologically realistic parameter than the more commonly used LUE_{canopy} as an input to large-scale photosynthesis models. In other words, $fAPAR_{chl}$ and LUE_{chl} provide more ecophysiologically realistic information than the more commonly used $fAPAR_{canopy}$ and LUE_{canopy}. Validation examples for crop fields can be found in (Zhang, Q., *et al.*, 2014).

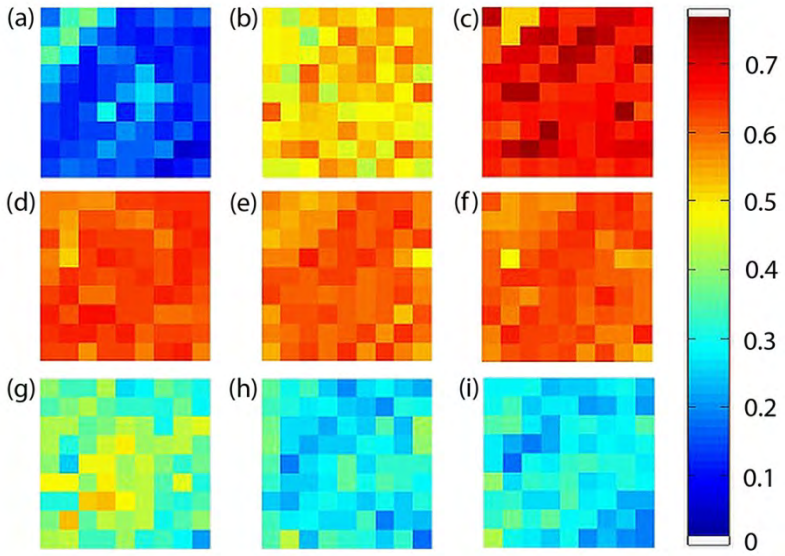

Figure 7-72. $fAPAR_{chl}$ maps for 9 x 9 MODIS pixel area around the Harvard Forest tower site for day of year/Year: (a) 105/2008 (early spring), (b) 149/2008 (late spring), (c) 185/2008 (early July), (d) 233/2008 (August), (e) 241/2008 (late August), (f) 265/2008 (September), (g) 289/2008 (October), (h) 297/2008 (October) and (i) 305/2008 (early November).

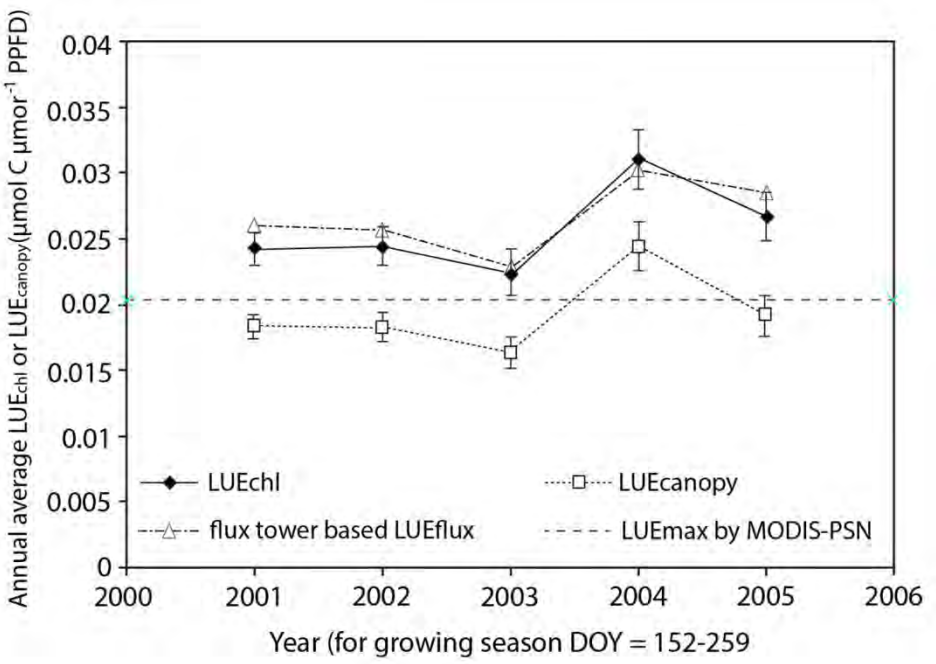

Figure 7-73. Comparison of the annual means ± SE for MODIS-derived LUE_{chl} and LUE_{canopy} during the five-year period (2001-2005) for the growing season between DOY =152-259. LUE_{chl} was significantly higher than LUE_{canopy} in every year, averaging a 0.007 µmol C µmol^{-1} PPFD difference. Annual LUE_{flux} values (Krishnan *et al*., 2006) agree well with LUE_{chl}, falling within the SE range in 4 of 5 years. The maximum LUE (LUE_{max}) used by the MOD17 (a MODIS GPP product) is shown as a horizontal dashed line.

12 STRUCTURE FROM MOTION AND 3D RECONSTRUCTION

12.1 *Introduction*

The geospatial field has witnessed an explosion on the measuring, representation, and manipulation of the third dimension. Significant advances in our ability to measure and represent terrain elevation and the dimensions of targets on Earth are increasing user access to 3D data and transforming how scientists interact with software tools while adopting or proposing solutions to spatial problems. Traditional survey methods for 3D extraction are demonstrated to be accurate, but costly and sometimes infeasible. Recently, with the popularization of LiDAR technologies, novel data acquisition methods and metrics have expanded our analytical capabilities for identifying multi-point elevation and the reconstruction of surface models. In particular, ground-based LiDAR systems have been used widely in many fields, including urban planning, architecture, forestry, and military operations.

CV and algorithm developments for image processing and analysis have also advanced considerably in recent years. As a result, many CV analytical procedures have been developed and are now available at different stages of maturity. Among these procedures, the reconstruction of 3D geometry by using Structure from Motion (SfM) and related technologies, including the generation of 3D models from images acquired from multiple perspectives and use of UASs, is expanding the toolset(s) available to geospatial analysts. This section presents recent developments in 3D reconstruction and modeling based on non-metric

photography/imagery applied to the geospatial field. Here, SfM is explored to introduce the principles involved in reconstructing 3D structures from a set of photographs acquired from multiple camera positions. The section discusses applications of the SfM technology, including practical aspects affecting 3D reconstruction results. Study cases involving point cloud generation using SfM-based 3D reconstruction are presented.

12.2 *Structure from Motion and Multiple Image Matching*

Dating back to the 1950s, objects of interest have been reconstructed using 3D geometry, including the generation of point clouds. Traditionally, information regarding scene geometry, camera parameters, camera orientation, and GCPs were required when using stereo photogrammetry, including a series of overlapping, offset images. However, when using SfM, the main requirement to resolve 3D structure is overlapping images only. Neither ground-control reference targets nor knowledge of the camera exposures are required (Dellaert *et al.*, 2000, Westoby *et al.*, 2012). In place of operator collected data, the camera and scene parameters are solved automatically during the SfM process. This process was conceived in the CV community which integrates automatic feature matching/extraction algorithms to combine multiple overlapping images (Westoby *et al.*, 2012). Features are extracted automatically using simultaneous, highly redundant and iterative bundle adjustment procedures resulting in very accurate point matching across photographs. Combining overlapping photographs in this manner extracts a dense RGB-encoded point cloud (Mancini, 2013). SfM performs best with highly overlapping images, >60% overlap, and a range of perspectives of the 3D structure. Both of these requirements can be extracted from a moving sensor by using individual frames from video.

Although internally consistent, models derived from SfM typically lack scale and orientation provided by using GCPs. The 3D point clouds generated from SfM are created in a relative image-space coordinate system and are thus often satisfactory for many basic applications since they can still be scaled by using a known distance imaged in a scene. However, a multidimensional data adjustment can be achieved by utilizing 3D similarity transforms using a few GCPs measured after the model is complete. Thus, if more precise measurements are needed for analysis and repeatability, the data must be aligned to a real world, object space coordinate system. To meet high accuracy workflow requirements, known control points and the definition of direction and dimension must be made. Control points can be implemented into the model output by defining specific 3D points calculated by the model. Several software solutions exist to process a series of images and generate a point cloud dataset: cloud based (Autodesk® 123D Catch®), free or open source desktop software (e.g., Visual SfM, Insight3D), and commercial (e.g., Agisoft PhotoScan, Eos Systems PhotoModeler, University of Stuttgart SURE) (Madden *et al.*, 2015). Examples below demonstrate the SfM workflow for 3D point clouds, digital surface models and microterrain extraction for building vegetation and geomorphic structure representation.

Algorithms for SfM vary and here we present a set of principles and frequently found steps and data structures used by softwares and services while performing 3D reconstruction. Vergauwen and Luc Van Gool (2006) introduce their Web service based SfM and list four procedural steps for 3D reconstruction, including comparison procedures for the identification of image pairs out of the multiple images presented to the algorithm. Comparisons and the identification of pair candidates also involve image subsampling.

Pair matching supports subsequent steps of the 3D reconstruction pipeline associated with analog feature identification and guarantees that photographs can be used without the need for identifying a particular image sequence.

The success of SfM while reconstructing a DEM or objects far from the camera can be affected by atmospheric conditions during photograph acquisition. Contrast reduction by haze obfuscates detail and may offer considerable challenges during the SfM pipeline, particularly during the identification of matching pairs and analog features on photographs acquired from different angles. Atmospheric correction can, in theory, be added to the 3D reconstruction workflow aiming to increase contrast and feature recognition. However, besides involving the manipulation of multiple photographs, these procedures may result in the creation of image aberrations or artifacts which have also the potential to impact processing.

12.3 *3D Models of Natural and Cultural Resources Using UAS Imagery*

Researchers at the Center for Geospatial Research (CGR) within the Department of Geography at the University of Georgia have used DJI Phantom 2 Vision and Phantom 2 Vision Plus quadcopters to collect imagery. Based on the objectives of a specific mission, both operator-controlled first-person view (FPV) and automated navigation to preplanned waypoints can be utilized. As an example, images acquired at the Georgia State Botanical Garden demonstrate the advantage of using a multi-rotary UAS to document seasonal changes in a cultural landscape. Specifically, the flexibility and ease of deployment of UAS allowed the operator to take advantage of optimal flying conditions (i.e., calm winds and clear skies) synchronized with plant phenology and the planting schedule of the gardens. This simple application provided managers with a vantage point that allows them to better plan planting and maintenance, to inspect infrastructure, and to evaluate visitor experience (Figure 7-74).

Figure 7-74. Bird's-eye-view of the Georgia State Botanical Gardens acquired with a rotary-wing Phantom 2 Vision Plus (DJI) quadcopter used for image acquisition and resource mapping.

More precise information was gathered once the quadcopter was lowered to an altitude of 30*m*. At this height, with the camera positioned at roughly 15° from nadir, video was recorded while the UAV was flown at ~2*m*/s. Multiple overlapping frames were selected from the video to be used as input for PhotoScan (AgiSoft, Inc.) for SfM processing. To achieve optimal alignment images should overlap by at least 70%. While some images overlapping by only 50% were able to be aligned, the output from these images resulted in poor data quality. The product from images with proper overlap was able to produce 3D point clouds and image models of the gardens for unique geovisualizations (Figure 7-75). Furthermore. the images and models were georeferenced using specific objects located within the images.

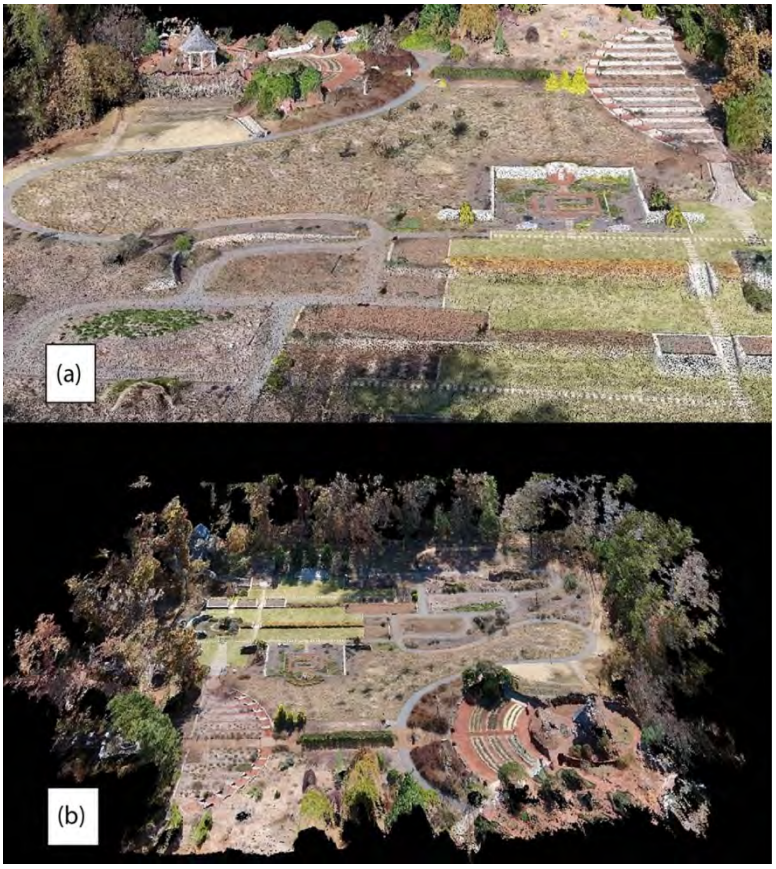

Figure 7-75 (a) 3D point cloud of the Georgia State Botanical Gardens, and (b) geovisualization of the area.

Images acquired of the Abbey of the Holy Cross in Cañon City, Colorado, demonstrate the advantage of using a multi-rotary UAS to document heritage buildings and gardens in a cultural landscape. Built in 1866 of Gothic Revival style as a monastery, the Abbey was subsequently used as a boarding school for boys and a winery, and is now listed on the USA National Register of Historical Places (Figure 7-76a). Navigation by FPV was used to guide the Phantom 2 Vision Plus quadcopter with its RGB camera pointing at a low oblique angle and record video of the cultural landscape following roughly parallel flight lines (Figure 7-76b). Although flight missions will vary depending on the physical configuration of the ground features of interest, typical data sets should involve at least three flight lines with the camera tilted at slightly different angles to obtain multiple views of the features. Errors in the resulting products are minimized by flying

low oblique video in two to four directions to ensure all surfaces are visible in multiple overlapping images (Figure 7-76c).

In practice, the UAS imagery is collected and preliminary processing is performed on a laptop in the field. The first pass performs a low or medium density point matching and low-density point cloud. If the resulting point cloud is not complete (e.g., there are gaps) the video can be reflown without the added expense of traveling to the site for a second time. Further processing, typically reserved for the lab because of the needed computing power/time, includes high accuracy point matching and the creation of a high-density point cloud. This processing step usually takes substantially more time than the generation of low-density point cloud and benefit from dedicated hardware and batch mode processing. Point matching refinement is based on lens distortion and removes the barrel distortion caused by typical cameras of wide angle and short focal length.

(a)

(b)

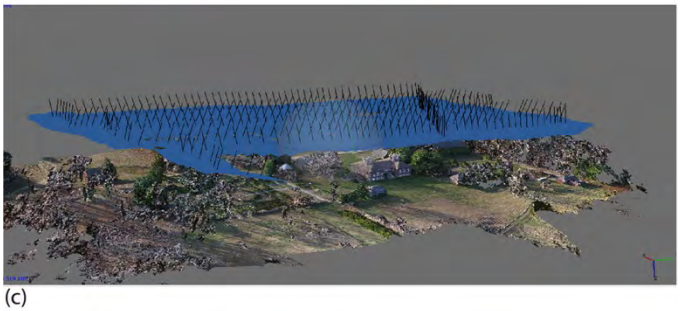

(c)

Figure 7-76. (a) Frame selected from the UAS video for the Colorado Abbey, (b) black lines indicate 418 frames extracted from video collected along multi-directional flight lines, and (c) the same 418 frames demonstrating the low oblique angles used for data collection. The accompanying video was obtained using a DJI Phantom 2Vison+ quad-coppter equipped with a digital camera.

Nine GCPs, well-distributed corners of sidewalks surrounding the Abbey, were identified in Google Earth™ and X, Y, and Z coordinates extracted from high-resolution DigitalGlobe imagery in Google Earth for all GCPs (Figure 7-77a). To avoid having to input the locations of the nine GCPs on each of the 418 images as required by PhotoScan to rectify the images individually, a point cloud consisting of 10.6 million points was created in PhotoScan, scaled *a priori* in LASTools and then transformed in Quick Terrain Modeler (Applied Imagery, LLC) by measuring the nine GCPs once. The QTModeler software transformed the point cloud to an accuracy of 0.34*m* in XY, 0.30*m* in Z and 0.45*m* in XYZ (Figure 7-77b). This level of 3D point cloud accuracy is suitable for most natural and cultural resource applications.

Figure 7-77. (a) Control points obtained from high resolution images are used to assign real-world coordinates to 3D models, and (b) The resulting RGB 3D point cloud.

12.4 *Conclusions*

Detailed point clouds and comprehensive spatial information can be gathered from basic photographic techniques using SfM. UASs provide the best platforms for this analysis because of their ability to gather images quickly, with sufficient overlap (>80%), and from different perspectives. By utilizing photogrammetric techniques performed by readily available software, images, or screen grabs from video, can be transformed into 3D models with associated RGB values, providing an accurate, multidimensional perspective of a variety of natural to anthropogenic features.

12.5 *Acknowledgements*

The authors thank the students and staff of the CGR, Department of Geography, University of Georgia, for their assistance and contributions to this research. Appreciation also is extended to the Georgia State Botanical Garden.

13 IMAGE PROCESSING OF VERY LARGE DATASETS

13.1 *Introduction*

This section focuses on requirements for, and examples of, processing very large image datasets. Data from the Landsat series of satellites provides an exemplar of the type of large image datasets ripe for data mining. Since 1971, the Earth Resource Observation and Science (EROS) has received and processed petabytes of Landsat data, comprising over five million scenes of roughly 185*km* by 180*km*. Recent advances in cloud computing have made it possible to access and process the entire catalog of Landsat scenes and other sizable image data catalogs. This section describes some of the requirements for processing datasets of this size, and provides examples of how these analyses are happening today.

13.2 *Examples*

To provide a sense for what kinds of analyses are possible, and the computational complexity of performing image processing on large image datasets, two examples are presented of large scale analyses performed in Earth Engine®, Google's public cloud-based platform for geospatial analysis: the creation of a 30-meter scale global animation of change from 1984 to 2012, called Timelapse, and a global analysis of forest change from 2000 to 2012.

13.2.1 *TIME's Timelapse Project*

The Timelapse project is a global, zoomable, time-lapse 30-meter resolution map of change over the Earth from 1984 to 2012, built through a collaboration by Google, NASA, USGS, the CREATE Lab at Carnegie Mellon University, and TIME magazine. This animation is comprised of one 1.78 terapixel image for each year of the animation. The images were created by combing through 909 terabytes of Landsat-4, -5, and -7 data to find the best available pixels and to extract clouds and data errors. An additional 20 terabytes of MODIS data were used to account for seasonal effects. The Landsat, MODIS, and petabytes

of other Earth observation data are stored in Earth Engine's catalog and available for analysis on Google's infrastructure using a geospatial analysis programming interface. Once the yearly mosaics were complete, they were transformed into multiresolution, overlapping video tiles so that they could be viewed in a Web browser. The combined process required 1.8 million core-hours (i.e., over 200 core-years), but because it was spread over 66,000 cores running in parallel, it took approximately 3 days to complete.

13.2.2 *Global Forest Change*

Hansen, *et al*. (2013) provides an example of mining the Landsat catalog for measurable change detection. The study used Earth Engine's archive of Landsat-7 data and 10 000 central processing unit (CPU)-cores to characterize tree cover in the year 2000, and subsequent tree cover loss and gain through 2012. The browsable dataset revealed a total loss of 2.3 million square kilometers over the study period. This analysis involved 143 billion Landsat pixels drawn from 654 178 Landsat ETM+ scenes. Earth Engine was used to resample images, convert raw DNs to TOA reflectance, screen for clouds, cloud shadows, and water, and normalize the data. It handled all the necessary data format conversion, reprojection and resampling, and data access. The resulting imagery was then used to create a set of metrics over the study interval, including per-band reflectance percentiles and a slope of linear regression of band reflectance value versus image date. These metrics were related to a set of percent tree cover, forest loss, and forest gain training data using decision trees, and the resulting model was applied to generate global forest cover, loss, and gain. Earth Engine provides both an interactive mode, which the researchers used for debugging and development, and a batch mode, which is meant for longer tasks such as rendering the global forest change image.

13.3 *Challenges*

These analyses require a computational framework that provides access to the data, the ability to combine datasets that come with different resolutions and projections, the ability to perform analyses on a global scale in a reasonable amount of time and the ability to analyze the data in an interactive mode that allows analysts to refine their methods before applying them to complete petabyte-scale datasets.

13.4 *Requirements*

13.4.1 *Accessing the Data*

The first challenge is to access the data for analysis. There are two main approaches to data access: (1) centralized, and (2) distributed. In the centralized mode, all of the data to be analyzed are stored in a central repository. In a distributed system, the data are stored on a variety of servers and downloaded when needed. Although there are many schemes for distributed databases, none of these scale well when trying to analyze petabytes of data. It simply takes too long to download all of the necessary data. The rest of this section assumes that data reside in a centralized data store before analysis begins.

A related challenge in data access involves data availability. Different storage media have different cost and latency profiles. Less expensive storage media, like tape, have slower access times when arbitrary parts of the dataset are required. Active media, like optical drives or solid state drives, are considerably more

expensive, but provide quicker access. In any case, intelligent indexing of data assets is critical for fast data access, which, in turn, is critical for enabling analyses of large amounts of image data.

Even when a data provider makes their data available for analysis, there are limits on how quickly data can be accessed. For example, most data providers limit the number of connections any given entity can use to download data which impacts the speed at which data may be acquired.

13.4.2 *Combining Disparate Datasets*

Geospatial image datasets represent their data using specific resolutions, bit depths, band names, projections and datums. These factors vary both between datasets and among images within a single dataset. In addition, datasets often attach arbitrary metadata to each image. Any system that combines large image datasets needs to be able to deal with this variability. This variability can be dealt with at various places in the pipeline from data ingestion, to data access, to data analysis, to output production. When dealing with only a few datasets, it may be possible to select a common representation system into which to cast datasets upon ingestion that degrades the datasets minimally As a centralized data store involves a larger number of datasets or is applied in a wider range of applications, however, it becomes valuable to store the input datasets in their native formats. That way, a different common format can be determined for each pair of datasets at the time of analysis. This approach requires an ability to reproject and redescribe datasets on demand, potentially increasing the computation involved in any analysis.

13.4.3 *Global-scale Processing*

Analyses that take advantage of large amounts of image data will demand some kind of parallelism. As seen in the case studies, global analyses can require the analysis of hundreds of terabytes of data and millions of CPU hours. Running them on a single commodity CPU is simply not feasible. Alternatives include running analyses on supercomputer clusters, like the Pleiades[5] supercomputer, leveraging conventional cloud computing infrastructure, such as Google's Compute Engine, Amazon EC2, or Microsoft Azure Virtual Machines, or using a cloud-based geospatial analysis platform such as Google Earth Engine.

Any implementation will require an interface that lets analysts access the image data and apply the required analyses. Graphical interfaces are simple to use, but tend to be inflexible. Programming interfaces offer more flexibility at the cost of a steeper learning curve. In any case, the operations available via the interface must be able to access the imagery in the datastore and run analyses in parallel over a number of CPUs.

The literature related to parallel processing of images is quite rich. Some tasks are "pleasingly parallel." These are tasks where very little or no communication is needed between tasks. For example, per-pixel analyses of images, where the value of a pixel in the output is dependent only on the values that occur in that pixel, are straightforward to parallelize. Consider the NDVI of a Landsat scene, for example. The output of each pixel is simply the difference of the values of NIR and red band at that pixel divided by their sum. In the most extreme case, each pixel could be analyzed using a different CPU, and the resulting image

[5] *http://www.nas.nasa.gov/hecc/resources/pleiades.html*

would be a collection of the outputs. In practice, an image would be divided into tiles and each tile would be sent to a separate machine for analysis.

Some operations require neighborhood-based parallelization, which offers additional challenges. A basic example is image convolution, in which a given spatial kernel is used to compute pixel values using the values from many surrounding pixels. Even more challenging to parallelize are tasks that inherently involve iteration. For example, finite element models which use iteration to find approximate solutions to boundary problems involve data interdependencies that make them difficult to parallelize. Flow models, where flow is computed by executing an unknown number of iterations, are also difficult to parallelize. In such cases, it is often necessary to rely on methods that are non-parallel, and therefore less scalable.

13.4.4 *Local-scale Processing*

Any system that supports analysis of large image datasets needs to subset the data in a variety of ways (e.g., temporally, spatially, and spectrally). A calculation of NDVI on a part of global MODIS image, for example, should apply that calculation to just the area of interest. An analysis of springtime surface water must apply to only those images that were taken at the appropriate times. One of the critical factors impacting the performance of any analysis is the simple act of retrieving the relevant data from disk. Therefore, these filters should restrict not only which output pixels are computed, but also which input pixels are retrieved from disk in the first place. Two means to these ends are lazy evaluation and filter propagation.

13.5 *Conclusion*

A number of requirements have been presented for systems analyzing large image datasets. Some or all of these features have been implemented by a number of systems, for example Google Earth Engine, the NASA Earth Exchange (NEX), and any number of institution-specific systems like the one created by the EROS data center to process Landsat imagery. Increasingly, commercial cloud infrastructure providers, such as Amazon EC2 are providing access to large image datasets as well, without explicitly providing many of the services described above. We believe that adding services on top of the data greatly improves their utility and impact. More is presented in the section on cloud computing.

Our already large image datasets are growing larger. Operational satellites collect more data continually, and more satellites are being added to this existing swarm. In addition, aerial imagery, imagery collected by people, and a variety of ground-based image sensors all provide datasets that present their own challenges. Integrating datasets within a given stratum (e.g., integrating Landsat and MODIS imagery), and analyses that involve multiple strata, such as integrations between aerial and ground data, remains an interesting area of work and provides many future challenges.

14 CLOUD-BASED IMAGE PROCESSING

14.1 *Introduction*

In 2013, Seagate reported that more than 60% of information technology managers have moved to cloud based processing. Since then that number has continued to increase. Managers see improvements in cost of

computing infrastructure, environmental benefits, extended collaboration support and improved security. The benefits of cloud computing apply to image processing as well. This section describes cloud computing in general and provides several case studies of different cloud implementations of image processing.

14.1.1 *Definition of Cloud Computing*

The U.S. National Institute of Standards and Technology (NIST) has defined cloud computing as "a model for enabling ubiquitous, convenient, on-demand network access to a shared pool of configurable computing resources (e.g., networks, servers, storage, applications, and services) that can be provisioned and released rapidly with minimal management effort or service provider interaction." They go on to define five essential characteristics: on-demand self-service, broad network access, resource pooling, rapid elasticity, and measured service.

14.1.2 *Cloud Services*

Cloud services are typically defined as falling into one of three categories: Infrastructure as a Service (IaaS), Platform as a Service (PaaS), and Software as a Service (SaaS).

IaaS suppliers generally provide access to virtual machines that effectively replace computer servers that an organization would need to purchase and maintain on-site. These virtual machines offer traditional processing and storage just as a set of physical servers would. The benefit is that these servers are, in effect, rented and can be used only when needed. This situation is suited perfectly to conditions where computers are not utilized 24 hours a day. Current examples of IaaS services are Google Compute Engine, Amazon EC2, and Microsoft Azure Virtual Machines.

PaaS suppliers offer toolkits and application programming interfaces (APIs) that are designed for developers to leverage into products and services of their own. These services often include databases, Web servers, programming environments, and networking tools. Examples of PaaS are Google App Engine, Amazon Web Services, and services built into Microsoft Azure.

Finally, SaaS supplies provide full Web-based software that runs in their clouds. Web-based solutions for email, tax preparation, social media, data-file storage, spreadsheets and word processing are all examples of SaaS.

Each of these types of services has been used to process images. Google Compute Engine, Amazon EC2, and Microsoft Azure Virtual Machines have all been used to process Earth observation imagery. Google Earth Engine, a cloud-based PaaS for large scale geospatial analysis provides APIs that enable developers to rely on Earth Engine for their geospatial processing. Parts of Earth Engine are also SaaS, providing a Web interface for performing geospatial analysis. Esri ArcGIS® online is another example of SaaS, providing a cloud-based interface to Esri GIS tools.

14.2 *A Menu of Cloud Geospatial Image Processing Features*

Existing cloud-based image processing systems provide a wide variety of features. No system currently supports all the below features, but each of the features occurs in at least one of the systems that was discussed above. The discussion will focus on processing geospatial images such as data collected from Earth observation satellites.

14.2.1 *Core Raster Processing Facilities*

All cloud-based geospatial image processing systems provide raster operations at their foundation. Consider a single scene collected by Landsat-8, the most recent of the Landsat satellites. The core features of any geospatial processing system will support viewing the scene using a single satellite band, composing three satellite bands into an RGB image, stretching the band values to highlight certain sets of values, and performing simple arithmetic on the bands to create indices, such as NDVI. In addition, a geospatial image processing system should be able to reproject imagery into different map projections, subsample imagery to provide a zoomed-out visualization, and combine raster data with geospatially defined vector data.

In addition, geospatial image processing systems should be able to work with collections of images. For example, the Landsat series of satellites takes an image of the same part of the Earth every 16 days. Some of those images are cloudy. However, given that clouds move, a cloud-free composite image can be created. Take a set of images that cover the same area of the Earth and stack them with the most recent Landsat image on the top, making a cube where the X-dimension runs North/South, the Y-dimension runs East/West, and the Z-dimension cuts through time. Then, for each X, Y position, choose the most recent cloud-free pixel to represent that position. If there is a cloud-free pixel, and the cloud detection algorithm is sound, this process will result in a cloud-free mosaic. Any geospatial processing system should be able to manage sets of images in this way. This involves accessing images that are stored in the cloud, and providing tools to filter large collections of images to retrieve just those that are necessary for a given analysis.

Finally, performing statistics on regions on images is a key aspect of any geospatial image processing framework. Computing averages over areas of interest, collecting histograms of values, and calculating slopes of time series are typical examples.

14.2.2 *Interfaces*

Any image processing system requires an interface. That interface can be a GUI that requires no programming abilities, or it can be nothing other than a programming interface that can be called using a given programming language. Cloud image processing systems cover the gamut of possible interfaces.

14.2.3 *Graphical User Interfaces*

Some cloud image processing frameworks rely entirely on a GUI. These services present a set of features that can be configured using options panels. For example, a viewing feature can be configured to select a set of satellite image bands to assign to red, green, and blue, and perhaps provide min and max values to constrain the range of values displayed. More advanced GUIs could apply algorithms as complex as machine learning, or morphological operators like dilation and erosion.

14.2.4 *Application Programming Interfaces*

On the other extreme, some cloud image processing systems have no GUI and are controlled entirely via a programming language. These systems exchange ease of use with flexibility. An API allows other systems, such as Web sites, to issue commands to the image processing system, which then return results that may be visualized in the Web sites. Alternatively, the image processing system can return tables of values

when queried. In each of these cases, a programming language, such as Java, JavaScript, Python, C++, or R is used to issue commands to the image processing system.

14.2.5 *Integrated Development Environments*

Integrated development environments (IDE) can fall between these two extremes. IDEs provide developers a framework for programming against APIs combined with the ability to visualize, debug, and profile the results of their programming efforts. A geospatially informed IDE can provide rapid prototyping of algorithms and methods. When integrated with code versioning systems, an IDE can also provide a framework for collaboration.

14.2.6 *Delivery*

Any cloud image processing system requires mechanisms for disseminating the results of its processing. This can involve storing imagery, either on local computers or in the cloud. It can also involve providing mechanisms to display the results live via Web pages, Web services, or other online mechanisms. The former case is fairly straightforward. The image processing system is required to write bits out to files that are then stored on one or more computers. The main requirement here is that the files are readily available for the intended recipients. The main complexity is determining how best to store the output given the limitations of whatever file format is chosen.

The latter case, providing live access to the data, is more complex. A major consideration here is whether to store the results of analyses on disk, or simply recreate them on demand. Especially when generating extremely large datasets, such as global 30*m* data, it may be that certain areas are never visited. For example, consider the dataset of NDVI for each of the millions of Landsat images. The number of times that the NDVI value of a given pixel in Antarctica in 2012 will be requested is quite small, and probably does not merit being stored when the calculation of NDVI from the source data is quite simple. The complexity of a calculation and the frequency with which that data are requested determines whether or not storing the data makes sense. Given that the costs of processing units are currently dropping more rapidly than the costs of storage, the decision to recompute rather than store will shift steadily toward the side of recompute. This assumes an environment where the processing capabilities of a cloud framework are always available, and not brought up only when processing is needed.

Caching the results of an analysis falls in between storing processed bits on data for download, and reprocessing bits on demand. With caching, the results of an analysis are stored temporarily and eventually age out. The expectation is that if a bit of data is requested once, there is a good chance it will be requested again, but that chance drops over time. Many cloud systems provide caching as a service available to developers building applications.

14.2.7 *Processing Models*

Cloud processing tends to occur in one of two modes: interactive or batch. In interactive mode, an operator can iterate with the system in real-time, running an analysis, checking the results, and adjusting the methodology until it is ready to apply to a larger area. At some point of complexity or scale analyses will take too long for interactive processing, at which point batch mode is used. In batch processing, a set of

resources is reserved for a task, and that task is divided among the allocated processing units. The task is then executed and the results stored in some format.

Both of these modes benefit from being able to parallelize tasks over thousands of computer processing units. The standard map-reduce framework introduced by Google and made open-source through the Hadoop project generally relies on parallelizing operations over many relatively simple computers. Some operations lend themselves easily to being parallelized. For example, operations such as band math on single satellite images can be split easily among as many CPUs as necessary. Simply divide the image into as many pieces as necessary, send each piece to a different CPU, and when each piece is complete, gather and stitch them together to get the result. Other operations, such as computing image segmentation are harder to run in parallel. Since any given object in the image might span the entire image and splitting the image into smaller pieces and segmenting those will result in a set of segmented images, recombining these into a single result presents challenges. What is the best way to join segments that cross the borders of two or more of the divided pieces? In some cases relying on a single computer with a great deal of random access memory (RAM) is more suitable.

14.3 *Cloud Image Processing Implementations*

This section presents three different examples of cloud geospatial image processing systems running on Google infrastructure today, one from each type of cloud computing service type as examples of how cloud computing is currently being applied to geospatial data processing.

14.4 *Infrastructure as a Service*

Google Cloud Platform (GCP) provides data storage through Google Cloud Storage, a variety of database tools such as BigQuery, and computational infrastructure through Google Compute Engine. A number of organizations have used GCP for analysis of Earth Observation data. For example, Descartes Labs has used a petabyte of Landsat data stored in Google Cloud Storage and 30 000 processor cores in Google Compute Engine to estimate global corn crop yields. Having the data already available in Google Cloud Storage meant that Descartes Labs did not have to download and manage the data themselves. Relying on Compute Engine meant that they did not have to purchase and house their own servers. Instead, they could, in effect, borrow the 30 000 cores, perform their analysis and then, give all the cores back. However, Descartes Labs needed to manage all 30 000 cores, ensuring that they were running the appropriate software and managing the processing on their own.

14.5 *Platform as a Service*

While IaaS platforms like Compute Engine provide scalable hardware, they offer little software support for geospatial analyses. In the previous example, Descartes Labs[6] created their own software, installed it on all the processors, and managed all the data. *Platform as as Service* solutions for geospatial analysis provide more software support. The Google Earth Engine platform, for example, provides access to multiple

[6] *http://www.descarteslabs.com/*

petabytes of satellite data and a programming interface to analyze the data. Earth Engine also supports the upload of user specific data, and the download and saving of analyses and the raw input data. The approximately 800 geospatial imaging operations in the Earth Engine library can be combined to create a wide variety of applications, ranging from global forest monitoring (Hansen, *et al.*, 2013) to crop yield estimation (Lobell *et al.*, 2015), and computing urban extents (Zhang, Q., *et al.*, 2015). Earth Engine handles details like parallelizing analyses over a cluster of computers, reprojecting data when necessary, and using filters to access exactly the required data. In addition to using Python or JavaScript to create scripts using its library, called Earth Engine provides an interface for Web sites that would like to call out to the platform to execute geospatial queries. For example, the Global Forest Watch application calls Earth Engine when a user circles an area to discover how much tree cover loss and gain occurred over that area. Similarly the Map of Life application uses Earth Engine to refine species habitat ranges using additional data such as elevation and land cover type. Earth Engine can be called in both an interactive mode, described more below, and in a batch mode for large and complex analyses.

14.6 *Software as a Service*

The Earth Engine platform described above has two main graphical interfaces, each of which can be considered SaaS. The Google Earth Engine Explorer provides a GUI that lets users browse the collection of satellite imagery available and create simple image processing pipelines supporting band math, morphological operations, and machine learning algorithms. This interface is effectively a Web-based version of a desktop system for geospatial image analysis. However, unlike traditional desktop software, analyses run on the Earth Engine Explore are executed by a cluster of computers in parallel. This enables very large analyses that would otherwise not be possible. The Earth Engine Explorer has been used mostly for educational purposes, but has also been used in scientific applications such as measuring mangrove extent in South Asia (Giri *et al.*, 2015).

The Earth Engine Code Editor is an integrated development environment which provides access to documentation, tools for debugging and profiling algorithms developed using the Earth Engine library of operators, an interface into the Earth Engine data catalog, mechanisms for sharing scripts with collaborators, and tools for managing user-uploaded imagery. It supports both an interactive mode, where the results of an analysis can be seen on a map, and a batch mode with simple tools for monitoring the progress of long-running jobs. The Code Editor is one of the primary interfaces into the Earth Engine Platform and has been used to develop all of the methodologies described in the PaaS section of the chapter.

14.7 *Challenges*

Cloud computing has proven itself to be cost effective, energy efficient, and secure. However, moving image processing to the cloud has a number of challenges.

14.7.1 *Internet Access*

The cloud cannot be used without access to the internet. Internet access has been expanding rapidly worldwide. Approximately 40% of the world has access to the internet in 2015, up from 6% in 2000.

Projects such as Project Loon and internet.org, plus more traditional infrastructure expansion aim to remove this limitation over time. That said, people in areas with limited internet connectivity will have limited opportunities to use the cloud for image processing.

14.7.2 *Trust*

A serious hurdle in cloud processing across-the-board is user trust in the cloud. Geospatial data are often sensitive, and people question whether data uploaded to the cloud are secure. Cloud providers counter that data are safer in the cloud than on local machines because cloud providers hire teams of computer security professionals to ensure that their clouds are secure and this claim is borne out by data. Alert Logic's Annual State of Cloud Security, for example, shows regularly that cloud solutions are more secure than on-premise solutions. However, trust continues to be one of the largest barriers to cloud adoption.

14.7.3 *Licensing*

Centralizing the data poses challenges of its own, political and technical. The political challenges relate to data licensing: not all datasets that are useful for performing a required analysis may have licensing that permits their sharing. Some data providers would rather not share their data in this way, due to concerns about processes for updating the data in the future, or due to restrictions on how they would like the data to be used. Non-commercial use policies are not unusual, but can be difficult to enforce in a centralized system and can prevent commercial cloud service providers from hosting data for their users in the first place.

14.7.4 *Versioning*

The version of traditional desktop software can be frozen. Although most modern software packages provide constant updates to improve the software or patch security holes, a user can ensure that the version of the software being used does not change. Similarly, data on a desktop computer can be controlled by the computer's owner. This is different in the cloud, where the cloud provider can update software regularly and may not guarantee that old versions of the software will be maintained or even be available. This absence of guaranteed stability can be a challenge for people who want to ensure that the results of their analyses can be replicated years in the future.

14.8 *Conclusion*

This chapter has described cloud computing as it applies to geospatial imagery analysis, and has given examples of how different kinds of cloud services can apply to the imagery analysis space. Cloud computing is in its infancy, and although impressive results have already been achieved, we are just scratching the surface of what is possible. As more satellite data are made available via these platforms, and more services are provided, the scope of geospatial analyses will continue to expand. Some of the greatest advances may be made in the application of machine learning and artificial intelligence, which are currently revolutionizing applications throughout the cloud. One area to watch is the ability for geospatial analysis platforms to move beyond monitoring the Earth to predicting areas of likely change.

15 CURRENT STATUS AND FUTURE DEVELOPMENTS IN IMAGE PROCESSING AND ANALYSIS

Processing remotely-sensed data is key to a large variety of project workflows and activities, including environmental resource management, food production, and diseases monitoring, among many others. These activities, involving academia, government, non-governmental organizations and the private sector, use data processing techniques to bring immeasurable benefits to human life on Earth, This chapter presented important theory and techniques involved in processing and analyzing those remotely-sensed data. The text introduced pre-processing strategies involved in data preparation and enhancement, and included data processing techniques associated with information extraction. Concepts were illustrated by examples that incorporated the preparation and analysis of those datasets. Future developments in the field are closely associated with the increased availability of remotely-sensed data. For instance, UASs are revolutionizing remote sensing, as well as many fields that use remotely-sensed data for information extraction. Use of rotary or fixed wing aircraft of many sizes and capable of carrying a rich array of sensors has led to high control over image acquisition. Benefits resulting from UAS include shortening revisiting intervals for data collection, as well as full control over the time (e.g., time of the day, season) and environmental conditions when remotely-sensed data are acquired. Small satellites and sensors mounted on orbital platforms (e.g., on the International Space Station) have become an important alternative for data acquisition and should bring significant increase in data availability. The incorporation of UAS and other data sensors into projects also brings multiple image processing and analysis challenges, including those associated with variations in platform attitude, changes in acquisition geometry, atmospheric correction, data fusion, image mosaicking and management of increased volume of data.

In addition, image processing and analysis have benefitted greatly from advances in computing, including multiple development fronts in hardware and software. The large volume of data being acquired challenges our ability to process and use those data efficiently. The increased processing power of computer systems, including the use of multicore systems and applications that make use of specialized GPU to accelerate processing, contribute to reduce processing time and expedite product generation. Initiatives involving cloud processing, such as the NEX and Google Earth Engine, have made available unprecedented processing power to the community of users of remotely-sensed data. A rich image processing and analysis toolset is being produced by those and other initiatives, including the free and open source software efforts. Some of this software include transformative approaches and algorithms, such as deep learning. These advances are empowering the user community and making possible the processing and analysis of vast amounts of data, including multitemporal wall-to-wall renditions of the entire globe at multiple spatial resolutions.

Further, advances in CAL/VAL of sensors have facilitated data processing steps and, in some cases, users may not need to preprocess their data. Agencies, such as the ESA and the USGS, have gone beyond the distribution of raw data and have incorporated multiple processing steps into their image distribution workflows. Geometrically and atmospherically corrected images converted into surface reflectance or into derived products (e.g., vegetation indices and metrics indicating light absorption by vegetation and productivity) are now routinely produced and made available by these groups at no extra cost to the user

community. Current efforts exist to incorporate intelligent payloads into sensor systems, which will enable onboard processing and the downlink of resulting products.

Finally, analyses using data from remote sensors have traditionally emphasized the spatial domain. Increased data availability and longer time series, associated with the increased ability to process and compare these data, have allowed investigations to incorporate changes increasingly over space and time into their analyses and to consider the dynamics of processes happening on our changing planet. Indeed, as our observations and explorations expand beyond the Earth's surface to the subsurface, ocean depths, within and beyond Earth's atmospheric layers and through space, we will continue to stretch our image horizons and understand a myriad of dynamic processes. As a result, these are transformative and exciting times for those involved in image processing and analysis, which is facilitated by the increasing availability of rich datasets and tools to analyze them.

The text presented here will be augmented and revised to reflect the dynamic nature of remote sensing. Future developments in image processing and analysis will be incorporated into this chapter, following a living document concept. Additions to the chapter will include the processing of data acquired in different regions of the electromagnetic spectrum (e.g., thermal and radar) as well as by a variety of sensor platforms that are now becoming available.

16 SECTION AUTHORS

Section 1: Sergio Bernardes and Marguerite Madden (Center for Geospatial Research, Department of Geography, University of Georgia, Athens, GA, USA)

Section 2: E. Lynn Usery (U.S. Geological Survey, Rolla, MO, USA)

Section 3: Eric Vermote (NASA Goddard Space Flight Center, Greenbelt, MD, USA), Jean-Claude Roger and Belen Franch-Gras (Department of Geographical Sciences, University of Maryland, College Park, MD and NASA Goddard Space Flight Center, Greenbelt, MD, USA), and Chris Justice (Department of Geographical Sciences, University of Maryland, College Park, MD, USA)

Section 4:

4.1: Wanxiao Sun (Grand Valley State University, Allendale, MI, USA)

4.2: Sergio Bernardes (Center for Geospatial Research, Department of Geography, University of Georgia, Athens, GA, USA),

Section 5: Tomoaki Miura (Department of Natural Resources and Environmental Management, University of Hawaii at Manoa, Honolulu, HI, USA), Alfredo Huete (University of Technology, Sydney, Sydney, Australia) and Hiroki Yoshioka (Aichi Prefectural University, Nagakute, Japan)

Section 6: Dar A. Roberts (Department of Geography, University of California, Santa Barbara, CA, USA), Ben Somers (Division of Forest, Nature and Landscape, Katholieke Universiteit Leuven, Leuven, Belgium), Laurent Tits (Flemish Institute for Technological Research [VITO], Remote Sensing Unit, Mol., Belgium) and Philip E. Dennison (Department of Geography, University of Utah, Salt Lake City, UT, USA)

Section 7: Akira Hirano (Japan International Research Center for Agricultural Sciences, Tsukuba, Ibaraki, Japan)

Section 8: Wenjing Xu, Caren Remillard and David Cotten (Center for Geospatial Research, Department of Geography, University of Georgia, Athens, GA, USA) and Zhi Zhang (School of Public Administration, China University of Geosciences, Wuhan, China)

Section 9:

9.1: Sergio Bernardes (Center for Geospatial Research, Department of Geography, University of Georgia, Athens, GA, USA)

9.2: Giorgos Mountrakis (Department of Environmental Resources Engineering, State University of New York College of Environmental Science and Forestry, Syracuse, NY, USA)

9.3: Mahesh Pal (Department of Civil Engineering, National Institute of Technology, Kurukshetra, Haryana, India) and Rick L. Lawrence (Spatial Sciences Center, Montana State University, Bozeman, MT, USA)

9.4: Lei Zhang (Center for Urban and Environmental Change, Department of Earth and Environmental Systems, Indiana State University, Terre Haute, IN, USA and The State Key Laboratory of Information Engineering in Surveying, Mapping and Remote Sensing, Wuhan University, Wuhan, China), Xuefei Hu (Department of Environmental Health, Rollins School of Public Health, Emory University, Atlanta, GA, USA) and Qihao Weng (Center for Urban and Environmental Change, Department of Earth and Environmental Systems, Indiana State University, Terre Haute, IN, USA)

9.5: Akira Hirano (Japan International Research Center for Agricultural Sciences, Tsukuba, Ibaraki, Japan)

9.6: Iryna Dronova (Department of Landscape Architecture and Environmental Planning, College of Environmental Design, University of California Berkeley, Berkeley, CA, USA) and Peng Gong (Center for Earth System Science, Tsinghua University, Beijing, China)

Section 10:

10.1 – 10.4: Emilio Chuvieco (Environmental Remote Sensing Research Group, Department of Geology, Geography and Environment, Universidad de Alcalá, Spain), Ioannis Gitas and Dimitris Stavrakoudis (Laboratory of Forest Management and Remote Sensing, School of Forestry and Natural Environment, Aristotle University of Thessaloniki, Greece)

10.5: Cuizhen Wang (Department of Geography, University of South Carolina, Columbia, SC, USA), Linlin Lu (Institute of Remote Sensing and Digital Earth, Chinese Academy of Sciences, Beijing, China)

10.6.1: Mingshu Wang (Center for Geospatial Research, Department of Geography, University of Georgia, Athens, GA, USA)

Section 11:

11.1: Deepak R. Mishra and Ike Astuti (Center for Geospatial Research, Department of Geography, University of Georgia, Athens, GA, USA) and Sachidananda Mishra (Dow Agrosciences LLC, Indianapolis, IN, USA)

11.2: Kunwar K. Singh (Center for Geospatial Analytics, North Carolina State University, Raleigh, NC, USA and Department of Forestry & Environmental Resources, North Carolina State University, Raleigh, NC, USA)

11.3: Allison Howard (Department of Psychology, University of Georgia, Athens, GA, USA and Department of Biology, University of Maryland, College Park, MD, USA)

11.4: Qingyuan Zhang and Tian Yao (Universities Space Research Association, Goddard Earth Sciences and Technology Center and NASA Goddard Space Flight Center, Biospheric Sciences Lab, Greenbelt, MD, USA), Guoqing Sun (Department of Geographical Sciences, University of Maryland, College Park, MD, USA and NASA Goddard Space Flight Center, Biospheric Sciences Lab, Greenbelt, MD, USA) and Sergio Bernardes (Center for Geospatial Research, Department of Geography, University of Georgia, Athens, GA, USA)

Section 12: David L. Cotten, Thomas Jordan, Marguerite Madden and Sergio Bernardes (Center for Geospatial Research, Department of Geography, University of Georgia, Athens, GA, USA)

Section 13: David Thau and Matt Hancher (Google, Mountain View, CA, USA)

Section 14: David Thau and Matt Hancher (Google, Mountain View, CA, USA)

Section 15: Sergio Bernardes and Marguerite Madden (Center for Geospatial Research, Department of Geography, University of Georgia, Athens, GA, USA)

17 REFERENCES

Ablain, M., A. Cazenave, G. Larnicol, M. Balmaseda, P. Cipollini, Y. Faugère, M.J. Fernandes, O. Henry, J.A. Johannessen, P. Knudsen, O. Andersen, J. Legeais, B. Meyssignac, N. Picot, M. Roca, S. Rudenko, M.G. Scharffenberg, D. Stammer, G. Timms and J. Benveniste. 2015. Improved sea level record over the satellite altimetry era (1993-2010) from the Climate Change Initiative project. *Ocean Science.* 11(1):67-82.

Adams, J.B. and A.R. Gillespie. 2006. *Remote Sensing of Landscapes with Spectral Images: A Physical Modeling Approach*. Cambridge University Press. Cambridge, UK. 378 p.

Adams, J.B., D.E. Sabol, V. Kapos, R. Almeida Filho, D.A. Roberts, M.O. Smith, and A.R. Gillespie, 1995. Classification of multispectral images based on fractions of endmembers: Application to land-cover change in the Brazilian Amazon. *Remote Sensing of Environment.* 52:137-154.

Adams, J.B., M.O. Smith and A.R. Gillespie. 1993. Image spectroscopy: Interpretation based on spectral mixture analysis. *Remote Geochemical Analysis: Elemental and Mineralogical Composition.* C.M. Pieters and P.A. Englert, eds., Cambridge University Press, pp. 145-166.

Adams, J.B., M.O. Smith and P.E. Johnson. 1986. Spectral mixture modeling: A new analysis of rock and soil types at the Viking Lander-1 site. *Journal of Geophysical Research: Solid Earth (1978–2012).* 91(B8):8098-8112.

Adams, M.L., W.D. Philpot and W.A. Norvell. 1999. Yellowness index: An application of the spectral second derivative to estimate chlorosis of leaves in stressed vegetation. *International Journal of Remote Sensing.* 20(18):3663-3675.

Addink, E.A., S.M. de Jong and E.J. Pebesma. 2007. The importance of scale in object-based mapping of vegetation parameters with hyperspectral imagery. *Photogrammetric Engineering & Remote Sensing.* 73(8):905-912.

Agca, M., S.C. Popescu and C.W. Harper. 2011. Deriving forest canopy fuel parameters for loblolly pine forests in eastern Texas. *Canadian Journal of Forest Research-Revue Canadienne De Recherche Forestiere.* 41:1618-1625.

Aiazzi, B., L. Alparone and S. Baronti. 2002. Context-driven fusion of high spatial and spectral resolution images based on oversampled multiresolution analysis. *Institute of Electrical and Electronic Engineers Transactions on Geoscience and Remote Sensing.* 40(10).

Alcaraz-Segura, D., E. Chuvieco, H.E. Epstein, E.S. Kasischke and A. Trishchenko. 2010. Debating the greening vs. browning of the North American boreal forest: differences between satellite datasets. *Global Change Biology.* 16(2):760-770.

Amici, G., F. Dell'Acqua, P. Gamba and G. Pulina. 2004. A comparison of fuzzy and neuro-fuzzy data fusion for flooded area mapping using SAR images. *International Journal of Remote Sensing.* 25(20):4425-4430.

Amolins, K., Y. Zhang and P. Dare. 2007. Wavelet based image fusion techniques - An introduction, review and comparison. *ISPRS Journal of Photogrammetry and Remote Sensing.* 62:249-63.

Andersen, H.E., R.J. McGaughey and S.E. Reutebuch. 2005. Estimating forest canopy fuel parameters using LIDAR data. *Remote Sensing of Environment.* 94:441-449.

Anderson, R.P., M. Gómez-Laverde and A. Peterson. 2002. Geographical distributions of spiny pocket mice in South America: Insights from predictive models. *Global Ecology and Biogeography.* 11(2):131-141.

Andrieu, B., F. Baret, S. Jacquemoud, T. Malthus and M. Steven. 1997. Evaluation of an improved version of SAIL model for simulating bidirectional reflectance of sugar beet canopies. *Remote Sensing of Environment.* 60:247-257.

Apte, C. and S. Weiss. 1997. Data mining with decision trees and decision rules. *Future Generation Computer Systems.* 13(2):197-210.

Arangio, S., F. Calò, M.D. Mauro, M. Bonano, M. Marsella and M. Manunta. 2014. An application of the SBAS-D InSAR technique for the assessment of structural damage in the city of Rome. *Structure and Infrastructure Engineering.* 10(11):1469-1483.

Arroyo, L.A., C. Pascual and J.A. Manzanera. 2008. Fire models and methods to map fuel types: The role of remote sensing. *Forest Ecology and Management.* 256:1239-1252.

Asner, G.P. and D.B. Lobell. 2000. A biogeophysical approach for automated SWIR unmixing of soils and vegetation. *Remote Sensing of Environment.* 74(1):99-112.

Asner, G.P. and K.B. Heidebrecht. 2002. Spectral unmixing of vegetation, soil and dry carbon cover in arid regions: Comparing multispectral and hyperspectral observations. *International Journal of Remote Sensing.* 23(19):3939-3958.

Asner, G.P. and K.B. Heidebrecht. 2003. Imaging spectroscopy for desertification studies: Comparing AVIRIS and EO-1 Hyperion in Argentina drylands. *Institute of Electrical and Electronic Engineers. Transactions Geoscience and Remote Sensing.* 41(6):1283-1296.

Asner, G.P. and K.B. Heidebrecht. 2005. Desertification alters regional ecosystem–climate interactions. *Global Change Biology.* 11(1):182-194.

Asner, G.P., M. Keller, R. Pereira Jr., J.C. Zweede and J.N. Silva. 2004. Canopy damage and recovery after selective logging in Amazonia: Field and satellite studies. *Ecological Applications.* 14(sp4):280-298.

Asrar, G., M. Fuchs, E.T. Kanemasu and J.L. Hatfield. 1984. Estimating absorbed photosynthetic radiation and leaf area index from spectral reflectance in wheat. *Agronomy Journal.* 76:300-306.

Atkinson, P.M. and A.R.L. Tatnall. 1997. Introduction: Neural networks in remote sensing. *International Journal of Remote Sensing.* 18:699-709.

Attila, J., S. Koponen, K. Kallio, A. Lindfors, S. Kaitala and P. Ylöstalo. 2013. MERIS Case II water processor comparison on coastal sites of the northern Baltic Sea. *Remote Sensing of Environment.* 128:138-149.

Augustine, J.A. and E.G. Dutton. 2013. Variability of the surface radiation budget over the United States from 1996 through 2011 from high-quality measurements. *Journal of Geophysical Research-Atmosphere.* 118(1):43-53.

Azzali, S., and M. Menenti. 2000. Mapping vegetation-soil-climate complexes in southern Africa using temporal Fourier analysis of NOAA-AVHRR NDVI data. *International Journal of Remote Sensing*, 21:973-196.

Baatz, M. and A. Schäpe. 2000. Multiresolution Segmentation – an optimization approach for high quality multi-scale image segmentation. *Angewandte Geographische Informationsverarbeitung XII* (Strobl, J. *et al*., editors). Wichmann, Heidelberg. pp. 12-23.

Badhwar, G.D., W. Verhoef and N.J.J. Bunnik. 1985. Comparative study of SUITS and SAIL canopy reflectance models. *Remote Sensing of Environment.* 17:179-195.

Baker, C., R. Lawrence, C. Montagne and D. Patten. 2006. Mapping wetlands and riparian areas using Landsat ETM+ imagery and decision tree-based models. *Wetlands.* 26: 465-474.

Balch, J.K. 2014. Atmospheric science: Drought and fire change sink to source. *Nature.* 506:41-42.

Ballantine, J-A C., G.S. Okin, D.E. Prentiss and D.A. Roberts. 2005. Mapping African landforms using continental scale unmixing of MODIS imagery. *Remote Sensing of Environment.* 97:470-483.

Baret, F. and G. Guyot. 1991. Potentials and limits of vegetation indexes for LAI and APAR assessment. *Remote Sensing of Environment.* 35(2-3):161-173.

Baret, F. and T. Fourty. 1997. Radiometric estimates of nitrogen status in leaves and canopies. *Diagnosis of the Nitrogen Status in Crops.* G. Lemaire, editor. Berlin: Springer. pp. 201-227.

Bateson, C., G.P. Asner and C. Wessman. 2000. Endmember bundles: A new approach to incorporating endmember variability into spectral mixture analysis. *Institute of Electrical and Electronic Engineers on Geoscience and Remote Sensing.* 38(2):1083-1094.

Bauer, E. and R. Kohavi. 1999. An empirical comparison of voting classification algorithms: Bagging, boosting, and variants. *Machine Learning.* 36:105-142.

Bazi, Y. and F. Melgani. 2007. Semisupervised PSO-SVM regression for biophysical parameter estimation. *Institute of Electrical and Electronic Engineers Transactions on Geoscience and Remote Sensing.* 45(6):1887-1895.

Beaumont, L.J. and L. Hughes. 2002. Potential changes in the distributions of latitudinally restricted Australian butterfly species in response to climate change. *Global Change Biology.* 8(10):954-971.

Beck, P.S.A., C. Atzberger, K.A. Høgda, B. Johansen and A.K. Skidmore. 2006. Improved monitoring of vegetation dynamics at very high latitude: A new method using MODIS NDVI. *Remote Sensing of Environment.* 100:321-334.

Beck, R. 2003. EO-1 user guide v.2.3. Department of Geography. University of Cincinnati.

Benz, U.C., P. Hofmann, G. Willhauck, I. Lingenfelder and M. Heynen. 2004. Multi-resolution object-oriented fuzzy analysis of remote sensing data for GIS-ready information. *ISPRS Journal of Photogrammetry and Remote Sensing.* 58(3-4):239-258.

Beriaux, E., C. Lucau-Danila, E. Auquiere and P. Defourny, 2013. Multiyear independent validation of the water cloud model for retrieving maize leaf area index from SAR time series. *International Journal of Remote Sensing.* 34(12):4156-4181.

Berk, A., L.S. Bernstein and D.C. Robertson. 1987. MODTRAN: A moderate resolution model for LOWTRAN. *Scientific Report No.1, AFGL-TR-87-0220.* Hanscom AFB, Massachusetts. 35p.

Bernstein, R. 1983. Image geometry and rectification. *Manual of Remote Sensing. 2nd Edition, Volume 1* (R.N. Colwell, editor). American Society for Photogrammetry. Falls Church, VA, pp. 873-922.

Betbeder, J., S. Rapinel, S. Corgne, E. Pottier and L. Hubert-Moy. 2015. TerraSAR-X dual-pol time-series for mapping of wetland vegetation. *ISPRS Journal of Photogrammetry and Remote Sensing.* 107:90-98.

Bhandari, S., S. Phinn and T. Gill, 2012. Preparing Landsat Image Time Series (LITS) for monitoring changes in vegetation phenology in Queensland, Australia. *Remote Sensing.* 4(6):1856-1886.

Biging, G., D.R. Colby and R.G. Congalton. 1998. Sampling Systems for Change Detection Accuracy Assessment. *Remote Sensing Change Detection. Environmental Monitoring Methods and Applications* (R.S. Luneta and C.D. Elvidge, editors). Ann Arbor Press. Chelsea, MI. pp. 281-308.

Bioucas-Dias, J.M., A. Plaza, N. Dobigeon, M. Parente, Q. Du, P. Gader and J. Chanussot. 2012. Hyperspectral unmixing overview: Geometrical, statistical, and sparse regression-based approaches. *Institute of Electrical and Electronic Engineers. Journal of Selected Topics in Applied Earth Observations and Remote Sensing.* 5(2):354-379.

Bishop, C. 1995. *Neural networks for pattern recognition*. New York: Oxford University Press.

Blackburn, G.A. and J.G. Ferwerda. 2008. Retrieval of chlorophyll concentration from leaf reflectance spectra using wavelet analysis. *Remote Sensing of Environment.* 112:1614-1632.

Blanco, P.D., R.R. Colditz, G. López Saldaña, L.A. Hardtke, R.M. Llamas, N.A. Mari, A. Fischer, C. Caride, P.G. Aceñolaza, H.F. del Valle, M. Lillo-Saavedra, F. Coronato, S.A. Opazo, F. Morelli, J.A. Anaya, W.F. Sione, P. Zamboni and V.B. Arroyo. 2013. A land cover map of Latin America and the Caribbean in the framework of the SERENA project. *Remote Sensing of Environment.* 132:13-31.

Blaschke, T. 2010. Object based image analysis for remote sensing. *ISPRS Journal of Photogrammetry and Remote Sensing.* 65(1):2-16.

Blaschke, T., S. Lang and G.J. Hay. 2008. Object-Based Image Analysis: Spatial Concepts for Knowledge-Driven Remote Sensing Applications. Springer Verlage. Berlin. 817 p.

Blaschke, T. and J. Strobl. 2001. What's wrong with pixels? Some recent developments interfacing remote sensing and GIS. *Geo-Information-Systemes.* 14(6):12-17.

Blaschke, T., G.J. Hay, M. Kelly, S. Lang, P. Hofmann, E. Addink, R. Queiroz Feitosa, F. van der Meer, H. van der Werff, F. van Coillie and D. Tiede. 2014. Geographic object-based image analysis - towards a new paradigm. *ISPRS Journal of Photogrammetry and Remote Sensing.* 87:180-191.

Bloomfield, P. 2000. *Fourier analysis of time series: an introduction.* 2nd ed. Wiley. New York. 261 p.

Boardman, J.W. 1989. Inversion of imaging spectrometry data using singular value decomposition. *Proceedings IGARSS 1989.* Vancouver, CA. pp. 2069-2072.

Boardman, J.W. 1993. Automating spectral unmixing of AVIRIS data using convex geometry concepts. *4th JPL Airborne Geoscience Workshop*. JPL Publication 93-26. 1:11-14.

Boardman, J.W. and F.A. Kruse. 1994. Automated spectral analysis: A geological example using AVIRIS data (from) north Grapevine Mountains, Nevada. *Proceedings, Tenth Thematic Conference on Geologic Remote Sensing.* Ann Arbor, Michigan (Environmental Research Institute of Michigan). I: 407-418.

Boardman, J.W., F.A. Kruse and R.O. Green. 1995. Mapping target signatures via partial unmixing of AVIRIS data. *Summaries of the 5th Airborne Earth Science Workshop.* 23-26 January. JPL Publication. Vol. 95(1):23-26.

Bojinski, S., M. Verstraete, T.C. Peterson, C. Richter, A. Simmons and M. Zemp. 2014. The concept of essential climate variables in support of climate research, applications, and policy. *Bulletin of the American Meteorological Society.* 95(9):1431-1443.

Bolstad, P.V. 2008. GIS Fundamentals: A First Textbook on Geographic Information Systems. Eider Press, White Bear Lake, MN.

Bontemps, S., P. Bogaert, N. Titeux and P. Defourny. 2008. An object-based change detection method accounting for temporal dependences in time series with medium-to-coarse spatial resolution. *Remote Sensing of Environment.* 112(6):3181-3191.

Borel, C.G. and S.A.W. Gerstl. 1994. Nonlinear spectral mixing models for vegetative and soil surfaces. *Remote Sensing of Environment.* 47:403-416.

Boschetti, M., D. Stroppiana, P.A. Brivio and S. Bocchi. 2009. Multi-year monitoring of rice crop phenology through time series analysis of MODIS images. *International Journal of Remote Sensing.* 30(18):4643-4662.

Bovolo, F. and L. Bruzzone. 2005. A detail-preserving scale-driven approach to change detection in multitemporal SAR images. *Institute of Electrical and Electronic Engineers Transactions on Geoscience and Remote Sensing*, 43:2963-2972.

Bradley, B.A., A.D. Olsson, O. Wang, B.G. Dickson, L. Pelech, S.E. Sesnie and L.J. Zachmann. 2012. Species detection vs. habitat suitability: Are we biasing habitat suitability models with remotely sensed data? *Ecological Modelling.* 244:57-64.

Bradley, B.A., R.W. Jacob, J.F. Hermance and J.F. Mustard. 2007. A curve fitting procedure to derive inter-annual phenologies from time series of noisy satellite NDVI data. *Remote Sensing of Environment.*106:137-145.

Brandt, M., C. Mbow, A.A. Diouf, A. Verger, C. Samimi and R. Fensholt. 2015. Ground- and satellite-based evidence of the biophysical mechanisms behind the greening Sahel. *Global Change Biology.* 21(4):1610-1620.

Braswell, B.H., D.S. Schimel, J.L. Privette, B. Moore, W.J. Emery, E.W. Sulzman and A.T. Hudak. 1996. Extracting ecological and biophysical information from AVHRR optical data: An integrated algorithm based on inverse modeling. *Journal of Geophysical Research.* 101:23335-23348.

Braswell, B.H., W.J. Sacks, E. Linder and D.S. Schimel. 2005. Estimating diurnal to annual ecosystem parameters by synthesis of a carbon flux model with eddy covariance net ecosystem exchange observations. *Global Change Biology.* 11:335-355.

Breiman, L. 1996. Bagging predictors. *Machine Learning.* 24:123-140.

Breiman, L. 2001. Random forests. *Machine Learning.* 45:5-32.

Breiman, L., J.H. Friedman, R.A. Olshen and C.J. Stone. 1984. *Classification and Regression Trees.* Wadsworth International Group, Belmont, California. USA.

Brigham, E.O. 1988. *The fast Fourier transform and its applications.* Prentice Hall, Englewood Cliffs, New Jersey. 448 p.

Brodley, C.E. and P.E. Utgoff. 1992. Multivariate versus univariate decision trees. *Technical Report 92-8.* Department of Computer Science, University of Massachusetts, Amherst, Massachusetts, USA.

Bruce, L.M., C.H. Koger and J. Li. 2002. Dimensionality reduction of hyperspectral data using discrete wavelet transform feature extraction. *Institute of Electrical and Electronic Engineers Transactions on Geoscience and Remote Sensing.* 40:2331-2338.

Bruzzone, L. and D. Fernández-Prieto. 2000. An adaptive parcel-based technique for unsupervised change detection. *International Journal of Remote Sensing.* 21(4):817-822.

Burges, C.J.C. 1998. A tutorial on support vector machines for pattern recognition. *Data Mining and Knowledge Discovery.* 2(2):121-167.

Burns, J. 2012. Applications of LIDAR in wildlife management: an opportunity in British Columbia. Forestry Undergraduate Essay/Thesis. University of British Columbia Library.

Burrough, P.A. 1981. Fractal dimensions of landscapes and other environmental data. *Nature* 294: 240-242.

Burrough, P.A. 1993. Fractals and geostatistical methods in landscape studies. *Fractals in Geography.* (N. S.-N. Lam and L. De Cola, editors). Prentice Hall, New Jersey. pp. 87-121.

Busby, J.R. 1991. BIOCLIM-A bioclimatic analysis and prediction system. In: C.R. Margules and M.P. Austin (eds.). *Nature Conservation: Cost effective Biological Surveys and Data Analysis*. 64-68. Canberra, CSIRO.

Camacho, F., J. Cernicharo, R. Lacaze, F. Baret and M. Weiss. 2013. GEOV1: LAI, FAPAR essential climate variables and FCOVER global time series capitalizing over existing products. Part 2: Validation and intercomparison with reference products. *Remote Sensing of Environment.* 137:310-329.

Camps-Valls, G., L. Gomez-Chova, J. Calpe-Maravilla, J.D. Martin-Guerrero, E. Soria-Olivas, L. Alonso-Chorda and J. Moreno. 2004. Robust support vector method for hyperspectral data classification and knowledge discovery. *Institute of Electrical and Electronic Engineers. Transactions on Geoscience and Remote Sensing.* 42(7):1530-1542.

Cao, C., F.J. DeLuccia, X. Xiong, R. Wolfe and F. Weng. 2014. Early on-orbit performance of the Visible Infrared Imaging Radiometer Suite onboard the Suomi National Polar-Orbiting Partnership (S-NPP) satellite. *Institute of Electrical and Electronic Engineers. Transactions on Geoscience and Remote Sensing.* 52(2):1142-1156.

Cao, C., X. Xiong, A. Wu and X. Wu. 2008. Assessing the consistency of AVHRR and MODIS L1B reflectance for generating fundamental climate data records. *Journal of Geophysical Research.* 113(D9).

Caraux, D. and R.W. Austin. 1983. Delineation of seasonal changes of chlorophyll frontal boundaries in Mediterranean coastal waters with Nimbus-7 Coastal Zone Color Scanner data. *Remote Sensing of Environment.*13:239-249.

Carpenter, G., A.N. Gillison and J. Winter. 1993. Domail: A flexible modelling procedure for mapping potential distributions of plants and animals. *Biodiversity and Conservation*. 2:667-680.

Carpenter, G.A., S. Gopal, S. Macomber, S. Martens, C.E. Woodcock and J. Franklin. 1999. A neural network method for efficient vegetation mapping. *Remote Sensing of Environment.* 70(3):326-338.

Carter, G.A. and A.K. Knapp. 2001. Leaf optical properties in higher plants: linking spectral characteristics to stress and chlorophyll concentration. *American Journal of Botany.* 88(4):677-684.

Cascini, L., D. Peduto, D. Reale, L. Arena, S. Ferlisi, S. Verde and G. Fornaro. 2013. Detection and monitoring of facilities exposed to subsidence phenomena via past and current generation SAR sensors. *Journal of Geophysics and Engineering*. 10(6):064001.

Cavanaugh, K.C., D.A. Siegel, D.C. Reed and P.E. Dennison. 2011. Environmental controls of giant-kelp biomass in the Santa Barbara Channel, California. *Marine Ecology Progress Series.* 429:1-17.

Chander, G., B.L. Markham and D.L. Helder. 2009. Summary of current radiometric calibration coefficients for Landsat MSS, TM, ETM+ and EO-1 ALI sensors. *Remote Sensing of Environment.* 113(5):893-903.

Chavez, P.S. 1988. An improved dark-object subtraction technique for atmospheric scattering correction of multispectral data. *Remote Sensing of Environment.* 24:459-479.

Chavez, P.S. 1996. Image-based atmospheric corrections revisited and improved. *Photogrammetric Engineering & Remote Sensing.* 62(9):1025-1036.

Chen, B., H. Gong, X. Li, K. Lei, M. Gao, C. Zhou and Y. Ke. 2015. Spatial–temporal evolution patterns of land subsidence with different situation of space utilization. *Natural Hazards.* 77(3):1765-1783.

Chen, C.F., N.T. Son, L.Y. Chang and C.R. Chen. 2011. Classification of rice cropping systems by empirical mode decomposition and linear mixture model for time-series MODIS 250*m* NDVI data in the Mekong Delta, Vietnam. *International Journal of Remote Sensing.* 32(18):5115-5134.

Chen, C.M., G.F. Hepner and R.R. Forster. 2003. Fusion of hyperspectral and radar data using the HIS transformation to enhance urban surface features. *ISPRS Journal of Photogrammetry & Remote Sensing.* 58:19-30.

Chen, J., P. Gong, C. He, R. Pu and P. Shi. 2003. Land use/land cover change detection using improved change-vector analysis. *Photogrammetric Engineering and Remote Sensing.* 69(4):369-379.

Chen, J., J. Wu, L. Zhang, J. Zou, G. Liu, R. Zhang and B. Yu. 2013. Deformation trend extraction based on multitemporal InSAR in Shanghai. *Remote Sensing.* 5(4):1774-1786.

Chen, J., P. Jonsson, M. Tamura, Z.H. Gu, B. Matsushita and L. Eklundh. 2004. A simple method for reconstructing a high-quality NDVI time-series data set based on the Savitzky–Golay filter. *Remote Sensing of Environment.* 91:332-344.

Chen, Q.S., M. Defrise and F. Deconinck. 1994. Symmetrical phase-only matched filtering of Fourier-Mellin transforms for image registration and recognition. *Institute of Electrical and Electronic Engineers. Transactions on Pattern Analysis and Machine Intelligence* 16:1156-1168.

Chen, S., R. Zhang, H. Su, J. Tian and J. Xia. 2010. SAR and multispectral image fusion using generalized IHS transform based on Atrous wavelet and EMD decompositions. *Institute of Electrical and Electronic Engineers IEEE Sensors Journal.* 10(3):737-745.

Chen, S-H, H. Su, Z. Renhua and T. Jing. 2008. Fusing remote sensing images using à trous wavelet transform and empirical mode decomposition. *Pattern Recognition Letters.* 29(3):330-342.

Chen, X. and L. Vierling. 2006. Spectral mixture analyses of hyperspectral data acquired using a tethered balloon. *Remote Sensing of Environment.* 103(3):338-350.

Chen, X., J. Chen, X. Jia, B. Somers, J. Wu and P. Coppin. 2011. A quantitative analysis of virtual endmembers' increased impact on the collinearity effect in spectral unmixing. *Institute of Electrical and Electronic Engineers. IEEE Transactions on Geoscience and Remote Sensing.* 49:2945-56.

Cheng, T., B. Rivard, A.G. Sanchez-Azofeifa, J.B. Feret, S. Jacquemoud and S.L. Ustin. 2014. Deriving leaf mass per area (LMA) from foliar reflectance across a variety of plant species using continuous wavelet analysis. *ISPRS Journal of Photogrammetry and Remote Sensing*.87:28-38.

Christopoulos, C., A. Skodras and T. Ebrahimi. 2000. The JPEG2000 still image coding system: An overview. *Institute of Electrical and Electronic Engineers. Transactions on Consumer Electronics* 46:1103-1127.

Chuvieco, E. 2016. Fundamentals of Satellite Remote Sensing: An Environmental Approach. CRC Press, Boca Raton, Florida.

Chuvieco, E., C. Yue, A. Heil, F. Mouillot, I. Alonso-Canas, M. Padilla, J.M. Pereira, D. Oom and K. Tansey. 2016. A new global burned area product for climate assessment of fire impacts. *Global Ecology and Biogeography*. 25: 619-629.

Chuvieco, E., G. Ventura, M.P. Martín and I. Gómez. 2005. Assessment of multitemporal compositing techniques of MODIS and AVHRR images for burned land mapping. *Remote Sensing of Environment.* 94(4):450-462.

Chuvieco, E., S. Opazo, W. Sione, H. Del Valle, J. Anaya, C. Di Bella, I. Cruz, L. Manzo, G. López, N. Mari, F. González-Alonso, F. Morelli, A. Setzer, I. Csiszar, J.A. Kanpandegi, A. Bastarrika and R. Libonati. 2008. Global burned land estimation in Latin America using MODIS composite Data. *Ecological Applications.* 18(1):64-79.

Cihlar, J. 1996. Identification of contaminated pixels in AVHRR composite images for studies of land biosphere. *Remote Sensing of Environment.* 56:149-153.

Cihlar, J., D. Manak and N. Voisin. 1994. AVHRR bidirectional reflectance effects and compositing. *Remote Sensing of Environment.* 48(1):77-88.

Cihlar, J., H. Ly, Z. Li, J. Chen, H. Pokrant and F. Huang. 1997. Multitemporal, multichannel AVHRR data sets for land biosphere studies - Artifacts and corrections. *Remote Sensing of Environment.* 60(1):35-57.

Clark, R.N., A.J. Gallagher and G.A. Swayze. 1990. Material absorption band depth mapping of imaging spectrometer data using the complete band shape least-squares algorithm simultaneously fit to multiple spectral features from multiple materials. *Proceedings Third Airborne Visible/Infrared Imaging Spectrometer (AVIRIS) Workshop.* JPL Publication 90-54:176-186.

Clarke, K.C. 1986. Computation of the fractal dimension of topographic surfaces using the triangular prism surface area method. *Computers & Geosciences.* 12:713-722.

Clarke, K.C. and D.M. Schweizer. 1991. Measuring the fractal dimension of natural surfaces using a robust fractal estimator. *Cartography and Geographic Information Systems.* 18:37-47.

Clinton, N., A. Holt, J. Scarborough, L. Yan and P. Gong. 2010. Accuracy assessment measures for object-based image segmentation goodness. *Photogrammetric Engineering & Remote Sensing.* 76(3):289-299.

Cochrane, M.A., 2003. Fire science for rainforests. *Nature.* 421:913-919.

Cohen, W.B., Z. Yang and R. Kennedy. 2010. Detecting trends in forest disturbance and recovery using yearly Landsat time series: 2. TimeSync - Tools for calibration and validation. *Remote Sensing of Environment.* 114(12):2911-2924.

Coldewey-Egbers, M., D.G. Loyola, M. Koukouli, D. Balis, J.-C. Lambert, T. Verhoelst, J. Granville, M.van Roozendael, C. Lerot, R. Spurr, S.M. Frith and C. Zehner. 2015. The GOME-type Total Ozone Essential Climate Variable (GTO-ECV) data record from the ESA Climate Change Initiative. *Atmospheric Measurements Techniques.* 8(9):3923-3940.

Congalton, R.G. 1991. A review of assessing the accuracy of classifications of remotely sensed data. *Remote Sensing of Environment.* 37(1):35-46.

Congalton, R. and K. Green. 2009. *Assessing the Accuracy of Remotely Sensed Data: Principles and Practices* (2nd ed.). RC/Taylor and Francis. Boca Raton, Florida.

Coops, N.C., N. Goodwin and C. Stone. 2006. Predicting *Sphaeropsis sapinea* damage in *Pinus radiata* canopies using spectral indices and spectral mixture analysis. *Photogrammetric Engineering & Remote Sensing.* 72(4):405-416.

Coppin, P.R. and M.E. Bauer. 1994. Processing of multitemporal Landsat TM imagery to optimize extraction of forest cover change features. *Institute of Electrical and Electronic Engineers Transactions on Geoscience and Remote Sensing.* 32:918-927.

Coulson, K.L., J.V. Dave and Z. Sckera. 1960. *Tables Related to Radiation Emerging from a Planetary Atmosphere with Rayleigh Scattering*. Berkeley. University of California Press. 548 p.

Craig, S.E., S.E. Lohrenz, Z. Lee, K.L. Mahoney, G.J. Kirkpatrick, O.M. Schofield and R.G. Steward. 2006. Use of hyperspectral remote sensing reflectance for detection and assessment of the harmful algae, *Karenia brevis*. *Applied Optics. 45*(21):5414-5425.

Crist, E.P and R.C. Cicone. 1984. A physically-based transformation of Thematic Mapper data - The TM Tasseled Cap. *Institute of Electrical and Electronic Engineers. Transactions on Geoscience and Remote Sensing.* GE-22(3):256-263.

D'Odorico, P., A. Gonsamo, B. Pinty, N. Gobron, N. Coops, E., Mendez and M.E. Schaepman. 2014. Intercomparison of fraction of absorbed photosynthetically active radiation products derived from satellite data over Europe. *Remote Sensing of Environment.* 142:141-154.

Dall'Olmo, G. and A.A. Gitelson. 2005. Effect of bio-optical parameter variability on the remote estimation of chlorophyll-*a* concentration in turbid productive waters: Experimental results. *Applied Optics*. 44: 412-422.

Dall'Olmo, G., A.A. Gitelson and D.C. Rundquist. 2003. Towards a unified approach for remote estimation of chlorophyll-*a* in both terrestrial vegetation and turbid productive waters. *Geophysical Research Letters.* 30(18).

Damerval, C., S. Meignen and V. Perrier. 2005. A fast algorithm for bidimensional EMD. *Institute of Electrical and Electronic Engineers. Signal Processing Letters.* 12(10):701-704.

Datt, B., T.R. McVicar, T.G. Van Niel, D.L. Jupp and J.S. Pearlman. 2003. Preprocessing EO-1 Hyperion hyperspectral data to support the application of agricultural indexes. *Institute of Electrical and Electronic Engineers IEEE. Transactions on Geoscience and Remote Sensing.* 41(6):1246-1259.

Dave, C.P., R. Joshi and S.S. Srivastava. 2015. A Survey on geometric correction of satellite imagery. *International Journal of Computer Applications.* 116(12):24-27.

Davidson, E.A., G.P. Asner, T.A. Stone, C. Neill and R.O. Figueiredo. 2008. Objective indicators of pasture degradation from spectral mixture analysis of Landsat imagery. *Journal of Geophysical Research: Biogeosciences (2005–2012).*113(G1).

De'ath, G. 2007. Boosted trees for ecological modelling and prediction. *Ecology.* 88:243-251.

De Bernardis, C.G., F. Vicente-Guijalba, T. Martinez-Marin and J.M. Lopez-Sanchez. 2015. Estimation of key dates and stages in rice crops using dual-polarization SAR time series and a particle filtering approach. *Institute of Electrical and Electronic Engineers. Journal of Selected Topics in Applied Earth Observations and Remote Sensing.* 8(3):1008-1018.

de Beurs, K.M. and G.M. Henebry. 2004. Land surface phenology, climatic variation, and institutional change: Analyzing agricultural land cover change in Kazakhstan. *Remote Sensing of Environment.* 89:497-509.

De Cola, L. 1989. Fractal Analysis of a classified Landsat scene. *Photogrammetric Engineering and Remote Sensing*. 55:601-610.

De Jong, S.M. and P.A. Burrough. 1995. A fractal approach to the classification of Mediterranean vegetation types in remotely sensed images. *Photogrammetric Engineering and Remote Sensing.* 61:1041-1053.

De Keersmaecker, W., S. Lhermitte, L. Tits, O. Honnay, B. Somers and P. Coppin. 2015. A model quantifying global vegetation resistance and resilience to short-term climate anomalies and their relationship with vegetation cover. *Global Ecology and Biogeography.* 24(5):539-548.

Definiens, A. 2009. *Definiens eCognition Developer 8 User Guide*. Definens AG, Munchen, Germany.

DeFries R.S. and J.C.W. Chan. 2000. Multiple criteria for evaluating machine learning algorithms for land cover classification from satellite data. *Remote Sensing of Environment.* 37:35-46.

Dehecq, A., N. Gourmelen and E. Trouve. 2015. Deriving large-scale glacier velocities from a complete satellite archive: Application to the Pamir–Karakoram–Himalaya. *Remote Sensing of Environment.* 162:55-66.

Delaplace, K.L.W., F.M.B. Van Coillie, R.R. De Wulf, D. Gabriels, K. De Smet, M. Ouessar, A.O. Belgacem and T. Houcine. 2010. Object-based assessment of tree attributes of *Acacia tortilis* in Bou-Hedma, Tunisia. *Geobia 2010: Geographic Object-Based Image Analysis. 38-4-C7.*

Dellaert, F., S.M. Seitz, C.E. Thorpe and S. Thrun. 2000. Structure from motion without correspondence. *Proceedings of the Institute of Electrical and Electronic Engineers Conference on Computer Vision and Pattern Recognition.* Hilton Head Island, South Carolina, USA. pp. 557-564.

Demarchi, L., F. Canters, J.C.W. Chan and T. Van de Voorde. 2012. Multiple endmember unmixing of CHRIS/Proba imagery for mapping impervious surfaces in urban and suburban environments. *Institute of Electrical and Electronic Engineers Transactions on Geoscience and Remote Sensing.* 50(9):3409-3424.

Demarez, V., J.P. Gastellu-Etchegorry, E. Mougin, G. Marty, C. Proisy, E. Dufrene and V. Le Dantec. 1999. Seasonal variation of leaf chlorophyll content of a temperate forest. Inversion of the PROSPECT model. *International Journal of Remote Sensing.* 20:879-894.

Demetriades-Shah, T.H., M.D. Steven and J.A. Clark. 1990. High resolution derivative spectra in remote sensing. *Remote Sensing of Environment.* 33:55-64.

Demir, B. and S. Erturk. 2010. Empirical mode decomposition of hyperspectral images for support vector machine classification. *Institute of Electrical and Electronic Engineers Transactions on Geoscience and Remote Sensing.* 48(11):4071-4084.

Deng, C. and C. Wu. 2012. BCI: A biophysical composition index for remote sensing of urban environments. *Remote Sensing of Environment.* 127:247-259.

Deng, C. and C. Wu. 2013. A spatially adaptive spectral mixture analysis for mapping subpixel urban impervious surface distribution. *Remote Sensing of Environment.* 133:62-70.

Dennison, P.E. and D.A. Roberts. 2003a. Endmember selection for Multiple Endmember Spectral Mixture Analysis using endmember average RSME. *Remote Sensing of Environment*. 87(2-3):123-125.

Dennison, P. E. and D.A. Roberts. 2003b. Effects of vegetation phenology on endmember selection and species mapping in Southern California chaparral. *Remote Sensing of Environment.* 87(2):295-309.

Dennison, P.E., K. Charoensiri, D.A. Roberts, S.H. Peterson and R.O. Green. 2006. Wildfire temperature and land cover modeling using hyperspectral data. *Remote Sensing of Environment.* 100(2):212-222.

Dennison, P.E., K.Q. Halligan and D.A. Roberts. 2004. A comparison of error metrics and constraints for multiple endmember spectral mixture analysis and spectral angle mapper. *Remote Sensing of Environment.* 93:359-367.

Deschamps, P.Y., M. Herman and D. Tanre. 1983. Modeling of the atmospheric effects and its application to the remote sensing of ocean color. *Applied Optics*. 22(23):3751-3758.

Dezso, B., R. Giachetta, I. Laszlo and I. Fekete. 2012. Experimental study on graph-based image segmentation methods in the classification of satellite images. *EARSeL eProceedings.* 11(1):12-24.

Di Bella, C.M., J.M. Paruelo, J.E. Becerra, C. Bacour and F. Baret. 2004. Effect of senescent leaves on NDVI-based estimates of f APAR: experimental and modelling evidences. *International Journal of Remote Sensing.* 25:5415-5427.

Di, K., R. Ma and R.X. Li. 2003. Rational functions and potential for rigorous sensor model recovery. *Photogrammetric Engineering & Remote Sensing.* 69(1):33-41.

Didan, K., A. Barreto-Munoz, T. Miura, J. Tsend-Ayush, X.Y. Zhang, M. Friedl, J. Gray, W. van Leeuwen, J. Czapla-Myers, S. Doman-Bennett, C. Jenkerson, T. Maiersperger and D. Meyer. 2015. Multi-Sensor Vegetation Index and Phenology Earth Science Data Records: Algorithm Theoretical Basis Document and User Guide (Version 4.0). *https://vip.arizona.edu/VIP_ATBD_UsersGuide.php.* University of Arizona. Tucson, Arizona.

Dierssen, H.M. 2010. Perspectives on empirical approaches for ocean color remote sensing of chlorophyll in a changing climate. *Proceedings of the National Academy of Sciences.* 107(40):17073-17078.

Dils, B., M. Buchwitz, M. Reuter, O. Schneising, H. Boesch, R. Parker, S. Guerlet, I. Aben, T. Blumenstock, J.P. Burrows, A. Butz, N.M. Deutscher, C. Frankenberg, F. Hase, O.P. Hasekamp, J. Heymann, M. De Mazière, J. Notholt, R. Sussmann, T. Warneke, D. Griffith, V. Sherlock and D. Wunch. 2014. The Greenhouse Gas Climate Change Initiative (GHG-CCI): comparative validation of GHG-CCI SCIAMACHY/ENVISAT and TANSO-FTS/GOSAT CO2 and CH4 retrieval algorithm products with measurements from the TCCON. *Atmospheric Measurements Techniques.* 7(6):1723-1744.

Diner, D.J., J.C. Beckert, T.H. Reilly, C.J. Bruegge, J.E. Conel, R.A. Kahn, J.V. Martonchik, T.P. Ackerman, R. Davies, S.A.W. Gerstl, H.R. Gordon, J.-P. Muller, R.B. Myneni, P.J. Sellers, B. Pinty and M.M. Verstraete. 1998. Multi-angle Imaging SpectroRadiometer (MISR) instrument description and experiment overview. *Institute of Electrical and Electronic Engineers. Transactions on Geoscience and Remote Sensing.* 36(4):1072-1087.

Dixon, B. and N. Candade. 2008. Multispectral landuse classification using neural networks and support vector machines: one or the other, or both? *International Journal of Remote Sensing.* 29(4):1185-1206.

Dobigeon, N., L. Tits, B. Somers, Y. Altmann and P. Coppin. 2014. A comparison of nonlinear mixing models for vegetated areas using simulated and real hyperspectral data. *Institute of Electrical and Electronic Engineers Journal of Selected Topics in Applied Earth Observations and Remote Sensing.* 7(6):1869-1878.

Dong, W., X. Li, X. Lin and Z. Li. 2014. A bidimensional empirical mode decomposition method for fusion of multispectral and panchromatic remote sensing images. *Remote Sensing.* 6(9):8446.

Dong, X., S. Quegan, U. Yumiko, C. Hu and T. Zeng. 2015. Feasibility study of C- and L-band SAR time series data in tracking Indonesian plantation and natural forest cover changes. *Institute of Electrical and Electronic Engineers. Journal of Selected Topics in Applied Earth Observations and Remote Sensing.* 8(7):3692-3699.

Dorigo, W.A., A. Gruber, R.A.M. De Jeu, W. Wagner, T. Stacke, A. Loew, C. Albergel, L. Brocca, D. Chung, R.M. Parinussa and R. Kidd. 2015. Evaluation of the ESA CCI soil moisture product using ground-based observations. *Remote Sensing of Environment.* 162:380-395.

Dowman, I. and J.T. Dolloff. 2000. An evaluation of rational functions for photogrammetric restitution. *International Archives of Photogrammetry and Remote Sensing. Vol. XXXIII, Part B3:* 254-266, Amsterdam.

Dragotti, P.L., C. Poggi and A.R.P. Ragozini. 2000. Compression of multispectral images by three-dimensional SPIHT algorithm. *Institute of Electrical and Electronic Engineers. Transactions on Geoscience and Remote Sensing.* 38:416-428.

Dragut, L., C. Eisank and T. Strasser. 2011. Local variance for multi-scale analysis in geomorphometry. *Geomorphology.* 130(3-4):162-172.

Dragut, L., D. Tiede and S.R. Levick. 2010. ESP: A tool to estimate scale parameter for multiresolution image segmentation of remotely sensed data. *International Journal of Geographical Information Science.* 24(6):859-871.

Dragut, L., O. Csillik, C. Eisank and D. Tiede. 2014. Automated parameterisation for multi-scale image segmentation on multiple layers. *ISPRS Journal of Photogrammetry and Remote Sensing.* 88:119-127.

Drobot, S., D. Robinson, A. Laing, R. Barry, J. Campbell, R. Defries, B. Emery, M. Halem, J. Hurrell, R. Miller, R. Myneni, R. Somerville, P. Try and T.V. Haar. 2004. Climate data records from environmental satellites. 13th Conference on Satellite Meteorology and Oceanography. 20-23 September. Norfolk, VA, USA.

Dronova, I. 2015. Object-based image analysis in wetland research: A review. *Remote Sensing.* 7(5):6380-6413.

Dronova, I., P. Gong, L. Wang and L. Zhong. 2015. Mapping dynamic cover types in a large seasonally flooded wetland using extended principal component analysis and object-based classification. *Remote Sensing of Environment.* 158:193-206.

Dronova, I., P. Gong, N.E. Clinton, L. Wang, W. Fu, S. Qi and Y. Liu. 2012. Landscape analysis of wetland plant functional types: The effects of image segmentation scale, vegetation classes and classification methods. *Remote Sensing of Environment.* 127:357-369.

Du, W., K. Inoue and K. Urahama. 2005. Robust kernel fuzzy clustering. *Proceedings Second International Conference on Fuzzy Systems and Knowledge Discovery.* Changsha, China. pp. 454-461.

Dubovik, O., A. Smirnov, B.N. Holben, M.D. King, Y.J. Kaufman, T.F. Eck and I. Slutsker. 2000. Accuracy assessments of aerosol optical properties retrieved from Aerosol Robotic Network (AERONET) sun and sky radiance measurements. *Journal of Geophysical Research.* 105(D8):9791-9806.

Dubovik, O., B. Holben, T.F. Eck, A. Smirnov, Y.J. Kaufman, M.D. King, D. Tanré and I. Slutsker. 2002. Variability of absorption and optical properties of key aerosol types observed in worldwide locations. *Journal of the Atmospheric Sciences.* 59(3):590-608.

Dubuisson-Jolly, M.P. and A. Gupta. 2000. Color and texture fusion: Application to aerial image segmentation and GIS updating. *Image and Vision Computing.* 18(10):823-832.

Duncanson, L.I., K.O. Niemann and M.A. Wulder. 2010. Estimating forest canopy height and terrain relief from GLAS waveform metrics. *Remote Sensing of Environment.* 114(1):138-154.

Durieux, L., J. Kropacex, G.D.D. Grandi and F. Achard. 2007. Object-oriented and textural image classification of the Siberia GBFM radar mosaic combined with MERIS imagery for continental scale land cover mapping. *International Journal of Remote Sensing.* 28(18):4175-4182.

Eastman, J.R. 2006. *IDRISI Andes: Guide to GIS and image processing.* Clark University, Worcester, Massachusetts.

Eastman, J.R., J. McKendry and M. Fulk. 1994. UNITAR Explorations in GIS Technology, vol. 1: Change and Time Series Analysis, Geneve, Switzerland.

Eckmann, T., D.A. Roberts and C. Still. 2008. Using Multiple Endmember Spectral Mixture Analysis to retrieve subpixel fire properties from MODIS. *Remote Sensing of Environment.* 112(10):3773-3783.

Ecognition. 2012. e-Cognition Reference Book v. 8.8. Trimble Inc.

Eerens, H., D. Haesen, F. Rembold, F. Urbano, C. Tote and L. Bydekerke. 2014. Image time series processing for agriculture monitoring. *Environmental Modelling & Software.* 53:154-162.

Elith, J. and J.R. Leathwick. 2009. Species distribution models: Ecological explanation and prediction across space and time. *Systematics.* 677-697.

Elith, J., C.H. Graham, R.P. Anderson, M. Dudík, S. Ferrier, A. Guisan, R.J. Hijmans, F. Huettmann, J.R. Leathwick, A. Lehmann, J. Li, L.G. Lohmann, B.A. Loiselle, G. Manion, C. Moritz, M. Nakamura, Y. Nakazawa, J.C.M. Mc Overton, A. Townsend Peterson, S.J. Phillips, K. Richardson, R. Scachetti-Pereira, R.E. Schapire, J. Soberón, S. Williams, M.S. Wisz and N.E. Zimmermann. 2009. Novel methods improve prediction of species' distributions from occurrence data. *Ecography.* 29(2):129-151.

Elmore, A.J., J.F. Mustard and S.J. Manning. 2003. Regional patterns of plant community response to changes in water: Owens Valley, California. *Ecological Applications.* 13:443-460.

Emerson, C.W., N.S.-N Lam and D.A. Quattrochi. 1999. Multiscale fractal analysis of image texture and pattern. *Photogrammetric Engineering and Remote Sensing.* 65:51-61.

Emerson, C.W., N.S.-N Lam and D.A. Quattrochi. 2005. A comparison of local variance, fractal dimension, and Moran's I as aids to multispectral image classification. *International Journal of Remote Sensing.* 26(8):1575-1588.

Epting, J., D. Verbyla and B. Sorbel. 2005. Evaluation of remotely sensed indices for assessing burn severity in interior Alaska using Landsat TM and ETM+. *Remote Sensing of Environment.* 96:328-339.

Erdody, T.L. and L.M. Moskal. 2010. Fusion of LiDAR and imagery for estimating forest canopy fuels. *Remote Sensing of Environment.* 114:725-737.

Escuin, S., R. Navarro and P. Fernandez. 2008. Fire severity assessment by using NBR (Normalized Burn Ratio) and NDVI (Normalized Difference Vegetation Index) derived from LANDSAT TM/ETM images. *International Journal of Remote Sensing*. 29:1053-1073.

Eugenio, F. and F. Marqués. 2003. Automatic satellite image georeferencing using a contour-matching approach. *Institute of Electrical and Electronic Engineers Transactions on Geoscience and Remote Sensing.* 41(12):2869-2880.

Farber, O. and R. Kadmon. 2003. Assessment of alternative approaches for bioclimatic modelling with special emphasis on the Mahalanobis Distance. *Ecological Modeling*. 160:115-130.

Fattahi, H., M.J.V. Zoej, M.R. Mobasheri, M. Dehghani, and M.R. Sahebi. 2009. Windowed Fourier transform for noise reduction of SAR interferograms. *Institute of Electrical and Electronic Engineers Geoscience and Remote Sensing Letters*, 6:418-422.

Feder, J. 1988. Fractals. Plenum Press, New York. 286p.

Feng, G., D. Ming, M. Wang and J. Yang. 2017. Connotations of pixel-based scale effect in remote sensing and the modified fractal-based analysis method. *Computers & Geosciences.* 103:183-190.

Fensholt, R., I. Sandholt and M.S. Rasmussen. 2004. Evaluation of MODIS LAI, fAPAR and the relation between fAPAR and NDVI in a semi-arid environment using *in situ* measurements. *Remote Sensing of Environment.* 91(3-4):490-507.

Fensholt, R., I. Sandholt and S. Stisen. 2006a. Evaluating MODIS, MERIS, and VEGETATION - Vegetation indices using *in situ* measurements in a semiarid environment. *Institute of Electrical and Electonic Engineers Transactions on Geoscience and Remote Sensing.* 44(7):1774-1786.

Fensholt, R., I. Sandholt, S. Stisen and C. Tucker. 2006b. Analysing NDVI for the African continent using the geostationary Meteosat Second Generation SEVIRI sensor. *Remote Sensing of Environment.* 101(2):212-229.

Fernandes, R., S. Plummer, J. Nightingale, F. Baret, F. Camacho, H. Fang, S. Garrigues, N. Gobron, M. Lang, R. Lacaze, S. LeBlanc, M. Meroni, B. Martinez, T. Nilson, B. Pinty, J. Pisek, O. Sonnentag, A. Verger, J. Welles, M. Weiss and J.L. Widlowski. 2014. Global leaf area index product validation good practices, Version 2.0. *Best Practice for Satellite-Derived Land Product Validation* (M. Román and J. Nickeson, editors), Land Product Validation Subgroup (WGCV/CEOS). 72pp.

Fernández, A., P. Illera and J.L. Casanova. 1997. Automatic mapping of surfaces affected by forest fires in Spain using AVHRR NDVI composite image data. *Remote Sensing of Environment.* 60(2):153-162.

Fernandez-Manso, A., C. Quintano and D.A. Roberts. 2012. Evaluation of potential of multiple endmember spectral mixture analysis (MESMA) for surface coal mining affected area mapping in different world forest ecosystems. *Remote Sensing of Environment.* 127:181-192.

Ficetola, G.F., W. Thuiller and C. Miaud. 2007. Prediction and validation of the potential global distribution of a problematic alien invasive species - the American bullfrog. *Diversity and Distributions.* 13(4):476-485.

Filippi, A.M. and J.R. Jensen. 2006. Fuzzy learning vector quantization for hyperspectral coastal vegetation classification. *Remote Sensing of Environment.* 100(4):512-530.

Fisher, P.F. and S. Pathirana. 1990. The evaluation of fuzzy membership of land cover classes in the suburban zone. *Remote Sensing of Environment.* 34(2):121-132.

Fitzgerald, G.J., P.J. Pinter, D.J. Hunsaker and T.R. Clarke. 2005. Multiple shadow fractions in spectral mixture analysis of a cotton canopy. *Remote Sensing of Environment.* 97(4):526-539.

Fitzgerald, G.J., S.J. Maas and W.R. Detar. 2004. Spider mite detection and canopy component mapping in cotton using hyperspectral imagery and spectral mixture analysis. *Precision Agriculture.* 5(3):275-289.

Foody, G.M. 1996. Approaches for the production and evaluation of fuzzy land cover classifications from remotely-sensed data. *International Journal of Remote Sensing.* 17(7):1317-1340.

Foody, G.M. 1998. Sharpening fuzzy classification output to refine the representation of sub-pixel land cover distribution. *International Journal of Remote Sensing.* 19(13):2593-2599.

Foody, G.M. and D.P. Cox. 1994. Sub-pixel land cover composition estimation using a linear mixture model and fuzzy membership functions. *International Journal of Remote Sensing.* 15(3):619-631.

Foody, G.M., R.M. Lucas, P.J. Curran and M. Honzak. 1997. Non-linear mixture modelling without end-members using an artificial neural network. *International Journal of Remote Sensing.* 18:937-953.

Fox, C. and D.E. Hayes. 1985. Quantitative methods for analyzing the roughness of the seafloor. *Reviews of Geophysics.* 23:1-48.

Franch, B., E.F. Vermote, J.A. Sobrino, E. and E. Fédèle. 2013. Analysis of directional effects on atmospheric correction. *Remote Sensing of Environment. 128:*276-288.

Franke, J., D. Roberts, K. Halligan and G. Menz. 2009. Hierarchical multiple endmember spectral mixture analysis (MESMA) of hyperspectral imagery for urban environments. *Remote Sensing of Environment.* 113:1712-1723.

Fraser, R.H., R. Fernandes and R. Latifovic. 2003. Multi-temporal Mapping of Burned Forest over Canada Using Satellite-based Change Metrics. *Geocarto International.* 18(2):37-47.

Fretwell, P.T., I.J. Staniland and J. Forcada. 2014. Whales from space: Counting southern right whales by satellite. *PLoS ONE.* 9(2):e88655.

Freund, Y. and R.E. Schapire. 1996. Experiments with new boosting algorithm. *Machine Learning: Proceedings of the Thirteenth International Conference*, Bari, Italy, July 3-6.

Freund, Y., R.E. Schapire and N. Abe. 1999. A short introduction to boosting. *Journal-Japanese Society for Artificial Intelligence*.14:1612.

Friedl, M.A. and C.E. Brodley.1997. Decision tree classification of land cover from remotely sensed data. *Remote Sensing of Environment.* 61:399-409.

Friedl, M.A., C.E. Brodley and A.H. Strahler. 1999. Maximizing land cover classification accuracies produced by decision tree at continental to global scales. *Institute of Electrical and Electronic Engineers Transactions on Geoscience and Remote Sensing*, 37: 969-977.

Friedl, M.A., D.K. McIver, J.C.F. Hodges, X.Y. Zhang, D. Muchoney, A.H. Strahler, C.E. Woodcock, S. Gopal, A. Schneider, A. Cooper, A. Baccini, F. Gao and C. Schaaf. 2002. Global land cover mapping from MODIS: algorithms and early results. *Remote Sensing of Environment.* 83(1-2):287-302.

Friedman, J.H. 2001. Greedy function approximation: A gradient boosting machine. *Ann. Stats.* 29(5): 1189-1232.
Friedman, J.H. 2002. Stochastic gradient boosting. *Computational Statistics & Data Analysis*, 38:367-378.
Fu, T.C. 2011. A review on time series data mining. *Engineering Applications of Artificial Intelligence.* 24(1):164-181.
Fung, T. 1992. Land use and land cover change detection with Landsat MSS and SPOT-HRV Data in Hong Kong. *Geocarto International.* 7:33-40.
Fung, T. and E. LeDrew. 1988. The determination of optimal threshold levels for change detection using various accuracy indices. *Photogrammetric Engineering and Remote Sensing.* 54:1449-1454.
Gajardo, J., M. Garcia and D. Riano. 2014. Applications of airborne laser scanning in forest fuel assessment and fire prevention. *Forestry Applications of Airborne Laser Scanning: Concepts and Case Studies.* 27:439-462.
Gamon, J.A., J. Peñuelas and C.B. Field. 1992. A narrow-waveband spectral index that tracks diurnal changes in photosynthetic efficiency. *Remote Sensing of Environment.* 41(1):35-44.
Gao, B. and A.F.H. Goetz. 1990. Column atmospheric water vapor and vegetation liquid water retrievals from airborne imaging spectrometer data. *Journal of Geophysical Research.* 95(D4):3549-3564.
Gao, B.C. 2000. A practical method for simulating AVHRR-consistent NDVI data series using narrow MODIS channels in the 0.5-1.0 μm spectral range *Remote Sensing of Environment.* 38:1969-1975.
Gao, F., E.B. de Colstoun, R. Ma, Q. Weng, J.G. Masek, J. Chen, Y. Pan and C. Song. 2012. Mapping impervious surface expansion using medium-resolution satellite image time series: A case study in the Yangtze River Delta, China. *International Journal of Remote Sensing.* 33(24):7609-7628.
Gao, F., J. Masek and R.E. Wolfe. 2009. Automated registration and orthorectification package for Landsat and Landsat-like data processing. *Journal of Applied Remote Sensing.* 3(1): 033515-033520.
Gao, X., A.R. Huete, W. Ni and T. Miura. 2000. Optical-biophysical relationships of vegetation spectra without background contamination. *Remote Sensing of Environment.* 74(3):609-620.
Gauthier, S., P. Bernier, T. Kuuluvainen, A.Z. Shvidenko and D.G. Schepaschenko. 2015. Boreal forest health and global change. *Science.* 349:819-822.
GCOS. 2010. Implementation Plan for the Global Observing System for Climate in Support of the UNFCCC (2010 Update). Geneva, Switzerland: Secretariat of the World Meteorological Organization. No. GCOS-138.
Gelfand, S.B., C.S. Ravishankar and E.J. Delp. 1991. An iterative growing and pruning algorithms for classification tree design. *Institute of Electrical and Electronic Engineers Transactions on Pattern Analysis and Machine Intelligence,* 13:163-174.
Gelman, A., J.B. Carlin, H.S. Stern and D.B. Rubin (Editors). 2000. Markov chain simulation. *Bayesian Data Analysis.* New York: Champman & Hall /CRC.
Ghosh, A., N.R. Pal and J. Das. 2006. A fuzzy rule based approach to cloud cover estimation. *Remote Sensing of Environment.* 100(4):531-549.
Gilabert, M.A., F.J. Garcia-Haro and J. Meli. 2000. A mixture modeling approach to estimate vegetation parameters for heterogeneous canopies in remote sensing. *Remote Sensing of Environment.* 72(3):328-345.
Gilerson, A., J. Zhou, S. Hlaing, I. Ioannou, B. Gross, F. Moshary and S. Ahmed. 2008. Fluorescence component in the reflectance spectra from coastal waters. II. Performance of retrieval algorithms. *Optics Express. 16*(4):2446-2460.
Gilerson, A., J. Zhou, S. Hlaing, I. Ioannou, J. Schalles, B. Gross, F. Moshary and S. Ahmed. 2007. Fluorescence component in the reflectance spectra from coastal waters. Dependence on water composition. *Optics Express.* 15(24):15702-15721.
Gillespie, A.R. 1992. Spectral mixture analysis of multispectral thermal infrared images. *Remote Sensing of Environment.* 42(2):137-145.
Giri, C., J. Long, S. Abbas, R.M. Murali, F.M. Qamer, B. Pengra and D. Thau. 2015. Distribution and dynamics of mangrove forests of South Asia. *Journal of Environmental Management.* 148:101-111.
Gitelson, A.A., G. Dall'Olmo, W. Moses, D.C. Rundquist, T. Barrow, T.R. Fisher, D. Gurlin and J. Holz. 2008. A simple semi-analytical model for remote estimation of chlorophyll-*a* in turbid waters: Validation. *Remote Sensing of Environment.* 112(9):3582-3593.
Gitelson, A.A., J.F. Schalles and C.M. Hladik. 2007. Remote chlorophyll-*a* retrieval in turbid, productive estuaries: Chesapeake Bay case study. *Remote Sensing of Environment. 109*(4):464-472.
Gitelson, A.A. and Y.J. Kaufman. 1998. MODIS NDVI optimization to fit the AVHRR data series – spectral considerations. *Remote Sensing of Environment.* 66:343-350.
Gitelson, A.A., Y. Peng and K.F. Huemmrich. 2014. Relationship between fraction of radiation absorbed by photosynthesizing maize and soybean canopies and NDVI from remotely sensed data taken at close range and from MODIS 250*m* resolution data. *Remote Sensing of Environment.* 147:108-120.

Gobron, N., B. Pinty, M.M. Verstraete and J.L. Widlowski. 2000. Advanced vegetation indices optimized for upcoming sensors: Design, performance, and applications. *Institute of Electrical and Electronic Engineers Transactions on Geoscience and Remote Sensing.* 38(6):2489-2505.

Goel, N.S., and D.W. Deering. 1985. Evaluation of a canopy reflectance model for LAI estimation through its inversion. *Institute of Electrical and Electronic Engineers Transactions on Geoscience and Remote Sensing.* 23:674-684.

Goel, N.S. and R.L. Thompson. 1984. Inversion of vegetation canopy reflectance models for estimating agronomic variables 5. Estimation of leaf-area index and average leaf angle using measured canopy reflectances. *Remote Sensing of Environment.* 16:69-85.

Goetz, A.F.H., G. Vane, J.E. Solomon and B.N. Rock. 1985. Imaging spectrometry for Earth remote sensing, *Science.* 228(4704):1147-1153.

Goetz, S., A. Bunn, G. Fiske and R.A. Houghton. 2005. Satellite-observed photosynthetic trends across boreal North America associated with climate and fire disturbance. *Proceedings National Academy of Sciences* 102(38):13521-13525.

Gong, P., D.J. Marceau and P.J. Howarth. 1992. A comparison of spatial feature extraction algorithms for land-use classification with SPOT HRV data. *Remote Sensing of Environment.* 40:137-151.

Gong, P. and P.J. Howarth. 1990. The use of structural information for improving land-cover classification accuracies at the rural-urban fringe. *Photogrammetric Engineering and Remote Sensing.* 56:67-73.

Gons, H.J. 1999. Optical teledetection of chlorophyll*a* in turbid inland waters. *Environmental Science & Technology. 33*(7)1127-1132.

Gons, H.J., M. Rijkeboer and K.G. Ruddick. 2002. A chlorophyll-retrieval algorithm for satellite imagery (Medium Resolution Imaging Spectrometer) of inland and coastal waters. *Journal of Plankton Research. 24*(9):947-951.

Gons, H.J., M.T. Auer and S.W. Effler. 2008. MERIS satellite chlorophyll mapping of oligotrophic and eutrophic waters in the Laurentian Great Lakes. *Remote Sensing of Environment.* 112:4098-4106.

Gonsamo, A. and J.M. Chen. 2013. Spectral response function comparability among 21 satellite sensors for vegetation monitoring, *Institute of Electrical and Electronic Engineers Transactions on Geoscience and Remote Sensing.* 51(3):1319-1335.

González Vilas, L., E. Spyrakos and J.M. Torres Palenzuela. 2011. Neural network estimation of chlorophyll*a* from MERIS full resolution data for the coastal waters of Galician rias (NW Spain). *Remote Sensing of Environment.* 115:524-535.

Goodchild, M.F. 1980. Fractals and the accuracy of geographical measures. *Mathematical Geology.* 12:85-98.

Goodchild, M.F. and D.M. Mark. 1987. The fractal nature of geographic phenomena. *Annals of the Association of American Geographers.* 77:265-278.

Gordon, H.R., O.B. Brown, R.H. Evans, J.W. Brown, R.C. Smith, K.S. Baker and D.K. Clark. 1988. A semianalytic radiance model of ocean color. *Journal of Geophysical Research: Atmospheres. 93*(D9):10909-10924.

Gordon, S.I. 1980. Utilizing Landsat imagery to monitor land use change: A case study in Ohio. *Remote Sensing of Environment.* 9:189-196.

Goward, S.N. and K.F. Huemmrich. 1992. Vegetation canopy PAR absorptance and the Normalized Difference Vegetation Index: an assessment using the SAIL model. *Remote Sensing of Environment.* 39:119-140.

Gower, J. and S. King. 2007. Validation of chlorophyll fluorescence derived from MERIS on the west coast of Canada. *International Journal of Remote Sensing.* 28:625-635.

Gower, J.F.R. and G.A. Borstad. 2004. On the potential of MODIS and MERIS for imaging chlorophyll fluorescence from space. *International Journal of Remote Sensing.* 25(7-8):1459-1464.

Green, A.A., M. Berman, P. Switzer and M.D. Craig. 1988. A transformation for ordering multispectral data in terms of image quality with implications for noise removal. *Institute of Electrical and Electronic Engineers Transactions on Geoscience and Remote Sensing.* 26(1):65-74.

Guan, K., M. Pan, H. Li, A. Wolf, J. Wu, D. Medvigy, K.K. Caylor, J. Sheffield, E.F. Wood, Y. Malhi, M. Liang, J.S. Kimball, S.R. Saleska, J. Berry, J. Joiner and A.I. Lyapustin. 2015. Photosynthetic seasonality of global tropical forests constrained by hydroclimate. *Nature Geoscience* 8(4):284-289.

Guanter, L., C. Frankenberg, A. Dudhia, P.E. Lewis, J. Gomez-Dans, A. Kuze, H. Suto and R.G. Grainger. 2012. Retrieval and global assessment of terrestrial chlorophyll fluorescence from GOSAT space measurements. *Remote Sensing of Environment.* 121:236-251.

Guay, K.C., P.S.A. Beck, L.T. Berner, S.J. Goetz, A. Baccini and W. Buermann. 2014. Vegetation productivity patterns at high northern latitudes: a multi-sensor satellite data assessment. *Global Change Biology.* 20(10):3147-3158.

Guisan, A., R. Tingley, J.B. Baumgartner, I. Naujokaitis-Lewis, P.R. Sutcliffe, A.I. Tulloch, T.J. Regan, L. Brotons, E. McDonald-Madden, C. Mantyka-Pringle, T.G. Martin, J.R. Rhodes, R. Maggini, S.A. Setterfield, J. Elith,

M.W. Schwartz, B.A. Wintle, O. Broennimann, M. Austin, S. Ferrier, M.R. Kearney, H.P. Possingham and Y.M. Buckley. 2013. Predicting species distributions for conservation decisions. *Ecology Letters.* 16(12):1424-1435.

Gunther, K.P. and S.W. Maier. 2007. AVHRR compatible vegetation index derived from MERIS data. *International Journal of Remote Sensing.* 28(3/4):693-708.

Gupta, R.P., R.K. Tiwari, V. Saini and N Srivastava. 2013. A simplified approach for interpreting Principal Component images. *Advances in Remote Sensing.* 2:111-119.

Haala, N., R. Reulke, M. Thies and T. Aschoff. 2004. Combination of terrestrial laser scanning with high resolution panoramic images for investigations in forest applications and tree species recognition. *Proceedings of the ISPRS working group V/1,* 19-22 February 2004. Dresden, Germany.

Haboudane, D., J.R. Miller, E. Pattey, P.J. Zarco-Tejada and I.B. Strachan. 2004. Hyperspectral vegetation indices and novel algorithms for predicting green LAI of crop canopies: Modeling and validation in the context of precision agriculture. *Remote Sensing of Environment.* 90(3):337-352.

Haboudane, D., J.R. Miller, N. Tremblay, P.J. Zarco-Tejada and L. Dextraze. 2002. Integrated narrow-band vegetation indices for prediction of crop chlorophyll content for application to precision agriculture. *Remote Sensing of Environment,* 81(2-3):416-426.

Hall, F.G., Y.E. Shimabukuro and K.F. Huemmrich. 1995. Remote sensing of forest biophysical structure using mixture decomposition and geometric reflectance models. *Ecological Applications.* 993-1013.

Han, C., H. Guo, C. Wang and D. Fan, 2002. A novel method to reduce speckle in SAR images. *International Journal of Remote Sensing.* 23(23):5095-5101.

Hansen, M.C., P.V. Potapov, R. Moore, M. Hancher, S.A. Turubanova, A. Tyukavina, D. Thau, S.V. Stehman, S.J. Goetz, T.R. Loveland, A. Kommareddy, A. Egorov, L. Chini, C.O. Justice and J.R.G. Townshend. 2013. High-resolution global maps of 21st-Century forest cover change. *Science.* 342(6160):850-853.

Hansen, M.C., R. Dubayah and R. Defries. 1996. Classification trees: an alternative to traditional land cover classifiers. *International Journal of Remote Sensing.* 17:1075-1081.

Hantson, S. and E. Chuvieco. 2011. Evaluation of different topographic correction methods for Landsat imagery. *International Journal of Applied Earth Observation and Geoinformation.* 13(5):691-700.

Haralick, R.M., K. Shanmugan and I. Dinstein. 1973. Texture features for image classification, *Institute of Electrical and Electronic Engineers. Transactions on Systems, Man, and Cybernetics,* SMC-3:610-621.

Harding, L.W. Jr., E.C. Itsweire and W.E. Esaias. 1994. Estimates of phytoplankton biomass in the Chesapeake Bay from aircraft remote sensing of chlorophyll concentrations. 1989-92. *Remote Sensing of Environment.* 49:41-56.

Harsanyi, J.C. and C.I. Chang. 1994. Hyperspectral image classification and dimensionality reduction: An orthogonal subspace projection approach. *Institute of Electrical and Electronic Engineers Transactions on Geoscience and Remote Sensing.* 32:779-785.

Harvey, E.T., S. Kratzer and P. Philipson. 2015. Satellite-based water quality monitoring for improved spatial and temporal retrieval of chlorophyll-*a* in coastal waters. *Remote Sensing of Environment.* 158:417-430.

Hawinkel, P., E. Swinnen, S. Lhermitte, B. Verbist, J. Van Orshoven and B. Muys. 2015. A time series processing tool to extract climate-driven interannual vegetation dynamics using Ensemble Empirical Mode Decomposition (EEMD). *Remote Sensing of Environment.* 169:375-389.

Hazel, G.G. 2001. Object-level change detection in spectral imagery. Institute of Electrical and Electronic Engineers Transactions on Geoscience and Remote Sensing. 39(3):553-561.

He, K.S., B.A. Bradley, A.F. Cord, D. Rocchini, M.-N. Tuanmu, S. Schmidtlein, W. Turner, M. Wegmann and N. Pettorelli. 2015. Will remote sensing shape the next generation of species distribution models? *Remote Sensing in Ecology and Conservation.* 1(1):4-18.

Heine, I., T. Francke, C. Rogass, P.H.A. Medeiros, A. Bronstert and S. Foerster. 2014. Monitoring seasonal changes in the water surface areas of reservoirs using TerraSAR-X time series data in semiarid Northeastern Brazil. *Institute of Electrical and Electronic Engineers Journal of Selected Topics in Applied Earth Observations and Remote Sensing.* 7(8):3190-3199.

Heinz, D. C. and C.I. Chang. 2001. Fully constrained least squares linear spectral mixture analysis method for material quantification in hyperspectral imagery. *Institute of Electrical and Electronic Engineers Transactions on Geoscience and Remote Sensing.* 39(3):529-545.

Herawati, H., J.R. Gonzalez-Olabarria, A. Wijaya, C. Martius, H. Purnomo and R. Andriani. 2015. Tools for assessing the impacts of climate variability and change on wildfire regimes in forests. *Forests.* 6:1476-1499.

Hernandez, P.A., C.H. Graham, L.L. Master and D.L. Albert. 2006. The effect of sample size and species characteristics on performance of different species distribution modeling methods. *Ecography.* 29(5): 773-785.

Herold, M., M.E. Gardner and D.A. Roberts. 2003. Spectral resolution requirements for mapping urban areas. *Institute of Electrical and Electronic Engineers Transactions on Geoscience and Remote Sensing.* 41(9):1907-1919.

Herzfeld, U.C. and B. Wallin. 2014. Spatio-temporal analysis of surface elevation changes in Pine Island Glacier, Antarctica, from ICESat GLAS data and ERS-1 radar altimeter data. *Annals of Glaciology.* 55(66):248-258.

Herzfeld, U.C., B. McDonald, B.F. Wallin, W. Krabill, S. Manizade, J. Sonntag, H. Mayer, W.A. Yearsley, P.A. Chen and A. Weltman. 2014. Elevation changes and dynamic provinces of Jakobshavn Isbrae, Greenland, derived using generalized spatial surface roughness from ICESat GLAS and ATM data. *Journal of Glaciology.* 60(223):834-848.

Heylen, R., M. Parente and P. Gader. 2014. A review of nonlinear hyperspectral unmixing methods. Institute of Electrical and Electronic Engineers Journal of Selected Topics in Applied Earth Observations and Remote Sensing. 7(6):1844-1868.

Hilbert, D. 2004. Golden bowerbird (*Prionodura newtonia*) habitat in past, present and future climates: Predicted extinction of a vertebrate in tropical highlands due to global warming. *Biological Conservation.* 116(3):367-377.

Hirzel, A.H., J. Hausser, D. Chessel and N. Perrin. 2002. Ecological-niche factor analysis: How to compute habitat suitability maps without absence data? *Ecology.* 83:2027-2036.

Hodgson, A., N. Kelly and D. Peel. 2013. Unmanned aerial vehicles (UAVs) for surveying marine fauna: A Dugong case study. *PLoS ONE.* 8(11):e79556.

Hofmann, T., J. Puzicha and J.M. Buhmann. 1998. Unsupervised texture segmentation in a deterministic annealing framework. *Institute of Electrical and Electronic Engineers Transactions on Pattern Analysis and Machine Intelligence.* 20(8):803-818.

Holben, B.N. 1986. Characteristics of maximum-value composite images from temporal AVHRR data. *International Journal of Remote Sensing.* 7(11):1417-1434.

Holben, B.N., D. Tanré, A. Smirnov, T.F. Eck, I. Slutsker, N. Abuhassan, W.W. Newcomb, J.S. Schafer, B. Chatenet, F. Lavenu, Y.J. Kaufman, J. Vande Castle, A. Setzer, B. Markham, D. Clark, R. Frouin, R. Halthore, A. Karneli, N.T. O'Neill, C. Pietras, R.T. Pinker, V. Voss and G. Zibordi. 2001. An emerging ground-based aerosol climatology: Aerosol optical depth from AERONET. *Journal of Geophysical Research.* 106:12,067-12,097.

Hollmann, R., C.J. Merchant, R. Saunders, C. Downy, M. Buchwitz, A. Cazenave, E. Chuvieco, P. Defourny, G. de Leeuw, R. Forsberg, T. Holzer-Popp, F. Paul, S. Sandven, S. Sathyendranath, M. van Roozendael and W. Wagner. 2013. The ESA Climate Change Initiative: Satellite data records for essential climate variables. *Bulletin of the American Meteorological Society.* 94(10):1541-1552.

Holt, A.C., E.Y.W. Seto, T. Rivard and P. Gong. 2009. Object-based detection and classification of vehicles from high-resolution aerial photography. *Photogrammetric Engineering & Remote Sensing.* 75(7):871-880.

Hoogenboom, H.J., A.G. Dekker and I.A. Althuis. 1998. Simulation of AVIRIS sensitivity for detecting chlorophyll over coastal and inland waters. *Remote Sensing of Environment.* 65:333-340.

Horowitz, H.M., R.F. Nalepka, P.D. Hyde and J.P. Morganstern. 1971. Estimating the proportion of objects within a single resolution element of a multispectral scanner. University of Michigan, Ann Arbor, NASA contract NAS-9-9784.

Hosgood, B., S. Jacquemoud, G. Andreoli, J. Verdebout, G. Pedrini and G. Schmuck. 1995. Leaf Optical Properties EXperiment 93 (LOPEX93). *European Commision, Joint Research Center, Institute for Remote Sensing Applications. Report EUR 16095 EN.*

Houghton, J., J. Townshend, K. Dawson, P. Mason, J. Zillman and A. Simmons. 2012. The GCOS at 20 years: the origin, achievement and future development of the Global Climate Observing System. *Weather.* 67(9):227-235.

Hsu, N.C., S.C. Tsay, M.D. King and J.R. Herman. 2006. Deep blue retrievals of Asian aerosol properties during ACE-Asia. *Institute of Electrical and Electronic Engineers Transactions on Geoscience and Remote Sensing.* 44(11): 3180-3195.

Hu, C., F.E. Muller-Karger, C. Taylor, K.L. Carder, C. Kelble, E. Johns and C.A. Heil. 2005. Red tide detection and tracing using MODIS fluorescence data: A regional example in SW Florida coastal waters. *Remote Sensing of Environment.* 97:311-321.

Hu, X. and Q. Weng. 2011. Estimating impervious surfaces from medium spatial resolution imagery: A comparison between fuzzy classification and LSMA. *International Journal of Remote Sensing.* 32(20):5645-5663.

Hu, Y., A. Croitoru and V. Tao. 2004. Understanding the rational function model: Methods and applications. *International Archives of Photogrammetry and Remote Sensing.* 12-23 July, Istanbul. 20: 663-668.

Hu, Y. and V. Tao. 2002. Updating solutions of the rational function model using additional control information. *Photogrammetric Engineering & Remote Sensing*. 68(7):715-723.

Huang, H., J. Chen, Z. Li, F. Gong and N. Chen. 2017. Ontology-guided image interpretation for GEOBIA of high spatial resolution remote sensing imagery: A coastal area case study. *ISPRS International Journal of Geo-Information*. 6(4): 105-121.

Huang, N.E. and Z.H. Wu. 2008. A review on Hilbert-Huang transform: Method and its applications to geophysical studies. *Reviews of Geophysics.* 46(2).

Huang, N.E., Z. Shen, S.R. Long, M.L.C. Wu, H.H. Shih, Q.N. Zheng, N.C. Yen, C.C. Tung and H.H. Liu. 1998. The empirical mode decomposition and the Hilbert spectrum for nonlinear and non-stationary time series analysis. *Proceedings of the Royal Society a-Mathematical Physical and Engineering Sciences.* 454(1971):903-995.

Huemmrich, K.F., T.A. Black, P.G. Jarvis, J.H. McCaughey and F.G. Hall. 1999. High temporal resolution NDVI phenology from micrometeorological radiation sensors. *Journal of Geophysical Research-Atmospheres.* 104(D22):27935-27944.

Huete, A., F. Keita, K. Thome, J. Privette, W. van Leeuwen, C. Justice and J. Morisette. 1999. A light aircraft radiometric package for MODLAND Quick Airborne Looks (MQUALS). *The Earth Observer.* 11(1):22-25.

Huete, A., K. Didan, T. Miura, E.P. Rodriguez, X. Gao and L.G. Ferreira. 2002. Overview of the radiometric and biophysical performance of the MODIS vegetation indices. *Remote Sensing of Environment.* 83(1-2):195-213.

Huete, A., K. Didan, W. van Leeuwen, T. Miura and E. Glenn. 2011. MODIS Vegetation Indices. *Land Remote Sensing and Global Environmental Change: NASA's Earth Observing System and the Science of ASTER and MODIS* (B. Ramachandran, C. O. Justice, and M. J. Abrams, editors), Springer. pp. 579-602.

Huete, A., T. Miura, H. Yoshioka, P. Ratana and M. Broich. 2014. Indices of vegetation activity. *Biophysical Applications of Satellite Remote Sensing* (J. M. Hanes, editor). Springer, pp.1-41.

Huete, A.R. 1987. Soil and Sun angle interactions on partial canopy spectra. *International Journal* of *Remote Sensing.* 8(9):1307-1317.

Huete, A.R. 1988. A soil-adjusted vegetation index (SAVI). *Remote Sensing of Environment.* 25(3):295-309.

Huete, A.R., K. Didan, Y.E. Shimabukuro, P. Ratana, S.R. Saleska, L.R. Hutyra, W.Z. Yang, R.R. Nemani and R. Myneni. 2006. Amazon rainforests green-up with sunlight in dry season. *Geophysical Research Letters.* 33(6):L06405.

Huete, A.R., N. Restrepo-Coupe, P. Ratana, K. Didan, S.R. Saleska, K. Ichii, S. Panuthai and M. Gamo. 2008. Multiple site tower flux and remote sensing comparisons of tropical forest dynamics in Monsoon Asia. *Agricultural and Forest Meteorology.* 148(5):748-760.

Huete, A.R., R.D. Jackson and D.F. Post. 1985. Spectral response of a plant canopy to different soil backgrounds. *Remote Sensing of Environment.* 17:37-53.

Hurst, H.E., R.P. Black, and Y.M. Simaika. 1965. *Long Term Storage: An Experimental Study*, Constable, London, 145 p.

Hurtt, G.C. and R.A. Armstrong. 1996. A pelagic ecosystem model calibrated with BATS data. *Deep-Sea Research Part II-Topical Studies in Oceanography. 43:* 653-683.

Ichoku, C. and A. Karnieli. 1996. A review of mixture modeling techniques for sub-pixel land cover estimation. *Remote Sensing Reviews.* 13(3-4):161-186.

Iglesias, R., A. Aguasca, X. Fabregas, J.J. Mallorqui, D. Monells, C. Lopez-Martinez and L. Pipia. 2015. Ground-based polarimetric SAR interferometry for the monitoring of terrain displacement phenomena–Part II: Applications. *Institute of Electrical and Electronic Engineers Journal of Selected Topics in Applied Earth Observations and Remote Sensing.* 8(3):994-1007.

Ingebritsen, S.E. and R.J.P. Lyon. 1985. Principal components analysis of multitemporal image pairs. *International Journal of Remote Sensing.* 6:687-695.

Iordache, D.-M., J. Bioucas-Dias, A. Plaza and B. Somers. 2014a. Music-CSR Hyperspectral unmixing via multiple signal classification and collaborative sparse regression. *Institute of Electrical and Electronic Engineers Transactions on Geoscience and Remote Sensing.* 52:4364-4382.

Iordache, D.-M., L. Tits, A. Plaza, J. Bioucas-Dias and B. Somers. 2014b. A dynamic unmixing framework for site specific monitoring of plant production systems. *Institute of Electrical and Electronic Engineers Journal of Selected Topics in Applied Earth Observations and Remote Sensing.* 7:2016-2034.

Jacquemoud, S. and F. Baret. 1990. PROSPECT - a model of leaf optical-properties spectra. *Remote Sensing of Environment.* 34:75-91.

Jacquemoud, S., C. Bacour, H. Poilve and J.P. Frangi. 2000. Comparison of four radiative transfer models to simulate plant canopies reflectance: Direct and inverse mode. *Remote Sensing of Environment.* 74:471-481.

Jaggi, S., D.A. Quattrochi and N.S.-N. Lam. 1993. Implementation and operation of three fractal measurement algorithms for analysis of remote-sensing data. *Computer & Geosciences,* 19:745-767.

Jakubauskas, M.E., D.R. Legates and J.H. Kastens. 2001. Harmonic analysis of time-series AVHRR NDVI data. *Photogrammetric Engineering and Remote Sensing.* 67: 461-470.

Jakubauskas, M.E., D.R. Legates and J. Kastens. 2002. Crop identification using harmonic analysis of time-series AVHRR NDVI data. *Computers and Electronics in Agriculture.* 37(4):127-139.

Jakubowski, M.K., Q.H. Guo and M. Kelly. 2013. Tradeoffs between lidar pulse density and forest measurement accuracy. *Remote Sensing of Environment.* 130:245-253.

Jarnevich, C. S. and T. J. Stohlgren. 2009. Near-term climate projections for invasive species distributions. *Biological Invasions.* 11:1373-1379.

Jensen, J.R. 2005. *Introductory Digital Image Processing: A Remote Sensing Perspective, 3rd ed.*, Pearson Prentice Hall, Upper Saddle River, New Jersey, 526 p.

Jensen, R. and C. Yang. 2009. Hyperspectral remote sensing – Sensors and applications. *Earth Observing Platforms & Sensors, Manual of Remote Sensing, 3rd ed.* (M. Jackson, editor). ASPRS, Maryland. pp. 205-224.

Jensen, R.J. 2015. Introductory Digital Image Processing: A Remote Sensing Perspective, 4th ed., Pearson Education. Glenview, Illinois. 544 p.

Jiang, Z., A.R. Huete, K. Didan and T. Miura. 2008. Development of a two-band enhanced vegetation index without a blue band. *Remote Sensing of Environment.* 112(10):3833-3845.

Jin, S. and S.C. Chen. 2012. Application of QuickBird imagery in fuel load estimation in the Daxinganling region. China. *International Journal of Wildland Fire.* 21:583-590.

Jin, Z. and B. Xu. 2013. A novel compound smoother – RMMEH to reconstruct MODIS NDVI time series. *Institute of Electrical and Electronic Engineers Geoscience and Remote Sensing Letters.* 10(4):942-946.

Johnson, P.E., M.O. Smith and J.B. Adams. 1985. Quantitative analysis of planetary reflectance spectra with principle components analysis. *Journal of Geophysical Research.* 90, supplement C805-C810.

Joiner, J., L. Guanter, R. Lindstrot, M. Voigt, A.P. Vasilkov, E.M. Middleton, K.F. Huemmrich, Y. Yoshida and C. Frankenberg. 2013. Global monitoring of terrestrial chlorophyll fluorescence from moderate-spectral-resolution near-infrared satellite measurements: methodology, simulations, and application to GOME-2. *Atmospheric Measurement Techniques.* 6(10):2803-2823.

Jönsson, A.M., L. Eklundh, M. Hellström, L. Bärring and P. Jönsson. 2010. Annual changes in MODIS vegetation indices of Swedish coniferous forests in relation to snow dynamics and tree phenology. *Remote Sensing of Environment.* 114(11):2719-2730.

Jönsson, P. and L. Eklundh. 2002. Seasonality extraction by function fitting to time-series of satellite sensor data. *Institute of Electrical and Electronic Engineers Transactions on Geoscience and Remote Sensing.* 40(8):1824-1832.

Jönsson, P. and L. Eklundh. 2004. TIMESAT - a program for analyzing time-series of satellite sensor data. *Computers & Geosciences.* 30(8):833-845.

Jönsson, P. and L. Eklundh. 2015. *Timesat 3.2 Software Manual.* Sweden: Lund and Malmö University.

Ju, J., D.P. Roy, E. Vermote, J. Masek and V. Kovalskyy. 2012. Continental-scale validation of MODIS-based and LEDAPS Landsat ETM+ atmospheric correction methods. *Remote Sensing of Environment.* 122:175-184.

Ju, W. and N.S.N. Lam. 2009. An improved algorithm for computing local fractal dimension using the triangular prism method. *Computers & Geosciences.* 35:1224-1233.

Justice, C.O., E. Vermote, J.R.G. Townshend, R. Defries, D.P. Roy, D.K. Hall, V.V. Salomonson, J.L. Privette, G. Riggs, A. Strahler, W. Lucht, R.B. Myneni, Y. Knyazikhin, S.W. Running, R.R. Nemani, Z.M. Wan, A.R. Huete, W. van Leeuwen, R.E. Wolfe, L. Giglio, J.P. Muller, P. Lewis and M.J. Barnsley. 1998. The Moderate Resolution Imaging Spectroradiometer (MODIS): Land remote sensing for global change research. *Institute of Electrical and Electronic Engineers Transactions on Geoscience and Remote Sensing.* 36(4):1228-1249.

Kaewpijit, S., J. Le moigne and T. El-Ghazawi. 2003. Automatic reduction of hyperspectral imagery using wavelet spectral analysis. *Institute of Electrical and Electronic Engineers Transactions on Geoscience and Remote Sensing,* 41:863-871.

Kandasamy, S. and R. Fernandes. 2015. An approach for evaluating the impact of gaps and measurement errors on satellite land surface phenology algorithms: Application to 20 year NOAA AVHRR data over Canada. *Remote Sensing of Environment.* 164:114-129.

Karami, A., M. Yazdi and G. Mercier. 2012. Compression of hyperspectral images using discerete wavelet transform and Tucker decomposition. *Institute of Electrical and Electronic Engineers Journal of Selected Topics in Applied Earth Observations and Remote Sensing,* 5:444-550.

Karlsson, K.G. and E. Johansson. 2014. Multi-sensor calibration studies of AVHRR-heritage channel radiances using the simultaneous nadir observation approach. *Remote Sensing.* 6(3):1845-1862.

Kasischke, E.S., N.H.F. French, P. Harrell, N.L. Christensen, S.L. Ustin and D. Barry. 1993. Monitoring of wildfires in boreal forests using large area AVHRR NDVI composite image data. *Remote Sensing of Environment.* 45:61-71.

Kaufman, Y.J. and D. Tanré. 1992. Atmospherically Resistant Vegetation Index (ARVI) for EOS-MODIS. *Institute of Electrical and Electronic Engineers Transactions on Geoscience and Remote Sensing.* 30(2):261-270.

Kaufmann, H., S. Förster, H. Wulf, K. Segl, L. Guanter, M. Bochow, U. Heiden, A. Müller, W. Heldens, T. Schneiderhan, P.J. Leitão, S. van der Linden, P. Hostert, J. Hill, H. Buddenbaum, W. Mauser, T. Hank, H. Krasemann, R. Röttgers, N. Oppelt and B. Heim. 2012. *Science plan of the Environmental Mapping and Analysis Program (EnMAP).* Scientific Technical Report, Deutsches GeoForschungs Zentrum GFZ, Potsdam, 60 p.

Kauth, R.J. and G.S. Thomas. 1976. The tasseled cap - A graphic description of the spectral-temporal development of agricultural crops as seen by LANDSAT. *Proceedings of the Symposium on Machine Processing of Remotely Sensed Data. Purdue University of West Lafayette, Indiana.* 4B:41-51.

Keane, R.E., R. Burgan and J. van Wagtendonk. 2001. Mapping wildland fuels for fire management across multiple scales: Integrating remote sensing, GIS, and biophysical modeling. *International Journal of Wildland Fire.* 10:301-319.

Keiner, L.E. and X.-H. Yan. 1998. A neural network model for estimating sea surface chlorophyll and sediments from Thematic Mapper imagery. *Remote Sensing of Environment.* 66:153-165.

Keller, J.M., S. Chen and R.M. Crownover. 1989. Texture description and segmentation through fractal geometry, *Computer Vision, Graphics, and Image Processing.* 45:150-166.

Kelly, M., K.A. Tuxen and D. Stralberg. 2011. Mapping changes to vegetation pattern in a restoring wetland: Finding pattern metrics that are consistent across spatial scale and time. *Ecological Indicators.* 11(2):263-273.

Kennedy, R.E., Z. Yang and W.B. Cohen. 2010. Detecting trends in forest disturbance and recovery using yearly Landsat time series: 1. LandTrendr - Temporal segmentation algorithms. *Remote Sensing of Environment.* 114(12):2897-2910.

Kennedy, R.E., Z. Yang, J. Braaten, C. Copass, N. Antonova, C. Jordan and P. Nelson, 2015. Attribution of disturbance change agent from Landsat time-series in support of habitat monitoring in the Puget Sound region, USA. *Remote Sensing of Environment.* 166:271-285.

Kennedy, S.K. and W. Lin. 1986. FRACT – A Fortran subroutine to calculate the variables necessary to determine the fractal dimension of closed forms. *Computers & Geosciences.* 12:705-712.

Kern, S., K. Khvorostovsky, H. Skourup, E. Rinne, Z.S. Parsakhoo, V. Djepa, P. Wadhams and S. Sandven. 2015. The impact of snow depth, snow density and ice density on sea ice thickness retrieval from satellite radar altimetry: results from the ESA-CCI Sea Ice ECV Project Round Robin Exercise. *The Cryosphere.* 9(1):37-52.

Keshava, N. and J.F. Mustard. 2002. Spectral unmixing. *Institute of Electrical and Electronic Engineers. Signal Processing Magazine*. 19(1):44-57.

Khan, S.I., Y. Hong, J.J. Gourley, M.U. Khattak and T. De Groeve. 2014. Multi-sensor imaging and space-ground cross-validation for 2010 Flood along Indus River, Pakistan. *Remote Sensing.* 6(3):2393-2407.

Khatami R., G. Mountrakis and S. Stehman. 2016. A meta-analysis of remote sensing research on land-cover image classification processes: A guide for practitioners and directions for future research. *Remote Sensing of Environment* 177:89-100.

Khlopenkov, K.V. and A.P. Trishchenko. 2007. SPARC: New cloud, snow, and cloud shadow detection scheme for historical 1-km AVHHR data over Canada. *Journal of Atmospheric and Oceanic Technology.* 24(3):322-343.

Kilham, N.E. and D.A. Roberts. 2011. Amazon River time series of surface sediment concentration from MODIS. *International Journal of Remote Sensing.* 32(10):2659-2679.

Kim, B. and D.A. Landgrebe. 1991. Hierarchical classifier design in high-dimensional, numerous class cases. *Institute of Electrical and Electronic Engineers Transactions on Geoscience and Remote Sensing*, 29:518-528.

Kim, J.-W., D. Kim, S.H. Kim, H.K. Ha and S.H. Lee. 2015a. Disintegration and acceleration of Thwaites Ice Shelf on the Amundsen Sea revealed from remote sensing measurements. *GIScience & Remote Sensing.* 52(4):498-509.

Kim, J.-W., Z. Lu, Y. Jia and C.K. Shum. 2015b. Ground subsidence in Tucson, Arizona, monitored by time-series analysis using multi-sensor InSAR datasets from 1993 to 2011. *ISPRS Journal of Photogrammetry and Remote Sensing*.107:126-141.

Kim, M., M. Madden and T.A. Warner. 2009. Forest type mapping using object-specific texture measures from multispectral Ikonos imagery. *Photogrammetric Engineering & Remote Sensing.* 75(7):819-829.

Kim, M., T.A. Warner, M. Madden and D.S. Atkinson. 2011. Multi-scale GEOBIA with very high spatial resolution digital aerial imagery: Scale, texture and image objects. *International Journal of Remote Sensing*. 32(10):2825-2850.

Kim, Y., A.R. Huete, T. Miura and Z. Jiang. 2010. Spectral compatibility of vegetation indices across sensors: A band decomposition analysis with Hyperion data. *Journal of Applied Remote Sensing.* 4:043520.

King, M.D., Y.J. Kaufman, D. Tanré and T. Nakajima. 1999. Remote sensing of troposheric aerosols from space: Past, present and future. *Bulletin of the American Meteorological Society.* 80(11):2229-2259.

Kirk, J.T.O. 1996. *Light and Photosynthesis in Aquatic Ecosystems.* 2nd edition. Cambridge University Press. Melbourne, Australia.

Klinkenberg, B. 1992. Fractal and morphometric measures: Is there a relationship? *Geomorphology.* 5:5-20.

Klinkenberg, B. 1994. A review of methods used to determine the fractal dimension of linear features. *Mathematical Geology.* 26:23-46.

Klinkenberg, B., and M.F. Goodchild. 1992. The fractal properties of topography: A comparison of methods, *Earth Surface Processes and Landforms.* 17:217-234.

Knerr, S., L. Personnaz and G. Dreyfus. 1990. Single–layer learning revisited: A stepwise procedure for building and training a neural network. *Neurocomputing: Algorithms, Architectures and Applications*, NATO ASI Series. Springer.

Kononenko, I. and J.S. Hong. 1997. Attribute selection for modelling. *Future Generation Computer Systems*, 13:181-195.

Kotchenova, S.Y. and E.F. Vermote. 2007. Validation of a vector version of the 6S radiative transfer code for atmospheric correction of satellite data. Part II. Homogeneous Lambertian and anisotropic surfaces. *Applied Optics.* 46(20):4455-4464.

Kotchenova, S.Y., E.F. Vermote, R. Levy and A. Lyapustin. 2008. Radiative transfer codes for atmospheric correction and aerosol retrieval: intercomparison study. *Applied Optics.* 47(13):2215-2226.

Kotchenova, S.Y., E.F. Vermote, R. Matarrese and F.J. Klemm, Jr., 2006. Validation of a vector version of the 6S radiative transfer code for atmospheric correction of satellite data. Part I: Path radiance. *Applied Optics.* 45(26):6762-6774.

Kramer, H.A., B.M. Collins, M. Kelly and S.L. Stephens. 2014. Quantifying ladder fuels: A new approach using LiDAR. *Forests.* 5:1432-1453.

Kruse, F.A. 2003. Preliminary results-hyperspectral mapping of coral reef systems using EO-1 Hyperion, Buck Island, US Virgin Islands. *2nd JPL Airborne Earth Science Workshop,* 24-28 February 2003. Pasadena, California.

Kruse, F.A., A.B. Lefoff, J.W. Boardman, K.B. Heidebrecht, A.T. Shapiro, J.P. Barloon and A.F.H. Goetz. 1993. The spectral image processing system (SIPS)—Interactive visualization and analysis of imaging spectrometer data. *Remote Sensing of Environment*.44:145-163.

Kruse, F.A., J.W. Boardman and J.F. Huntington. 2003. Comparison of airborne hyperspectral data and EO-1 Hyperion for mineral mapping. *Institute of Electrical and Electronic Engineers Transactions on Geoscience and Remote Sensing.* 41(6):1388-1400.

Kruse, F.A., K.S. Kierein-Young and J.W. Boardman. 1990. Mineral mapping at Cuprite, Nevada with a 63-channel imaging spectrometer. *Photogrammetric Engineering and Remote Sensing*. 56:83-92.

Kumar S. and T.J. Stohlgren. Environmental Modelling for Health. 2013. In: S.A Morain, A. Budge. *Environmental Tracking for Public Health Surveillance*. (eds.) CRC Press. pp. 293-332.

Kwiatkowska, E.J. and G.S. Fargion. 2003. Application of machine-learning techniques toward the creation of a consistent and calibrated global chlorophyll concentration baseline dataset using remotely sensed ocean color data. *Institute of Electrical and Electronic Engineers Transactions on Geoscience and Remote Sensing*, 41(12):2844-2860.

Laliberte, A.S., M. Goforth, C.M Steele and A. Rango. 2011. Multispectral remote sensing from unmanned aircraft: Image processing workflows and applications for rangeland environments. *Remote Sensing*. 3(11):2529-2551.

Laliberte, A.S. and A. Rango. 2009. Texture and scale in object-based analysis of subdecimeter resolution unmanned aerial vehicle (UAV) imagery. *Institute of Electrical and Electronic Engineers Transactions on Geoscience and Remote Sensing.* 47(3):761-770.

Lam, N.S.-N. 1990. Description and measurement of Landsat TM images using fractals. *Photogrammetric Engineering and Remote Sensing.* 56:187-195.

Lam, N.S.-N., D.A. Quattrochi, H.L. Qiu and W. Zhao. 1998. Environmental assessment and monitoring with image characterization and modeling system using multiscale remote sensing data. *Applied Geographical Studies*, 2(2):77-93.

Lam, N.S.-N., H.L. Qiu, D.A. Quattrochi and C.W. Emerson. 2002. An evaluation of fractal methods for characterizing image complexity. *Cartography and Geographic Information Science.* 29:25-35.

Lam, N. S.-N. and L. De Cola, 1993a. *Fractals in Geography*, Prentice Hall, Englewood Cliffs, New Jersey. 308 p.

Lam, N. S.-N. and L. De Cola. 1993b. Fractal measurement, *Fractals in Geography* (N. S.-N. Lam and L. De Cola, editors), Prentice Hall, New Jersey, pp. 23-55.

Landeweerd, G.H., T. Timmers and E.S. Gelsema. 1983. Binary tree verses single level tree classification of white blood cells. *Pattern Recognition.* 16:571-577.

Landwehr, N., M. Hall and E. Frank. 2005. Logistic model trees. *Machine Learning.* 59:161-205.

Lang, S., E. Schopfer and T. Langanke. 2009. Combined object-based classification and manual interpretation – synergies for a quantitative assessment of parcels and biotopes. *Geocarto International*. 24(2):99-114.

Lasaponara, R. and A. Lanorte. 2012. Satellite time-series analysis. *International Journal of Remote Sensing.* 33(15):4649-4652.

Latifovic, R., Z.L. Zhu, J. Cihlar, C. Giri and I. Olthof. 2004. Land cover mapping of North and Central America - Global Land Cover 2000. *Remote Sensing of Environment.* 89(1):116-127.

Lauknes, T.R., A. Piyush Shanker, J.F. Dehls, H.A. Zebker, I.H.C. Henderson and Y. Larsen. 2010. Detailed rockslide mapping in northern Norway with small baseline and persistent scatterer interferometric SAR time series methods. *Remote Sensing of Environment.* 114(9):2097-2109.

Lavery, P., C. Pattiaratchi, A. Wyllie and P. Hick. 1993. Water quality monitoring in estuarine waters using the Landsat thematic mapper. *Remote Sensing of Environment.* 46:268-280.

Lawrence, R.L. 2017. Rigorous comparison of diverse classification algorithms. *37th International Symposium on Remote Sensing of the Environment*. Tswane, South Africa. 8-12 May 2017.

Lawrence, R.L., A. Bunn, S. Powell and M. Zambon. 2004. Classification of remotely sensed imagery using stochastic gradient boosting as a refinement of classification tree analysis. *Remote Sensing of Environment.* 90:331-336.

Lawrence, R.L. and C.J. Moran. 2015. The AmericaView classification methods accuracy comparison project: A rigorous approach for model selection. *Remote Sensing of Environment.* 170: 115-120.

Lawrence, R.L., S. Wood and R. Sheley. 2006. Mapping invasive plants using hyperspectral imagery and Breiman Cutler classifications (randomForest). *Remote Sensing of Environment.* 100:356-362.

Le, C., C. Hu, D. English, J. Cannizzaro and C. Kovach. 2013. Climate-driven chlorophyll-*a* changes in a turbid estuary: Observations from satellites and implications for management. *Remote Sensing of Environment.* 130:11-24.

Le, C., Y. Li, Y. Zha, D. Sun, C. Huang and H. Lu. 2009. A four-band semi-analytical model for estimating chlorophyll-*a* in highly turbid lakes: The case of Taihu Lake, China. *Remote Sensing of Environment.* 113:1175-1182.

Lee, S. and R.G. Lathrop. 2002. Sub-pixel estimation of urban land cover intensity using fuzzy c-means clustering. *Proceedings of the 2002 Annual Conference of the American Society for Photogrammetry and Remote Sensing.* 19-26 April 2002. Washington, D.C.

Lee, S. and R.G. Lathrop. 2005. Sub-pixel estimation of urban land cover components with linear mixture model analysis and Landsat Thematic Mapper imagery. *International Journal of Remote Sensing.* 26(22):4885-4905.

Lee, Z., K.L. Carder and R.A. Arnone. 2002. Deriving inherent optical properties from water color: A multiband quasi-analytical algorithm for optically deep waters. *Applied Optics. 41*(27):5755-5772.

Lee, Z., S. Shang, C. Hu, M. Lewis, R. Arnone, Y. Li and B. Lubac. 2010. Time series of bio-optical properties in a subtropical gyre: Implications for the evaluation of interannual trends of biogeochemical properties. *Journal of Geophysical Research: Oceans. 115*(C9).

Lehmann, E.A., P. Caccetta, K. Lowell, A. Mitchell, Z.-S. Zhou, A. Held, T. Milne and I. Tapley. 2015. SAR and optical remote sensing: Assessment of complementarity and interoperability in the context of a large-scale operational forest monitoring system. *Remote Sensing of Environment.* 156:335-348.

Leinss, S., A. Wiesmann, J. Lemmetyinen and I. Hajnsek, 2015. Snow water equivalent of dry snow measured by differential interferometry. *Institute of Electrical and Electronic Engineers Journal of Selected Topics in Applied Earth Observations and Remote Sensing.* 8(8):3773-3790.

Lenoble, J., M. Herman, J.L. Deuzé, B. Lafrance, R. Santer and D. Tanré, 2007. A successive order of scattering code for solving the vector equation of transfer in the earth's atmosphere with aerosols. *Journal of Quantitative Spectroscopy and Radiative Transfer.* 107(3):479-507.

Letelier, R.M. and M.R. Abbott. 1996. An analysis of chlorophyll fluorescence algorithms for the moderate resolution imaging spectrometer (MODIS). *Remote Sensing of Environment.* 58:215-223.

Levine, M.D. and A.M. Nazif. 1985. Dynamic measurement of computer generated image segmentations. *Institute of Electrical and Electronic Engineers Transactions on Pattern Analysis and Machine Intelligence.* 7(2):155-164.

Levy, R.C., L.A. Remer, R.G. Kleidman, S. Mattoo, C. Ichoku, R. Kahn and T.F. Eck. 2010. Global evaluation of the Collection 5 MODIS dark-target aerosol products over land. *Atmospheric Chemistry and Physics.* 10(21):10399-10420.

Li, A., C. Huang, G. Sun, H. Shi, C. Toney, Z. Zhu, M.G. Rollins, S.N. Goward and J.G. Masek. 2011. Modeling the height of young forests regenerating from recent disturbances in Mississippi using Landsat and ICESat data. *Remote Sensing of Environment.* 115(8):1837-1849.

Li, L. and J.F. Mustard. 2003. Highland contamination in lunar mare soils: Improved mapping with multiple end-member spectral mixture analysis (MESMA). *Journal of Geophysical Research E: Planets.* 108(6):7-1.

Li, L., S.L. Ustin and M. Lay. 2005. Application of multiple endmember spectral mixture analysis (MESMA) to AVIRIS imagery for coastal salt marsh mapping: A case study in China Camp, CA, USA. *International Journal of Remote Sensing.* 26(23):5193-5207.

Li, X. and A.G.O. Yeh. 1998. Principal component analysis of stacked multi-temporal images for the monitoring of rapid urban expansion in the Pearl River Delta. *International Journal of Remote Sensing.* 19(8):1501-1518.

Li, X., P. Gong and L. Liang. 2015. A 30-year (1984-2013) record of annual urban dynamics of Beijing City derived from Landsat data. *Remote Sensing of Environment.* 166:78-90.

Li, Z., C. Xue, X. Dong, Z. Liu, T. Zhong and S. Qi. 2013a. Ore geology, S-and Pb-isotopic compositions of the Wulagen Zn-Pb deposit, Wuqia County, Xinjiang. *Earth Science Frontiers.* 20(1):15.

Li, Z.-L., B.-H. Tang, H. Wu, H. Ren, G. Yan, Z. Wan, I.F. Trigo and J.A. Sobrino. 2013b. Satellite-derived land surface temperature: Current status and perspectives. *Remote Sensing of Environment.* 131:14-37.

Liao, T. W., 2005. Clustering of time series data-a survey. *Pattern recognition.* 38(11):1857-1874.

Liaw A. and M. Wiener. 2002. Classification and regression by randomForest. *R News,* 2/3:18-22.

Lillesand, T.M., R.W., Kiefer and J.W. Chipman. 2015. *Remote Sensing and Image Interpretation. 7th ed.*, John Wiley & Sons, Inc., New York, New York. 720 p.

Linderman, M., J. Liu, J. Qi, L. An, Z. Ouyang, J. Yang and Y. Tan. 2004. Using artificial neural networks to map the spatial distribution of understorey bamboo from remote sensing data. *International Journal of Remote Sensing*. 25(9):1685-1700.

Lippitt, C.D., A. Stow and L.C. Coulter (eds.). 2015. Time Sensitive Remote Sensing. Springer. 198p. ISBN 978-11-4939-2601-5.

Liu, Y, H. Xue, J. Wang and H. Zhou. 2012. Comparison and analysis of two fractal dimension computing algorithms for upscaling remote sensing leaf area index map. *IGARSS 2012.* 1684-1687.

Lo, T.H.C., F.L. Scarpace and T.M. Lillesand. 1986. Use of multitemporal spectral profiles in agricultural land-cover classification. *Photogrammetric Engineering & Remote Sensing.* 52:535-544.

Lobell, D. B. and G.P. Asner. 2004. Cropland distributions from temporal unmixing of MODIS data. *Remote Sensing of Environment.* 93(3):412-422.

Lobell, D.B., D. Thau, C. Seifert, E. Engle and B. Little. 2015. A scalable satellite-based crop yield mapper. *Remote Sensing of Environment.* 164:324-333.

Lobser, S.E. and W.B. Cohen. 2007. MODIS tasselled cap: land cover characteristics expressed through transformed MODIS data. *International Journal of Remote Sensing.* 28(22):5079-5101.

Lorimer, N.D., R.G. Haight and R.A. Leary. 1994. *The Fractal Forest: Fractal Geometry and Applications in Forest Science* (USDA: General Technical Report NC-170).

Los, S.O. 1993. Calibration adjustment of the NOAA AVHRR Normalized Difference Vegetation Index without resource to component channel-1 and channel-2 data. *International Journal of Remote Sensing.* 14(10):1907-1917.

Lovejoy, S. 1982. Area-perimeter relation for rain and cloud areas. *Science.* 216:185-187.

Lu, D. and Q. Weng. 2004. Spectral mixture analysis of the urban landscape in Indianapolis city with Landsat ETM+ imagery. *Photogrammetric Engineering & Remote Sensing*. 70(9):1053-1062.

Lu, D. and Q. Weng. 2006. Spectral mixture analysis of ASTER images for examining the relationship between urban thermal features and biophysical descriptors in Indianapolis, Indiana, USA. *Remote Sensing of Environment.* 104(2):157-167.

Lu, D., M. Batistella, E. Moran and P. Mausel. 2004. Application of spectral mixture analysis to Amazonian land-use and land-cover classification. *International Journal of Remote Sensing.* 25(23):5345-5358.

Lu, L., C. Wang, H. Guo and Q. Li. 2014. Detecting winter wheat phenology with SPOT-VEGETATION data in the North China Plain. *Geocarto International.* 29(3):244-255.

Luneta, R.S. and C.D. Elvidge. 1998. Remote Sensing Change Detection. *Environmental Monitoring Methods and Applications.* Ann Arbor Press. Chelsea, MI.

Lyapustin, A., Y. Wang, I. Laszlo, R. Kahn, S. Korkin, L. Remer, R. Levy and J. S. Reid. 2011. Multiangle implementation of atmospheric correction (MAIAC): 2. Aerosol algorithm. *Journal of Geophysical Research: Atmospheres.* (1984-2012). 116(D3).

Lyapustin, A.I., Y. Wang, I. Laszlo, T. Hilker, F.G. Hall, P.J. Sellers, C.J. Tucker and S.V. Korkin. 2012. Multi-angle implementation of atmospheric correction for MODIS (MAIAC): 3. Atmospheric correction. *Remote Sensing of Environment.* 127:385-393.

Ma, Y., H. Wu, L. Wang, B. Huang, R. Ranjan, A. Zomaya and W. Jie. 2015. Remote sensing big data computing: Challenges and opportunities. *Future Generation Computer Systems.* 51:47-60.

Madden, M., T. Jordan, D.L. Cotten, N. O'Hare, A. Pasqua and S. Bernardes. 2015. The future of unmanned aerial systems (UAS) for monitoring natural and cultural resources. *Photogrammetric Week. 2015.* 7-11 September 2015. Universität Stuttgart.

Mafanya, M., P. Tsele, J. Botai, P. Manyama, B. Swart and T. Monate. 2017. Evaluating pixel and object based image classification techniques for mapping plant invasions from UAV derived aerial imagery: Harrisia pomanensis as a case study. *ISPRS Journal of Photogrammetry and Remote Sensing*. 129:1-11.

Maglione, P., C. Parente and A. Vallario. 2014. Coastline extraction using high resolution Worldview-2 satellite imagery. *European Journal of Remote Sensing.* 47:685-699.

Maguya, A.S., K. Tegel, V. Junttila, T. Kauranne, M. Korhonen, J. Burns, V. Leppanen and B. Sanz. 2015. Moving voxel method for estimating canopy base height from airborne laser scanner data. *Remote Sensing.* 7:8950-8972.

Mainali, K.P., D.L. Warren, K. Dhileepan, A. McConnachie, L. Strathie, G. Hassan, D. Karki, B.B. Shrestha and C. Parmesan. 2015. Projecting future expansion of invasive species: Comparing and improving methodologies for species distribution modeling. *Global Change Biology.* 21(12):4464-4480.

Maini, R. and H. Aggarwal. 2010. A comprehensive review of image enhancement techniques. *Journal of Computing.* 2(3):8-13.

Major, D.J., G.B. Schaalje, C. Wiegand and B.L. Blad. 1992. Accuracy and sensitivity analyses of SAIL model-predicted reflectance of maize. *Remote Sensing of Environment.* 41:61-70.

Malenovský, Z., H. Rott, J. Cihlar, M.E. Schaepman, G. García-Santos, R. Fernandes and M. Berger. 2012. Sentinels for science: Potential of Sentinel-1, -2, and -3 missions for scientific observations of ocean, cryosphere, and land. *Remote Sensing of Environment.* 120:91-101.

Mallat, S.G. 2009. *A wavelet tour of signal processing: the sparse way.* Elsevier/Academic Press, Boston. 805 p.

Mancini, F., M. Dubbini, M. Stecchi Gattelli, S.F. Fabbri and G. Gabbianelli. 2013. Using unmanned aerial vehicles (UAV) for high-resolution reconstruction of topography: The structure from motion approach on coastal environments. *Remote Sensing.* 5(12):6880-6898.

Mandelbrot, B. B. 1967. How long is the coast of Britain? Statistical self-similarity and fractional dimension. *Science*, 156:636-638.

Mandelbrot, B. B. 1977. *Fractals: Form, Chance and Dimension.* W. H. Freeman and Company, San Francisco. 365p.

Mandelbrot, B. B. 1982. *The Fractal Geometry of Nature.* W. H. Freeman and Company, New York. 468 p.

Mandelbrot, B. B. 1985. Self-affine fractals and the fractal dimension, *Physica Scripta.* 32:257-260.

Mandelbrot, B. B., 1989. Multifractal measures, especially for the geophysicist. *Pageoph.* 131:5-42.

Mantero, P., G. Moser and S.B. Serpico. 2005. Partially supervised classification of remote sensing images through SVM-based probability density estimation. *IGARSS 2012. IEEE Transactions on Geoscience and Remote Sensing*, 43(3):559-570.

Maritorena, S., D.A. Siegel and A.R. Peterson. 2002. Optimization of a semi-analytical ocean color model for global-scale applications. *Applied Optics. 41*(15):2705-2714.

Mark, D.M. and P.B. Aronson. 1984. Scale-dependent fractal dimensions of topographic surfaces: An empirical investigation with application in geomorphology and computer mapping. *Mathematical Geology.* 16:671-683.

Marshall, M., E. Okuto, Y. Kang, E. Opiyo and M. Ahmed. 2016. Global assessment of Vegetation Index and Phenology Lab (VIP) and Global Inventory Modeling and Mapping Studies (GIMMS) version 3 products. *Biogeosciences.* 13(3):625-639.

Martha, T.R., N. Kerle, C.J. van Westen, V. Jetten and K.V. Kumar. 2011. Segment optimization and data-driven thresholding for knowledge-based landslide detection by object-based image analysis. *Institute of Electrical and Electronics Engineers Transactions on Geoscience and Remote Sensing.* 49(12):4928-4943.

Martín, G. and A. Plaza. 2011. Region-based spatial preprocessing for endmember extraction and spectral unmixing. *Institute of Electrical and Electronics Engineers Geoscience and Remote Sensing Letters.* 8(4):745-749.

Martin, L.R.G. 1989. Accuracy assessment of Landsat-based visual change detection methods applied to the rural-urban fringe. *Photogrammetric Engineering and Remote Sensing.* 55:209-215.

Martín, M.P. and E. Chuvieco. 1995. Mapping and evaluation of burned land from multitemporal analysis of AVHRR NDVI images. *EARSeL Advances in Remote Sensing.* 4(3):7-13.

Maselli, F. 1998. Multiclass spectral decomposition of remotely sensed scenes by selective pixel unmixing. *Institute of Electrical and Electronics Engineers Transactions on Geoscience and Remote Sensing.* 36(5):1809-1820.

Matheson, D. S. and P.E. Dennison. 2012. Evaluating the effects of spatial resolution on hyperspectral fire detection and temperature retrieval. *Remote Sensing of Environment.* 124:780-792.

Matsushita, B., W. Yang, G. Yu, Y. Oyama, K. Yoshimura and T. Fukushima. 2015. A hybrid algorithm for estimating the chlorophyll-*a* concentration across different trophic states in Asian inland waters. *ISPRS Journal of Photogrammetry and Remote Sensing.* 102:28-37.

Mazer, A.S., M. Martin, M. Lee and J.E. Solomon. 1988. Image processing software for imaging spectrometry analysis. *Remote Sensing of Environment.* 24:201-210.

McCullagh, P. and J.A. Nelder. 1989. *Generalized linear models*. London: Chapman & Hall.

Medeiros, S.C., S.C. Hagen, N. Chaouch, J. Feyen, M. Temimi, J.F. Weishampel, Y. Funakoshi and R. Khanbilvardi, 2013. Assessing the performance of a Northern Gulf of Mexico tidal model using satellite imagery. *Remote Sensing.* 5(11):5662-5679.

Melaas, E.K., M.A. Friedl and Z. Zhu. 2013. Detecting interannual variation in deciduous broadleaf forest phenology using Landsat TM/ETM + data. *Remote Sensing of Environment.* 132:176-185.

Melgani, F. 2006. Contextual reconstruction of cloud-contaminated multitemporal multispectral images. *Institute of Electrical and Electronics Engineers Transactions on Geoscience and Remote Sensing.* 44(2):442-455.

Mélin, F. and V. Vantrepotte. 2015. How optically diverse is the coastal ocean? *Remote Sensing of Environment.* 160:235-251.

Merchant, C.J., G. de Leeuw and W. Wagner. 2015. Selecting algorithms for Earth observation of climate within the European Space Agency Climate Change Initiative: Introduction to a special issue. *Remote Sensing of Environment.* 162:239-241.

Meroni, M., M. Rossini, L. Guanter, L. Alonso, U. Rascher, R. Colombo and J. Moreno. 2009. Remote sensing of solar-induced chlorophyll fluorescence: Review of methods and applications. *Remote Sensing of Environment.* 113(10):2037-2051.

Mertes, L.A., M.O. Smith and J.B. Adams. 1993. Estimating suspended sediment concentrations in surface waters of the Amazon River wetlands from Landsat images. *Remote Sensing of Environment.* 43(3):281-301.

Metropolis, N., A.W. Rosenbluth, M.N. Rosenbluth, A.H. Teller and E. Teller. 1953. Equations of state calculations by fast computing machines. *Journal of Chemical Physics.* 21:1087-1092.

Meyer, F.J., D.B. McAlpin, W. Gong, O. Ajadi, S. Arko, P.W. Webley and J. Dehn. 2015. Integrating SAR and derived products into operational volcano monitoring and decision support systems. *ISPRS Journal of Photogrammetry and Remote Sensing.* 100:106-117.

Middleton, E.M., K.F. Huemmrich, Y.B. Cheng and H.A. Margolis. 2011. Spectral bio-indicators of photosynthetic efficiency and vegetation stress. *Hyperspectral Remote Sensing of Vegetation.* In: P.S. Thenkabail, J.G. Lyon, and A. Huete (editors). Taylor and Francis. pp. 265-288.

Miller, J.R., S.C. Jain, N.T. O'Neill, W.R. McNeil and K.P.B. Thomson. 1977. Interpretation of airborne spectral reflectance measurements over Georgian Bay. *Remote Sensing of Environment.* 6:183-200.

Milne, B. T. 1991. Lessons from applying fractal models to landscape patterns. *Quantitative Methods in Landscape Ecology.* M. G. Turner and R. H. Gardern, editors. Springer-Verlag, New York, pp. 199-235.

Mingers, J. 1989a. An empirical comparison of selection measures for decision tree induction. *Machine Learning.* 3: 319-342.

Mingers, J. 1989b. An empirical comparison of pruning methods for decision tree induction. *Machine Learning* 4: 227-243.

Mishra, D.R. 2014. Editorial on “Coastal Remote Sensing”. *GIScience and Remote Sensing.* 51(2):115-119.

Mishra, S. and D.R. Mishra. 2012. Normalized difference chlorophyll index: A novel model for remote estimation of chlorophyll-*a* concentration in turbid productive waters. *Remote Sensing of Environment.* 117:394-406.

Mishra, S., D.R. Mishra, Z. Lee and C.S. Tucker. 2013. Quantifying cyanobacterial phycocyanin concentration in turbid productive waters: A quasi-analytical approach. *Remote Sensing of Environment.* 133:141-151.

Mitri, G.H. and I.Z. Gitas. 2008. Mapping the severity of fire using object-based classification of IKONOS imagery. *International Journal of Wildland Fire.* 17:431-442.

Miura, T., A.R. Huete and H. Yoshioka. 2000. Evaluation of sensor calibration uncertainties on vegetation indices for MODIS. *Institute of Electrical and Electronics Engineers Transactions on Geoscience and Remote Sensing.* 38(3):1399-1409.

Miura, T., A.R. Huete and H. Yoshioka. 2006. An empirical investigation of cross-sensor relationships of NDVI and red/near-infrared reflectance using EO-1 Hyperion data. *Remote Sensing of Environment.* 100(2):223-236.

Miura, T., J.P. Turner and A.R. Huete. 2013. Spectral compatibility of the NDVI across VIIRS, MODIS, and AVHRR: An analysis of atmospheric effects using EO-1 Hyperion. *Institute of Electrical and Electronics Engineers Transactions on Geoscience and Remote Sensing.* 51(3):1349-1359.

MODIS Land Team. 2015. Validation status for Vegetation Indices (MOD13). URL: http://landval.gsfc.nasa.gov/ProductStatus.php? ProductID=MOD13. National Aeronautics and Space Administration.

Moeller, M., L. Lymburner and M. Volk. 2007. The comparison index: A tool for assessing the accuracy of image segmentation. *International Journal of Applied Earth Observation and Geoinformation.* 9(3):311-321.

Moffett, K.B. and S.M. Gorelick. 2013. Distinguishing wetland vegetation and channel features with object-based image segmentation. *International Journal of Remote Sensing.* 34(4):1332-1354.

Mohan, B.K., B.B. Madhavan and U.M.D. Gupta. 2000. Integration of IRS-1A L2 data by fuzzy logic approaches for land use classification. *International Journal of Remote Sensing.* 21(8):1709-1723.

Molina, J.R., F.R.Y. Silva, E. Merida and M.A. Herrera. 2014. Modelling available crown fuel for *Pinus pinaster* stands in the Cazorla, Segura and Las Villas Natural Park (Spain). *Journal of Environmental Management.* 144:26-33.

Montealegre, A.L., M.T. Lamelas, M.A. Tanase and J. de la Riva. 2014. Forest fire severity assessment using ALS data in a Mediterranean environment. *Remote Sensing.* 6:4240-4265.

Montes-Hugo, M.A., K. Carder, R.J. Foy, J. Cannizzaro, E. Brown and S. Pegau. 2005. Estimating phytoplankton biomass in coastal waters of Alaska using airborne remote sensing. *Remote Sensing of Environment.* 98:481-493.

Morsdorf, F., E. Meier, B. Kotz, K.I. Itten, M. Dobbertin and B. Allgower. 2004. LIDAR-based geometric reconstruction of boreal type forest stands at single tree level for forest and wildland fire management. *Remote Sensing of Environment.* 92:353-362.

Morton, D.C., J. Nagol, C.C. Carabajal, J. Rosette, M. Palace, B.D. Cook, E.F. Vermote, D.J. Harding and P.R.J. North. 2014. Amazon forests maintain consistent canopy structure and greenness during the dry season. *Nature.* 506(7487):221-224.

Moses, W.J., A.A. Gitelson, S. Berdnikov and V. Povazhnyy. 2009. Satellite estimation of chlorophyll-*a* concentration using the red and NIR bands of MERIS-The Azov Sea Case Study. *Institute of Electrical and Electronics Engineers Geoscience and Remote Sensing Letters.* 6(4):845-849.

Moses, W.J., A.A. Gitelson, S. Berdnikov, V. Saprygin and V. Povazhnyi. 2012. Operational MERIS-based NIR-red algorithms for estimating chlorophyll-*a* concentrations in coastal waters: The Azov Sea case study. *Remote Sensing of Environment.* 121:118-124.

Motagh, M., H.-U. Wetzel, S. Roessner and H. Kaufmann. 2013. A TerraSAR-X InSAR study of landslides in southern Kyrgyzstan, Central Asia. *Remote Sensing Letters.* 4(7):657-666.

Mouat, D.A., G.G. Mattin and J. Lancaster. 1993. Remote sensing techniques in the analysis of change detection. *Geocarto International.* 8:39-50.

Mountrakis, G., J. Im and C. Ogole. 2011. Support vector machines in remote sensing: A review. *ISPRS Journal of Photogrammetry and Remote Sensing.* 66(3):247-259.

Mouw, C.B., S. Greb, D. Aurin, P.M. DiGiacomo, Z. Lee, M. Twardowski, C. Binding, C. Hu, R. Ma, T. Moore, W. Moses and S.E. Craig. 2015. Aquatic color radiometry remote sensing of coastal and inland waters: Challenges and recommendations for future satellite missions. *Remote Sensing of Environment.* 160:15-30.

Muldashev, T.Z., A.I. Lyapustin and U.M. Sultangazin. 1999. Spherical harmonics method in the problem of radiative transfer in the atmosphere-surface system. *Journal of Quantitative Spectroscopy and Radiative Transfer.* 61(3):393-404.

Murthy, S.K., S. Kasif and S. Salzberg. 1994. A system for induction of oblique decision trees. *Journal of Artificial Intelligence Research.* 2:1-32.

Myint, S.W. 2003. Fractal approaches in texture analysis and classification of remotely sensed data: Comparisons with spatial autocorrelation techniques and simple descriptive statistics. *International Journal of Remote Sensing.* 24:1925-1947.

Myint, S.W., N. S.-N. Lam. 2005. Examining lacunarity approaches in comparison with fractal and spatial autocorrelation techniques for urban mapping. *Photogrammetric Engineering and Remote Sensing.* 71(8):927-937.

Myint, S.W., P. Gober, A. Brazel, S. Grossman-Clarke and Q. Weng. 2011. Per-pixel vs. object-based classification of urban land cover extraction using high spatial resolution imagery. *Remote Sensing of Environment.* 115(5):1145-1161.

Myneni, R.B., C.D. Keeling, C.J. Tucker, G. Asrar and R.R. Nemani. 1997. Increased plant growth in the northern high latitudes from 1981- 1991. *Nature.* 386:698-702.

Nascimento, J.M. and J.M.B. Dias. 2005. Vertex component analysis: A fast algorithm to unmix hyperspectral data. *Institute of Electrical and Electronics Engineers Transactions on Geoscience and Remote Sensing.* 43(4):898-910.

Nash, D.B. and J.E. Conel. 1974. Spectral reflectance systematics for mixtures of powdered hypersthene, labradorite, and ilmenite. *Journal of Geophysical Research.* 79(11):1615-1621.

Navalgund, R.R. and R.P. Singh. 2011. Climate change studies using space based observation. *Journal of the Indian Society of Remote Sensing.* 39(3):281-295.

Negrón-Juárez, R.I., J.Q. Chambers, D.M. Marra, G.H.P.M. Ribeiro, S.W. Rifai, N. Higuchi and D.A. Roberts. 2011. Detection of subpixel treefall gaps with Landsat imagery in Central Amazon forests. *Remote Sensing of Environment.* 115:3322-3328.

Newnham, G.J. and T. Burt. 2001. Validation of a leaf reflectance and transmittance model for three agricultural crop species. *International Geoscience and Remote Sensing Symposium.* 7:2976-2978.

Niedermeier, A., E. Romaneessen, and S. Lehner, 2000. Detection of coastlines in SAR images using wavelet methods. *IEEE Transactions on Geoscience and Remote Sensing.* 38:2270-2281.

Normant, F. and C. Tricot. 1993. Fractal simplification of lines using convex hulls. *Geographical Analysis* 25:118-129.

Numata, I., D.A. Roberts, Y. Sawada, O.A. Chadwick, J.P. Schimel and J.V. Soares. 2007. Regional characterization of pasture changes through time and space in Rondonia, Brazil. *Earth Interactions.* 11(Paper No. 14):25 pp.

O'Connor, B., E. Dwyer, F. Cawkwell and L. Eklundh. 2012. Spatio-temporal patterns in vegetation start of season across the island of Ireland using the MERIS Global Vegetation Index. *ISPRS Journal of Photogrammetry and Remote Sensing.* 68:79-94.

O'Neil-Dunne, J.P.M., S.W. MacFaden, A.R. Royar and K.C. Pelletier. 2013. An object-based system for LiDAR data fusion and feature extraction. *Geocarto International.* 28(3):227-242.

Obata, K., T. Miura, H. Yoshioka and A.R. Huete. 2013. Derivation of a MODIS-compatible enhanced vegetation index from visible infrared imaging radiometer suite spectral reflectances using vegetation isoline equations. *Journal of Applied Remote Sensing.* 7(1):073467.

Obata, K., T. Miura, H. Yoshioka, A.R. Huete and M. Vargas. 2016. Spectral cross-calibration of VIIRS Enhanced Vegetation Index with MODIS: A case study using year-long global data. *Remote Sensing.* 8(1):34.

OGC. 1999. The Open GIS™ abstract specification. Volume 7: The Earth Imagery Case (99-107.doc). http://www.opengis.org/techno/specs.htm.

Okeke, F. and A. Karnieli. 2006a. Methods for fuzzy classification and accuracy assessment of historical aerial photographs for vegetation change analyses. Part I: Algorithm development. *International Journal of Remote Sensing*. 27(1/2):153-176.

Okeke, F. and A. Karnieli. 2006b. Methods for fuzzy classification and accuracy assessment of historical aerial photographs for vegetation change analyses. Part II: Practical application. *International Journal of Remote Sensing.* 27(9):1825-1838.

Okin, G.S. 2007. Relative spectral mixture analysis-A multitemporal index of total vegetation cover. *Remote Sensing of Environment.* 106(4):467-479.

Okin, G.S., D.A. Roberts, B. Murray and W.J. Okin. 2001. Practical limits on hyperspectral vegetation discrimination in arid and semiarid environments. *Remote Sensing of Environment.* 77:212-225.

Opitz D. and R. Maclin. 1999. Popular ensemble methods: An empirical study. *Journal of Artificial Intelligence Research.* 11:169-198.

O'Reilly, J.E., S. Maritorena, B.G. Mitchell, D.A. Siegel, K.L. Carder, S.A. Garver, M. Kahru and C. McClain. 1998. Ocean color chlorophyll algorithms for SeaWiFS. *Journal of Geophysical Research: Oceans.* 103:24937-24953.

O'Reilly, J.E., S. Maritorena, D.A. Siegel, M.C. O'Brien, D. Toole, B.G. Mitchell, M. Kahru, F.P. Chavez, P. Strutton, G.F. Cota and S.B. Hooker. 2000. Ocean color chlorophyll-*a* algorithms for SeaWiFS, OC2 and OC4: Version 4. *SeaWiFS post-launch calibration and validation analyses. Part 3*:9-23.

Orford, J.D. and W.B. Whalley. 1983. The use of the fractal dimension to quantify the morphology of irregular-shaped particles. *Sedimentology* 30:655-668.

Otsu, N. 1979. Threshold selection method from gray-level histograms. Institute of Electrical and Electronics Engineers. Transactions on Systems Man and Cybernetics. 9(1):62-66.

Ouaidrari, H. and E.F. Vermote. 1999. Operational atmospheric correction of Landsat TM data. *Remote Sensing of Environment.* 70:4-15.

Ozdogan, M. 2010. The spatial distribution of crop types from MODIS data: Temporal unmixing using Independent Component Analysis. *Remote Sensing of Environment.* 114(6):1190-1204.

Padilla, M., S.V. Stehman, R. Ramo, D. Corti, S. Hantson, P. Oliva, I. Alonso-Canas, A.V. Bradley, K. Tansey, B. Mota, J.M. Pereira and E. Chuvieco, 2015. Comparing the accuracies of remote sensing global burned area products using stratified random sampling and estimation. *Remote Sensing of Environment.* 160:114-121.

Painter, T.H., D.A. Roberts, R.O. Green and J. Dozier. 1998. The effect of grain size on spectral mixture analysis of snow-covered area from AVIRIS data. *Remote Sensing of Environment.* 65:320-332.

Painter, T.H., J. Dozier, D.A. Roberts, R.E. Davis and R.O. Green. 2003. Retrieval of subpixel snow-covered area and grain size from imaging spectrometer data. *Remote Sensing of Environment.* 85(1):64-77.

Pal, M. 2005. Random forest classifier for remote sensing classifications. *International Journal of Remote Sensing.* 26:217-222.

Pal, M. 2007. Ensemble learning with decision tree for remote sensing classification, *Proceedings of World Academy of Science, Engineering and Technology*, December 14-16, Bangkok, 36:258-260.

Pal, M. and P.M. Mather. 2003. An assessment of the effectiveness of decision tree methods for land cover classification. *Remote Sensing of Environment.* 86:554-565.

Palmer, S.C.J., D. Odermatt, P.D. Hunter, C. Brockmann, M. Présing, H. Balzter and V.R. Tóth. 2015. Satellite remote sensing of phytoplankton phenology in Lake Balaton using 10 years of MERIS observations. *Remote Sensing of Environment.* 158:441-452.

Palsule, S.S., G. Paswan, S.S.S. Kopparthi and B. Shah. 2004. Assessment of geo-positioning accuracy achieved using rational function model for Cartosat-1 stereo data. *Archives of Photogrammetry and Remote Sensing.* Istanbul.

Pan, Z., J. Huang, Q. Zhou, L. Wang, Y. Cheng, H. Zhang, G.A. Blackburn, J. Yan and J. Liu. 2015. Mapping crop phenology using NDVI time-series derived from HJ-1 A/B data. *International Journal of Applied Earth Observation and Geoinformation.* 34:188-197.

Panciera, R., J.P. Walker, T.J. Jackson, D.A. Gray, M.A. Tanase, D. Ryu, A. Monerris, H. Yardley, C. Rudiger, X. Wu, Y. Gao and J.M. Hacker. 2014. The Soil Moisture Active Passive Experiments (SMAPEx): Toward soil moisture retrieval from the SMAP mission. *Institute of Electrical and Electronics Engineers Transactions on Geoscience and Remote Sensing.* 52(1):490-507.

Parks, M.M., J. Biggs, P. England, T.A. Mather, P. Nomikou, K. Palamartchouk, X. Papanikolaou, D. Paradissis, B. Parsons, D.M. Pyle, C. Raptakis and V. Zacharis. 2012. Evolution of Santorini Volcano dominated by episodic and rapid fluxes of melt from depth. *Nature Geoscience.* 5(10):749-754.

Paul, F., T. Bolch, A. Kääb, T. Nagler, C. Nuth, K. Scharrer, A. Shepherd, T. Strozzi, F. Ticconi, R. Bhambri, E. Berthier, S. Bevan, N. Gourmelen, T. Heid, S. Jeong, M. Kunz, T.R. Lauknes, A. Luckman, J.P. Merryman Boncori, G. Moholdt, A. Muir, J. Neelmeijer, M. Rankl, J. VanLooy and T. Van Niel. 2015. The glaciers climate change initiative: Methods for creating glacier area, elevation change and velocity products. *Remote Sensing of Environment.* 162:408-426.

Pearson, R.G., T.P. Dawson, P.M Berry and P.A. Harrison. 2002. Species: A Spatial Evaluation of climate impact on the envelope of species. *Ecological Modelling.* 154: 289-300.

Peitgen, H.O. and D. Saupe. 1988. *The Science of Fractal Images*, Springer-Verlag, New York, 312 p.

Pentland, A.P. 1984. Fractal-based descriptions of natural scenes, Institute of Electrical and Electronics Engineers Transactions on Pattern Analysis and Machine Intelligence, 6:661-674.

Penuelas, J., T. Rutishauser and I. Filella. 2009. Phenology feedbacks on climate change. *Science.* 324(5929):887-888.

Perkins, T., S. Adler-Golden, M.W. Matthew, A. Berk, L.S. Bernstein, J. Lee and M. Fox. 2012. Speed and accuracy improvements in FLAASH atmospheric correction of hyperspectral imagery. *Optical Engineering.* 51:111707/1. DOI doi: 10.1117/1.OE.51.11.111707.

Peterson, A. 2006. Uses and requirements of ecological niche models and related distributional models. *Biodiversity Informatics.* 3:59-72.

Peterson, A., M. Papes and D.A. Kluza. 2003. Predicting the potential invasive distributions of four alien plant species in North America. *Weed Science.* 51(6):863-868.

Peterson, B., K. Nelson and B. Wylie. 2013. Towards integration of GLAS into a national fuel mapping program. *Photogrammetric Engineering and Remote Sensing.* 79:175-183.

Peterson, B., K.J. Nelson, C. Seielstad, J. Stoker, W.M. Jolly and R. Parsons. 2015. Automated integration of lidar into the LANDFIRE product suite. *Remote Sensing Letters.* 6:247-256.

Peterson, S.H., D.A. Roberts, M. Beland, R.F. Kokaly and S.L. Ustin. 2015. Oil detection in the coastal marshes of Louisiana using MESMA applied to band subsets of AVIRIS data. *Remote Sensing of Environment.* 159:222-231.

Petropoulos, G.P., C. Kalaitzidis and K. Prasad Vadrevu. 2012. Support vector machines and object-based classification for obtaining land-use/cover cartography from Hyperion hyperspectral imagery. *Computers & Geosciences.* 41:99-107.

Pfeifer, M., A. Gonsamo, M. Disney, P. Pellikka and R. Marchan. 2012. Leaf area index for biomes of the Eastern Arc Mountains: Landsat and SPOT observations along precipitation and altitude gradients. *Remote Sensing of Environment.* 118:103-115.

Pflugmacher, D., W.B. Cohen, R.E. Kennedy and Z. Yang. 2014. Using Landsat-derived disturbance and recovery history and lidar to map forest biomass dynamics. *Remote Sensing of Environment.* 151:124-137.

Pharr, M. and G. Humphreys. 2004. *Physically Based Rendering: From Theory to Implementation*. Morgan Kaufmann Publishers. San Francisco, USA. 1056 p.

Phillips, S.J., M. Dudík, J. Elith, C.H. Graham, A. Lehmann, J. Leathwick and S. Ferrier. 2009. Sample selection bias and presence-only distribution models: implications for background and pseudo-absence data. *Ecological Applications.* 19(1):181-97.

Phillips, S.J., R.P. Anderson and R.E. Shapire. 2006. Maximum entropy modelling of species geographic distributions. *Ecological Modelling.* 190:231-259.

Phinn, S., M. Stanford, P. Scarth, A.T. Murray and P.T. Shyy. 2002. Monitoring the composition of urban environments based on the vegetation-impervious surface-soil (VIS) model by subpixel analysis techniques. *International Journal of Remote Sensing.* 23(20):4131-4153.

Pilon, P., P.J. Howarth, R.A. Bullock and P.O. Adeniyi. 1988. An enhanced classification approach to change detection in semi-arid environments. *Photogrammetric Engineering & Remote Sensing.* 54:1709-1716.

Pinzon, E.J. and J.C. Tucker. 2014. A non-stationary 1981–2012 AVHRR NDVI3g time series. *Remote Sensing.* 6(8):6929-6960.

Pinzon, E.J., M.E. Brown and C.J. Tucker. 2005. EMD correction of orbital drift artifacts in satellite data stream, *Hilbert-Huang Transform and Applications* (N.E. Huang and S.S.P. Shen. eds.). World Scientific Publishing Co. Pty. Ltd. pp.167-186.

Platt, R.V. and L. Rapoza. 2008. An evaluation of an object-oriented paradigm for land use/land-cover classification. *The Professional Geographer.* 60(1):87-100.

Plaza, A., Q. Du, Y.L. Chang and R.L. King. 2011. Foreword to the special issue on high performance computing in earth observation and remote sensing. *Institute of Electrical and Electronics Engineers Transactions on Geoscience and Remote Sensing Journal of Selected Topics in Applied Earth Observations and Remote Sensing.* 3(4):503-507.

Plourde, L.C., S.V. Ollinger, M.L. Smith and M.E. Martin. 2007. Estimating species abundance in a northern temperate forest using spectral mixture analysis. *Photogrammetric Engineering & Remote Sensing.* 73(7):829-840.

Pohl, C. and J. van Genderen. 1998. Review article multisensor image fusion in remote sensing: concepts, methods and applications. *International Journal of Remote Sensing.* 19(5):823-854.

Ponce-Campos, G.E., M.S. Moran, A. Huete, Y. Zhang, C. Bresloff, T.E. Huxman, D. Eamus, D.D. Bosch, A.R. Buda, S.A. Gunter, T.H. Scalley, S.G. Kitchen, M.P. McClaran, W.H. McNab, D.S. Montoya, J.A. Morgan, D.P. C. Peters, E.J. Sadler, M.S. Seyfried and P.J. Starks. 2013. Ecosystem resilience despite large-scale altered hydroclimatic conditions. *Nature.* 494(7437):349-352.

Pontius, J., G. Robert, E. Shusas and M. McEachern. 2004. Detecting important categorical land changes while accounting for persistence. *Agriculture, Ecosystems & Environment.* 101(2-3):251-268.

Porcar-Castell, A., E. Tyystjärvi, J. Atherton, C. van der Tol, J. Flexas, E.E. Pfündel, J. Moreno, C. Frankenberg, and J.A. Berry. 2014. Linking chlorophyll-*a* fluorescence to photosynthesis for remote sensing applications: mechanisms and challenges. *Journal of Experimental Botany.* 65(15):4065-4095.

Powell, R., D.A. Roberts, L. Hess and P. Dennison. 2007. Sub-pixel mapping of urban land cover using multiple endmember spectral mixture analysis: Manaus, Brazil. *Remote Sensing of Environment.*106:253-267.

Powell, S.L., W.B. Cohen, R.E. Kennedy, S.P. Healey and C. Huang. 2013. Observation of trends in biomass loss as a result of disturbance in the Conterminous U.S.: 1986-2004. *Ecosystems.* 17(1):142-157.

Pratt, W.K. 2014. *Digital Image Processing*.4th ed., CRC press, Boca Raton, Florida. 756 p.

Price, J.C. 1992. Estimating vegetation amount from visible and near infrared reflectances. *Remote Sensing of Environment.* 41(1):29-34.

Privette, J.L., G.P. Asner, J. Conel, K.F. Huemmrich, R. Olson, A. Rango, A.F. Rahman, K. Thome and E.A. Walter-Shea. 2000. The EOS Prototype Validation Exercise (PROVE) at Jornada: Overview and Lessons Learned, *Remote Sensing of Environment.* 74(1):1-12.

Qiu, H., N.S.N. Lam, D.A. Quattrochi and J.A. Gamon. 1999. Fractal characterization of hyperspectral imagery. *Photogrammetric Engineering and Remote Sensing.* 65:63-71.

Quarmby, N.A., J.R.G. Townshend, J.J. Settle, K.H. White, M. Milnes, T.L. Hindle and N. Silleos. 1992. Linear mixture modelling applied to AVHRR data for crop area estimation. *International Journal of Remote Sensing*. 13(3):415-425.

Quattrochi, D.A., N.S.N. Lam, H.L. Qiu and W. Zhao. 1997. Image characterization and modeling system (ICAMS): a geographic information system for the characterization and modeling of multiscale remote sensing data. *Scale in Remote Sensing and GIS* (D.A. Quattrochi and M.F. Goodchild, editors), CRC press, Boca Raton, Florida. pp. 295-308.

Quinlan, J.R. 1987. Simplifying decision trees. *International Journal of Man-Machine Studies.* 27:221-234.

Quinlan, J.R. 1993. *C4.5: Programs for Machine Learning*. Morgan Kaufmann. San Mateo.

Quintano, C., A. Fernandez-Manso and D.A. Roberts. 2013. Multiple Endmember Spectral Mixture Analysis (MESMA) to map burn severity levels from Landsat images in Mediterranean countries. *Remote Sensing of Environment.* 136:76-88.

Quintano, C., A. Fernandez-Manso, O. Fernandez-Manso and Y. Shimabukuro. 2006. Mapping burned areas in the Mediterranean using Spectral Mixture Analysis. *International Journal of Remote Sensing.* 27(4):645-662.

Radoux, J. and P. Bogaert. 2014. Accounting for the area of polygon sampling units for the prediction of primary accuracy assessment indices. *Remote Sensing of Environment.* 142:9-19.

Radoux, J. and P. Defourny. 2007. A quantitative assessment of boundaries in automated forest stand delineation using very high resolution imagery. *Remote Sensing of Environment.* 110(4):468-475.

Radoux, J., C. Lamarche, E. Van Bogaert, S. Bontemps, C. Brockmann and P. Defourny. 2014. Automated training sample extraction for global land cover mapping. *Remote Sensing.* 6(5):3965-3987.

Radoux, J., P. Bogaert, D. Fasbender and P. Defourny. 2011. Thematic accuracy assessment of geographic object-based image classification. *International Journal of Geographical Information Science.* 25(6):895-911.

Rahman, A.F., D.A. Sims, V.D. Cordova and B.Z. El-Masri. 2005. Potential of MODIS EVI and surface temperature for directly estimating per-pixel ecosystem C fluxes. *Geophysical Research Letters.* 32(19):L19404.

Ranchin, T., B. Aiazzi, L. Alparone, S. Baronti and L. Wald. 2003. Image fusion-the ARSIS concept and some successful implementation schemes. *ISPRS Journal of Photogrammetery & Remote Sensing.* 58(2003):4-18.

Ranjbar, H. and M. Honarmand. 2004. Integration and analysis of airborne geophysical and ETM+ data for exploration of porphyry type deposits in the Central Iranian Volcanic Belt using fuzzy classification. *International Journal of Remote Sensing.* 25(21):4729-4741.

Raxworthy, C., C. Ingram, N. Rabibisoa and R. Pearson. 2007. Applications of ecological niche modeling for species delimitation: A review and empirical evaluation using day geckos (*Phelsuma*) from Madagascar. *Systematic Biology.* 56(6):907-923.

Ray, T.W. and B.C. Murray. 1996. Nonlinear spectral mixing in desert vegetation. *Remote Sensing of Environment.* 55:59-64.

Ray, T.W. and B.C. Murray, 1996. Nonlinear Spectral Mixing in Desert Vegetation. *Remote Sensing of Environment.* 55:59-64.

Read, J.M. and N.S.-N. Lam. 2002. Spatial methods for characterizing land cover and detecting land-cover changes for the tropics. *International Journal of Remote Sensing*.23:2457-2474.

Reed, B.C., M.D. Schwartz and X. Xiao. 2009. Remote sensing phenology: Status and the way forward. *Phenology of Ecosystem Processes* (A. Noormets, editor). Springer, New York. pp. 231-246.

Reiche, J., J. Verbesselt, D. Hoekman and M. Herold, 2015. Fusing Landsat and SAR time series to detect deforestation in the tropics. *Remote Sensing of Environment.* 156:276-293.

Ren, H., Y.-L. Wang, M.-Y. Huang, Y.-L. Chang and H.-M. Kao. 2014. Ensemble empirical mode decomposition parameters optimization for spectral distance measurement in hyperspectral remote sensing data. *Remote Sensing.* 6(3):2069.

Ressel, R., A. Frost and S. Lehner. 2015. A neural network-based classification for sea ice types on X-band SAR images. Institute of Electrical and Electronics Engineers Transactions on Geoscience and Remote Sensing Journal of Selected Topics in Applied Earth Observations and Remote Sensing. 8(7):3672-3680.

Riano, D., E. Chuvieco, S.L. Ustin, R. Zomer, P.E. Dennison, D.A. Roberts and J. Salas. 2002. Assessment of vegetation regeneration after fire through multitemporal analysis of AVIRIS images in the Santa Monica Mountains. *Remote Sensing of Environment.* 79(1):60-71.

Riccio, D. and G. Ruello. 2015. Synthesis of fractal surfaces for remote-sensing applications. *Institute of Electrical and Electronics Engineers Transactions on Geoscience and Remote Sensing.* 53(7):3803-3814.

Richards, C.L., B.C. Carstens and L. Lacey Knowles. 2007. Distribution modelling and statistical phylogeography: an integrative framework for generating and testing alternative biogeographical hypotheses. *Journal of Biogeography.* 34(11):1833-1845.

Richardson, A.D., B.H. Braswell, D.Y. Hollinger, J.P. Jenkins and S.V. Ollinger. 2009. Near-surface remote sensing of spatial and temporal variation in canopy phenology. *Ecological Applications.* 19(6):1417-1428.

Richardson, A.J. and C.L. Wiegand. 1977. Distinguishing vegetation from soil background information. *Photogrammetric Engineering and Remote Sensing.* 43(12):1541-1552.

Richardson, L.F. 1961. The problem of contiguity: An appendix to "Statistics of Deadly Quarrels" *General Systems Yearbook.* 6:139-187.

Richter, R. and D. Schläpfer. 2014a. *Atmospheric/Topographic Correction for Satellite Imagery.* DLR report DLR-IB 565-02/14. Wessling, Germany. 231 p.

Richter, R. and D. Schläpfer. 2014b. *Atmospheric/Topographic Correction for Airborne Imagery.* DLR report DLR-IB 565-02/14. Wessling, Germany. 240 p.

Ricotta, C., G.C. Avena and F. Volpe. 1999. The influence of principal component analysis on the spatial structure of a multispectral dataset. *International Journal of Remote Sensing.* 20(17):3367-3376.

Riffler, M., G. Lieberherr and S. Wunderle. 2015. Lake surface water temperatures of European Alpine lakes (1989–2013) based on the Advanced Very High Resolution Radiometer (AVHRR) 1 km data set. *Earth System Science Data.* 7(1):1-17.

Rios, R.A., L. Parrott, H. Lange and R.F. de Mello. 2015. Estimating determinism rates to detect patterns in geospatial datasets. *Remote Sensing of Environment.* 156:11-20.

Ripullone, F., A.R. Rivelli, R. Baraldi, R. Guarini, R. Guerrieri, F. Magnani, J. Peñuelas, S. Raddi and M. Borghetti. 2011. Effectiveness of the photochemical reflectance index to track photosynthetic activity over a range of forest tree species and plant water statuses. *Functional Plant Biology.* 38(3):177-186.

Roberts, D.A. 1991. *Separating Spectral Mixtures of Vegetation and Soils.* PhD. Dissertation, University of Washington. 180 pp.

Roberts, D.A., D.A. Quattrochi, G.C. Hulley, S.J. Hook and R.O. Green. 2012. Synergies between VSWIR and TIR data for the urban environment: An evaluation of the potential for the Hyperspectral Infrared Imager (HyspIRI) Decadal Survey mission. *Remote Sensing of Environment.* 117:83-101.

Roberts, D.A., I. Numata, K.W. Holmes, G. Batista, T. Krug, A. Monteiro, B. Powell and O. Chadwick. 2002. Large area mapping of land-cover change in Rondônia using multitemporal spectral mixture analysis and decision tree classifiers. *Journal of Geophysical Research: Atmospheres.* 107(D20), 8073, LBA 40-1 to 40-18.

Roberts, D.A., J.B. Adams and M.O. Smith. 1990. Predicted distribution of visible and near-infrared radiant flux above and below a transmittant leaf. *Remote Sensing of Environment.* 34:1-17.

Roberts, D.A., M. Alonzo, E. Wetherley, K. Dudley and P. Dennison. 2016. Multiscale analysis of urban areas using mixing models. *Scale in Remote Sensing and GIScience Applications.* D.A. Quattrochi, E. Wentz, N.S. Lam and C. W. Emerson. Editors. CRC press.

Roberts, D.A., M. Gardner, R. Church, S. Ustin, G. Scheer and R.O. Green. 1998. Mapping chaparral in the Santa Monica Mountains using multiple endmember spectral mixture models. *Remote Sensing of Environment.* 65:267-279.

Roberts, D.A., M. Gardner, R. Church, S.L. Ustin and R.O. Green. 1997a. Optimum Strategies for Mapping Vegetation using Multiple Endmember Spectral Mixture Models. SPIE Conference Vol 3118. Imaging Spectrometry III. July 27-Aug 1, 1997. San Diego, California. pp. 108-119.

Roberts, D.A., M.O. Smith and J.B. Adams. 1993. Green vegetation, nonphotosynthetic vegetation, and soils in AVIRIS data. *Remote Sensing of Environment.* 44(2-3):255-269.

Roberts, D.A., P.E. Dennison, K.L. Roth, K. Dudley and G. Hulley. 2015. Relationships between dominant plant species, fractional cover and land surface temperature in a Mediterranean ecosystem. *Remote Sensing of Environment.* 167:152-167.

Roberts, D.A., P.E. Dennison, M. Gardner, Y. Hetzel, S.L. Ustin and C. Lee. 2003. Evaluation of the potential of Hyperion for fire danger assessment by comparison to the Airborne Visible/Infrared Imaging Spectrometer. *Institute of Electrical and Electronics Engineers Transactions on Geoscience and Remote Sensing. Transactions on Geoscience and Remote Sensing.* 41 (6 Part 1):1297-1310.

Roberts, D.A., R.O. Green and J.B. Adams. 1997b. Temporal and spatial patterns in vegetation and atmospheric properties from AVIRIS. *Remote Sensing of Environment.* 62:223-240.

Roberts, D.A., S.L. Ustin, S. Ogunjemiyo, J. Greenberg, S.Z. Dobrowski, J. Chen and T.M. Hinckley. 2004. Spectral and structural measures of Northwest forest vegetation at leaf to landscape scales. *Ecosystems.* 7:545-562.

Rocha, A.V. and G.R. Shaver. 2009. Advantages of a two band EVI calculated from solar and photosynthetically active radiation fluxes. *Agricultural and Forest Meteorology.* 149(9):1560-1563.

Roderick, M., R. Smith and G. Lodwick. 1996. Calibrating long-term AVHRR-derived NDVI imagery. *Remote Sensing of Environment.* 58(1):1-12.

Roerink, G.J., M. Menenti and W. Verhoef. 2000. Reconstructing cloud-free NDVI composites using Fourier analysis of time series. *International Journal of Remote Sensing.* 21(9):1911-1917.

Rogge, D.M., B. Rivard, J. Zhang and J. Feng. 2006. Iterative spectral unmixing for optimizing per-pixel endmember sets. Institute of Electrical and Electronics Engineers Transactions on Geoscience and Remote Sensing. Transactions on Geosciences and Remote Sensing. 44(12):3725-3736.

Rollins, M.G., R.E. Keane and R.A. Parsons. 2004. Mapping fuels and fire regimes using remote sensing, ecosystem simulation, and gradient modeling. *Ecological Applications.* 14:75-95.

Román, M.O., C.B. Schaaf, C.E. Woodcock, A.H. Strahler, X. Yang, R.H. Braswell, P.S. Curtis, K.J. Davis, D. Dragoni and M.L. Goulden. 2009. The MODIS (Collection V005) BRDF/albedo product: Assessment of spatial representativeness over forested landscapes. *Remote Sensing of Environment.* 113(11):2476-2498.

Rosso, P.H., S.L. Ustin and A. Hastings. 2005. Mapping marshland vegetation of San Francisco Bay, California using hyperspectral data. *International Journal of Remote Sensing.* 26(23):5169-5191.

Roth, K.L., P.E. Dennison and D.A. Roberts. 2012. Comparing endmember selection techniques for accurate mapping of plant species and land cover using imaging spectrometer data. *Remote Sensing of Environment.* 127:139-152.

Rouse, J.W., R.H. Haas, J.A. Schell and D.W. Deering. 1973. Monitoring vegetation systems in the Great Plains with ERTS. *Third Earth Resources Technology Satellite-1 Symposium:* Volume I, NASA SP-351:309-317.

Roy, A.G., G. Gravel and C. Gauthier. 1987. Measuring the dimension of surfaces: A review and appraisal of different methods. *Proceedings of the Eighth International Symposium on Computer-Assisted Cartography* (Auto-Carto 8). March 29- April 3 1987. Baltimore, Maryland. pp. 68-77.

Roy, D. 2000. The impact of misregistration upon composited wide field-of-view satellite data and implications for change detection. *Institute of Electrical and Electronics Engineers Transactions on Geoscience and Remote Sensing.* 38(4):2017-2032.

Roy, D.P., M. Wulder, T. Loveland, C. Woodcock, R. Allen, M. Anderson, D. Helder, J. Irons, D. Johnson and R. Kennedy. 2014. Landsat-8: Science and product vision for terrestrial global change research. *Remote Sensing of Environment.*145:154-172.

Running, S.W., D.D. Baldocchi, D.P. Turner, S.T. Gower, P.S. Bakwin and K.A. Hibbard. 1999. A global terrestrial monitoring network integrating tower fluxes, flask sampling, ecosystem modeling and EOS satellite data. *Remote Sensing of Environment.* 70(1):108-127.

Russ, J.C. 1990. Processing images with a local Hurst operator to reveal textural differences. *Journal of Computer-Assisted Microscopy,* 2(4):249-257.

Russ, J.C. 1993. *Fractal Surfaces.* Plenum Press. 309 p.

Russ, J.C. 2011. *The Image Processing Handbook.* 5th Ed., CRC Press, Boca Raton, 849 p.

Russ, J.C. 2017. *The Image Processing Handbook.* 7th Ed. CRC Press, New York. 1053 p.

Sabol, D.E., J.B. Adams and M.O. Smith. 1992. Quantitative sub-pixel spectral detection of targets in multispectral images. *Journal of Geophysical Research.* 97:2659-2672.

Sader, S.A. and J.C. Winne. 1992. RGB-NDVI colour composites for visualizing forest change dynamics. *International Journal of Remote Sensing.* 13:3055-3067.

Safavian, S. R. and D. Landgrebe. 1991. A survey of decision tree classifier methodology. *Institute of Electrical and Electronics Engineers Transactions of Systems, Man, and Cybernetics.* 21:660-675.

Sakamoto, T., M. Yokozawa, H. Toritani, M. Shibayama, N. Ishitsuka, and H. Ohno. 2005. A crop phenology detection method using time-series MODIS data. *Remote Sensing of Environment.* 96:366-374.

Saleska, S.R., J. Wu, K. Guan, A.C. Araujo, A. Huete, A.D. Nobre and N. Restrepo-Coupe. 2016. Dry-season greening of Amazon forests. *Nature.* 531(7594):E4-E5.

Samanta, A., S. Ganguly, H. Hashimoto, S. Devadiga, E. Vermote, Y. Knyazikhin, R. R. Nemani and R. B. Myneni. 2010. Amazon forests did not green-up during the 2005 drought. *Geophysical Research Letters.* 37(5):L05401.

Sandmeier, S.R. and K.I. Itten. 1999. A Field Goniometer System (FIGOS) for acquisition of hyperspectral BRDF data. Institute of Electrical and Electronics Engineers Transactions on Geoscience and Remote Sensing. Transactions on Geoscience and Remote Sensing. 37(2):978-986.

Sarkar, N. and B.B. Chaudhuri. 1992. An efficient approach to estimate fractal dimension of textural images, *Pattern Recognition.* 25:1035-1041.

Saunders, R.W and K.T. Kriebel. 1988. An improved method for detecting clear sky and cloudy radiances from AVHRR data. *International Journal of Remote Sensing.* 9(1):123-150.

Saupe, D., 1988. Algorithms for random fractals. *The Science of Fractal Images* (H.O. Peitgen and D. Saupe, editors). Springer-Verlag, New York. pp. 71-136.

Savitzky, A. and M.J.E. Golay. 1964. Smoothing and differentiation of data by simplified least squares procedures. *Analytical Chemistry.* 36:1627-1639.

Schaaf, A.N., P.E. Dennison, G.K. Fryer, K.L. Roth and D.A. Roberts. 2011. Mapping plant functional types at multiple spatial resolutions using imaging spectrometer data. *GIScience and Remote Sensing.* 48(3):324-344.

Schaaf, C.B., F. Gao, A.H. Strahler, W. Lucht, X. Li, T. Tsang, N.C. Strugnell, X. Zhang, Y. Jin, J.-P. Muller, P. Lewis, M. Barnsley, P. Hobson, M. Disney, G. Roberts, M. Dunderdale, C. Doll, R. P. d'Entremont, B. Hu, S. Liang, J. L. Privette and D. Roy. 2002. First operational BRDF albedo nadir reflectance products from MODIS. *Remote Sensing of Environment.* 83(1-2):135-148.

Schneider, A. 2012. Monitoring land cover change in urban and peri-urban areas using dense time stacks of Landsat satellite data and a data mining approach. *Remote Sensing of Environment.* 124:689-704.

Scholkopf, B. and A.J. Smola. 2001. Learning with Kernels. The MIT Press.

Schriever, J.R. and R.G. Congalton. 1995. Evaluating seasonal variability as an aid to cover-type mapping from Landsat Thematic Mapper data in the Northeast. *Photogrammetric Engineering & Remote Sensing.* 61:321-327.

Schulz, J., P. Albert, H.-D. Behr, D. Caprion, H. Deneke, S. Dewitte, B. Dürr, P. Fuchs, A. Gratzki, P. Hechler, R. Hollmann, S. Johnston, K.-G. Karlsson, T. Manninen, R. Müller, M. Reuter, A. Riihelä, R. Roebeling, N. Selbach, A. Tetzlaff, W. Thomas, M. Werscheck, E. Wolters and A. Zelenka. 2009. Operational climate monitoring from space: the EUMETSAT Satellite Application Facility on Climate Monitoring (CM-SAF). *Atmospheric Chemistry and Physics.* 9(5):1687-1709.

Scott, J.H. and E.D. Reinhardt. 2001. Assessing crown fire potential by linking models of surface and crown fire behavior. *USDA Forest Service Rocky Mountain Research Station Research Paper.* RMRS-RP-29. 49p.

Seddon, A.W.R., M. Macias-Fauria, P.R. Long, D. Benz and K.J. Willis. 2016. Sensitivity of global terrestrial ecosystems to climate variability. *Nature.* 531(7593):229-232.

Sellers, P.J., C.J. Tucker, G.J. Collatz, S.O. Los, C.O. Justice, D.A. Dazlich and D.A. Randall. 1994. A global NDVI data set for climate studies: Part II. The generation of global fields of terrestrial biophysical parameters from the NDVI. *International Journal of Remote Sensing.* 15(17):3519-3545.

Senf, C., D. Pflugmacher, M.A. Wulder and P. Hostert. 2015. Characterizing spectral–temporal patterns of defoliator and bark beetle disturbances using Landsat time series. *Remote Sensing of Environment.* 170:166-177.

Settle, J.J. and N.A. Drake. 1993. Linear mixing and the estimation of ground cover proportions. *International Journal of Remote Sensing.* 14(6):1159-1177.

Sexton, J.O., D.L. Urban, M.J. Donohue and C. Song. 2013. Long-term land cover dynamics by multi-temporal classification across the Landsat-5 record. *Remote Sensing of Environment.* 128:246-258.

Sezgin, M. and B. Sankur. 2004. Survey over image thresholding techniques and quantitative performance evaluation. *Journal of Electronic Imaging.* 13(1):146-168.

Shabanov, N., M. Vargas, T. Miura, A. Sei and A. Danial. 2015. Evaluation of the performance of Suomi NPP VIIRS top of canopy vegetation indices over AERONET sites. *Remote Sensing of Environment.* 162(0):29-44.

Shang, H., L. Jia and M. Menenti. 2014. Analyzing the inundation pattern of the Poyang Lake floodplain by passive microwave data. *Journal of Hydrometeorology.* 16(2):652-667.

Shelberg, M.C., H. Moellering and N.S.-N. Lam. 1982. Measuring the fractal dimension of empirical cartographic curves. *Proceedings of the Fifth International Symposium on Computer-Assisted Cartography* (Auto-Carto 5), August 22-28. Crystal City, Virginia, United States. pp. 481-490.

Shelberg, M.C., N.S.-N. Lam and H. Moellering. 1983. Measuring the fractal dimension of surfaces. *Proceedings of the Sixth International Symposium on Computer-Assisted Cartography* (Auto-Carto 6), October 16-21, 1983. Hull, Ottawa, Canada. pp. 319-328.

Shepherd, J.D. and J.R. Dymond. 2000. BRDF correction of vegetation in AVHRR imagery. *Remote Sensing of Environment.* 74:397-408.

Shi, X., L. Zhang, T. Balz and M. Liao. 2015. Landslide deformation monitoring using point-like target offset tracking with multi-mode high-resolution TerraSAR-X data. *ISPRS Journal of Photogrammetry and Remote Sensing.* 105:128-140.

Shimabukuro, Y. E. and J. Smith. 1991. The least-squares mixing models to generate fraction images derived from remote sensing multispectral data. *Institute of Electrical and Electronics Engineers Transactions on Geoscience and Remote Sensing.* 29(1):16-20.

Shimabukuro, Y.E., B.N. Holben and C.J. Tucker. 1994. Fraction images derived from NOAA AVHRR data for studying the deforestation in the Brazilian Amazon. *International Journal of Remote Sen*sing. 15:517-520.

Shipman H. and J.B. Adams. 1987. Detectability of minerals in desert alluvial fans using reflectance spectra. *Journal of Geophysical Research.* 92(B10):10391-10492.

Shiraishi, T., T. Motohka, R.B. Thapa, M. Watanabe and M. Shimada. 2014. Comparative assessment of supervised classifiers for land use-land cover classification in a tropical region using time-series PALSAR mosaic data. *Institute of Electrical and Electronics Engineers Transactions on Geoscience and Remote Sensing. Journal of Selected Topics in Applied Earth Observations and Remote Sensing.* 7(4):1186-1199.

Silvetti, A. and C. Delrieux. 2013. Quadratic self-correlation: An improved method for computing local fractal dimension in remote sensing imagery. *Computers & Geosciences.* 60:142-155.

Simis, S.G.H., S.W.M. Peters, H.J. Gons. *Remote sensing of the cyanobacterial pigment phycocyanin in turbid inland water*. Limnology Oceanography. 2005;50:237–45.

Sims, D.A., A.F. Rahman, E.F. Vermote and Z. Jiang. 2011. Seasonal and inter-annual variation in view angle effects on MODIS vegetation indices at three forest sites. *Remote Sensing of Environment.* 115(12):3112-3120.

Sims, D.A., A.F. Rahman, V.D. Cordova, B.Z. El-Masri, D.D. Baldocchi, L.B. Flanagan, A.H. Goldstein, D.Y. Hollinger, L. Misson, R.K. Monson, W.C. Oechel, H.P. Schmid, S.C. Wofsy and L.K. Xu. 2006. On the use of MODIS EVI to assess gross primary productivity of North American ecosystems. *Journal of Geophysical Research-Biogeosciences.* 111(G4):G04015.

Sinclair, S. and G.G.S. Pegram. 2005. Empirical mode decomposition in 2-D space and time: A tool for space-time rainfall analysis and nowcasting. *Hydrology and Earth System Sciences Discussions.* 9(3):127-137.

Singer, R. B. and T.B. McCord. 1979. Mars - Large scale mixing of bright and dark surface materials and implications for analysis of spectral reflectance. *Proceedings of the 10th Lunar and Planetary Science Conference.* 19-23 March 1979. Houston, Texas. Volume 2. (A80-23617 08-91) New York. Pergamon Press, Inc. pp. 1835-1848.

Singh, A. 1986. Change detection in the tropical forest environment of Northeastern India using Landsat. *Remote Sensing and Tropical Land Management.* (M.J. Eden and J.T. Parry, eds.). John Wiley, Chichester. pp. 237-254.

Singh, S.K., S.N. Devakanth, T.P. Srinivasan, B.G. Krishna and P.K. Srivastava. 2008. Rational polynomial modelling for Cartosat-1 data. *The International Archives of the Photogrammetry. Remote Sensing and Spatial Information Sciences.* Vol. XXXVII. Part B1. Beijing.

Skowronski, N., K. Clark, R. Nelson, J. Hom and M. Patterson. 2007. Remotely sensed measurements of forest structure and fuel loads in the Pinelands of New Jersey. *Remote Sensing of Environment.* 108:123-129.

Slater, P.N., S.F. Biggar, J.M. Palmer and K.J. Thome. 2001. Unified approach to absolute radiometric calibration in the solar-reflective range. *Remote Sensing of Environment.* 77(3):293-303.

Small, C. 2001. Estimation of urban vegetation abundance by spectral mixture analysis. *International Journal of Remote Sensing.* 22(7):1305-1334.

Smith, M.O., S.L. Ustin, J.B. Adams and A.R. Gillespie. 1990. Vegetation in deserts: A regional measure of abundance from multispectral images. *Remote Sensing of Environment.* 31:1-26.

Smits, P. and A. Annoni. 2000. Toward specification-driven change detection. Institute of Electrical and Electronics Engineers Transactions on Geoscience and Remote Sensing. 38(3):1484-1488.

Solberg, A.H.S. 2006. Data fusion for remote sensing applications. *Signal and Image Processing for Remote Sensing.* (C.H. Chen, editor). CRC Press. Boca Raton. pp. 515-537.

Somers, B. and G.P. Asner. 2013. Invasive species mapping in Hawaiian rainforests using multi-temporal Hyperion spaceborne imaging spectroscopy. *Institute of Electrical and Electronics Engineers Transactions on Geoscience and Remote Sensing. Journal of Selected Topics in Applied Earth Observations and Remote Sensing.* 6(2):351-359.

Somers, B. and G.P. Asner. 2014. Tree species mapping in tropical forests using multi-temporal imaging spectroscopy: Wavelength adaptive spectral mixture analysis. *International Journal of Applied Earth Observation and Geoinformation*.31:57-66.

Somers, B., G.P. Asner, L. Tits and P. Coppin. 2011. Endmember variability in spectral mixture analysis: A review. *Remote Sensing of Environment.* 115(7):1603-1616.

Somers, B., J. Verbesselt, E.M. Ampe, N. Sims, W.W. Verstraeten and P. Coppin. 2010b Spectral mixture analysis to monitor defoliation in mixed aged *Eucalyptus globules* Labill plantations in southern Australia using Landsat 5TM and EO-1 Hyperion data. *International Journal of Applied Earth Observation and Geoinformation.* 12:270-277.

Somers, B., K. Cools, S. Delalieux, J. Stuckens, D. Van der Zande, W.W. Verstraeten and P. Coppin. 2009a. Nonlinear hyperspectral mixture analysis for tree cover estimates in orchards. *Remote Sensing of Environment.* 113(6):1183-1193.

Somers, B., M. Zortea, A. Plaza and G.P. Asner. 2012. Automated extraction of image-based endmember bundles for improved spectral unmixing. *Institute of Electrical and Electronics Engineers Transactions on Geoscience and Remote Sensing. Journal of Selected Topics in Applied Earth Observations and Remote Sensing.* 5:396-408.

Somers, B., S. Delalieux, J. Stuckens, W.W. Verstraeten and P. Coppin. 2009b. A weighted linear spectral mixture analysis approach to address endmember variability in agricultural production systems. *International Journal of Remote Sensing.* 30(1):139-147.

Somers, B., S. Delalieux, W.W. Verstraeten, J.A.N. Van Aardt, G.L. Albrigo and P. Coppin. 2010a. An automated waveband selection technique for optimized hyperspectral mixture analysis. *International Journal of Remote Sensing.* 31(20):5549-5568.

Son, N.T., C.F. Chen, C.R. Chen and L.Y. Chang. 2013. Satellite-based investigation of flood-affected rice cultivation areas in Chao Phraya River Delta, Thailand. *ISPRS Journal of Photogrammetry and Remote Sensing.* 86:77-88.

Song, D.-X., C. Huang, J.O. Sexton, S. Channan, M. Feng and J.R. Townshend. 2015. Use of Landsat and Corona data for mapping forest cover change from the mid-1960s to 2000s: Case studies from the Eastern United States and Central Brazil. *ISPRS Journal of Photogrammetry and Remote Sensing.* 103:81-92.

Song, R., H. Guo, G. Liu, Z. Perski, H. Yue, C. Han and J. Fan. 2014. SAR interferometric phase filtering technique based on bivariate empirical mode decomposition. *Remote Sensing Letters.* 5(8):743-752.

Sonnentag, O., J.M. Chen, D.A. Roberts, J. Talbot, K.Q. Halligan and A. Govind. 2007. Mapping tree and shrub leaf area indices in an ombrotrophic peatland through multiple endmember spectral unmixing. *Remote Sensing of Environment.* 109:342-360.

Souza, C., D.A. Roberts and M.A. Cochrane. 2005. Combining spectral and spatial information to map canopy damages from selective logging and forest fires. *Remote Sensing of Environment.* 98:329-343.

Souza, C., L. Firestone, L. M. Silva and D. Roberts. 2003. Mapping forest degradation in the Eastern Amazon from SPOT 4 through spectral mixture models. *Remote Sensing of Environment.* 87(4):494-506.

Souza, C.M., J.V. Siqueira, M.H. Sales, A.V. Fonseca, J.G. Ribeiro, I. Numata, M.A. Cochrane, C.P. Barber, D.A. Roberts and J. Barlow. 2013. 10-year Landsat classification of deforestation and forest degradation in the Brazilian Amazon. *Remote Sensing.* 5(11):5493-5513.

Spyrakos, E., L. González Vilas, J.M. Torres Palenzuela and E.D. Barton. 2011. Remote sensing chlorophyll-*a* of optically complex waters (rias Baixas, NW Spain): Application of a regionally specific chlorophyll-*a* algorithm for MERIS full resolution data during an upwelling cycle. *Remote Sensing of Environment.* 115:2471-2485.

Steven, M.D., T.J. Malthus, F. Baret, H. Xu and M.J. Chopping. 2003. Intercalibration of vegetation indices from different sensor systems. *Remote Sensing of Environment.* 88(4):412-422.

Stockwell, D.R.B. and I.R. Noble. 1992. Induction of sets of rulesfrom animal distribution data: A robust and informative method of data analysis. *Math & Computer Simulation.* 33:385-390.

Stockwell. D.R.B. and D. Peters. 1999. The GARP modelling system: Problems and solutions to automated spatial prediction. *International Journal of Geographical Information Sciences.* 13(2): 143-158.

Stuckens, J., B. Somers, S. Delalieux, W.W. Verstraeten and P. Coppin. 2009. The impact of common assumptions on canopy radiative transfer simulations: A case study in citrus orchards. *Journal of Quantitative Spectroscopy and Radiative Transfer.* 110(1):1-21.

Sun, D., Y. Li and Q. Wang. 2009. A unified model for remotely estimating chlorophyll-*a* in Lake Taihu, China, based on SVM and *in-situ* hyperspectral data. *Institute of Electrical and Electronics Engineers Transactions on Geoscience and Remote Sensing.* 47(8):2957-2965.

Sun, J. and J. Southworth. 2013. Remote sensing-based fractal analysis and scale dependence associated with forest fragmentation in an Amazon tri-national frontier. *Remote Sensing.* 5:454-472.

Sun, W. 2006. Three new implementations of the triangular prism method for computing the fractal dimension of remote sensing images. *Photogrammetric Engineering and Remote Sensing.* 72(4):373-382.

Sun, W., A.Z. Kolappal and P. Gong. 2005. Two computational methods for detecting anisotropy in image texture. *Geographic Information Science.* 11(2):87-96.

Sun, W., G. Xu, G. P. Gong and S. Liang. 2006. Fractal analysis of remote sensing images: A review of methods and applications. International Journal of Remote Sensing. 27(22):4963-4990.

Surdu, C.M., C.R. Duguay, L.C. Brown and D. Fernández Prieto. 2014. Response of ice cover on shallow lakes of the North Slope of Alaska to contemporary climate conditions (1950–2011): radar remote-sensing and numerical modeling data analysis. *The Cryosphere.* 8(1):167-180.

Swain, P.H. and H. Hauska. 1977. The decision tree classifier: design and potential. Institute of Electrical and Electronics Engineers Transactions on Geoscience and Remote Sensing. 3:142-147.

Swets, D.L., B.C. Reed, J.D. Rowland and S.E. Marko. 1999. A weighted least squares approach to temporal NDVI smoothing. *Proceedings of the American Society of Photogrammetry and Remote Sensing.* 17-21 May 1999. Portland, OR, USA. pp. 526-536.

Swinnen, E. and F. Veroustraete. 2008. Extending the SPOT-VEGETATION NDVI time series (1998–2006) back in time with NOAA-AVHRR data (1985–1998) for Southern Africa. *Institute of Electrical and Electronics Engineers Transactions on Geoscience and Remote Sensing. Transactions on Geoscience and Remote Sensing.* 46(2):558-572.

Tachikawa, T., O. Kashimura, J Tanii, A. Iwasaki, T. Matsunaga, S. Tsuchida and H. Yamamoto. 2012. Outline and prospect of Hyperspectral Imager Suite (HISUI). *Journal of the Remote Sensing Society of Japan.* 32(5):280-286. (Japanese with English abstract).

Tan, C., A. Samanta, X. Jin, L. Tong, C. Ma, W. Guo, Y. Knyazikhin and R. Myneni. 2013. Using hyperspectral vegetation indices to estimate the fraction of photosynthetically active radiation absorbed by corn canopies. *International Journal of Remote Sensing.* 34(24):8789-8802.

Tang, J., L. Wang and S.W. Myint. 2007. Improving urban classification through fuzzy supervised classification and spectral mixture analysis. *International Journal of Remote Sensing.* 28(18):4047-4063.

Tao, C.V. and Y. Hu. 2001. A comprehensive study of the rational function model for photogrammetric processing, *Photogrammetric Engineering & Remote Sensing.* 67(12):1347-1357.

Tao, C.V., Y. Hu, J.B. Mercer, S. Schnick and Y. Zhang. 2000. Image rectification using a generic sensor model – rational function model. *International Archives of Photogrammetry and Remote Sensing. Vol. XXXIII, Part B3.* Amsterdam.

Tapia, R., A. Stein and W. Bijker. 2005. Optimization of sampling schemes for vegetation mapping using fuzzy classification. *Remote Sensing of Environment.* 99(4):425-433.

Tebbs, E.J., J.J. Remedios and D.M. Harper. 2013. Remote sensing of chlorophyll-*a* as a measure of cyanobacterial biomass in Lake Bogoria, a hypertrophic, saline–alkaline, flamingo lake, using Landsat ETM. *Remote Sensing of Environment.* 135:92-106.

Teillet, P.M., B. Guindon and D.G. Goodeonugh. 1982. On the slope-aspect correction of multispectral scanner data. *Canadian Journal of Remote Sensing.* 8(2):84-106.

Teillet, P.M., K. Staenz and D.J. William. 1997. Effects of spectral, spatial, and radiometric characteristics on remote sensing vegetation indices of forested regions. *Remote Sensing of Environment.* 61(1):139-149.

Teo, T.A. and C.C. Lau. 2012. Pyramid-based image empirical mode decomposition for the fusion of multispectral and panchromatic images. *Eurasip Journal on Advances in Signal Processing.* 2012(1):1-12.

Thenkabail, P.S., C.M. Biradar, P. Noojipady, V. Dheeravath, Y. Li, M. Velpuri, M. Gumma, O.R.P. Gangalakunta, H. Turral, X. Cai, J. Vithanage, M.A. Schull and R. Dutta. 2009. Global irrigated area map (GIAM) derived from remote sensing for the end of the last millennium. *International Journal of Remote Sensing.* 30(14):3679-3733.

Thenkabail, P.S., I. Mariotto, M.K. Gumma, E.M. Middleton, D.R. Landis and K.F. Huemmrich. 2013. Selection of hyperspectral narrowbands (HNBs) and composition of hyperspectral two band vegetation indices (HVIs) for biophysical characterization and discrimination of crop types using field reflectance and Hyperion/EO-1 data. *Institute of Electrical and Electronics Engineers Transactions on Geoscience and Remote Sensing. Journal of Selected Topics in Applied Earth Observations and Remote Sensing.* 6(2):427-439.

Thenkabail, P.S., L.G. Lyon and A. Huete. 2012. *Hyperspectral Remote Sensing of Vegetation.* CRC Press, Boca Raton. 705 p.

Thomas, C., T. Ranchin, L. Wald and J. Chanussot. 2008. Synthesis of multispectral images to high spatial resolution: A critical review of fusion methods based on remote sensing physics. *Institute of Electrical and Electronics Engineers Transactions on Geoscience and Remote Sensing.* 46(5):1301-1312.

Thomas, N., C. Hendrix and R.G. Congalton. 2003. A comparison of urban mapping methods using high-resolution digital imagery. *Photogrammetric Engineering & Remote Sensing.* 69(9):963-972.

Thorp, K.R., A.N. French and A. Rango. 2013. Effect of image spatial and spectral characteristics on mapping semi-arid rangeland vegetation using multiple endmember spectral mixture analysis (MESMA). *Remote Sensing of Environment.* 132:120-130.

Thuiller, W. 2004. Patterns and uncertainties of species' range shifts under climate change. *Global Change Biology.* 10(12):2020-2027.

Tian, F., R. Fensholt, J. Verbesselt, K. Grogan, S. Horion and Y. Wang. 2015. Evaluating temporal consistency of long-term global NDVI datasets for trend analysis. *Remote Sensing of Environment.* 163:326-340.

Tilstone, G.H., I.M. Angel-Benavides, Y. Pradhan, J.D. Shutler, S. Groom and S. Sathyendranath. 2011. An assessment of chlorophyll-*a* algorithms available for SeaWiFS in coastal and open areas of the Bay of Bengal and Arabian Sea. *Remote Sensing of Environment.* 115:2277-2291.

Tits, L., B. Somers and P. Coppin. 2012. The potential and limitations of a clustering approach for the improved efficiency of multiple endmember spectral mixture analysis in plant production system monitoring. *Institute of Electrical and Electronics Engineers Transactions on Geoscience and Remote Sensing.* 50(6):2273-2286.

Tits, L., B. Somers, J. Stuckens and P. Coppin. 2014. Validating nonlinear mixing models: Benchmark datasets from vegetated areas. *Proceedings of the 6th Workshop on Image and Signal Processing: Evolution in Remote Sensing (WHISPERS)*. June 25-27. Lausanne, Switzerland.

Tofani, V., C. Del Ventisette, S. Moretti and N. Casagli. 2014. Integration of remote sensing techniques for intensity zonation within a landslide area: A case study in the Northern Apennines, Italy. *Remote Sensing.* 6(2):907-924.

Tompkins, S., J.F. Mustard, C.M. Pieters and D.W. Forsyth. 1997. Optimization of endmembers for spectral mixture analysis. *Remote Sensing of Environment.* 59:472-489.

Toutin, T. 2004. Review article: Geometric processing of remote sensing images: Models, algorithms and methods, *International Journal of Remote Sensing.* 25(10):1893-1924.

Townsend, P.A. 2000. A quantitative fuzzy approach to assess mapped vegetation classifications for ecological applications. *Remote Sensing of Environment.* 72(3):253-267.

Townshend, J.R.G., C.O. Justice, C. Gurney and J. McManus. 1992. The impact of misregistration on change detection. *Institute of Electrical and Electronics Engineers Transactions on Geoscience and Remote Sensing.* 30:1054-1060.

Trishchenko, A.P. 2009. Effects of spectral response function on surface reflectance and NDVI measured with moderate resolution satellite sensors: Extension to AVHRR NOAA-17, 18 and METOP-A. *Remote Sensing of Environment.* 113(2):335-341.

Trishchenko, A.P., J. Cihlar and Z.Q. Li. 2002. Effects of spectral response function on surface reflectance and NDVI measured with moderate resolution satellite sensors. *Remote Sensing of Environment.* 81(1):1-18.

Tsai, F. and W. Philpot. 1998. Derivative analysis of hyperspectral data. *Remote Sensing of Environment.* 66:41-52.

Tso, B. and P.M. Mather. 2009. *Classification Methods for Remotely Sensed Data,* CRC Press, London. 376 p.

Tuanmu, M.N., A. Viña, S. Bearer, W. Xu, Z. Ouyang, H. Zhang and J. Liu. 2010. Mapping understory vegetation using phenological characteristics derived from remotely sensed data. *Remote Sensing of Environment.* 114(8):1833-1844.

Tucker, C.J. 1979. Red and photographic infrared linear combinations for monitoring vegetation. *Remote Sensing of Environment.* 8(2):127-150.

Tucker, C.J., J.E. Pinzon, M.E. Brown, D.A. Slayback, E.W. Pak, R. Mahoney, E.F. Vermote and N. El Saleous. 2005. An extended AVHRR 8-km NDVI dataset compatible with MODIS and SPOT vegetation NDVI data. *International Journal of Remote Sensing.* 26(20):4485-4498.

Turcotte, D.L. 1992. *Fractals and Chaos in Geology and Geophysics.* Cambridge University Press, Cambridge. 221 p.

Turner II, B.L., E.F. Lambin and A.A. Reenberg. 2007. The emergence of land change science for global environmental change and sustainability. *Proceedings of the National Academy of Sciences (PNAS). USA.* 104:20666-20671.

Tzortziou, M., A. Subramaniam, J.R. Herman, C.L. Gallegos, P.J. Neale and L.W. Harding, Jr. 2007. Remote sensing reflectance and inherent optical properties in the mid Chesapeake Bay. *Estuarine Coastal and Shelf Science.* 72:16-32.

Usery, E.L., M.P. Finn and C. Mugnier. 2009. Coordinate systems and map projections. *Manual of Geographic Information Systems.* American Society for Photogrammetry and Remote Sensing. Bethesda, MD. pp. 87-112.

Ustin, S.L., D.A. Roberts, J.A. Gamon, G.P. Asner and R.O. Green. 2004. Using imaging spectroscopy to study ecosystem processes and properties. *Bioscience.* 54(6):523-534.

Utgoff, P.E. and C.E. Brodley. 1990. An incremental method for finding multivariate splits for decision trees. *Proceedings of the Seventh International Conference on Machine Learning*, Morgan Kaufmann, Austin, TX, 58-65.

van Den Eeckhaut, M., N. Kerle, J. Poesen and J. Hervas. 2012. Object-oriented identification of forested landslides with derivatives of single pulse LiDAR data. *Geomorphology.* 173:30-42.

van der Meer, F. 2006. The effectiveness of spectral similarity measures for the analysis of hyperspectral imagery. *International Journal of Applied Earth Observation and Geoinformation*. 8:3-17.

van der Meer, F. and S.M. De Jong. 2000. Improving the results of spectral unmixing of Landsat Thematic Mapper imagery by enhancing the orthogonality of end-members. *International Journal of Remote Sensing.* 21(15):2781-2797.

van Leeuwen, W.J.D., A.R. Huete and T.W. Laing. 1999. MODIS vegetation index compositing approach: A prototype with AVHRR data. *Remote Sensing of Environment.* 69(3):264-280.

van Leeuwen, W.J.D., B.J. Orr, S.E. Marsh and S.M. Herrmann. 2006. Multi-sensor NDVI data continuity: Uncertainties and implications for vegetation monitoring applications. *Remote Sensing of Environment.* 100(1):67-81.

van Vliet, A.J.H. and M.D. Schwartz. 2002. Phenology and climate: the timing of life cycle events as indicators of climatic variability and change. *International Journal of Climatology.* 22(14):1713-1714.

Vapnik, V. 1979. *Estimation of Dependences Based on Empirical Data* [in Russian]. Nauka, Moscow (English translation: Springer Verlag, New York. 1982.

Vargas, M., T. Miura, N. Shabanov and A. Kato. 2013. An initial assessment of Suomi NPP VIIRS vegetation index EDR. *Journal of Geophysical Research-Atmospheres.* 118:1-16.

Varghese, J., S. Subash, and N. Tairan. 2016. Fourier transform-based windowed adaptive switching minimum filter for reducing periodic noise from digital images. *IET Image Processing.* 10:646-656.

Vasconcelos, S.S., P.M. Fearnside, P.M.L.A. Graça, D.V. Dias and F.W.S Correia. 2013. Variability of vegetation fires with rain and deforestation in Brazil's state of Amazonas. *Remote Sensing of Environment.* 136:199-209.

Veefkind, J.P., I. Aben, K. McMullan, H. Förster, J. de Vries, G. Otter, J. Claas, H.J. Eskes, J.F. de Haan, Q. Kleipool, M. van Weele, O. Hasekamp, R. Hoogeveen, J. Landgraf, R. Snel, P. Tol, P. Ingmann, R. Voors, B. Kruizinga, R. Vink, H. Visser and P.F. Levelt. 2012. TROPOMI on the ESA Sentinel-5 Precursor: A GMES mission for global observations of the atmospheric composition for climate, air quality and ozone layer applications. *Remote Sensing of Environment.* 120:70-83.

Veraverbeke, S. and S.J. Hook. 2013. Evaluating spectral indices and spectral mixture analysis for assessing fire severity, combustion completeness and carbon emissions. *International Journal of Wildland Fire.* 22(5):707-720.

Veraverbeke, S., E.N. Stavros and S.J. Hook. 2014. Assessing fire severity using imaging spectroscopy data from the Airborne Visible/Infrared Imaging Spectrometer (AVIRIS) and comparison with multispectral capabilities. *Remote Sensing of Environment.* 154:153-163.

Verbesselt, J., A. Zeileis and M. Herold. 2012. Near-real-time disturbance detection using satellite image time series. *Remote Sensing of Environment.* 123:98-108.

Verbesselt, J., R. Hyndman, G. Newnham and D. Culvenor. 2010. Detecting trend and seasonal changes in satellite image time series. *Remote Sensing of Environment.* 114(1):106-115.

Vergauwen, M. and L. Van Gool. 2006. Web-based 3D reconstruction service. *Machine Vision Applications.* 17:411-426.

Verger, A., F. Baret, M. Weiss, I. Filella and J. Peñuelas. 2015. GEOCLIM: A global climatology of LAI, FAPAR, and FCOVER from vegetation observations for 1999-2010. *Remote Sensing of Environment.* 166:126-137.

Verhoef, W. and H. Bach. 2003. Simulation of hyperspectral and directional radiance images using coupled biophysical and atmospheric radiative transfer models. *Remote Sensing of Environment.* 87:23-41.

Vermote, E. and Y.J. Kaufman. 1995. Absolute calibration of AVHRR visible and near infrared channels using ocean and cloud views. *International Journal of Remote Sensing.* 16(13):2317-2340.

Vermote, E., C.O. Justice and F.M. Breon. 2009. Towards a generalized approach for correction of the BRDF effect in MODIS directional reflectances. *Institute of Electrical and Electronics Engineers Transactions on Geoscience and Remote Sensing.* 47(3):898-908.

Vermote, E., N. El Saleous, Y.J. Kaufman and E. Dutton. 1997. Data pre-processing: Stratospheric aerosol perturbing effect on the remote sensing of vegetation: Correction method for the composite NDVI after the Pinatubo eruption. *Remote Sensing Reviews.* 15:7-21.

Vermote, E.F. and S. Kotchenova. 2008. Atmospheric correction for the monitoring of land surfaces. *Journal of Geophysical Research: Atmospheres*. 13(D23).

Vermote, E.F., D. Tanré, J.L. Deuzé, M. Herman and J.J. Morcette. 1997. Second simulation of the satellite signal in the solar spectrum, 6S: An overview. *Institute of Electrical and Electronics Engineers Transactions on Geoscience and Remote Sensing. Transactions on Geoscience and Remote Sensing.* 35(3):675-686.

Verstraete, M.M. and B. Pinty. 1996. Designing optimal spectral indexes for remote sensing applications. *Institute of Electrical and Electronics Engineers Transactions on Geoscience and Remote Sensing.* 34(5):1254-1265.

Viollier, M., P.Y. Deschamps and P. Lecomte. 1978. Airborne remote sensing of chlorophyll content under cloudy sky as applied to the tropical waters in the Gulf of Guinea. *Remote Sensing of Environment.* 7:235-248.

Viovy, N., O. Arino and A.S. Belward. 1992. The best index slope extraction (BISE) - a method for reducing noise in NDVI time-series. *International Journal of Remote Sensing.* 13:1585-1590.

Voss, R. 1988. Fractals in nature: From characterization to simulation. *The Science of Fractal Images* (H. O. Peitgen and D. Saupe, editors). Springer-Verlag, New York. pp. 21-70.

Wagenseil, H. and C. Samimi. 2006. Assessing spatio-temporal variations in plant phenology using Fourier analysis on NDVI time series: results from a dry savannah environment in Namibia. *International Journal of Remote Sensing*, 27:3455-3471.

Wald, L. 1999. Some terms of reference in data fusion. Institute of Electrical and Electronics Engineers Transactions on Geoscience and Remote Sensing. 37(3):1190-1193.

Wang, C., C. Zhong and Z. Yang. 2015. Assessing bioenergy-driven agricultural land use change and biomass quantities in the U.S. Midwest with MODIS time series. *Journal of Applied Remote Sensing.* 8(1):015198 1-16.

Wang, C., E.R. Hunt Jr., L. Zhang and H. Guo. 2013. Spatial distributions of C_3 and C_4 grass functional types in the U.S. Great Plains and their dependency on inter-annual climate variability. *Remote Sensing of Environment.* 128:90-101.

Wang, C., F.B. Fritschi, G. Stacey and Z. Yang. 2011. Phenology-based assessment of energy crops in North American Tallgrass Prairie. *Annals of the Association of American Geographers.* 101(4):742-751.

Wang, D., D. Morton, J. Masek, A. Wu, J. Nagol, X. Xiong, R. Levy, E. Vermote and R. Wolfe. 2012. Impact of sensor degradation on the MODIS NDVI time series. *Remote Sensing of Environment.* 119:55-61.

Wang, F. 1990. Fuzzy supervised classification of remote-sensing images. Institute of Electrical and Electronics Engineers Transactions on Geoscience and Remote Sensing. 28(2):194-201.

Wang, L., D. Liu and Q. Wang. 2013. Geometric method of fully constrained least squares linear spectral mixture analysis. *Institute of Electrical and Electronics Engineers Transactions on Geoscience and Remote Sensing.* 51(6):3558-3566.

Wang, L., W.P. Sousa and P. Gong. 2004. Integration of object-based and pixel-based classification for mapping mangroves with IKONOS imagery. *International Journal of Remote Sensing.* 25(24):5655-5668.

Wang, P., E.S Boss and C. Roesler. 2005. Uncertainties of inherent optical properties obtained from semi-analytical inversions of ocean color. *Applied Optics.* 44(19):4074-4085.

Wang, Q., J. Tenhunen, N.Q. Dinh, M. Reichstein, T. Vesala and P. Keronen. 2004. Similarities in ground- and satellite-based NDVI time series and their relationship to physiological activity of a Scots pine forest in Finland. *Remote Sensing of Environment.* 93(1-2):225-237.

Wang, X., X. Cheng, P. Gong, C.K. Shum, D. M. Holland and X. Li. 2014. Freeboard and mass extraction of the disintegrated Mertz Ice Tongue with remote sensing and altimetry data. *Remote Sensing of Environment.* 144:1-10.

Wang, Y., A.I. Lyapustin, J.L. Privette, J.T. Morisette and B. Holben. 2009. Atmospheric correction at AERONET locations: A new science and validation data set. *Institute of Electrical and Electronics Engineers Transactions on Geoscience and Remote Sensing.* 47(8):2450-2466.

Wang, Z., D. Ziou, C. Armenakis, D. Li. and Q. Li. 2005. A comparative analysis of image fusion methods. *Institute of Electrical and Electronics Engineers Transactions on Geoscience and Remote Sensing.* 43(6):1391-1402.

Warrick, J.A., L.A.K. Mertes, D.A. Siegel and C. Mackenzie. 2004. Estimating suspended sediment concentrations in turbid coastal waters of the Santa Barbara Channel with SeaWiFS. *International Journal of Remote Sensing.* 25(10):1995-2002.

Watanachaturaporn, P., M.K. Arora and P.K. Varshney. 2008. Multisource classification using support vector machines: An empirical comparison with decision tree and neural network classifiers. *Photogrammetric Engineering & Remote Sensing.* 74(2):239-246.

Weng, Q. and D. Lu. 2008. A sub-pixel analysis of urbanization effect on land surface temperature and its interplay with impervious surface and vegetation coverage in Indianapolis, United States. *International Journal of Applied Earth Observation and Geoinformation.* 10(1):68-83.

Westoby, M.J., J. Brasington, N.F. Glasser, M.J. Hambrey and J.M. Reynolds. 2012. Structure-from-Motion. Photogrammetry: A low-cost, effective tool for geoscience applications. *Geomorphology.* 179:300-314.

White, M.A., F. Hoffman, W.W. Hargrove and R.R. Nemani. 2005. A global framework for monitoring phenological responses to climate change. *Geophysical Research Letters*, 32(4).

White, M.A., K.M. de Beurs, K. Didan, D.W. Inouye, A.D. Richardson, O.P. Jensen, J. O'Keefe, G. Zhang, R.R. Nemani, W.J.D. van Leeuwen, J.F. Brown, A. de Wit, M. Schaepman, X.M. Lin, M. Dettinger, A.S. Bailey, J. Kimball, M.D. Schwartz, D.D. Baldocchi, J.T. Lee and W.K. Lauenroth. 2009. Intercomparison, interpretation, and assessment of spring phenology in North America estimated from remote sensing for 1982-2006. *Global Change Biology.* 15:2335-2359.

White, M.A., R.R. Nemani, P.E. Thornton and S.W. Running. 2002. Satellite evidence of phenological differences between urbanized and rural areas of the eastern United States deciduous broadleaf forest. *Ecosystems.* 5:260-273.

Wilfong, B.N., D.L. Gorchov and M.C. Henry. 2009. Detecting an invasive shrub in deciduous forest understories using remote sensing. *Weed Science.* 57(5):512-520.

Willis, K.S. 2015. Remote sensing change detection for ecological monitoring in United States protected areas. *Biological Conservation.* 182:233-242.

Wilson, T.B. and T.P. Meyers. 2007. Determining vegetation indices from solar and photosynthetically active radiation fluxes. *Agricultural and Forest Meteorology.* 144(3-4):160-179.

Winter, M.E. 1999. N-FINDR: An algorithm for fast autonomous spectral end-member determination in hyperspectral data. *Proceedings SPIE Conference on Imaging Spectrometry V*, Denver, Colorado. pp. 266-275.

Witharana, C. and H.J. Lynch. 2016. An object-based image analysis approach for detecting penguin guano in very high spatial resolution satellite images. *Remote Sensing*. 8(5):375-403.

Wolfe, R.E., M. Nishihama, A.J. Fleig, J.A. Kuyper, D.P. Roy, J.C. Storey and F.S. Patt. 2002. Achieving sub-pixel geolocation accuracy in support of MODIS land science. *Remote Sensing of Environment.* 83(1-2):31-49.

Wu, C. 2004. Normalized spectral mixture analysis for monitoring urban composition using ETM+ imagery. *Remote Sensing of Environment.* 93:480-492.

Wu, C. and A.T. Murray. 2003. Estimating impervious surface distribution by spectral mixture analysis. *Remote sensing of Environment.* 84(4):493-505.

Wu, X., J.T. Sullivan and A.K. Heidinger. 2010. Operational calibration of the Advanced Very High Resolution Radiometer (AVHRR) visible and near-infrared channels. *Canadian Journal of Remote Sensing.* 36(5):602-616.

Wu, Z.H. and N.E. Huang. 2009. Ensemble empirical mode decomposition: a noise-assisted data analysis method. *Advances in Adaptive Data Analysis, Theory and Applications.* 1(1):1-41.

Xiao, X., B. Braswell, Q. Zhang, S. Boles, S. Frolking and B. Moore. 2003. Sensitivity of vegetation indices to atmospheric aerosols: continental-scale observations in Northern Asia. *Remote Sensing of Environment.* 84:385-392.

Xiao, X., Q. Zhang, B. Braswell, S. Urbanski, S. Boles, S. Wofsy, B. Moore and D. Ojima. 2004. Modeling gross primary production of temperate deciduous broadleaf forest using satellite images and climate data. *Remote Sensing of Environment.* 91(2):256-270.

Xiao, X., Q. Zhang, S. Saleska, L. Hutyra, C. De, Plinio, S. Wofsy, S. Frolking, S. Boles, M. Keller and B. Moore. 2005. Satellite-based modeling of gross primary production in a seasonally moist tropical evergreen forest. *Remote Sensing of Environment.* 94(1):105-122.

Xie, X., H. Wang and W. Zhang. 2015. Statistic estimation and validation of in-orbit modulation transfer function based on fractal characteristics of remote sensing images. *Optics Communications.* 354:202-208.

Xiong, W., C.I. Chang, C.C. Wu, K. Kalpakis and H.M. Chen. 2011. Fast algorithms to implement N-FINDR for hyperspectral endmember extraction. *Institute of Electrical and Electronics Engineers Transactions on Geoscience and Remote Sensing. Journal of Selected Topics in Applied Earth Observations and Remote Sensing.* 4(3):545-564.

Xu, Y., B. Liu, J. Liu and S. Riemenschneider. 2006. Two-dimensional empirical mode decomposition by finite elements. *Proceedings of the Royal Society of London A: Mathematical, Physical and Engineering Sciences.* 462(2074):3081-3096.

Yamamoto, H., T. Hashimoto, M. Seki, N. Yuda, Y. Mitomi, H. Yoshioka, Y. Honda and T. Igarashi. 2005. Evaluation of GLI reflectance and vegetation indices with MODIS products. *Proceedings of 2005 Institute of Electrical and Electronics Engineers Transactions on Geoscience and Remote Sensing. International Geoscience and Remote Sensing Symposium.* Seoul, South Korea. 25-29 July. pp. 5584-5587.

Yang, X. 1997. *Georeferencing CAMS data: Polynomial rectification and beyond.* Ph.D.dissertation. University of South Carolina, Columbia, SC. 161 p.

Yang, X. 2000. Accuracy of rational function approximation in photogrammetry. *Proceedings of ASPRS Annual Convention.* 22-26 May. Washington D.C. CD-ROM.

Yilmaz, A., O.T. Ozerbil, O. Eker, M. Erdogan, E.E. Marasb, H.G. Komutanligi, F. Dairesi and D. Ankara. 2004. Investigation of 3D Geopositioning and DEM Accuracy of Cartosat-1 Stereo Imagery. *International Archives of Photogrammetry and Remote Sensing.* 12-23 July Istanbul. Vol. XX: 799-804.

Yoshioka, H., A.R. Huete and T. Miura. 2000a. Derivation of vegetation isoline equations in red-NIR reflectance space. *Institute of Electrical and Electronics Engineers Transactions on Geoscience and Remote Sensing.* 38(2):838-848.

Yoshioka, H., T. Miura, A.R. Huete and B.D. Ganapol. 2000b. Analysis of vegetation isolines in red-NIR reflectance space. *Remote Sensing of Environment.* 74(2):313-326.

Yoshioka, H., T. Miura and K. Obata. 2012. Derivation of relationships between spectral vegetation indices from multiple sensors based on vegetation isolines. *Remote Sensing.* 4(3):583-597.

Youngentob, K.N., D.A. Roberts, A.A. Held, P.E. Dennison, X. Jia and D.B. Lindenmayer. 2011. Mapping two Eucalyptus subgenera using multiple endmember spectral mixture analysis and continuum-removed imaging spectrometry data. *Remote Sensing of Environment.* 115(5):1115-1128.

Yu, Q., P. Gong, N. Clinton, G. Biging, M. Kelly and D. Schirokauer. 2006. Object-based detailed vegetation classification with airborne high spatial resolution remote sensing imagery. *Photogrammetric Engineering & Remote Sensing.* 72(7):799-811.

Yuan, F. and M.E. Bauer. 2007. Comparison of impervious surface area and normalized difference vegetation index as indicators of surface urban heat island effects in Landsat imagery. *Remote Sensing of Environment.* 106(3):375-386.

Zakharov, I. and T. Toutin. 2012. Subpixel image matching based on Fourier phase correlation for Radarsat-2 stereo-radargrammetry. *Canadian Journal of Remote Sensing* 38:487-495.

Zambon, M., R.L. Lawrence, A. Bunn and S. Powell. 2006. Effect of alternative splitting rules on image processing using classification tree analysis. *Photogrammetic Engineering & Remote Sensing* 72:25-30.

Zare, A. and K.C. Ho. 2014. Endmember variability in hyperspectral analysis: Addressing spectral variability during spectral unmixing. *Institute of Electrical and Electronics Engineers Transactions on Geoscience and Remote Sensing. Signal Processing Magazine.* 31(1):95-104.

Zare, A. and P. Gader. 2010. PCE: Piecewise convex endmember detection. *Institute of Electrical and Electronics Engineers Transactions on Geoscience and Remote Sensing.* 48(6):2620-2632.

Zare, A., P. Gader, O. Bchir and H. Frigui. 2013. Piecewise convex multiple-model endmember detection and spectral unmixing. *Institute of Electrical and Electronics Engineers Transactions on Geoscience and Remote Sensing.* 51(5):2853-2862.

Zhang, D.Q. and S.C. Chen. 2003. Kernel-based fuzzy and possibilistic c-means clustering. *Proceedings of the International Conference Artificial Neural Network.* pp. 122-125.

Zhang, G., H. Xie, T. Yao and S. Kang. 2013. Water balance estimates of ten greatest lakes in China using ICESat and Landsat data. *Chinese Science Bulletin.* 58(31):3815-3829.

Zhang, J. 2010. Multi-source remote sensing data fusion: status and trends. *International Journal of Image and Data Fusion.* 1(1):5-24.

Zhang, J. and G.M. Foody. 1998. A fuzzy classification of suburban land cover from remotely sensed imagery. *International Journal of Remote Sensing.* 19(14):2721-2738.

Zhang, J. and G.M. Foody. 2001. Fully-fuzzy supervised classification of sub-urban land cover from remotely sensed imagery: Statistical and artificial neural network approaches. *International Journal of Remote Sensing.* 22(4):615-628.

Zhang, L. and Q. Weng. 2016a. Annual dynamics of impervious surface in the Pearl River Delta, China, from 1988 to 2013 using time series Landsat data. *ISPRS Journal of Photogrammetry and Remote Sensing.* 113(3):86-96.

Zhang, L. and Q. Weng, 2016b. Assessment of urban growth in the Pearl River Delta, China using time series Landsat imagery. *Remote Sensing for Sustainability.* (Q. Weng, editor). CRC Press, Taylor & Francis Group. Boca Raton, Florida, U.S.A.

Zhang, Q., B. Li, D. Thau and R. Moore. 2015. Building a better urban picture: Combining day and night remote sensing imagery. *Remote Sensing.* 7(9):11887-11913.

Zhang, Q., E.M. Middleton, B.-C. Gao and Y.-B. Cheng. 2012. Using EO-1 Hyperion to simulate HyspIRI products for a coniferous forest: the fraction of PAR absorbed by chlorophyll (fAPARchl) and leaf water content (LWC). *Institute of Electrical and Electronics Engineers Transactions on Geoscience and Remote Sensing.* 50:1844-1852.

Zhang, Q., E.M. Middleton, H.A. Margolis, G.G. Drolet, A.A. Barr and T.A. Black. 2009. Can a MODIS-derived estimate of the fraction of PAR absorbed by chlorophyll (FAPARchl) improve predictions of light-use efficiency and ecosystem photosynthesis for a boreal aspen forest? *Remote Sensing of Environment.* 113:880-888.

Zhang, Q., E.M. Middleton, Y.-B. Cheng and D.R. Landis. 2013. Variations of foliage chlorophyll fAPAR and foliage non-chlorophyll fAPAR (fAPARchl, fAPARnon-chl) at the Harvard Forest. *Institute of Electrical and Electronics Engineers Transactions on Geoscience and Remote Sensing. Journal of Selected Topics in Applied Earth Observations and Remote Sensing.* 6:2254-2264.

Zhang, Q., X. Xiao, B. Braswell, E. Linder, S. Ollinger, M.L. Smith, J.P. Jenkins, F. Baret, A.D. Richardson, B. Moore and R. Minocha. 2006. Characterization of seasonal variation of forest canopy in a temperate deciduous broadleaf forest using daily MODIS data. *Remote Sensing of Environment.* 105:189-203.

Zhang, Q., X.M. Xiao, B. Braswell, E. Linder, F. Baret and B. Moore. 2005. Estimating light absorption by chlorophyll leaf and canopy in a deciduous broadleaf forest using MODIS data and a radiative transfer model. *Remote Sensing of Environment.* 99:357-371.

Zhang, Q., Y.-B. Cheng, A. Lyapustin, Y. Wang, X. Zhang, A. Suyker, S. Verma, Y. Shuai and E.M. Middleton. 2015. Estimation of crop gross primary production (GPP): II. Do the scaled vegetation indices improve performance? *Agricultural and Forest Meteorology.* 200:1-8.

Zhang, Q., Y.-B. Cheng, A.I. Lyapustin, Y. Wang, F. Gao, A. Suyker, S. Verma and E. Middleton. 2014. Estimation of crop gross primary production (GPP): fAPARchl versus MOD15A2 FPAR. *Remote Sensing of Environment.* 153:1-6.

Zhang, X. 2015. Reconstruction of a complete global time series of daily vegetation index trajectory from long-term AVHRR data. *Remote Sensing of Environment.* 156(0):457-472.

Zhang, X., B. Tan and Y. Yu. 2014. Interannual variations and trends in global land surface phenology derived from enhanced vegetation index during 1982-2010. *International Journal of Biometeorology*. 58(4):547-564.

Zhang, X., M.A. Friedl, C.B. Schaaf, A.H. Strahler, J.C.F. Hodges and F. Gao. 2003. Monitoring vegetation phenology using MODIS. *Remote Sensing of Environment.* 84:471-475.

Zhang, X., M.A. Friedl and C.B. Schaaf. 2006. Global vegetation phenology from Moderate Resolution Imaging Spectroradiometer (MODIS): Evaluation of global patterns and comparison with *in situ* measurements. *Journal of Geophysical Research.* 111(G4):G04017.

Zheng, G., D. Stramski and R.A. Reynolds. 2014. Evaluation of the quasi-analytical algorithm for estimating the inherent optical properties of seawater from ocean color: Comparison of Arctic and lower-latitude waters. *Remote Sensing of Environment.*155:194-209.

Zhou, G. and N.S.-N. Lam. 2005. A comparison of fractal dimension estimators based on multiple surface generation algorithms, *Computers & Geosciences*, 31:1260-1269.

Zhou, J., L. Jia, M. Menenti, and B. Gorte. 2016. On the performance of remote sensing time series reconstruction methods - A spatial comparison. *Remote Sensing of Environment*, 187:367-384.

Zhu, G. and D.G. Blumberg. 2002. Classification using ASTER data and SVM algorithms: The case study of Beer Sheva, Israel. *Remote Sensing of Environment.* 80(2):233-240.

Zhu, Z. and C.E. Woodcock. 2014. Continuous change detection and classification of land cover using all available Landsat data. *Remote sensing of Environment.* 144(25):152-171.

Zimmermann, N.E., T.C. Edwards, G.G. Moisen, T.S. Frescino and J.A. Blackard. 2007. Remote sensing-based predictors improve distribution models of rare, early successional and broadleaf tree species in Utah. *Journal of Applied Ecology.* 44(5):1057-1067.

Zimmermann, T., J. Rietdorf and R. Pepperkok. 2003. Spectral imaging and its applications in live cell microscopy. *Federation of European Biochemical Societies Letters.* 546(1):87-92.